PACIFIC EARTHQUAKE ENGINEERING RESEARCH CENTER

The Fourth U.S.-Japan Workshop on Performance-Based Earthquake Engineering Methodology for Reinforced Concrete Building Structures

22–24 October 2002
Toba, Japan

Sponsors:

Japan Ministry of Education, Science, Sports and Culture
Pacific Earthquake Engineering Research Center
U.S. National Science Foundation

PEER 2002/21
DEC. 2002

The Fourth U.S.-Japan Workshop on Performance-Based Earthquake Engineering Methodology for Reinforced Concrete Building Structures

22–24 October 2002
Toba, Senpokaku, Japan

Organizers

Toshimi Kabeyasawa
Earthquake Research Institute
University of Tokyo

Jack P. Moehle
Pacific Earthquake Engineering Research Center
University of California, Berkeley

Sponsors

Japan Ministry of Education, Science, Sports and Culture
Pacific Earthquake Engineering Research Center
U.S. National Science Foundation

Research Report

PEER Report 2002/21
Pacific Earthquake Engineering Research Center
College of Engineering
University of California, Berkeley

December 2002

PREFACE

Considerable research is under way throughout the world to establish performance-based assessment and design methodology for buildings. Japan and the United States are at the forefront of this research effort, as well as efforts to implement the research results. The U.S.-Japan Cooperative Research in Urban Earthquake Disaster Mitigation, sponsored in Japan by the Ministry of Education, Science, Sports and Culture, and in the U.S. by the National Science Foundation, is funding collaborative research in Japan and the U.S. The Pacific Earthquake Engineering Research Center in the U.S. has established the development of performance-based earthquake engineering methodology as its primary mission. Because of the importance of this topic, it is timely for researchers and practitioners from the U.S. and Japan to meet to exchange technical data and ideas as well as to identify issues of mutual concern and opportunities for cooperative study.

The Fourth Workshop on Performance-Based Earthquake Engineering Methodology for Reinforced Concrete Building Structures was organized to meet the needs and opportunities for research and practice in performance-based engineering. The objectives of the workshop were threefold: (1) to discuss different perspectives on performance-based engineering as it is applied to new and existing concrete buildings in Japan and the U.S., (2) to exchange the latest findings related to the same subject, and (3) to enhance communication and promote opportunities for new and continuing collaboration.

The Fourth Workshop was held 22–24 October 2002 in Toba, Senpokaku, Japan. It was attended by 14 Japanese and 10 U.S. participants. The participants are identified on the following page.

JAPAN SIDE	U.S. SIDE
Toshimi Kabeyasawa, ERI, U Tokyo Toshikatsu Ichinose, Nagoya IT Daisuke Kato, Niigata U Kazuhiro Kitayama, Tokyo Metro U Hiroshi Kuramoto, BRI Koichi Kusunoki, IIS, U Tokyo Masaki Maeda, Tohoku U Minehiro Nishiyama, Kyoto U Shunsuke Otani, U Tokyo Hitoshi Shiohara, U Tokyo Masaomi Teshigawara, BRI Hitoshi (Jin) Tanaka, DPRI, Kyoto U Akira Tasai, Yokohama U Manabu Yoshimura, Tokyo Metro U	Jack Moehle, UC Berkeley Craig Comartin, Comartin Reis Allin Cornell, Stanford U Sashi Kunnath, U Central Florida Laura Lowes, U Washington Eduardo Miranda, Stanford U Santiago Pujol, Purdue U Mark Sinclair, Degenkolb Engineers John Wallace, UCLA Yan Xiao, USC

Front row: Yan Xiao, Craig Comartin, Santiago Pujol, Jack Moehle, Toshimi Kabeyasawa, Shunsuke Otani, Eduardo Miranda, Hiroshi Kuramoto

Middle row: Hitoshi Shiohara, Laura Lowes, Koichi Kusunoki, Masaomi Teshigawara, Sashi Kunnath, Kazuhiro Kitayama, John Wallace, Akira Tasai, Allin Cornell

Back row: Masaki Maeda, Mark Sinclair , Hitoshi (Jin) Tanaka, Manabu Yoshimura, Daisuke Kato, Toshikatsu Ichinose, Minehiro Nishiyama

HOST ORGANIZATIONS AND SPONSORS

The workshop was organized under the auspices of the U.S.-Japan Cooperative Research in Earthquake Disaster Mitigation, with funding in Japan by the Ministry of Education, Science, Sports and Culture, and in the U.S. by the National Science Foundation, the Pacific Earthquake Engineering Research Center, and the State of California.

The technical program was developed by Professor Toshimi Kabeyasawa, Division of Disaster Mitigation Science, Earthquake Research Institute, University of Tokyo, and Professor Jack P. Moehle, Director of the Pacific Earthquake Engineering Research Center, University of California, Berkeley.

ACKNOWLEDGMENTS

This work was supported in part by the Pacific Earthquake Engineering Research Center through the Earthquake Engineering Research Centers Program of the National Science Foundation under Award number EEC-9701568.

On the Japan side, this work was supported as part of the Development of Performance-Based Design Methodologies, subtheme (2-1) of the U.S.-Japan Cooperative Research in Earthquake Disaster Mitigation program under grant number 11209203, a grant-in-aid for Scientific Research on Priority Area, Category B, by the Ministry of Education, Science, Sports and Culture.

CONTENTS

SESSION B-3: BEAM-COLUMN JOINTS ♦ Chaired by Hitoshi Tanaka and Yan Xiao

SESSION B-4: BEAM-COLUMN JOINTS ♦ Chaired by Masaki Maeda and Santiago Pujol

PLENARY SESSION II: RESOLUTIONS AND CLOSING ♦ Chaired by Jack Moehle and Toshimi Kabeyasawa

PLENARY SESSION I: STATE OF THE ART OF SEISMIC DESIGN IN THE U.S. AND JAPAN

Chaired by

♦ Jack Moehle and Toshimi Kabeyasawa ♦

AN OUTLINE OF AIJ GUIDELINES FOR SEISMIC PERFORMANCE EVALUATION OF REINFORCED CONCRETE BUILDINGS

Toshimi KABEYASAWA, Toshikatsu ICHINOSE, Daisuke KATO, Hitoshi TANAKA, Yuuki SAKAI, Hiroshi KURAMOTO, Hideyuki KINUGASA, Taizo MATSUMORI, Nobuyuki IZUMI, Kazuhiro KITAYAMA, Masaki MAEDA, Kazuaki TSUDA, Masaru TERAOKA, Hajime OKANO

ABSTRACT

This paper outlines the draft of AIJ guidelines on seismic performance evaluation which was proposed by a subcommittee of reinforced concrete committee of Architectural Institute of Japan(AIJ) and is to be published in the near future. The guidelines is to evaluate actual seismic performance level of a reinforced concrete building, which has been designed based on an appropriate design guidelines. The performance level is expressed with the basic seismic capacity index by a deterministic procedure. The basic seismic capacity index is defined as the amplitude ratio of the limit earthquake intensity to the standard earthquake intensity for each limit state, when the estimated response of the structure attained to the limit state. The limit states of the structures are selected on the inelastic load-deformation curve based on the residual damage levels of members as four levels: (1) serviceability, (2) minor repair, (3) major repair, and (4) safety. Probabilistic evaluation of the seismic performance is also presented as an additional procedure. Performance levels are expressed as the excessive probability of the response over the limit state within the design service life of the building considering deviations of earthquake intensity, response estimation, and limit state evaluation.

1. INTRODUCTION

The Building Standard Law of Japan was revised in 2001, where design earthquake response spectrum was explicitly specified at the bedrock and the comparison of the inelastic response with the limit states was introduced as the design criteria, although the verification is to be made through comparison of demand and capacity of lateral strength. The basic concepts for defining the limit states were specified. However, the detailed and general calculation methods for evaluating the limit states were not presented with sufficient verification data. A Subcommittee on Performance-Based Design* in the Reinforced Concrete Committee, the Architectural Institute of Japan, has investigated on a new seismic design guidelines, which is

*Members of the committee in addtion to above authors:
Hitoshi SHIOHARA, Matsutaro SEKI, Kazuo TAMURA, Masaomi TESHIGAWARA, Yoshiaki NAKANO, Shigeru FJII, Taiki SAITO, Satoru NAGAI, Eiji FUKUZAWA, Motomi TAKAHASHI

to evaluate actual seismic performance level of a reinforced concrete building. The guidelines includes the similar concepts on the performance objectives with the BSL and the detailed evaluation methods have been verified through test data. This paper outlines the draft of AIJ guidelines on seismic performance evaluation of reinforced concrete buildings, which was proposed by the subcommittee and is to be published in the near future.

2. REVIEW OF AIJ GUIDELINES FOR SEISMIC DESIGN OF REINFORCED CONCRETE BUILDINGS

Architectural Institute of Japan has proposed seismic design guidelines for reinforced concrete buildings[1][2], where calculation methods and detailing of reinforced concrete members are presented to assure ductile beam-yielding mechanism of the building structures. The method has been used in practical design, especially for shear design and ductility design of members. The method has also promoted research on design and perfomance as a standard model code.

AIJ design guidelines(1988draft, 1990) [1] has specified an method for ensuring the overall beam-yielding collapse mechanism based on capacity design philosophy. The hinge region and the non-hinge region are clearly selected and the design actions for non-hinge regions are amplified considering variations in calculation. Also the guidelines presents the new methods of (1) shear design to ensure target ductility, (2) bond design in conjunction with shear design, (3) design method for beam-column joints, (4) detailing against high axial load, (5) design of non-structural components.

The revision of above guidelines started from around 1994 to make the scope wider or to make the specifications in a practical form, or to reflect new research. . However, 1995 Hyogoken-Nambu earthquake occurred during the revision, and the target of the revision was modified. It was drawn as the lessons from the earthquake that (1) characteristics of near source motion, (2) ultimate earthquake level for safety, (3) performance objectives such as functional use or restorability, (4) expression of performance to owner, and (5) performance level higher than minimum requirement, should be considered in design. On the other hand, the performance-based design including reliability concept became a new worldwide trend. As a result, the revision was made widely towards performance-based design guidelines and as a trial base. Therefore, AIJ design guidelines (1997 draft, 1999) [2] was published as a new design guidelines based on inelastic displacement concept, although it was originally proposed as the revision of 1990 edition.

The AIJ design guidelines 1999[2] has introduced or presented (1) design criteria or limit states clearly defined using inelastic deformations, (2) performance verification format, (3) use of various analytical tools, (4) design against bi-directional motions, (5) potential hinge region in addition to hinge and non-hinge regions, (6) new design equation for shear and bond reflecting recent research, (7) explicit formula for deformability, (8) quantitative design for confinement details, and (9) practical verification procedure with a design example. The method for design or verification is based on deterministic and equivalent static procedure, although the required deformability or displacement criteria were related to the responses, which were also interpreted with exceed probability estimated from historical earthquake data and an attenuation model. Also the scope of the guidelines is limited to regular shaped building structures.

On the other hand, the Building Standard of Japan was revised in 2001, where the design earthquake spectrum was specified at the engineering bedrock and also the calculation methods for the soil amplification factors and the inelastic displacement responses of the buildings were presented.

The followings were introduced into the new draft of the AIJ guidelines for seismic performance evaluation, although some of them should be examined and refined futher:

(1) definition of performance index expressing seismic performance level, both in deterministic and probabilistic ways,
(2) specification of standard earthquake and site earthquake for performance evaluation
(3) simple and practical formula for estimating soil amplification
(4) equivalent linearization as well as time-history analysis for estimating inelastic response of the building,
(5) limit states defined with deformation based on member damage levels,
(6) performance evaluation considering the structural collapse mechanisms,
(7) a method of performance evaluation by exceed probability of limit state.

3. CONTENTS AND ABRIDGED TRANSLATION OF THE DRAFT

The followings are the table of contents with abridged translation of the draft of "AIJ guidelines for seismic performance evaluation of reinforced concrete building structures (in Japanese)," which is to be published in 2003.

---

1 General

1.1 Scope

This guidelines specifies an method for the verification or evaluation of seismic performance level of reinforced concrete buildings, the detailed design of which has been determined by an appropriate design code. The guidelines may be applied to buildings under design procedure for new construction, using materials in Chapter 4, and less than 60m height.

1.2 Definitions

1.3 Unit

2 Principles for performance evaluation

(1) Seismic performance of a building shall be evaluated for serviceability, reparability, and safety.

(2) Seismic performance of a building shall be expressed in principle using the deterministic seismic capacity indices defined in Chapter 7.

(3) Seismic performance of a building may be expressed additionally using the excess probabilities of limit states during service life defined in Chapter 8.

3 Performance objectives

Seismic performance of a building shall be evaluated for the following performance objectives as the deterministic capacity index by the limit earthquake levels by which the responses attain the corresponding limit states, or in addition by the excess probability of the limit states during the service life:

(1) Serviceability - Serviceability limit state

(2) Reparability - Reparable limit state I(minor) or II(major)

(3) Safety - Safety limit state

4 Materials

4.1 Properties of reinforcing steel

Performance evaluation may be applied to the building if the mechanical, durable and fireproof properties of the reinforcing steel are specified, assured, and if the structural performance of members with the steel can be evaluated. Characteristic values and appropriate models for stress-strain relations shall be used in design and analysis.

4.2 Properties of concrete

Performance evaluation may be applied to the building if the mechanical, durable and fireproof properties of the concrete are specified, assured, and if the structural performance of members with the concrete can be evaluated. Characteristic values and appropriate models for stress-strain relations shall be used in design and analysis.

4.3 Models for confined concrete

Stress-strain relations for confined concrete shall be modified considering the effect of confinement by transverse reinforcement, confining steel plate or fiber sheet.

4.4 Models for joint surface

Effect of joint interface between concrete and steel or in the concrete shall be considered in analysis for performance evaluation, if necessary

4.5 Other materials (omitted)

5 Earthquake Loading

5.1 Standard earthquake

5.1.1 Standard earthquake

Standard earthquake is defined at the engineering bedrock by the response spectrum or the time-history waveforms, which shall be used for the evaluation of the seismic capacity index.

5.1.2 Response spectrum

The response spectrum of the standard earthquake at the base of the building shall be computed from the following standard acceleration spectrum Sa (m/sec/sec) with 5 percent of critical damping (h=0.05) defined at the outcrop bedrock considering the soil amplification.

$Sa(T, h=0.05)=3.2+30T$ if $T \leqq 0.16$

$Sa(T, h=0.05)=8$ if $0.16 \leqq 0.T<0.64$

$Sa(T, h=0.05)=5.12/T$ if $0.64 \leqq 0.T<5.0$

where, T: fundamental period and damping coefficient of the system.

5.1.3 Time-history

The time-history waveforms of the standard earthquake shall be generated from the sine wave components of appropriate phases and duration so that the response spectrum fits to the formula in 5.1.2. More than three waves of different phase characteristics should be used for performance evaluation.

5.1.4 Soil-structure interaction

Soil-structure interaction should be introduced into the modeling of the soil-structure system or the flexibility at the base boundary.

5.2 Site earthquake

5.2.1 Site earthquake

Site earthquake shall be defined at the construction site considering recurrence probability, which shall be used for the evaluation of the excess probability of limit states during the service life.

5.2.2 Evaluation of site earthquake

Site earthquake shall be evaluated considering seismicity at the site, source characteristics, seismic wave propagation property, detailed properties or irregularities of soil structures and soil-structure interactions.

5.3 Amplification through surface soil

The amplification of earthquake motions through surface soil on the bedrock shall be evaluated based on the nonlinear properties of soil.

5.4 Dead loads and live loads

The dead load and live load for performance evaluation shall be calculated based on the actual state.

6 Analysis

6.1 Principles for structural analysis

Structural analysis shall be used for performance evaluation, by which maximum inelastic responses of members under the design motion can be calculated with sufficient accuracy. Inaccuracy, errors and variations which are neglected in the analytical model may be considered by simple estimation methods.

6.2 Nonlinear pushover analysis

Nonlinear pushover analysis of the structure shall be carried out using member models and hysteresis models which satisfies:

(1) Three-dimensional equilibrium and compatibility

(2) Nonlinear properties of materials

(3) Two-dimensional or three-dimensional constitutive law of materials or member models

6.3 Estimation of response from equivalent SDF system

Dynamic responses of members in the building may be derived by a static pushover analysis and an equivalent single-degree-of-freedom (SDF) system in the following or another procedure, the accuracy of which is verified.

(1) Static load-deformation relations are derived by static pushover analysis under assumed lateral load distribution,

(2) The relations are reduced into the equivalent load - equivalent displacement relations of SDF system with the modes of the lateral forces and calculated deformations,

(3) The maximum displacement response of the equivalent displacement is estimated from equivalent linear system with substitute damping coefficient,

(4) The maximum responses of member forces and deformations are derived as the corresponding actions in the static pushover analysis,

(5) The member forces and deformations are amplified with appropriate factors considering the inaccuracy in the above estimation, such as effect of higher mode, upper bound strength of inelastic members.

6.4 Calculation of response from MDF system

Dynamic responses of members in the building may be derived by a static pushover analysis and an equivalent multi-degrees-of-freedom (MDF) system in the following or another procedure, the accuracy of which is verified.

(1) Static load-deformation relations are derived by static pushover analysis under assumed lateral load distribution,

(2) The relations are reduced into the equivalent load - equivalent drift relations of MDF system by idealizing the relations of calculated inter-story shear forces and drifts into simple hysteresis rules,

(3) The maximum inter-story displacement responses are calculated from the MDF system by time-history analysis,

(4) The maximum responses of member forces and deformations are derived as the corresponding actions in the static pushover analysis,

(5) The member forces and deformations are amplified with appropriate factors considering the inaccuracy in the above estimation, such as effect of upper bound strength of inelastic members.

6.5 Calculation of response from frame model

Dynamic responses of members in the building may be calculated by a time-history response analysis with a member-based frame model, which includes:

(1) member models in 6.2

(2) appropriate hysteresis models under cyclic load reversals

(3) appropriate viscous damping

6.6 Calculation of response from soil-structure system (omitted)

7 Evaluation of seismic capacity

7.1 Seismic capacity index for buildings

7.1.1 Definition of seismic capacity index

The seismic capacity indices of the structure are defined for the serviceability, reparable and safety limit states as the ratios of the intensity of the limit earthquake to that of the standard earthquake.

7.1.2 Limit earthquake levels

The intensity of the limit earthquake is defined as amplification factor of the standard earthquake, which induces each limit deformation of the structure.

7.2 Limit deformations

7.2.1 Structural limit deformations

The structural limit deformation is defined for each limit state in each horizontal direction as the corresponding equivalent SDF lateral deformation, when any of the inter-story deformations attained its story limit deformation.

7.2.2 Story limit deformations

The story limit deformations shall be evaluated based on the maximum damage level of the column, wall, beam or beam-column joint.

7.2.3 Damage level of members

The damage level of members shall be estimated by the methods in 7.3 considering the residual responses, variations in load and materials and inaccuracy, which shall be classified into the following four levels with the corresponding limit states:

(1) Level I: serviceability limit and the members are functional on use without repair

(2) Level II: reparability limit and the members are restorable with minor repair

(3) Level III: reparability limit and the members are restorable with major repair

(4) Level IV: safety limit and the members are stable without strength decay but beyond reparable state

7.3 Performance evaluation of members

7.3.1 Performance evaluation of beams

The hysteresis relations of the beam member shall be evaluated by a reliable method with the following corresponding limit states in the relations.

(1) Serviceability limit state: the residual crack width shall be less than 0.2mm and the reinforcing bar shall remain elastic.

(2) Reparability limit state(I): the residual crack width shall be less than 1.0mm and the reinforcing bar shall remain within small inelastic strain. Slight damage to concrete may occur.

(3) Reparability limit state(II): the residual crack width shall be less than 2.0mm and the reinforcing bar may be with large inelastic strain but without buckling. Falling-off of cover concrete may occur but no damage to core concrete.

(4) Safety limit state: deformability limit without significant decay of seismic resistance (not less than 80% of maximum strength), which may be caused by crushing of concrete, buckling or rupture of reinforcing bars, shear failure or bond failure.

7.3.2 Performance evaluation of columns

The hysteresis relations of the column member shall be evaluated by a reliable method with the following corresponding limit states in the relations.

(1) Serviceability limit state: the residual crack width shall be less than 0.2mm and the reinforcing bar shall remain elastic.

(2) Reparability limit state(I): the residual crack width shall be less than 1.0mm and the reinforcing bar shall remain small inelastic strain. Slight damage to concrete may occur.

(3) Reparability limit state(II): the residual crack width shall be less than 2.0mm and the reinforcing bar may be with large inelastic strain but without buckling. Falling-off of cover concrete may occur but no damage to core concrete.

(4) Safety limit state: deformability limit without significant decay of seismic resistance (not less than 80% of maximum strength), which may be caused by crushing of concrete, buckling or rupture of reinforcing bars, shear failure or bond failure.

7.3.3 Performance evaluation of walls

The hysteresis relations of the wall member shall be evaluated by a reliable method with the following corresponding limit states in the relations.

(1) Serviceability limit state: the residual crack width shall be less than 0.2mm and the reinforcing bar shall remain elastic.

(2) Reparability limit state(I): the residual flexural and shear crack widths shall be less than 1.0mm and 0.5mm, respectively. The reinforcing bar shall remain within small inelastic strain. Slight damage to concrete may occur.

(3) Reparability limit state(II): the residual flexural and shear crack widths shall be less than 2.0mm and 1.0mm, respectively. The reinforcing bar may be with large inelastic strain but without buckling. Falling-off of cover concrete may occur but no damage to concrete of column core and wall panel.

(4) Safety limit state: deformability limit without significant decay of seismic resistance (not less than 80% of maximum strength), which may be caused by crushing of concrete, buckling or rupture of reinforcing bars, or shear failure.

7.3.4 Performance evaluation of beam-column joints

The hysteresis relations of the beam-column joint shall be evaluated by a reliable method with the following corresponding limit states in the relations.

(1) Serviceability limit state: the residual crack width shall be less than 0.2mm and the reinforcing bar shall remain elastic.

(2) Reparability limit state(I): the residual crack width shall be less than 0.5mm and the reinforcing bar shall remain within small inelastic strain. Slight damage to concrete may occur.

(3) Reparability limit state(II): the residual crack width shall be less than 1.0mm and the reinforcing bar may be with large inelastic strain but without buckling. Falling-off of cover concrete may occur but no damage to core concrete.

(4) Safety limit state: deformability limit without significant decay of seismic resistance (not less than 80% of maximum strength), which may be caused by crushing of concrete, buckling or rupture of reinforcing bars, shear failure or anchorage failure.

7.3.5 Performance evaluation of non-structural components (omitted)

8 Evaluation of seismic performance risk

8.1 Seismic performance risk

Seismic performance of a building may be expressed using the excess probabilities of limit states during the service life, in addition to the seismic capacity indices, by estimating the site earthquake hazard and variations of structural capacities.

8.2 Evaluation of site earthquake hazard

The site earthquake hazard for the site shall be estimated considering the seismicity from historical earthquake data, seismic wave propagation property, soil-structure, and active faults.

8.3 Excess probability of limit states

The seismic performance risk shall be expressed as the excess probabilities of limit states during the service life, which shall be evaluated.

----

4. CONCLUSION

The draft of AIJ guidelines on seismic performance evaluation was outlined which was proposed by a subcommittee of reinforced concrete committee of Architectural Institute of Japan(AIJ) and is to be published in the near future.

REFERENCES

[1] Architectural Institute of Japan(1990). Design Guidelines for Earthquake-Resistant Reinforced Concrete Buildings Based on Ultimate Strength Concept 1988(draft), 1990(the first edition in Japanese), 1994(in English version), AIJ, Tokyo.

[2] Architectural Institute of Japan(1999). Design Guidelines for Earthquake-Resistant Reinforced Concrete Buildings Based on Inelastic Displacement Concept 1997(draft), 1999(the first edition in Japanese). AIJ, Tokyo.

KEYWORDS

Reinforced concrete structure; Performance-based design; Seismic performance; Limit state; Serviceability; Reparability; Safety; Seismic Risk

Japanese State of Practice in Design of Seismically Isolated Buildings

Shunsuke Otani[1] and Nagahide Kani[2]

ABSTRACT

Building Standard Law of Japan was revised in 1998 with objectives partly to introduce performance-based design regulations. Building Standard Law Enforcement Order was revised in 2000 to introduce additional technical requirements for the law revision. Ministry of Construction (presently reorganized to Ministry of Land, Infrastructure and Transport) issued Notification No. 2009 in October, 2000, to define the technical standard for structural specifications and structural calculation methods for the structural design of seismically isolated buildings. This paper briefly introduces new requirements and the state of practices in the design of seismically isolated buildings in Japan for gravity loads, snow loads, wind forces and earthquake forces.

1. INTRODUCTION

The idea of seismic isolation of a building to protect the super-structure was as old as the earthquake resistant design methods. Flexible rubber bearing isolators were first used in an elementary school building in Yugoslavia in 1969. William Clayton Building in New Zealand may be the first practical and engineered use of laminated rubber isolators with lead plug dampers in 1981. Several experimental applications of seismic isolators in buildings could be found in Japan in the 1970s. The use of seismic isolators in buildings was not popular before the 1995 Hyogo-ken Nambu (Kobe) earthquake. There were less than 90 buildings with base-isolator devices in 1995. People realized the danger of an earthquake through the 1995 Hanshin-Awaji earthquake disaster, and the number of base-isolated buildings reached 800 in five years.

This paper briefly introduces the current code requirements on the design of seismically isolated buildings in Japan.

2. BUILDING CODE SYSTEM IN JAPAN

2.1 Building Standard Law

The Building Standard Law of Japan, a national law, was proclaimed in May 1950 to "safeguard the life, health, and property of people by providing minimum standards concerning the site, structure, equipment, and use of buildings." The 1998 revision introduced of performance-based engineering. The law requires the structural performance in Article 20

---

1) Department of Architecture, Graduate School of Engineering, University of Tokyo
Email: otani@sake.t.u-tokyo.ac.jp
2) Managing Director, Japan Society of Seismic Isolation
Email: kani@jssi.or.jp

that “the building shall be constructed safe against dead and live loads, snow loads, wind forces, soil and water pressures, and earthquake and other vibration forces and impacts.” The article also requires that the construction and structural calculation shall conform to the technical standard outlined by a cabinet order, Building Standard Law Enforcement Order. The structural calculation is, however, exempted from “small-size buildings” such as (a) Buildings of total floor area not more than 100 m^2, (b) Timber construction not more than two stories or not more than 500 m^2 total floor area and not more than 13 m in height, and (c) Buildings, other than timber construction, of single-story or of total floor area not more than 200 m^2.

2.2 Building Standard Law Enforcement Order

Building Standard Law Enforcement Order was revised in 2000 to enforce the 1998 revision of the law. The construction and structural calculation requirements are specified in Chapter 3 “Structural Strength.” Specification requirements about construction are outlined in Sections 1 through 7, including specific requirements associated with durability (“durability related provisions”). Structural calculation methods are outlined in Section 8 for (a) Allowable Stress Calculation (old procedure) and (b) Ultimate Strength Calculation (new procedure). Three performance objectives were defined; i.e.,

(1) Maintenance of building serviceability under permanent loading conditions,

(2) Prevention of structural damage under frequent loading conditions (events corresponding to a return period of approximately 50 years), and

(3) Protection of occupants’ life under extraordinary loading conditions (events corresponding to a return period of approximately 500 years.

The Allowable Stress Calculation requires;

(1) Stresses in structural members under combined dead and live loads (and 70 percent of snow load in specified heavy snow areas) shall not exceed the allowable stresses of materials set forth for the long-term loading.

(2) Stresses in structural members (a) under combined dead, live and snow loads, (b) under combined dead and live loads and wind forces, and (c) under combined dead and live loads and earthquake forces, shall not exceed the allowable stresses of materials set forth for the short-term loading. Story drift under earthquake force shall be not more than 1/200.

(3) Story shears at the formation of collapse mechanisms under lateral loading shall be not less than values specified taking into account (a) expected deformation capacity of yielding members forming the collapse mechanism and (b) irregular stiffness and mass distribution in structural plan and along building height.

The Ultimate Strength Calculation (Ref. 1) requires

(1) Stresses in structural members developed by combined dead and live loads (and 70

percent of snow load in specified heavy snow areas) shall not exceed the allowable stresses of materials set forth for the long-term loading,

(2) Stresses in structural members developed by (a) combined dead, live and snow loads, and (b) combined dead and live loads and wind forces, shall not exceed the allowable stresses of materials set forth for the short-term loading, and

(3) Seismic design is based on the capacity-spectrum and demand-spectrum method. The design acceleration spectra of design earthquake motion for damage-control and collapse-control levels are specified at the engineering bed rock. The amplification of earthquake motion by surface geology shall be evaluated separately for the two intensity levels of ground motion. The capacity spectra shall be formulated by the push-over analysis taking into account the nonlinear stiffness characteristics and energy dissipation at the expected response.

The Building Standard Law Enforcement Order requires that the construction and structural calculation shall conform to one of the following routes;

Route 1: Construction shall conform to the specification provisions of Sections 1 to 7 of Chapter 3. The structural calculation shall conform to the Allowable Stress Calculation of Section 8, or one of the calculation methods outlined by the Minister of Land, Infrastructure and Transport (hereafter abbreviated as “MOLIT”) as a procedure equivalent to the Allowable Stress Calculation.

Route 2: Construction shall conform to the durability related provisions of the specification provisions of Sections 1 through 7 of Chapter 3. The structural calculation shall conform to the Ultimate Strength Calculation of Section 8, or one of the calculation methods outlined by MOLIT as a procedure deemed to ensure a safety level of a building equivalent to or higher than the Ultimate Strength Calculation.

Route 3: Construction shall conform to the durability related provisions. The structural calculation shall conform to one of the structural calculation methods, outlined by MOLIT, examining the safety of a building by the stress and deformation of structural members under combined design loads and forces taking into account the dynamic characteristics and construction of a building; e.g., the construction and structural calculation for buildings more than 60 m in height (Ref. 2).

Construction and structural calculation methods outlined by MOLIT are issued in the form of Notifications of the Minister.

2.3 Notifications for Seismically Isolated Buildings

Minister of Construction (presently MOLIT) issued Notification No. 2009 on October 17, 2000, to define the technical standard for construction specifications and structural calculation methods for seismically isolated buildings. Notification 2009 is deemed to ensure the safety of buildings equivalent to or higher than that of the Ultimate Strength Calculation. The construction and structural calculation of seismically isolated buildings can be exercised in one of the following three routes;

Route 1: No structural calculation route for small construction;

Route 2: Notification 2009 route for normal construction; and

Route 3: Other route for special construction.

Some technical terms are defined in Notification 2009;

Seismic isolation devices: Building materials which are used with specific objectives to reduce the intensity of input earthquake motion of a building, including seismic isolators, damping devices and stiffness elements;

Seismic isolator: A device, placed in the horizontal plane, which resists the vertical load of the super-structure but allows horizontal deformation with small resistance. Types of seismic isolators are listed in Table 1.

Table 1: Types of seismic isolators

Type	Materials
a) Elastic system	Laminated rubber or similar elastic materials
b) Sliding system	Tetra-fluorethylene (PTFE) or similar sliding materials
c) Rolling system	Steel ball or similar rolling materials

Damping device: A device, which dissipates kinetic energy of the super-structure with the velocity or deformation of the device. Types of damping devices are listed in Table 2.

Table 2: Types of damping devices

Type	Materials
a) Hysteretic system	Lead, steel or similar materials
b) Fluid system	Hydraulic fluid or similar materials

Stiffness element: An elastic device which is placed in the seismic isolation layer to adjust the period of a structure.

Seismic isolation layer: A horizontal part of a building where seismic isolation devices are inserted between floor systems.

Seismically isolated building: A building having a seismic isolation layer.

Super-structure: A part of a seismically isolated building above the seismic isolation layer.

Sub-structure: A part of a seismically isolated building below the seismic isolation layer.

Design deformation limit of the seismic isolation layer: Story drift δ_s (m) of the seismic isolation layer at which one of seismic isolation devices first reaches its design deformation limit ${}_{\max}\delta_d$ (m) calculated by the following equation;

$$ {}_{\max}\delta_d = \beta\, \delta_u \qquad (1) $$

in which δ_u : Nominal ultimate deformation (m) of a seismic isolation device, and β : Reduction factor, shown in Table 3, reflecting the load support condition of seismic isolation devices. Other values may be used if the safety is proven by taking into consideration the deformation characteristics of seismic isolation devices under loading.

Table 3: Reduction factor representing support conditions of seismic isolation devices

Type of seismic isolation devices		β
Seismic isolator	Elastic system	0.8
	Sliding and rolling systems	0.9
Damping device		1.0
Stiffness element		1.0

Nominal Ultimate Deformation of Seismic Isolator Devices: Nominal ultimate deformation δ_u of a seismic isolator is a lateral deformation at the lateral strength of the seismic isolator under compression stress corresponding to one-third of design compression limit σ_{design}. Existing axial stress reduces the lateral strength and associated lateral deformation limit of an elastic seismic isolator due to buckling (Fig. 1). A structural designer can choose the level of design compression limit σ_{design} smaller than the nominal compressive strength σ_c. Lateral resistance of sliding and rolling isolators is not affected by the compression stress level; i.e., the nominal ultimate deformation δ_u does not change with the compression stress level. Nominal ultimate deformation of a damping device and stiffness element is a lateral deformation at the lateral strength of the device and element.

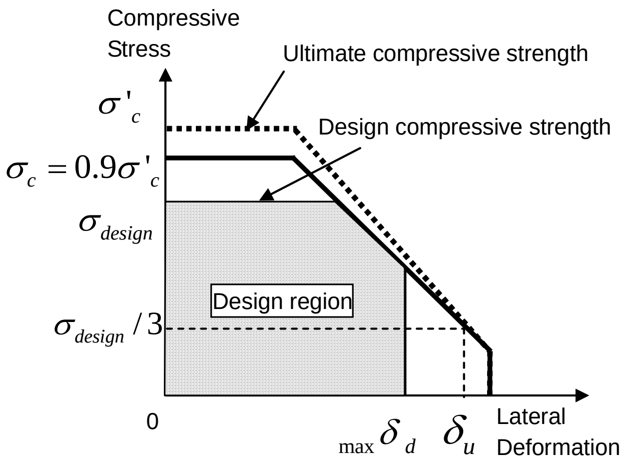

Fig. 1: Nominal ultimate deformation of elastic seismic isolators

Minister of Construction Notification No. 1446 defines the quality and characteristics of seismic isolators and damping devices.

3. SEISMICALLY ISOLATED SMALL CONSTRUCTION

The application of the following route is limited to these small-size buildings whose structural calculation is exempted by the Building Standard Law. The construction must conform to the specification provisions outlined in Sections 3 to 7 of Chapter 3 of the Building Standard Law Enforcement Order and also the durability related provisions of Notification 2009.

Construction Specifications for Seismic Isolation Layer: The construction of the seismic isolation layer must satisfy the following requirements for the safety;

(1) The seismic isolation devices must be rigidly connected to the bottom of the slab or the structural element in the lowest floor of the super-structure, and to the top of the foundation floor or the structural element of the sub-structure.

(2) The ratio of total floor area per story of the super-structure to the number of seismic isolators must be not more than 15 m^2. The ratio of the sum of horizontal forces (kN) in the seismic isolation devices at the "yielding" of the seismic isolation layer to the building floor area per floor must be bounded by values in columns (a) and (b) of Table 4. The ratio of the sum of horizontal forces (kN) in the seismic isolation devices at the design deformation limit δ_s of the seismic isolation layer to the building floor area per floor must be bounded by values in columns (c) and (d) of Table 4.

Table 4: Limit of forces per floor area in seismic isolation devices

Building type		(a)	(b)	(c)	(d)
Light-weight buildings, such as timber construction	Single storied	0.22	0.36	0.72	1.09
	Two storied	0.29	0.49	0.98	1.47
Other buildings		0.34	0.58	1.17	1.75

(3) Design deformation limit δ_s of the seismic isolation layer must be not less than 350 mm. The equivalent viscous damping factor at the design deformation limit must be not less than 20 percent.

(4) The seismic isolation devices must be able to transmit loads and external forces acting on the super-structure to the sub-structure. The seismic isolation devices must be installed at locations in good balance with the position of columns and structural walls.

(5) The space sufficient for the ease of inspections of isolation devices, piping and architectural equipments must be provided in the seismic isolation layer. The seismic isolation devices must be installed at locations easy for examination and inspection.

Construction Specifications for Super-structure: The construction of the super-structure must satisfy the structural and construction specification provisions outlined in Sections 3 to 7 of Chapter 3, Building Standard Law Enforcement Order, excluding the provisions on foundation structures.

The plan and elevation of the super-structure must be regular. The length ratio of the longitudinal direction to the transverse direction must be not more than 4.0. The use of the super-structure is limited to those having small variation of live loads during the usage. The distance between the super-structure and peripheral buildings and the border line of the plot must be not less than 500 mm.

The base of columns and structural walls and ground sills must be rigidly connected to the floor in the lowest floor of the super-structure for the transmission of existing stresses. Floor slabs in the lowest floor of the super-structure must be cast-in-place reinforced concrete construction of thickness not less than 180 mm, and reinforced in double layers by deformed bars of diameter not less than 12 mm placed at 200 mm on centers in the two directions.

Construction Specifications for Sub-structure: The sub-structure must be monolithic reinforced concrete construction. In case the seismic isolation devices are connected to the top of the floor slab of the sub-structure, the slab thickness must be not less than 180 mm; the slab must be reinforced in double layers by deform bars of diameter not less than 12 mm placed at 200 mm on centers in the two directions and must be connected to the surrounding structural members for the transmission of existing stresses. In case a basement is constructed, the uniform lateral soil pressure must act on all four faces of exterior walls.

Construction Specifications for Foundation: The building must rest on the foundation soil having allowable stresses for the long-term loading not less than 50 kN/m^2. The structure must be supported by either pile foundation or monolithic reinforced concrete mat foundation. The base of the foundation must be supported on the soil layer other than alluvium layers that consist of organic or other soft soil; there should be no danger of liquefaction.

Foundation piles must be located to safely support the structure above the foundation. Construction of the pile foundation must conform to the requirements of foundation piles outlined in Minister of Construction Notification No. 1347 (2000).

For mat foundation, the slab thickness must be not less than 250 mm. The mat foundation must be embedded in the soil by not less than 150 mm unless the base of the mat foundation rests on the compact firm soil layer without any danger from the influence of rain. The base of the mat foundation must be embedded below freezing depth and also special measures must be taken to prevent the soil underneath the base of the mat foundation from freezing. The erected vertical part of the mat foundation must be reinforced longitudinally by deformed bars of not less than 12 mm in diameter; one or more longitudinal bars must be placed at the top of the erected vertical part and more than one bar must be placed at the base; these longitudinal bars must be tied to lateral reinforcing bars of not less than 9 mm in diameter, placed vertically at not more than 300 mm on centers. The base of mat foundation must be reinforced, both at the top and bottom, by reinforcing bars of not less than 12 mm diameter, placed at not more than 200 mm on centers in the longitudinal and transverse directions.

Other Specification Requirements: A sign must be posted at the location easy for the occupants and visitors to observe that the building uses seismic isolation devices. The structure of the seismic isolation layer must be such that seismic isolation devices can be replaced as needed. Special measures, if necessary, must be taken to permit free lateral movement of a seismically isolated building against piled snow. Drainage must be provided to the foundation to prevent submergence of seismic isolation devices if the danger of flooding is anticipated in the seismic isolation layer.

4. DESIGN BASED ON NOTIFICATION 2009

Building not more than 60 m in height can be designed and constructed if the durability related provisions of Building Standard Law Enforcement Order and a special structural calculation procedure outlined in Article 6 of Notification 2009 are satisfied.

Design for Serviceability under Permanent Loading: Stresses developed in structural members by the combination of dead and live loads ("long-term loading") must not exceed the allowable stresses of materials set forth for the long-term loading. The deformation and vibration of structural members must not interfere with the serviceability of the building.

Design for Damage Prevention from Frequent Loading and Forces: Stresses developed in structural members by the combined dead, live and snow loads and the combined dead and live loads and wind forces ("short-term loading") must not exceed the allowable stresses of materials set forth for the short-term loading. The amplitudes of snow and wind pressure have been determined for the events of 50 years return period. The allowable stresses of seismic isolation devices are listed in Table 5.

Table 5: Allowable stresses of seismic isolation devices (MPa)

Types	Long-term loading		Short-term loading	
	Compression	Shear	Compression	Shear
Seismic isolators	$F_c/3$	F_{s1}	$(2/3)F_c$	F_{s2}
Damping devices	-	F_{s1}	-	F_{s2}
Stiffness elements	-	F_{s1}	-	F_{s2}

F_c: Nominal compressive strength (MPa) of seismic isolators,
F_{s1}: Shear stress (MPa) of a seismic isolation device developed at one-third of the nominal ultimate deformation δ_u of the device,
F_{s2}: Shear stress (MPa) of a seismic isolation device developed at two-thirds of the nominal ultimate deformation δ_u of the device.

Design for Life Safety from Extraordinary Loading: Member actions, calculated in structural members under extraordinary snow loading and extraordinary wind-storm loading cases, must not exceed the resistance of members, calculated using material strength;

Heavy snow loading: (Dead load) + (Live load) + 1.4 x (Snow load)

Extraordinary wind-storm loading: (Dead load) + (Live load) + 1.6 x (Wind force)

The wind force and snow load are defined for events at 50 year return period. The multipliers of snow load and wind force for the life safety were determined as the ratio of load or force for events at 500 year and 50 year return periods. Material strength of seismic isolation devices is listed in Table 6.

Table 6: Material strength of seismic isolation devices

Types	Material strength (MPa)	
	Compression	Shear
Seismic isolators	F_c	F_s
Damping devices	-	F_s
Stiffness elements	-	F_s
F_c : Nominal compressive strength (MPa) of a seismic isolator, defined as 90 percent of the compression strength of the seismic isolator, F_s : Shear stress (MPa) of a seismic isolation device developed at the nominal ultimate deformation δ_u of the device.		

Roofing materials, cladding and curtain walls facing the outside shall be structurally safe against strong wind pressure.

Seismic Design Requirements: Seismic design requirements are listed separately; i.e., (a) Response deformation of the seismic isolation layer under design seismic forces shall not exceed the design deformation limit δ_s, (b) Response velocity of fluid dampers under design seismic forces shall not exceed the velocity limit of the device, (c) Ratio of the story shear carried by hysteretic and fluid damping devices to the total story shear of the seismic isolation layer shall be not less than 0.03, (d) Tangent period of the structure at the probable maximum response deformation shall be not less than 2.5 sec, (e) Axial force acting in seismic isolators shall not be in tension, and (f) Stresses developed in structural members of the super-structure and sub-structure shall not exceed the allowable stresses of the material set forth for the short-term loading.

Design Earthquake Force in Seismic Isolation Layer: Design earthquake force Q (kN) in terms of lateral shear in the seismic isolation layer is calculated by the following expression;

$$Q = S_A \cdot G_s \cdot M \cdot F_h \cdot Z \tag{2}$$

in which,

S_A : Acceleration spectrum of design earthquake motion at the engineering bedrock,

G_s : Amplification factor of earthquake motion from the engineering bedrock to the ground surface by surface geology.

M : Total mass (ton) of a super-structure,

F_h : Acceleration response reduction factor by the effect of damping, and

Z : Seismic zone factor defined in Building Standard Law Enforcement Order.

The design acceleration spectrum at the engineering bedrock is given in Table 7 for equivalent period T_{eq} ;

Table 7: Design earthquake spectrum at engineering bedrock

$T_{eq} < 0.16 \sec$	$S_A = (3.2 + 30T_{eq}) \quad m/\sec^2$
$0.16 \le T_{eq} < 0.64 \sec$	$S_A = 8 \quad m/\sec^2$
$0.64 \le T_{eq} \sec$	$S_A = \dfrac{5.12}{T_{eq}} \quad m/\sec^2$

The equivalent period T_{eq} of a seismically isolated building is calculated by the following expression at the design deformation limit of the seismic isolation layer unless the period is evaluated by an eigen value analysis considering the stiffness and damping of the seismic isolation layer;

$$T_{eq} = 2\pi\sqrt{\frac{M}{K_{eq}}} \tag{3}$$

in which

M : Total mass (ton) of the super-structure (the sum of dead and live loads divided by gravitational acceleration),

K_{eq} : Equivalent stiffness (kN/m) of the seismic isolation layer (the sum of horizontal forces acting in each seismic isolation device at the design deformation limit δ_s of the seismic isolation layer divided by the design deformation limit δ_s).

Acceleration response reduction factor F_h due to damping effect is calculated by the following expression unless the reduction factor is evaluated by a procedure taking into consideration the effect of stiffness and damping in the seismic isolation layer;

$$F_h = \frac{1.5}{1 + 10(h_d + h_v)} \qquad \textit{but not less than } 0.4 \tag{4}$$

in which h_d : Equivalent damping factor of seismic isolators and hysteretic damping devices in the seismic isolation layer, and h_v : Equivalent damping factor of fluid damping devices in the seismic isolation layer.

The equivalent damping factor h_d of seismic isolators and hysteretic damping devices is calculated by the following expression;

$$h_d = \frac{0.8}{4\pi} \frac{\sum \Delta W_i}{\sum W_i} \tag{5}$$

in which

ΔW_i : Area enclosed (kN-m) by the hysteretic curve of each hysteretic damping device and seismic isolator at the maximum displacement under the design deformation limit δ_s of the seismic isolation layer, and

W_i : One half of the product (kN-m) of displacement and force acting in each hysteretic damping device and seismic isolator at the design limit deformation δ_s of the seismic isolation layer.

The equivalent damping factor h_v of fluid damping devices is calculated by the following expression;

$$h_v = \frac{1}{4\pi} \frac{T_{eq} \sum C_{vi}}{M} \tag{6}$$

in which

T_{eq} : Equivalent period (sec) of the structure,

M : Total mass (ton) of a super-structure, and

C_{vi} : Damping coefficient of each fluid damping device, defined as the ratio of damping force to velocity in each fluid damping device when equivalent velocity V_{eq} (m/sec), defined by the following expression, is developed in the seismic isolation layer;

$$V_{eq} = 2\pi \frac{\delta_s}{T_{eq}} \tag{7}$$

in which δ_s : design deformation limit (m) of the seismic isolation layer.

Deformation Limit of Seismic Isolation Layer: Maximum story drift of the seismic isolation layer under the design earthquake force must not exceed the design deformation limit δ_s of the seismic isolation layer.

Response deformation δ_r of the seismic isolation layer is calculated by the following expression;

$$\delta_r = 1.1\,\delta_{r'} \tag{8}$$

in which $\delta_{r'}$: Representative response deformation (m) of the seismic isolation layer calculated by the following equation unless the maximum value of the representative deformation of the seismic isolation layer is evaluated taking into consideration the variation of characteristics of seismic isolation devices,

$$\delta_{r'} = \alpha\,\delta \tag{9}$$

in which

α : Factor associated with variation of characteristics due to the change in environment and decay of characteristics with time, of seismic isolation devices. The value must be 1.2 if it is estimated less than 1.2,

δ : Basic deformation (m) of the seismic isolation layer calculated by dividing the design earthquake force Q in the seismic isolation layer by equivalent stiffness K_{eq} of the seismic isolation layer at the design deformation limit.

The horizontal distance from the super-structure and sub-structure to neighboring structures and other objects must be not less than 1.25 times response deformation δ_r of the seismic isolation layer nor 200 mm plus response deformation δ_r. If the space between the building and neighboring buildings or other objects is used as passage, additional 0.6 m horizontal distance must be provided.

<u>Velocity Limit of Fluid Damping Device:</u> Response velocity V_r in a fluid damping device must be evaluated by the following expression unless the response velocity of each seismic isolation device is evaluated taking into consideration the variation of characteristics of the seismic isolation device. The response velocity V_r must not exceed velocity limit of the device specified in Notification 1446,

$$V_r = 2.0\sqrt{\frac{(Q_h + Q_e)\delta_r}{M}} \tag{10}$$

in which

Q_h : Sum of horizontal forces (kN) acting in each hysteretic damping device and seismic isolator having similar damping characteristics when the seismic isolation layer deforms to the nominal ultimate deformation,

Q_e: Sum of horizontal forces (kN) acting in each seismic isolator (other than those having damping characteristics similar to a hysteretic damping device) and stiffness element,

δ_r: Response deformation (m) of the seismic isolation layer, and

M : Total mass (ton) of a super-structure.

Minimum Shear Carried by Damping Devices and Isolators: Ratio μ of the shear carried by hysteretic and fluid damping devices to the total shear of the seismic isolation layer is calculated by the following expression. The ratio must be not less than 0.03;

$$\mu = \frac{\sqrt{(Q_h + Q_e)^2 + 2\varepsilon(Q_h + Q_e)Q_v + Q_v^2}}{M \cdot g} \frac{Q_h + Q_v}{Q_h + Q_v + Q_e} \tag{11}$$

in which

Q_h: Sum of horizontal forces (kN) acting in each hysteretic damping device and seismic isolator having similar damping characteristics when the seismic isolation layer deforms to the nominal ultimate deformation,

Q_e: Sum of horizontal forces (kN) acting in each seismic isolator (other than those having damping characteristics similar to a hysteretic damping device) and stiffness element,

ε : Factor defined in Table 8 for response velocity $V_{r'}$ of the seismic isolation layer;

$V_{r'}$: Response velocity (m/sec) of the seismic isolation layer evaluated by the following expression;

$$V_{r'} = 2.0\sqrt{\frac{(Q_h + Q_e)\delta_{r'}}{M}}$$

where $\delta_{r'}$: Representative response deformation of the seismic isolation layer,

Table 8: Factor ε for different fluid damping devices

$V_{r'} \le V_y$	0.0
$V_{r'} > V_y$	0.5
V_y : Relief velocity (m/sec) of fluid damping devices.	

Q_v: Sum of the products (kN) of response velocity in each fluid damping device when the seismic isolation layer reaches representative response velocity $V_{r'}$ and damping coefficient of the fluid damping device at the velocity, and

M : Total mass (ton) of a super-structure.

Minimum Tangent Period of Building: Tangent period T_t (sec) of a seismically isolated building, calculated by the following expression, must be not shorter than 2.5 sec (or 2.0 sec for buildings of less than 13.0 m in height);

$$T_t = 2\pi\sqrt{\frac{M}{K_t}} \tag{12}$$

in which M : Total mass (ton) of a super-structure, and K_t : Sum of tangent stiffness (kN/m) of each seismic isolation device when the basic response deformation δ is developed in the seismic isolation layer.

Compression Stress in Seismic Isolation Devices: Compression stresses in the vertical load carrying elements in the seismic isolation layer developed by the sum of 1.3 times the weight of a super-structure and compression forces due to the overturning effect of the design earthquake force must not exceed the design compression limit. Axial stress in the vertical load carrying elements in the seismic isolation layer developed by the sum of 0.7 times the weight of the super structure and tensile forces due to the overturning effect under earthquake forces must not be in tension.

Seismic Design of Super-Structure: Stresses developed in structural members in the super-structure and the seismic isolation layer by combined dead load, live load, and the design earthquake forces (and 0.35 times snow load in the designated heavy snow areas) must not exceed the allowable stress of materials specified for the short-term loading. The design earthquake force in terms of story shear coefficient C_{ri} is calculated by the following expression;

$$C_{ri} = \gamma \frac{\sqrt{(Q_h + Q_e)^2 + 2\varepsilon(Q_h + Q_e)Q_v + Q_v^2}}{M \cdot g} \frac{A_i(Q_h + Q_v) + Q_e}{Q_h + Q_v + Q_e} \tag{13}$$

in which γ: Factor associated with change of characteristics, environmental change and decay with time of the seismic isolation devices. The value must be not less than 1.3 unless the factor is evaluated taking into consideration the change of characteristics, environmental change and decay with time,

Story drift ratio (inter-story displacement divided by inter-story height under the design earthquake forces) shall be not more than 1/300 (1/200 for buildings less than 13 m in height).

Seismic Design of Sub-Structure: Stresses developed in structural members of the sub-structure under the combination of dead load, live load, earthquake forces Q_{iso} in the seismic isolation layer, defined in the following expression, and twice the earthquake force of the sub-structure (and 0.35 times the snow load in heavy snow areas) must not exceed the allowable stress of materials specified for short-term loading conditions;

$$Q_{iso} = \gamma \sqrt{(Q_h + Q_e)^2 + 2\varepsilon (Q_h + Q_e) Q_v + Q_v^2} \tag{14}$$

in which the symbols are defined above. The earthquake force of the sub-structure is calculated as the product of weight and seismic coefficient k defined below:

$$k \geq 0.1(1 - \frac{H}{40})Z \tag{15}$$

in which H : Depth (m) from the ground level, but the value is set 20 if the depth exceeds 20 m, and Z : Seismic zoning factor (varying from 0.7 to 1.0 in Japan).

<u>Other Structural Requirements:</u> The eccentricity ratio of the seismic isolation layer must be not more than 0.03 unless the safety can be proven by taking into consideration the displacement amplification by torsional effects. Pertinent measures shall be taken to prevent damages in those buildings located in designated earth-flow disaster areas.

<u>Durability Related Provisions:</u> The durability related provisions are a part of the specification provisions that cover construction methods, durability and quality control which cannot be ensured by the structural calculation. The additional durability related provisions for seismically isolated buildings outlined in Notification 2009 are as follows;

(1) The gravity loads and forces acting on the super-structure above the seismic isolation layer must be transmitted to the sub-structure by the seismic isolation devices. The seismic isolation devices shall be rigidly connected to the bottom of the super-structure and the top of the sub-structure. The bottom of the foundation shall reach the firm soil layer without any danger of liquefaction. If the basement is constructed in the sub-structure, soil pressure shall act uniformly from all sides in the basement.

(2) The height between slabs above and below the seismic isolation layer must be sufficient for the inspection of seismic isolation devices, piping and architectural facilities. The seismic isolation devices must be placed at the locations easy for the inspection. The structure of the seismic isolation layer must be such that seismic isolation devices can be replaced as needed.

(3) The displacement of a seismically isolated building shall not be interfered by snow. Drainage shall be provided to the foundation to prevent submergence of seismic isolation devices if the danger of flooding is anticipated in the seismic isolation layer.

(4) A sign must be posted at the location easy for the occupants and visitors to observe that the building uses seismic isolation devices.

5. DESIGN OF SPECIAL BUILDINGS

Construction and design of those buildings which do not satisfy the limitation of small size construction and construction specifications or those buildings which do not satisfy the construction specifications and structural calculations must be approved by the MOLIT that the structural calculation conforms to one of the structural calculation methods, outlined by MOLIT, examining the safety of a building by the stress and deformation of structural members under combined design loads and forces taking into account the dynamic characteristics. furthermore, the construction of those buildings must satisfy the durability related provisions.

One of the structural calculation methods outlined by the MOLIT is introduced in Ref. 2 for high-rise buildings taller than 60 m.

SUMMARY

The Japanese design requirements for seismically isolated buildings are briefly introduced in this paper. Small construction is exempted from structural calculation requirements. The construction and structural calculation of those buildings not satisfying Notification 2009 must be individually approved by Minister of Land, Infrastructure and Transport.

References

1) Shunsuke Otani, “New Seismic Design Provisions in Japan,” Proceedings, Second U.S.-Japan Workshop on Performance-Based Earthquake Engineering Methodology for Reinforced Concrete Building Structures, Sapporo, Japan, September 2000.

2) Shunsuke Otani, “Japanese State of Practices in Seismic Design of High-rise Reinforced Concrete Buildings,” Proceedings, Third U.S.-Japan Workshop on Performance-Based Earthquake Engineering Methodology for Reinforced Concrete Building Structures, Seattle, Washington, August 2001.

SESSION A-1: SYSTEMS ANALYSIS

Chaired by

♦ Sashi Kunnath and Daisuke Kato ♦

A PROGRESS REPORT ON
ATC 55: EVALUATION AND IMPROVEMENT OF INELASTIC SEISMIC ANALYSIS PROCEDURES

CRAIG D. COMARTIN[1]

Abstract

The Applied Technology Council (ATC), with primary funding provided by the Federal Emergency Management Agency (FEMA) and supplemental support from the Pacific Earthquake Engineering Research Center (PEER), is in the midst of a project (ATC 55) to evaluate and improve the application of inelastic analysis procedures for use with performance-based engineering methods for seismic design, evaluation, and rehabilitation of buildings. A previous paper (Comartin 2001) documents the first phase of the project. This current paper reports on the present status of the second phase of the project. The focus is on anticipated recommendations to improve inelastic analysis procedures as currently documented in *FEMA 356* (BSSC 2000) and *ATC 40* (ATC 1996). General categories of improvements include:

- Displacement modification procedures (Coefficient Method)
- Equivalent linearization procedures (Capacity Spectrum Method)
- Multi-degree-of-freedom effects
- Short period effects

INTRODUCTION AND BACKGROUND

The objectives of the ATC 55 project are the development of practical recommendations for improved prediction of inelastic structural response of buildings to earthquakes (i.e., guidance for improved application of simplified inelastic analysis procedures) and the identification of important issues for future research. Specific anticipated outcomes are:

1. Improved understanding of the inherent assumptions and theoretical underpinnings of existing and proposed new simplified analysis procedures.
2. Recognition of the applicability, limitations, and reliability of various procedures.
3. Guidelines for practicing engineers to apply the procedures to new and existing buildings.
4. Direction for researchers on issues for future improvements of simplified inelastic analysis procedures.

The results of the project will culminate in a project document to be published by FEMA. This document will provide a comprehensive discussion of simplified inelastic seismic analysis of new and existing buildings. It will contain guidelines for applications of selected procedures including their individual strengths, weaknesses and

---

[1] *Comartin-Reis, Stockton, California*
comartin@comartin-reis.com

limitations. The document will also contain illustrative examples and expert commentary on key issues. The document will serve to update and supplement existing publications including *FEMA 273/274, ATC 40,* and the *NEHRP Recommended Provisions*

The first phase of the project comprised an assessment of pertinent aspects of the state of research and practice. Information on the project and the results of the first phase may be accessed at the ATC web site (www.atcouncil.org). As of October 2002, the second phase of the project is nearing completion. This phase has focused upon the detailed evaluation of current procedures and the development of recommended improvements. The results of the evaluation process are documented by Miranda (2002ab). This paper summarizes the current status of the proposed improvements. These are being developed currently by the project team.

Contemplated improvements include better estimates of inelastic displacements when using nonlinear static procedures (NSP's). There are currently two alternatives. *FEMA 356* documents the Displacement Coefficient Method (DCM). The basis of this approach is the statistical analyses of the results of time histories of SDOF oscillators used to generate inelastic spectra or R-μ-T relationships. The results are used to formulate coefficients used to modify the response of a linear system. This basic approach is termed **displacement modification**. The other alternative is documented in *ATC 40* as the Capacity Spectrum Method (CSM). This approach relies on **equivalent linearization** of the inelastic system utilizing both a period shift (decrease in stiffness) and equivalent viscous damping to represent hysteretic energy loss. These parameters are specific to each system. They are also a function of ductility and current methods require iteration for solution. The development of improved procedures for both are outlined in the following sections of this paper.

The current NSP's of both *FEMA 356* and *ATC 40* rely primarily on single-degree-of-freedom analysis of response. Both documents touch upon variations in load vectors or other attempts to recognize the effects of higher modes of vibration. The results from Phase I indicate that there may be potential improvements. First, several studies suggest that modification of the load vector during the pushover analysis to reflect changes in the vertical distribution of forces resulting from inelastic behavior can improve NSP results compared with actual MDOF analyses. Secondly, other studies appear to show that combining the results of several pushovers representative of different mode shapes for the same structure can lead to improved comparisons with actual MDOF analyses. These potential improvements are outlined in a subsequent section on **multi-degree-of-freedom effects**.

For a number of reasons, short period buildings may not respond to seismic shaking as adversely as might be predicted analytically. Traditional design and evaluation procedures, including *FEMA 356*, recognize this with various provisions. These provisions are not based directly upon empirical or theoretical justifications. In order to at least begin to address this shortcoming, the ATC 55 project scope has been recently expanded with an effort to document and discuss **short period effects** within an improve technical context. The last section of this paper provides an outline of the issues currently being investigated.

DISPLACEMENT MODIFICATION

The ATC 55 project team is contemplating several recommended improvements (Miranda 2002c) to the displacement modification procedure in *FEMA 356* (BSSC 2000). These relate to the basic coefficient method equation for the target displacement, δ_t in estimating the maximum inelastic global deformation demands on buildings for earthquake ground motions

$$\delta_t = C_0 C_1 C_2 C_3 S_a \frac{T_e^2}{4\pi^2} g$$

where the coefficients are currently defined as follows:

C_o = modification factor to relate spectral displacement of an equivalent SDOF system to the roof displacement of the building MDOF system.

C_1 = modification factor to relate the expected maximum inelastic displacements to displacements calculated for linear elastic response.

= 1.0 for $T_e \geq T_s$

= $[1.0 + (R\text{-}1)T_s/T_e]/R$ for $T < T_s$

C_1 computed by the above equations can by capped the limiting equations

C_1 = 1.5 for T_e < 0.1s.

C_1 = 1.0 for $T_e \geq T_s$.

Linear interpolation is allowed for the intermediate values $0.1 < T_e \leq T_s$.

R = Ratio of elastic strength demand to calculated yield strength.

T_e = Effective fundamental period of the building.

T_s = Characteristic period of the response spectrum, defined as the period associated with the transition from the constant acceleration segment of the spectrum to the constant velocity spectrum of the spectrum.

C_2 = Modification factor to represent the effect of pinched hysteretic shape, stiffness degradation and strength deterioration on the maximum displacement response. Values of C_2 for different framing systems and Structural Performance Levels (i.e. immediate occupancy, life safety and collapse prevention) are obtained from Table 3.3 of the FEMA-356. Alternatively, C_2 can take the value of one.

C_2 values from FEMA-356 (BSSC, 2000)

Structural performance level	$T \leq 0.1$second		$T > T_s$	
	Framing Type 1[1]	Framing Type 2[2]	Framing Type 1[1]	Framing Type 2[2]
Immediate occupancy	1.0	1.0	1.0	1.0
Life safety	1.3	1.0	1.1	1.0
Collapse prevention	1.5	1.0	1.2	1.0

[1] Structures in which more than 30% of the shear at any level by combination of the following components, elements or frames: ordinary moment resisting frame, concentrically moment braced frame, frames with partially restrained connections, tension only braces, unreinforced masonry walls, shear-critical, piers and spandrels of reinforced concrete and masonry.

[2] All frames not assigned to Frame Type 1.

[3] Linear interpolation shall be used for intermediate values of T.

C_3 = Modification factor to represent increased displacements due to dynamic P-Δ effects. For buildings with positive post-yield stiffness, C_3 is set equal to 1. For buildings with negative post-yield stiffness, values of C_3 is calculated using the following expression:

$$C_3 = 1.0 + \frac{|\alpha| (R-1)^{3/2}}{T_e}$$

Based on the analyses of the current procedures (Miranda 2002a) two alternatives for improvement of the factor C_1 are being considered:

ALTERNATIVE 1:

$$C_1 = 1 + \left[\frac{1}{a \cdot (T_e / T_g)^b} - \frac{1}{c} \right] \cdot (R-1)$$

Soil profile	***a***	***b***	***c***	**T_g (s)**
B	42	1.60	45	0.75
C	48	1.80	50	0.85
D	57	1.85	60	1.05

ALTERNATIVE 2:

$$C_1 = 1 + \left[\frac{1}{a \cdot (T_e / T_g)^b} \right] \cdot (R-1)$$

Soil profile	***a***	***b***	**T_g (s)**
B	151	1.60	1.60
C	199	1.83	1.75
D	203	1.91	1.85

where T_g = a site dependent period.

These are both compared to the current definition in Figure 1. Figure 2 illustrates the substantial improvement in error reduction with either alternative

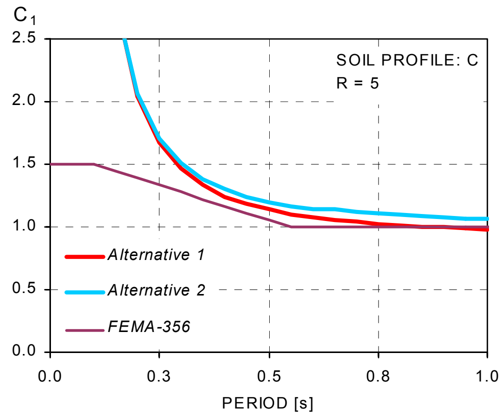

Figure 1: Comparison of current and potential C_1 coefficients (from Miranda 2002c)

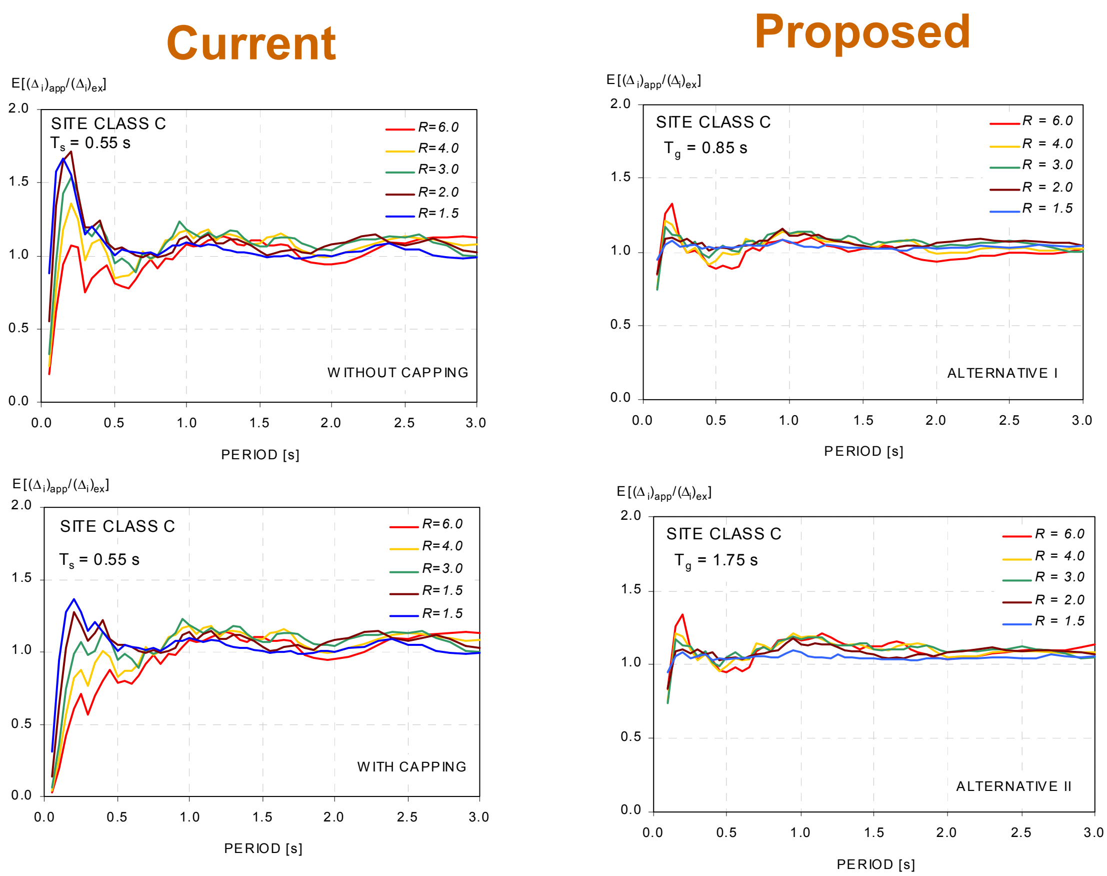

Figure 2: Comparison of mean errors for C_1 coefficients for site class C (from Miranda 2002c)

Miranda (2002a) points out that the current definitions C_2 and C_3 are not clearly independent of one another. C_2 is intended to represent changes in hysteretic behavior due to pinching, stiffness degradation, and strength degradation. However, strength and stiffness degradation due to P-Δ effects are supposedly addressed by C_3 as well. The proposed improvements include a clearer separation of these coefficients outlined as follows:

C_2 = Modification factor to represent CYCLIC DEGRADATION (both stiffness and strength degradation).

ALTERNATIVE 1:

$C_2 > 1$ for $Te < 0.5$s

$C_2 = 1$ for $Te \geq 0.5$s

ALTERNATIVE 2:

$C_2 = 1$

Figure 3 illustrates that for stiffness degrading (SD) and strength-and-stiffness degrading (SDD) behavior C_2 is actually less than 1.0 except for low strength short period oscillators.

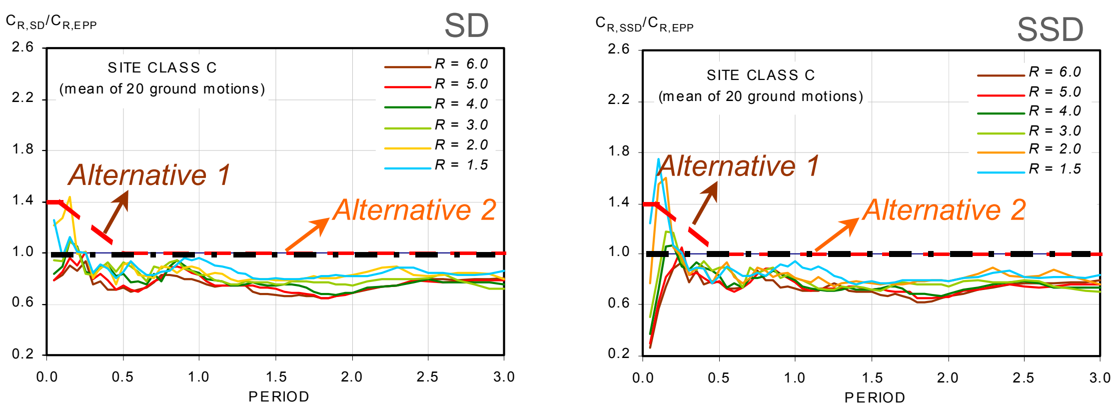

Figure 3: Comparison of proposed C_2 coefficients with the results of RHA (from Miranda 2002c)

C_3 = Modification factor to represent the effect of STRENGTH DEGRADATION WITHIN A CURRENT HALF-CYCLE, when there is a negative stiffness in the pushover curve. For buildings with positive yield stiffness, C_3 is set equal to 1.

The negative stiffness can come from geometric nonlinearities (i.e., P-Δ effects), material nonlinearities (strength degradation, brittle failures, etc) or combination of these phenomena. The analytical definition of this coefficient is being studied based on a number of parameters that control the point at which instability (collapse) occurs. The general shape of the relationship to strength is shown in Figure 4. This figure suggests that an alternative to the C_3 coefficient might be to impose some limitations on directly on the strength of buildings with negative post-elastic stiffness to avoid collapse. This is also under consideration.

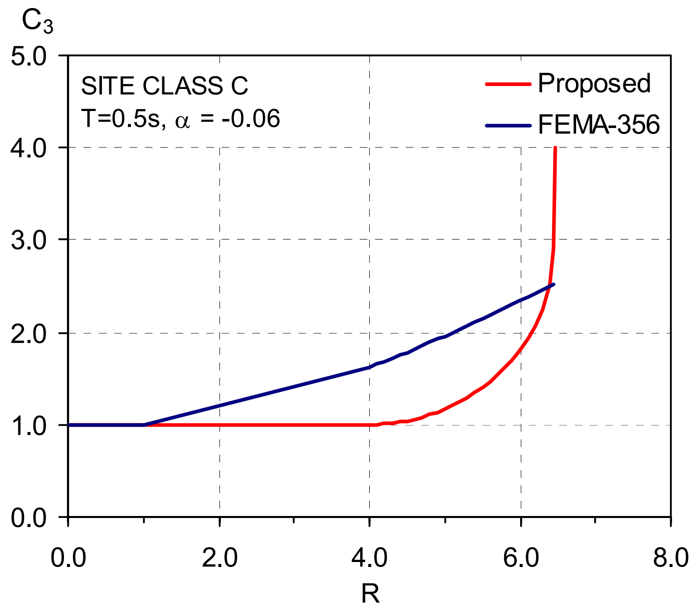

Figure 4: Comparison of general shape of current and proposed C_3 coefficients (from Miranda 2002c)

EQUIVALENT LINEARIZATION

The capacity spectrum method documented in *ATC 40* (ATC 1997) is a form of equivalent linearization based on two fundamental assumptions. The period of the equivalent linear system is assumed to the secant period and the equivalent damping is related to the area under the capacity curve associated with the inelastic displacement demand. The focus of the ATC 55 effort (Iwan 2002) has been to develop better procedures to estimate equivalent period and equivalent damping. This is an extension of previous work (Iwan 1978 and 1980) in which both parameters are expressed as functions of ductility. These relationships are based on an optimization process whereby the error between the displacement predicted using the an equivalent linear oscillator and using nonlinear response history analysis is minimized. Conventionally, the measurement of error has been the mean of the absolute difference between the displacements. Although this seems logical, it might not lead to particularly good results from an engineering standpoint. This is illustrated in Figure 5 from. It is possible to select linear parameters for which the mean error is zero as for the broad, flat distribution. However, the narrower curve might represent equivalent linear parameters that provide better results from an engineering standpoint, since the chance of errors outside say a –20% to +10% range are much lower. This is owing to the smaller standard deviation in spite of the –5% mean error.

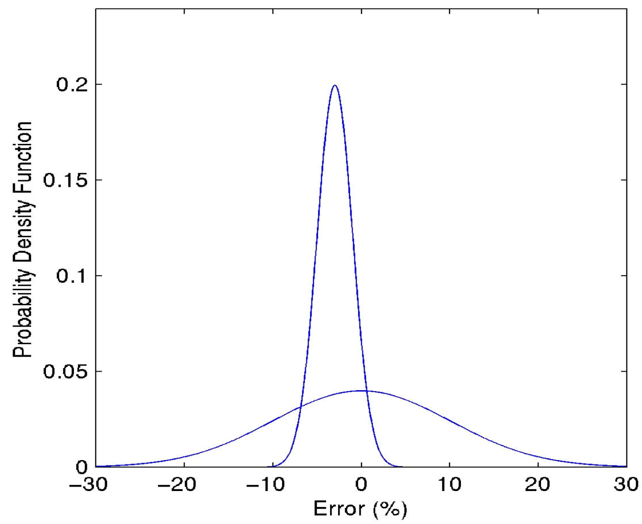

Figure 5. Illustration of probability density function of displacement error for a Gaussian distribution-from (Iwan 2002).

This general strategy has been applied to a series of elasto-plastic, stiffness degrading, and strength-and-stiffness-degrading hysteretic models generate optimal equivalent linear parameters for a range on periods and ductilities as illustrated in Figure 6.

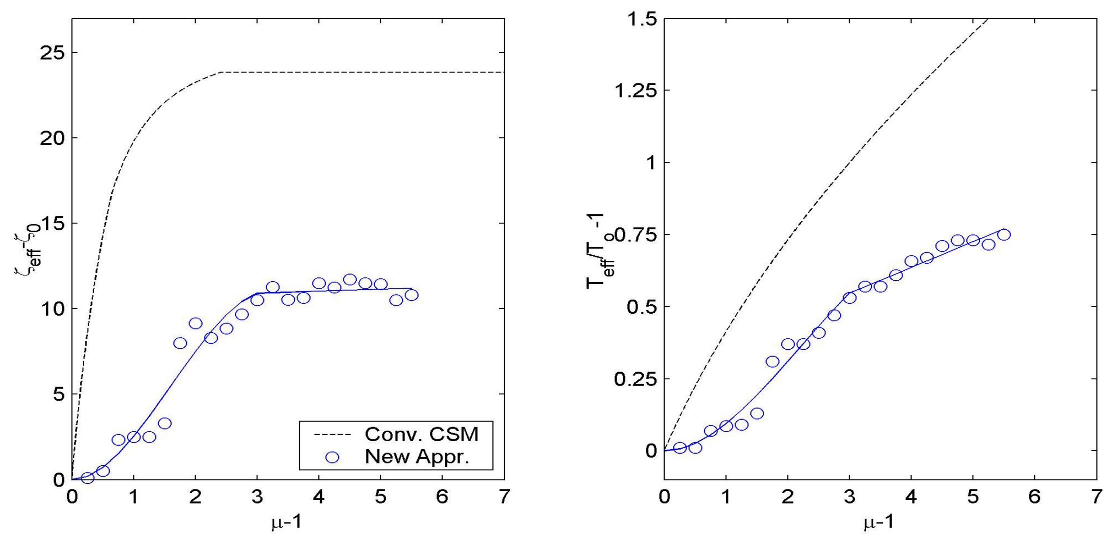

Figure 6: New optimal effective (equivalent) linear parameters for elastoplastic system.T_0=0.1-2.0 (from Iwan 2002).

Using the results for discrete values of ductility, a curve fitting process has leads to analytical expressions relating effective period, T_{eff} , and effective damping, ξ_{eff} , to ductility, μ , similar to the following:

For μ<4.0:

$$T_{eff}/T_o - 1 = 0.111(\mu - 1)^2 - 0.0167(\mu - 1)^3$$
$$\zeta_{eff} - \zeta_o = 3.19(\mu - 1)^2 - 0.660(\mu - 1)^3$$

For μ≥4.0:

$$T_{eff}/T_o - 1 = 0.279 + 0.0892(\mu - 1)$$
$$\zeta_{eff} - \zeta_o = 10.6 + 0.116(\mu - 1)$$

In practical applications, the parameter of interest is most often the maximum inelastic displacement which is directly related to ductility. Consequently, the application of these expressions generally require iteration, as with the previous capacity spectrum method. In contrast to the previous procedure however, the use of the optimal effective period and damping directly produces a point on an acceleration and displacement response diagram (ADRS) that does not lie on the capacity spectrum for the structure (see Figure 7). Although the intersection of T_{eff} with the ADRS demand reduced by ξ_{eff} identifies the proper maximum displacement, $D_{max,}$ the corresponding maximum acceleration, A_{max} , must lie on the capacity spectrum. This may be easily corrected graphically by multiplying the value of the acceleration at every displacement on the reduced ADRS by the ratio of the corresponding secant period, T_{sec}, of the capacity spectrum at that displacement to the effective period, T_{eff}, for the same displacement. This results in what has been termed a Modified ADRS (MADRS) that is a function of ductility and the specific capacity spectrum. Thus a family of curves maybe generated for a given structure as shown in Figure 8. The intersection of the radial effective period lines and the MADRS curves corresponding to the same ductilities trace the locus of potential performance points. The actual performance point for the structure is then the intersection of this locus and the capacity spectrum. Characterized in this manner the application improved is analogous to the previous capacity spectrum method.

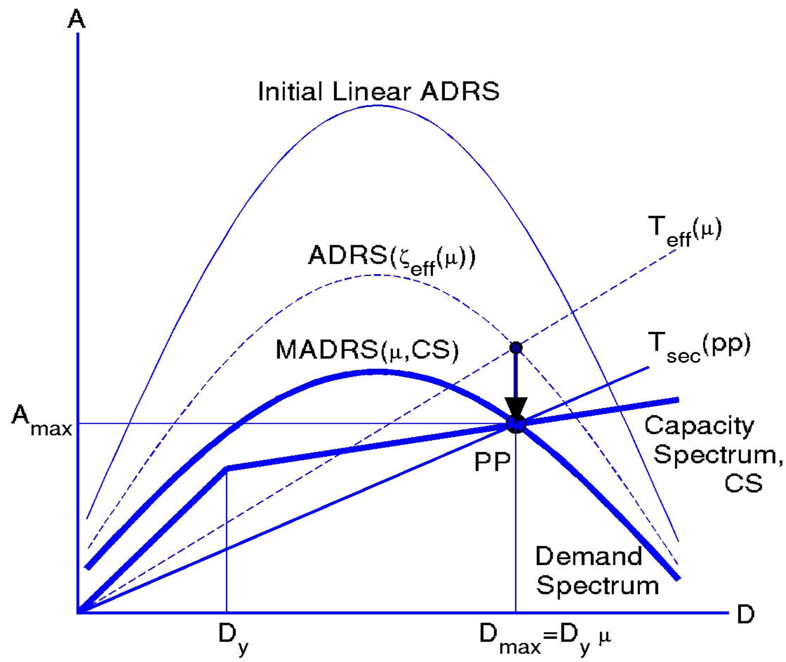

Figure 7: Description of the Modified ADRS (MADRS) and its use (from Iwan 2002).

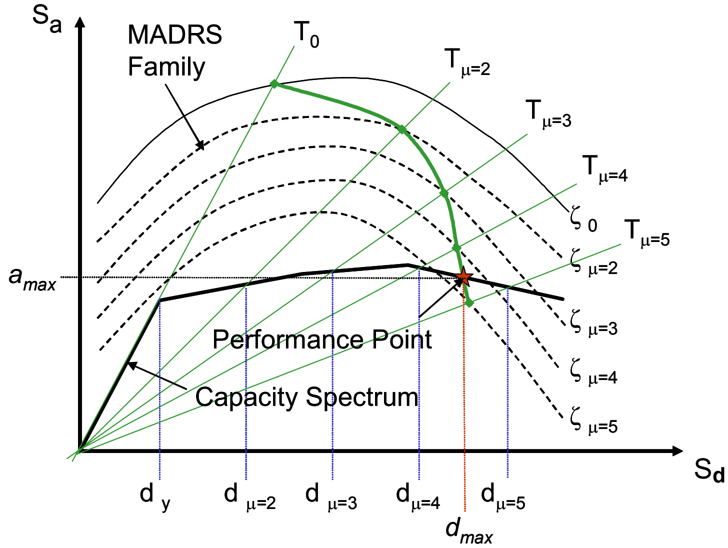

Figure 8: Illustration of a graphical procedure for finding the Performance Point using a family of MADRS (from Iwan 2002).

Figure 9 provides a comparison between the previous capacity spectrum method approach of ATC 40 and the proposed improved MADRS procedures for the UBC design spectrum.

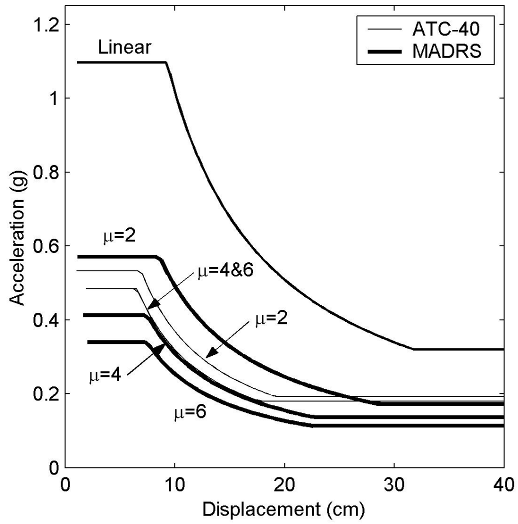

Figure 9: UBC based reduced ADRS from conventional ATC-40 approach and MADRS from new optimal parameters for an elastoplastic system (from Iwan 2002).

For low levels of ductility it is evident that the MADRS procedure will predict relatively higher displacements. However, for higher ductility demands the improved procedures will predict significantly lower displacements than the ATC 40 approach. This effect is most evident for systems with very short initial periods (high initial stiffness) or long initial periods (low stiffness). These differences can be important in evaluating the performance of older buildings and may partially address the question of why the conventional CSM approach appears to be overly conservative for some short period, low strength structures based on actual earthquake performance. This issue needs to be examined further.

MULTI-DEGREE-OF-FREEDOM EFFECTS

In order to compare and illustrate techniques for improving the results of nonlinear static procedures related to the effects of higher modes, five example buildings have been analyzed (Aschheim 2002). The basic outline of this effort is as follows:

<u>Objective</u> Compare estimates made using simplified inelastic procedures with results obtained by nonlinear dynamic analysis

<u>Example Buildings</u>

3-Story Steel Frame (SAC LA Pre-Northridge M1 Model)

3-Story Weak Story Frame (lowest story at 50% of strength)

8-Story Shear Wall (Escondido Village)

9-Story Steel Frame (SAC LA Pre-Northridge M1 Model)

<u>Ground Motions</u>

11 Site Class C Motions, 8-20 km, 5 events

4 Near Field Motions: Erzincan, Northridge (Rinaldi Receiving Station & Sylmar County Hospital), and Landers

Drift Levels

Ordinary Motions (scaled)

0.5, 2, 4% for frames

0.2, 1, 2% for wall

Near-Field (unscaled)

1.8 to 5.0% for 3-story frames, 1.7-2.1% for 9-story frames

0.6 – 2.1% for wall

Load Vectors/Methods Illustrated

First Mode

Inverted Triangular

Rectangular (Uniform)

Code

Adaptive

SRSS

Multimode Pushover (MPA)

Response Quantities (Peak values generally occur at different instants in time)

Floor and roof displacements

Interstory Drifts

Story Shears

Overturning Moment

Errors

Mean over all floors

Maximum over all floors

Major observations from MDOF examples are summarized as follows:

Displacements

Displacements are estimated well by approximate methods, except:

> Displacement response is not always predominantly in a first mode.
>
> Weak story mechanisms can occur for some motions and not others. Pushover analyses show weak story mechanisms.

The load vectors result in similar displacement estimates.

> The rectangular, code, and SRSS vectors are a little worse than the others.
>
> The adaptive does not result in a substantial difference.

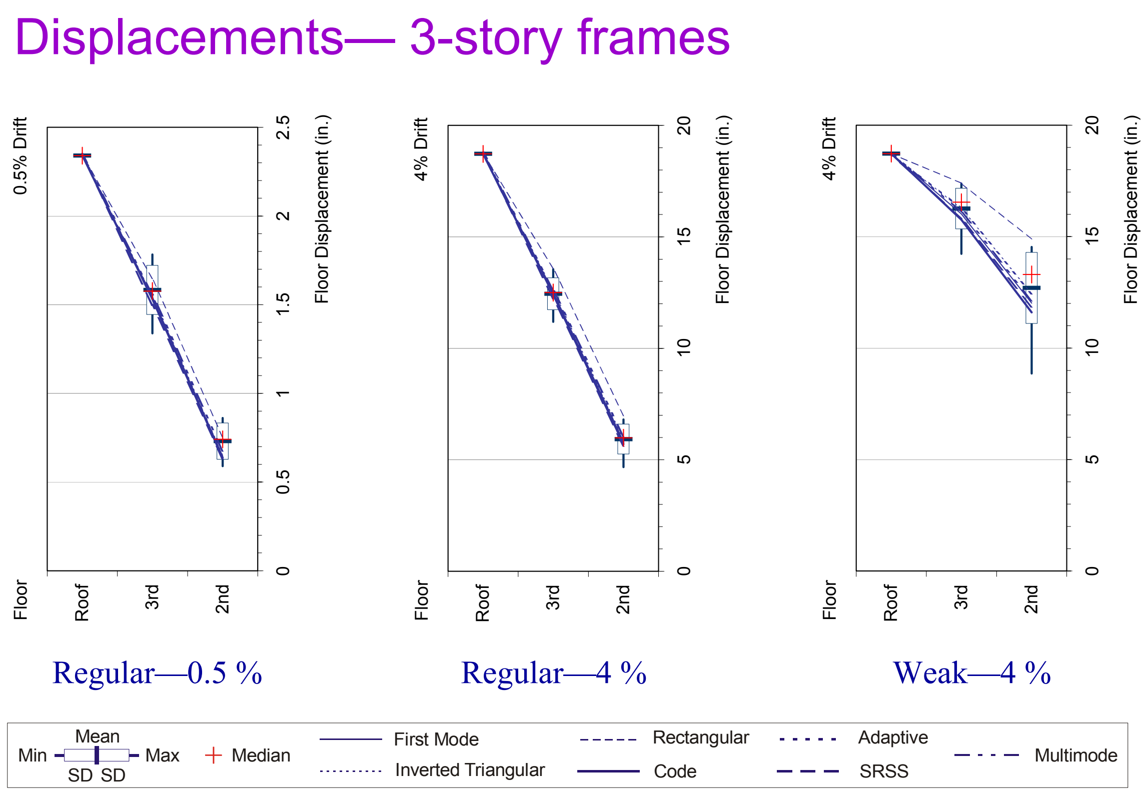

Figure 10: Example results from MDOF examples for displacements (from Aschheim 2002).

Interstory drifts

8-story wall:

> Interstory drifts were dominated by the first mode and were estimated well by quasi-first mode vectors. (Interstory shears are estimated poorly by these vectors)

Weak-story frames:

Interstory drifts at the weak story were estimated well by all load vectors. Elsewhere could be severely underestimated.

Regular frames:

Interstory drifts were underestimated by quasi-first mode load vectors.

While much better, even the modified MPA could significantly underestimate interstory drifts for the 9-story frames.

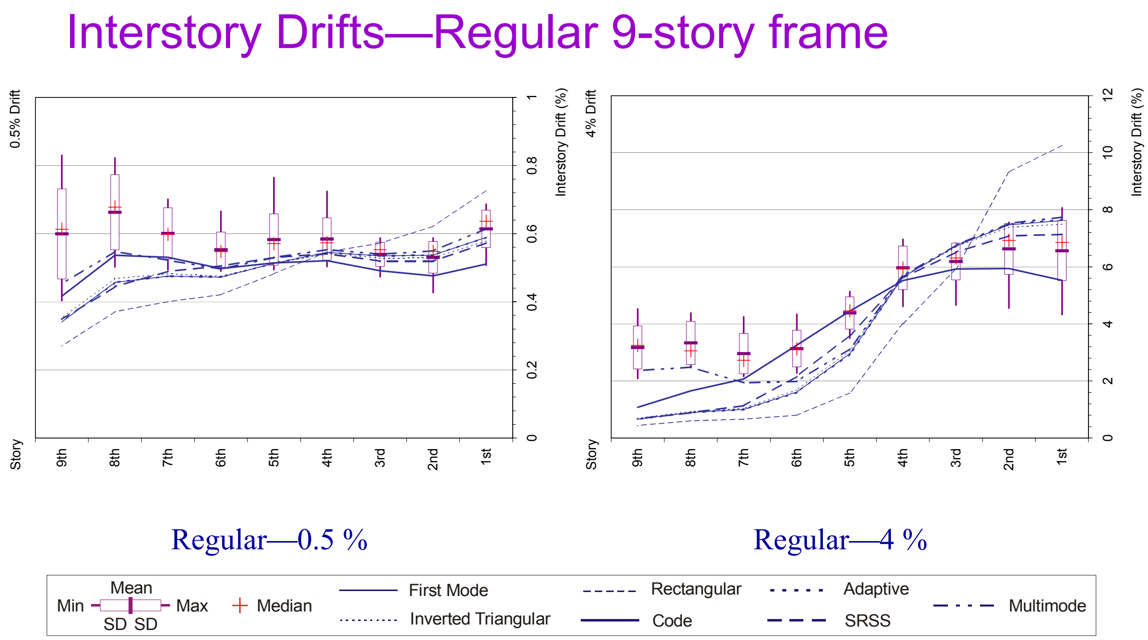

Figure 11: Example results from MDOF examples for interstory drifts (from Aschheim 2002).

Story shears

Story shears generally were underestimated by quasi-first mode load vectors (except at the weak story of the weak-story frames).

A modified MPA method overestimated story shears for the 3-story frames, and could underestimate or overestimate story shears for the 8 and 9-story buildings. (Improvements might involve more modes, with each reduced as nonlinearity increases.)

The Code ELF procedure significantly underestimates shears at large drifts.

A revised F_t approach would require as much as 75% of the base shear to be applied at the top.

Story Shears— 8-story wall

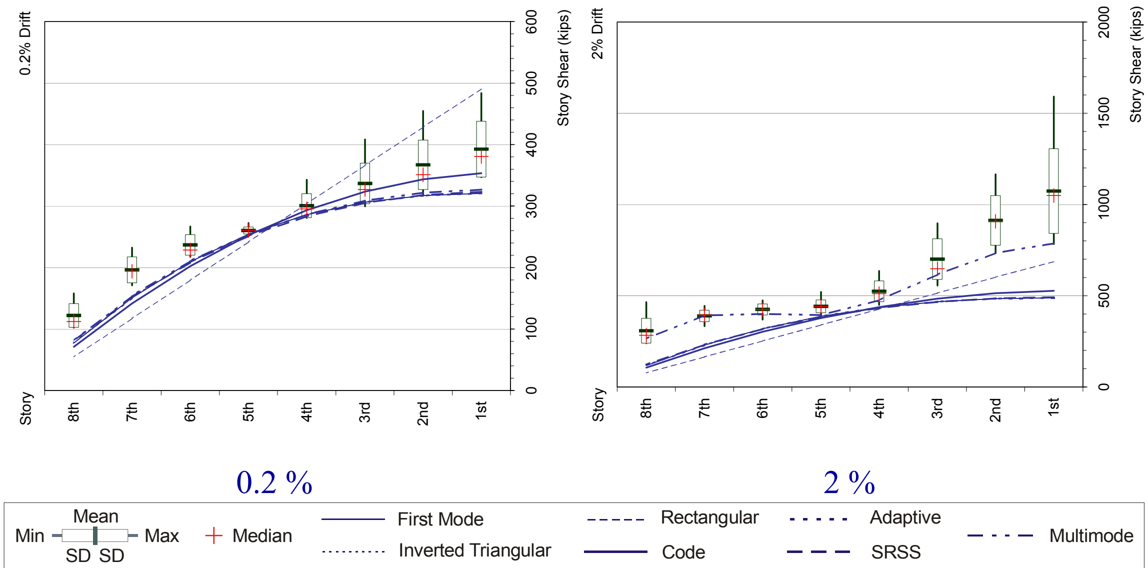

Figure 12: Example results from MDOF examples for story shears (from Aschheim 2002).

Overturning moment

Underestimated by quasi-first mode techniques

MPA is can be accurate, but can also significantly underestimate or overestimate overturning moments.

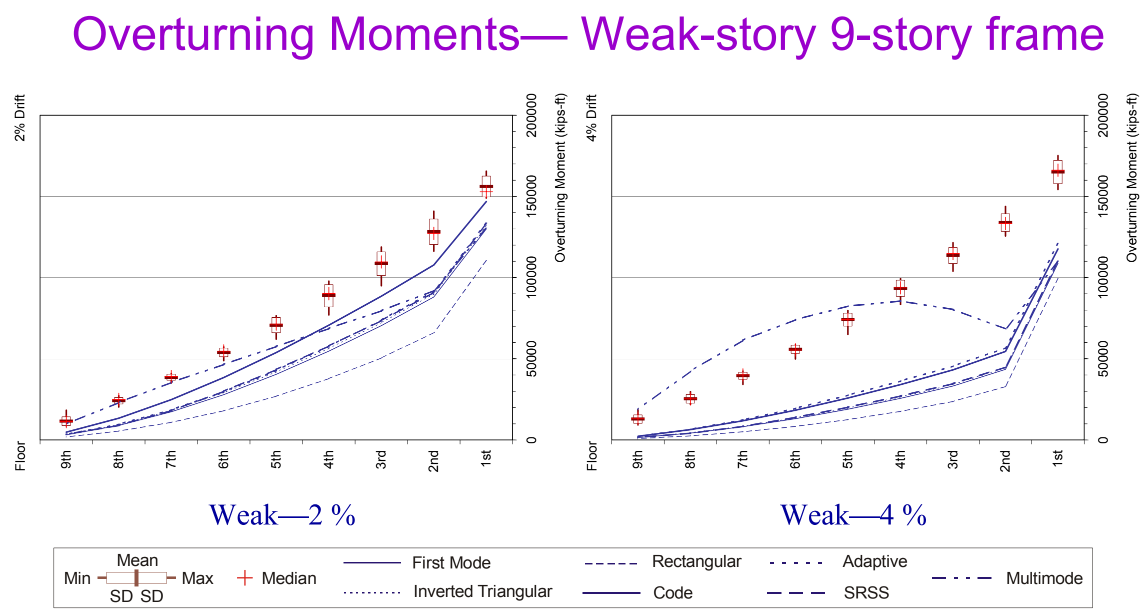

Figure 13: Example results from MDOF examples for overturning (from Aschheim 2002).

Key observations and implications

Displacement response usually is dominated by a first mode. Displacements are estimated well.

Pushover analysis shows weak story mechanisms that do not always occur dynamically.

ESDOF estimates:

For positive post-yield stiffness: are slightly conservative, are applicable to ordinary and near-field motions.

For negative post-yield stiffness, ESDOF estimates can be much too large.

Peak displacements generally estimated well by all load vectors. Complex or multiple load vectors are not needed.

Errors for interstory drifts, story shears, and overturning moments can be substantial. Complex or multiple load vectors still do not give reliable estimates.

SHORT PERIOD EFFECTS

FEMA 356 currently contains limitations (caps) on the maximum value of the coefficient C_1, the ratio of the maximum inelastic displacement of a single degree of freedom elasto-plastic oscillator to the maximum response of the fully elastic oscillator. The authors of *FEMA 356* apparently included the capping limitations for two related reasons. First, there is a belief in the practicing engineering community that short stiff buildings simply do not respond to seismic shaking as adversely as might be predicted analytically. Secondly, authors felt that the required use of the empirical equation without out relief in the short period range would motivate practitioners to revert to the more traditional, and apparently less conservative, linear procedures. Although there may be technical justification for limitations on the maximum value of C_1 particularly for short period structures, the current limitations are not adequately founded on theoretical principles or empirical data. Capping leads to prediction of maximum inelastic displacements that are less than the current empirical relationship by a margin that varies widely depending on period, strength, and site conditions. For periods of interest for most buildings (>0.3 sec. or so), the margin ranges from relatively small (<20%) for firm (Class B) sites to rather large(>200%) for soft (Class E) sites (see Figure 14).

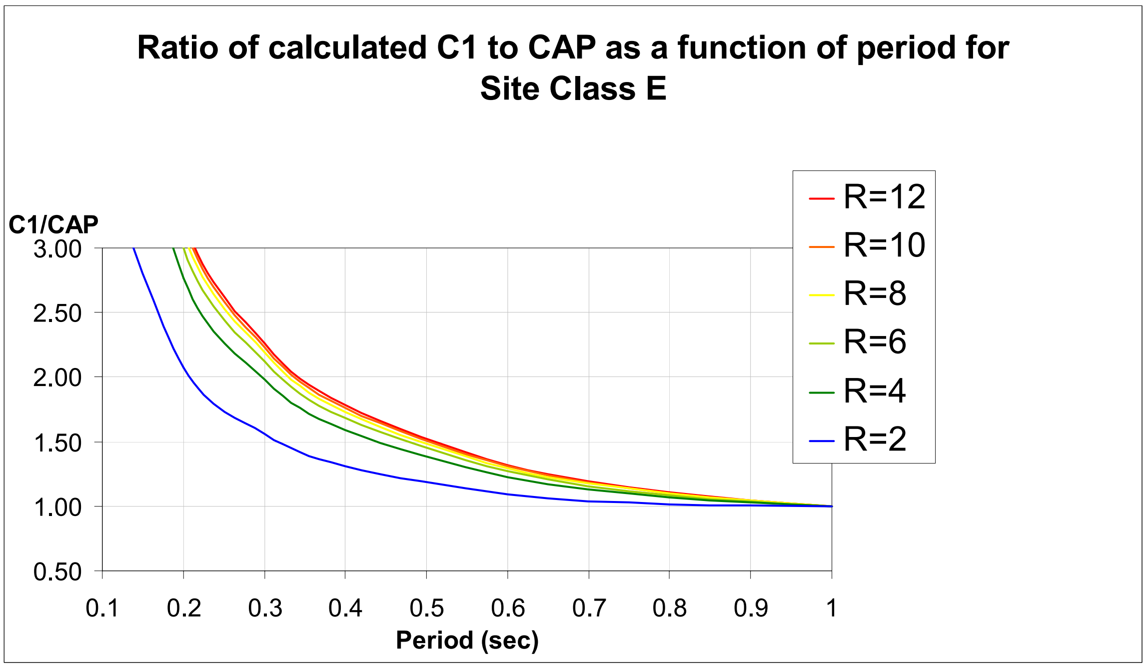

Figure 14: Example of error introduced by capping

There are several interrelated reasons why inelastic displacements for apparently short period buildings might be less than predicted by nonlinear analyses of idealized SDOF systems.

1. Practicing engineers tend to neglect the ascending branch of design spectra when considering first mode response and use the acceleration plateau in this region, assuming that period lengthening resulting from nonlinear behavior will shift the structure to the spectral plateau, during response.

2. Short, stiff buildings generally are more sensitive to interaction between soil material strength and stiffness with that of the structure and its foundations than are longer period structures.

3. Radiation and material damping in supporting soils cause the motion imparted to structures to differ from that of the free field.

4. Full and partial basements, and foundation depth more generally, can modify the motion that a structure feels compared to that in the free field.

5. Building foundations can act as filters effectively cutting off motions at a characteristic period related to the plan dimension of the foundation relative to the shear wave velocity of the supporting soils.

6. Conventional structural analysis procedures lump building masses at floor and roof levels.

The ATC 55 Project is investigating these in a effort to provide guidance and practical procedures for including short period effects more rationally in inelastic analyses. This effort is funded by the Pacific Earthquake Engineering Research Center and is being done under the direction of Jonathan Stewart at the University of California, Los Angeles.

REFERENCES

Aschheim, M., T. Tjhin, and M. Inel, ATC-55 MDOF Studies (ATC 55 draft working paper), University of Illinois-Urbana, 2002

ATC, 1996, *The Seismic Evaluation and Retrofit of Concrete Buildings, Volume 1 and 2*, ATC-40 Report, Applied Technology Council, Redwood City, California.

BSSC (2000), *A prestandard and commentary for the seismic rehabilitation of buildings*, prepared by the Building Seismic Safety Council; published by the Federal Emergency Management Agency, FEMA 356 Report, Washington, DC.

Comartin, C.D., ATC 55: Evaluation and Improvement of Inelastic Seismic Analysis Procedures, US-Japan Workshop, Seattle, August, 2001.

Iwan, W. D. (1980). Estimating inelastic response spectra from elastic spectra. *Intl. J. Earthq. Engng. and Struc. Dyn.*, **8**, 375-388.

Iwan, W. D. and N. C. Gates (1978), The effective period and damping of a class of hysteretic structures, *Intl. J. Earthq. Engng and Struc. Dyn.*, **7**, 199-211.

Iwan, W. D., and A. C. Guyader, An improved equivalent linearization procedure for the capacity spectrum method (ATC 55 draft working paper), California Institute of Technology, Pasadena, California, USA, 2002.

Miranda, E., Evaluation of methods to estimate target displacement in PBEE, 4th US-Japan Workshop on Performance-Based Earthquake Engineering Methodology for Reinforced Concrete Buildings, Toba, Japan, October, 2002a.

Miranda, E., S. Akkar and J. Ruiz-García, Summary of evaluation of current nonlinear static procedures (ATC 55 draft working paper), Stanford University, 2002b.

Miranda, E., S. Akkar and J. Ruiz-García, *FEMA 356* Nonlinear Static Procedure – Proposed Improvements for C1, C2 and C3 (ATC 55 draft working paper), Stanford University, 2002c.

Development of Health Monitoring System for an Existing Building

TESHIGAWARA Masaomi [1], and ISODA Hiroshi [2]

Abstract

The objective of this paper is to propose a hybrid health monitoring system combined a sensing system with analytical modeling system. This study has been conduced under the US/Japan research program on Smart Structure System that started in 1998 as a 5-year project. The health monitoring system applied into the BRI ANNEX building is proposed and discussed. This system consists of four parts; Sensing parts, Analytical parts, Modeling part, and Display part. In the sensing part, acceleration, displacements, strain, and any other information are being measured as many points as possible. In addition, Accelerometer, RWSS[1)], maximum response memory sensor[2)], AE[2)] and so on are planned to be installed. In the analytical part, global seismic performances are calculated. Those are response and capacity computed by spectrum analysis method. Other damage identification methods will be installed in this part. In the modeling part, three-dimensional (3-D) numerical model, such as the one made by the NAStran 3-D, will be installed. The effective parameters are the treatment of non-structural elements and evaluation of yielding stiffness. These two main parameters are modified by the data from sensing and analytical parts. As for the strength, we can estimate it with a very small error. Through the several trial of modification of the modeling, analytical results are displayed. Finally the sensing data and computational results that are the combination of the direct sensing and the analytical modeling are displayed. It's impossible to avoid the change/deterioration of structural performance during the lifetime of building, which is caused by aging, earthquakes and some other actions. We should constantly watch and monitor the structural condition of buildings to keep its required performance. Maintenance and rehabilitation would be operated based on the performance that leads to the balance of total cost/life cycle cost of building.

1. INTRODUCTION

US/Japan Coordinated Research Program on Smart Structure System (SSS) is a 5-year project which started in 1998. SSS is the system with function of Sensing, Processing, and Actuating. These three functions make a structure Auto Adaptive that provides effectively safety and serviceability to the structure. That leads to an improvement of Structural Performance, and Performance Based Maintenance and Sustainable Structure (see Fig.1).

---

1) Structural Department, Building Research Institute, E-mail: Teshi@bri.go.jp

2) ditto

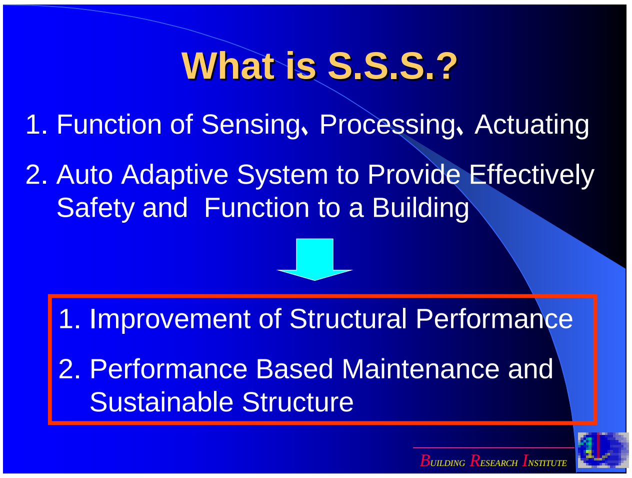

Fig.1 Smart Structure System

In this program, Japan side has set three main research items that are Sensing, Effector, and System. Research plan is tabulated in Fig. 2. These three main research items are based on the definition of an SSS that consists of Sensing, Actuating, and Processing. Research of Processing is considered as common through the research for Sensing, Effector, and System. Research issue of System is unique for Japan side. In this research issue, concept and example of SSS will be proposed. Outputs of each research issues are SSS evaluation Guidelines (GLs, hereafter) for System, Sensor & Monitoring GLs for Sensing, and Usage of Smart Materials GLs for Effectors through the verification by large scale test.

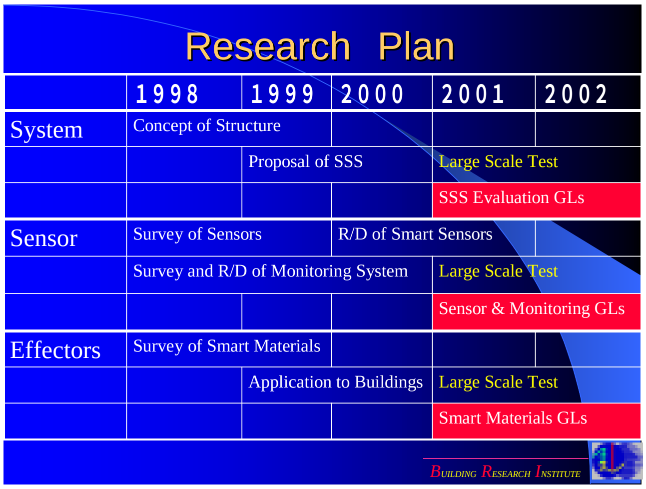

	1998	1999	2000	2001	2002
System	Concept of Structure				
		Proposal of SSS		Large Scale Test	
				SSS Evaluation GLs	
Sensor	Survey of Sensors		R/D of Smart Sensors		
	Survey and R/D of Monitoring System			Large Scale Test	
				Sensor & Monitoring GLs	
Effectors	Survey of Smart Materials				
		Application to Buildings		Large Scale Test	
				Smart Materials GLs	

Fig.2 Research Plan

The objective of this paper is to propose a hybrid health monitoring system combined a sensing system with an analytical modeling system. The health monitoring system applied into the BRI ANNEX building is proposed and discussed. This study has conduced to the Sensor Sub-Committee under the US/Japan research program on SSS.

2. NECESSITY OF HEALTH MONITORING

The change/deterioration of structural performance during the lifetime of building is illustrated in Fig. 3.Aging, earthquake and some other actions decrease the structural performance. We should constantly watch the condition of building to keep its required performance. Aging gradually deteriorates the structural performance. Earthquake damage decreases the structural performance suddenly. At any time, especially after earthquake, structural performance should be evaluated. If performance level would be lower than required one, structural performance should be recovered.

Maintenance, and recovering would be operated based on performance, then that leads to a reduction of total cost/life cycle cost of building

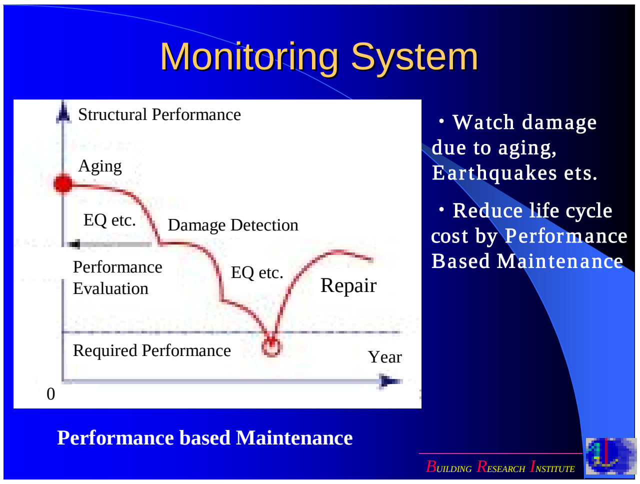

Fig.3 The change/deterioration of structural performance during the lifetime of building

3. CONSTRUCTION OF SYSTEM

Figure 4 is a sketch of monitoring system planned for BRI ANNEX. This system consists of four parts; Sensing parts, Analytical parts, Modeling part, and Display part. In the sensing part, acceleration, displacements, strain, and any other information are being measured as many points as possible. In addition, Accelerometer, RWSS[1), Maximum response memory sensor[2) AE[2) and so on are planned to be installed. In the analytical part, global seismic performances are calculated. Those are response and capacity of building computed by spectrum analysis method. Other damage identification methods will be installed in this part. In the modeling part, 3-D numerical model, such as the one made by the NAStran 3D, will be installed.

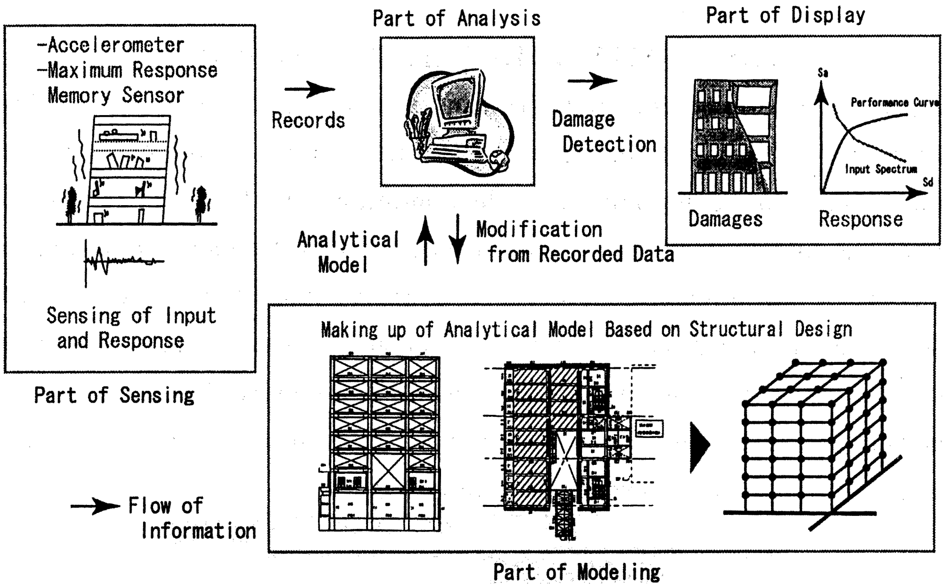

Fig. 4 Proposed hybrid monitoring system

The effective parameters on the modeling are non-structural elements and evaluation of yielding stiffness. These two main parameters are modified by the data from sensing and analytical parts. Through the several trial of modification of the modeling, analytical results are displayed, and so is the damage condition of each member on which any sensor has not been installed yet. Finally the results of sensing and computational results by the combination of the direct sensing and the analytical modeling are displayed.

(1) Verification of Model at initial stage

In order to make an appropriate model to trace the behavior during earthquakes, parametric study based on structural design document Implementation is conducted following the flow shown in Figure 5. At first, the finite element model including non-structural elements is prepared, and then the frame model to trace the result of finite elements model is made. Some earthquake response records is analyzed. Response spectrum is computed. These data are input into the frame model, and the response is also computed. Based on the comparison between records and the results of analysis for the model, finite element model is modified. This effort is continued until analysis corresponds to records. The pushover analysis is conducted to this final model. Earthquake records analyzed so far are shown in Table 1. Maximum accelerations on the basement were less than 30 cm/sec^2. It is expected that the structure still remains in linear range.

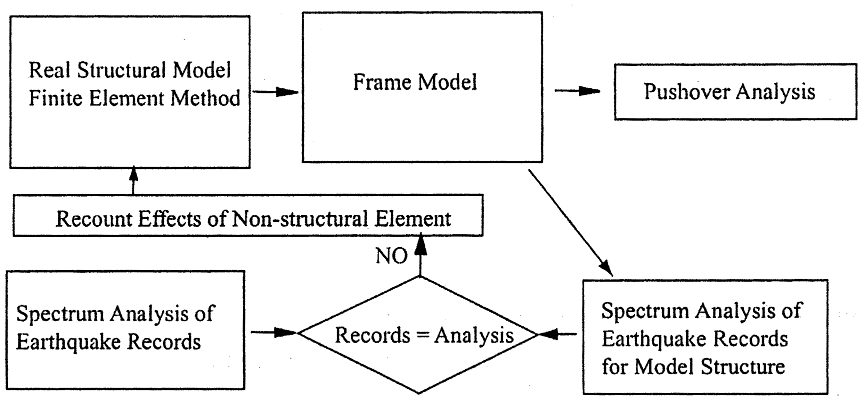

Fig. 5 Flow of analysis

Table 1 Earthquake records

No.	Date	Magnitude	Depth	Distance	Max.Acc
1	06/24/98	4.6	73km	2.2km	14.3gal
2	08/29/98	5.1	67	58.4	6.4
3	11/08/98	4.6	78	57.7	3.2
4	03/26/99	4.9	58	60.4	27.7
5	04/25/99	5.1	58	62.4	25.1
6	07/15/99	4.9	56	42.1	4.2
7	08/09/99	4.4	116	34.3	3.6

Effect of non-structural element

The numerical model corresponding with records was the 3-D model including non-structural element such as finishing and wing walls. Two-dimensional waves were input into this model. Figure 6 shows the example of response spectrum compared with records and analysis.

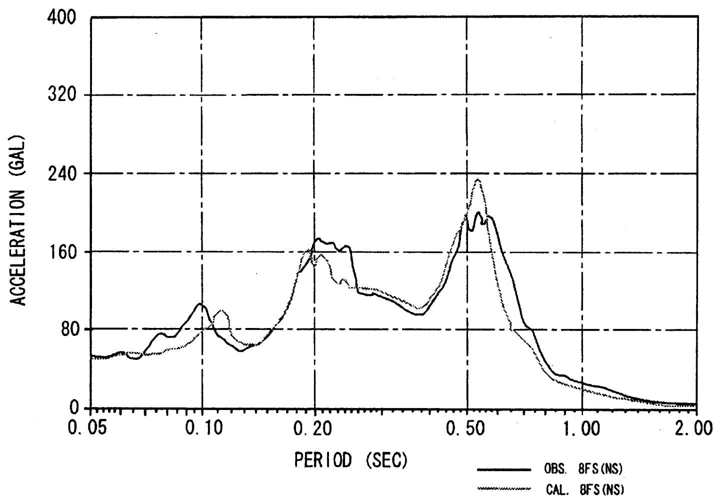

Fig.6 Comparison of records and analysis

Expected damage parts by push-over analysis

Figure 7 shows the result of the push-over analysis. It is expected that damaged will be occurred to the different components in accordance with the change of the external lateral force distributions along the height of building. Here the external lateral force distribution that has been widely used as structural design is adopted. In case of analysis for estimating effects of non-structural elements, wing walls in Figure 8 were considered. But in push-over analysis they were ignored. The capacity of shear force is shown in figure 7 as a result of analysis. The failure mechanism came into existence in the column base of second floor and beam edges on from the third floor to the six floor at the base shear coefficient of 0.52 in the X direction. In Y direction, the same failure mechanism is expected at the base shear coefficient of 0.57. Figure 8 shows the components where yielding is expected earlier than at any others. Smart sensors will be installed in these expected damage components.

(2) Evaluation of Total Seismic Performance

In the analytical part, total seismic performances of buildings, that are response and capacity, are calculated based on a spectrum analysis method[3)]. The total seismic performance is displayed in the right top corner in Fig. 4. Other damage identification methods will be installed in this part as well. In order to evaluate total seismic performance, minimum two accelerometers are necessary, that are installed at the base and top as shown in Fig. 10. From the data of the accelerometer at the base, response spectrum will be obtained. From the data of two accelerometers, response of building will be calculated by the spectrum method where a specific deformation mode is assumed. This method is the base of a new calculation method, "Calculation of Response and Limit Strength", specified in Japan Building Code (JBC) revised in 2000. If more than two accelerometers would be installed in a building, mode shape would be more precise.

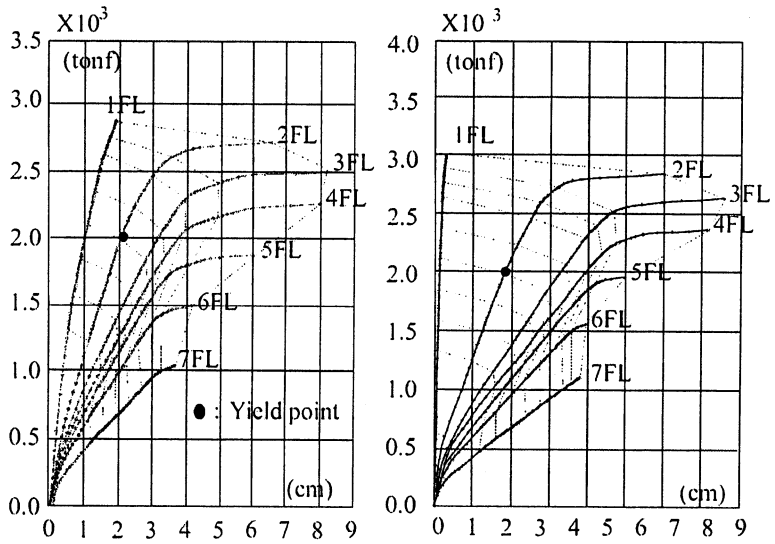

Fig. 7 result of push-over analysis

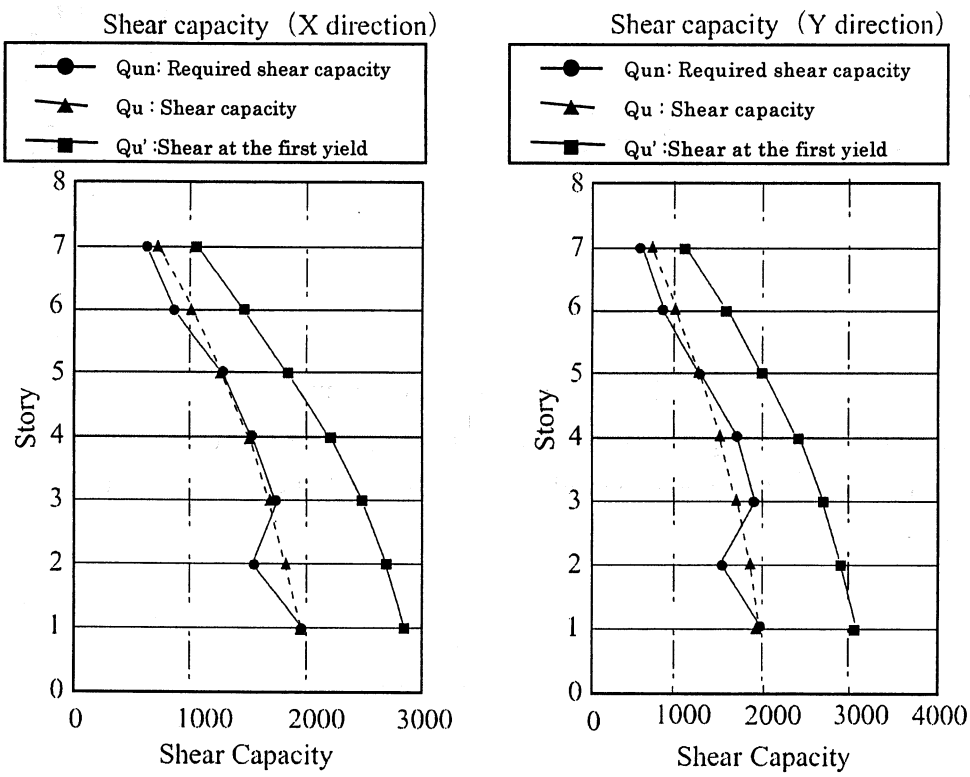

Fig. 8 Shear capacity

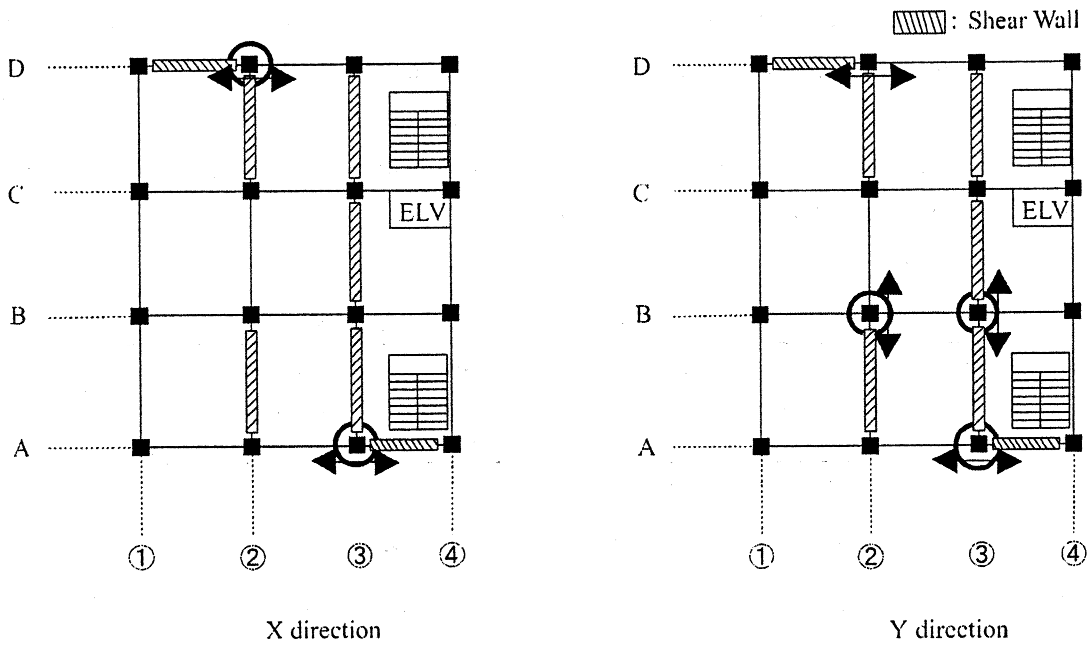

Fig. 9 Vulnerable components

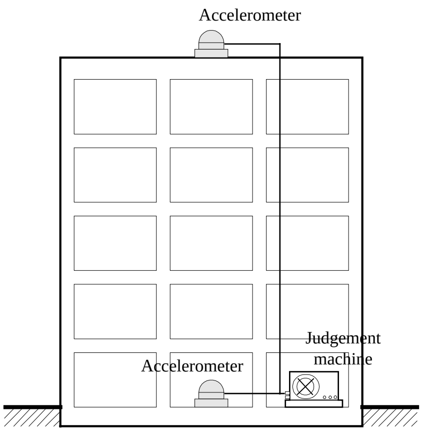

Fig. 10 Minimum configuration of system for analytical part

Figure 11 is a performance curve of building and a required performance curve against an earthquake. There is some damping in the response of a building, so that required performance curve is reduced according to the amount of damping as shown in this figure. And we can get the response point as the cross point of these two curves, that are performance and required curves.

We can judge the seismic performance of the building by following steps,
1) extending the performance curve line until its limit deformation (approximately limit deformation is assumed by construction year and construction method),
2) in case of the limit point being beyond the spectrum of main shock, this building is judged to be safe, otherwise dangerous.

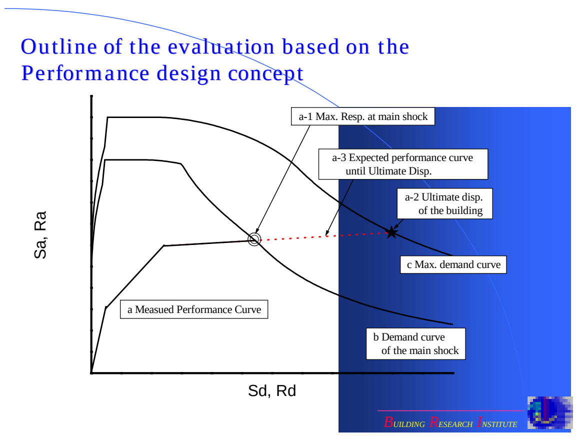

Fig. 11 Outline of the evaluation based on the calculation of response and limit strength in JBC

Figure 12 shows the correlation between this method and the shaking test. Black line shows test data, and red line shows this method. This method can follow the test result.

Solid and this line in Fig. 13 shows required performance, that is response spectrum, and marked Line is capacity spectrum. In this case this building is unsafe and is estimated to suffer large damage. Test results also show large damage.

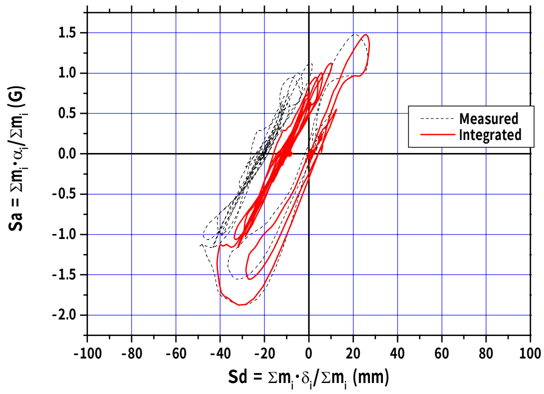

Fig.12 Shaking table test

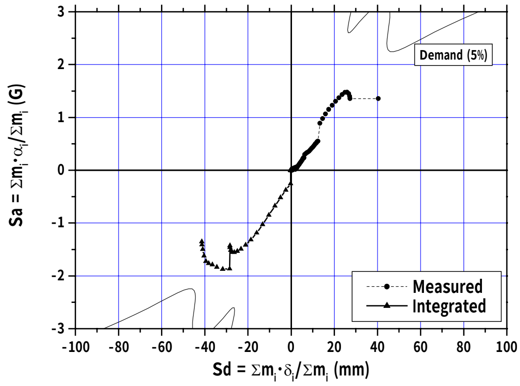

Fig. 13 Demand and performance curve

(3) A Display part

This is an example display of sensing data. We can choice the installed sensor, and display the data. This is also an example display of analytical part. Much information of all structural members are calculated and displayed. Lower left is total performance of building, and lower right is condition of specific member.

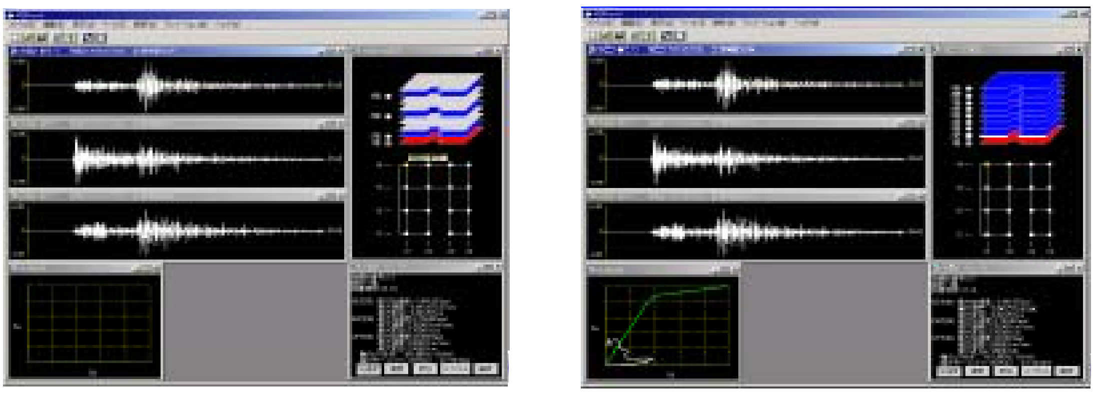

(a) sensing results (b)analytical and modeling results

Fig. 14 Example of health monitoring display

5. CONCLUSIONS

A hybrid health monitoring system combined a sensing system with analytical modeling system is proposed.

1) This system consists of four parts; Sensing parts, Analytical parts, Modeling part, and

Display part.

2) Through the direct sensing analytical, and modeling results are displayed, the damage condition of each member on which any sensor has not been installed yet. And,
3) Maintenance and rehabilitation would be operated based on the performance that leads to the balance of total cost/life cycle cost of building.

REFERENCES

[1] Noguchi K., Kaminosono T. and Sakata K.," U.S.-Japan Cooperative Research Project on Smart Structure System (Part 23: Experimental study on Damage detection by Reduced-wiring system)", Architectural Institute of Japan, B-2, 2001, pp.227

[2] The report of U.S.-Japan Cooperative Research Project on Smart Structure System, 2001

[3] Teshigawara M. and Kusunoki K. "Development of Real-time Residual Seismic Capacity Evaluation System", Workshop on Smart Structural Systems organized for U.S.-Japan Cooperative Research Programs on Smart Structural Systems (Auto-adaptive Media) and Urban Earthquake Disaster Mitigation, 2002

Building-Specific Seismic Fatality Estimation Methodology

G.L. Yeo and C.A. Cornell[1]

ABSTRACT

We propose a building-specific methodology to estimate the expected annual number of fatalities due to the occurrence of an earthquake. The proposed procedure uses advanced nonlinear dynamic analyses to characterize the damage state of the building, and couples these results with information on the spatial locations of the occupants and the ground motion site hazard curve of the site, to obtain a full probability distribution of the annual number of fatalities due to structural damage. With further development the proposed methodology could become a useful tool for structural design based on optimizing resource allocation.

INTRODUCTION

The number of fatalities is one of the decision variables adopted by PEER (Pacific Earthquake Engineering Research Center) as a basis upon which the seismic adequacy of a specific structure is to be assessed. The objective here is to exploit the detailed nonlinear analysis associated with the assessments envisioned by PEER to enhance the precision of such fatality estimation. If generalized to families of buildings, earthquake fatality estimates are also important for emergency crisis management and broad policy making.

A number of fatality estimation models are available. (See for example, Lee and Ang 96, Murkami 92, Coburn, Spence and Pomonis 92, and Shino, Krimgold and Ohta 91) One of the most recent models for fatality estimation is that developed by Kircher. (HAZUS 99 Technical Manual) It is an extension of the model proposed by Stojanovski & Dong. (Stojanovski & Dong 94) This is the model that is employed in the HAZUS software (Natural Hazard Loss Estimation Methodology) for regional earthquake loss estimation in the U.S. This model is developed in the form of an event tree as shown in Figure 1.

The four damage states correspond to slight, moderate, extensive and complete damage. The formulation of the tree facilitates computation of the probability of an occupant being killed as well as the expected number of fatalities.

In an independent document for FEMA (Kircher 99) aimed at building-specific application, Kircher also proposes a similar model where the focus is on a more specific breakdown of the fourth or "complete damage" state. This breakdown is into a finer set of states more closely associated with fatalities. For this model, given that the building is in a complete

[1] *Department of Civil and Environmental Engineering, Stanford University, Stanford, California. Email:geeliek@stanford.edu*

state of damage, there are four possible collapse failure modes: No collapse, local collapse, story collapse and global collapse. With information on the probabilities of these four states and the fraction of building occupants exposed to them, an estimate of the fraction of occupants exposed to collapse given that the building is in a complete state of damage can be calculated. We follow this general scheme with even finer state breakdowns.

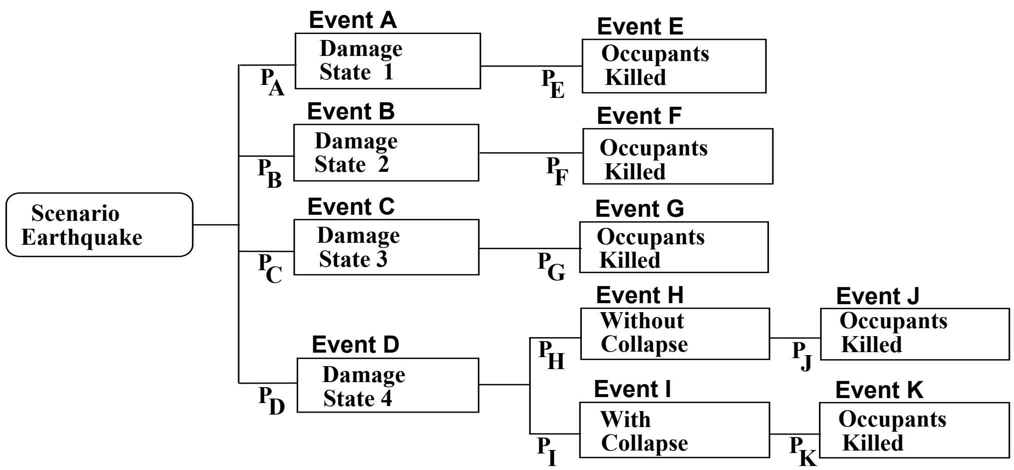

Figure 1: Event Tree for Casualty Estimation in HAZUS

Because initiating earthquakes are low-probability events, there is limited available historical data. Until empirical data is available, an approach is adopted where the results of multiple nonlinear dynamic structural predictions of local and global damage states under a sample of possible ground motion records are combined with limited historical data and professional judgement to obtain an estimate of the required probabilities. The accuracy of the model is dependent on the quality of the information available. The model and its estimates will improve as better structural models and more pertinent empirical data become available.

Current studies by PEER researchers and others into the nonlinear seismic behavior of buildings have significantly improved our ability to predict the performance of a building during an earthquake. PEER's research efforts have led to improved methodologies for the prediction of various damage cases. The HAZUS fatality estimation procedure does not take into account the actual design of the building in the prediction of earthquake fatalities. Kircher (99) does so via a deterministic nonlinear static pushover analysis. In this study, we shall use a building-specific model, nonlinear time history analyses, and multiple records that will permit probability estimates.

Neither HAZUS nor the later Kircher model considers the location and behavior of the occupants during an earthquake. According to Kircher, up to half the occupants on the first floor of a typical building will have sufficient time to escape during an earthquake. Personal communication with Krimgold also indicates that occupants have a tendency to react to the earthquake by escaping towards the stair cores. The stair cores, which may be enclosed by shear walls, may well have a lower likelihood of collapse than the remainder of the structure. Incorporation in the assessment of such observed occupant behavior, coupled with the predicted behavior of the building, will improve the validity of the fatality estimates. Also, given the above-mentioned behavioral trait demonstrated by occupants, the stairwells could, in response, be especially designed to be more robust so that the survival rates of occupants can be increased.

METHODOLOGY

Quantitative risk assessments (QRA) are common in the offshore industry where life safety risks on offshore platforms are often explicitly evaluated using event trees. Initiating events resulting in damage and/or failure of the system (fires, earthquakes, blowouts, etc.) are considered one by one in the risk assessment. The spatial distribution of personnel at the time of occurrence of the initiating event (be it global or localized) as well as possible escape and evacuation procedures are taken into consideration in the analysis. Also considered in the QRA are the time required for escape/evacuation and the temporal progress of the initiating event as its effects propagate through the system. A probabilistic estimate of the resulting number of fatalities is evaluated. (Vinnem 99)

Motivated by this approach, we propose a building-specific model that would take the above factors into consideration for earthquake fatality estimation due to structural collapses, both local and global. The model is divided into two distinct parts: Occupant Spatial Location and Building Fatality Potential. These factors are independent of each other; the results from both models are combined to provide us with a probabilistic estimate of the annual number of fatalities due to earthquakes. These two factors will next be described in details.

Occupant Spatial Location

The number and location of the occupants in the building play an important role in earthquake fatality estimation. The number of earthquake fatalities is highly dependent on the time of occurrence of the earthquake, the function of the building as well as the individual floor level usage, the level of the building in consideration, structural spatial discontinuities, the value of the full-occupancy population as well as occupant behavior during the earthquake. For example, if the earthquake happens late at night, the estimation of earthquake fatalities in a residential building would be much higher than that of a commercial office building. Such effects as well as the uncertain value of the full-occupancy population can be dealt with by a simple event tree and weighting of the results for individual cases; therefore we shall not pursue this further in this paper. As another example, an office building may have certain floors used for storage and/or mechanical equipment purposes. Such areas usually have a smaller number of occupants. The proposed model enables one to account for such situations.

Spatial variability of occupants is especially important when it correlates with structural variations. There are also examples of structural spatial discontinuities that exist in buildings, which, coupled with the presence of a high concentration of occupants for a significant proportion of the time, might lead to an increased estimate of the number of fatalities at that location. Examples of such spatial discontinuities are the lecture halls in academic institutions, where their main function is to accommodate a large concentration of occupants over an extended period of time during the day. Such lecture halls usually have larger spans and higher ceilings as compared to the rest of the building, resulting in a discontinuity in the structural spatial configuration. Such spatial irregularities, when considered with the fact that lecture halls are commonly located on the first floor of the building, may result in the formation of soft stories during an earthquake. This condition may significantly increase the probability of collapse of the first story. Also, because there is a constant high concentration of occupants in that location during the day, such spatial discontinuities may significantly increase the predicted number of fatalities over those estimates based on simple averages over many buildings.

The last factor to consider is occupant behavior during an earthquake. Despite warnings to take cover, building occupants are known to have a tendency to move towards exits such as the stair cores during an earthquake. Hence, we expect a higher concentration of occupants near the stair cores as compared to the rest of the building. If the stair cores (which, may, for example, be reinforced concrete shear walls) perform better than the rest of the building, the percentage of survivors will be higher compared to the case where the occupants remain in their original locations. The proposed model enables us to consider such behavior when estimating the number of fatalities.

Proposed Methodology to Quantify Occupant Spatial Location

In order to take the above-mentioned factors into consideration when estimating the number of earthquake fatalities, we propose to model the number and location of the occupants by dividing the floor area into smaller grid areas. One recommended grid size is the area supported by four adjacent columns. As a first step of our analysis, we need to obtain estimates of the expected number of occupants per grid area for all the grid areas in the building. This involves the estimation of a "snapshot" of the locations of all building occupants at the end of the earthquake. For example, for the SAC three story steel moment-resisting frame (SMRF) building, a typical floor can be divided into 24 grid areas as shown in Figure 2. Assuming 150 people on each floor and that the occupants are spatially uniformly distributed, the expected number of occupants per grid area is 6.25.

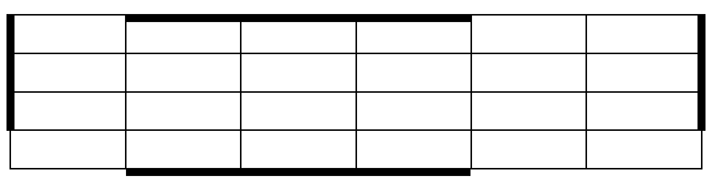

Figure 2: Typical Floor of SAC Building and Proposed Grid Areas

Dividing the floor area into smaller grid sizes will allow us to take the above-mentioned factors into consideration. For example, we could assume a density higher than average near exits and lower elsewhere.

Building Fatality Potential

A second independent factor that needs to be taken into consideration is the building fatality potential. This is analogous to the damage states of the building as described in the HAZUS methodology. (Figure 1) Motivated by Kircher's approach but further extending it to a level of finer detail, we develop our model based first on the four damage states defined by Kircher: no collapse, local collapse, story collapse and global collapse.

To predict the likelihood of performance levels of the structure, including the state of each grid, and to estimate the number of fatalities under earthquakes of different intensities, we perform "multiple-stripe" nonlinear dynamic analyses. This term implies that we perform a number of nonlinear dynamic analyses of the structure using a sample (in our example to follow, of size ten) of ground motions scaled to a common ground motion intensity level (here, first-mode period Sa) value, collect the information on the damage sustained by the structure in terms of appropriate engineering demand parameters (EDPs), scale up the ground motion to a higher Sa value, and repeat the process. (Jalayer and Cornell, 2002)

As an example to be used in an illustration to follow, for a steel moment-resisting frame structure, we propose to predict the state of the damaged building based on the complete set of beam-end rotations sustained by the structure. Each beam rotation is then compared to its rotational capacity, which is assumed to be uniformly distributed between 0.05 radians and 0.09 radians. Beams with rotations greater than their respective (randomly generated) rotational capacities are assumed to have failed in shear, resulting in the collapse of the slab that it supports and the death of the occupants located under the area. These represent local collapses. Of course, the simple assumption made here that all occupants below the failing slab die is surely conservative; here is one critical location where carefully collected post-earthquake empirical data can improve the assumptions within this model.

We can also look at other possible failure modes of the building. For example, we can look at individual story collapses, as observed in Kobe, or global collapses, as the SAC project did. The flexibility of the proposed methodology allows one or a combination of such failure modes together with, for example, the local shear failure, slab-collapse cases. In the example, one could also look at other EDPs to determine the types of collapse sustained by the structure. For example, the peak inter-story drifts could be used to determine if the building is in a state of story collapse. As global instability assessments might use the slope obtained from incremental dynamic analysis (IDA) (Yun et al, 2002 and Vamvatsikos and Cornell, 2002), all these cases of damage states can be collected from the "multiple-stripe" analyses. From each given level of the "multiple-stripe" nonlinear dynamic analyses, we use the observed frequencies to estimate the conditional probabilities of the different damage states "conditional on" or given that Sa level. We identify in each case, first, whether the building is in one of the mutually exclusive damage states: a local collapse state, a story collapse state, or the building-wide, global collapse state. The fraction of the records in which the building is in, say, the global collapse state is an estimate of this conditional probability given this intensity level.

Consider next those cases when the structure is in a state of story collapse. There is a number of mutually exclusive collapse "scenarios" that we can envision. For example, given a state of story collapse, there are six possible "scenarios" at any particular Sa level: only the first story collapses, only the second story collapses, only the third story collapses, only the first and second story collapse, only the first and third story collapse and only the second and third story collapse. (If all collapse, it is a global collapse.) A similar set of (many) individual "scenarios" exists for the state of local collapse. These will be illustrated below. Computers make the bookkeeping straightforward.

Fatality Estimation

After obtaining the expected number of occupants per grid area and the conditional probabilities of the damage states, we can estimate the expected number of fatalities. For any particular floor level in consideration, we assume that all the occupants who are located directly under a collapsed floor slab will be killed. Since we have performed a number (e.g., ten) of nonlinear dynamic analyses at any particular Sa level, we can easily obtain the expected or average number of occupants who are killed at any floor level given any particular damage state. (or given any possible collapse "scenario" if the building is in a state of story collapse or local collapse) We can also obtain its corresponding standard deviation.

Denoting the set of ground motions that result in collapse "scenario" k and damage state j at Sa level i by Ω, where n = number of ground motions in Ω, CS_k = collapse "scenario" k, DSj = damage state j, Sa_i = Sa level i and X_l = number of occupants killed on floor level l, then

$$E[X_{\text{level l}} \mid CS_k, DSj, Sa_i] = \frac{1}{n}\sum_{\Omega} X_{\text{level l}} \mid CS_k, DSj, Sa_i \qquad (1)$$

$$E[X^2_{\text{level l}} \mid CS_k, DSj, Sa_i] = \frac{1}{n}\sum_{\Omega} X^2_{\text{level l}} \mid CS_k, DSj, Sa_i \qquad (2)$$

$$\text{Also,} \quad E[X|Sa_i] = \sum_j\sum_k\sum_l E[X_{\text{level l}} \mid CS_k, DSj, Sa_i]P[CS_k|DS_j, Sa_i]P[DS_j|Sa_i] \qquad (3)$$

$$E[X^2| Sa_i] = \sum_j\sum_k\sum_l E[X^2_{\text{level l}} \mid CS_k, DSj, Sa_i]P[CS_k|DS_j, Sa_i]P[DS_j|Sa_i] \qquad (4)$$

$$\sigma_{x|Sa_i} = \sqrt{E(X^2 \mid Sa_i) - (E(X \mid Sa_i))^2} \tag{5}$$

If we assume that the number of occupants killed at a given Sa level can be represented approximately by a lognormal distribution matching the mean and standard deviation given by the above expressions, we can sum these several distributions weighted by the likelihood of each Sa level, as obtained from a site probabilistic hazard curve, to obtain the function P(number of occupants killed > x). Given the hazard curve, we can also obtain the expected number of people killed and the standard deviation of the number of people killed by:

$$E(X) = \sum_i E[X \mid Sa_i]P[Sa_i] \tag{6}$$

$$E(X^2) = \sum_i E[X^2 \mid Sa_i]P[Sa_i] \tag{7}$$

$$\sigma_x = \sqrt{E(X^2) - (E(X))^2} \tag{8}$$

ILLUSTRATION

To demonstrate the methodology, we consider the three-story post-Northridge SAC steel building developed as part of the SAC project (Gupta and Krawinkler 99). We assume 150 occupants/floor, with half the people on the first floor being capable of escaping in an earthquake. A typical floor layout divided into 24 grid areas is shown in Figure 2. The expected number of occupants/grid area is computed assuming uniform distribution of occupants, with 6.25 occupants/grid area on the second and third floors, and half that on the first floor.

We perform ten nonlinear dynamic analyses of the structure for each Sa level from 0.4g to 4.0g. At each Sa level for every ground motion, we classify the building into the appropriate damage state by looking at the "snapshots" of the building on all floors. Such an assessment is based on the comparison of the beam rotations with random beam capacities described earlier.[2] We can estimate the number of people killed based on these "snapshots". For example, at Sa = 1.6g with ground motion number 1, the following "snapshots" are obtained for the 3 floors of the building. The shaded areas indicate the slabs that have collapsed. From the "snapshots" below, we can conclude that the building is in a state of local collapse[3]. The number of collapsed grid areas for the first, second and third floor is equal to 5, 7 and 22 respectively. Thus the number of people killed on the first, second and third floor is equal to 15.625, 43.75 and 137.5.

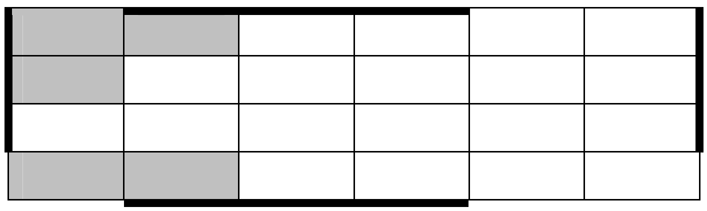

First Floor of Building

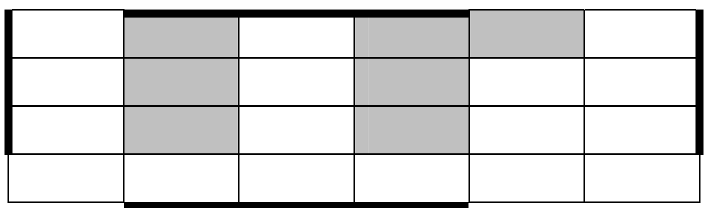

2nd Floor of Building

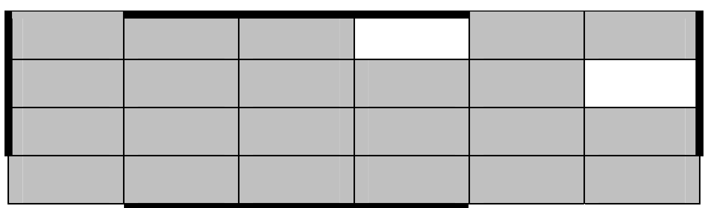

3rd Floor of Building

Figure 3: Collapsed Grid Areas for Ground Motion 1 at Sa = 1.6g

After the bookkeeping described above, we obtain Figure 4. We adopted a simplified ground motion site hazard curve for the purpose of illustration that has a 2% chance in 50 years of exceeding a one-second spectral acceleration of 1.5g. If we assume further that the number of occupants killed at a given Sa level can be represented by a lognormal distribution, we obtain Figure 5 after numerical integration. The intercept on the y-axis provides us with the annual probability of any loss of life. (i.e., more than zero lives) The expected annual number of fatalities is estimated to be 0.06. These numbers are only illustrative; they should not be taken out of context. We also performed a disaggregation of the expected number of fatalities with regard to the type of collapse and the Sa level. The complete disaggregation is shown in Figure 6. For example, the figure states that local collapse contributes 61% to the expected annual

---

[2] The simplified example above serves only to illustrate the proposed methodology. Bilinear beam and column hinge models are used. Shear connection failures are predicted from moment rotations with no interaction between moments and shear forces. Two-dimensional frame analyses are used to estimate three-dimensional responses. Only the longitudinal direction is considered.

[3] For simplicity of illustration, it was assumed here that if an interior connection failed, then both adjacent slabs failed, and that floor collapse required all slabs on a floor to fail, and global collapse required all floors to fail.

number of fatalities, story collapse contributes 18% and global collapse contributes 21%, while local collapse at a Sa level of 1.6g contributes almost 26% to the expected annual number of fatalities. These numbers are very dependent on the simplified definitions of rotational capacity and of story and global collapse adopted for the illustration and should not be considered accurate.

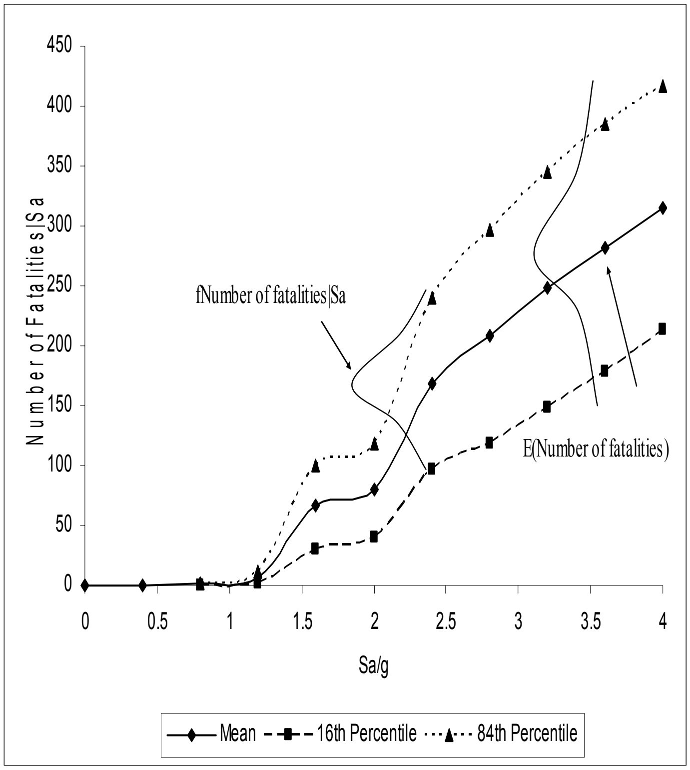

Figure 4: Distribution of Annual Number of Fatalities at different Sa

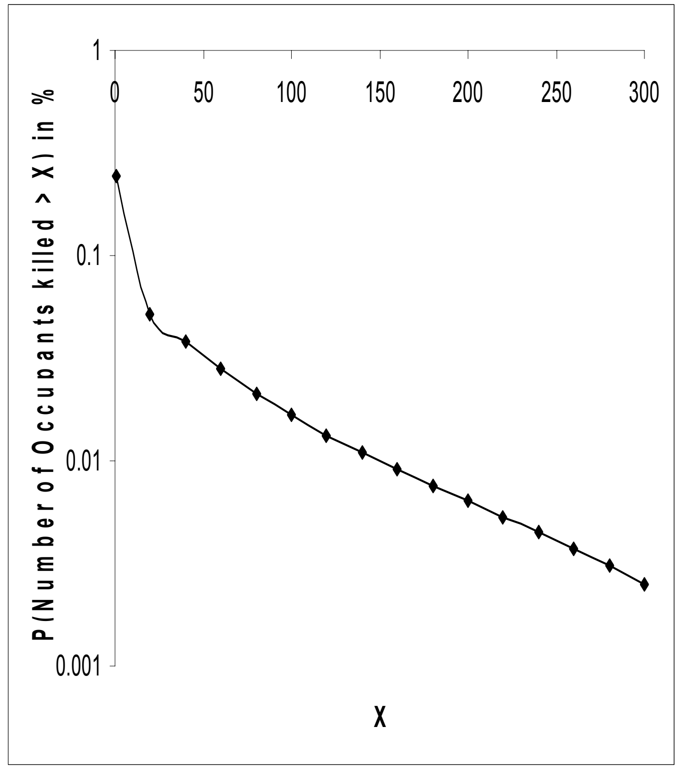

Figure 5: Distribution of Annual Number of Fatalities

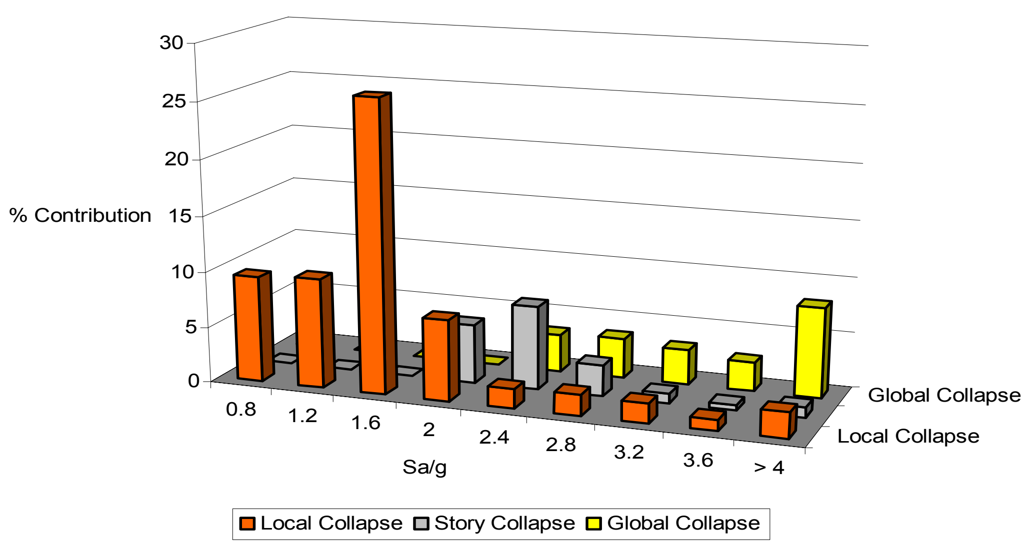

Figure 6: Disaggregation of Expected Fatalities with respect to Collapse Type & Sa values

CONCLUSION

We propose a building-specific methodology to estimate the expected value and the probability distribution of the annual number of fatalities due to earthquakes. The proposed procedure uses advanced nonlinear dynamic analyses to characterize detailed damage states of the building, and couples these with information on the spatial locations of the occupants, to obtain these results. Such information is a proposed component of the performance-based earthquake assessment procedures under development at PEER. Fatality and injury estimates will be coupled with parallel economic loss estimates and with more traditional limit-state information.

RECOMMENDATION FOR FURTHER STUDY

The proposed procedure provides a full probability distribution of the annual number of fatalities due to local and other structural collapses. We have not considered explicitly fatalities due to other causes such as non-structural failures, leakages of hazardous waste materials or non-fatal injuries. The proposed method of characterization of the spatial location of the occupants may prove useful, however, in evaluating the number of fatalities and injuries due to all such causes. In applying the above procedure to non-structural fatalities and injuries, other EDPs may need to be used to characterize the damage state of the building. An example is peak floor accelerations for non-structural content-related deaths.

To obtain more accurate estimates of the number of fatalities, this model highlights the need for the development of more advanced structural models to predict the damage states of the structure at both local and system levels. The propagation of local failures to partial and full system failure needs to be represented more faithfully than current modeling aims at. With the development of such an engineering-oriented fatalities estimation model, it is important to obtain data to calibrate (estimate parameters) and validate the accuracy of the model. A public health research group in UCLA, led by Dr. Kimberly Shoaf and Ms. Hope Seligson (Reference 15), is developing a standardized classification scheme for earthquake-related fatalities, including injury mechanisms and building damages. Data for earthquake-related fatalities is being collected through interviews. The survey forms such as theirs could be modified to obtain more detailed information on occupant spatial locations and building damage state characterizations as a means to calibrate and validate the accuracy of our proposed model. It can be hoped that such models will stimulate and guide data collection, and that new data will in turn encourage still better models.

ACKNOWLEDGMENT

The authors acknowledge the use of a nonlinear dynamic analysis software and three-story post-Northridge SAC model from Professor Charles Menun in Stanford University. Financial support by PEER (project number 3202001) is greatly appreciated.

REFERENCES

1. Benjamin, J.R., and Cornell, C.A. (1970). *Probability, Statistics and Decision for Civil Engineers.* McGraw-Hill Book Company, New York.
2. Coburn, A.W., Spence, R.J.S. and Pomonis, A. (1992). Factors determining human casualty levels in earthquakes: Mortality prediction in building collapse. *Proceedings of the 10th WCEE, Balkema, Rotterdam*:pp 5989-5994.
3. FEMA 351. (2000). *Recommended Seismic Evaluation and Upgrade Criteria for Existing Welded Steel Moment-Frame Buildings*. SAC Joint Venture for the Federal Emergency Management Agency, Washington, DC.
4. Gupta, A., and Krawinkler, H. (1999). *Seismic demands for performance evaluation of steel moment resisting frame structures*. John A. Blume Earthquake Engineering Report No. 132.
5. HAZUS 99 Technical Manual. (1999). Federal Emergency Management Agency, Washington, DC.
6. Jalayer, F., and Cornell, C.A. (2002). Alternative Nonlinear Demand Estimation Methods for Probability-Based Seismic Assessment. *To be submitted to Earthquake Spectra*.
7. Krimgold, F. (2002). Personal Communication. Comments on Fatality Issues.
8. Lee, J.C. and Ang, A. H-S. (1996). *Reliability-Based Cost-Effective Aseismic Design of Reinforced Concrete Frame-Wall Buildings.* Ph.D. Dissertation, University of California at Irvine, Irvine, CA, U.S.
9. Lee, K. and Foutch, D. A. (2000). *Performance Prediction and Evaluation of Steel Special Moment Frames for Seismic Loads.* SAC Background Document SAC/BD-00/25, SAC Joint Venture, Richmond, CA.
10. May, P. (2002). *PBEE Decision Variable Considerations.* Unpublished PEER Testbed Discussion Summary for Session Held 5/23/02, Richmond, CA: PEER.
11. Murkami, H.O. (1992). A Simulation Model to Estimate Human Loss for Occupants of Collapsed Buildings in an Earthquake. *Proceedings of the 10th WCEE, Madrid, Spain*: pp 5969-5974.
12. Okada, S. (1992). Indoor-zoning map on dwelling space safety during an earthquake. *Proceedings of the 10th WCEE, Balkema, Rotterdam*: pp 6037-6042.

13. Charles Kircher & Associates. (1999). *Procedures for Developing HAZUS-Compatible Building-Specific Damage and Loss Function.* National Institute of Building Sciences, Washington, DC and the Federal Emergency Management Agency, Washington, DC.

14. Rahimi, M. (1992). Classification and analysis of occupant behavior during earthquake shaking. *Proceedings of the 10th WCEE, Balkema, Rotterdam*: pp 5989-5994.

15. Seligson, H.A., Shoaf, K.I., Peek-Asa, C. and Mahue-Giangreco, M. (2002). Engineering-based earthquake casualty modeling: Past, Present and Future. *Presented at the 7th U.S. National Conference on Earthquake Engineering (7NCEE).*

16. Shino, K., Krimgold, F. and Ohta, Y. (1991). A Method for the Estimation of Earthquake Fatalities and its Applicability to the Global Macro-Zonation of Human Casualty Risk. *Proc. 4th International Conference on Seismic Zonation, Stanford, CA, 3:* pp 277-284.

17. Shino, K., Krimgold, F. and Ohta, Y. (1992). Modeling of Search-and-Rescue activity in an earthquake. *Proceedings of the 10th WCEE, Balkema, Rotterdam*: pp 6043-6048.

18. Shoaf, K.I., and Bourque, L.B. (1999). Correlates of Damage to Residences Following the Northridge Earthquake, as Reported in a Population-Based Survey of Los Angeles Country Residents. *Earthquake Spectra, v. 15,* 1:145-172.

19. Stojanovski, P., and Dong, W. (1994). Simulation Model for Earthquake Casualty Estimation. *Proc. 5th U.S. National Conference on Earthquake Engineering, Paper No. 00592, Chicago, Illinois*.

20. Vamvatsikos, D., and Cornell, C.A. (2002). Incremental Dynamic Analysis. *Earthquake Engineering and Structural Dynamics, 31(3):*491-514.

21. Vinnem. (1999). *Offshore Risk Assessment: Principles, Modelling and Applications of QRA Studies.* Netherlands: Kluwer Academic Publishers.

22. Yun, S.Y., Hamburger, R.O., Cornell, C.A., and Foutch, D.A. (2002). Seismic Performance Evaluation for Steel Moment Frames. *ASCE Journal of Structural Engineering, 128(4):*534-547.

SESSION A-2: DEMAND ESTIMATION

Chaired by

♦ Craig Comartin and Masaomi Teshigawara ♦

Evaluation of Approximate Methods to Estimate Target Displacements in Nonlinear Static Procedures

Eduardo MIRANDA[1] and Sinan D. AKKAR[2]

ABSTRACT

Approximate methods included in Nonlinear Static Procedures recommended in ATC-40 and FEMA-356 to estimate target displacements are evaluated. In order to take into account the difference in deformation demands in inelastic and elastic structures ATC-40 uses equivalent linearization while FEMA-356 uses displacement modification factors. Target displacements computed with these approximate methods are compared with results computed with nonlinear response history analyses. A wide range of periods, lateral strengths and hysteretic behaviors is considered in combination with 100 earthquake ground motions recorded in a wide range of site conditions. The bias introduced by these methods is evaluated by computing mean ratios of approximate to exact displacement demands. It is concluded that for short periods structures target displacements computed following the recommendations in these documents can not only be significantly different from each other but also significantly different from results from response history analyses. The equivalent linear procedure implemented in ATC-40 does not adequately address changes in deformations demands produced by changes in period of vibration for systems with short periods of vibration. Meanwhile the upper limit imposed in the inelastic displacement ratio in the coefficient method ignores changes in displacement demands produced by changes in lateral strength in this spectral region. For intermediate and long periods these approximate methods may yield adequate estimations, conservative or unconservative deformation estimates depending on the lateral strength and hysteretic behavior of the system. It is concluded that both types of methods tend to overestimate the variation in deformation demands with changes in the hysteretic behavior of the system. Areas of possible improvements in both methods are identified and discussed.

1. INTRODUCTION

The ATC-40 (ATC, 1996) and FEMA-356 (BSSC, 2000a) documents include simplified nonlinear seismic analysis procedures that are referred to as Nonlinear Static Procedures (NSP). The two approaches use nonlinear static analysis (pushover analysis) to estimate the lateral capacity of the structure. In both procedures the global inelastic deformation demand on the structure is computed from the response of an equivalent single-degree-of-freedom (SDOF) system. Similarly in both methods, for a given ground motion, the maximum inelastic deformation of the equivalent SDOF system is approximated from the maximum deformation of an elastic SDOF system. They differ, however, in the technique used to estimate the target displacement.

The NSP in ATC-40 is based on the Capacity Spectrum Method that was developed using equivalent linearization in which the maximum deformation of an inelastic system is *approximated* as the maximum deformation of an elastic system with a lateral stiffness smaller than that of the initial stiffness of the inelastic system and with a damping ratio larger than that of the inelastic system. On the other hand, the so-called displacement coefficient method in FEMA-

[1] *Assistant Professor, Dept. of Civil and Envir. Engrg., Stanford University, Stanford, CA, USA.*
[2] *Visiting Postdoctoral Scholar, Dept. of Civil and Envir. Engrg., Stanford University, Stanford, CA, USA.*

356 is based on the use of a series of modification factors. In this method the maximum deformation of an inelastic system is *approximated* as the maximum deformation of an elastic system with the same stiffness and same damping ratio as the inelastic system times a displacement modification factor that depends on the lateral strength and period of vibration of the structure.

Various researchers and practicing engineers have more recently found that in some cases simplified procedures in ATC-40 and FEMA-356 may yield for a given system and ground motion substantially different estimates for target displacement demands (Aschheim et al., 1998; Chopra and Goel 1999; MacRae and Tagawa, 2002). The disparities in displacement predictions highlight the need for comparison and further study of these different approaches.

The objective of this manuscript is to summarize the results of an investigation whose main goal was to study the accuracy of the approximate methods recommended in ATC-40 and FEMA-356 to estimate the maximum inelastic deformation demand of SDOF systems using the maximum response of linear elastic systems. This investigation was conducted as part of the Applied Technology Council ATC-55 project whose main goal is to evaluate and improve the application of simplified inelastic analysis procedures for use with performance-based engineering methods for seismic design, seismic evaluation, and seismic rehabilitation of buildings.

2. METHODOLOGY

Five percent damped single-degree-of-freedom (SDOF) systems with 50 periods of vibration between 0.05s and 3.0s were used in this investigation. Nine levels of lateral strength ratios were considered corresponding to R=1, 1.5, 2, 3, 4, 5, 6, 7 and 8. The lateral strength ratio, R, corresponds to the lateral strength required to maintain the system elastic normalized by the yielding strength of the system. Four different hysteretic behaviors were used in this study: (a) elasto-perfectly plastic (EPP); (b) stiffness degrading (SD); (c) strength and stiffness degrading (SSD); and (d) nonlinear elastic (NE) model that unloads on the same branch as the loading curve and therefore exhibits no hysteretic energy dissipation. Combinations of period of vibration, lateral strength and hysteretic behavior represent a total of 1,800 different SDOF systems.

Each SDOF system was subjected to 100 earthquake ground motions recorded on different site conditions with average shear wave velocities ranging from 1,500 m/s to less than 100 m/s. The ensemble of recorded ground motions also included 20 records with forward directivity effects.

In order to evaluate the accuracy of the procedures in ATC-40 and FEMA-356 ratios of approximate displacement demands to “exact” displacements demands were computed for each period, each strength ratio, each hysteretic behavior and for each ground motion. The “exact” displacements were computed using nonlinear response history analyses. A total number of 160,000 nonlinear response history analyses and 320,000 individual errors were considered as part of this investigation. To evaluate whether these methods on average tend to overestimate or underestimate the maximum inelastic deformation of SDOF mean errors averaged over all records were computed.

3. EVALUATION OF ATC-40

The simplified inelastic analysis procedure in ATC-40 is based on equivalent linearization. The basic assumption in equivalent linear methods is that the maximum inelastic deformation of a nonlinear SDOF system can be estimated from the maximum deformation of a linear elastic SDOF system that has a period and a damping ratio that are larger than those the nonlinear system. The elastic SDOF system that is used to estimate the maximum inelastic deformation of the nonlinear system is usually referred to as the equivalent or substitute system. Similarly, the period of vibration and damping ratio of the elastic system are commonly referred to as equivalent period and equivalent damping ratio, respectively. In equivalent linear methods the equivalent period is computed from the initial period of vibration of the nonlinear system and from the maximum displacement ductility ratio, μ. The equivalent damping ratio is computed as a function of damping ratio in the nonlinear system and the displacement ductility ratio. The main differences between the many equivalent linear methods stems primarily from the functions used to compute the equivalent period and equivalent damping ratio

In the equivalent linear method implemented in the ATC-40 report the equivalent period T_{eq} and equivalent damping ratio (referred to as effective viscous damping, β_{eff}, in ATC-40) are computed as

$$T_{eq} = T_o \sqrt{\frac{\mu}{1+\alpha\mu-\alpha}} \tag{1}$$

$$\beta_{eff} = 0.05 + \kappa \frac{2}{\pi} \frac{(\mu-1)(1-\alpha)}{\mu(1+\alpha\mu-\alpha)} \tag{2}$$

where T_o is the initial period of vibration of the nonlinear system, α is the post-yield stiffness ratio and κ is an adjustment factor to approximately account for changes in hysteretic behavior in reinforced concrete structures. ATC-40 proposes three equivalent damping levels that change according to the hysteretic behavior of the system. Type A hysteretic behavior denotes new structures with reasonably full hysteretic loops and the corresponding equivalent damping ratios take the maximum values. Type C hysteretic behavior represents severely degraded hysteretic loops resulting the smallest equivalent damping ratios. Type B hysteretic behavior is intermediate between type A and type C hysteretic behaviors. The value of κ decreases for degrading systems (hysteretic behaviors types B and C).

The main observations on the approximate method in ATC-40 to estimate target displacements can be summarized as follows:

A1. One of the main disadvantages of the nonlinear static procedure in ATC-40 is the need to iterate in order to obtain an approximate solution. In equations (1) and (2) the displacement ductility ratio μ must be known in order to compute the equivalent damping β_{eff} and the equivalent period T_{eq}. However, when evaluating existing buildings the maximum displacement ductility ratio is not known. Hence, the equivalent linear method in ATC-40 requires iteration in order to estimate the maximum inelastic deformation. ATC-40 describes 3 iterative procedures to estimate the maximum inelastic deformation of the equivalent SDOF system.

A2. If in the iterative procedure A the displacement estimate found in any iteration is taken as the assumed displacement in the next iteration, the iterative procedure becomes a fixed-point iterative procedure, which may not always converge. An example corresponding to an elastoplastic 5%-damped SDOF system with a 1.0s fundamental period and a yield displacement of 4.302cm subjected to the north-south component of the well-known El Centro 1940 ground motion is shown in figure 1. Displacements were computed with equivalent linear equations of ATC-40 for closely-spaced assumed displacements D_a between 0 and 12cm. In figure 1 the horizontal axis corresponds to the assumed displacement D_a and the vertical axis corresponds to the computed displacement, D_c. The diagonal line corresponds to points in which the computed displacement is equal to the assumed displacement. Shown in this form, it is clear that convergence using iteration methods in equivalent linearization is essentially a root-solving problem. The dotted line follows the iterations starting with an assumed displacement of 5.0 cm. It can be seem that despite having initiated the iterations with an initial displacement that is very close to the root (5.32cm), the method diverges moving away from the root and then going into a non-converging alternating pattern.

If at any point of the iteration process a displacement smaller than the yield displacement is computed (fourth iteration), equation 2 will yield an equivalent damping ratio equal to the initial damping. Then, if the demand spectrum computed with $\beta_{eff} = \xi_o$ (initial viscous elastic damping) intersects the capacity diagram at a displacement that, when used as an assumed displacement D_a produces a computed displacement D_c smaller than the yield displacement, then the iterative method goes into an alternating pattern and will never converge. This flip-flop non-converging behavior is produced in this method when a displacement smaller than the yield displacement is computed at any two non-consecutive iterations i and i+2.

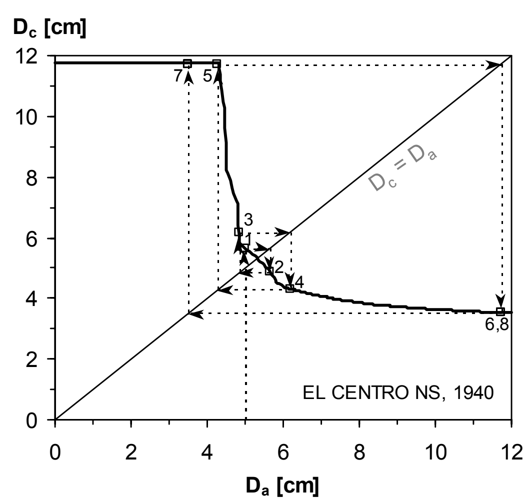

Figure 1. Example of non-converging behavior using ATC-40 Procedure A for a 1s SDOF system subjected to the El Centro 1940 ground motion.

A3. Iterative procedure B is guaranteed to converge but it has a slow rate of convergence. For a more complete discussion of iterative procedures in equivalent linear methods, including convergence problems and rates of convergence, the reader is referred to Miranda and Akkar (2002).

A4. Is particularly important to be aware that even if convergence is achieved, iteration schemes in ATC-40 do not converge to the exact deformation but just to an approximate deformation, which, in some cases may differ significantly from the deformation computed from nonlinear response history analyses. Hence, and as previously noted by Chopra and Goel (2000) achieving convergence in ATC-40 is deceptive as it may provide a false sense of accuracy.

A5. The use of equivalent linear methods in some cases may lead to multiple solutions. An example is shown in Figure 2 for a SDOF system having an initial period of 1.65s with a yield displacement of 7.82cm when using iterative Procedure B and Type C hysteretic behavior. It can be seen that in this case procedure B may converge to any of the three displacements shown with a circle.

A6. Equation (1) that is used to compute the equivalent period in ATC-40 is based on the secant stiffness at maximum deformation. From comparisons of the deformations computed with ATC-40 and those computed using response history analyses it was found that this large period shift, when used in combination with equivalent damping factors like those in ATC-40, leads to large overestimation of inelastic deformations for short period structures. An example is shown in figure 3, where mean errors corresponding to ground motions recorded in site class C and for hysteretic behavior types A, B and C are shown. Miranda and Ruiz-García (2002) also reported large overestimations of inelastic deformations for SDOF systems with short periods of vibration for other equivalent linear methods that are also based on secant stiffness.

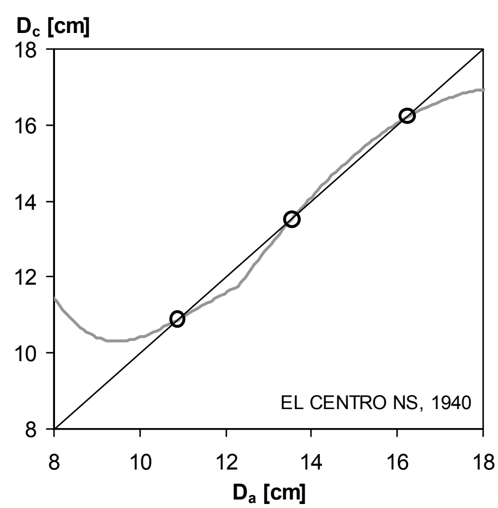

Figure 2. Example of multiple solutions using ATC-40 Procedure B in combination with hysteretic behavior Type C.

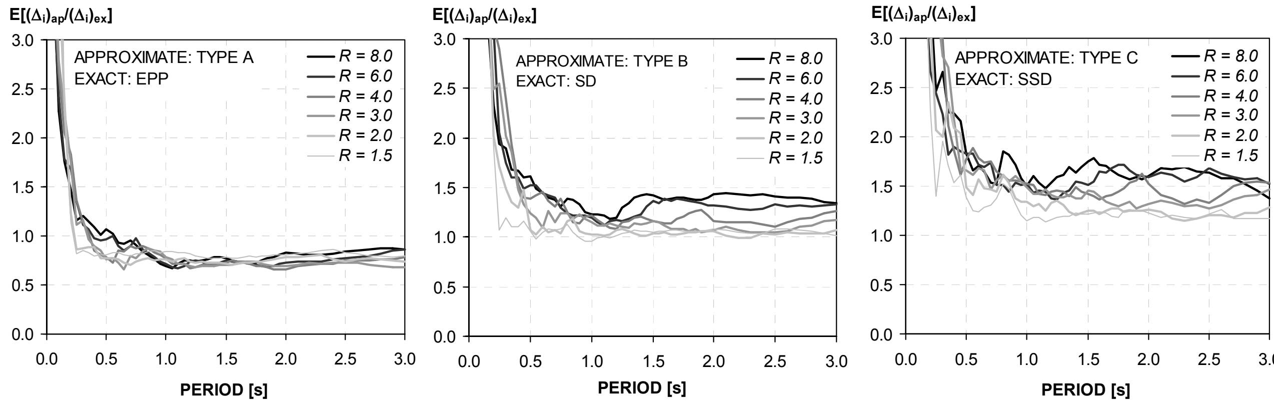

Figure 3. Mean error in computing the inelastic deformation of SDOF systems with hysteretic behavior types A, B and C when subjected to ground motions recorded on site class C.

A7. For systems with periods longer than about 0.7s, the equation for computing the equivalent damping ratio in structures with hysteretic behavior type A overestimates the damping ratio which, when used in combination with the secant stiffness and recorded earthquake ground motions, leads to underestimations of the maximum deformation that on average are 30% to 40% for systems with periods longer than about 0.7s.

A8. ATC-40 assumes that the inelastic deformation demands in structures with behavior type B will be larger than those in structures with behavior type A, while results of nonlinear response history analyses show that the deformations are actually approximately the same or slightly larger for the elasto-perfectly plastic model compared to the stiffness-degrading model. Hence, for structures that may exhibit stiffness degradation ATC-40 will lead to overestimations of deformation demands for systems with periods longer than about 0.6s. The level of overestimation increase as the *R* increases. Average overestimations range approximately from 5% to 55%.

A9. For structures with hysteretic behavior type C (with strength and stiffness degradation), ATC-40 assumes inelastic deformations larger than those of structures with hysteretic behavior type B and much larger than those of structures with hysteretic behavior type A. Hence, for structures that may exhibit a hysteretic behavior type C, ATC-40 leads to significant overestimations of the maximum inelastic deformation for systems with periods longer than 0.5s. Overestimations increases as the *R* increases. Average overestimations range from approximately 20% for systems with *R*=1.5 to about 90% for systems with *R*=8.

A10. Spectral reduction factors in the constant-acceleration region SR_A are smaller than spectral reductions factors in the constant velocity region SR_V. This means that larger reductions in spectral ordinates will be applied in the constant-acceleration region (short-periods) than in the constant-velocity region. This is opposite to the trend observed by various investigators that have studied the reductions in spectral ordinates with increasing damping ratios. Furthermore, this is also opposite to the spectral reduction factors in FEMA 273 and FEMA 368 in which larger reductions in the spectral ordinates are recommended in the constant-velocity spectral region than in the short-period region.

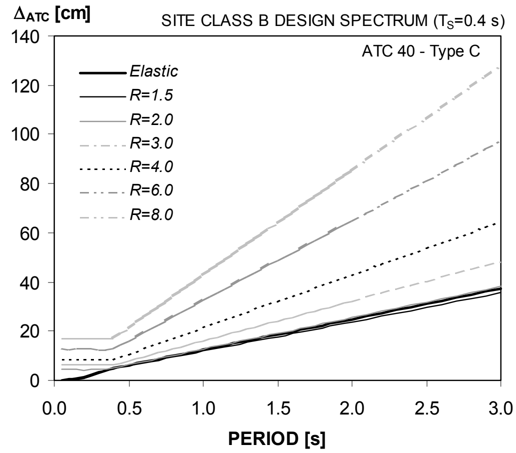

Figure 4. Maximum inelastic deformation estimates on SDOF systems computed using ATC-40 spectral reduction factors proposed and design spectrum.

A11. As illustrated in figure 4, minimum values of SR_A and SR_V in ATC-40 when used in combination with design spectra leads to constant inelastic deformations for systems with the same R and periods smaller than T_s (corner period between constant-acceleration and –velocity spectral regions). This is contrary to observations from nonlinear response history analyses that indicate that in the short period region systems with the same R will experience increasing inelastic deformations with increases periods of vibration.

A12. Minimum values imposed on SR_A and SR_V are such that when the NSP in ATC-40 is used in combination with design spectra, it will lead to significant overestimations in inelastic deformations, particularly for large values of R and for periods longer than the characteristic period T_s. In this spectral region, the inelastic deformations computed with ATC-40 can be more than twice than those computed with the equal displacement approximation when R=5 and more than four times larger than those computed with the equal displacement approximation when R=8.

4. EVALUATION OF FEMA-356

The nonlinear static procedure (NSP) in FEMA-356 estimates the maximum inelastic global deformation demand on a building (target displacement, δ_t) as follows

$$\delta_t = C_0 C_1 C_2 C_3 S_a \frac{T_e^2}{4\pi^2} g \tag{3}$$

where C_0 is a modification factor to relate the spectral displacement of the equivalent SDOF system to the roof displacement of the building, C_1 is a modification factor to relate expected maximum inelastic displacements to elastic displacements computed with linear elastic analysis, C_2 is a modification factor to represent the effect of pinched hysteretic shape, stiffness degradation and strength deterioration on maximum displacement response, while C_3 accounts for displacements due to dynamic P-Δ effects.

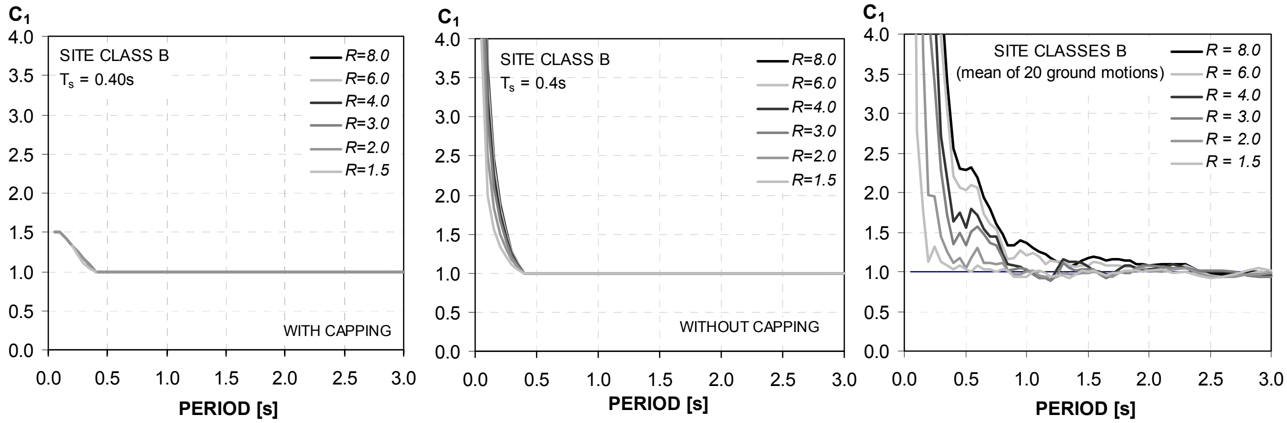

Figure 5. Comparison between C_1 factors in FEMA-356 (with and without capping) to mean C_1 computed with nonlinear response history analyses.

Figure 5 compares the coefficient C_1 currently specified in FEMA-356 with mean values of the ratio of maximum inelastic deformation to maximum elastic deformation (actual trend in C_1) computed from SDOF systems with elasto-perfectly-plastic hysteretic model when subjected to 20 ground motions recorded on site B. The main observations on the approximate procedure in FEMA-356 to estimate target displacements are summarized as follows:

B1. The use of the equal displacement approximation to compute the coefficient C_1 for systems with periods longer than the characteristic periods leads to relatively good approximations of maximum inelastic deformations for systems with elastoplastic hysteretic behavior for periods longer than about 1s. Only small overestimations in the order of 5 or 15% are produced. For very soft soil sites and near-fault records the equal displacement approximation is only adequate for systems with period of vibration that are approximately 1.5 times longer than the predominant period and the pulse periods, respectively.

B2. For systems with *R* larger than about 2.5 the limiting values of C_1 in the NSP not to exceed those of the Linear Static Procedure (LSP) will control the design.

B3. The capping on C_1 imposed by maximum values from the LSP lead to significant underestimations of the maximum inelastic deformation demands for structures in the short period range when *R* is larger than 2.

B4. An effect of the capping, perhaps even more important, is that according to the FEMA-356 Prestandard short period structures will see the same global displacement demand whether they are strong or weak and that an increase in lateral strength in short period structures will not lead to reductions is inelastic displacements. This is contrary to basic observations made by various researchers in the last forty years based on results of response history analyses.

B5. Current characteristic periods are based on the corner period between the constant-acceleration spectral region and the constant-velocity spectral region. These characteristic periods are shorter than those observed from response history analyses, hence underestimation of inelastic deformations are produced for periods between the characteristic period and periods that are approximately 1.5 times the characteristic period.

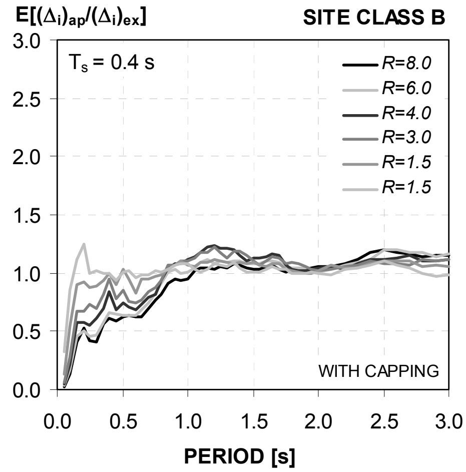

Figure 6. Mean error on the maximum inelastic deformations computed using FEMA-356 and elasto-perfectly plastic error.

B6. Even if the capping were to be removed and the characteristic period lengthened, it was observed that equation to estimate C_1 does not capture adequately the changes in inelastic deformation demands that are produced with changes in *R* for short-period structures. In particular the changes in target displacement demands with changes in lateral strength for short period structures are larger than those implied by FEMA-356.

B7. There is not a clear division of the intent of coefficients C_2 and C_3. In particular C_2 is supposed to account for changes in lateral displacement produced by departures of the hysteretic behavior from an elasto-perfectly plastic model (such as pinching, stiffness degradation and strength degradation.). However, $P\text{-}\Delta$ effects that are accounted for by C_3 will also produce changes in the hysteretic behavior. In particular, $P\text{-}\Delta$ effects will also produce decreases in both the lateral stiffness and the lateral strength that could also be described as stiffness and strength degradation.

B7. In FEMA-356 the structural performance of many structural elements is determined as a function of the lateral deformation of the structure. Hence, deformation demands need to be determined in order to estimate the structural performance. However, in the NSP in FEMA-356 the structural performance level is required in order to compute the coefficient C_2, which implies that the structural performance is needed to estimate the lateral deformation. Clearly this leads to confusion in the use and interpretation of the NSP as is not clear how the performance level can be estimated without the deformation demand.

B8. For structures with framing type I and life safety and collapse prevention structural performance levels the coefficient C_2 can take values larger than one. However, since the modification factor C_2 is not necessarily equal unity when *R* is unity, the predicted peak displacement may be greater than the elastic deformation demand even when the structure is strong enough to remain elastic.

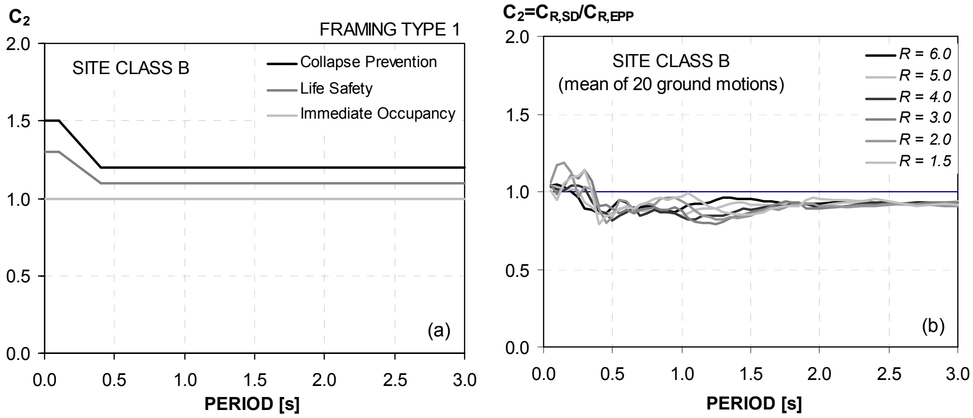

Figure 7. Comparison of modification factors to account for hysteretic behavior: (a) in FEMA-356; (b) computed with response history analyses.

B9. With the exception of periods of vibration smaller than about 0.4s, response history analyses conducted as part of this investigation indicate that the maximum deformation of stiffness-degrading systems is very similar and on average only slightly smaller (5 to 15% smaller) than the maximum deformation of elastoplastic systems. Although this seems counter-intuitive given the hysteresis loops of stiffness degrading models or of strength and stiffness degrading models, results shown in this study are consistent with many previous investigations. While results from response history analyses suggest that stiffness degradation will practically not affect or will even produce small reductions in lateral deformation, coefficient C_2 in FEMA 356 increases lateral deformations. For periods longer than about 0.5s, coefficient C_2 will lead to overestimations of the maximum inelastic deformation. While for short periods this coefficient may lead in some cases to overestimations and in some cases to underestimations of the maximum inelastic deformation.

B10. Coefficient C_3 does not adequately addresses the possibility of having dynamic instability.

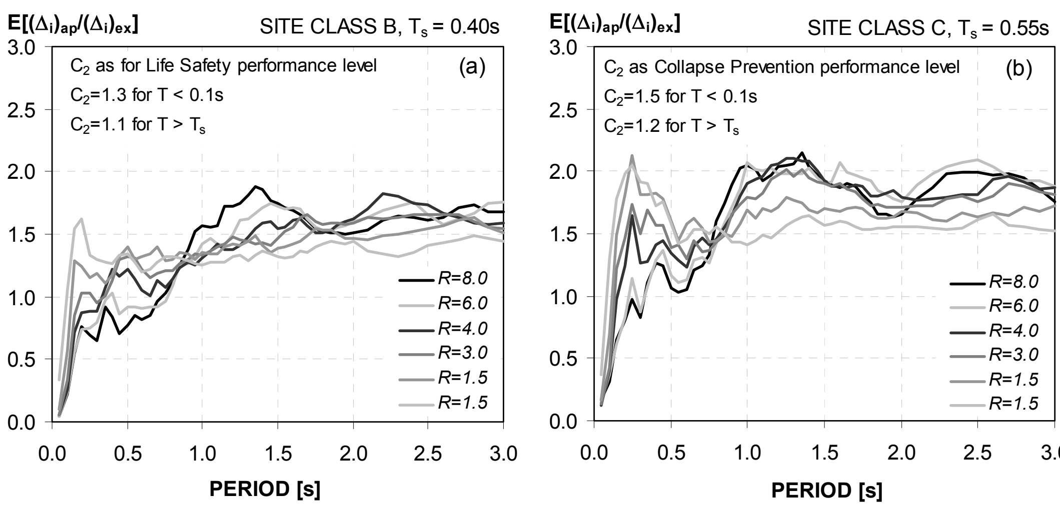

Figure 8. Mean error of maximum inelastic deformations for Life Safety and Collapse Prevention performance levels.

5. SUMMARY AND CONCLUSIONS

Approximate methods to estimate target displacements in ATC-40 and FEMA-356 were evaluated. A total number of 1,800 different SDOF systems corresponding to a wide range of periods of vibration with different levels of lateral strength and four types of hysteretic models were considered when subjected to an ensemble of earthquake ground motions recorded on different site classes together with some near-fault records influenced by forward directivity effects were considered. Approximate inelastic displacements were compared to results from nonlinear response history analyses. It was found that in many cases the target displacements computed with ATC-40 and FEMA-356 can depart significantly from results from response history analyses.

The observations highlighted in this study have very important practical implications when upgrading existing structures. In particular, the resulting retrofitting strategies suggested for the same structure could be very different if one uses ATC-40 or FEMA-356. For structures with periods of vibration smaller then T_s and whose maximum global deformation capacity is being exceeded, ATC-40 would suggest a retrofitting strategy of primarily increasing the lateral strength, since according to this procedure, an increase in lateral stiffness would not lead to reductions in displacement demands. Meanwhile, FEMA 356 would suggest a retrofitting strategy of primarily increasing lateral stiffness as the capping for $T < T_s$ does not reduce the displacement demand for increases in lateral strength. In this spectral region both methods contradict fundamental observations from nonlinear response history analyses that show that for short period structures the maximum inelastic deformation is very sensitive to *both* lateral stiffness and lateral strength.

In the case of structures with periods of vibration longer than T_s, also different retrofitting strategies may result from the use of these guidelines. For a structure in this period range whose global deformation capacity is being exceeded ATC-40 would suggest that reductions in displacement demands could be achieved by increasing both the lateral stiffness and the lateral strength of the structure. Meanwhile the displacement coefficient method in FEMA-356, that in this spectral region uses the equal displacement approximation, suggests that an increase in lateral strength would not result in reductions in displacement demands and that an increase in lateral stiffness is what is needed. In this spectral region, the simplified analysis procedure in FEMA-356 is closer to observations from the nonlinear response history analyses.

6. ACKNOWLEDGEMENTS

The investigation reported was partially supported by the ATC-55 Project: “Evaluation and Improvement of Inelastic Analysis Procedures” of the Applied Technology Council with funding from the Federal Emergency Management Agency. The substance of such work is dedicated to the public. The authors are solely responsible for the accuracy of statements or interpretations contained in this publication. Special thanks are given to Craig Comartin and other participants of the ATC-55 project (Mark Aschheim, Ron Hamburger, Robert Hanson, William Holmes, Wilfred

Iwan, Michael Mahoney, Jack Moehle, and Christopher Rojahn) for their comments to this work. These organizations and individuals do not assume any legal liability or responsibility for the accuracy, completeness, or usefulness of any of the information in this publication.

7. REFERENCES

Akkar S.D. and Miranda, E., (2002), "Statistical evaluation of approximate methods for estimating maximum deformation demands on existing structures," submitted for review and possible publication to *J. Struc. Eng.*, ASCE.

Applied Technology Council, (1996), "Seismic evaluation and retrofit of concrete buildings," *Report ATC-40*, Applied Technology Council, Redwood City, California.

Aschheim, M.A., Maffei, J., and Black, E. F., (1998), "Nonlinear static procedures and earthquake displacement demands," *Proceedings 6th US National Conference on Earthquake Engineering*, Seattle, Washington, Earthquake Engineering Research Institute, June, CD-ROM, Paper 167.

Building Seismic Safety Council, (1997), "NEHRP guidelines for the seismic rehabilitation of buildings," *Reports FEMA-273 (Guidelines) and FEMA-274 (Commentary)*, Federal Emergency Management Agency, Washington, DC.

Building Seismic Safety Council, (2000a), "Prestandard and commentary for the seismic rehabilitation of buildings," *Report FEMA-356*, Washington, D.C.

Building Seismic Safety Council, (2000b), "Global topics report on the prestandard and commentary for the seismic rehabilitation of buildings," *Report FEMA-357*, Washington, D.C.

Chopra, A.K. and Goel, R.K., (1999), "Capacity-demand-diagram methods for estimating seismic deformation of inelastic structures: SDF systems," *Report PEER-1999/02*, Pacific Earthquake Engineering Research Center, University of California, Berkeley, California.

Iwan, W.D., (1980), "Estimating inelastic response spectra from elastic spectra," *Earthquake Eng. Struct. Dyn*., **8**, 375–388.

Kunnath, S. K. and Gupta, B., (2000), "Validity of deformation demand estimates using nonlinear static procedures," *Proceedings of the US-Japan Workshop on Performance-Based Engineering of Reinforced Concrete Building Structures*, Sapporo, Hokkaido, Japan.

MacRae, G.A., Morrow, D.V. and Roeder C.V., (2001), "Near-fault ground motion effects on simple structures," *J. Struc. Eng.*, ASCE, **127**(9), 996-1004.

Miranda, E., Akkar, S.D. and Ruiz-García J., (2002), "Summary of evaluation of current nonlinear static procedures–sdof studies," Interim report prepared for the *Phase 2 of Project to Evaluation and Improvement of Inelastic Seismic Analysis Procedures (ATC-55 project)*.

Miranda, E. and Ruiz-García J., (2002), "Evaluation of approximate methods to estimate maximum inelastic displacement demands," *Earthquake Eng. Struct. Dyn.,* **31**, 539-560.

Miranda, E. and Akkar, S.D., (2002), "Evaluation of iterative schemes in equivalent linear methods,' submitted for review and possible publication to *Earthquake Spectra*, EERI.

Ruiz-García, J. and Miranda, E., (2002), "Inelastic displacement ratios for evaluation of existing structures," accepted for publication in *Earthquake Eng. Struct. Dyn.*, **31**.

PROBABILISTIC ESTIMATION OF SEISMIC STORY DRIFTS FOR RC BUILDINGS

Thuat V. DINH[1] and Toshikatsu ICHINOSE[2]

ABSTRACT

This paper proposes a procedure for evaluating the mean and standard deviation of seismic story drifts for RC buildings by considering both total and story failure mechanisms. The estimation process consists of a pushover analysis of the structure against inverted triangular forces to evaluate the most probable mechanism during earthquakes, and consideration of the relative reserve strengths to evaluate the probability of other mechanisms. The relative reserve strengths against story and total mechanisms are expressed by two newly defined story-safety and total-reduction factors, respectively. The application of the proposed procedure is examined by conducting dynamic response analyses of structures with various story-safety and total-reduction factors using 36 real motion records. The proposed procedure well predicted the mean and standard deviation of story drift ratios for RC buildings.

1. INTRODUCTION

For seismic evaluation of RC buildings, there have been numerous researches on the evaluation of global deformation demands by replacing multistory structures with an equivalent single-degree-of-freedom (SDOF) system. Freeman (1978) introduced the capacity spectrum method, Moehle (1992) proposed a method based on the displacement spectrum, and Chopra and Goel (2001) further developed the method using inelastic design spectra. Studies investigating the evaluation of local deformation demands have also been performed. Saiidi and Sozen (1981) developed a modification factor to convert the SDOF response to a multi-degree-of-freedom (MDOF) response, which has been improved in papers including Gupta and Krawinkler (2000). However, almost all of these researches assume that the building will deform as predicted during

[1]*Doctoral Student, Dept. of Architecture and Civil Engineering, Nagoya Inst. of Tech., Nagoya 466-8555, Japan. E-mail: k01@archi.ace.nitech.ac.jp*

[2]*Professor, Dept. of Architecture and Civil Engineering, Nagoya Inst. of Tech., Nagoya 466-8555, Japan. E-mail: ichinose@archi.ace.nitech.ac.jp*

pushover analysis. This is not appropriate for actual buildings, which may fail in a variety of mechanisms due to the different dynamic characteristics of earthquake motions and uncertainties in the estimation of member strengths. This paper proposes a procedure for evaluating the mean and standard deviation of seismic story drifts for RC buildings by considering both total and story mechanisms. The proposed procedure is examined by conducting dynamic response analyses of various analytical models using 36 motion records.

2. BASES OF THE PROPOSED PROCEDURE

2.1 Definition of Story-Safety and Total-Reduction Factors

In a building with structural walls, the probability of a story mechanism decreases as the shear strength of the walls increases, as discussed by Park and Paulay (1975). In a frame building, the probability of a story mechanism decreases as the column-to-beam strength ratio increases, as discussed by Dooley and Bracci (2001). To integrate these tendencies, a story-safety factor, f_i, is defined by

$$f_i = \frac{\Delta V_i}{V_{ui}} \quad \text{for} \quad \Delta V_i = V_{si} - V_{ui} \tag{1}$$

where V_{si} = strength under the forces causing a story mechanism of the *i*th story as shown in Figure 1b, and V_{ui} = shear force of the *i*th story when a failure mechanism occurs under inverted triangular forces as shown in Figure 1a. The difference between V_{si} and V_{ui} represents the strength margin against a story mechanism.

The probability of a total mechanism is not necessarily zero even if a building fails due to a story mechanism under static loading. Conservatively, designers may neglect this probability. However, for symmetry of the theory, a total-reduction factor, f_t, is defined as follows:

$$f_t = \frac{\Delta V_t}{V_{u1}} \quad \text{for} \quad \Delta V_t = V_{t1} - V_{u1} \tag{2}$$

where V_{t1} = imaginary base shear strength of the building that is modified to deform in a total mechanism. The difference between V_{t1} and V_{u1} represents the shortage of story strength to realize the total mechanism.

2.2 Assumptions of Story Drift and Deformation

We assume that the peak drift in the *i*th story of a building consists of three parts:

$$d_i = d_{ei} + d_{pti} + d_{psi} \tag{3}$$

where d_{ei} = elastic deformation, d_{pti} = plastic deformation due to a total mechanism, and d_{psi} = plastic deformation due to a story mechanism. Summation of both sides of Equation 3 for all stories leads to the total deformation:

$$D_{total} = D_e + D_{pt} + \sum_{i=1}^{n} d_{psi} \tag{4}$$

where D_e = total elastic deformation and D_{pt} = roof displacement due to a total mechanism as shown in Figure 1a. The sum of the second and the third terms on the right-hand side of Equation 4 is called the total plastic deformation, denoted by D_p. Since a total mechanism provides a uniform drift angle, Equation 3 becomes

$$d_i = d_{ei} + R_{pt} D_p \frac{h_i}{H} + R_{psi} D_p \tag{5}$$

where $R_{pt} = D_{pt}/D_p$ and $R_{psi} = d_{psi}/D_p$, representing the allotment of plastic deformations in a building. The ratios R_{pt} and R_{psi} are assumed as

$$R_{pt} = \frac{D_{pt}}{D_p} = \frac{\lambda_t \exp(-\beta f_t)}{\lambda_t \exp(-\beta f_t) + \sum_{j=1}^{n} \lambda_j \exp(-\beta f_j)} \tag{6}$$

$$R_{psi} = \frac{d_{psi}}{D_p} = \frac{\lambda_i \exp(-\beta f_i)}{\lambda_t \exp(-\beta f_t) + \sum_{j=1}^{n} \lambda_j \exp(-\beta f_j)} \tag{7}$$

where λ_t and λ_i = random variables representing the normalized contributions of the total and *i*th story mechanisms of a building respectively, and $-\beta$ = constant representing the inverse relationships between R_{pt} and f_t, and between R_{psi} and f_i. The elastic deformation, d_{ei}, in Equation 5 is defined as the story drift when a mechanism occurs by pushover analysis under inverted triangular forces.

2.3 Probabilistic Formulation of Story Drift

The equation for estimating the mean of story drift is

$$\mu_{di} = d_{ei} + \mu_{Rpt}\mu_{Dp}\frac{h_i}{H} + \mu_{Rpsi}\mu_{Dp} \tag{8}$$

where

$$\mu_{Rpt} \approx \frac{\mu_{\lambda t} \exp(-\beta f_t)}{\mu_{\lambda t} \exp(-\beta f_t) + \sum_{j=1}^{n} \mu_{\lambda j} \exp(-\beta f_j)} \tag{9}$$

$$\mu_{Rpsi} \approx \frac{\mu_{\lambda i} \exp(-\beta f_i)}{\mu_{\lambda t} \exp(-\beta f_t) + \sum_{j=1}^{n} \mu_{\lambda j} \exp(-\beta f_j)} \tag{10}$$

Next, the equation for estimating the standard deviation of story drift is

$$\sigma_{di}^2 = \left(V_{Dpt}\mu_{Dpt}\frac{h_i}{H}\right)^2 + \left(V_{dpsi}\mu_{dpsi}\right)^2 \tag{11}$$

where

$$1 + V_{Dpt}^2 = \left(1 + V_{Rpt}^2\right)\left(1 + V_{Dp}^2\right) \tag{12}$$

$$1+V_{dpsi}^2 = \left(1+V_{Rpsi}^2\right)\left(1+V_{Dp}^2\right) \tag{13}$$

$$V_{Rpt}^2 = \left(\frac{\sigma_{Rpt}}{\mu_{Rpt}}\right)^2 \approx \left(\frac{\sigma_{\lambda t}}{\mu_{\lambda t}}\right)^2 + \frac{\left[\sigma_{\lambda t}\exp(-\beta f_t)\right]^2 + \sum_{j=1}^{n}\left[\sigma_{\lambda j}\exp(-\beta f_j)\right]^2}{\left[\mu_{\lambda t}\exp(-\beta f_t) + \sum_{j=1}^{n}\mu_{\lambda j}\exp(-\beta f_j)\right]^2} \tag{14}$$

$$V_{Rpsi}^2 = \left(\frac{\sigma_{Rpsi}}{\mu_{Rpsi}}\right)^2 \approx \left(\frac{\sigma_{\lambda i}}{\mu_{\lambda i}}\right)^2 + \frac{\left[\sigma_{\lambda t}\exp(-\beta f_t)\right]^2 + \sum_{j=1}^{n}\left[\sigma_{\lambda j}\exp(-\beta f_j)\right]^2}{\left[\mu_{\lambda t}\exp(-\beta f_t) + \sum_{j=1}^{n}\mu_{\lambda j}\exp(-\beta f_j)\right]^2} \tag{15}$$

(Haugen 1968)

2.4 Procedure for Estimating Story Drifts

Figure 2 shows an overview of the process for estimating the mean and the standard deviation of the seismic story drift for an RC building. First, perform a pushover analysis under inverted triangular forces to evaluate the failure mechanism and to determine V_{ui} and d_{ei} at the mechanism point of the building. Next, calculate the story-safety factor of each story, f_i, by Equation 1. Then, calculate the total-reduction factor, f_t, as follows. If the building fails in a total mechanism, f_t = 0 automatically. If the building fails in a story mechanism, modify the building to fail in a total mechanism (by increasing the strengths of columns and walls) and then perform another pushover analysis to calculate the factor f_t by Equation 2. Finally, estimate the mean and standard deviation of the seismic story drift in each story by Equations 8 and 11, respectively.

3. WALL AND FRAME STRUCTURES

3.1 Input Ground Motions

The input ground motions were 36 motion records downloaded from the web site of the Pacific Earthquake Engineering Research Center (APEER@ 2001) after screening for a peak ground velocity of between 75 cm/s and 120 cm/s and a peak ground acceleration of between 0.4 g and 2.0 g. Such a number of earthquakes and ground motion records sufficiently represent the variety of seismic characteristics and intensities that affect the inelastic responses of buildings.

3.2 Analytical Models

Two 9-story wall and frame structures with their dimensions shown in Figure 3 were considered. These structures had equal story weights of 900 and 600 kN, respectively. Wall panels with two boundary columns at each story were modeled as an equivalent column member with two flexural springs at the top and bottom and a shear spring in the middle, while frame beams and columns were modeled as members with flexural springs at the ends. At these springs, the Takeda model (Takeda *et al.* 1970) was used to present flexural deformation and the origin-oriented degrading stiffness model to present shear deformation. The secant stiffness ratio was 0.3, and the post-yield stiffness ratios were 0.001 and 0.01 for the wall and frame structures, respectively. The damping factor was 0.05 in proportion to the tangential stiffness. The resulting fundamental periods of the wall and frame structures were 0.416 and 0.891 sec, respectively.

The initial strength assignments of the wall and frame structures were in accordance with the inverted triangular forces by assuming the base shear coefficients of 0.6 and 0.3, respectively. For the wall structure, the flexural strengths of wall were increased as shown in Figure 3a (Paulay and Priestley 1992). For the frame structure, the flexural strengths of the *i*th story column were obtained from the story shear force multiplied by half of the story height. The flexural strengths of beams at each column-beam joint were the average flexural strengths of the connecting columns. The strengths of roof and foundation beams were increased by factors of 1.5 and 2, respectively. Thus, we obtained the prototype structures denoted T-1.0, whose failure mechanisms under inverted triangular forces were simultaneous total and story mechanisms. The cracking strengths of wall and frame members were assumed as half and one-third of the corresponding yield strengths, respectively.

Additional models were derived based on model T-1.0. T-models were obtained by multiplying the shear strengths of wall model T-1.0 by a factor of ψ_i = 1.1, 1.2, or 1.3 and the column flexural strengths of frame model T-1.0 by a factor of ψ_i = 1.1, 1.2, … or 1.5. The failure mechanism of the T-models under inverted triangular forces was total mechanism. TS-models were identical to the T-models except for one or two selected weak stories with ψ_i = 1.0. The failure mechanism of the TS-models under inverted triangular forces was simultaneous total and story mechanisms. Figure 4b shows the shear strength distributions of wall models T-1.0 and TS1-1.2 (weak first story with ψ_i = 1.2). Figure 5 shows the relationship between the story shear and story drift ratio obtained from pushover analysis under inverted triangular forces for wall model T-1.2.

3.3 Allotment of Plastic Deformations for T-Models

Figure 6 shows the relationship between the ratio R_{pt} and the global ductility factor, D_{total}/D_e, for all T-models of the wall structure under the given ground motions. The factor D_{total}/D_e exhibits no correlation with R_{pt}, indicating that the failure mechanism was insensitive to the intensity of the ground motion. Furthermore, R_{pt} could be nearly zero though all the data were from T-models, indicating that the failure mechanism under seismic excitation differed from that under static loading.

Figure 7 shows the relationships of the ratio R_{ps1} at the first story and the ratio R_{psi} at each the upper story to the story-safety factors. Note that results corresponding with D_{total}/D_e less than 1.25 were neglected because they represent approximately elastic responses of the structure. The results indicate that the higher the story-safety factor, the lower the contribution of story mechanism at that story. When the story-safety factor was greater than 0.2, almost no story mechanism occurred. The results also indicate that a larger contribution of story mechanism was obtained at the first story than at upper stories. This contribution was much larger for the wall models (Figure 7a-1) than the frame models (Figure 7b-1). We analyzed other wall and frame models, and found that the contribution of story mechanism at the first story depended upon the fundamental period of the structure. Figure 8 shows the relationship between the mean of λ_1 and the fundamental period, T_1, in which the circles and rectangles indicate the results from solving Equations 9 and 10 for model T-1.0 (with $f_t = f_i = 0$). The mean of λ_t is assumed as two for wall and 10 for frame structures, and the means of λ_i at all upper stories as unity. The standard deviation of λ_t and λ_i at all stories are assumed as half of the corresponding means. Further analyses of models T-1.1 through T-1.3 gave the constant β = 20. Finally, the solid and broken curves in Figure 7 show the estimation of means and mean-plus-one-standard-deviations of R_{pt} and R_{psi} for all T-models under consideration.

3.4 Estimation of Story Drift Ratios for TS-Models

In Figure 9, the dotted lines show the drift responses of the TS-wall and frame models under the given ground motions. In wall model TS1&5-1.2 (Figure 9a), plastic deformation was concentrated in the first story rather than in the middle story. In frame model TS5-1.2 (Figure 9b), a larger dispersion of the seismic story drift ratio was observed compared with the wall model. This means that the contribution of a partial mechanism existed in the frame structure. We should also note that the mechanism varies depending on the characteristics of the ground motions: In some cases, plastic deformation mainly occurred in the lower stories, whereas in other cases, it occurred in the upper stories (Figure 9b). However, the estimated means and standard deviations of story drift ratios agreed well with those obtained from the dynamic analyses.

4. WALL-FRAME STRUCTURE

For wall-frame structures, we define a participation ratio of structural walls in resisting lateral forces as follows

$$r_w = \frac{V_{w,base}}{V_{w,base} + V_{f,base}} \tag{16}$$

where $V_{w,base}$ and $V_{f,base}$ = shear resistances of the wall and frame elements at the base respectively, obtained from pushover analysis of the structure under inverted triangular forces at a roof displacement of D_{roof} = 0.02 H. Figure 10 shows the relationship between the mean of λ_t and the ratio r_w, in which the circles and triangles show the results of dynamic analyses while the solid line shows the proposal. Note that r_w equals unity for wall and zero for frame structures.

Figure 11a shows a wall-frame structure considered that consisted of one structural wall and 18 identical frame structures as previously described. The initial assignment of strengths was derived based on an elastic analysis of the structure under inverted triangular forces with the base shear coefficient assumed as 0.35. Then, the flexural and shear strengths of wall (except at the base) were increased according to Paulay and Priestley (1992). Figure 11b shows good agreement between the results of the estimation and the dynamic analysis for model TS3-1.2.

5. TOTAL DEFORMATION

Figure 12 shows a comparison of D_{total} and D_{roof} obtained from dynamic analyses of all the T- and TS-models of the wall and frame structures under the 36 ground motions. The result indicates that the mean and standard deviation of the ratio D_{total}/D_{roof} were 1.1 and 0.1, respectively. We should note that the ratio D_{total}/D_{roof} was affected by other parameters. For example, the ratio tended to be nearly 1.0 for the models with a total mechanism only and to be large for models that had several weak stories. However, such effects were minor and negligible.

6. CONCLUSIONS

1. The failure mechanism of an RC building under seismic excitation may differ from that under static loading. For a building failing due to a total mechanism under inverted triangular forces, the contribution of a story mechanism existed under seismic excitation in many cases.
2. The story-safety factor represents the relative reserve strength against a story mechanism. When the story-safety factors of all the stories were greater than 0.2, the probability of a total mechanism was approximately 100 %.
3. When the story-safety factors of the first and some other upper stories were simultaneously zero, the contribution of plastic deformations at the first story was larger than those at the upper stories.
4. In a wall-frame building, the contribution of a partial mechanism tends to reduce with the increased participation ratio of structural walls in resisting lateral forces.
5. The proposed procedure well predicted the mean and standard deviation of story drifts for RC buildings against a given level of ground motion causing plastic deformation.

7. REFERENCES

Chopra, A. K. and Goel, R. K. (2001). "Direct displacement-based design: Use of inelastic vs. elastic design spectra." *Earthquake Spectra*, 17(1), 47-64.

Dooley, L., and Bracci, J. M. (2001). "Seismic evaluation of column-to-beam strength ratios in reinforced concrete frames." *ACI Struct. J.*, 98(6), 834-851.

Freeman, S. A. (1978). "Prediction of response of concrete buildings to severe earthquake motion." *Douglas McHenry Int. Symp. on Concrete and Concrete Struct.*, *ACI SP-55*, American Concrete Institute, Detroit, 589-605.

Gupta, A., and Krawinkler, H. (2000). "Estimation of seismic drift demands for frame structures." *Earthquake Engrg. and Struct. Dyn.* 29(3), 1287-1305.

Haugen, E. B. (1968). *Probabilistic approaches to design*. John Wiley.

Moehle, J. P. (1981). "Displacement-based design of RC structures subjected to earthquakes." *Earthquake Spectra*, 8(3), 403-428.

Park, R., and Paulay, T. (1975). *Reinforced concrete structures*. John Wiley & Sons, New York.

Paulay, T., and Priestley, M. J. N. (1992). *Seismic design of reinforced concrete and masonry buildings*. John Wiley & Sons: A Wiley Interscience Publications.

"PEER Strong Motion Database." (2000). <http://peer.berkeley.edu/smcat/search.html> (Sep. 2. 2001).

Saiidi, M., and Sozen, M. A. (1981). "Simple nonlinear seismic analysis of R/C structures." *J. Struct. Engrg.*, ASCE, 107(5), 937-951.

Takeda, T., Sozen, M. A., and Nielson, N. N. (1970). "Reinforced concrete response to simulated earthquakes." *J. Struct. Engrg.*, ASCE, 96(4), 2557-2573.

8. KEYWORDS

Seismic response; Reinforced concrete building; Total mechanism; Story mechanism; Partial Mechanism; Story-safety factor; Total-reduction factor.

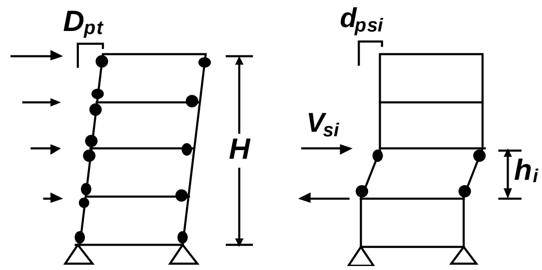

(a) Total (b) Story

Figure 1. Failure Mechanisms of Frame

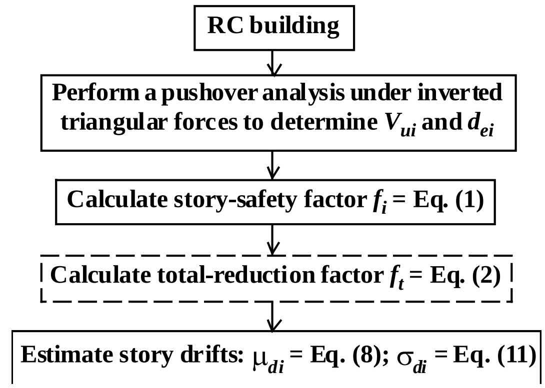

Figure 2. Procedure for Estimating Mean and Standard Deviation of Story Drifts

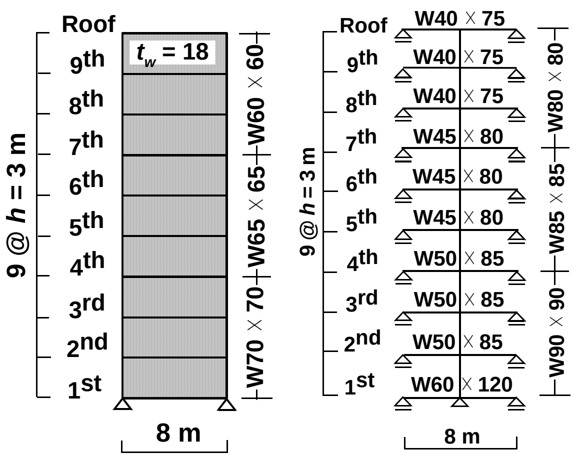

(a) Wall (b) Frame

Figure 3. Analytical Models with 9 Stories

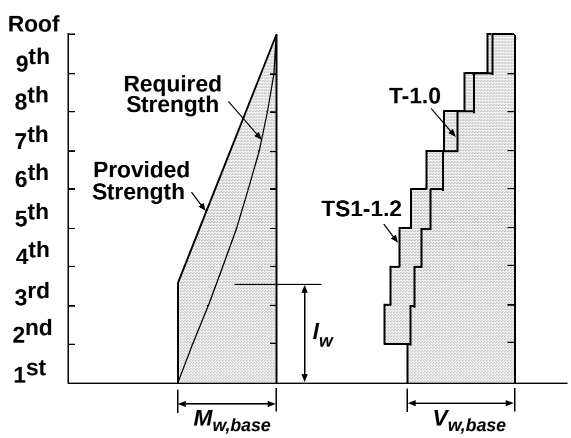

(a) Flexural (b) Shear

Figure 4. Flexural and Shear Strengths of Wall Models

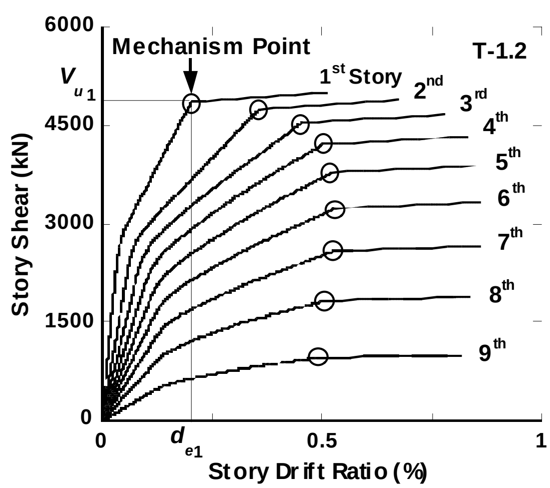

Figure 5. Story Shear - Drift Ratio Relationship for Wall Model T-1.2

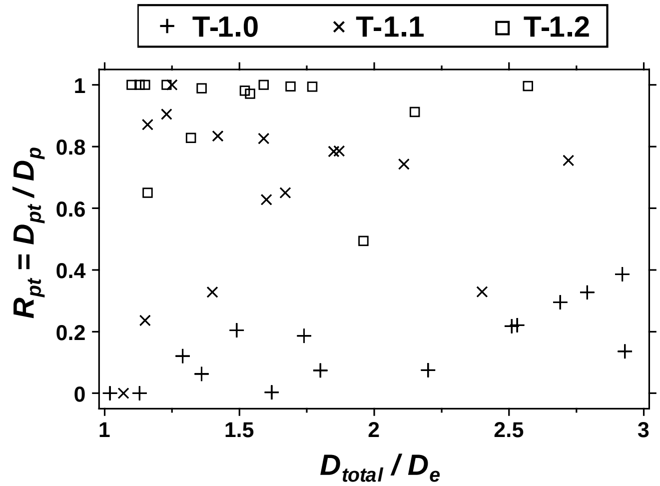

Figure 6. Relationship between Plastic Deformation Allotment due to Total Mechanism and Global Ductility Factor for T-Models of Wall Structure

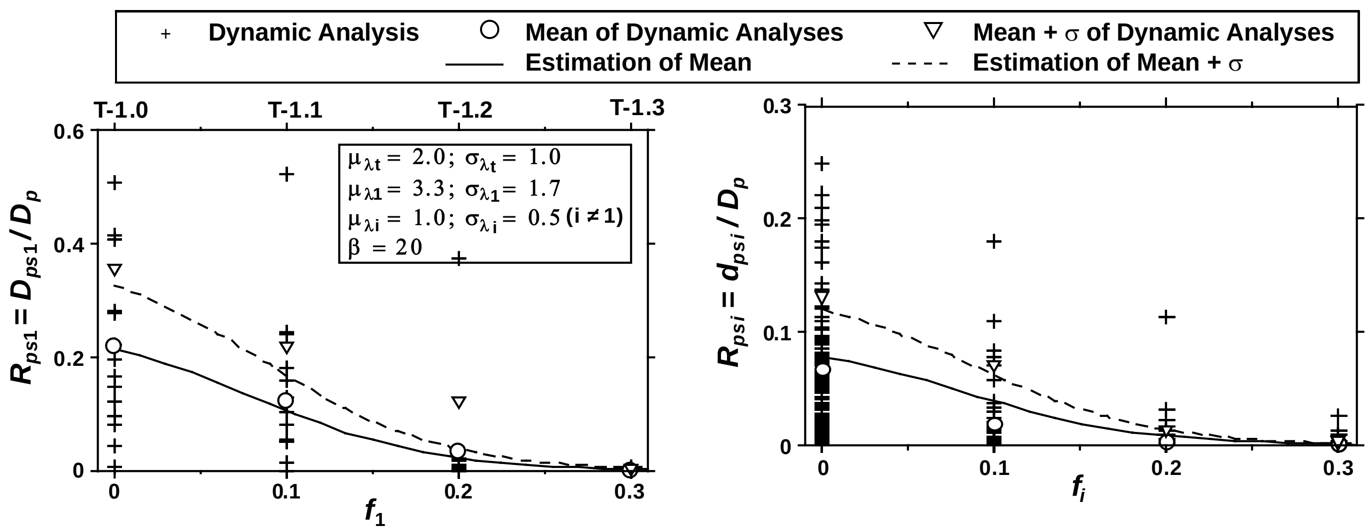

(a-1) First Story

(a-2) Upper Story

(a) Wall Models

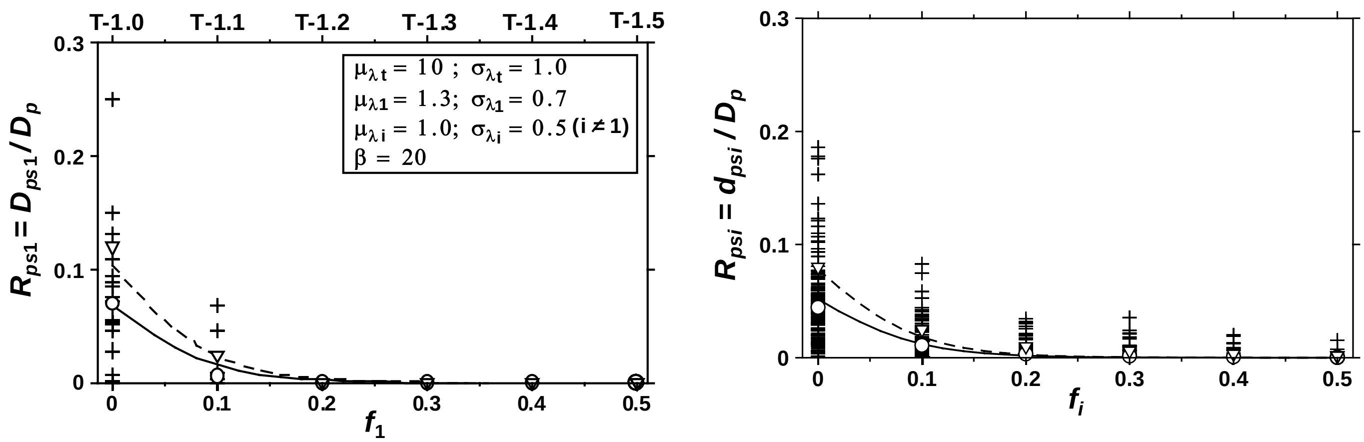

b-1) First Story **(b-2) Upper Story**

(b) Frame Models

Figure 7. Relationships of Plastic Deformations Allotments to Story-Safety Factors for T-Models

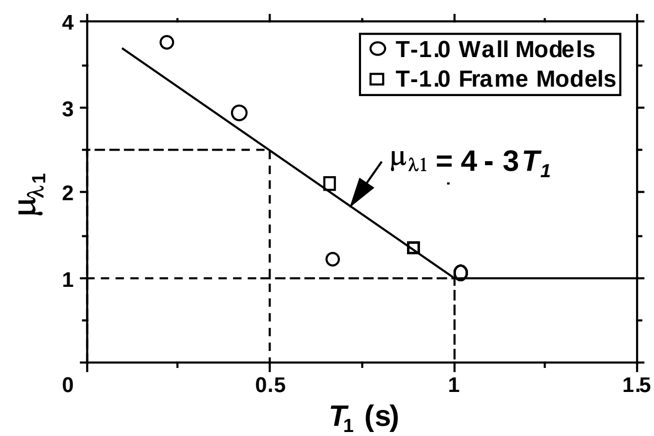

Figure 8. Relationship between Mean of λ_1 and Fundamental Period

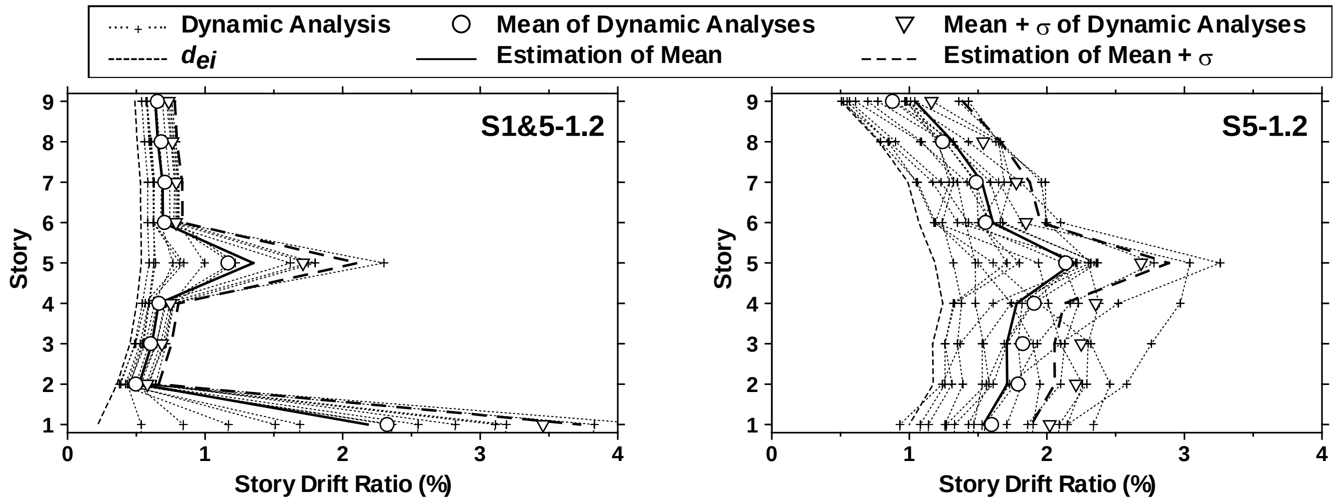

(a) TS1&5-1.2 Wall Model **(b) TS5-1.2 Frame Model**

Figure 9. Story Drift Ratios Obtained from Estimation and Dynamic Analysis

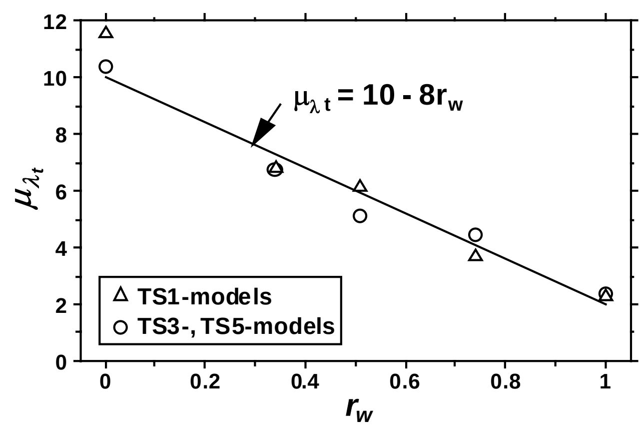

Figure 10. Relationship between Mean of λ_t and r_w

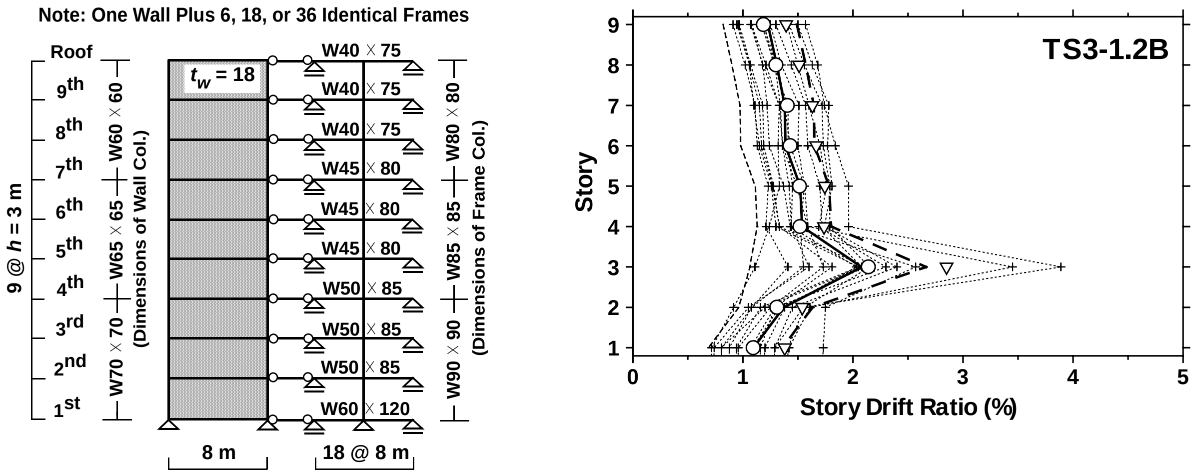

(a) Model (1 Wall and 18 Frames) **(b) Estimation of Story Drift Ratios**

Figure 11. Wall-Frame Structure with 9 Stories

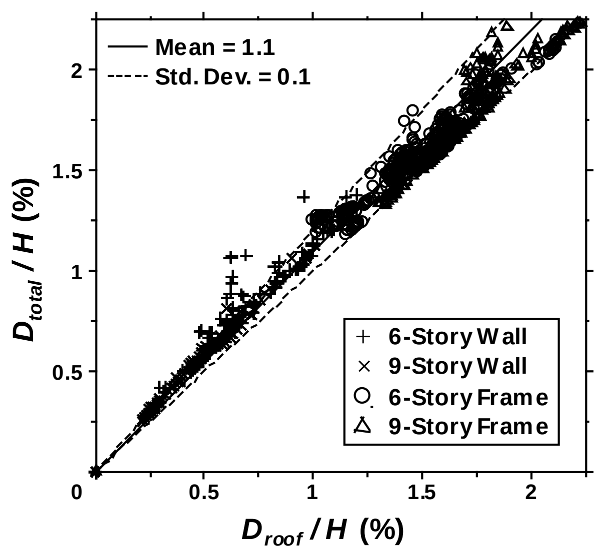

Figure 12. Comparison of D_{total} and D_{roof}

RELEVANCE OF LOW-CYCLE FATIGUE DAMAGE IN PERFORMANCE-BASED SEISMIC DESIGN

Sashi K. KUNNATH[1]

ABSTRACT

The emergence of performance-based procedures as a new paradigm in seismic design has brought into focus several critical issues related to the response and behavior of structures that merit closer scrutiny. The low-cycle fatigue characteristic of structural components that undergo reversed inelastic cyclic loading during intense ground-shaking is one such issue. This paper explores the relevance of cumulative damage, arising from considerations of low-cycle fatigue, in establishing performance criteria for seismic design and evaluation of structures. It is argued that damage estimates based on peak deformation demands may be an inadequate measure of performance and that cumulative effects must be incorporated into the evaluation process.

1. INTRODUCTION

The transition from traditional force-based design procedures to performance-based procedures, which are largely based on principles of displacement or deformation-controlled design, has brought into focus numerous issues that were previously on the fringe of reinforced concrete research. The subject of damage modeling, for example, which gained considerable attention in the late 1980s and early 1990s (Park et al, 1987; Chung et al, 1987; Kratzig et al, 1989; DiPasquale et al, 1990; Kunnath et al, 1992) has now re-emerged as researchers look for ways to correlate demand with performance. Damage indices can be regarded as the precursors of performance-based acceptance criteria. Similarly, the topic of low-cycle fatigue found its way into mainstream RC literature primarily through its application in damage modeling procedures (Mander and Cheng 1995; El-Bahy et al., 1999).

The release of the *NEHRP Prestandard and Commentary for the Seismic Rehabilitation of Buildings*, FEMA-356 (2000) marked a major step in the advancement of seismic evaluation procedures. There is reason to believe that this document contains the blueprint for future

[1] *Department of Civil & Environmental Engineering, University of California, Davis 95616; skkunnath@ucdavis.edu*

performance-based seismic design codes. One significant outcome of the provisions in FEMA-356 is the fact that it brought into focus the importance of inelastic analysis methods to achieve improved estimates of deformation demands. This is evident from the increasing use of pushover analyses in routine seismic evaluation studies. However, the validity and reliability of deformation estimates from monotonic pushover analyses is an entirely different issue. The publication of FEMA-356 is only a first step in the goal of advancing performance-based seismic engineering. Hence, the guidelines need to be systematically and critically evaluated before engineers can begin to use new methodologies with confidence.

The central idea in this paper is to raise questions and flag concerns about the prevalent thinking in performance-based seismic engineering, such as the FEMA document referenced above, so that some of the provisions may be re-examined.

2. LOW-CYCLE FATIGUE FAILURE OF STRUCTURAL COMPONENTS

Current practice and much of the proposed and/or ongoing developments for seismic design and assessment of structures are primarily concerned with peak deformation demands. Given the analytical and computational tools commonly available for analysis and design at the time seismic codes evolved during the early 1970s, it is not surprising that seismic design principles were formulated from simplified approaches based on equivalent single-degree-of-freedom (SDOF) models and response spectrum analyses. However, the notion of cumulative fatigue damage resulting from earthquake loads was brought to the attention of researchers around the same time (Kasiraj, 1972; Suidan and Eubanks, 1973). Later, as seismic design criteria relied more on laboratory testing of structural components and connections, Krawinkler et al. (1983) carried out a comprehensive study on deformation demands imposed on steel structures by one or more earthquakes. Findings from these studies led to the development of testing protocol for steel components and sub-assemblies (ATC-24, 1992). More recently, studies by Barsom and Pellagino (2002) highlight the role of low-cycle fatigue damage in the fracture of welded steel moment connections subjected to inelastic cyclic loading.

The prevalent feeling, which does not appear to have changed significantly today, was that earthquakes imposed very few large inelastic excursions, hence the peak deformation amplitude would generally be adequate for design. While the dominant effect of the peak amplitude is unquestionable, the issue of survivability in a future event or the assessment of reserve capacity in a component following a seismic event is not addressed by current evaluation methodologies.

2.1 Low-Cycle Fatigue of Well-Detailed Flexural Columns

In an attempt to investigate cumulative damage effects in reinforced concrete, Kunnath et al. (1997) carried out both constant-amplitude and random amplitude fatigue tests on a series of identical quarter-scale flexural bridge columns. The response of the model column to two sets of constant amplitude loads is shown in Figure 1. As is evident from the results shown, an increase in the drift amplitude by approximately 1.4% (from 4.2% to 5.6%) reduced fatigue life by over 65% (from 26 to 9 cycles).

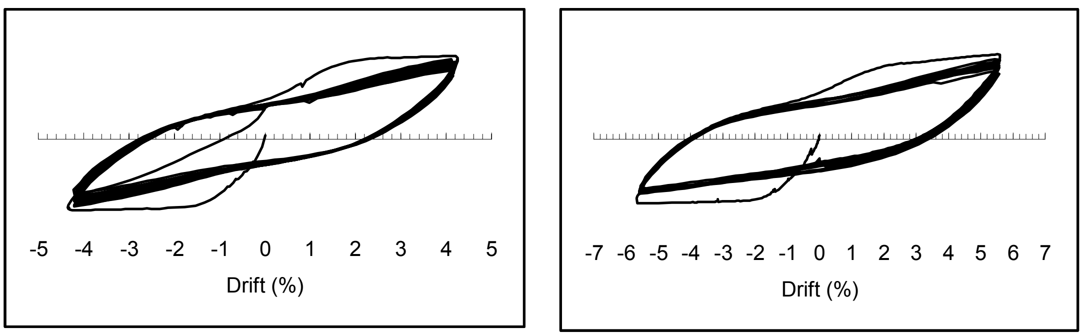

Figure 1. Force-deformation loops under constant amplitude loading

Constant amplitude testing at different drift amplitudes provides a basis for the development of fatigue life relationships. In the case of the flexural columns referenced above, the following equation was derived from curve-fitting the experimental data on a log-log scale:

$$\delta\,(\%) = 10.6\,(N_{2f})^{-0.285} \tag{1}$$

The equation above can also be recast in alternative formats, depending upon the objective of the application. For example, if an expression involving the ductility of the system is sought, it is possible to modify Equation (1), following a re-evaluation of the data, as follows:

$$\mu = 8.25(2N_f)^{-0.25} \tag{2}$$

In the above expressions, δ is the drift demand expressed as a percentage, μ is the ductility demand, and N_{2f} is the number of complete cycles to failure and $2N_f$ is the number of half-cycles to failure. Traditionally, fatigue life expressions are based on the number of reversals or the number of half-cycles since it is more convenient to deal with peak-to-peak amplitudes when applying these equations to irregular cycles.

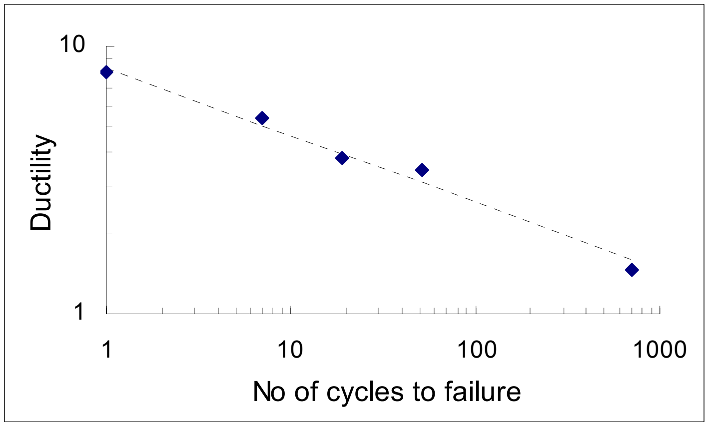

Figure 2. Low-cycle fatigue relationship for a well-detailed flexural column

The fatigue-life relationship given in Equation (2) is plotted in Figure 2. These plots illustrate the decay of fatigue life with increasing deformation demand.

2.2 Low-Cycle Fatigue of Reinforcing Bars

In the previous section, the low-cycle fatigue failure of an RC component was presented. The response of the member incorporated the fatigue characteristics of the composite section including shear-flexure-axial interaction of the member. Since the response of an RC member is influenced by numerous factors, it may be necessary to develop fatigue life expressions which consider these variables independently. Another alternative is to consider the fatigue behavior of constituent materials independently and utilize them in analytical simulation studies which can be used to calibrate global fatigue models. Additionally, from a performance-based design viewpoint, it may be useful to monitor the response of the constituent materials such as the strain in the extreme fibers of the concrete and reinforcing steel so that damage parameters such as concrete spalling, rebar buckling, etc. may be identified.

As an extension of the previous research, Brown and Kunnath (2000) investigated the low-cycle fatigue behavior of the longitudinal reinforcement used in the model tests reported in the previous section. Figure 3 shows a typical set of response data for a #6 reinforcing bar subjected to repeated cycles at constant strain. There is both a visible increase in the rate of decay as well as loss of fatigue life capacity when the strain amplitude is increased from 0.015 to 0.025. It is probably important to note that the measured strain in these cases is the average strain across a gage length of six bar diameters.

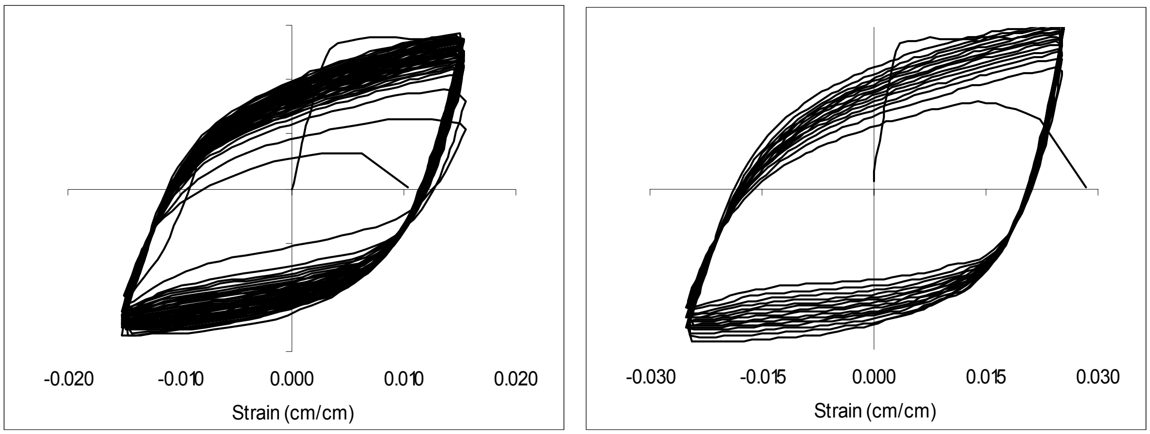

Figure 3. Cyclic response of A615 grade 60 reinforcing steel subjected to constant amplitude strain reversals

Fatigue life expressions for different strain parameters (plastic strain, total strain, etc), similar to the Coffin-Manson type expressions of Equation (1) and (2), have been derived and are reported in Brown and Kunnath (2000). These expressions and the data generated from the testing provide a basis for developing cumulative damage models and consequently, a quantative measure of performance.

2.3 Cumulative Damage Modeling

Standard low-cycle fatigue tests consist of inelastic cycles of constant amplitude. This facilitates the development of fatigue-life curves such as the one displayed in Figure 2. In earthquake analysis of structures, where a system is subjected to irregular deformation reversals, it is necessary to develop a model of cumulative damage that can deal with random histories. Several approaches have been proposed to model the cumulative effects of damage resulting from inelastic cycles, the most common being Miner's hypothesis (Miner 1945) which assumes linear accumulation of damage:

$$D_I = \sum \frac{n_i}{(2N_{fi})} \tag{3}$$

In order to use the above expression, it is first necessary to convert the random deformation history into a series of so-called "half-cycles" or double-amplitude reversals. To illustrate this process, consider the deformation history shown in Figure 4.

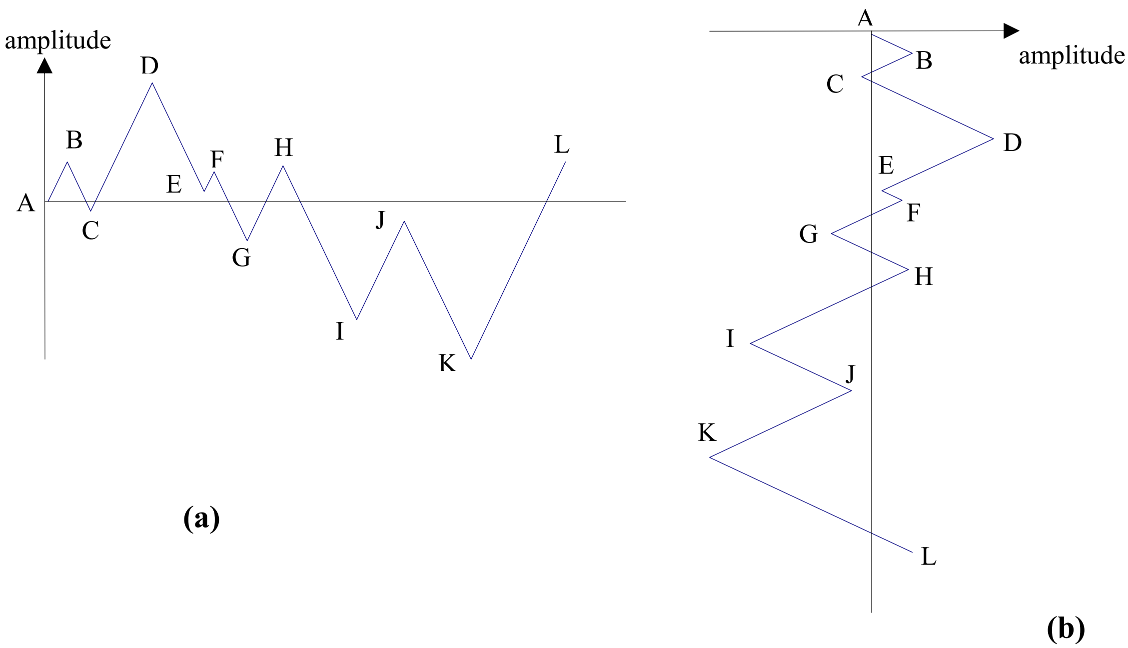

Figure 4. Sample random history to demonstrate amplitude counting methods

A relatively simple approach to counting half-cycles is to consider peak-to-valley or valley-to-peak amplitudes. In the sample history shown in Fig.4a, AB, BC, CD, DE, etc. would each represent one reversal and the vertical distance between the peaks and valleys would represent double amplitudes of deformation. An alternative approach is shown in Figure 4b. For random histories in which there are relatively few cycles to failure and the majority of damage is attributed to a few large reversals, the rainflow cycle counting (Suidan and Eubanks, 1973) offers distinct advantages. If the random load history (Fig.4a) is rotated 90 degrees (to result in Fig.4b), the resulting profile resembles a series of pagoda style roofs. Equivalent full and half cycles can be determined by carefully monitoring the behavior of a fictitious rainfall (hence the name) as it flows down the series of roofs. Rules governing the flow of rain are as follows: A new water source begins to flow down the roof at every peak. Flow from each source will continue until: (a) it falls from a roof and does not land on a roof below; (b) water falling from a peak crosses a stream flowing in the same direction that originated at a peak of larger opposite magnitude than the flow being terminated; or (c) water running down a roof is met by water falling from a higher roof. Table 1 provides a summary of the resulting amplitudes when this method is applied to the sample random history.

Table 1. Results of rainflow counting applied to sample history

Double Amplitude	Number of Half Cycles
A-B	1
B-C	1
C-D	1
D-K	1
E-F	2
G-H	2
I-J	2
K-L	1

2.3.1 Application to RC Columns

The computation of cumulative damage using the principles described in the previous section will now be applied to a displacement history obtained from random-cyclic testing of an identical flexural column for which the fatigue life relationship shown in Equation (1) was derived. The displacement history was calculated from separate inelastic time-history analysis of the prototype bridge column subjected to a series of four earthquakes: a major event, an after-shock, a minor event and a design-level event. Figure 5a shows the force-deformation hysteresis under the imposed loading. The next series of plots show the displacement history, the computed peak-valley and valley-peak displacement amplitudes and the cumulative damage index. The fact that the cumulative damage index attains a value of unity near failure of the testing is not incidental nor coincidental: the parameters of the fatigue model were calibrated from an identical column and the resulting finding validates the applicability of Miner's linear damage model.

2.3.2 Application to Reinforcing Bars

Modern computational tools for the analysis of RC structures are often based on tracing the cyclic behavior of constituent materials. Hence, the strain history of reinforcing bars can be recorded with reasonable accuracy. This information can be processed in real-time during the analysis or post-processed following the analysis.

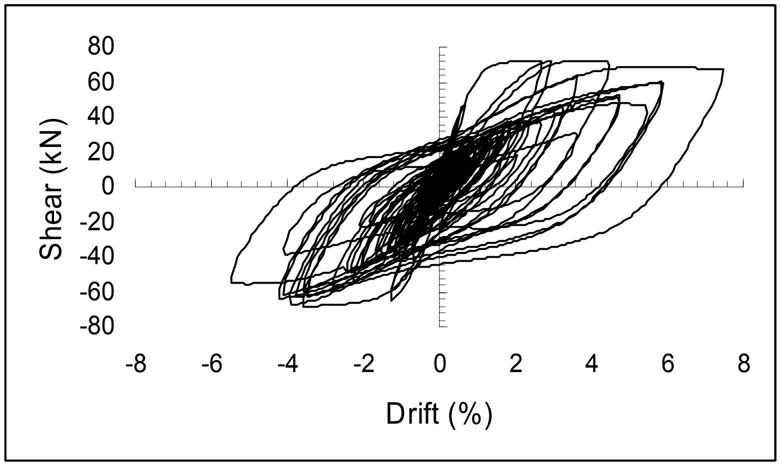

(a)

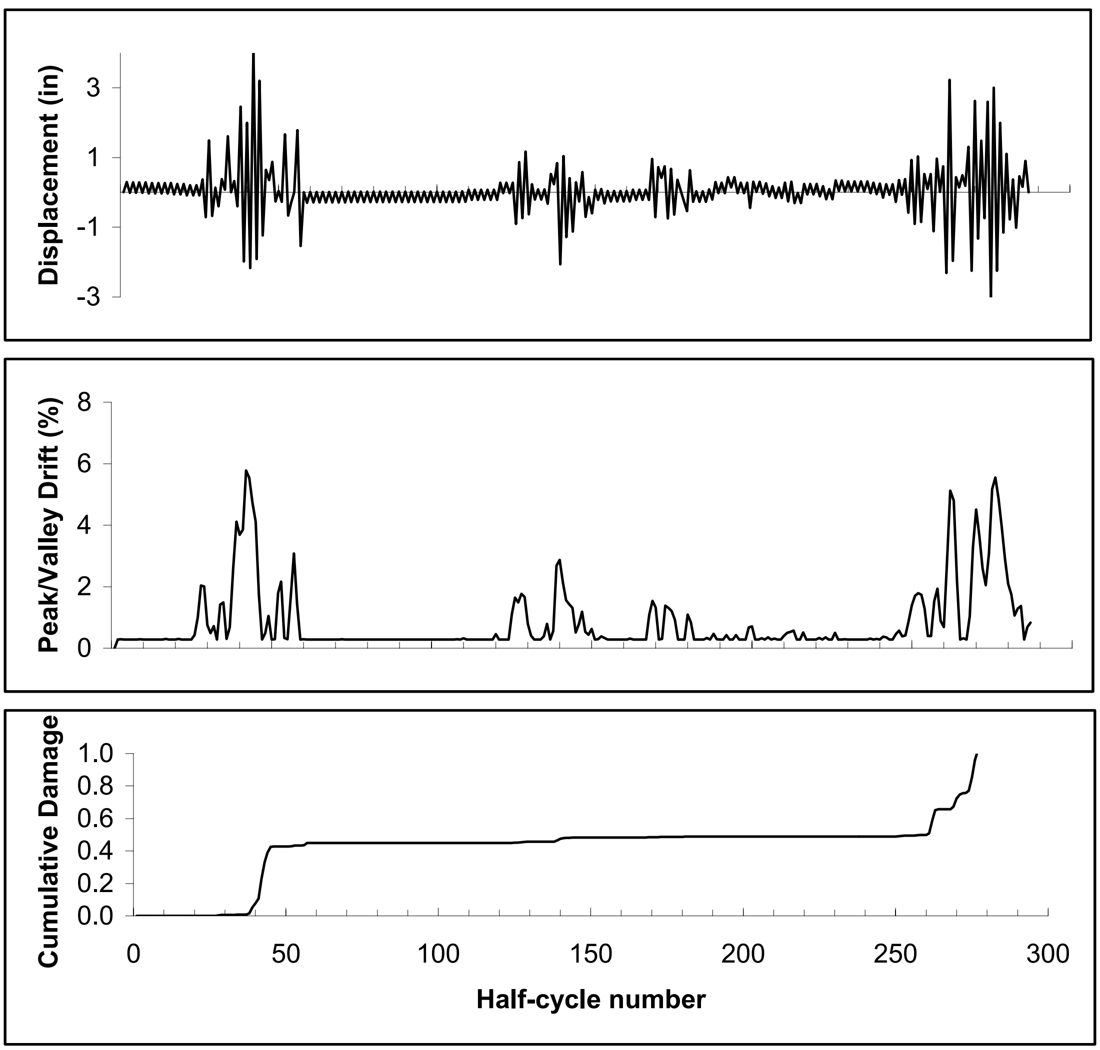

(b)

Figure 5. Application of fatigue-based damage model to simulated seismic loads

Alternatively, approximate expressions can be used to estimate the strain history. Given the response of an element in terms of force and deformation, it is possible to approximate the strain history in the rebar based on several simplifying assumptions. The plastic curvature at a section can be estimated if an equivalent hinge length is assumed, as follows:

$$\Phi_p = \frac{\Delta_p /(L-0.5l_p)}{l_p} \tag{4}$$

where: Φ_p = plastic curvature

l_p = plastic hinge length

Δ_p = plastic tip displacement

L = length of the element in single curvature

Once the equivalent plastic curvature has been computed, plastic strains can be estimated from:

$$\varepsilon_p = \frac{\Phi_p d'}{2} \tag{5}$$

where: ε_p = plastic strain

d' = distance between extreme longitudinal rebars

This relationship assumes that depth of the neutral axis remains essentially the same for both forward and reverse cycles, which is reasonable for bridge columns with low levels of axial loads. Further, the plastic rotation is assumed to be concentrated at the mid-section of the hinge. The resulting expressions are only meant to illustrate some basic principles which explore the applicability of fatigue-based models in damage estimation and correlation of physical damage states to measured performance.

3. PEAK DEMAND VS. CUMULATIVE EFFECTS: AN ILLUSTRATION

The information presented in the previous section outlined procedures to estimate cumulative damage resulting from low-cycle fatigue. The need to incorporate low-cycle fatigue effects in seismic evaluation is now investigated. This is best illustrated through an example. The response of an existing six-story building to earthquake-induced lateral loads is considered. The details of the building and the characteristics of the earthquake ground motion are not relevant to the illustration (though they are important parameters if a generalized design procedure is being developed). Figure 6 shows the shear vs. drift response resulting from a pushover analysis of the building. In addition to the base shear vs. roof drift, the response for the first story level is also shown, which has been identified as the critical story with the largest deformation demands.

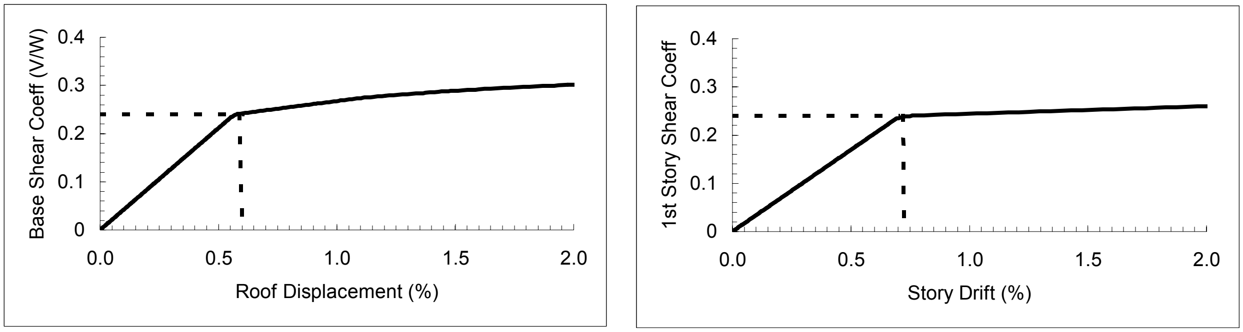

Figure 6. Pushover Analysis of Example 6-Story Frame: Shear-Drift Response

Next, the building is subjected to an earthquake load of reasonable magnitude so as to induce inelastic behavior. The resulting response is shown in Figure 7a. In traditional seismic evaluation, only the peak response of the system is considered. In fact, the specifications in FEMA-356 list the same acceptance criteria for nonlinear methods: pushover or time-history thereby implying that cumulative effects are not important. This is equivalent to considering only one cycle of response as indicated in Figure 7b. However, critical elements on the first floor of the building are subjected to several inelastic reversals. For the case study considered, every cycle of response after first yield is an inelastic cycle. The effects of cycles below the peak demand can be evaluated using principles of low-cycle fatigue introduced in the previous section. In the next section, some general characteristics of such effects will be investigated.

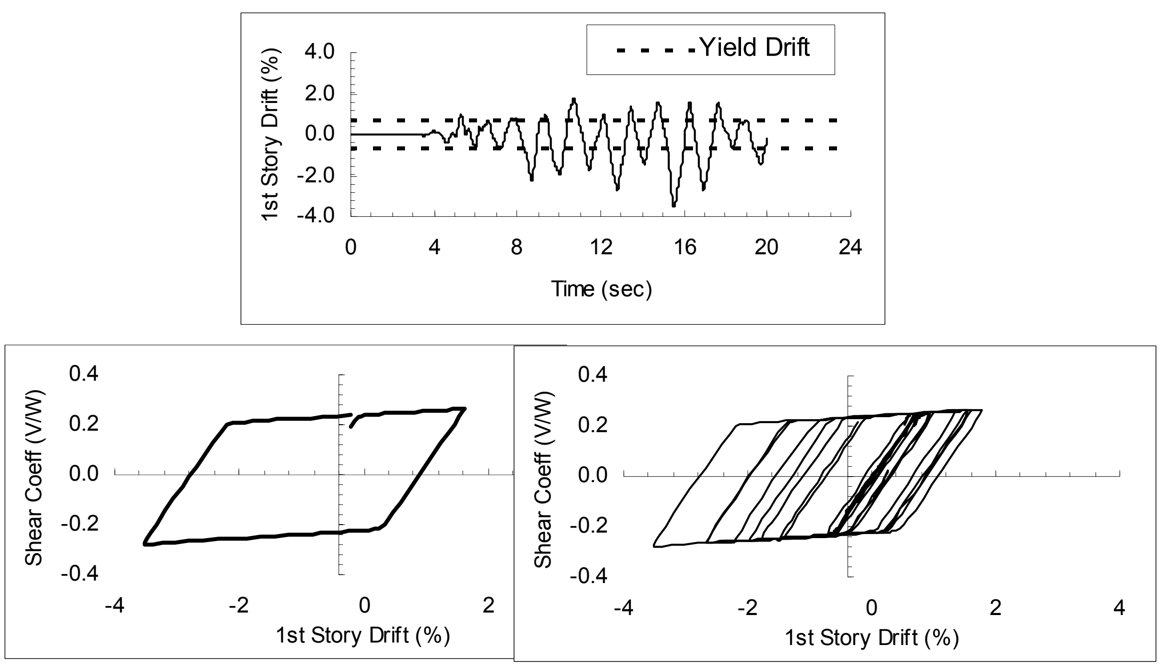

Figure 7. Response of the Building to a Severe Earthquake

4. INCORPORATING CUMULATIVE DAMAGE INTO SEISMIC DESIGN

The incorporation of low-cycle fatigue effects into a seismic design process requires a comprehensive study of deformation demands of representative structures subject to a suite of ground motions that characterize the seismic hazard at the site. The resulting deformations are then converted into equivalent cycles at a specified drift or ductility demand. This permits the application of cumulative damage models discussed in Section 2. One possible design implementation is discussed here by means of an example. A SDOF model is analyzed using an earthquake record that represents a seismic event with a 10% probability of exceedance in 50 years. The resulting force-deformation behavior is represented by a bilinear hysteretic relationship with a post-yield stiffness of 5% and a damping coefficient of 5% of critical damping. The resulting inelastic responses for a range of fundamental periods are transformed into equivalent cycles at the peak deformation demand. In order to permit a comparative evaluation of monotonic versus cyclic demand, the damage index defined in Equation (3) and the fatigue life expressions given in Equation (2) are used.

If only the peak deformation demand was considered in design and evaluation, the resulting damage index would contain only a single term in the summation represented by Equation (3). Cumulative effects, on the other hand, would also incorporate the effects of damage resulting from smaller amplitudes. Though the contribution of the peak amplitude is dominant, Figure 8 illustrates the effect of considering cyclic demand when evaluating the resulting damage. In this case, the response at T=0.2 seconds is elastic. With increasing period, the cyclic damage increases relative to the corresponding monotonic estimate. Eventually, as the period increases further, the imposed seismic demands decrease and damage computed using monotonic peak estimates are comparable to cyclic demands.

5. CONCLUDING REMARKS

Modern seismic codes rely mostly on the use of a response spectrum to provide engineers with a measure of seismic demand. However, in the light of the above discussion on cumulative effects, it is clear that such an approach may be an insufficient means of estimating the real cyclic demand imposed on a structure. The example used to illustrate the effects of cumulative damage (Figure 8) was based on a single earthquake and simplified SDOF models assuming a bilinear force-deformation behavior. Similar simulations using a suite of ground motions can provide an improved estimate of cumulative effects. Further, consideration of other critical factors such as degrading material behavior, or the application of the methodology to MDOF models of multistory buildings will yield a more comprehensive understanding of the need to include low-cycle fatigue damage in performance-based seismic design and evaluation.

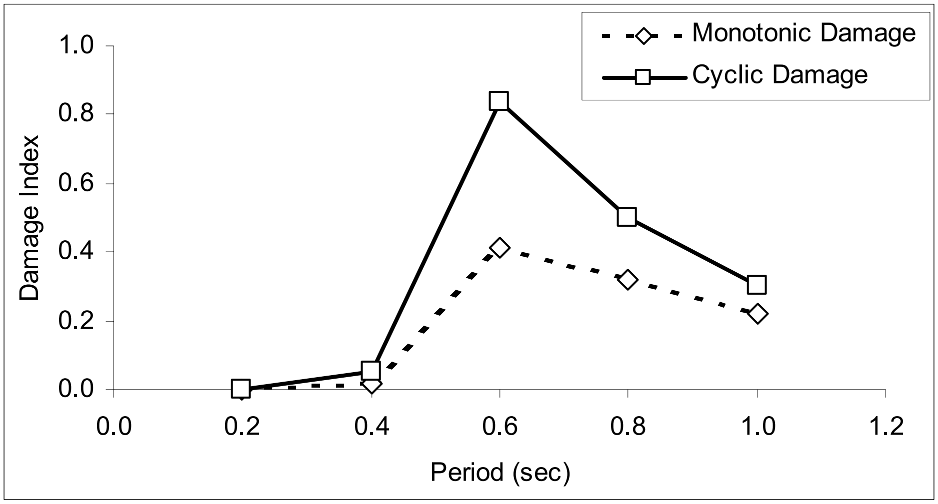

Figure 8. Incorporating cumulative effects into acceptance criteria

6. REFERENCES

ATC-24 (1992). *Guidelines for Cyclic Seismic Testing of Components of Steel Structures.* Applied Technology Council, Redwood City, CA.

Barsom, J.M. and Pellagino, Jr. J.V. (2002). Failure analysis of welded beam-to-column connections. *ASCE Journal of Materials in Civil Engineering.* Vol.14, No.1., 24-34.

Brown, J. and Kunnath, S.K. (2000). *Low Cycle Fatigue Behavior of Longitudinal Reinforcement in RC Bridge Columns.* Technical Report MCEER-00-0007, Multidisciplinary Center for Earthquake Engineering Research. Buffalo, NY.

Chung, Y.S., Meyer, C. and Shinozuka, M. (1989). Modeling of concrete damage. *ACI Structural Journal*. Vol. 86, No.3, 259-271.

DiPasquale, E., Ju J-w., Askar, A. and Cakmak, A. (1990). Relationship between global damage indices and local stiffness degradation. *ASCE Journal of Structural Engineering.* Vol. 116, No.5, 1440-1456.

El-Bahy, A. Kunnath, S.K., Stone, W.C. and Taylor, A.W. (1999). Cumulative seismic damage of circular bridge columns: benchmark and low-cycle fatigue tests. *ACI Structural Journal.* Vol. 96, No.4, 633-641.

FEMA-356 (2000), *Prestandard and Commentary for the Seismic Rehabilitation of Buildings*, Federal Emergency Management Agency, Washington, D.C.

Kasiraj, I. (1972). Fatigue failure of nonlinear multistory seismic structure. *ASCE Journal of Structural Division*. Vol.98, No. ST3, 655-670.

Kratzig, W.B., Meyer, I.F. and Meskouris, K. (1989). Damage evolution in reinforced concrete members under cyclic loading. *Proc. 5th International Conf. On Structural Safety and Reliability*. San Francisco. Vol. II, 795-802.

Krawinkler, H., Zohrei, M., Lashkari-Irvani, B., Cofie, N.G. and Hadidi-Tamjed, H. (1983). *Recommendations for Experimental Studies on the Seismic Behavior of Steel Components and Materials.* Technical Report No.61, John Blume Earthquake Engineering Center, Stanford University, CA.

Kunnath, S.K., Reinhorn, A.M. and Lobo, R.F. (1992). *IDARC Version 3.0: A Program for Inelastic Damage Analysis of RC Structures.* Technical Report NCEER-92-0022, National Center for Earthquake Engineering Research. Buffalo, NY.

Kunnath, S.K., El-Bahy, A., Taylor, A.W. and Stone, W.C. (1997). *Cumulative Seismic Damage of Reinforced Concrete Bridge Piers.* Technical Report NCEER-97-0006, National Center for Earthquake Engineering Research. Buffalo, NY.

Mander, J.B. and Cheng, C. (1995). Renewable Hinge Detailing for Bridge Columns. *National Seismic Conference on Bridges and Highways.* San Diego, Dec.10-13.

Miner, M.A. (1945). Cumulative Damage in Fatigue. *Journal of Applied Mechanics.* Vol.12, pp.A-159.

Park, Y.J. and Ang, A.H.S. (1985). Mechanistic seismic damage model for reinforced concrete. *ASCE Journal of Structural Division*. Vol.111, No. ST4, 722-739.

Suidan, M.T. and Eubanks, R.A. (1973). Cumulative fatigue damage in seismic structures. *ASCE Journal of Structural Division*. Vol.99, No. ST5, 923-943.

SESSION A-3: FRAME TESTS

Chaired by

♦ Allin Cornell and Manabu Yoshimura ♦

SHAKING TABLE TEST OF REINFORCED CONCRETE FRAMES WITH/WITHOUT STRENGTHENING FOR ECCENTRIC SOFT FIRST STORY

Yousok KIM[1] and Toshimi KABEYASAWA[2]

ABSTRACT

Dynamic tests were conducted on a third scale reinforced concrete pilotis-type wall-frame structures with considerable stiffness and strength eccentricity in the first story. Two specimens with the same sectional dimensions and reinforcement details were constructed and tested simultaneously on the large shaking table at NIED, Tsukuba. One was a bare reinforced concrete structure designed following old reinforcement detail practice in Japan, while the other was strengthened before the test with polyester fiber sheet, called as SRF method. The torsional response in the first story magnified the displacement of the independent columns on the weak side row due to the large eccentricity, and the torsional coupling effects were a little lager in inelastic response rather than in elastic. These two columns without strengthening failed in shear resulting in collapse associated with loss of the axial load carrying capacity, whose collapse process was traced on the basis of test results. On the other hand, the frame strengthened by SRF not only responded stably to the same input motion with minor damage but also survived still higher levels of succeeding input motions.

.

1. INTRODUCTION

Among the characteristics of structures that suffered severe damage or collapse during past earthquake, the subject to be investigated herein is as follows: (1) the lack of shear strength in RC columns designed following 1970's Japanese reinforcement detail practice, which lead to shear failure and the loss of axial load carrying capacity, (2) asymmetric plan system composed of independent column frame and wall frame, which induce considerable stiffness and strength eccentricity concentrating damage on weak frame. Two frame specimens with these characteristics, except that one specimen was strengthened by polyester sheet while the other was not, were tested simultaneously on the shake table. The objectives of this study, therefore, are to understand the collapse process of columns with poor shear capacity, to assess the influence of stiffness and strength eccentricities on elastic and inelastic earthquake responses and to verify the effectiveness of polyester sheet as the seismic retrofit materials.

[1] *Graduate student, Department of Architecture, The University of Tokyo*
Email:yskim@eri.u-tokyo.ac.jp
[2] *Earthquake Research Institute, The University of Tokyo*
Email: kabe@eri.u-tokyo.ac.jp

2. SHAKING TABLE TEST

2.1 Description of specimen

A one-third scale reinforced concrete specimen was used in this experiment, which comprises wall and column frame in the first story and wall frames only in the second story as shown in Figure 1. The cross-sectional dimensions and details of wall and column are illustrated in Table 1. Asymmetric plan in the first floor generate considerable stiffness and strength eccentricity amount up to 0.24 and 0.25, respectively. The stiffness eccentricity in the first story is given by:

$$R_{e_{kx}} = \frac{e_{kx}}{\sqrt{a^2 + b^2}}, \qquad e_{kx} = \frac{\sum {}_i k_x \cdot {}_i l_y}{\sum {}_i k_x} \tag{1}$$

where, e_{kx} = the distance between center of stiffness and mass, ${}_i l_y$ = the distance of each frame from center of mass, a, b = the dimension of plan in longitudinal and transverse direction, ${}_i k_x$ = stiffness of i frame in loading direction, x, which was calculated from pushover analysis in elastic range, and $\sum {}_i k_x$ = the sum of stiffness of all frames in loading direction.

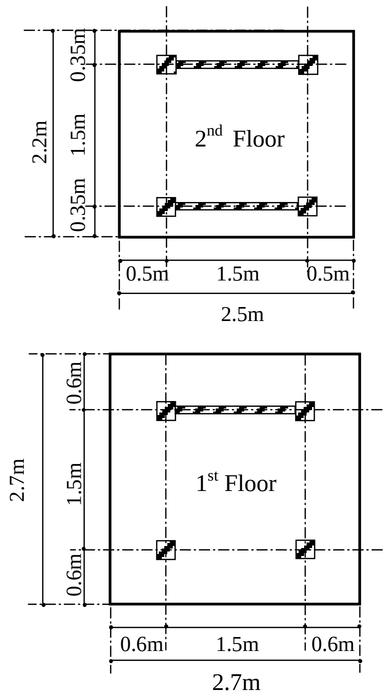

Figure 1: Plan of specimen

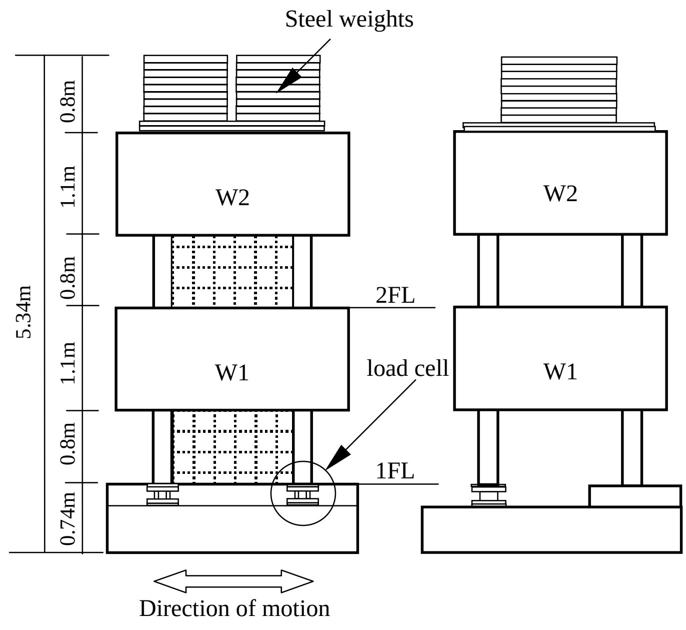

Figure 2: Elevation of specimen

The strength eccentricity was calculated using equation (2), where each frame's strength, ${}_iq_x$, was calculated using material properties from concrete cylinder test and tensile test of sample bars, and then used to calculate the capacity eccentricity of the frames to the mass, e_{qx}, together with the base shear coefficient, C_B and the distance, ${}_il_y$.

$$R_{e_{qx}} = \frac{e_{qx}}{\sqrt{a^2+b^2}}, \qquad e_{qx} = \frac{\sum {}_iq_x \cdot {}_il_y}{\sum {}_iq_x} \cdot C_B \tag{2}$$

Table 1: Section details of members

Floor	Column		Wall	
2	X×Y	200×200	Thickness	50
	Main bar	12-D10	Vertical and horizontal bar	D6@100
	Hoop	2-D6@50		
1	X×Y	200×200	Thickness	50
	Main bar	12-D10	Vertical and horizontal bar	D6@100
	Hoop	2-D4@50		

Table 2: Material properties of concrete

	σ_B (MPa)	ε_c (μ)	E_c (MPa)	σ_t (MPa)	age (days)
Superstructure	24.1	1894	21556	2.38	86
Base	25.37	2060	23096	2.22	108

Table 3: Material properties of steels

	E_s (MPa)	σ_y (MPa)	ε_y (μ)
D4	156490	188.4	1210
D6	185288	439.1	2372
D10	175137	352.4	2011

Table 4: Stiffness and strength eccentricity ('( )' indicate shear coefficient)

	Column side	Wall side
Elastic stiffness (N/mm)	9.1×10^4	4.57×10^5
Strength (KN)	125.5 (0.28)	429.7 (0.97)
Base shear coefficient	1.25	
Stiffness eccentricity	0.24	
Strength eccentricity	0.25	

Total height of specimen is 5340mm, which is the sum of base (500mm), load cell (240mm), the first story (800mm), W1 (1100mm), the second story (800mm), W2 (1100mm) and steel plates (800mm) (Figure 2). Two concrete masses, W1 and W2 (284.6 KN), and steel plates (148.3 KN) on the specimen produced axial load stress, $0.15 A_g f_c$ ($f_c = 18MPa$) in the first story column, which corresponded to that of six-story building. The first story independent columns were designed following 1970’s Japanese reinforcement detail practice, which could be vulnerable to shear failure after flexural yielding, as shown in Figure 3.

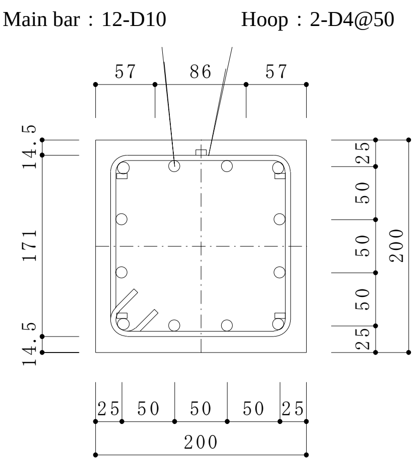

Figure 3: reinforcement details of column

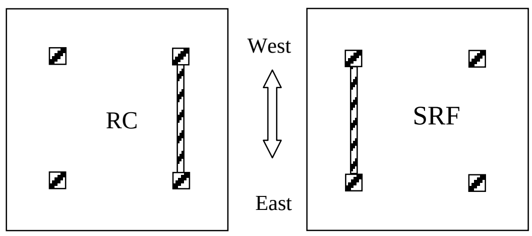

Figure 4: Specimen arrangement on shake table

2.2 Strengthening Method

Two specimens with the same properties and dimension were constructed and tested on the shake table simultaneously as shown in Figure 4, one of which was strengthened with polyester fiber sheet and belt (SRF specimen) and the other was not (RC specimen). The polyester sheet used for reinforcing materials in this experiment was developed to improve the capability of vertical member sustaining axial load under large lateral deformation caused by severe earthquake loading, whose effectiveness had been verified through the static column tests with various conditions ([1]-[5]). The characteristics of the sheet are such as toughness, durability, heat-resistance and flexibility, which improve workability and need no special technique in reinforcing process. The properties of SRF sheet and belt are summarized in Table 5 and the results of tensile test showed almost linear relationship between stress-strain relations, and the sheet failed at relatively large strains of 0.10 to 0.35. Only the first story in the SRF specimen was reinforced. The reinforcing method and materials are a little different in column and wall side. Column side was wrapped with 3mm single-layer polyester belt (Figure 5(a)), while the wall with boundary columns were wrapped with double layer polyester sheet of 0.9mm, using epoxy-urethane adhesive (Figure 5(b)).

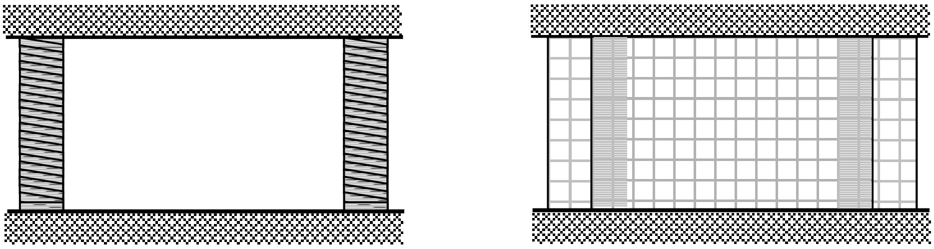

(a) column **(b) wall side**

Figure 5: SRF specimen

Table 5: Material properties of sheet and belt

	Model	Thickness (mm)	Width (mm)	Tensile strength (MPa)	Modulus of elasticity (MPa)
Belt	SRF3050	3	50	532	2904
Sheet	SRF905	0.9		203	1355

2.3 Base Motion Input Plan and Instrumentation

The two specimens were subjected to the series of recorded motions with selected five levels as shown in Table 6: TOH, Miyagi-ken Oki earthquake recorded at Tohoku university in 1978, ELC, Imperial Valley earthquake recorded at El centro in 1940, JMA, Hyogo-Ken Nambu earthquake recorded at Japan Meteorological Agency in 1995, CHI, Chile earthquake in 1985. The SRF specimen, which survived these motions, were subjected to additional three motions with higher levels of TAK, Hyogo-Ken Nambu earthquake recorded at Takatori station in 1995 and CHI, after removing the collapsed RC specimen from the table.

Table 6: Base motion input plan

Earthquake data	Maximum target velocity	Ratio to the prototype	Maximum acceleration of prototype	Maximum velocity of prototype	Maximum acceleration input to specimen	Maximum velocity input to specimen
	(kine)		(gal)	(kine)	(gal)	(kine)
TOH	12.5	0.3	258.2	40.9	77.5	7.2
TOH	25	0.6	258.2	40.9	155	14.4
ELC	37.5	1.1	341.7	34.8	375.9	21.7
JMA	50	0.6	820.6	85.4	492.4	28.9
CHI	50	0.7	884.4	70.6	619	28.3
TAK*	125	1.0	605.5	124.2	605.5	71.6
CHI*	63	0.9	884.4	70.6	796	36.4
CHI*	50	0.7	884.4	70.6	619	28.3

* only for SRF specimen

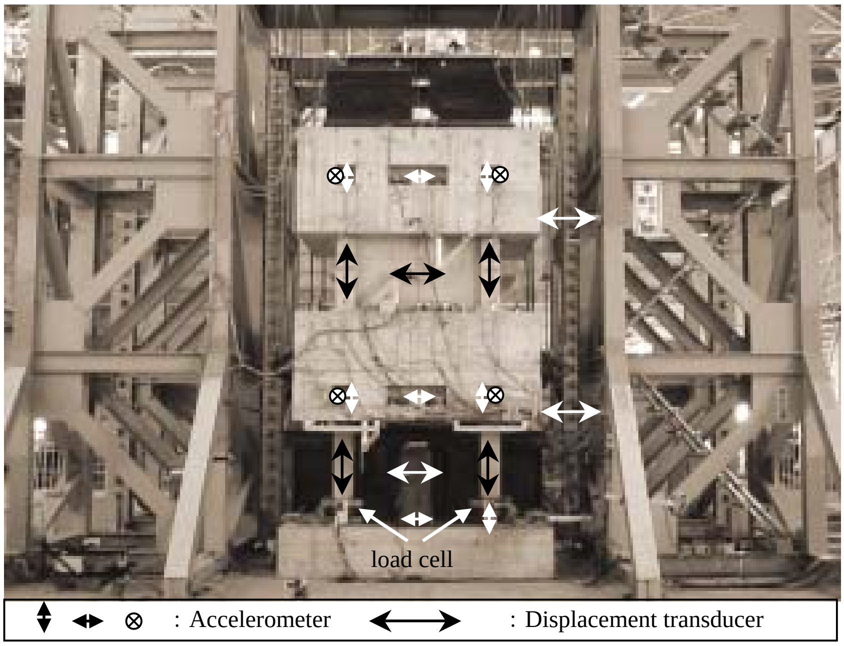

Figure 6: Experimental setup and instrumentation

The levels of the base motions were determined on the basis of preliminary analysis results, from which the RC specimen was expected to collapse at the stage 5 (CHI50). The duration time of the base motions was scaled by $1/\sqrt{3}$ to satisfy the similitude law. The axial stresses and shear coefficients were also corresponded to the proto-type six-story building by the additional mass (steel plates) on the specimen. Before and after the input of base motions, a white noise motions with small level was input to observe the change of the natural frequency of the damaged specimens.

The responses of the specimens to the base motion, such as acceleration, displacement, strain in steel bars and shear and axial forces in the first story columns, were recorded in 1000Hz sampling rate using accelerometers (22 channels), displacement transducers (20 channels), strain gauges (36 channels) and load cells (4 channels), respectively. The experimental setup and location of measuring instruments are identical for both specimens as shown in Figure 6. Also four different types of accelerometers were used for another objective, the development of economical and mass-productive accelerometers as standard tools for damage detective system or disaster prevention system. From the recorded accelerograms in each story, the maximum inter story drift can be calculated after the earthquake events, by which the warning during the earthquake or the post-earthquake safety evaluation can be done automatically.

3. TEST RESULTS

3.1 Damage Process of Specimen

The damage process of the specimens was evaluated by three methods, which were observation of cracks generated in specimen, the number of yielded strain gauge attached to reinforcing bars and the change of natural frequency calculated from system identification method. In case of the SRF specimen, however, the sheet and belt covering the surface of the specimen made it impossible to observe cracking, so only the two methods were available.

Table 7: Number of yielded strain gauges

	Main bars		Hoop	
	West column	East column	West column	East column
ELC37.5	0/8 (3/8)	0/8 (2/8)	0/7 (1/7)	0/7 (0/7)
JMA50	8/8 (8/8)	8/8 (8/8)	0/7 (2/7)	0/7 (0/7)
CHI50-1	8/8 (8/8)	8/8 (8/8)	1/7 (7/7)	2/7 (7/7)
TAK125	8/8	8/8	1/7	3/7
CHI63	8/8	8/8	6/7	6/7
CHI50-2	8/8	8/8	6/7	6/7

Figure 7: Crack pattern developed in columns and wall after JMA50

The numbers of yielded strains per measured in the steel bars are summarized in Table 7, which shows that all the longitudinal steel bars of both specimens were yielded at JMA50 and all the hoop reinforcements of the RC specimen were yielded at CHI50-1. The discrepancy in the numbers of yielded stain gauges between the two specimens also support the effectiveness of the SRF retrofit method.

The initial crack was occurred on the wall rather than on the column after TOH25, which was not expected and may be responsible for the out-of-plane deformation due to the torsional response. Furthermore, it was after JMA50 when the first crack was observed on the column, as though it is not explained considering the number of yielded strain gauge attached on the longitudinal steel bars. The crack patterns developed on the columns and the wall after JMA50 is illustrated in Figure 7.

The change of the natural frequency for both specimens in the course of damaging was computed using ARX model[6], from acceleration records at the base and on the concrete mass W2 under the white noise input. As shown in Figure 8, the natural frequencies for both specimens gradually decrease with increasing of damage developed in the specimens, where the higher decreasing rate can be observed in the RC specimen than in the SRF specimen.

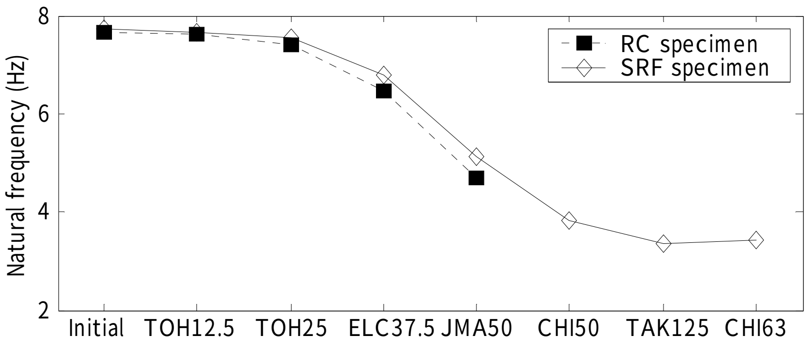

Figure 8: Transition of natural frequency

3.2 Lateral and Torsional Responses

Figure 9 shows the horizontal displacement responses of the wall and the column side during ELC37.5, which were recorded from the displacement transducer instrumented between the base and the bottom of W1. The horizontal displacement response of the column side was much larger than that of the wall side in both specimens, which resulted from the torsional response with considerable eccentricity. The similar responses were observed in the other input stages as though not presented here. Furthermore, the horizontal displacement responses of the RC specimen were slightly lager than those of the SRF specimen from TOH12.5 to CHI50-1 input, which became obvious in the first part of CHI50-1 input stage where the RC specimen was collapsed (Figure 10). Note that different scales on the vertical axis for displacement are used in Figure 10(b) and Figure 10(c).

The extent of the torsional response in elastic and inelastic range was evaluated by the index r, representing the relation between lateral displacement of center and rotation angle (Figure 11(a)). The value of r become zero in case of pure torsional mode and infinite in case of parallel translation mode. Namely, the torsional responses become dominant as the value of r decreases. As shown in Figures 11(b) and (c), the index r becomes small with increasing the load level, which means that the torsional response became more dominant in inelastic range rather than in elastic. These results may be explained in terms of the fact that strength eccentricity of this specimen, governing the characteristic of torsional response in inelastic range, is so high that the wall side was not yielded in spite of yielding in columns.

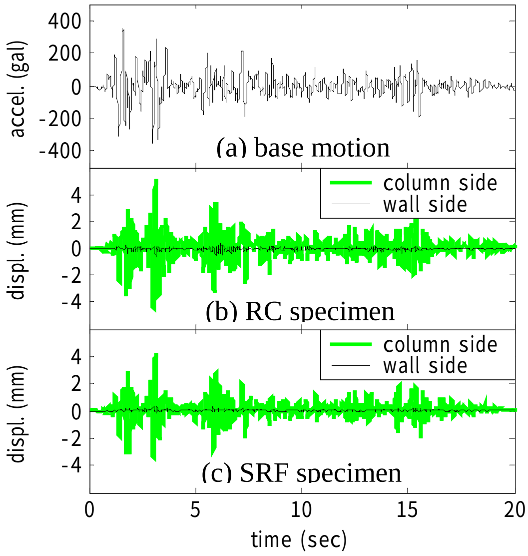

Figure 9: Horizontal displacement during ELC37.5

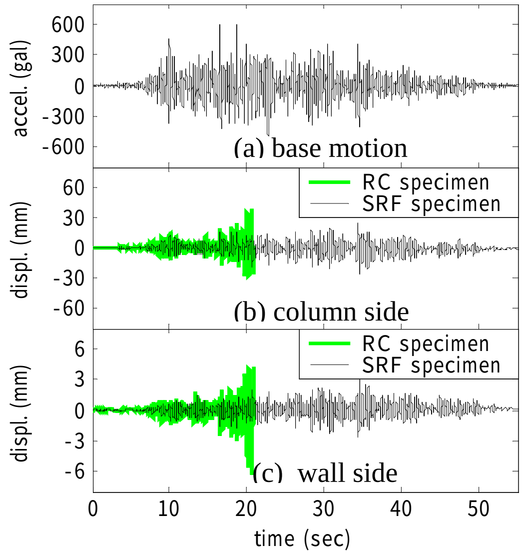

Figure 10: Horizontal displacement during CHI50-1

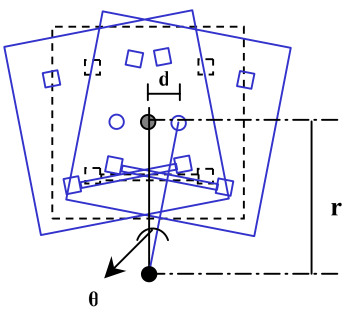

$$\theta \cong \frac{d}{r}$$

(a) Definition of r

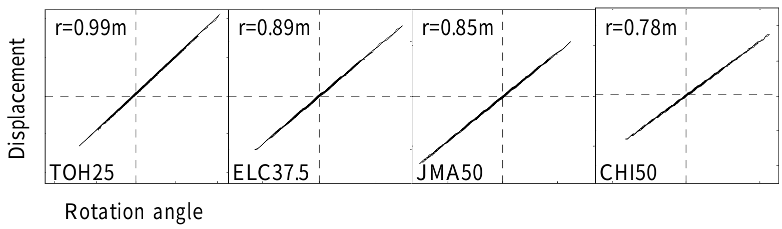

(b) RC specimen

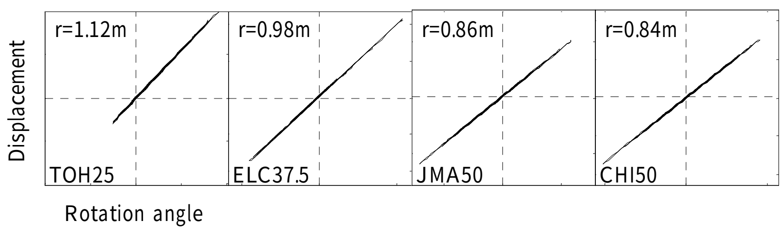

(c) SRF specimen

Figure 11: Relation between lateral displacement and rotation angle.

3.3 Shear Force Distribution

The base shear force was computed by summing the external forces calculated by multiplying masses of W1 and W2 to the acceleration record of them, from which shear forces carried by wall was obtained by subtracting shear force recorded at the load cells instrumented at the bases of the independent columns. Figure 12 (a) and (b) illustrates the shear forces carried by the columns and the wall in RC and SRF specimen, respectively, and the ratio of the column shear force to the base shear force is shown in Figure 12(c), where all the shear forces are the values at the time when the base shear force attained the peak in both directions.

From these figures, it is seen that the shear force carried by the columns is relatively smaller than that of wall and degrade gradually with increasing load level. Furthermore, the columns of the SRF specimen carry larger shear force compared to that of RC one, which accounts for the efficiency of SRF strengthening.

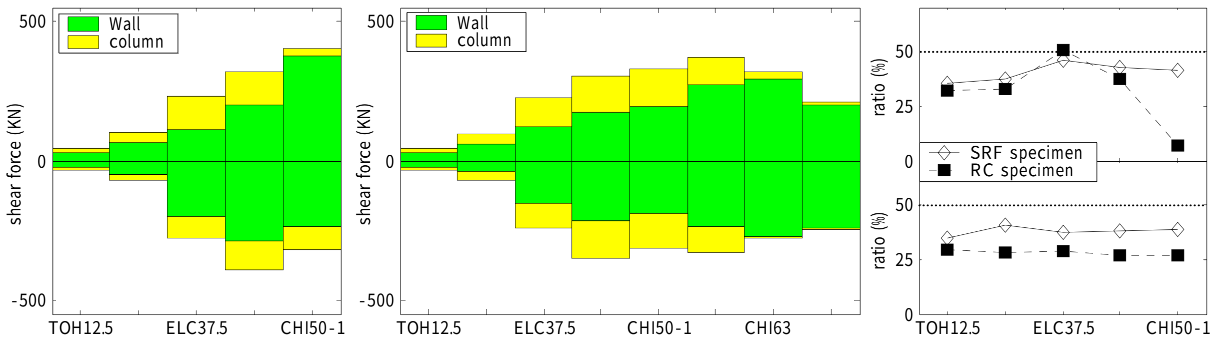

(a) RC specimen **(a) SRF specimen** **(c) ratio of column shear to base shear**

Figure 12: Shear force distribution carried by columns and wall.

3.4 Shear and Axial Hysteric Responses

The hysteresis relations between the horizontal displacement and the shear force in the two columns of the RC specimen are presented in Figure 13 together with those of the SRF specimen. The values of the maximum and minimum shear force and displacement, for which and those from RC specimens are indicated as in parentheses. The solid and dotted lines are calculated shear strength (112.9KN) and shear at calculated flexural strength (125.5KN) respectively, for the two RC columns.

In TOH12.5 and TOH25, the relations between two responses are almost linearly elastic. As the load level increases, the stiffness degrades and the lateral drift become larger, which is more obvious in RC specimen than in SRF one. The maximum shear forces were attained during JMA50 for both specimens, which was apparently larger in the SRF specimen than in the RC specimen. While the recorded maximum shear force in the RC specimen was almost the same as that of the calculated strength, that of SRF specimen exceeded that of calculated one, which may be due to the confinement of the SRF belts.

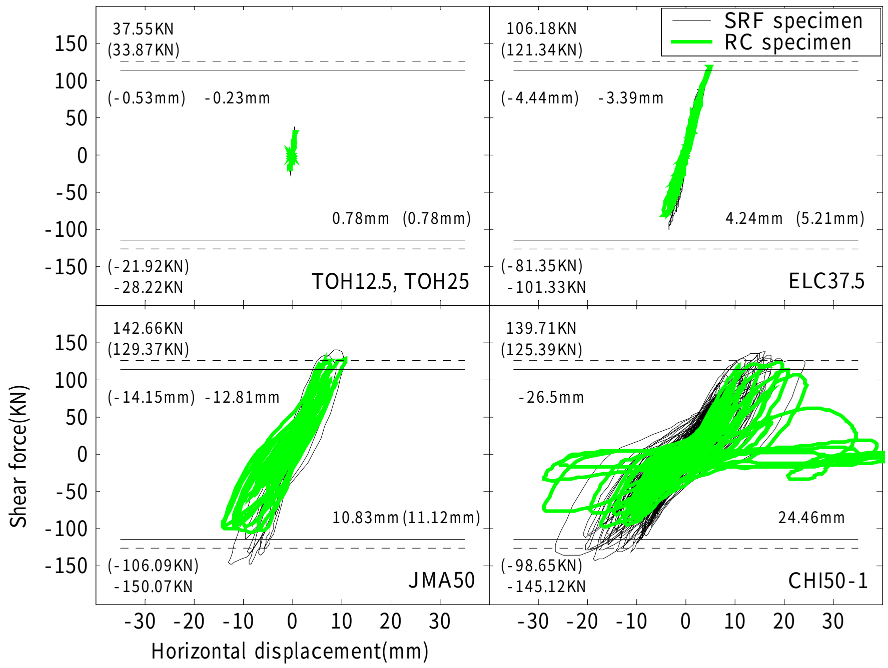

Figure 13: Shear force and displacement relation

(a) RC specimen **(b) SRF specimen**

Figure 14: Columns after CHI50-1

During the response to CHI50-1, the stiffness and strength degradations of the RC specimen became rapidly significant under reversed cyclic loadings and resulted in collapse when the elapsed time was around 20 sec. On the other hand, the hysteresis relations of the SRF specimen showed stable behavior without strength decay. Figure 14 shows the photos of the columns in both specimens after CHI50-1 input. The varying axial load vs axial deformation relations of one column of both specimens are compared in Figure 15. It is observed that the axial load-axial deformation relations of the columns were not much different for the two specimens, though axial compression rapidly increases with the progress of failure in RC specimen.

After removing the collapsed RC specimen from the shake table, the SRF specimen was tested under the three base motions with higher levels, TAK125, CHI63 and CHI50-2. The axial load-axial deformation relations and the shear force-horizontal displacement relations of the columns are shown in Figure 16 and 17, respectively. Response to one direction and considerable residual deformations was generated after CHI63 and CHI50-2, maybe due to the characteristics of the motions. Nevertheless, the SRF frame is structurally stable against axial collapse although the lateral stiffness and strength decayed and the axial deformation was accumulated.

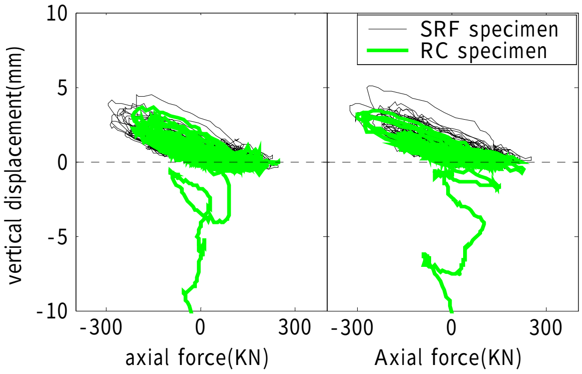

Figure 15: Relation between axial force and axial deformation under CHI50-1

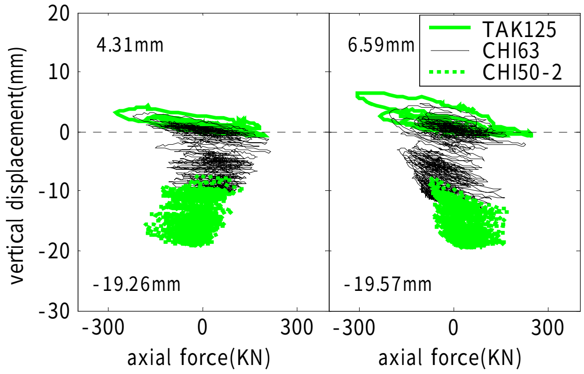

Figure 16: Relations between axial force and axial deformation of SRF specimen

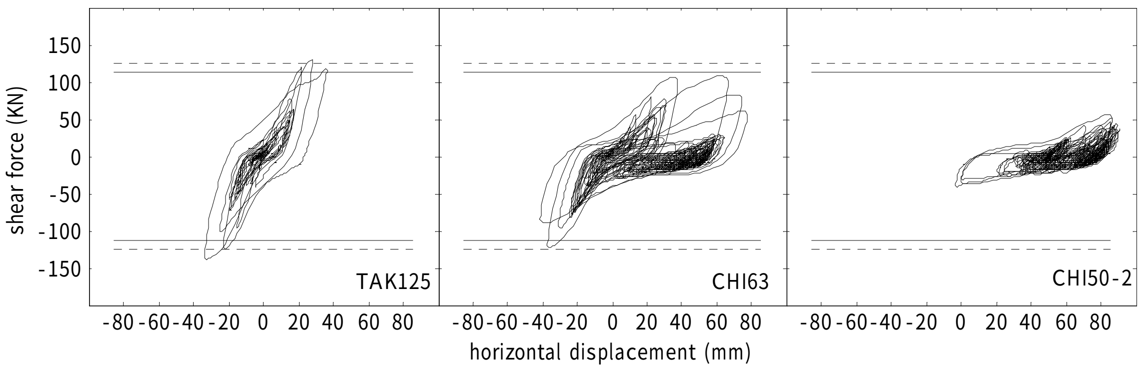

Figure 17: Hysteresis relations of SRF specimen after removing RC specimen.

3.5 Collapse Process of RC Columns

To understand the process of RC column failure, time-history responses and their relations for detailed data during CHI50-1 for 10 seconds (from 12 to 22 sec.) are illustrated in Figure 18. The strain of the hoop was measured at the mid-height of the column.

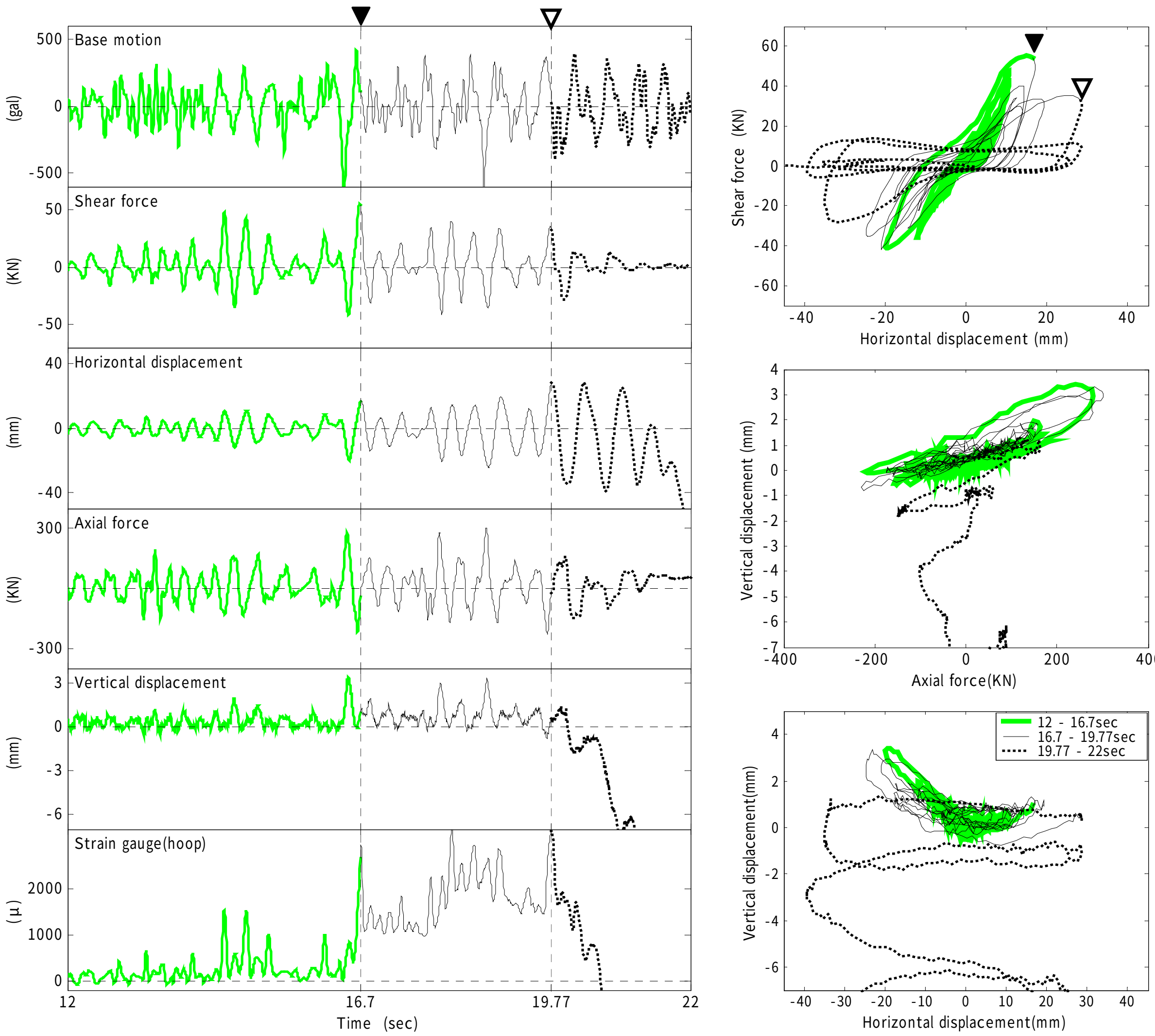

Figure 18: Responses of east column in RC specimen during CHI50-1

Two reference times, 16.7 sec. and 19.77 sec., marked with black and white triangles, were selected to divide the responses into three parts, because the large peak in shear force was recorded at the end of the first part, 16.7sec, from which both the stiffness and strength degraded considerably and lateral reinforcement bar started to expand. Also at 19.77sec the large lateral drift was recorded comparing to the previous one, lateral stiffness and strength was lost entirely and the loss of axial load-carrying capacity lead the RC specimen to collapse.

From these test data, the process and the cause of the column axial failure may be interpreted as follows: the column responded to the first peak of strength and drift to the point marked with the black triangle induced the critical cracking associated with the yielding of the hoop, which caused the residual hoop strains and the shear strength decay. The second peak drift with the white triangle exceeded the previous maximum, maybe partially due to the strength decay because it did not occurred in SRF specimen. Here, the hoop might be ruptured, because the residual strain fall down, and the loss of the interface shear transfer along the shear cracking might cause the fatal loss of the axial capacity. It should be noted that the inelastic strain of the hoop after yielding accumulated with cyclic load reversals in the second time region, which could be the main cause of the shear and axial failure of the column.

4. CONCLUSIONS

Two specimens with and without polyester sheet (SRF) strengthening for eccentric soft-first story were tested on the shake table simultaneously. The following conclusions can be drawn from the results of the earthquake simulation tests.

The collapse process of reinforced concrete columns without strengthening, that is, shear strength deterioration resulting in axial load failure along with inelastic load reversals, was shown using the responses during CHI50-1, while the SRF specimen still showed stable relations between lateral displacement and shear force with minor damage.

Throughout all the input stages, the lateral displacement responses of the column side were much lager than those of the wall side in both specimens. The torsional response was a little lager in inelastic responses than in elastic, which may be due to the large strength eccentricity. The torsional responses of the SRF specimen could be reduced from those of the RC specimen by the effect of strengthening.

With the above results, the fact that the SRF specimen survived and sustained the axial load after experiencing three additional base motions, although permanent lateral and axial deformations were considerable, verify the effectiveness of SRF reinforcing method used in this test.

ACKNOWLEDGEMENT

The test was carried out as a part of the research project "Development of post-earthquake performance evaluation using practical accelerometers," (Grant No. 12308018, PI: Toshimi Kabeyasawa) under the support of JSPS and Monbukagakusho. The dynamic test was conducted at NIED, Tsukuba, with Dr. Nobuyuki Ogawa and Mr. Atsushi Kato, NIED. The support and the cooperative works in the tests are gratefully acknowledged. The strengthening method reported herein has been international patent pending as "SRF" method by Square Inc., Japan.

REFERENCES

[1] KABEYASAWA, T., TASAI, A., IGARASHI, S., "An Economical and Efficient Method of Strengthening Reinforced Concrete Columns against Axial Load Collapse during Major Earthquake," Proceedings of the Third Workshop on Performance-based Engineering on Reinforced Concrete Building Structures, 2001, pp. 371-384.

[2] KABEYASAWA, T., TASAI, A., IGARASHI, S., "A New Method of Strengthening Reinforced Concrete Columns against Axial Load Collapse during Major Earthquake," Proceedings of EASEC-8, CD-ROM, Singapore, 2001.

[3] KABEYASAWA, T., TASAI, A., IGARASHI, S., "An Economical and Efficient Method of Preventing Old Reinforced Concrete Buildings from Collapse under Major Earthquake," Proceedings of 7NCEE, CD-ROM in print, Boston, 2002.

[4] OHSUGI, Y., KABEYASAWA, T., TASAI, A., IGARASHI, S., et al., "Effect of Sheet Strengthening on Seismic Behavior of Low-Strength Reinforced Concrete (in Japanese). Proceedings of The Third Symposium on Improvement of Preparedness to Earthquake Disaster by Investigating Collapse Process of Structures, JSCE, 2002, 183-187.

[5] KABEYASAWA, T., KIM, Y-S, et al, "Earthquake Simulation Test on Reinforced Concrete Buildings with Eccentric Soft-First Story, Part 1:Outline of Test and Part 2:Result of Test (in Japanese)," Proceedings of The Third Symposium on Improvement of Preparedness to Earthquake Disaster by Investigating Collapse Process of Structures, JSCE, 2002, 165-176.

[6] Erdal Safak (1991): Identification of Linear Structures Using Discrete-Time Filters, J. Struct. Eng. ASCE, Vol. 117(10), 3064-3085

KEYWORDS

Reinforced concrete structure; Shaking table test; Eccentricity; Polyester fiber sheet; Seismic retrofit; Shear failure; Axial load failure

SEISMIC PERFORMANCE OF FLAT PLATE SYSTEMS

John W. WALLACE, Thomas H.-K. KANG, Changsoon RHA[1]

ABSTRACT

Flat plate floor systems consisting of post-tensioned slab with shear reinforcement at the slab-column connection are commonly used in the western United States. The slab-column frame is not designed to resist the design earthquake lateral forces, but instead is checked for "deformation compatibility" to ensure it can undergo the design lateral displacements without loss of gravity load carrying capacity. Although the use of these systems is common, relatively little experimental work has been conducted to assess actual performance under either slowly varying cyclic loads or dynamic loads. The paper presents preliminary results of two, approximately one-third scale tests of two, two-bay by two story slab-column frames. One of the test frames consists of a reinforced concrete floor slab whereas the other test frame consists of a post-tensioned slab. The addition of shear reinforcement at the slab-column connection in the form of stud rails is provided in both test frames. The specimens were subjected to increasing intensity shaking using the earthquake simulator at the UC Berkeley Richmond Field Station. Overall, the test specimens performed well, with the shear reinforcement limiting the extent of the punching damage compared with tests on specimens without shear reinforcement. Excellent performance was observed for the post-tensioned slab-column frame. Background and preliminary results are provided.

1. INTRODUCTION

Common design practice in the western United States allows the structural engineer to design a building with a lateral-force-resisting-system (LFRS) and a non-participating system or gravity-force-resisting system (GFRS). The elements designated to be part of the LFRS are proportioned to resist the entire design seismic forces and provide sufficient stiffness to limit the lateral drift to acceptable levels. The elements designated to be part of the GFRS are proportioned assuming that they do not contribute to the seismic resistance, that is, these elements are designed to resist gravity forces only. The ability of the GFRS to support the gravity loads when subjected to the design lateral deformations must be checked, commonly referred to as a deformation compatibility check.

Given the practice of providing separate lateral and gravity force resisting systems, a typical building plan is shown in Fig. 1 for a four-story reinforced concrete building constructed in 1977. A plan view of the building is provided in Fig. 1(a), as are details of column geometry and

[1] *Department of Civil and Environmental Engineering, University of California, Los Angeles, USA*
Email: wallacej@ucla.edu, thkang@ucla.edu

reinforcement (Fig. 1b). The structure relies on a ductile perimeter moment frame to resist lateral loads and a post-tensioned slab – interior column system with drop panels to support gravity forces. The building suffered significant damage in the Northridge earthquake (Fig. 2) and has not been occupied since the earthquake. Damage from the earthquake consisted of first and second floor slab-column punching failures at approximately six connections at each floor level (Fig. 3). In addition, minor cracking and spalling of the perimeter frame were observed (Sabol, 1994).

For shorter buildings, it is common practice on the west coast of the U.S. to use a perimeter special moment frame with an interior slab-column gravity frame (Fig. 1). For taller buildings (10 to 25 stories), it is common practice on the west coast to use a core wall system to provide lateral strength and stiffness, and a slab-column gravity frame. This system has also been used on buildings with as many as 40 stories. The use of a post-tensioned floor slab also is common, as it allows for longer spans for the gravity frame and is easy to construct. The post-tensioning strands are typically banded in one direction, and distributed in the other direction.

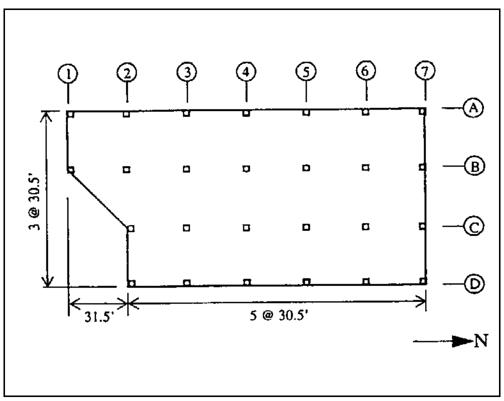

Fig. 1(a) Building floor plan

Fig. 2 Slab-column punching damage (Sabol, 1994)

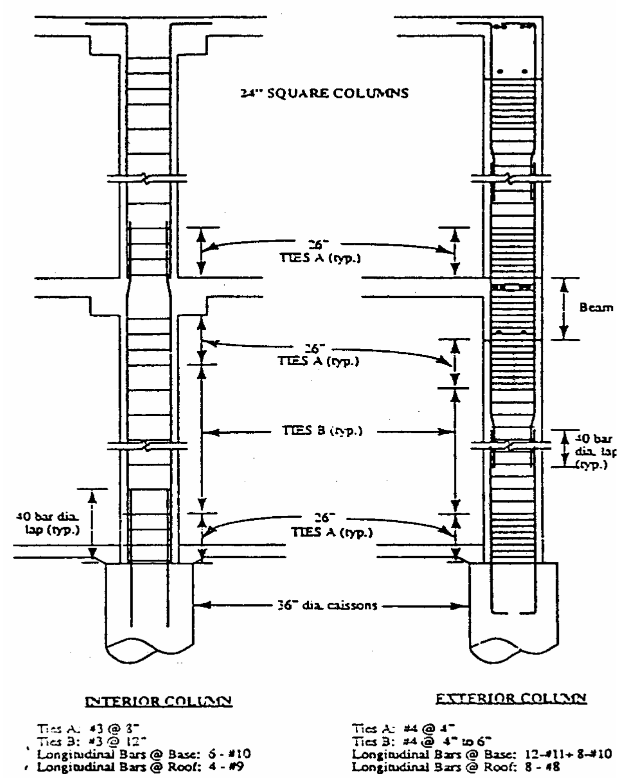

Fig. 1(b) Column elevation views

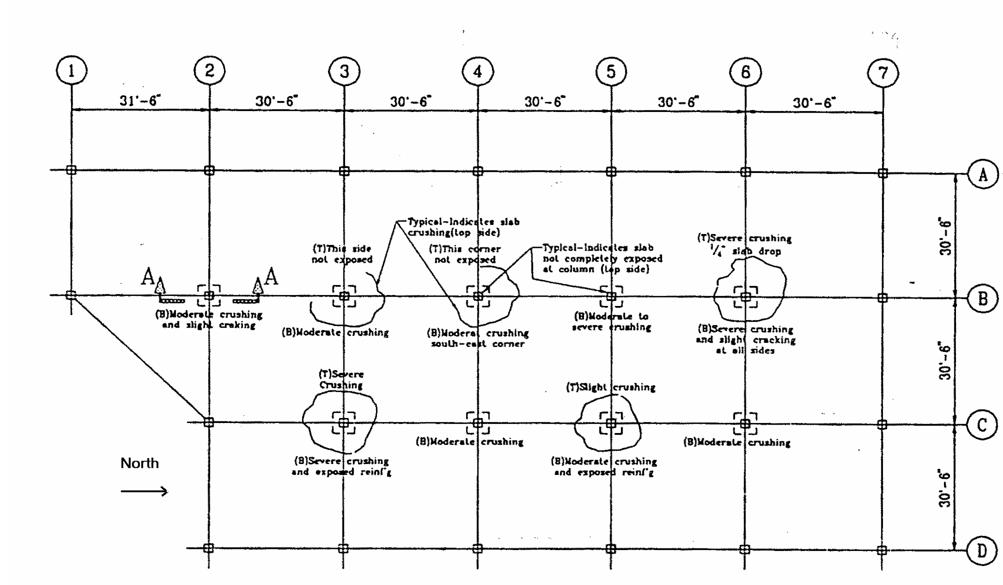

Fig. 3 Damage to first floor slab (from Sabol, 1994)

For shorter buildings, it is common practice on the west coast of the U.S. to use a perimeter special moment frame with an interior slab-column gravity frame (Fig. 1). For taller buildings (10 to 25 stories), it is common practice on the west coast to use a core wall system to provide lateral strength and stiffness, and a slab-column gravity frame. This system has also been used on buildings with as many as 40 stories. The use of a post-tensioned floor slab also is common, as it allows for longer spans for the gravity frame and is easy to construct. The post-tensioning strands are typically banded in one direction, and distributed in the other direction.

Given the longer spans for the post-tensioned floor system, the use of drop panels, as shown in Fig. 1(b), may be necessary due to the higher shear stresses that develop at the slab-column interface. The use of shear reinforcement within the slab adjacent to the column has emerged as the preferred solution to addressing the high slab-column connection shear stresses. Shear reinforcement may take the form of stirrups (e.g., Robertson et al., 2002), so-called shear bands (Pilakoutas, 2000), or so-called stud-rails (e.g., Elgabry and Ghali, 1988; Fig. 4). The use of stud-rails is very common because they are very easy to place and some test results have been published that have shown them to be effective. The use of shear reinforcement increases the shear strength of the slab-column connection ($V_n = V_c + V_s$), where V_c and V_s are the nominal shear strength provided by the concrete and shear reinforcement, respectively. The increased shear strength typically eliminates the need for a drop panel or a column capitol, resulting in reduced construction costs.

Fig. 4 Slab – column connection with stud rails (RC Specimen)

Design of slab-column connections is covered in the ACI 318 Building Code (“Building”, 2002; see Section 21.12.6) For combined lateral and gravity loads, sufficient flexural reinforcement must be placed within the column strip to resist the slab moments, and at least one-half of this reinforcement must be placed within $c_2 + 3h$ for an interior connection, where c_2 is the column dimension perpendicular to the direction of the applied loads and h is the slab thickness. In addition, the ability of the slab-column connection to transfer the unbalanced moment to the columns must be checked. Transfer of the unbalanced moment is assumed to occur through two mechanisms, flexure and eccentric shear. Reinforcement to resist the fraction of the unbalanced moment transferred in flexure $\gamma_f M_{unb}$ (e.g., 60%) must be placed within $c_2 + 3h$. The remaining fraction of the unbalanced moment $(1-\gamma_f)M_{unb} = \gamma_v M_{unb}$ (e.g., 40%) is transferred in eccentric shear on the slab critical section, defined to extend d/2 from the column face (Fig. 5).

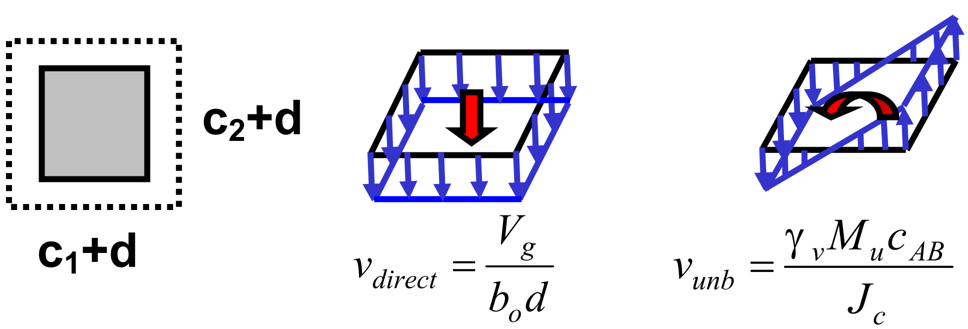

(a) slab-column critical section (b) Gravity shear (c) Eccentric shear

Fig. 5 Slab-column critical section and shear stress distributions

Where v_{direct} is the shear stress on the critical section, $b_0 = 2[(c_1+d) + (c_2+d)]d$, d is the effective section depth, V_g is the gravity force to be transferred from the slab to the column, v_{unb} is the shear stress on the critical section due to the unbalanced moment being transferred in eccentric shear, c_{AB} is the distance from the centroid of the critical section to the perimeter of the critical section, and J_c is the polar moment of inertia of the critical section (see Park and Gamble, 2000; Section 10.3.3). The combined shear stress on the critical section is found by adding the direct shear stress and the eccentric shear stress.

Experimental studies (Pan and Moehle, 1989, 1992; Moehle, 1996) have shown that the magnitude of the gravity shear stress on the critical section significantly influences the drift level at which a connection punching failure occurs (Fig. 6). For gravity shear stress ratios greater than 0.4, tests of slab-column connections reveal little displacement ductility capacity; therefore, ACI 318 (Building, 2002) puts a limit of $0.4\phi V_c$ on the concrete shear strength of the critical section (S21.12.6.8). The three data points plotted in Fig. 6 for isolated, post-tensioned, slab-column connections subjected to slowly varying drift cycles implies increased drift capacity prior to observed punching failures. However, due to the longer spans, post-tensioned slab-column floor systems tend to be more flexible than systems without post-tensioning, and also have higher gravity shear stress ratios.

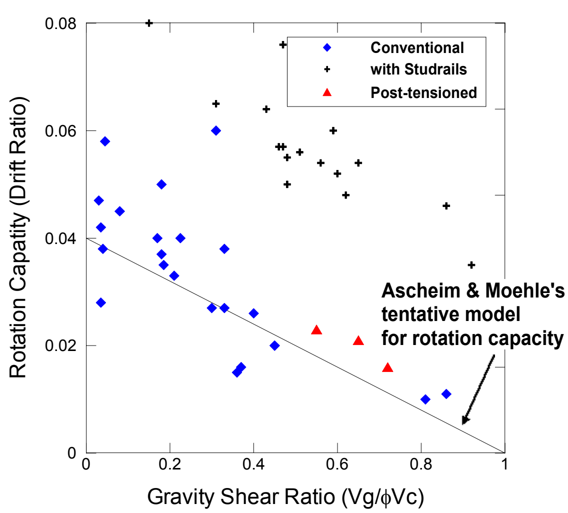

Fig. 6 Relationship between drift and gravity shear from experiments

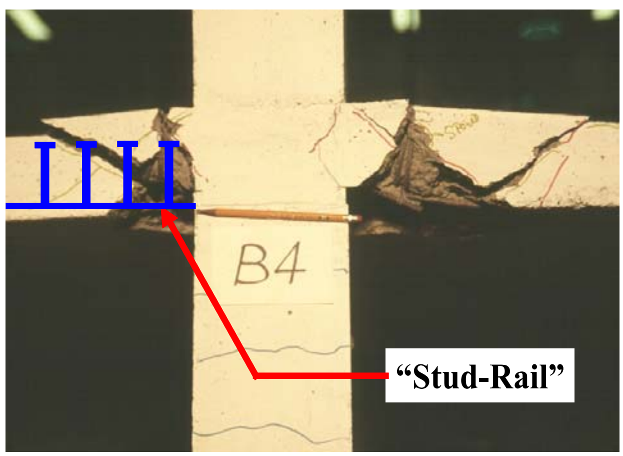

Fig. 7 Punched connection with studrail superimposed to failure plane.

In summary, US west coast design practice has evolved such that the lateral strength and stiffness are provided with either a perimeter frame or a core wall, or both (dual system). A slab-column frame is typically used for gravity loads. Post-tensioned floor slabs are common to increase span lengths, and the use of shear reinforcement in the form of stud-rails is used to increase the shear strength of the slab-column connection to allow for a thinner slab or to eliminate the need for drop panels or column capitols.

Limited test data exist from which to assess the appropriateness of current practice. The performance of stud-rail shear reinforcement is based on tests of isolated connections for cyclic loading (see Robertson et al., 2002; pp. 612). Data for post-tensioned connections are limited to three isolated slab-column connections tested at UC Berkeley (Martinez, 1993). Test results conducted on isolated specimens can be influenced by boundary conditions, and tests conducted under static loading conditions may overstate damage due to excessive crack propagation due to the application of sustained loads relative to a dynamic test. Given the prominent use of post-tensioned slab-column systems with stud-rail shear reinforcement, an experimental study for dynamic loading was undertaken to assess system performance.

2. TEST PROGRAM

The research program consisted of testing two, two-story, two-bay, slab-column systems on the shake table at UC Berkeley (Fig. 8). The specimens were approximately one-third scale representations of a full-scale prototype system. One specimen was constructed with a reinforced concrete (RC) flat-plate (Fig. 9) whereas the other specimen consisted of a post-tensioned (PT) flat-plate (Fig. 10). The shear capacity of the slab-column connections was enhanced by the use of stud-rails for both specimens (Fig. 9(b) and Fig. 10(a), (b)).

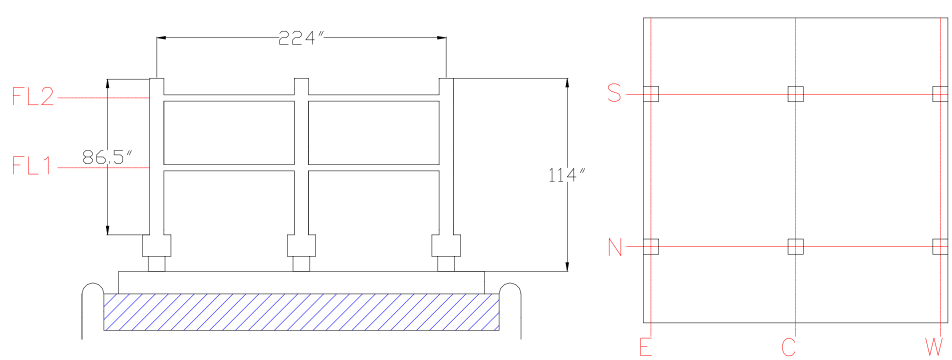

Fig. 8 Overview of shake table specimens

Fig. 9(a) Overview of RC slab reinforcement

Fig. 9(b) RC – Interior connection

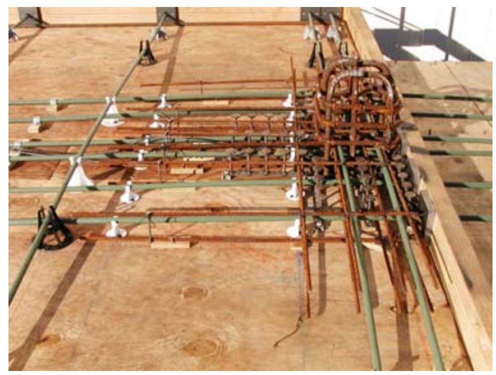

Fig. 10(a) PT – Exterior Connection

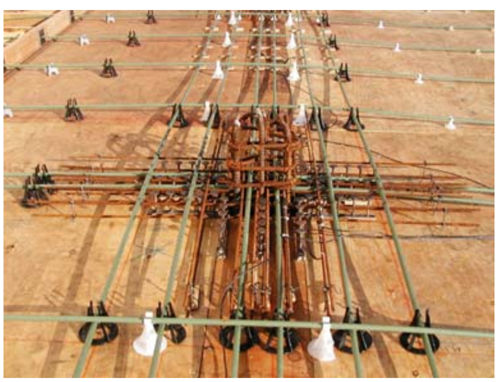

Fig. 10(b) PT – Interior connection

Fig. 10 (c) PT – Slab overview

2.1 Specimen Design & Construction

Plan views of the two specimens are shown in Fig. 11. The slab span-to-depth ratio is 23 for the RC specimen (2.06 m spans) and 37.3 for the PT specimen (2.84 m spans). Columns were 203 mm x 203 mm reinforced with 8 – 12.7 mm diameter bars with a nominal yield stress of 414 MPa. Design concrete compressive strength was 27.6 MPa. Slab reinforcement for the RC and PT specimens consisted of 9.5 mm and 6.35 mm diameter bars, respectively. Post-tensioning consisted of 8 mm nominal diameter, seven wire strand with an ultimate strength of 1,725 MPa (250 ksi). The gravity shear ratio for the interior connections was 0.26 and 0.34 for the design concrete strength of $f_c' = 27.6$ MPa (4.0 ksi) for the RC and PT specimens, respectively.

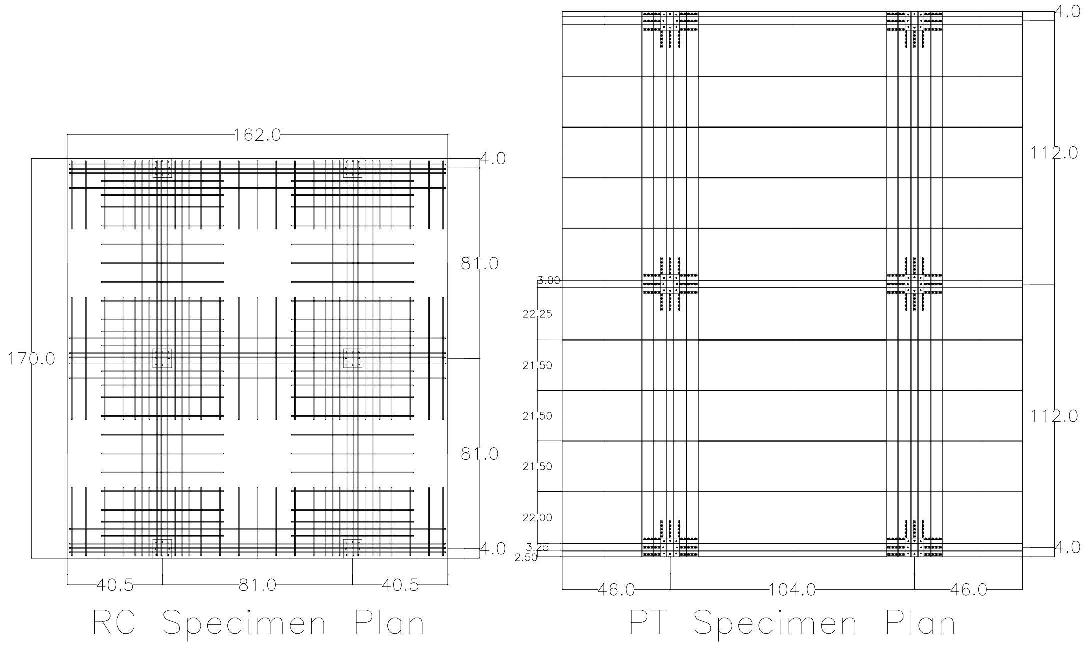

Fig. 11 Slab dimensions and top reinforcement

2.2 Specimen Instrumentation

Responses from approximately 200 instruments were monitored during the tests, including: (1) accelerometers on the table and on each floor level, (2) strain gauges on column and slab reinforcement, (3) load cells at the base of the first story columns, (4) load cells on some of the post-tensioning strands in the line of loading, (4) displacement gauges to measure average concrete strains on the slabs and columns, as well as absolute and relative displacements for each floor level, and (5) concrete strain gauges mounted on the surface of some columns. The instrumentation layout was selected to allow the determination of base shear, story displacements, overturning moment, and slab and column moments and curvatures, with a particular emphasis on evaluating the unbalanced moment transferred at slab-column connections during the dynamic tests.

2.3 Specimen Testing

The specimens were subjected to four (RC) and five (PT) table motions, with the intensity of the motions increasing with each test. The CHY087W record from the 21 September 1999 earthquake in Taiwan was selected and modified for the tests (time compressed and amplified). The tests represented: (1) low-level excitation, (2) service-level excitation to approximately 2/3 of yield displacement, (3) moderate-intensity excitation to produce limited yielding, and (4) damage-level excitation. For the PT specimen, a fifth test was run with very intense motions given that relatively little damage was observed at Run 4.

3. EXPERIMENTAL RESULTS

The tests were conducted in June and August of 2002; therefore, only preliminary results are available. Base shear versus relative displacement between the column base and the second story were determined and are plotted in Fig. 10 for the RC and PT specimens. Corrections due to rotation of the footing base were made.

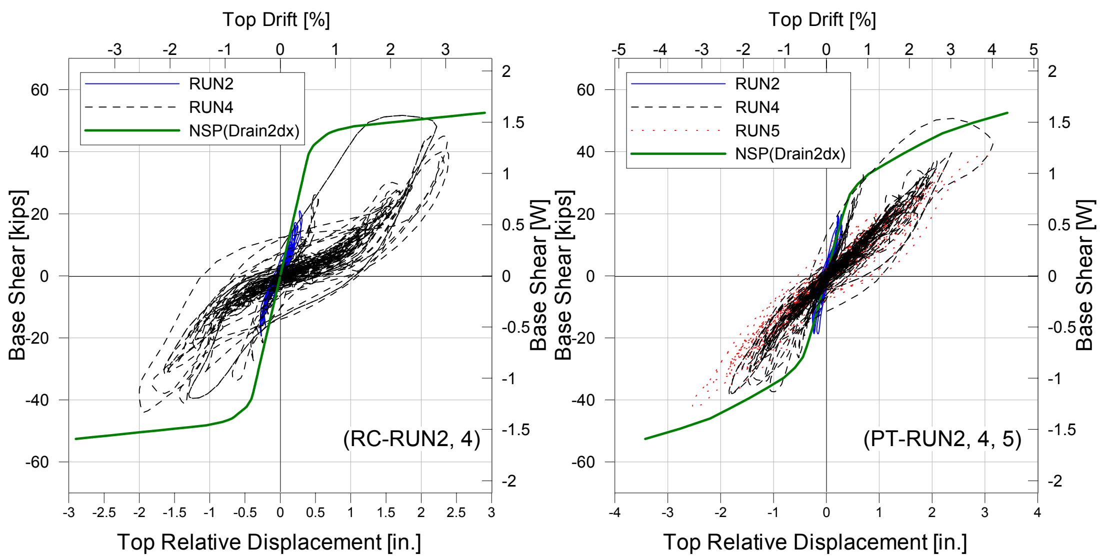

Fig. 12 Base shear vs top displacement relations

Figure 12 reveals that the RC specimen was subjected to drift levels of approximately 3% with only moderate strength deterioration. Deterioration in the lateral load capacity of the post-tensioned floor system is observed beyond 3% lateral drift. The loss of stiffness due to punching of the slab-column connections is apparent for both specimens. Results for the RC specimen reveal significant pinching of the hysteresis loops relative to the PT specimen. One approach to assessing when connection punching occurred is to plot the relationship between slab curvature and column curvature (Fig. 13). As slab curvature increases, the column curvature should also increase, unless slab moment capacity drops (i.e., punching occurs). For negative moment and curvature, Fig. 13 reveals that slab yielding occurs at close to the calculated yield curvature, and that the column curvature remains approximately constant for higher slab curvature values. This indicates slab yielding, and that the moment transfer capacity of the slab-column connection has not been reduced (no punching). In contrast, for positive curvatures, column curvatures begin to drop for higher slab curvatures, indicating that the moment transfer capacity of the slab-column connection is degrading. By examining similar relations for all connections, relationships for drift capacity at punching versus gravity shear ratio will be develop and compared to the existing database for monotonic and cyclic static tests of isolated connections. The data will be studied to address connection models for punching, including the influence of the stud-rails, as well as modelling issues associated with stiffness and ductility (e.g., see Fig. 6).

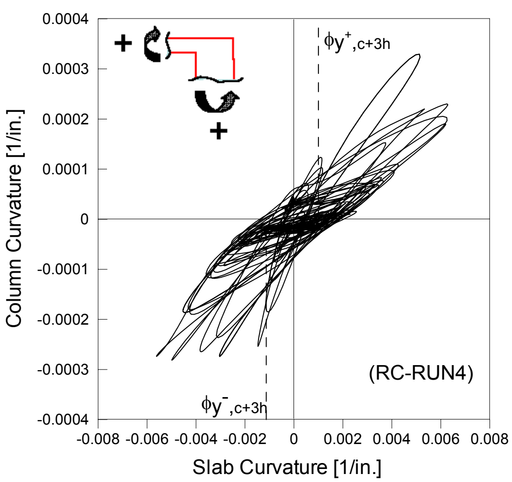

Fig. 13 Curvature diagram
(RUN 4, NW roof connection)

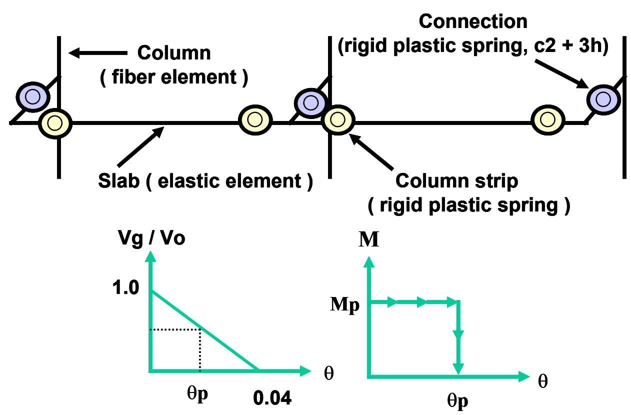

Fig. 14 Slab – column frame model with
connection springs to model punching

Review of models for slab-column behaviour requires that the direct shear and unbalanced moment at each connection be estimated. The data plotted in Fig. 13, for a roof connection, is relatively easy to assess. Additional work is being conducted to derive these quantities from the data measured during the tests. For example, data collected from rebar gauges on slab bars is plotted in Fig. 15.

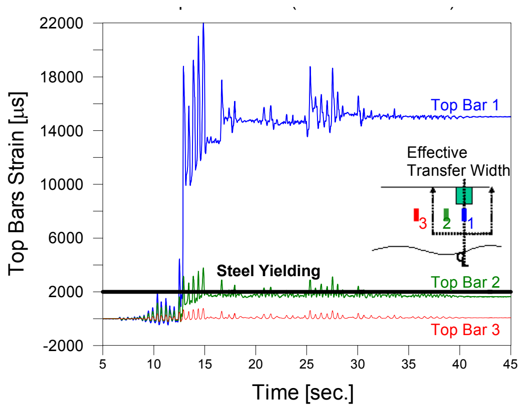

(a) Top bars

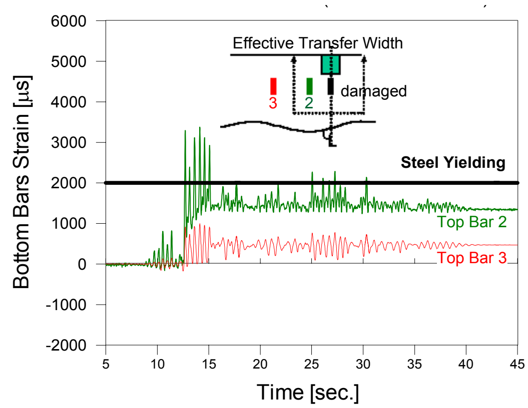

(b) Bottom bars

Fig. 15 Slab strain gauge data

Figure 16(a) shows a photo of the PT specimen on the earthquake simulator table. The added lead weights were provided to reproduce the mass and gravity stress needed to represent the prototype building. Fig. 16(b) shows the observed damage at an interior connection at the end of testing (after Run 5). Although the moment capacity of the connection has been reduced substantially (see loss of stiffness, Fig. 12), limited damage is observed relative to typical damage observed for RC specimens without shear reinforcement (e.g., Fig. 7). Given that it is relatively easy to add stud rails at slab-column connections, as well as the improved behaviour, code committees in the US (e.g., IBC and ACI) are considering code changes to require the use of shear reinforcement at slab-column connections depending on the connection gravity shear ratio and the story lateral drift ratio. The data collected from these tests should help shed light on this issue.

Fig. 16 (a) Test overview

(b) PT slab-column punching damage

4. SUMMARY & CONCLUSIONS

It is common in the western United States to provide separate systems to resist the design lateral and gravity forces. The lateral-load resisting system is required to resist the design lateral loads and to limit drift to acceptable levels. The gravity system is required to support the vertical loads when subjected to the design lateral displacements. Slab – column frames have proven to be economical gravity systems. An overview of a research program to investigate the behaviour of slab – column frames with shear reinforcement subjected to dynamic loads on the EERC/PEER shake table at the UC Berkeley Richmond Field Station was provided. Two, approximately one-third scale, specimens were subjected to increasing intensity shaking to provide detailed response data as well as damage data.

Details of the tests specimens as well as preliminary tests results were presented. Results indicate that deterioration of the moment capacity at the slab – column connections occurred during the tests; however, lateral drift ratios of 3% and 4% were achieved for the RC and PT specimens, respectively, with relatively little loss of lateral load capacity. The tests revealed relatively limited damage to the slab – column connection region compared with tests conducted under slowly varying loads on specimens of similar scale. In addition, the extent of damage observed in the slab for the dynamic tests does not appear as widespread as that noted for tests conducted under slowly varying cyclic displacements on isolated specimens.

The data collected in these tests should help define improved damage states for slab-column connections as a function of the design drift level, which is required to assess design requirements for the lateral force resisting system using current code procedures. Ultimately, design procedures that directly account for the interaction of the lateral and gravity systems should replace current procedures.

5. ACKNOWLEDGEMENTS

This research was conducted with funding provided by Phase IV of the joint CUREe – Kajima Research Program. Dr. Katsuya Igarashi and Dr. Norio Suzuki at Kajima Corporation are acknowledged for their significant contributions to the research program. Don Clyde and Wes Neighbour, from the UC Berkeley EERC/PEER Richmond Field Station, are thanked for providing valuable advice during the construction, instrumentation, and testing of the specimens. John Schuller at RPS Inc. are thanked for providing very useful information on post-tensioning procedure.

6. REFERENCES

Elgabry, A. A., and A. Ghali. (1988). *Tests on concrete slab-column connections with stud-shear reinforcement subjected to shear-moment transfer.* ACI Structural Journal, V. 84, No. 5., American Concrete Institute, Detroit MI, pp. 350-361.

Hwang, S. J., and J. P. Moehle. (1990). *An experimental study of flat-plate structures under vertical and lateral loads.* Report No. UCB/SEMM-90/11, Department of Civil Engineering, University of California at Berkeley.

Martinez-Cruzado J. A. (1993), *Experimental study of post-tensioned flat plate exterior slab-column connections subjected to gravity and biaxial loading.* PhD thesis, Department of Civil Engineering, University of California at Berkeley.

Moehle, J. P. (1996), *Seismic design considerations for flat-plate construction.* ACI SP-162: Mete A. Sozen Symposium, American Concrete Institute, Farmington Hills MI, 1996, pp. 1-34.

Pan, A. D., and J. P. Moehle. (1989). *Lateral displacement ductility of reinforced concrete flat plates.* ACI Structural Journal, V. 86, No. 3., American Concrete Institute, Detroit MI, pp. 250-258.

Pan, A. D., and J. P. Moehle. (1992). *An experimental study of slab-column connections.* ACI Structural Journal, V. 89, No. 6., American Concrete Institute, Detroit MI, pp. 626-638.

Park, R., and W. L. Gamble. (2000). *Reinforced Concrete Slabs 2ed.* New York: John Wiley & Sons.

Pilakoutas, K., and C. Ioannou. (2000). *Verification of a novel punching shear reinforcement system of flat slabs.* Procs International Workshop on Punching Shear Capacity of RC Slabs, TRITA-BKN Bulletin 57, Royal Institute of Technology, Stockholm.

Robertson, I. N., T. Kawai, J. Lee, and B. Enomoto. (2002). *Cyclic testing of slab-column connections with shear reinforcement*. ACI Structural Journal, V. 99, No. 5, American Concrete Institute, Detroit MI, pp. 605-613.

7. KEYWORDS

Flat plate, slab-column connections, post-tensioned slab, shake table test, punching failure, slab shear reinforcement, stud-rail, cyclic loading, gravity frame, non-participating frame.

TEST ON CONCRETE ENCASED STEEL COMPOSITE COLUMNS USING *FRC*

Hiroshi KURAMOTO [1], Tomohiro ADACHI [2] and Kiyohiko KAWASAKI [3]

ABSTRACT

In order to realize simplification and cost reduction in construction works for SRC structures, concrete encased steel structures consisting of only steel and concrete, hereafter referred to as CES structures, have been proposed by the authors. In the feasibility study to examine the structural performance of CES columns, it was conformed that damages of the columns with an increase of lateral deformation can be reduced by using high performance fiber reinforced cementitious composites, HPFRCC, instead of normal concrete. Moreover, the hysteretic characteristics of the CES columns were almost the same as those of SRC columns. However, significant reduction of the initial stiffness in the shear-drift relations and the development of drying shrinkage in the cover concrete were observed in the CES columns due to use of HPERCC without aggregates. In addition, the production and casting of HPFRCC were very difficult due to less workability.

Use of fiber reinforced concrete, FRC, for CES columns has been planed to solve the above-mentioned problems in the columns using HPFRCC. Proportioning tests of FRC using three types of fibers were conducted to obtain appropriate one for both the construction works and structural performance of CES structures. Then, using FRC selected from the proportioning tests, a total of tree CES columns were tested to investigate the structural performance and compare with the columns using HPFRCC. This paper outlines the proportioning and structural tests and shows the effectiveness of CES columns using FRC on the structural performance.

1. INTRODUCTION

Reinforced concrete encased steel structures referred to as SRC structures are typical composite structural systems consisting of steel and reinforced concrete and possess an excellent earthquake resistance with high capacities and deformability. However, SRC structures have a weak point in the construction due to complex works of both steel and reinforced concrete. In order to realize simplification and cost reduction in construction works for SRC structures, concrete encased steel structures consisting of only steel and concrete, hereafter referred to as CES structures, have

[1] *Associate professor, Toyohashi University of Technology, Toyohashi, Japan Email: kura@tutrp.tut.ac.jp*
[2] *Graduate Student, Toyohashi University of Technology, Toyohashi, Japan*
[3] *Manager, Fujimi Koken Engineering Co. Ltd., Tokyo, Japan*

been proposed by the authors (Kuramoto et al. 2000). In the feasibility study to examine the structural performance of CES columns, it was conformed that damages of the columns with an increase of lateral deformation such as cracking and crushing in concrete can be reduced by using high performance fiber reinforced cementitious composites, HPFRCC, instead of normal concrete. Moreover, the hysteretic characteristics of the CES columns were almost the same as those of SRC columns. However, significant reduction of the initial stiffness in the shear versus story drift relations and the development of drying shrinkage in the cover concrete were observed in the CES columns due to use of HPERCC without aggregates. In addition, the production and casting of HPFRCC were very difficult due to less workability.

Use of fiber reinforced concrete, FRC, for CES columns has been planed to solve the above-mentioned problems in the columns using HPFRCC. Proportioning tests of FRC using three types of fibers were conducted to obtain appropriate one for both the construction works and structural performance of CES structures. Then, using FRC selected from the proportioning tests, a total of tree CES columns were tested to investigate the structural performance and compare with the columns using HPFRCC. This paper outlines the proportioning tests and structural test and shows the effectiveness of CES columns using FRC on the structural performance.

2. PROPORTIONING TESTS OF FIBER REINFORCED CONCRETE

2.1 Materials Used and Test Parameter

Concrete used in FRC is mixed with Portland cement of 344kg/m^3, fine aggregate of 1,282 kg/m^3, coarse aggregate of 536kg/m^3 of which the maximum grading is 15mm, water of 182kg/m^3 and the high performance AE agent of 3%, respectively. Hence the water-cement ratio is 53% and the fine-total aggregate ratio is 70%.

Photo 1 Used Fibers

Stainless steel fibers and two types of poly-vinyl alcohol fibers are used as the reinforcing ones. The stainless steel fibers are dog-bone shape with the nominal diameter of 0.6mm and length of 35mm, hereafter referred to as F430D, and the poly-vinyl alcohol fibers are with the diameter and length of 0.66mm and 30mm, ditto RF4000, and those of 0.40mm and 24mm, ditto RF1500, respectively. A piece of F430D and RF4000 are shown in Photo 1.

Variables investigated are the type and content of reinforcing fibers. The contents are 1.0% and 2.0% in the volume ratio for each fiber. A total of six proportions are mixed.

2.2 Mixing

Using a two shafts typed batch mixer of which the maximum capacity is 100 liters, mixings of FRC of 30 liters per a batch were conducted according to the above-mentioned proportioning. The mixing were conducted with the following progress; 1) mixing with cement, fine aggregate and coarse aggregate for 30 seconds, 2) mixing for 120 seconds after adding water including the high performance AE agent, and 3) mixing for 60 seconds after adding reinforcing fibers.

2.3 Condition of Flesh Concrete

For FRC using RF1500 fibers, good workability was obtained in case of the volume content ratio of 1.0%, while the liquidity of concrete was not enough in that of 2.0% due to tangle between the fibers and coarse aggregates. For FRC using RF4000 fibers, relatively uniform dispersion between the fibers and coarse aggregates was observed in both cases of the volume content ratios of 1.0% and 2.0%. Although slight less workability was obtained with an increase of the volume content ratios, both FRC have enough workability to practical works. For FRC using F430D fibers, on the other hand, better workability was obtained in both cases of the volume content ratios of 1.0% and 2.0%.

2.4 Mechanical Properties of Hardened Concrete

In order to examine the mechanical properties of FRC with the above-mentioned mix proportions, compressive and tensile tests using cylinder specimens of $\phi 100 \times 200\text{mm}$ and flexural tests using rectangular parallelepiped specimens of $100 \times 100 \times 400\text{mm}$ were conducted.

2.4.1 Compressive strength

The compressive stress versus strain relations for each FRC with the volume content ratio of 2.0% are shown in Fig. 1. Compressive strength of FRC using RF1500 fibers was less than that of other two FRC due to insufficient casting caused by tangle between the fibers and coarse aggregates in the mixing, as mentioned above. Regardless of the type of fibers, the strains at the maximum strength were about 0.0045 and similar properties of the strain softening after reaching the maximum strength were observed.

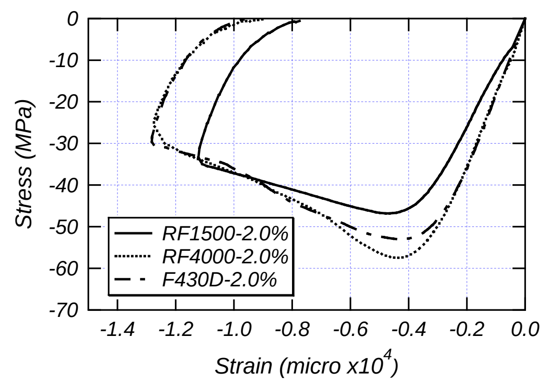

Fig. 1 Results of Compressive Test

2.4.2 Tensile strength

The tensile tests were conducted using the loading apparatus developed in the Building Research Institute (Sato et al. 2001), which adopts a direct tensile loading system by applying tension loads with gripping on both ends of a cylinder specimen. In all specimens, the maximum tensile strengths were developed at the strain of about 100micro, as shown in Fig. 2. The maximum tensile strengths of all specimens range from 1.8MPa to 2.8MPa regardless of the type and content of reinforcing fibers, though those of FRC using RF4000 fibers tend to be larger. The reason is considered to be because the splitting of concrete occurred at the section including the least fibers in all specimens. On the other hand, larger stress level of stable region after attaining to the maximum tensile strength and smaller strain reaching the stress level were observed with an increase of the content of fibers.

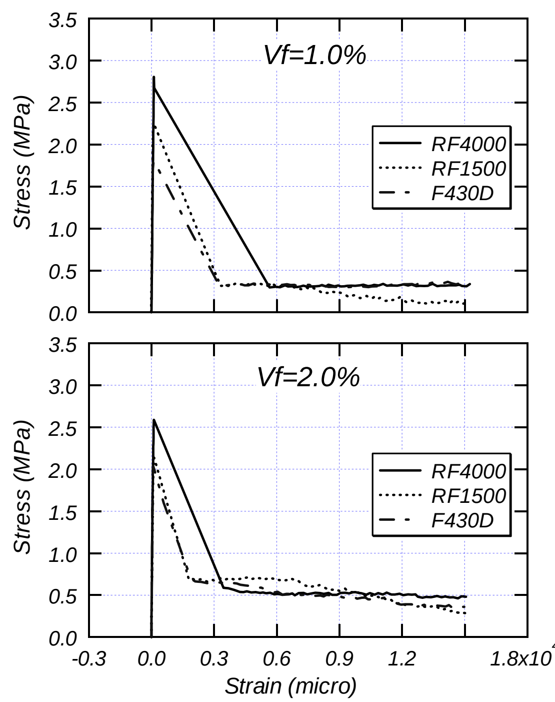

Fig. 2 Results of Tensile Test

2.4.3 Flexural strength

The results of flexural tests for FRC rectangular parallelepiped specimens are shown in Fig. 3. All specimens had almost the same initial stiffness and flexural cracking stress while the specimens using poly-vinyl alcohol fibers, RF1500 and RF4000, tend to show higher ductility after occurring flexural cracking than those using stainless steel fibers, F430D. In specimens with the volume content ratio of 2.0%, significant strain hardenings after occurring flexural cracking were observed regardless of the type of fibers included. This shows that the reinforcing fibers work effectively for preventing the propagation of flexural cracks.

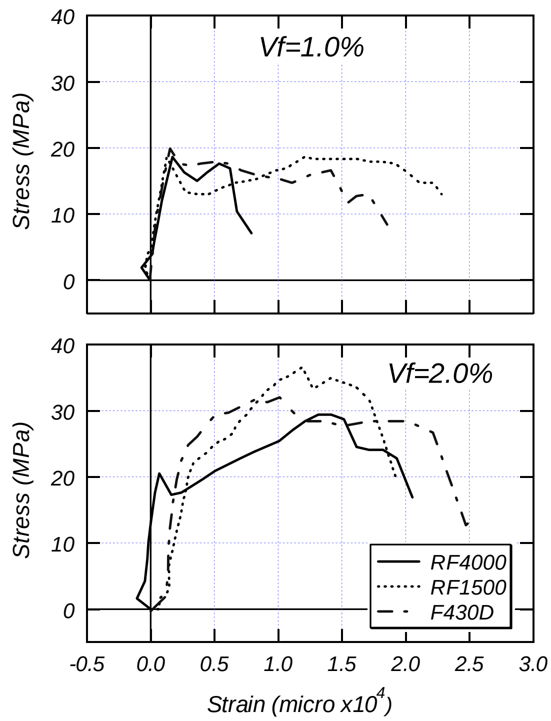

Fig. 3 Results of Flexural Test

3. STRUCTURAL TESTS OF *CES* COLUMNS USING *FRC*

3.1 Experimental Program

3.1.1 Specimens

Three CES column specimens using FRC of which the scale is about two-fifth were prepared. Based on the results of the above-mentioned proportioning tests, as shown in Table 1, the FRC with RF4000 of 1.0% and 2.0% and F430D of 2.0% in the volume content ratios were used for

Table 1 Test Plan

Specimen		VF1	VF2	SF2
Reinforcing Fibers	Type	RF4000	RF4000	F430D
	Volume Content (%)	1.0	2.0	2.0
Concrete	σ_B (MPa)	52.3	55.5	65.3
	E_c (GPa)	26.2	26.3	26.5
Steel	Built-in Steel (mm)	WH-$300 \times 150 \times 6.5 \times 9$		
	Tie Plate (mm)	PL-9		
Cross Section: $b \times D$ (mm)		400×400		
Column Height: h (mm)		1,600		
Axial Force	N (kN)	1,100		
	$N/(b \cdot D \cdot \sigma_B)$	0.131	0.124	0.105

Specimens VF1, VF2 and SF2, respectively. The proportioning of FRC used is shown in Table 2. The dimensions and details of the specimens are shown in Fig. 4. All specimens had columns with a 400mm square section and 1,600mm height, and the height-depth ratio was 4.0. Steels encased in each column had a cross shape section combining two H-section steels of $300 \times 150 \times 6.5 \times 9$ mm. The dimensions and details of the specimens were the same as those in the previous test (Kuramoto et al., 2000) with the intention of comparing with tested specimens using normal concrete and HPFRCC. The mechanical properties of steel used are listed in Table 3.

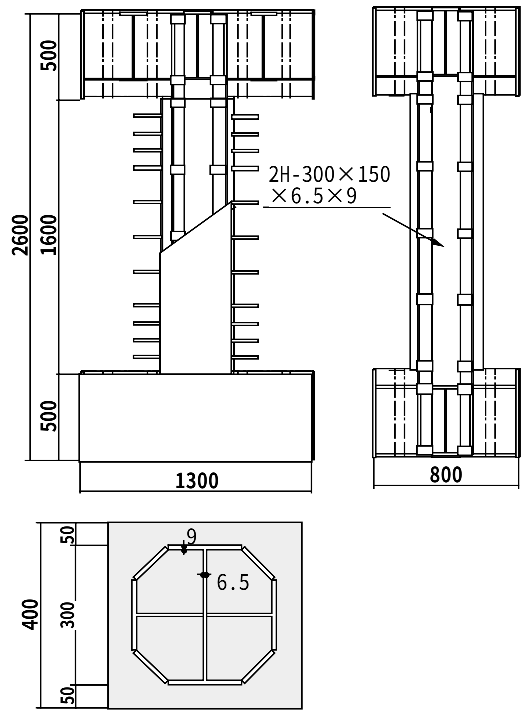

Fig. 4　Test Specimen

Table 2　Proportioning of FRC

Specimen	W/C (%)	S/(S+A) (%)	Vf vol(%)	Contents (for 0.5m^3)					
				Water W (kg)	Cement C (kg)	Fine Aggre. S (kg)	Coarse Aggre. A (kg)	Fiber vf (kg)	AE (g)
VF1	53	70	1.0	91	172	641	268	6.5	2.58
VF2			2.0					13.0	
SF2								40.0	

Table 3　Mechanical Properties of Steel

Steel	Spec.	Elastic Modulus E_s (GPa)	Yield Stress σ_y (MPa)	Notes
WH-300x150x6.5x9	SS400	207.6	336.8	Flange
		214.8	363.6	Web
PL-9	SS400	207.6	336.8	Tie Plate

Table 4　Calculated Strength

Specimen	VF1	VF2	SF2
Ultimate Flexural Strength: Q_{mcal} (kN)	649.1	664.4	710.5
Shear Strength: Q_{scal} (kN)	536.1	540.4	553.7

Calculated strengths for each specimen are shown in Table 4. The ultimate flexural strengths were calculated by fiber section analysis in which the Kent and Park model (Kent D.C. and R. Park, 1971) and the perfect elasto-plastic model were used for the stress-strain relationship of FRC and steels, respectively. In calculations of the shear strengths, on the other hand, the ultimate shear design equations in the AIJ standard for SRC structures (AIJ, 2001) were used.

3.1.2 Test Setup and Loading Procedures

The specimens were loaded lateral cyclic shear forces by using two horizontal hydraulic jacks, which were installed in parallel each other for one direction, and a constant axial compression of 1,100kN by using four vertical actuators, as shown in Photo. 2. The axial compression ratios, $N/(b \cdot D \cdot \sigma_B)$, were 0.131 for Specimen VF1, 0.124 for Specimen VF2 and 0.105 for Specimen SF2, respectively. The loads were applied through a steel frame attached at the top of a column that was fixed to the base. The four vertical actuators to apply the constant axial compression were also used to keep the column top beam parallel to the bottom beam, so that the column would be subjected to anti-symmetric moments.

Photo 2 Loading Set-up

The incremental loading cycles controlled by story drift angles, *R*, which was given by the ratio of lateral displacements to the column height, δ/h, were two for *R* of 0.005, 0.01, 0.02, 0.03 and 0.04 radians and one for that of 0.05 radian, respectively.

3.2 Experimental Results

3.2.1 Failure Mode and Shear-Displacement Response

The yield and maximum strengths and the corresponding story drift angles for each specimen are listed in Table 5. The yielding of each specimen was assumed when the first yielding of steel flange was observed that was corresponding to a triangle mark on the story shear versus story drift angle response shown in Fig. 5. Crack patterns after loadings for each specimen were

Table 5 Measured Strength

Specimen	at Yielding		at the Maximum Capacity	
	Q_y (kN)	R_y (rad.)	Q_{max} (kN)	R_{max} (rad.)
VF1	612.4	0.0109	689.4	0.0154
VF2	608.0	0.0103	703.2	0.0151
SF2	643.4	0.0110	737.5	0.0204

compared with those for Specimen SC using normal concrete and Specimen SFC using HPFRCC in the previous test (Kuramoto et al. 2000) in Photo 3.

In Specimen VF1 with RF4000 of 1.0% in the volume content ratio, flexural cracks occurred first at the story drift angle, *R*, of about 0.003 rad. at both top and bottom of the column. With an increase of the story drift angle, the flexural cracks propagated and thin shear cracks dispersed all over the column. The specimen showed stable and spindle shaped hysteresis loops with a little deterioration in load carrying capacity after attaining the maximum capacity at *R* of 0.0154 rad. Specimen VF2 with RF4000 of 2.0% in the volume content ratio showed slightly better hysteresis loops without distinct deterioration in load carrying capacity than those of Specimen VF1. Specimen VF2 also showed better propagation of cracks in cover concrete that means better performance in the damage limit state than Specimen VF1. Specimen SF2 with F430D of 2.0% showed high structural

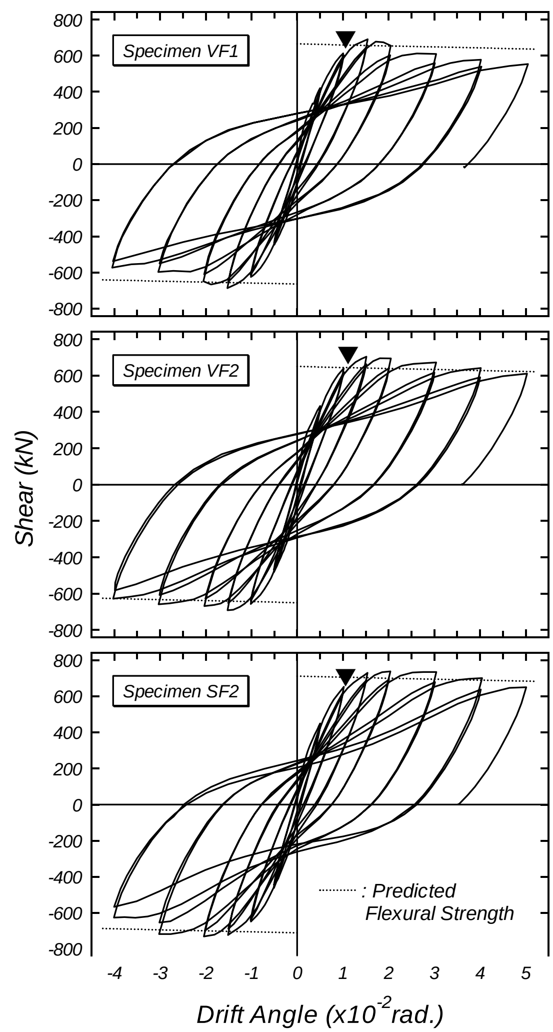

Fig. 5 Story Shear-Story Drift Relationship

VF1 VF2 SF2 SC SFC

Photo 3 Crack Patterns after Loading

performance with the highest maximum capacity among the tested specimens. As shown in Photo 3, the spalling of cover concrete due to the expansion of cracks, crushing in concrete and so on was not observed until *R* of 0.05 rad. in all specimens.

3.2.2 Initial Stiffness

The skeleton curves of all specimens in this test are compared with those of the specimens using normal concrete and HPFRCC, Specimens SC and SFC, in the previous test (Kuramoto et al. 2000) to examine the effects of FRC on the structural performance of CES columns in Fig.6. The initial stiffness of specimens using FRC is almost the same as or a little higher than that of Specimen SC and is considerably higher than that of Specimen SFC. Thus, distinct

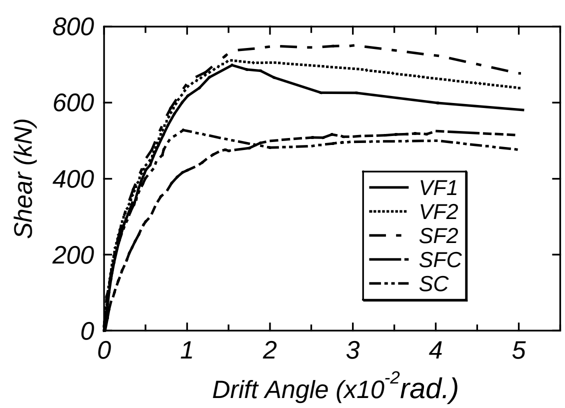

Fig.6 Comparison of Skeleton Curves

effectiveness of the use of FRC for CES columns is observed in improving the initially structural performance. Simultaneously, in comparison among specimens using FRC, it is indicated that the initial stiffness of CES columns is little affected by the type and content of fibers used in FRC.

3.2.3 Observed Cracking Width

The propagations of cracks in each column were photographed by a digital camera during the tests. The cracking widths at the peak and the unloading point in each loading cycle were measured from the photographs. The developments of the maximum residual cracking widths for flexure and shear with an increase of the story drift angles for each specimen are shown in Figs. 7 and 8. In the figures, the developments of the cracking widths of Specimens SC and SFC are also drawn to make a comparison with those of specimens with FRC.

In Specimens VF2 and SF2 with the fiber content of 2.0% in the volume ratio, similar tendencies with an increase of the story drift angles are observed in the developments of both the flexural and shear cracking widths. The values are about 1 mm even at the story drift angles of 0.04 rad. that is corresponding to relatively large lateral deformation. On the other hand, both the flexural and shear cracking widths in Specimen VF1 with the fiber content of 1.0% are almost 1.5 times as large as that in Specimens VF2 and SF2 in each loading cycle. These results imply that the developments of the cracking widths are affected by the content of fibers although the effect of the type of fibers is little. In comparison with Specimen SFC using HPFRCC, the flexural cracking widths in all specimens

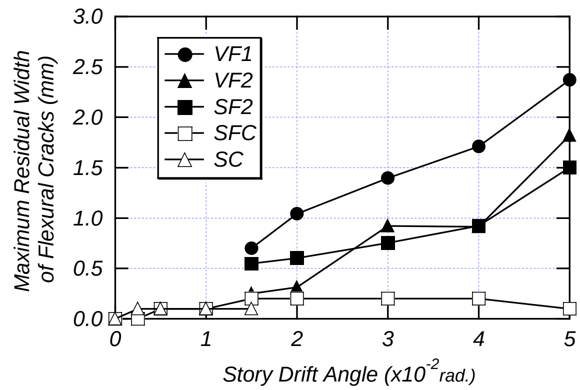

Fig. 7 Development of Maximum Residual Width of Flexural Cracks

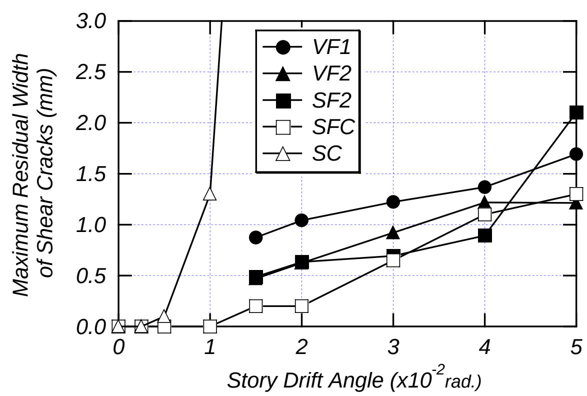

Fig. 8 Development of Maximum Residual Width of Shear Cracks

using FRC became larger with an increase of the story drift angles while the shear cracking widths are almost the same level.

In comparison with a CES column using HPFRCC, as mentioned above, although the damage of CES columns using FRC is obviously progressed by flexural cracks, the damage even at the relatively large deformation seems to be within the limits of making the relatively easy restoration possible. Thus, it is considered that the use of FRC is very effective for making CES columns practicable.

4. CONCLUSIONS

A total of three CES columns using FRC for which the type and content of reinforcing fibers were selected as the variables investigated were tested to examine the structural performance and the effectiveness for practical use. From the experimental results, the following conclusions can be drawn:

1) CES columns using FRC have almost the same structural performance as SRC columns which possess an excellent earthquake resistance with high capacities and deformability.

2) The use of FRC make the easy restoration of CES columns possible because the damages in cover concrete of the columns due to flexural and shear cracks are relatively light even at the large story drifts.

3) CES columns using FRC is effective for preventing the development of drying shrinkage in the cover concrete and enhancing the initially structural performance in comparison with the columns using HPFRCC.

4) CES columns using FRC is practical in the aspects of not only the structural performance but also the construction workability because the FRC can be easily produced by real concrete mixers.

ACKNOWLEDGEMENTS

The structural tests on CES columns and the tensile tests of FRC were conducted at the Building Research Institute with the cooperation of Mr. Haruhiko Suwada, NILIM. His cooperation is gratefully acknowledged.

REFERENCES

Architectural Institute of Japan (2001). *Standard for Structural Calculation of Steel Reinforced Concrete Structures*.

Kent, D.C. and R. Park (1971). Flexural Members with Confined Concrete. *Proceedings of ASCE*. Vol. 97. No. ST7: 1969-1990.

Kuramoto, H., H. Takahashi and M. Maeda (2000). Feasibility Study on Structural Performance of Concrete Encased Steel Columns using High Performance Fiber Reinforced Cementitious Composites. *Summaries of Technical Papers of Annual Meeting, AIJ*. Vol. C-1: 1085-1088. (in Japanese)

Sato, Y., H. Fukuyama and H. Suwada (2001). A Proposal of Tension-Compression Cyclic Loading Test Method for Ductile Cementitious Composite Materials. *Journal of Structural and Construction Engineering, AIJ*. No. 539: 7-12. (in Japanese)

KEYWORDS

CES Composite Column: Fiber Reinforced Concrete: Proportioning Test: Structural Test: Seismic Performance: Maximum Crack Width

SESSION A-4: AXIAL CAPACITY OF COLUMNS

Chaired by

♦ John Wallace and Hiroshi Kuramoto ♦

AXIAL LOAD CARRYING CAPACITY OF R/C COLUMNS WITH SIDE WALLS

Daisuke KATO[1] , Hao Yang SUN[2] and Yuji OTSUKA[2]

ABSTRACT

Recent earthquake resistant design concept of structures places explicit emphases on limit state design. Regarding reinforced concrete members three limit states have been discussed, i.e. operation limit state, repair limit state and safety limit state. The objectives of this study were to propose a simplified method to evaluate axial load carrying capacity of side walls connecting with reinforced concrete columns subjected to high axial load. Six column specimens were examined. Variables of those specimens were existence of side walls, direction of side walls to loading direction (parallel or crossing), location of side walls (centric or eccentric) and loading method of lateral force (two directional loading or one directional loading). Conclusions were as follows : (1)The effect of parallel side walls to loading direction on axial load carrying capacity is small. In other words axial load carrying capacity of columns with parallel side walls equals to that of isolated column. (2)Crossing side walls to main loading direction located at the center of the column enhanced the axial load carrying capacity. (3)The effect decreased by two directional loading. In other words damage of side walls due to lateral loading parallel to side walls lead to loss of axial load carrying capacity. (4)The effect decreased in case of side walls located eccentrically. This is because damage of eccentrically located side walls was more severe than that of centrally located side walls. This is because the contribution for shear and moment resistance of eccentrically located side walls was larger than that of centrally located side walls.

1. INTRODUCTION

Recent earthquake resistant design concept of structures places explicit emphases on limit state design. Regarding reinforced concrete members three limit states have been discussed, i.e. operation limit state, repair limit state and safety limit state. In the limit state design procedures a variety of evaluating methods of performances of members are expected to be proposed, i.e. initial stiffness, cracking strength, yield strength and deformation for operation limit state, reparability (crack width and concrete crush) for repair limit state and shear strength, deformation capacity, axial load carrying capacity for safety limit state.

On the other hand columns with side walls are widely used mainly in low rise R/C buildings. One of the benefit of side walls is that side walls are effective to enhance performance regarding operation limit state and repair limit state as well as safety limit state. In other words columns with side walls show higher elastic stiffness and higher reparability comparing to isolated columns for example.

1.Department. of Architecture, faculty of Engineering, Niigata University, Niigata, Japan.
Email:dkato@eng.niigata-u.ac.jp
2.Graduate student, Dept. of Architecture, faculty of Engineering, Niigata University

However their behavior regarding three limit states mentioned above have not been clearly understood. The objectives of this study were to propose evaluating methods of a variety of performance listed above. In this paper axial load carrying capacity of side walls connecting with reinforced concrete columns subjected to high axial load was discussed.

2. OUTLINE OF TEST

2.1 Specimens

Table 1 shows main variations of specimens. Six column specimens were examined(Sun 2001, Kato 2001, Otsuka 2002). Main variables of those specimens were existence of side walls, direction of side walls to loading direction (parallel or crossing), location of side walls (centric or eccentric) and loading method of lateral force (two directional loading or one directional loading). Figure 1 shows sections and loading directions of six specimens. Table 2 shows properties of specimens. Figure 2 shows examples of reinforcement of specimen. Table 3 shows characteristics of materials.

Specimen C-5 with a square section representing a prototype column was subjected to one directional lateral load under constant high axial load. Specimens CSW-1and CSW-2 with side walls located at the center of the column were also subjected to one directional lateral load under constant high axial load. The lateral loading direction of these two specimens was parallel to the side walls, which meant those side walls were expected to be effective for axial load resistance, moment resistance and shear resistance. From this view point hoop type reinforcement was adopted for side walls of these specimens.

Specimen CSWTR-1 with side walls located at the center of the column was subjected to one directional lateral load under constant high axial load. The lateral loading direction of the specimen was crossing at right angles to the side walls, which meant the side walls were expected to be effective for axial load resistance only. Although hoop type reinforcement was known to be effective for axial load resistance, single reinforcing bar was arranged in the side wall of this specimen for practical use.

Effects of loading direction should be taken into account because crossing side walls to main loading direction are easily damaged by parallel loading direction to the side wall. From this view point specimen CSWTR-2 with the same section as specimen CSWTR-1 was scheduled to be subjected to two directional loading.

Expected damage under main loading of eccentrically located side walls used in specimen CSWTR-3 is more severe than that of centrally located side walls in specimen CSWTR-2. This is because the contribution for shear and moment resistance of eccentrically located side walls is larger than that of centrally located side walls. From this view point specimen CSWTR-3 was planed.

2.2 Loading method

All specimen were subjected to constant axial load and the antisymmetric moment reversals. The two directional loading system was composed by pre loading and main loading. At first the lateral load was reversed at the drift angle of 1/200 rad twice in the parallel direction to the side wall (this is called pre loading) and then the main load was applied in the crossing direction to the side wall (this is called main loading).

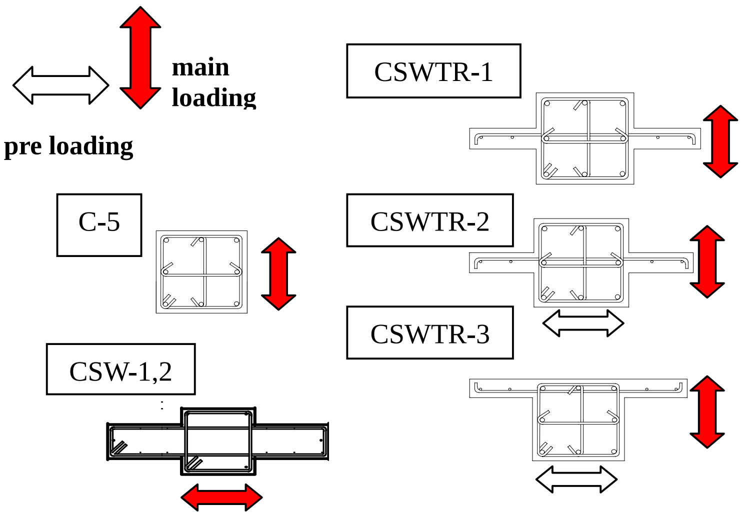

Figure 1 Section and loading direction

Table 1 Main variation of specimen

specimen	side wall	lateral force loading method
CSW-1	central	one directional (parallel to side wall)
CSW-2		
C-5	none	one directional
CSWTR-1	central	one directional (crossing side wall)
CSWTR-2		two directioanl
CSWTR-3	eccentrical	

Table 3 Characteristics of materials

	CSW-1,2		C-5、CSWTR-1		CSWTR-2、3	
	D6	D10	D6	D10	D6	D10
yield strength (MPa)	336	391	314	378	302	474
maximum strength (MPa)	512	541	483	517	389	543

Table 2 Properties of specimens

name	column section	side wall(one side)	height of column	total main bar of column	hoop (ratio)	peripheral reinforcement of side wall	reinforcement of side wall	concrete strength (MPa)	axial load (kN)
CSW－1	200×200mm	100×200mm	1200mm	4-D10	2-D6@75	1-D10	2-D6@75 (0.85%)	29.6	473
CSW－2									769
C－5	220×220mm	none	1100mm	8-D10	3-D6@70 (0.62%)	none	none	26.1	778
CSWTR－1		50×150mm				1-D6	1-D6@70 (0.91%)		
CSWTR－2									784
CSWTR－3									

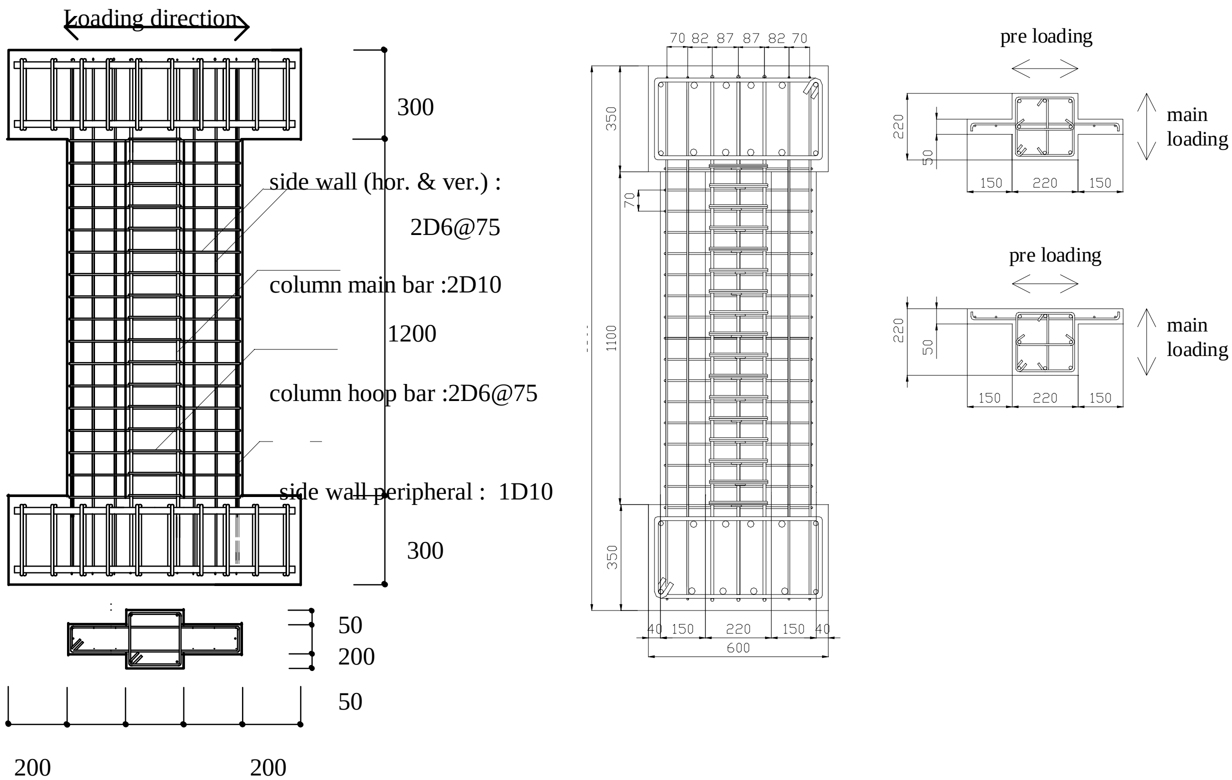

(a)Specimen CSW-1,2 **(b)Specimen CSWTR-1,2,3**

Figure 2 Example of reinforcement of specimen

3. EFFECTS OF PARALLEL SIDE WALLS TO LOADING DIRECTION

3.1 Test result of specimens CSW-1,2

Figure 3 shows relationship between lateral load and lateral deflection angle and relationship between axial strain and lateral deflection angle of specimens CSW-1 and CSW-2 with parallel side walls to loading direction. Lateral deflection angle was defined as lateral deformation divided by column height and axial strain was defined as axial deformation of the column divided by column height. These two specimens have same column sections and reinforcement. Only applied axial load was varied. The axial load ratios defined as axial load divided by axial compressive strength of column section only (side walls and reinforcement were ignored) were 0.4 for specimen CSW-1 and 0.65 for specimen CSW-2.

Circle marks in Fig. 3 represent losing points of lateral load carrying capacities defined as points where restoring force degraded to 80% of the maximum strength. Square mark in Fig 3 represents losing points of axial load carrying capacities defined as points where scheduled axial force could not be applied in the test. In specimen CSW-1 with smaller axial load ratio, losing point of axial load carrying capacity could not be observed. In other word the loading was terminated before the specimen lost it’s axial load carrying capacity in this specimen.

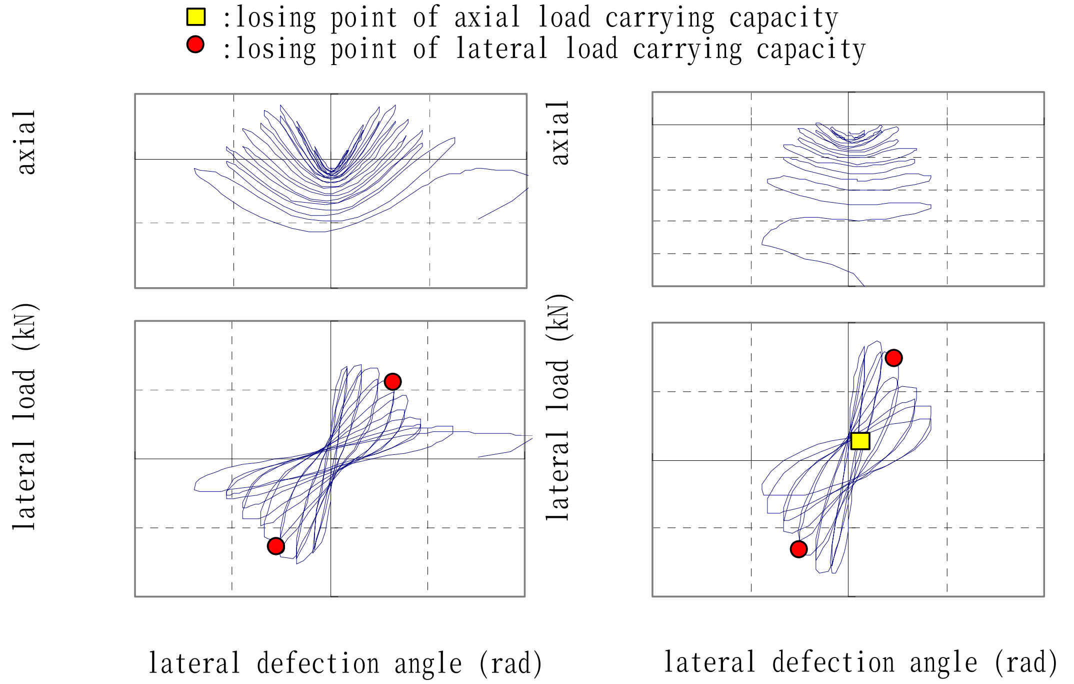

Figure 3 Lateral load, axial strain – lateral deflection relations of specimens with parallel side walls to loading direction

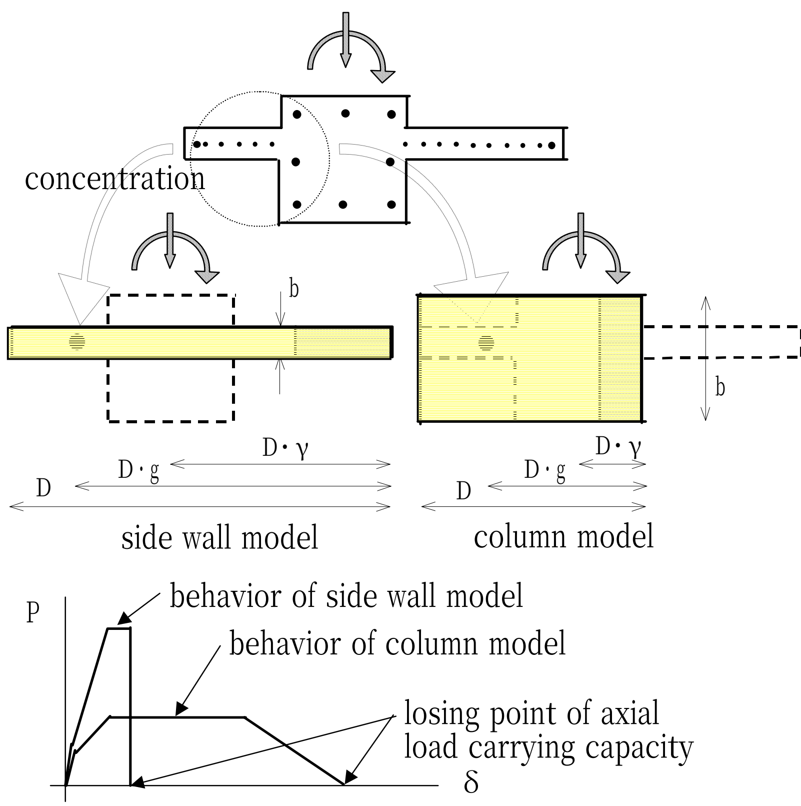

Figure 4 Two square section analogy models of column with side wall

3.2 Axial load carrying capacity of parallel side wall

Figure 4 shows two square section analogy models which can be used to explain the behavior of columns with parallel side walls to loading direction. In the early loading stage with slight damage in side walls side wall model is appropriate to explain the behavior of column with side walls. However with increasing the damage of side wall the behavior tend to match with the column model ignoring side walls in compression. Consequently the behavior of columns with side walls in the parallel direction to loading direction can be obtained as envelope curve of two square section analogy models.

Figure 5 shows comparison between two square section analogy model and experiment. Evaluated flexural strength and axial load carrying capacity using each analogy model are shown in straight lines in this figure. The behavior of columns with side walls in the parallel direction was found to be expressed by envelope curve of two square section analogy models.

As mentioned before axial load carrying capacity of specimen CSW-1 was not observed. So the feasibility of the model can not be discussed in this specimen. However the axial load carrying capacity of specimen CSW-2, the loading of which was terminated by losing axial load carrying capacity, was roughly estimated by column model. In other words the effect of parallel side walls to loading direction on axial load carrying capacity was found to be small.

4. EFFECTS OF CROSSING SIDE WALLS TO LOADING DIRECTION

4.1 Test result of specimens C-5 and CSWTR-1,2,3

Figure 6 shows relationship between lateral load and lateral deflection angle and relationship between axial strain and lateral deflection angle of specimens C-5 and CSWTR-1,2,3 with crossing side walls to loading direction. Square marks in Fig. 6 represent losing points of axial load carrying capacities. As shown in this figure losing points of axial load carrying capacity were observed in all specimens.

4.2 Axial load carrying capacity of crossing side walls

Figure 7 compares envelope curves of specimens with crossing side walls to loading direction. Results of comparisons regarding axial load carrying capacities between each specimen are summarized as follows. Side walls located at the center of the column enhanced the axial load carrying capacity (comparison between specimen C-5 and specimen CSWTR-1). However the effect decreased by two directional loading (comparison between specimen CSWTR-1 and specimen CSWTR-2). In other words damage of side walls due to lateral loading parallel to side walls (pre loading) lead to loss of axial load carrying capacity. Furthermore the effect decreased in case of side walls located eccentrically (comparison between specimen CSWTR-2 and specimen CSWTR-3). This is because damage of eccentrically located side walls used in specimen CSWTR-3 was more severe than that of centrally located side walls in specimen CSWTR-2. This is because the contribution for shear and moment resistance of eccentrically located side walls was larger than that of centrally located side walls.

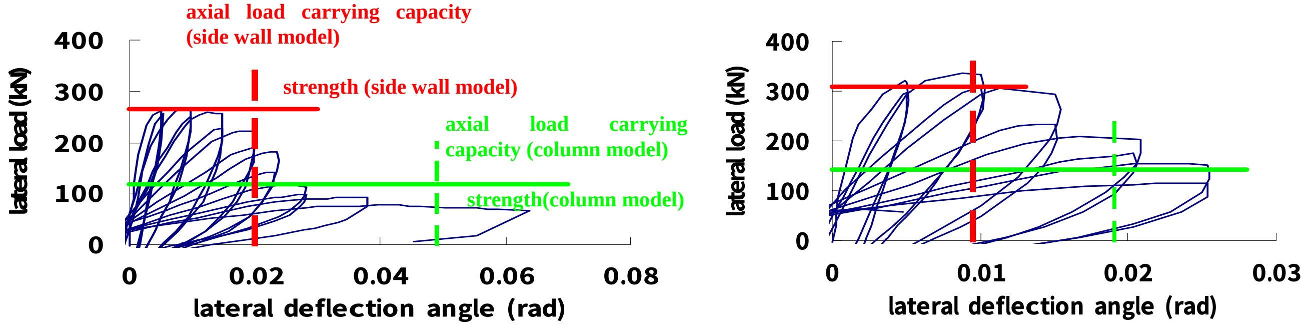

(a)Specimen CSW-1 (b)Specimen CSW2

Figure 5 Comparison between analogy models and experiment

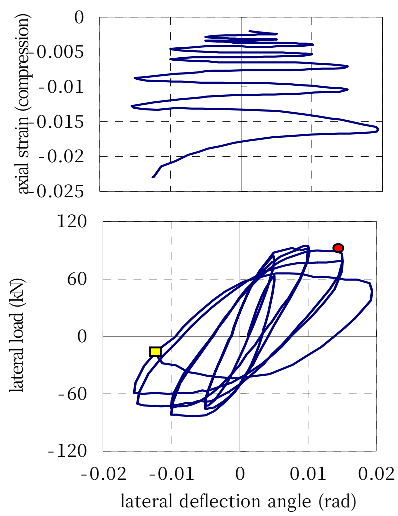

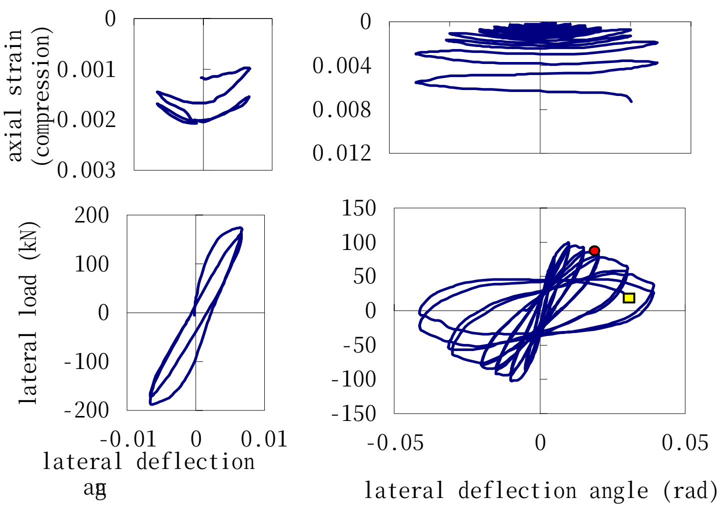

(pre loading) **(main loading)**

(a)Specimen C-5 **(c)Specimen CSWTR-2**

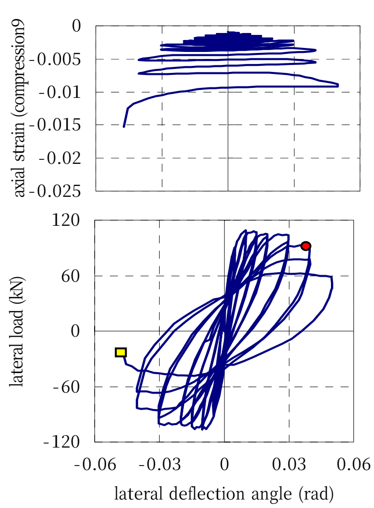

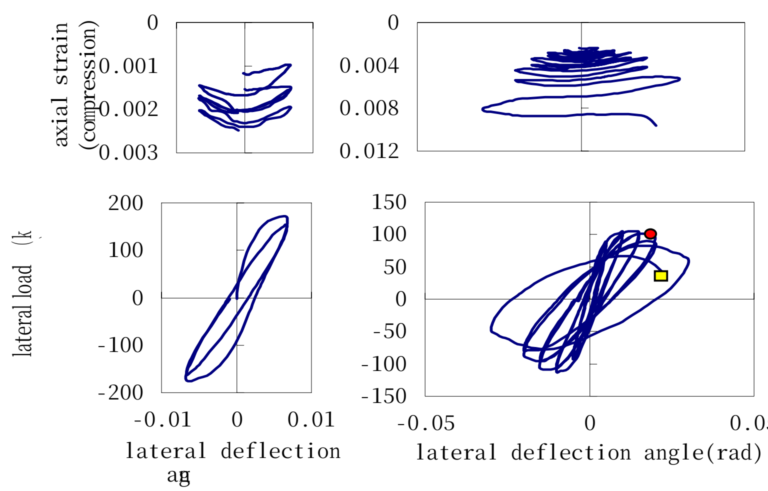

(pre loading) **(main loading)**

(b)Specimen CSWTR-1 **(d)Specimen CSWTR-3**

Figure 6 Lateral load, axial strain – lateral deflection relation of specimens with crossing side walls to main loading direction

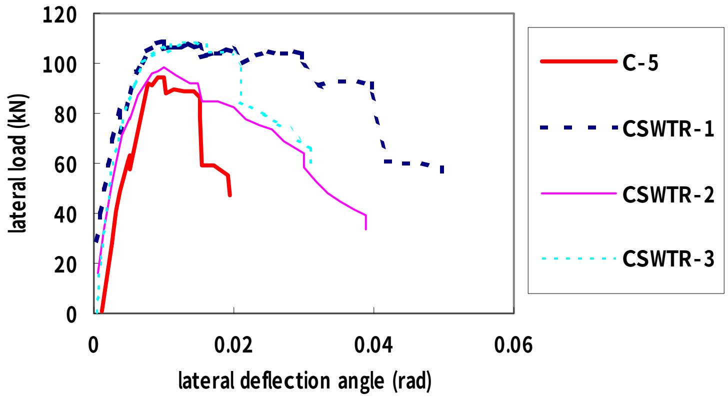

Figure 7 Compariosn of envelope curve of column with crossing side walls

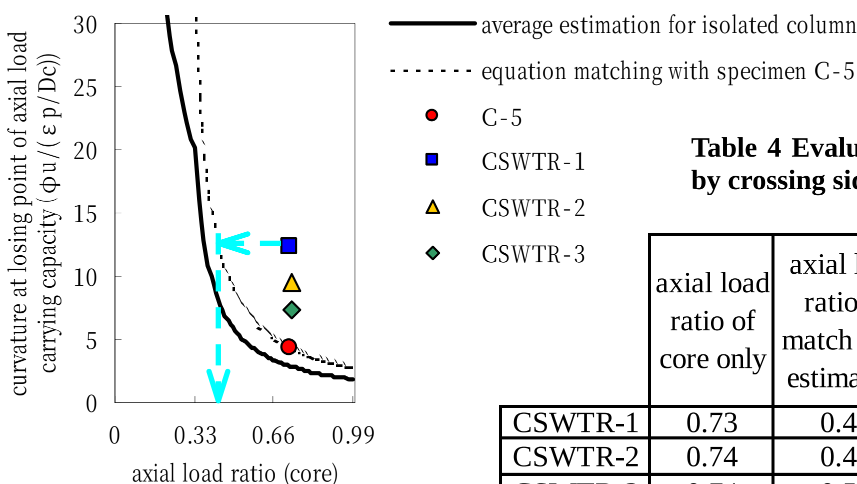

Table 4 Evaluation of axial load carried by crossing side walls

	axial load ratio of core only	axial load ratio to match with estimation	axial load carryed by side wall(kN)	effective axial load ratio of side wall (ratio to CSWTR-1)
CSWTR-1	0.73	0.43	317	0.81 (100%)
CSWTR-2	0.74	0.48	274	0.70 (86%)
CSWTR-3	0.74	0.54	211	0.54 (67%)

Figure 8 Effect of crossing side walls on axial load carrying capacity (evaluation of axial load carried by crossing side walls)

Figure 8 and Table 4 show trial to determine the axial load carried by crossing side walls of each specimen at the losing point of the axial load carrying capacity of specimens with crossing side walls. Figure 8 shows relations between axial load ratios of core section of columns and curvatures of the section at losing point of axial load carrying capacities. Solid curved line represents an average estimation for columns without side walls which was obtained using a number of experimental data(Kato 2001). Observed losing points of axial load carrying capacities of four specimens are also plotted in this figure using axial load ratios of core concrete of the column sections only. Dotted curved line represents an equation which matches the data of isolated column specimen C-5.

Using this dotted curved line axial load carried by crossing side walls can be estimated. Two broken arrow lines indicates this estimation in case of specimen CSWTR-1 showing the axial load ratio of core concrete of specimen CSWTR-1 was 0.43. In other words the curvature at losing point of axial load carrying capacity of specimen CSWTR-1 can be calculated using this dotted curved line and axial load ratio of 0.43. This axial load ratios to match with the estimation are listed in the second column of Table 4. Axial load carried by side walls can be estimated using the difference between the actual axial load ratio (listed in the first column of Table 4) and this axial load ratio to match with the estimation (listed in the second column of Table 4). These estimated axial load values carried by side walls are listed in the third column of Table 4. Consequently effective axial load ratios of side walls themselves are estimated as 0.81 for specimen CSWTR-1, 0.70 for specimen CSWTR-2 and 0.54 for CSWTR-3 as shown in the last column of table 4. Effective ratios to specimen CSWTR-1 are 86% for specimens CSWTR-2 and 67% for specimen CSWTR-3.

5. CONCLUSIONS

(1)The effect of parallel side walls to loading direction on axial load carrying capacity is small. In other words axial load carrying capacity of columns with parallel side walls equals to that of isolated column.

(2)Crossing side walls to main loading direction located at the center of the column enhanced the axial load carrying capacity.

(3)The effect decreased by two directional loading. In other words damage of side walls due to lateral loading parallel to side walls lead to loss of axial load carrying capacity.

(4)The effect decreased in case of side walls located eccentrically. This is because damage of eccentrically located side walls was more severe than that of centrally located side walls. This is because the contribution for shear and moment resistance of eccentrically located side walls was larger than that of centrally located side walls.

REFERENCES

Sun, H., Sasaki, J., Azukawa, K. and Kato,D. (2001)., *Tests of R/C Columns with Irregular Sections, Proceedings of the Japan Concrete Institute Vol.23.No.3, pp.151-156 (in Japanese)*

Kato,D., Ohnishi, K. (2001)., *Axial load carrying capacity of R/C columns under lateral load reversals, The third U.S.-Japan Workshop on performance-Based Earthquake Engineering Methodology for Reinforced Concrete Building Structures, pp.231-239*

Kato,D., Ohnishi, K., Otsuka, Y. and Doi, M. (2001)., *Tests of R/C Columns with Perpendicular Side Walls Subjected to Constant High Axial Load, Proceedings of the Japan Concrete Institute Vol.23.No.3, pp.163-168 (in Japanese)*

Otsuka, Y. and Kato,D. (2002)., *Tests of R/C Columns with Side Walls Subjected to Constant High Axial Load and Bi-lateral Load, Proceedings of the Japan Concrete Institute Vol.24.No.2, pp.259-264 (in Japanese)*

SHEAR AND AXIAL LOAD FAILURE MODEL FOR REINFORCED CONCRETE FRAMES SUBJECTED TO EARTHQUAKES

K. J. ELWOOD and J. P. MOEHLE [1]

ABSTRACT

Reinforced concrete frames with light transverse reinforcement may be susceptible to shear and subsequent axial load failures. An experimental program examined the behavior of two half-scale, one-story frames with axial loads representative of those expected for the lower story of a seven-story building. The frames were subjected to unidirectional simulated earthquake motion applied at the base. Shear failures of an interior column led to axial load failure and redistribution of internal forces to adjacent framing components. Analytical models are proposed to identify onset of shear and axial failure. The models are incorporated in a computer framework for numerical simulation of nonlinear dynamic response under earthquake base motion.

1. INTRODUCTION

Experimental research and post-earthquake reconnaissance have demonstrated that reinforced concrete columns constructed with light or widely spaced transverse reinforcement are vulnerable to shear failure during earthquakes. Such damage can also lead to a reduction in axial load capacity, although this process currently is not well understood. The resulting redistribution of gravity loads to the neighboring elements may play a role in progressing the collapse of the building frame. Shake table tests were conducted in an effort to investigate the process of column shear and axial load failures and the effect such failures have on the rest of the building frame.

2. DESIGN OF SHAKING TABLE TESTS

Shake table tests were designed to observe the process of dynamic shear and axial load failures in reinforced concrete columns when an alternative load path is provided for load redistribution. The test specimens were composed of three columns fixed at their base and interconnected by a beam at the upper level (Figure 1). The central column had wide spacing of transverse reinforcement making it vulnerable to shear failure, and subsequent axial load failure, during

[1] Pacific Earthquake Engineering Research Center, University of California, Berkeley

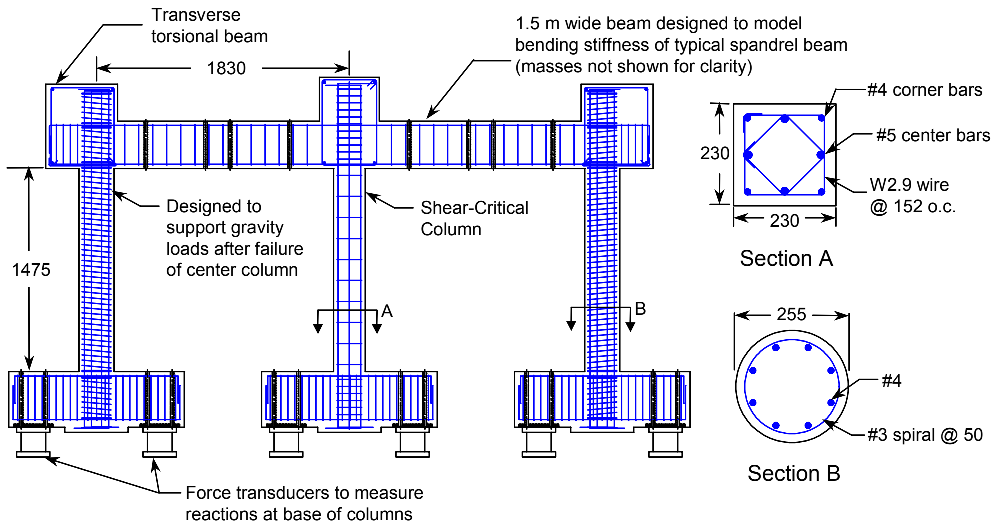

Figure 1: Shake table test specimen (units in mm).

testing. As the central column failed, shear and axial load would be redistributed to the adjacent ductile columns.

Two test specimens were constructed and tested. The first specimen supported a mass of 300 kN, producing column axial load stresses roughly equivalent to those expected for a seven-story building. The second specimen also supported a mass of 300 kN, but pneumatic jacks were added to increase the axial load carried by the central column from 128 kN (0.10 $f'_c A_g$) to 303 kN (0.24 $f'_c A_g$), thereby amplifying the demands for redistribution of axial load when the central column began to fail.

Specimens were constructed of normal-weight aggregate concrete (10-mm maximum aggregate size). See Table 1 for information on material properties.

Table 1: Properties for shake table test specimens

f'_c (columns and beam, Specimen 1)	24.5 MPa
f'_c (columns and beam, Specimen 2)	23.9 MPa
f_y (center column longitudinal bars)	479 MPa
f_y (outside column longitudinal bars)	424 MPa
f_y (center column transverse bars)	718 MPa
ρ_l (center column)	2.5 %
ρ_l (outside column)	2.0 %
ρ_h (center column)	0.18%

The stiffness of the beam in the three-column frame was selected such that the scaled maximum vertical deflection after axial failure of the center column for the first test specimen would be the same as the maximum deflection of the second story in a seven-story prototype building after axial failure of an interior first story column. The beam reinforcement was selected such that the ratio of the yield strength of the beam to the maximum moment demand from plastic analysis after axial failure of the center column was 1.59 for the Specimen 1 and 0.82 for Specimen 2.

Each test specimen was moved to the earthquake simulator prior to testing and supported on force transducers that monitored axial load, shear, and moment (Figure 1). The beam supported lead weights. Pneumatic jacks applied additional load to Specimen 2.

The planar frame specimens were to be subjected to one horizontal component from a scaled ground motion recorded at Viña del Mar during the 1985 Chile earthquake (Figure 2). An out-of-plane bracing system was developed to restrain motion out of the plane of the specimen; otherwise the bracing system allowed unrestrained in-plane horizontal and vertical motion.

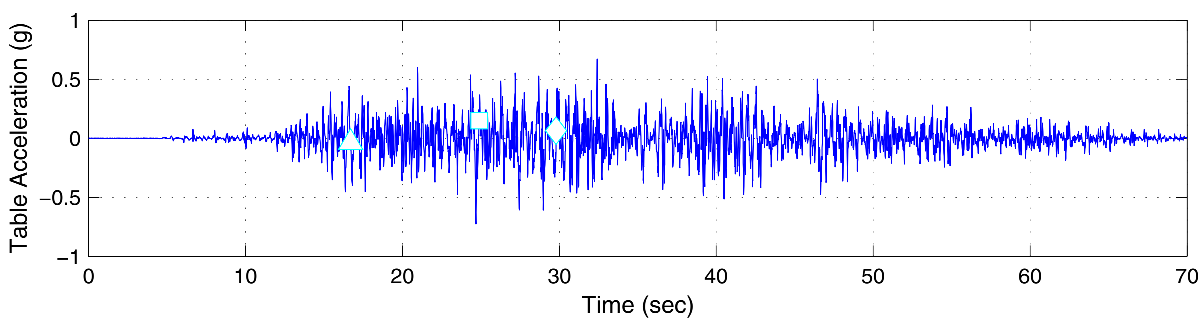

Figure 2: Table acceleration record (scaled Chile, 1985)

3. TEST RESULTS

Selected results from the shake table tests are plotted in Figures 3-6. The triangular marker indicates the approximate time at which the center column shear for Specimen 2 begins to drop off relative to the center column shear for Specimen 1. Also at this time, the center column axial load for both specimens drops by approximately 40 kN. This drop in load coincides with the development of significant cracks in the outside and center columns, and is thought to be caused by redistribution of gravity loads as the lengths of the columns change owing to flexural response.

The square marker indicates the pulse that initiates the axial failure of Specimen 2. Figures 4 and 5 demonstrate that by the time indicated by the square marker the center column shear capacity for Specimen 1 has only just begun to degrade, while the center column shear capacity of Specimen 2 has degraded to less than one-half of the previously attained center column shear.

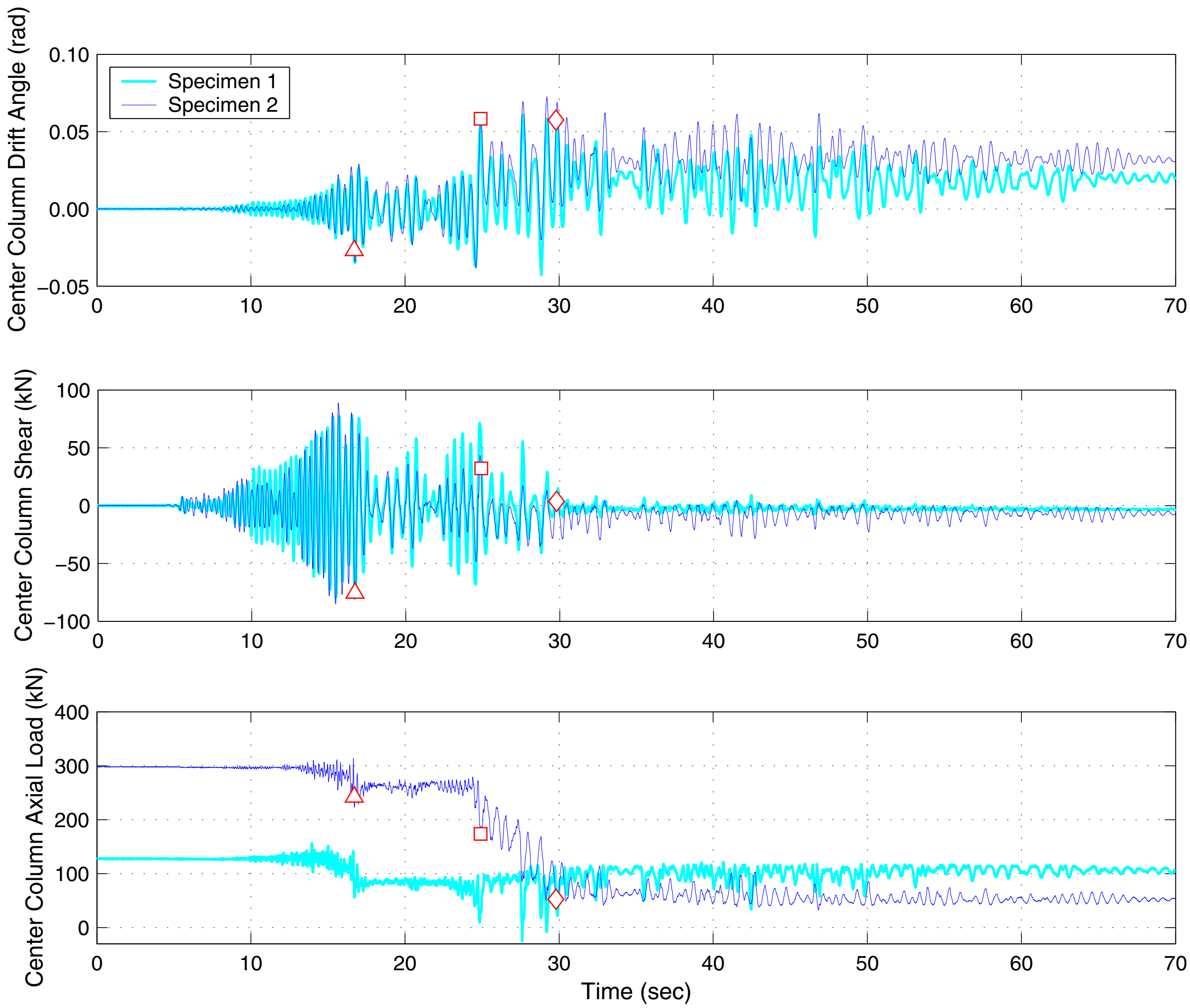

Figure 3: Response histories for shake table tests

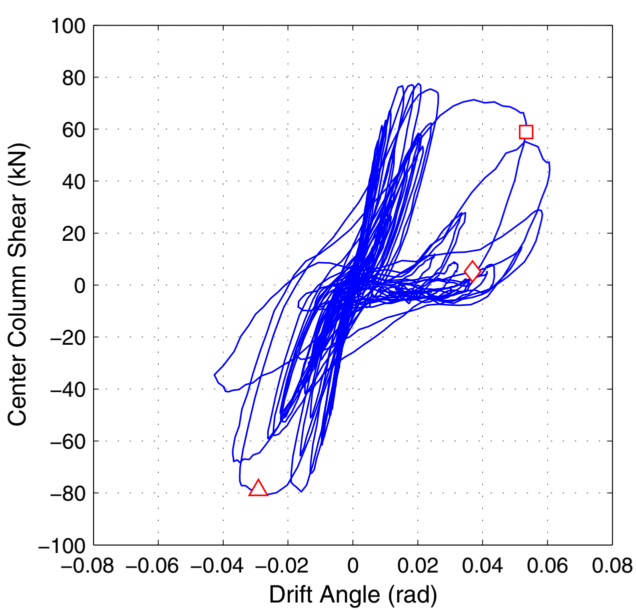

Figure 4: Specimen 1 center column shear hysteretic response

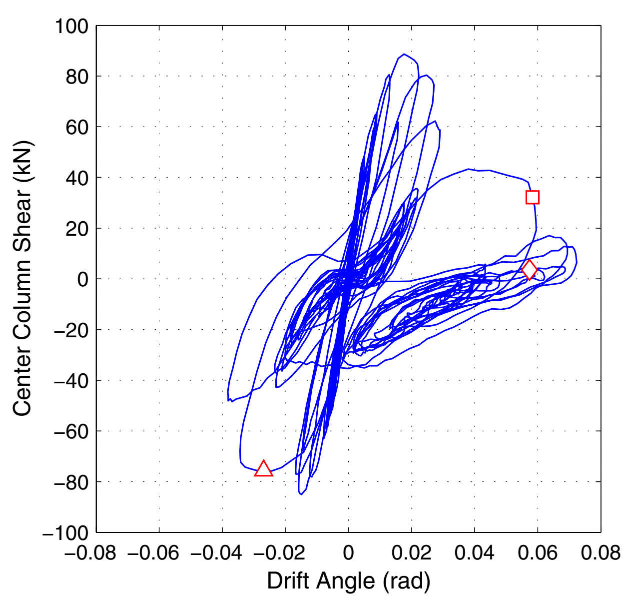

Figure 5: Specimen 2 center column shear hysteretic response

The diamond marker indicates the approximate time at which the minimum center column axial load is reached for the first time. By this point the center column shear capacity has all but disappeared for both specimens.

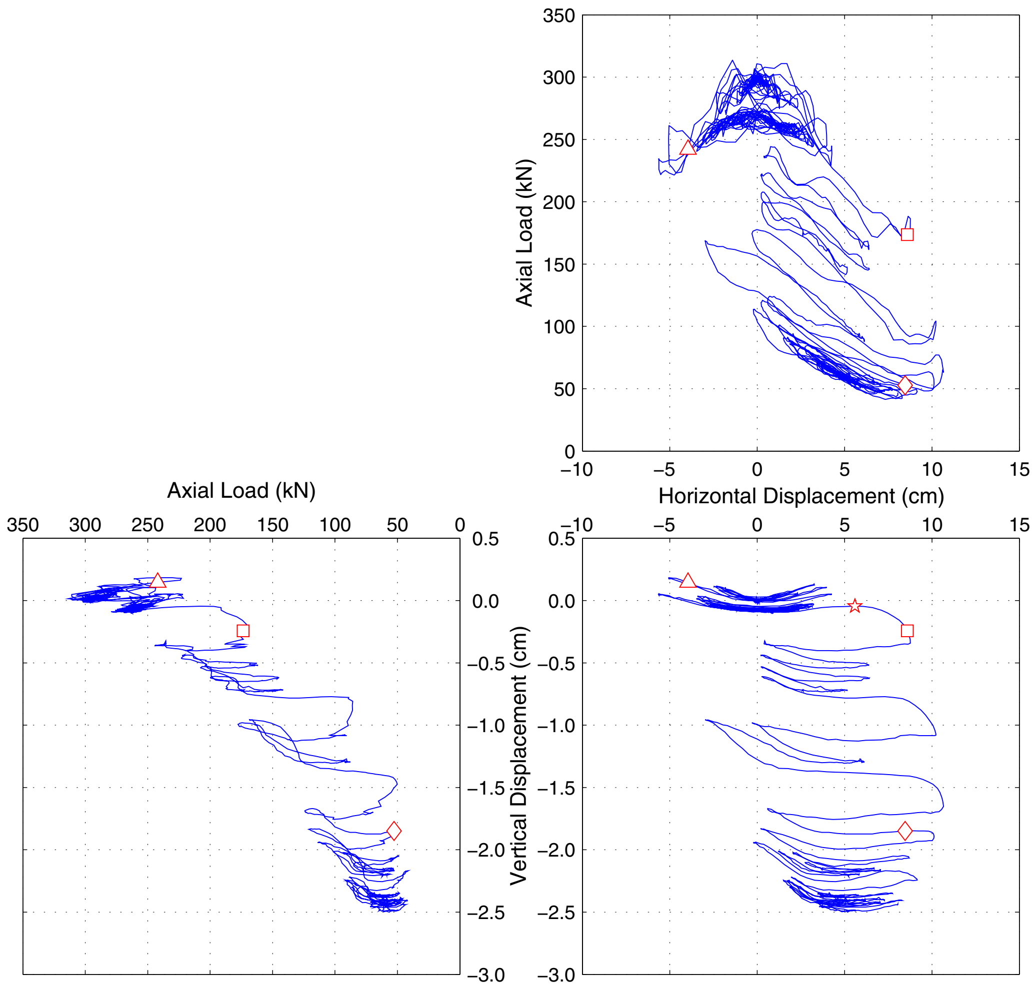

Figure 6: Relations between center column axial load, vertical displacement, and horizontal displacement of top of center column for Specimen 2

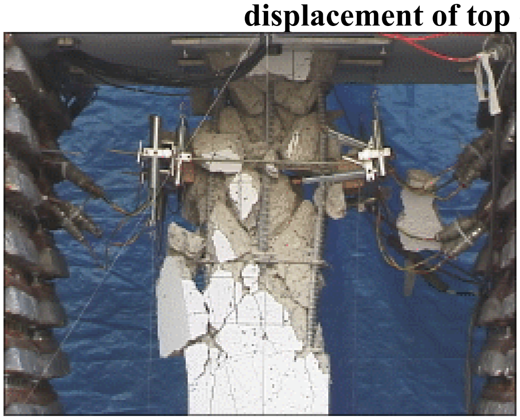

Figure 7a. Top of center column, Specimen 1 at end of test

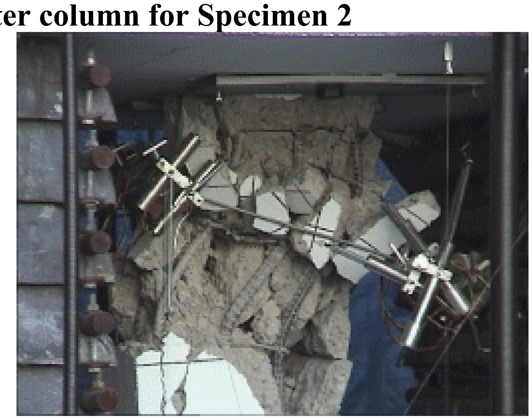

Figure 7b. Top of center column, Specimen 2 at end of test

The region between the square and the diamond markers in Figure 6 characterizes the behavior of the center column during axial failure for Specimen 2. The figure suggests that there are two mechanisms by which the vertical displacements increase: first, large pulses that cause a sudden increase in vertical displacement after a critical drift is attained; and second, smaller oscillations that appear to "grind down" the failure plane.

Figure 10 shows the state of both columns at the end of the tests.

4. DEFORMATION AT ONSET OF SHEAR FAILURE

Several models have been developed to represent the degradation of shear strength with increasing inelastic deformations (Watanabe and Ichinose, 1991; Aschheim and Moehle, 1992; Priestley et al. 1994; Sezen, 2002). While these shear strength models are useful for estimating the column strength as function of deformation demand, they are less useful for estimating displacement at shear failure. For example, the model by Sezen represents shear strength as a function of displacement ductility using the relation in Figure 8. A small variation in shear strength (or in flexural strength, not shown) can result in large variation in estimated displacement capacity. These models also suggest misleading trends in the relation between some critical parameters (such as axial load) and displacement capacity.

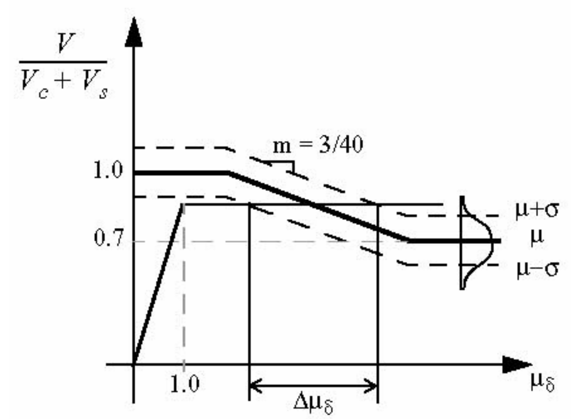

Figure 8: Displacement at shear failure as function of model variability

Pujol et al. (1999, 2000, 2002) have proposed drift capacity models for columns failing in shear. These models make an important contribution by focusing attention directly on displacement capacity and by analyzing data for model development. The database of Pujol et al. includes columns with transverse reinforcement ratios exceeding 0.01, which is larger than that which is of interest in the present study.

In the present study, a database of 50 columns having lower transverse reinforcement was studied. The database, compiled by Sezen (2002), consists of column specimens with observed shear distress at failure and tested in single or double curvature with the following range of properties: shear span to depth ratio: 2.0 < a/d < 4.0; concrete strength: 2500 < $f_c^{'}$ < 6500 psi; longitudinal reinforcement nominal yield stress: 40 < f_{yl} < 80 ksi; longitudinal reinforcement ratio: 0.01 < ρ_l < 0.08; transverse reinforcement ratio: 0.01 < $\frac{\rho^{"} f_{yt}}{f_c^{'}}$ < 0.12; maximum shear stress: 2.0 < $\frac{v}{\sqrt{f_c^{'}, psi}}$ < 9.0.

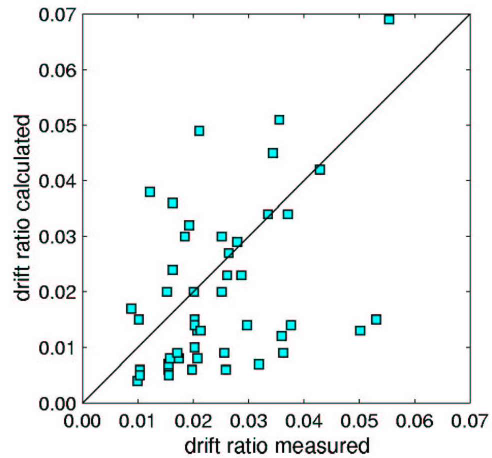

Figure 9: Comparison of measured and calculated drift capacities at onset of shear failure, Sezen shear strength model interpreted in terms of drift capacity.

The model of Sezen (2002) can be used to estimate mean shear strength as a function of displacement ductility. As suggested by Figure 8, the intersection of the shear corresponding to flexural strength with mean shear strength can be interpreted to indicate the expected displacement at shear failure. Figure 9 compares results obtained by this procedure with those actually observed during the tests. The correlation seems unsatisfactory.

A reanalysis of the data from a displacement-capacity perspective resulted in the following relationship to estimate displacement at onset of shear failure:

$$\frac{\Delta_s}{L} = 4\rho^{"} - \frac{1}{500}\frac{v}{\sqrt{f_c^{'}}} - \frac{1}{40}\frac{P}{A_g f_c^{'}} + \frac{3}{100} \geq \frac{1}{100} \qquad (1)$$

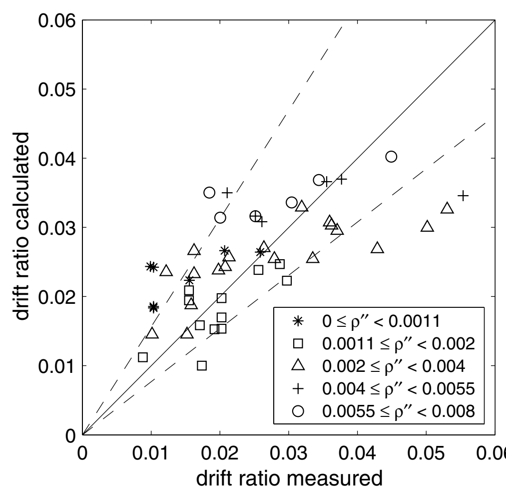

Figure 10: Comparison of measured and calculated drift capacities at onset of shear failure, Equation (1). (Dashed lines are +/- one standard deviation)

where $\frac{\Delta_s}{L}$ = drift ratio at shear failure, $\rho^{"}$ = transverse steel ratio, v = nominal shear stress (in psi), $f_c^{'}$ = concrete compressive strength (in psi), P is the axial load on the column, and A_g is the gross cross-sectional area. Figure 10 compares measured and calculated displacements at shear failure according to Equation (1).

5. DEFORMATION AT LOSS OF AXIAL-LOAD CAPACITY

Elwood (2002) has extended a shear-friction model, first presented in Moehle et al. (2001), to represent the general observation from experimental tests that the drift ratio at axial failure of a shear-damaged column is inversely proportional to the magnitude of the axial load. Considering a free-body diagram of the upper portion of a column under shear and axial load, the classic shear-friction equation from ACI 318 (1999) ($V_{sf} = N\mu$), and several simplifying assumptions, Elwood (2002) developed relations among axial load, transverse reinforcement, and drift at axial load collapse (Figure 11). While useful as a design chart for determining drift capacities, Figure 11 must only be used with a full appreciation for the limited accuracy of the results as discussed in Moehle et al. (2001) and the limitation that the results are based on unidirectional, pseudo-static tests.

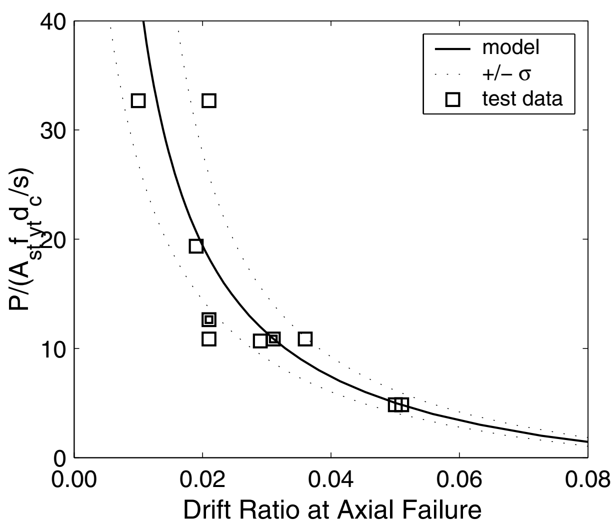

Figure 11: Drift capacity curve based on shear-friction model

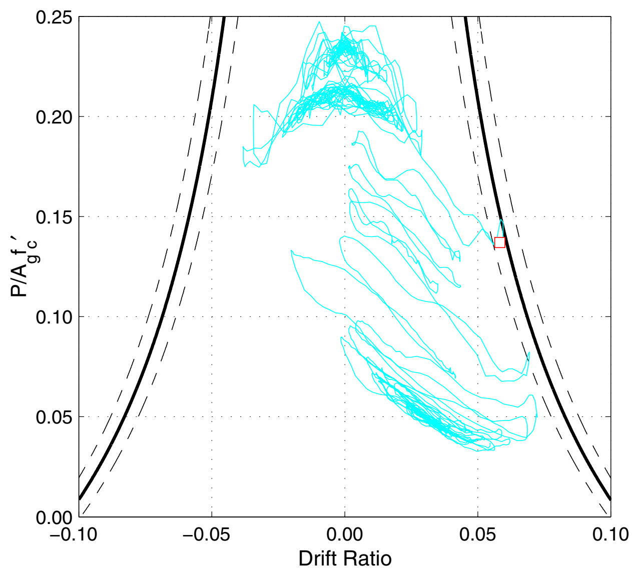

Figure 12: Comparison of shear-friction model with shake table test data from Specimen 2

Figure 12 plots the results from the shake table test (Specimen 2) along with the drift capacity curve for the center column based on the model discussed above. The intercept of the center column response and the model occurs at approximately 24.9 seconds, as indicated by the square marker (the same square marker appears in Figures 3-6). At 24.9 seconds significant distortion of the top of the center column, possibly due to sliding along the diagonal shear failure plane, could be observed visually. The center column response for Specimen 1 (not shown) lies entirely below the drift capacity curve, indicating that the shear-friction model correctly predicts no axial failure for the test column with low axial load.

6. IMPLEMENTATION IN NONLINEAR DYNAMIC ANALYSIS

An analytical model for reinforced concrete columns vulnerable to shear and axial load failures is under development within the OpenSees (2002) analytical platform. The analytical model incorporates the capacity model defining shear failure in addition to the capacity model described above for axial load failure. The column model consists of a beam-column element in series with zero-length shear and axial springs (Figure 13). As implemented, all deformations are accounted for by the beam-column element before shear or axial failure. Force and deformations in the beam-column element are used to trigger nonlinear response of zero-length springs. Figure 13 illustrates the choice of ordinate and abscissa for a shear failure spring. Since the springs are in series with the beam-column element, the springs will act as a fuse by limiting the loads carried by the entire column model. In the case of shear failure, the deformations of the entire system after the onset of failure is detected will be dominated by the shear deformations. A similar approach is implemented for axial failure using the interaction surface defined in Figure 11.

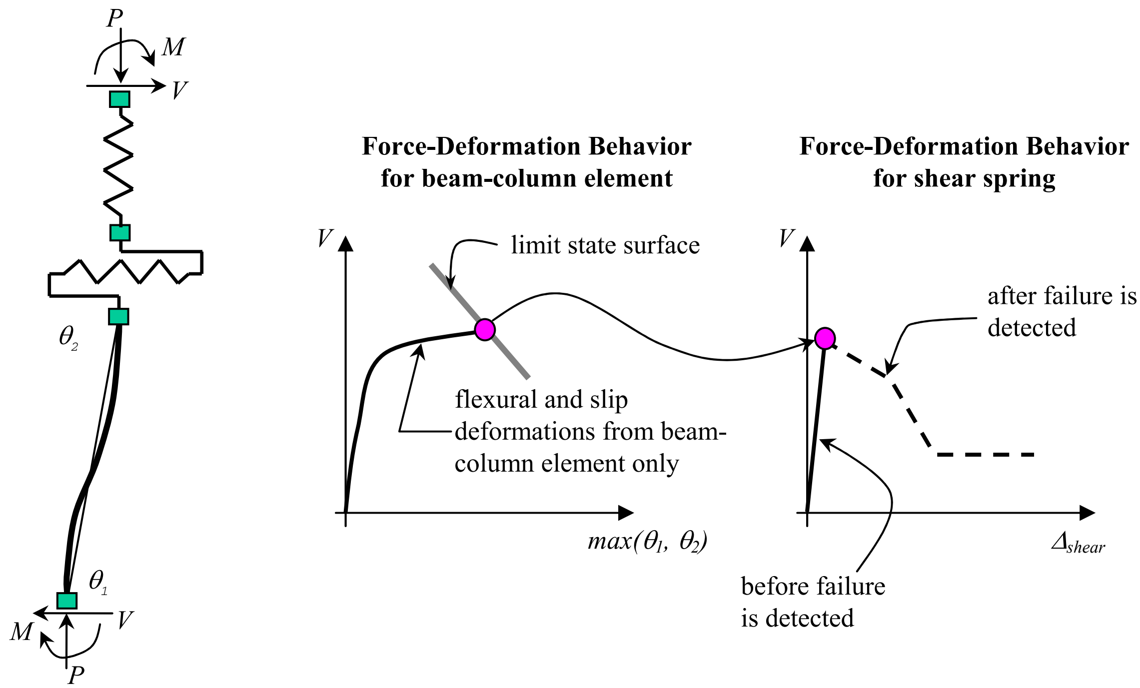

Figure 13: Limit state material used to model shear failure

The column model described above was used to model the shear failure observed in the center column of Specimen 2 described in Section 3. All columns were modeled using a fiber model to represent the interaction of flexural and axial response. The limit state surface defining the point of shear failure for the center column was determined based on the drift capacity model given by Equation 1, while the limit state surface defining the point of axial failure for the center column was based on the interaction surface shown in Figure 11. The model was subjected to the input base motion recorded during the test of Specimen 2. Equivalent viscous damping was set equal to two percent of critical.

The computed and measured base shear and drift ratio histories are compared in Figure 14. The analytical model adequately represents the measured response in terms of apparent vibration period and force amplitude throughout the test. The drifts are well predicted by the analytical results up to the point of axial failure (approximately t = 25 sec), at which point the permanent offset in the drifts observed in the test is not captured by the analysis. The analysis did not detect axial failure of the center column due to the underestimation of the lateral displacements.

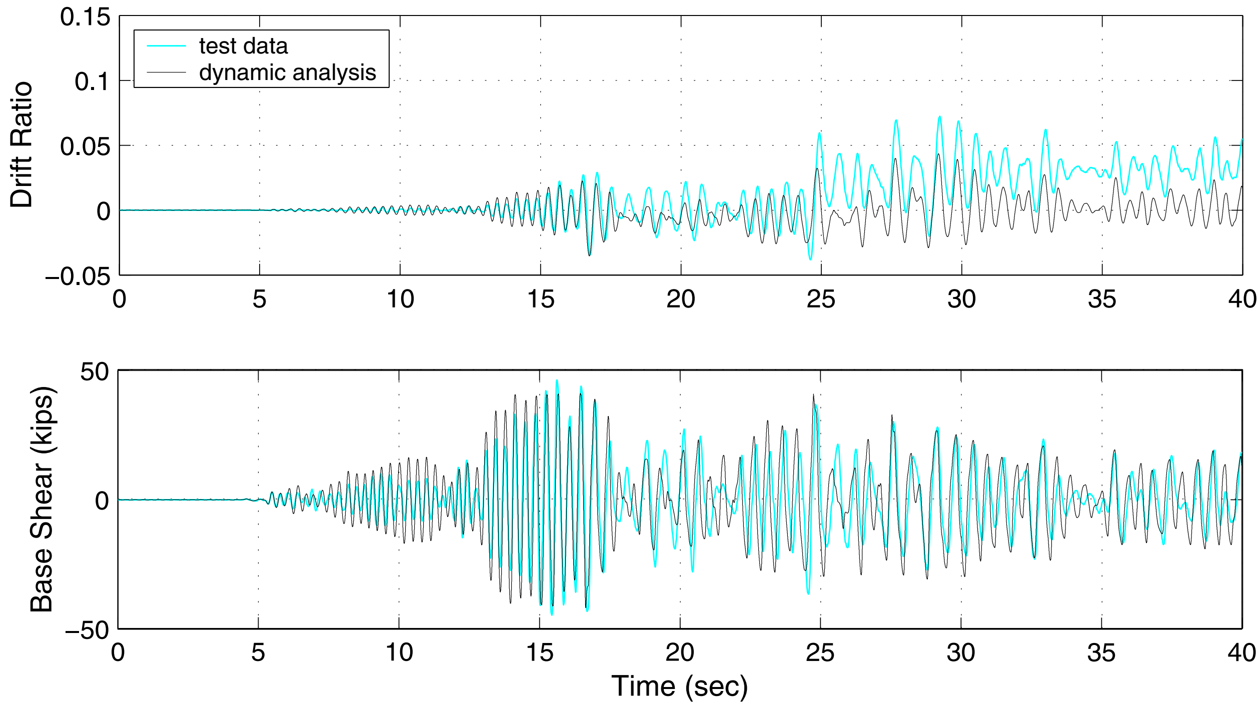

Figure 14: Comparison of experimental and analytical response histories for Specimen 2

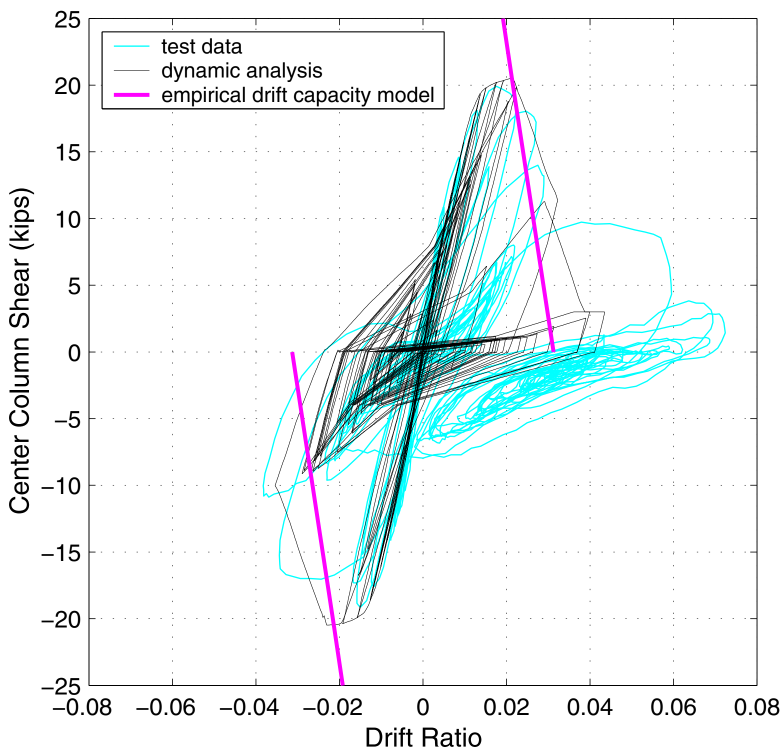

Figure 15: Comparison of experimental and analytical hysteretic response Center column, Specimen 2

Figure 15 shows the relation between shear force and lateral drift ratio for the center column. Equation 1 was used to define the drift capacity model shown in Figure 15. The response is reasonably well represented by the analytical model, although the model predicts that the shear strength degradation begins during a later cycle than observed during the test, leading to the underestimation of the permanent drifts. A closer agreement between the analytical model and the observed response can be achieved if the limit state surface defining shear failure is selected such that shear strength degradation in the model begins at the same time strength degradation was first observed during the test. Elwood (2002) investigates the influence of the variability in the position of the limit state surfaces and the degrading slope after shear failure.

7. CONCLUSIONS

Shake table tests were conducted to observe the process of dynamic shear and axial load failures in reinforced concrete columns when an alternative load path is provided for load redistribution. The test results show that the axial stress on the column influences the behavior of the column during shaking, particularly after shear failure. A column with an axial stress of $0.24f'_c$ failed to maintain its gravity loads, while another column with an axial stress of $0.10f'_c$ only saw minor gravity load redistribution. An axial failure model based on shear-friction compared favorably with the test results. A new analytical model for columns vulnerable to shear and axial load failures demonstrates the potential to reproduce the shake table test results analytically. Such a model would allow for the analysis of older reinforced concrete frame buildings vulnerable to gravity load collapse.

8. ACKNOWLEDGMENTS

This work was supported in part by the Pacific Earthquake Engineering Research Center through the Earthquake Engineering Research Centers Program of the National Science Foundation under Award number EEC-9701568. This support is gratefully acknowledged. The experimental studies were conducted in the research laboratories of PEER at the University of California, Berkeley.

9. REFERENCES

ACI Committee 318 (1999) *Building Code Requirements for Structural Concrete (318-99) and Commentary (318R-99)*, American Concrete Institute, Farmington Hills, Michigan.

Elwood, K. J., (2002) "Shake Table Tests and Analytical Studies on the Gravity Load Collapse of Reinforced Concrete Frames", *Ph.D. Dissertation*, Department of Civil and Environmental Engineering, University of California, Berkeley (to be submitted December 2002).

Lynn, A. C., Moehle, J. P., Mahin, S. A., and Holmes, W. T. (1996) "Seismic Evaluation of Existing Reinforced Concrete Columns", *Earthquake Spectra*, Earthquake Engineering Research Institute, Vol. 12, No. 4, November, pp. 715-739.

OpenSees (2002) Open System for Earthquake Engineering Simulation, (www.opensees.org), Berkeley, Calif.: Pacific Earthquake Engineering Research Center, University of California.

Moehle, J. P., Elwood, K. J., and Sezen, H., (2001) "Gravity Load Collapse of Building Frames during Earthquakes", *ACI SP-197, Behavior and Design of Concrete Structures for Seismic Performance*, American Concrete Institute.

Sezen, H. (2002) Seismic Response and Modeling of Lightly Reinforced Concrete Building Columns, *Ph.D. Dissertation*, Department of Civil and Environmental Engineering, University of California, Berkeley.

AXIAL COLLAPSE OF REINFORCED CONCRETE SHORT COLUMNS

M. Yoshimura[1] and T. Nakamura[2]

ABSTRACT

The loss of axial load carrying capacity or axial collapse of short columns is one of the most typical and dangerous damage to reinforced concrete (RC) buildings during severe earthquakes. Thus it was intended in this paper to study the axial collapse of short columns. Half-scale column specimens were laterally loaded until they came to be unable to sustain axial load. Axial load, loading history and main bar ratio were test variables. The test has revealed the general nature of axial collapse, the effect of test variables on it and so on.

1. INTRODUCTION

The loss of axial load carrying capacity or axial collapse of short columns following shear failure is one of the most typical and dangerous damage form RC building structures designed by the old codes suffered in the past earthquakes. There are still existing a number of old buildings including short columns, and it is necessary to prevent these buildings from collapsing during future severe earthquake events. To do so it is especially important to grasp the general nature of the axial collapse of short columns, such as how they come to collapse and how much associated lateral drift and vertical deformation (axial shortening) are.

While collapse tests of RC columns with ordinary length have been done in some institutes (Moehle and Elwood, 2001, Nakamura and Yoshimura, 2002 and others), those of short columns have not been done. Thus it was intended to study the axial collapse of short columns with shear mode.

[1]*Department of Architecture, Tokyo Metropolitan University, Hachioji, Japan*
Email: myoshim@arch.metro-u.ac.jp

[2]*Department of Architecture, Tokyo Metropolitan University, Hachioji, Japan*
Email: takaya@ecomp.metro-u.ac.jp

2. TEST PROCEDURES

Six half-scale model specimens were fabricated. They were designed such that shear failure might surely result. Specimen structural properties are listed in Table 1. Reinforcement details of the entire specimen and a column section are shown in Figs. 1 and 2. Height-to-depth ratio is 2 (height : 600mm and depth : 300mm). Main bar ratio (p_g) is 2.65% or 1.69%, and hoop ratio (p_w) is 0.21%. Material properties are listed in Table 2. Concrete strength in the table is an average of those determined before the first test and after the last test (24.0MPa and 26.3MPa).

Table 1: Specimen structural properties

<table>
<tr><th>Name①</th><th>b×D</th><th>h_0/D</th><th>Hoop
p_w (%)</th><th>Main bar
p_g (%)</th><th>Axial stress ratio②</th><th>Computed shear strength (kN)</th><th>Computed flexure strength (kN)</th></tr>
<tr><td>2M</td><td rowspan="6">300mm
×
300mm</td><td rowspan="6">2.0</td><td rowspan="6">0.21
(2-D6@100)</td><td rowspan="4">2.65
(12-D16)</td><td rowspan="2">0.19</td><td rowspan="2">279</td><td rowspan="2">430</td></tr>
<tr><td>2C</td></tr>
<tr><td>3M</td><td rowspan="2">0.29</td><td rowspan="2">295</td><td rowspan="2">486</td></tr>
<tr><td>3C</td></tr>
<tr><td>2M13</td><td rowspan="2">1.69
(12-D13)</td><td rowspan="2">0.19</td><td rowspan="2">260</td><td rowspan="2">319</td></tr>
<tr><td>2C13</td></tr>
</table>

①Numerals 2 and 3 denote axial stress ratio of about 0.2 and 0.3. Alphabets M and C denote monotonic and cyclic loading. Numeral 13 means D13 bar is used. ②Axial stress ratio, $\eta_c = N / (b \cdot D \cdot f_c')$ (N: Axial load)

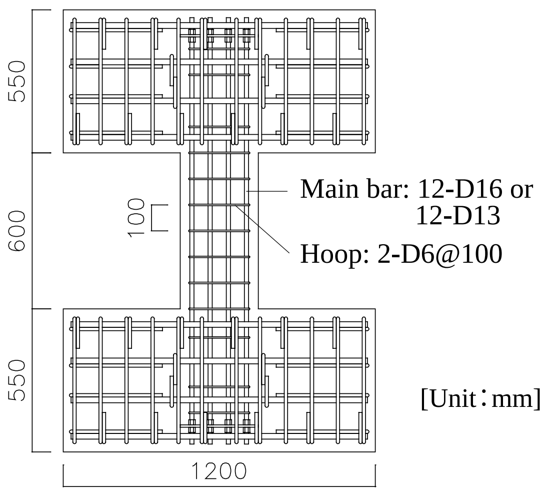

Fig. 1: Reinforcement details of specimen

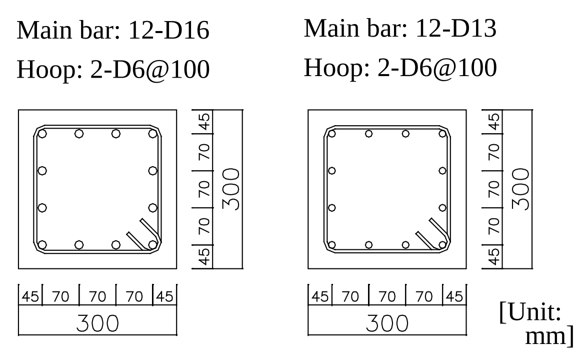

(a) 2M, 2C, 3M, 3C **(b) 2M13, 2C13**

Fig. 2: Column section

Table 2: Material properties

(a) Steel

	Yield stress (MPa)	Yield strain (%)
D16	396	0.22
D13	350	0.19
D6	392	0.24

(b) Concrete

Max. stress (MPa)	Strain at max. stress (%)
25.2	0.29

Test variables were axial load, loading history and main bar ratio. Two levels of axial load, 0.19 and 0.29 times as much as concrete strength (f_c') multiplied by column section, were considered. As for the loading history, monotonic and cyclic cases were used. The monotonic case was added taking account of the dynamic analysis results for the records from the Kobe earthquake that is a typical near-field earthquake. All specimens were finally loaded to the positive direction until the axial load could not be maintained. Two values of main bar ratio were considered. It is believed that hoop ratio has a significant effect on collapse, but it was not considered in this test.

Test apparatus is shown in Fig. 3, where the pantograph is placed so that the loading beam at the column top does not rotate (double curvature deformation is realized). A loading method is as follows. The specimens were loaded to the lateral direction under constant vertical load. The vertical actuator was controlled by load while the lateral actuator was by displacement. And the tests were terminated by the limiter of the vertical actuator that was set to operate when vertical deformation (axial shortening) reached 8.3% of the column height or 50mm.

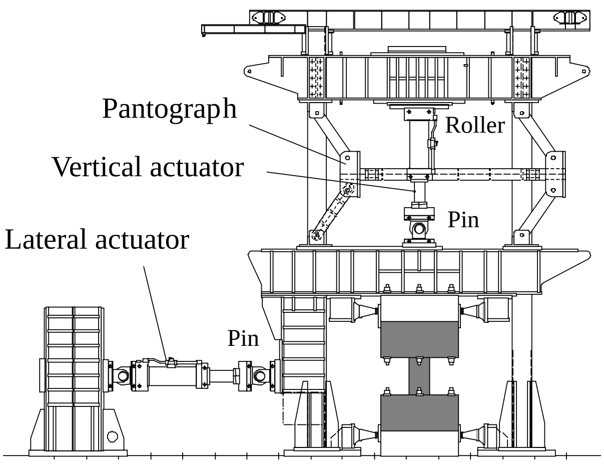

Fig. 3: Test apparatus

3. TEST RESULTS

All specimens finally lost their axial load carrying capacity. A load step immediately before the sudden increase of axial shortening is defined as a step of ‘collapse’ and maximum lateral drift experienced until that step is denoted as ‘collapse drift’. Damage states observed at and after collapse are shown in Photo 1 for 2M, 2C, 2M13 and 2C13. The note on 2M13, “Axial shortening once stopped increasing” is referred to later.

When lateral drift is large, differences in lateral load and shear force that is defined as force in the direction perpendicular to the column axis can not be neglected. Shear force is estimated by the way shown in Fig. 4. Lateral load (shear force) vs. drift relations are shown in Fig. 5. While lateral load at collapse was in some cases considerably negative, associated shear force was nearly zero because of the contribution of the vertical load to it.

Axial shortening vs. lateral drift relations are shown in Fig.6. For all specimens except 2M13, when the collapse occurred, the axial shortening suddenly increased reaching 8.3% (50mm) and the test was terminated by the limiter. However, for 2M13, when the collapse occurred, the axial shortening suddenly increased but stopped increasing at 5.1% (30.6mm). Therefore, the limiter did not operate. Note that the slope of the tangential at each load step tends to increase as the test proceeds. This phenomenon observed for all specimens will be discussed in 4.6.

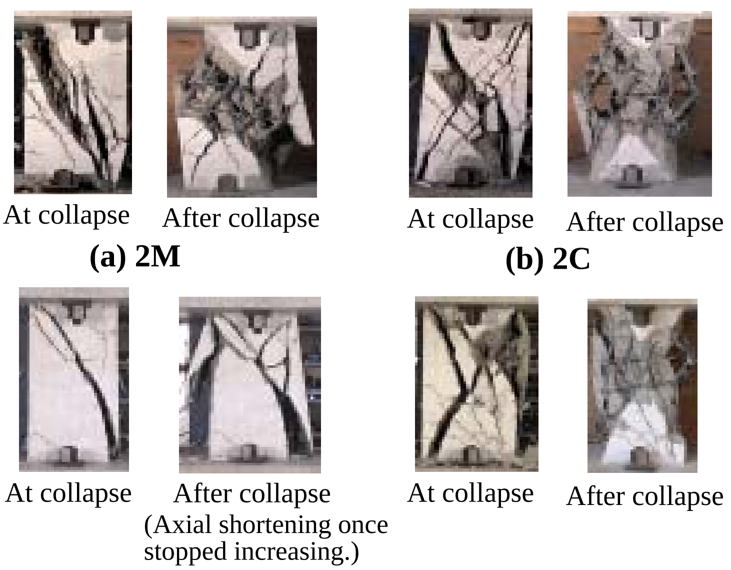

(a) 2M (b) 2C

(c) 2M13 (d) 2C13

Photo 1: Damage states

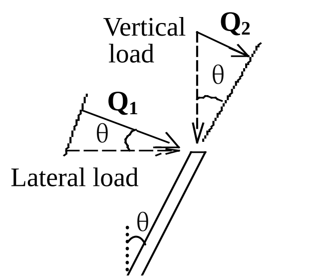

Shear force = Q_1+Q_2

where

Q_1 = Lateral load × cos θ

Q_2 = Vertical load × sin θ

$$\theta = \frac{\text{Lateral drift (mm)}}{\text{Column height (mm)}}$$

Fig. 4: Shear force

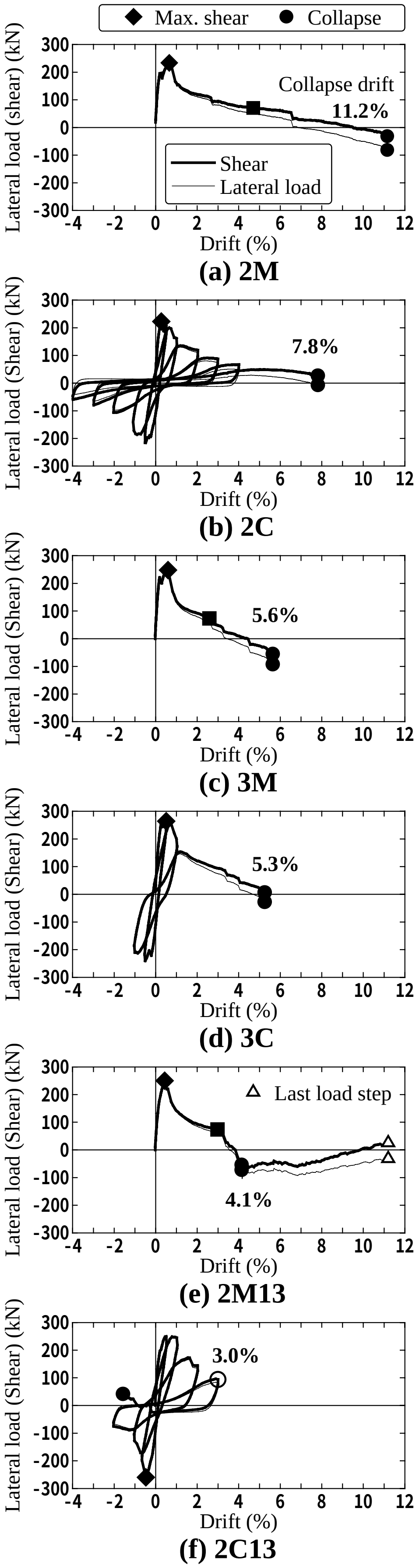

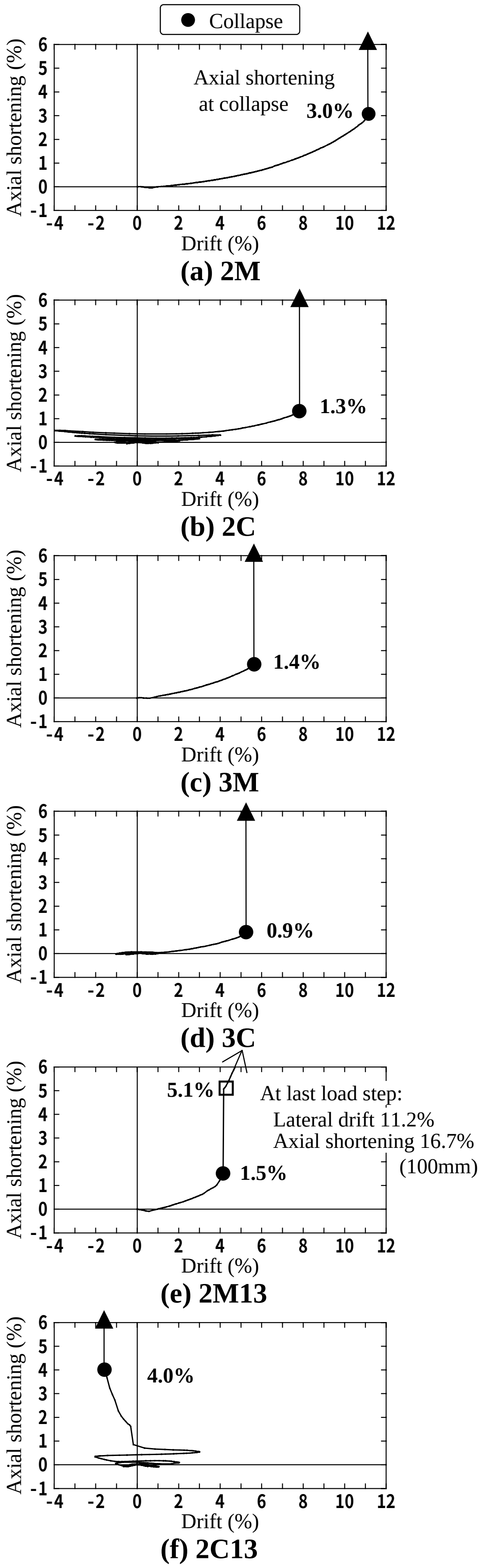

Fig. 5: Lateral load (Shear) vs. drift

Fig.6: Axial shortening vs. lateral drift

The test results are outlined in Table 3. Drift at 30% of the maximum shear in the table is discussed later. Collapse behavior is stated below for 2M, 2C, 2M13 and 2C13.

Table 3: Outline of test results

Name	Max. shear (kN)	Drift at max. shear (%)	Drift at 30% of max. shear (%)	Shear at collapse (kN)	Collapse drift (%)	Axial shortening at collapse (%)
2M	234	0.66	4.7	-31.5	11.2	3.0
2C	222	0.27		27.1	7.8	1.3
3M	248	0.60	2.6	-55.2	5.6	1.4
3C	264	0.51		6.7	5.3	0.9
2M13	250	0.43	3.0	-53.7	4.1	1.5
2C13	-260	-0.47		41.6	3.0	4.0

<u>2M</u> Collapse drift, and associated shear force and axial shortening were respectively 11.2% –31.5kN and 3.0%. At the moment of collapse hoop bars' fracture and their loosening at the hook as well as main bars' buckling were observed. Similar behavior was observed at the collapse for the other specimens too.

<u>2C</u> Collapse drift, associated shear force and axial shortening were 7.8%, 27.1kN and 1.3%. As compared to 2M, the portion of concrete crushing was large probably because of the effect of cyclic loading (Photo 1). Such difference depending on the loading history was also observed for the other specimens.

<u>2M13</u> Collapse drift, and associated shear force and axial shortening were 4.1%, –53.7kN and 1.5%. For this specimen the axial shortening stopped increasing before it reached the limit value. This is probably because at the moment of collapse the crushed concrete along the failure line was removed and the less damaged concrete existing above and below it came in contact. With the limit value increased to 16.7% (100m) the test was restarted. However, the sudden increase of axial shortening did not occur again.

<u>2C13</u> The collapse occurred at lateral drift of –1.6% during the loading from 3% to –3%. Associated shear force and axial shortening were 41.6kN and 4%. This was the only specimen that collapsed during the cyclic loading before the final collapse loading.

4. DISCUSSIONS

4.1 Main Bar Strains

It is confirmed for 3M that all stain gauges attached to the main bars functioned until near collapse. Damage state at collapse and locations of main bar strain measurement are shown in Photo 2 and Fig. 7 for this specimen. And main mar strains are shown in Fig. 8. At lateral drift of about 1% strains increased to compression for locations W1 and E4, and at lateral drift of about 2% they exceeded yield level in compression for locations W2 and E3. These four locations are close to the failure line (Photo 2), indicating the concrete crushing near the failure line led to the increase of compression strain in main bars for these locations. It is likely that the main bars played an important role in sustaining axial load at large drift level.

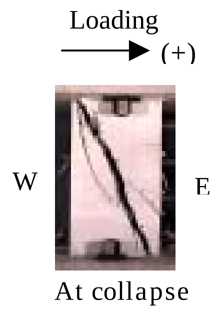

Photo 2: Damage state (3M)

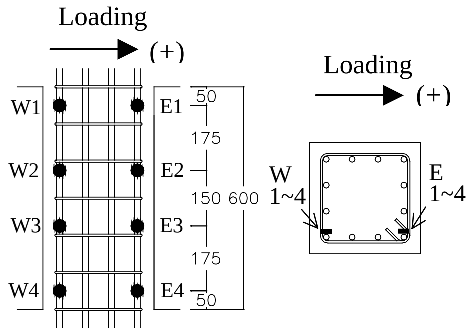

Fig. 7: Location of main bar strain measurement

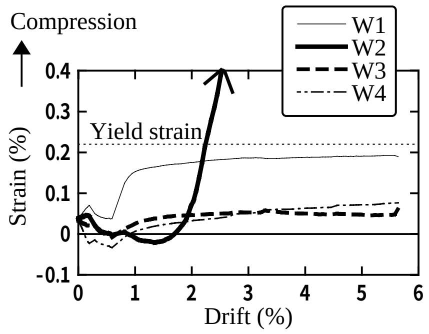

(a) W1~W4

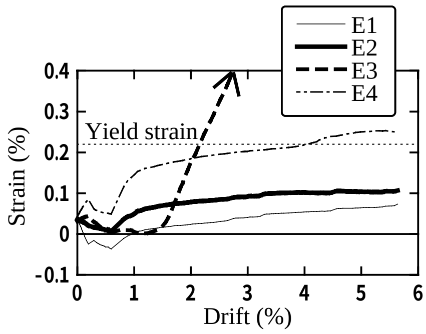

(b) E1~E4

Fig. 8: Main bar strain vs. lateral drift (3M)

4.2 Maximum Shear Force, and Shear Force and Axial Shortening at Collapse

Maximum shear force and shear force at collapse are shown in Fig. 9. Maximum shear force is close to the computed value for 2M13 and 2C13 though smaller than the computed by about 20% for the others. Shear force at collapse is within –55.2kN and 41.6kN, being nearly zero. This result indicates that the collapse occurs when shear force decreases to about zero.

Relations of axial shortening at collapse vs. collapse drift are shown in Fig. 10. It is apparent that 1) there is no interaction between these two values and 2) the axial shortening at collapse is, though varying much, at least about 1%, being considerably larger than 0.4% that is usually considered as crushing stain for plain concrete.

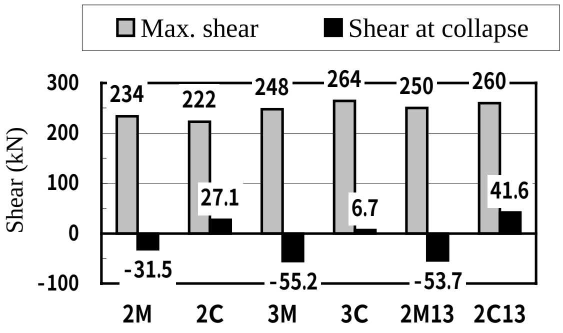

Fig. 9: Max. shear and shear at collapse

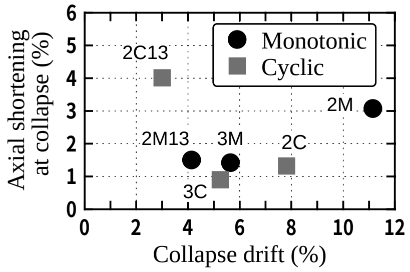

Fig. 10: Axial shortening at collapse vs. collapse drift

4.3 Reduction of Shear Force and Collapse

In most column tests the loading is stopped when the shear force decreases to some value. This value is arbitrary. Supposing it is 30% of the maximum shear force, and lateral drift at that shear force is read. Black square mark in Fig.5 shows this point. Ratio of the collapse drift to the drift so determined is shown in Fig. 11 for the monotonic cases. The collapse drift is occasionally more than twice as much as drift at 30% of the maximum shear force. If the loading is stopped at this level, it is far from the collapse.

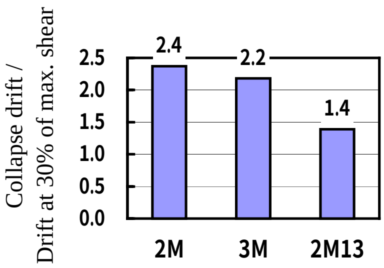

Fig. 11: Ratio of collapse drift to drift at 30% of max. shear

4.4 Effect of Test Variables on Collapse Drift

The collapse drift ranges from 3.0% to 11.2% (Table 3). The effect of the test variables on the collapse drift is discussed below.

<u>Effect of Axial Load</u>

The effect of axial load is shown in Fig. 12. Comparison of 2M (11.2%) and 2C (7.8%) with 3M (5.6%) and 3C (5.3%), all of which have same main bar ratio, indicates the collapse drift is smaller as the axial load increases.

<u>Effect of Loading History</u>

The collapse drift is compared in Fig. 13 with respect to the loading history. Ratios of the cyclic case to the monotonic case are 0.70 to 0.95, being not much smaller than unity. But this value can lower if the number of loading cycles is more than that used for this test.

Effect of Main Bar Ratio

In Fig. 12, comparison of 2M (11.2%) and 2C (7.8%) with 2M13 (4.1%) and 2C13 (3.0%), all of which have same axial load, indicates the collapse drift is smaller as the main bar ratio decreases. It is generally recognized that the deformation capacity of shear columns is similar irrespective of the main bar ratio if the other structural properties such as axial load and hoop ratio are same. However, the test shows the main bar ratio have a significant effect on the collapse drift.

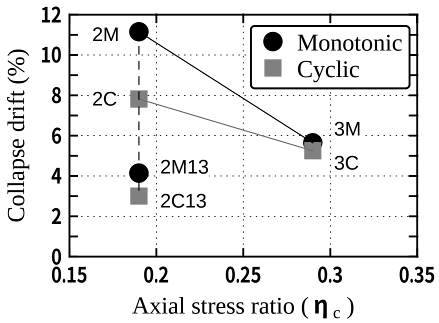

Fig. 12: Collapse drift vs. η_c

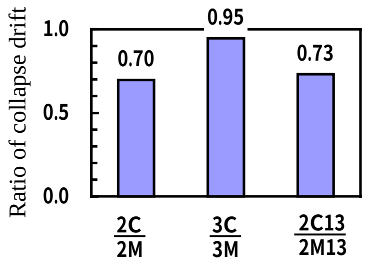

Fig. 13: Comparison of collapse drift with respect to loading history

4.5 Relations of Collapse Drift vs. Axial Stress Ratio Variously Defined

Axial stress ratio, η_C (N/(b・D・f_c')), based on the compression strength only by concrete can not explain the above fact that the collapse drift of 2M and 2C differs from that of 2M13 and 2C13. Hence axial stress ratio based on the compression strength by concrete and steel, η_{SC}, as defined by EQ (1), is computed.

$$\eta_{sc} = N / (A_g \cdot \sigma_y + A_c \cdot f_c') \qquad (1)$$

where A_g: total main bar area, σ_y: Main bar yield stress and A_c: Concrete area (= b・D - A_g).

Collapse drift vs. η_{SC} relations are shown in Fig. 14(a). Comparison of 2M and 2C with 2M13 and 2C13 shows the collapse drift is smaller as η_{SC} increases. However, comparison of 2M13 and 2C13 with 3M and 3C shows the collapse drift is larger as η_{SC} increases, which is opposite to the above result.

Then axial stress ratio based on the compression strength only by steel, η_S, as defined by EQ (2), is computed.

$$\eta_s = N / (A_g \cdot \sigma_y) \tag{2}$$

This equation was introduced by considering the fact stated earlier that the main bars had played an important role in sustaining axial load at large drift level. Collapse drift vs. η_S relations are shown in Fig. 14(b). It turns out the collapse drift is inversely proportional to η_S. The fitted lines are shown in the figure.

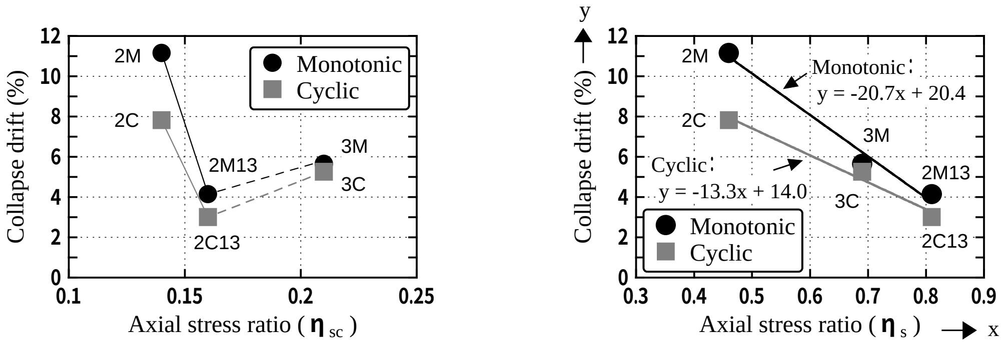

(a) Considering concrete and steel **(b) Considering only steel**

Fig. 14: Collapse drift vs. various axial stress ratios

4.6 Ratio of Axial Shortening Increment to Lateral Drift Increment

As stated earlier, the slope of the tangential at each load step in the axial shortening vs. lateral drift relations tends to increase with the increase of lateral drift or the decrease of shear force (Fig. 6). To study this phenomenon, the slope, as defined as a ratio of axial shortening increment to lateral drift increment is computed. This ratio is called Deformation Increment (DI) ratio. DI ratios are shown in Fig. 15 for 2M. DI ratio increases with the increase of lateral drift.

The reason DI ratio increases as the loading proceeds is discussed below. Figure 16 shows a conceptual sketch of shear strength vs. axial strength interaction curve (failure surface). Initial failure surface, which corresponds to the state of maximum shear force, was drawn such that the points of initial axial compression strength and initial axial tension strength might lie on it. The failure progress occurring after the maximum shear force is believed to accompany the deterioration of concrete, resulting in the reduction of axial compression strength as well as shear strength. But axial tension strength is considered to keep an initial value because it is not affected by concrete deterioration. The reduced failure surface in the figure was drawn by considering the above.

By the way one can know from the flow rule in plastic theory that DI ratio is equivalent to a direction normal to the failure surface. Though exactly speaking DI ratio has to be evaluated on the basis of plastic deformation, it is not a problem for this case because elastic deformation is small. As is shown in the figure, DI ratio increases as the loading proceeds (as the failure surface is reduced), which coincides with the observations.

The increase of DI ratio with the progress of failure can be explained by introducing the reduction of the failure surface.

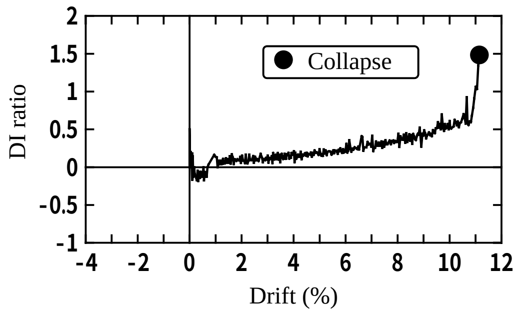

Fig. 15: DI ratio vs. lateral drift (2M)

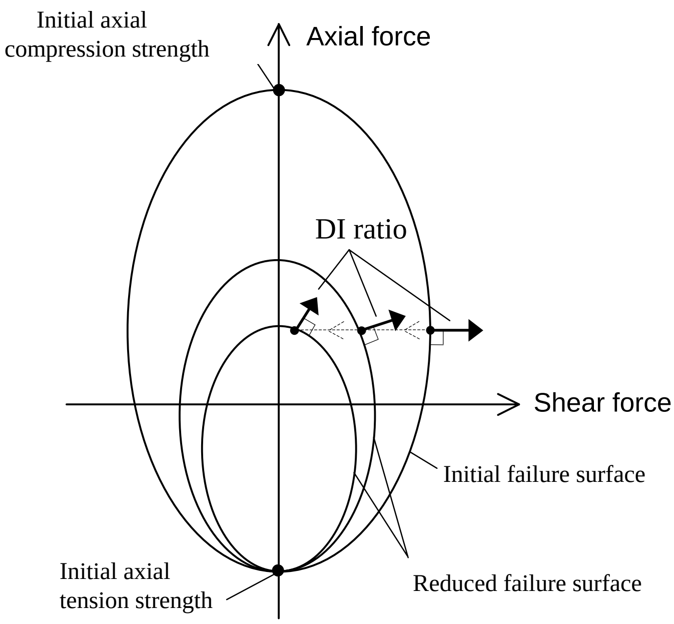

Fig. 16: Reduction of failure surface and changes of DI ratio

4.7 Collapse Inter-Story Drift

Collapse drift is converted to inter-story drift of a real-scale building with particular geometric properties. Assumed geometric properties are shown in Fig. 17. The column, twice as much as the specimens in size, is assumed to behave in the same way as the specimens did. The inter-story drift (%) of this building, at which the collapse occurs, is computed by multiplying the collapse drift (%) of the specimens by a factor of 1200/3600=1/3 (column clear height : 1200mm and story height : 3600mm). The collapse inter-story drift so determined is shown in Fig. 18. These values range from 1.0% to 3.7%. One has to note the collapse inter-story drift is occasionally as small as 1.0% because such extent of the inter-story drift possibly occurs during severe earthquakes.

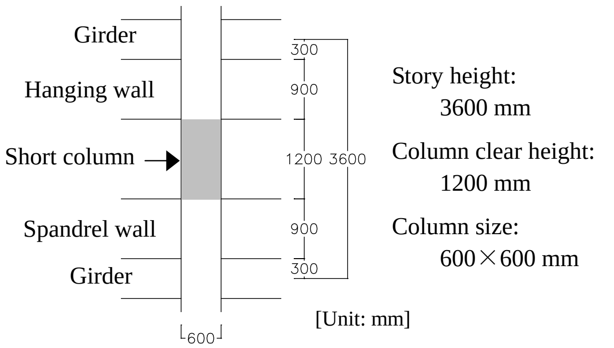

Fig. 17: Assumed real-scale building

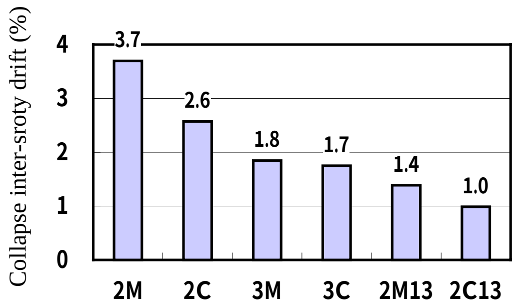

Fig. 18: Collapse inter-story drift

5. CONCLUSIONS

The axial collapse of shear-failing RC short columns was studied. The major findings from the study are as follows.

1) The collapse occurs when shear force decreases to about zero.
2) The collapse drift is 3.0% to 11.2% of column height. And the equivalent inter-story drift of real-scale buildings is 1.0% to 3.7% of story height, indicating it is occasionally as small as 1%.
3) It is generally recognized that the deformation capacity of shear columns is similar irrespective of the main bar ratios if the other structural properties are same. However, the test has revealed the collapse drift is smaller as the main bar ratio decreases.
4) An observed trend in the deformation increment ratio (DI ratio) can be explained by the flow rule in plastic theory by considering the reduced failure surface.

ACKNOWLEDGEMENT

The authors express their special gratitude to Mr. Seira, Ohwa, former graduate student of Tokyo Metropolitan University, who assisted them in studying in this text.

REFERENCES

Moehle, J. P., Elwood, K. J. and Sezen, H. (2001) Gravity Load Collapse of Building Frames during Earthquakes. ACI SP-197. *Behavior and Design of Concrete Structures for Seismic Performance.* American Concrete Institute.

Nakamura, T. and Yoshimura, M. (2002). Gravity Load Collapse of Reinforced Concrete Columns with Brittle Failure Modes. *Journal of Asian Architecture and Building Engineering.* Vol.1. No.1. 21-27.

KEYWORDS

collapse, axial load, loading history, lateral drift, axial shortening, deformation increment ratio, failure surface

SESSION B-1: PERFORMANCE ASSESSMENT

Chaired by

♦ Akira Tasai and Laura Lowes ♦

Post-Earthquake Capacity Evaluation of R/C Buildings Based on Pseudo-Dynamic Tests

Masaki MAEDA[1]

Daeeon KANG[2]

ABSTRACT

In this paper, Post-earthquake capacity evaluation method of reinforced concrete buildings was studied. Substructure pseudo-dynamic test and static loading test of first story column in a four-story R/C building was carried out in order to investigate the validity of the evaluation method proposed by authors. In pseudo-dynamic test, different levels of damage were induced in the specimens by pre-loading, and input levels of seismic motion, at which the specimens reached to the ultimate stage, were examined. From the experimental result, no significant difference in damage levels such as residual crack width between the specimens under static and pseudo-dynamic loading was found. It is shown that residual seismic capacity ratio η proposed by authors can provide a reasonable estimation of post-earthquake seismic capacity of R/C buildings suffered earthquakes.

1. INTRODUCTION

In damage investigation of building structures suffering from earthquake, estimation of residual seismic capacity is essential in order to access the safety of the building against aftershocks and to judge the necessity of repair and restoration. The authors have proposed an evaluation method for post-earthquake seismic capacity of reinforced concrete (R/C) buildings based on the residual energy dissipation capacity of structural members [Bunno and Maeda, 2000]. The proposed method was adopted in the Japanese “Damage Level Classification Standard” revised in 2001 [JBDPA, 2001].

In this paper, substructure pseudo-dynamic test of first story column in a four-story R/C building was carried out in order to investigate the validity of the proposed evaluation method for post-earthquake seismic capacity. In pseudo-dynamic test, different levels of damage were induced in the specimens by pre-loading, and input levels of seismic motion, at which the specimens reached to the ultimate stage, were examined. Evaluation method for post-earthquake seismic capacity was discussed based on the test results.

[1] *Department of Architecture and Building Science, Tohoku University, Sendai, Japan*
Email: maeda@struct.archi.tohoku.ac.jp
[2] *Department of Architecture and Building Science, Tohoku University, Sendai, Japan*
Email: kde0898@struct.archi.tohoku.ac.jp

2. OUTLINES OF EXPERIMENT

2.1 Description of Specimens

Four column specimens were tested in this study. The specimen represented an interior column in the first story of an existing 4-storied R/C building as shown in Figure 1. All specimens have the same dimension and reinforcement. The properties and reinforcing details are shown in Figure 2 and Table 1. The dimensions of a column section were 40 x 50 cm and shear span-to-depth ratio was 1.5 (150cm height). Ten D19 bars (nominal diameter of 1.91cm, nominal area of 2.87cm$_2$) were arranged as longitudinal reinforcement. 19ϕ bars (round bar, diameter of 1.9cm) were arranged as lateral reinforcement with 12.5cm spacing. Mechanical properties of concrete and reinforcement are shown in Table 2.

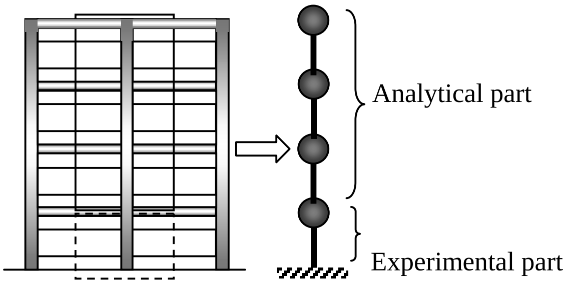

Figure 1: Objective building and analytical model for pseudo-dynamic test

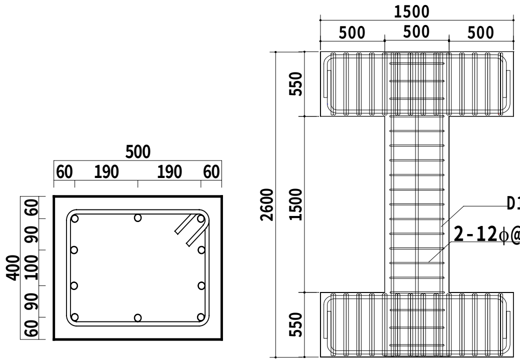

Figure 2: Dimensions and reinforcements distribution of specimens

Table 1: Dimensions and reinforcements of specimens

B X D	H_0	Longitudinal Reinforcement	p_t	Shear Reinforcement	p_w	N
400 X 500	1500	10–D19	0.57	2–12ϕ@125	0.45	953

H_0 : clear height (mm), P_t : tension reinf. ratio (%), P_w : lateral reinf. ratio (%), N : axial load (kN)

Table 2: Material properties of concrete and reinforcements

Concrete		Reinforcements		
σ_y (Mpa)	ε_{cu} (%)	Size and Quality	σ_y (Mpa)	ε_y (%)
27.2	0.18	D19	364	0.187
		12ϕ	329	0.161

σ_y : Compressive Strength, ε_{cu} : Strain at the Strength, σ_y : Yield Strength, ε_y : Yield Strain

2.2 Parameters of Experiment

Experimental parameters are shown in Table 3. Three specimens named PSD0, PSD2, and PSD3 were examined by pseudo-dynamic testing. The specimens PSD2 and PSD3 were damaged by pre-loadings. Target initial damage levels for PSD2 and PSD3 were minor damage (damage class II by the Damage Level Classification Standard, see Table 4) and moderate damage (damage class III), respectively. On the other hand, PSD0 was tested with no structural damage. The damaged and undamaged specimens were tested by pseudo-dynamic testing using amplified input seismic motion at which the specimens reached to the ultimate stage. The specimen ST was tested by static loading to compare the failure patterns, damage levels and hysterisis loops with the specimens under pseudo-dynamic testing.

Table 3: Parameters of experiment

	Loading	Initial damage	Damage class*
PSD0	Pseudo-Dynamic	None	0
PSD2		Minor	II
PSD3		Moderate (or Severe)	III
ST	Static	None	0

* Damage Level Classification Standard [JBPDA, 2001]

Table 4: Damage classification of structural members [JBPDA, 2001]

Damage class	Observed damage on structural members
I	Some cracks are found. Crack width is smaller than 0.2 mm.
II	Cracks of 0.2 - 1 mm wide are found.
III	Heavy cracks of 1 - 2 mm wide are found. Some spalling of concrete is observed.
IV	Many heavy cracks are found. Crack width is larger than 2 mm. Reinforcing bars are exposed due to spalling of the covering concrete.
V	Buckling of reinforcement, crushing of concrete and vertical deformation of columns and/or shear walls are found. Side-sway, subsidence of upper floors, and/or fracture of reinforcing bars are observed in some cases.

2.3 Test Method and Loading System

2.3.1 Loading apparatus

Loading apparatus is illustrated in Figure 3. The specimens were subjected to bending and shear by a horizontal jack. The vertical jacks on both side of the specimen kept the top and bottom stubs and applied constant axial. The specimen ST was subjected to two cycles at drift angle of 1/200, 1/100, 1/67, 1/50, 1/33 rad. after the first cycle at a drift angle of 1/400.

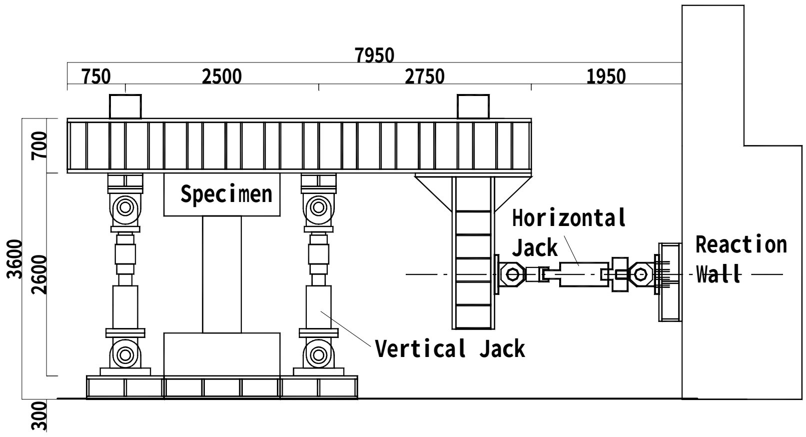

Figure 3: Testing apparatus

2.3.2 Method of Pseudo-Dynamic Test

The specimens PSD0, PSD2 and PSD3 were tested by sub-structure pseudo-dynamic method. The objected building was reduced to a 4-degree-of-freedom system. As shown in Figure 1, the column specimen represents the first story column and second to fourth stories were analyzed. The specimen was subjected to the target story drift angle which was calculated from step-by-step seismic response analysis of the 4-degree-of-freedom system. Takeda model was used as hysteresis model for the analytical parts in seismic response analyses. The crack and yielding strengths of the specimens are calculated according to the Japanese "Standard for Structural Calculation" [AIJ, 1999]. Time increment of response analysis was 0.005 second and OS-method [Nakajima et al., 1990] was applied to numerical integration. Viscous damping matrix was assumed to be proportional to stiffness matrix at yielding, which was 2% of natural frequency.

NS component of JMA (Japan Meteorological agency) KOBE recorded at 1995 Hyogo-ken-nambu Earthquake was adopted for the input ground motion. The input acceleration is shown in Figure 4. Table 5 shows the target structural damage levels of the specimens and the amplification factors of input ground acceleration for each RUNs, respectively. As mentioned earlier, specimens PSD2 and PSD3 were induced structural damage of damage class II and III, respectively, by pre-loading named "RUN0" in order to estimate the residual seismic capacity. Note that additional pre-loading "RUN0+" was applied to specimen PSD2 because the damage level due to the RUN0 remained damage class I. Then all specimens were subjected to amplified input acceleration so that the specimen reached to the ultimate state and failed (damage class V).

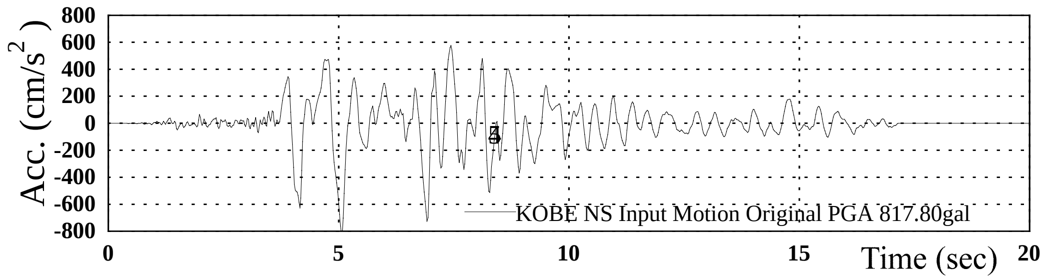

Figure 4: Acceleration record for input ground motion (JMA Kobe NS)

Table 5: Target structural damage and amplification factor of input acceleration

Specimen	Input	Target Damage Level	Amplification Factor
PSD2	RUN0	II	0.25
	RUN0$^+$		0.41
	RUN1	V	0.41
PSD3	RUN0	III	0.50
	RUN1	V	0.30
PSD5	RUN1	V	0.60

3. TEST RESULTS

3.1 Results of Static Loading

Figure 5 shows the observed shear force – lateral displacement relation for specimen ST. Crack pattern was shown in Photo 1. Longitudinal bars yielded at the drift angle of the order of 1/200 after generation of flexural and shear cracks. The process to failure was as follows; i.e., at a drift angle of 1/100rad., bond splitting cracks along longitudinal bars were observed. The lateral load began to decrease gradually with propagation of bond splitting cracks and, finally, bond splitting failure was observed.

The relationship between the maximum residual crack width and drift angle at the peak of each cycle was shown in Figure 6. The residual crack widths were measured by crack scale at the moment when the lateral force was unloaded. In the figure, crack width of 0.2, 1, and 2mm correspond to the borders between the damage classes of the structural members, according to Table 4 [JBDPA 2001]. The crack widths were smaller than 0.2mm, which correspond to the "damage class I (slight damage)", until flexural yielding occurred in a cycle at 1/200rad. After flexural yielding, the maximum residual crack widths increased markedly with increase in drift angle.

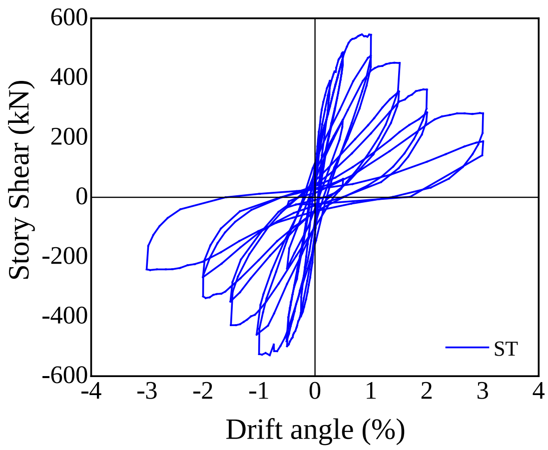

Figure 5: Story shear vs. drift angle

Photo 1: Crack patterns at the final cycle

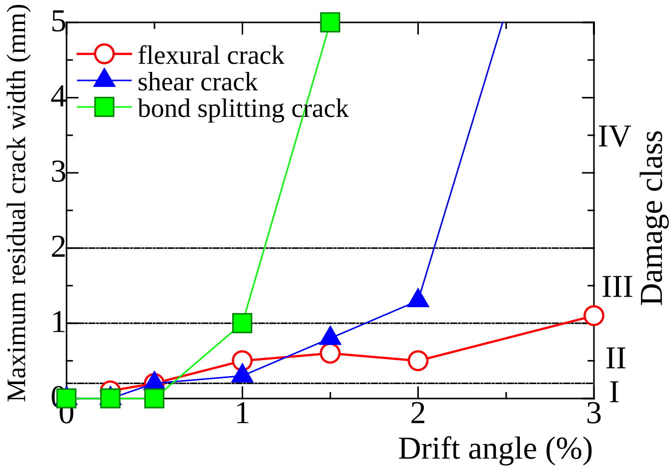

Figure 6: Maximum crack width vs. drift angle

3.2 Results of Pseudo-dynamic Loading

Figure 7 shows the observed shear force – lateral displacement relations of specimen PSD0, PSD2 and PSD3. The relationship between the maximum residual crack width and drift angle at the peak of each cycle was shown in Figure 8. Crack patterns after the pre-loading, RUN0, were shown in Photo 2.

The process to failure was almost similar to the specimens ST. In specimen PSD0 which was subjected to 0.60 time JMA Kobe NS record, after flexural yielding was observed at drift angle of 0.61%, shear force began to decrease with propagation bond splitting cracks and the specimen failed.

Maximum drift angle was 0.5% and maximum residual crack widths was 0.2mm (damage class I) in RUN0 of specimen PSD2, in which amplification factor for the input acceleration was 0.25. In the RUN0^{+} (amplification factor was 0.41), after the specimen yielded at the drift angle of 0.61% and maximum drift angle reached to 1.0% with maximum residual crack width of 0.5mm (damage class II). In the RUN1 (amplification factor was 0.41), the specimen failed in bond splitting due to rapid increase in drift angle.

Maximum drift angle of 2.24% and bond splitting crack of 3.5mm width, which was somewhat larger than the criteria of the target damage class III were induced by the RUN0 of specimen PSD3 (amplification factor was 0.50). In the RUN1 with amplification factor of 0.30, shear resistance was deteriorated gradually due to bond splitting failure, although maximum drift angle did not increase markedly.

As can be seen from Figure 8, no significant difference in residual crack widths between the specimens under static and pseudo-dynamic loading was found.

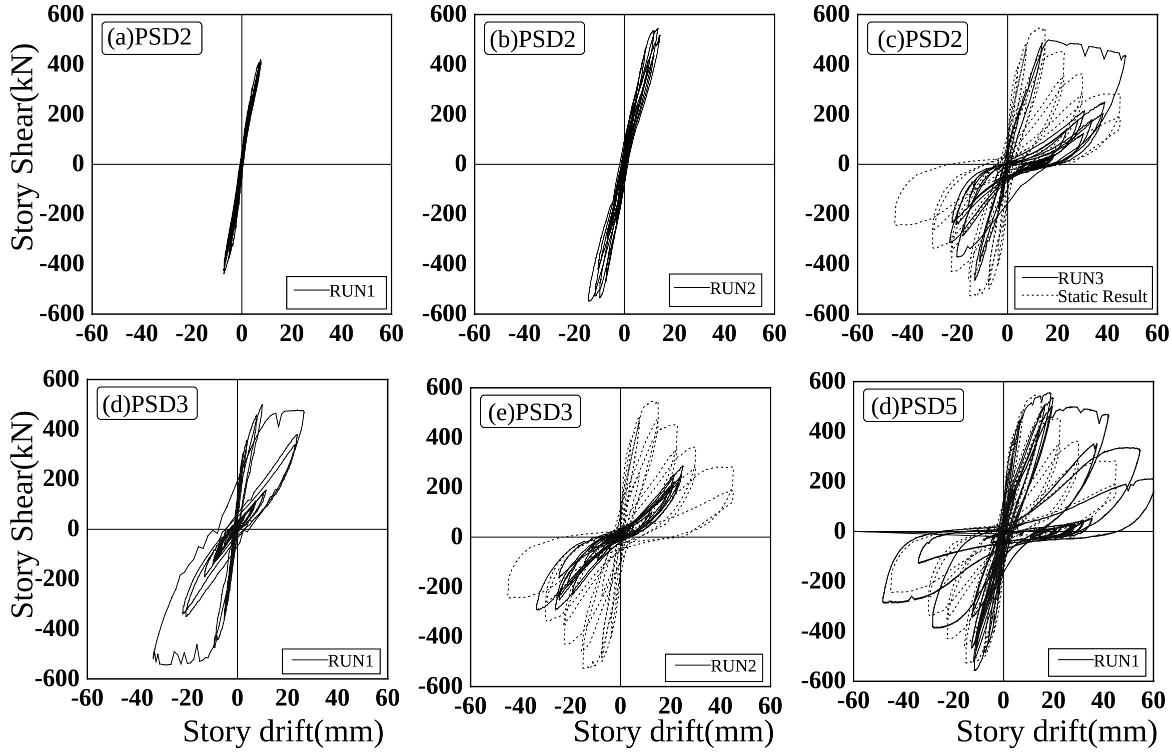

Figure 7: Relationships between story shear and drift angle

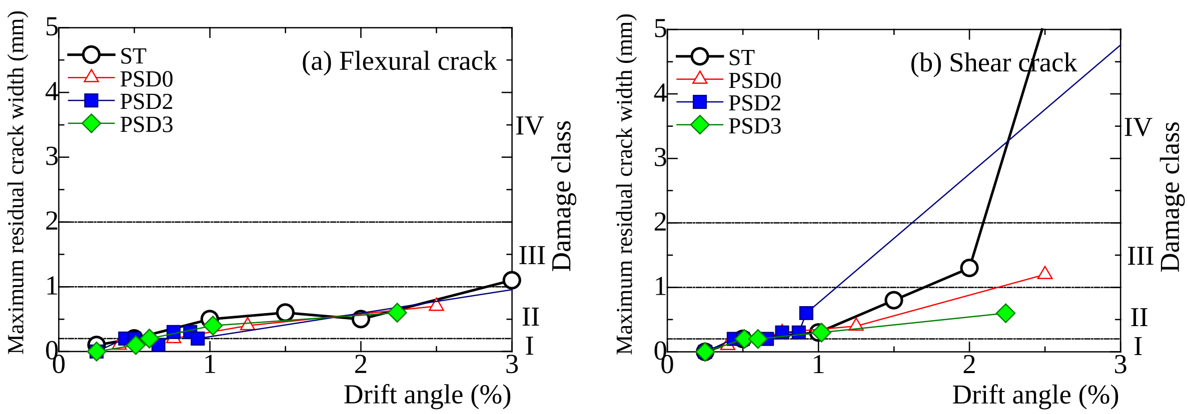

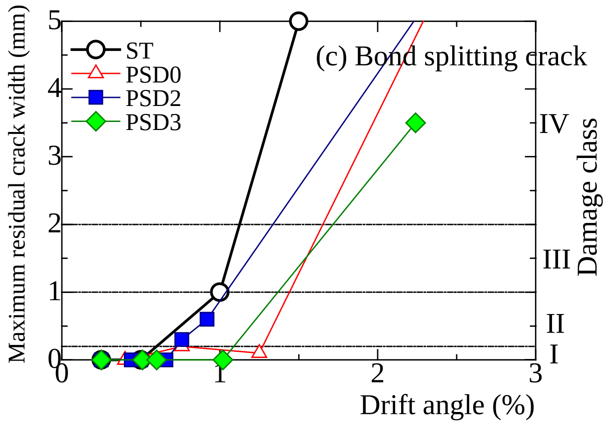

Figure 8: Maximum residual crack width vs. drift angle

(a) RUN0 of PSD2 **(b) RUN0$^+$ of PSD2** **(c) RUN0 of PSD3**

Photo 2: Crack patterns after pre-loading

The relationships between the amplification factor of input acceleration and maximum ductility factors are shown in Figure 9. In the figure, the lines indicate analytical results for the first story of the 4-degree-of-freedom system and the marks are experimental results. Figure 9(a) indicates the results without structural damage; i.e., RUN1 for PSD0 and RUN0 for PSD2 and PSD3. Figure 9(b), (c) and (d) indicate the results after pre-loading. From the figure, maximum ductility response increases with increase in amplification factor of input ground motion. The maximum ductility responses after some damage was induced (Figure 9(b), (c) and (d)) are generally larger than those without damage. Experimental results approximately agreed well with the analytical results although disagreement can be found for the results of ductility factor of larger than 5 because pinching behavior and deterioration of shear resistance were not taken into account in the hysteresis model for the analyses.

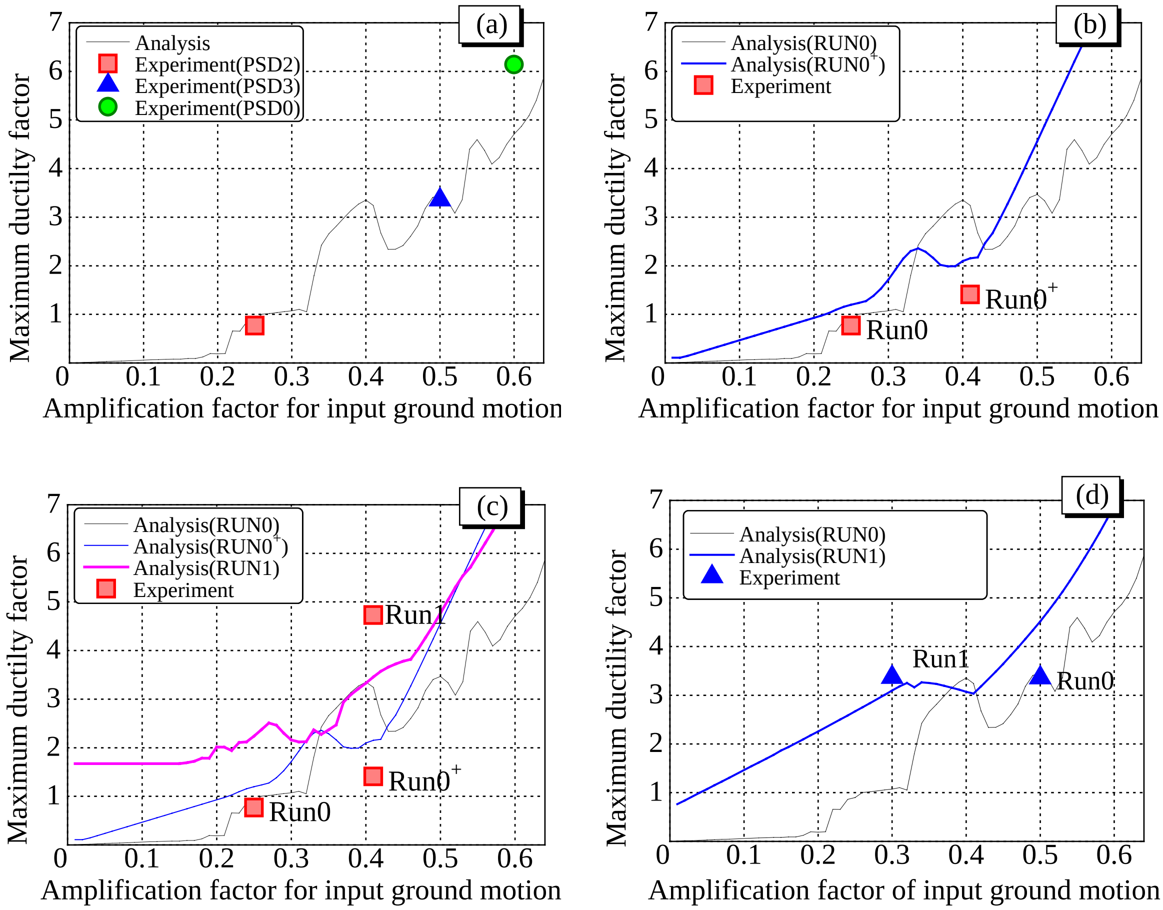

Figure 9: Relationship between amplification factor of input ground motion and maximum ductility factor

4. ESTIMATION OF RESIDUAL SEISMIC CAPACITY

The authors evaluated residual seismic capacity ratio η of structural members for each damage class as shown in Table 6 based on experimental data of beams and columns under static loading. The basic concept of residual seismic capacity ratio η is illustrated in Figure 10. Deterioration of seismic capacity was estimated by energy dissipation capacity in lateral force- displacement curve of each member. The residual seismic capacity ratio η was defined as the ratio of residual energy dissipation capacity to the total capacity and given by Eq.(1).

$$\eta = \frac{E_r}{E_t} \tag{1}$$

where, E_d : dissipated energy, E_r : residual energy capacity, E_t : entire energy capacity ($E_t = E_d + E_r$).

Table 6: Residual seismic capacity ratio η

Damage class	Brittle members	Ductile members
I	0.95	0.95
II	0.6	0.75
III	0.3	0.5
IV	0.0	0.1
V	0.0	0.0

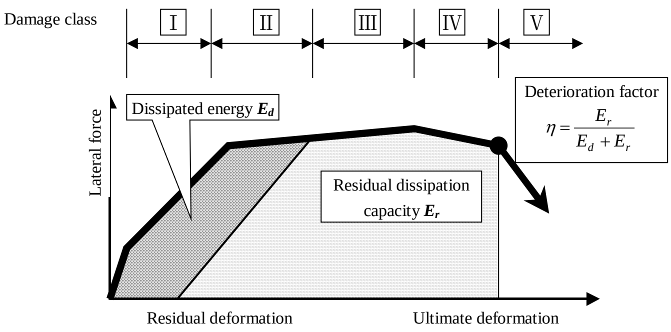

Figure 10: Seismic capacity reduction factor η

To investigate the validity of the proposed residual seismic capacity ratio η, input ground motion levels with which the specimen failed in the pseudo-dynamic testing were compared with residual seismic capacity ratio η in Figure 11. In the figure, thick line and broken line indicate residual seismic capacity ratio η for brittle and ductile members respectively. The circles indicate amplification factors of input acceleration in the pseudo-dynamic testing. Amplification factor of 0.60 for undamaged specimen PSD0 was assumed to correspond to the original capacity, η=1.0. As can be seen from the figure, amplification factor of 0.41 for RUN1 of PSD2 and 0.30 for RUN1 of PSD3 approximately correspond to the residual seismic capacity ratio η. Accordingly, the proposed residual seismic capacity ratio η might be useful for the reasonable estimation of post-earthquake seismic capacity of damaged R/C buildings.

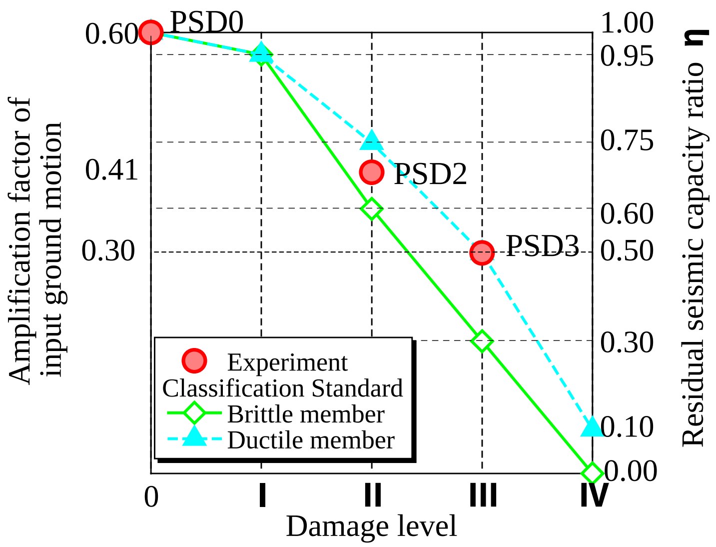

Figure 11: Comparison of seismic capacity reduction factor η with amplification factor of input ground motion

6. CONCLUSIONS

In this paper, static loading test and sub-structural pseudo-dynamic test of R/C columns were carried out to investigate the validity of the method for post-earthquake capacity evaluation proposed by the authors. From the experimental result, no significant difference in damage levels such as residual crack width between the specimens under static and pseudo-dynamic loading was found. It is shown that residual seismic capacity ratio η proposed by the authors can provide a reasonable estimation of post-earthquake seismic capacity of R/C buildings suffered earthquakes.

REFERENCES

AIJ / Architectural Institute of Japan (1999), *Standard for structural calculation of reinforced concrete structure*. (in Japanese)

Bunno, M., Maeda, M., and Nagata, M. (2000), "Damage level classification of reinforced concrete buildings based on member residual seismic performance (in Japanese)", *Proceedings of the Japan Concrete Institute*, Vol. 22, No. 3, JCI, pp.1447-1452.

Bunno, M., Nagayama, K., Maeda, M., and Tasai, A. (2001), "An evaluation of residual seismic capacity of reinforced concrete columns based on structural damage (in Japanese)", *Proceedings of the Japan Concrete Institute*, Vol. 23, No. 3, JCI, pp.259-264.

JBDPA / The Japan Building Disaster Prevention Association (2001), *Standard for Damage Level Classification of Reinforced Concrete Buildings*. (in Japanese)

Jung, M., Maeda, M., Tasai, A. and Nagata, M. (2001), "Relationship between residual seismic performance and damage level on seismic response of reinforced concrete buildings (in Japanese)", *Proceedings of the Japan Concrete Institute*, Vol. 23, No. 3, JCI, pp.1219-1224.

Nakajima, M., Ishida, M., and Ando, K (1990), "Integration Techniques for Substructure Pseudo Dynamic Test (Pseudo dynamic test using substructuring techniques) (in Japanese)", *Journal of structural and construction engineering, Transaction of AIJ*, No.417, pp.107-118,

LE CONTE HALL SEISMIC CORRECTIONS PROJECT

K. MARK SINCLAIR[1] and JANIELE MAFFEI[2]

ABSTRACT

The seismic performance of Le Conte Hall at the University of California, Berkeley, was investigated by Degenkolb Engineers, and a seismic strengthening scheme developed with Murukami/Nelson for the University of California Berkeley, Capital Projects Group.

The objective for the project was to increase the performance level of the structure from POOR to GOOD, in accordance with the University of California Policy on Seismic Safety. To achieve this level of performance the retrofitted structure was required to achieve Life Safety performance for the 10% probability of exceedance in 50 year earthquake, and Collapse Prevention performance for the 10% probability of exceedance in 100 year earthquake.

A number of challenges were encountered in the design and analysis of the seismic strengthening scheme, which was performed in accordance with the provisions of FEMA 356, *Prestandard and Commentary for the Seismic Rehabilitation of Buildings*, November 2000. These are summarized herein to illustrate some the challenges in implementing present performance based design procedures for this type of structure, and to highlight areas where additional research and development will assist practising design professionals.

1. INTRODUCTION

Le Conte Hall is located on the University of California, Berkeley's Campus within one kilometer of the Hayward Fault. The University's architect, John Galen Howard, designed the building in 1922. Degenkolb Engineers performed a detailed seismic evaluation of the existing structure of Le Conte Hall and developed a strengthening scheme to retrofit the building with Murakami/Nelson Architects for the University of California Berkeley, Office of Planning, Design, and Construction. The provisions of FEMA 356, *Prestandard and Commentary for the Seismic Rehabilitation of Buildings* [4] were used for the assessment of the existing structure and to develop the strengthening scheme.

[1] *Project Engineer, Degenkolb Engineers, San Francisco, California, USA, Email:sinclair@degenkolb.com*
[2] *Principal, Degenkolb Engineers, San Francisco, California, USA, Email:jmaffei@degenkolb.com*

The evaluation consisted of detailed two and three-dimensional modeling of the seismic force-resisting system using the SAP2000 computer program [2]. Two-dimensional models were used to understand the deformation mechanism of both the existing and the new lateral systems, and to create a nonlinear pushover curve for the overall structure. The overall pushover curve assembled from these analyses was used to calculate the target displacements for the Level II and Level III seismic demand spectrums using the target displacement approach, as presented in FEMA 356. Early in the assessment process the Level I earthquake was found to not govern and results for this assessment are not presented here. The three-dimensional model was used to assess the torsional behavior of the structure and to compute the maximum displacements of critical exterior wall components.

Figure 1: Le Conte Hall

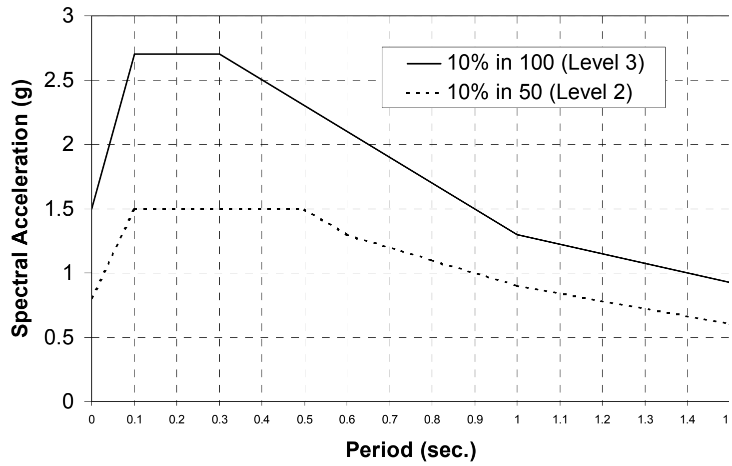

Figure 2: Le Conte Hall Seismic Demand Spectra

2. BUILDING DESCRIPTION

Le Conte Hall was designed in 1922 by the University's architect, John Galen Howard. The building is a four-story plus half basement cast-in-place concrete building with overall plan dimensions of about 190 feet by 95 feet and a gross square footage of approximately 76,000 square feet. The north half of the building is four stories and the south half has a basement level, which is above grade as a result of the sloping site. The majority of the roof is concrete construction, however at the center of the roof there is a large steel-framed glass skylight that protrudes roughly 14 feet above the peak of the main roof. The four-story portion of the building is 58 feet in height and the four-story plus basement portion is 70 feet in height to the top of the main roof. The typical story height is 15 feet with a 13 foot story height at the 4th floor and a 12 foot story height at the basement. The roof of the building is configured such that the fourth floor has the full story height for the inner portion of the building, but the roof slants down to meet the perimeter wall just 3½ feet or so above the fourth floor.

4. STRENGTHENING SCHEME

The strengthening scheme involved the addition of new concrete shear walls. Two walls were added in the transverse (east-west) direction, one each on column lines B and K. One wall was added in the longitudinal direction, located on column line 8. This configuration allowed for preservation of the existing historic corridors. The new walls were designed as a combination of cast-in-place concrete and shotcrete. Concrete collector beams were added in line with the walls to deliver seismic loads to the new walls. New concrete strip footings were placed below the new walls. In some locations, the footing / grade beam was extended beyond the end of the shear wall in order to mobilize additional dead load for overturning resistance.

The configuration of the building and the various components of the strengthening scheme are shown in Figures 3 through 6. The RW and RC notation refers to bays of new shear wall and collector that were removed from the preliminary scheme as a result of the presented three-dimensional pushover analysis.

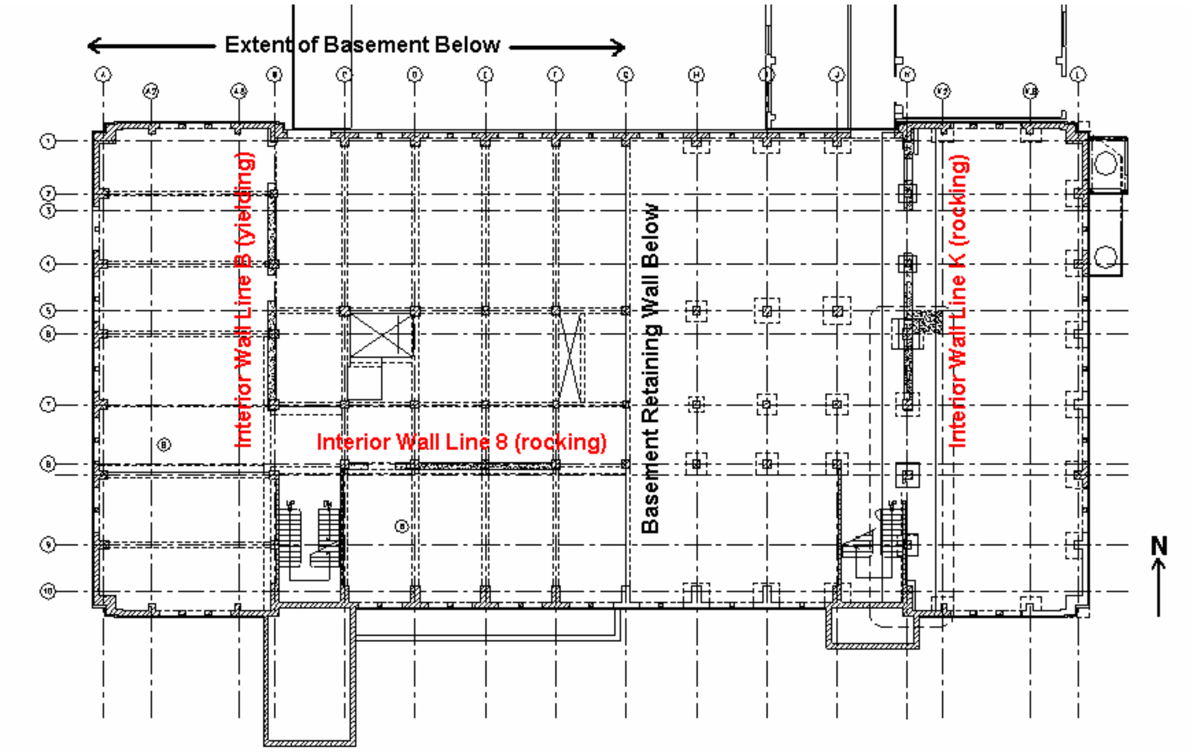

Figure 3: Le Conte Hall First Floor Plan

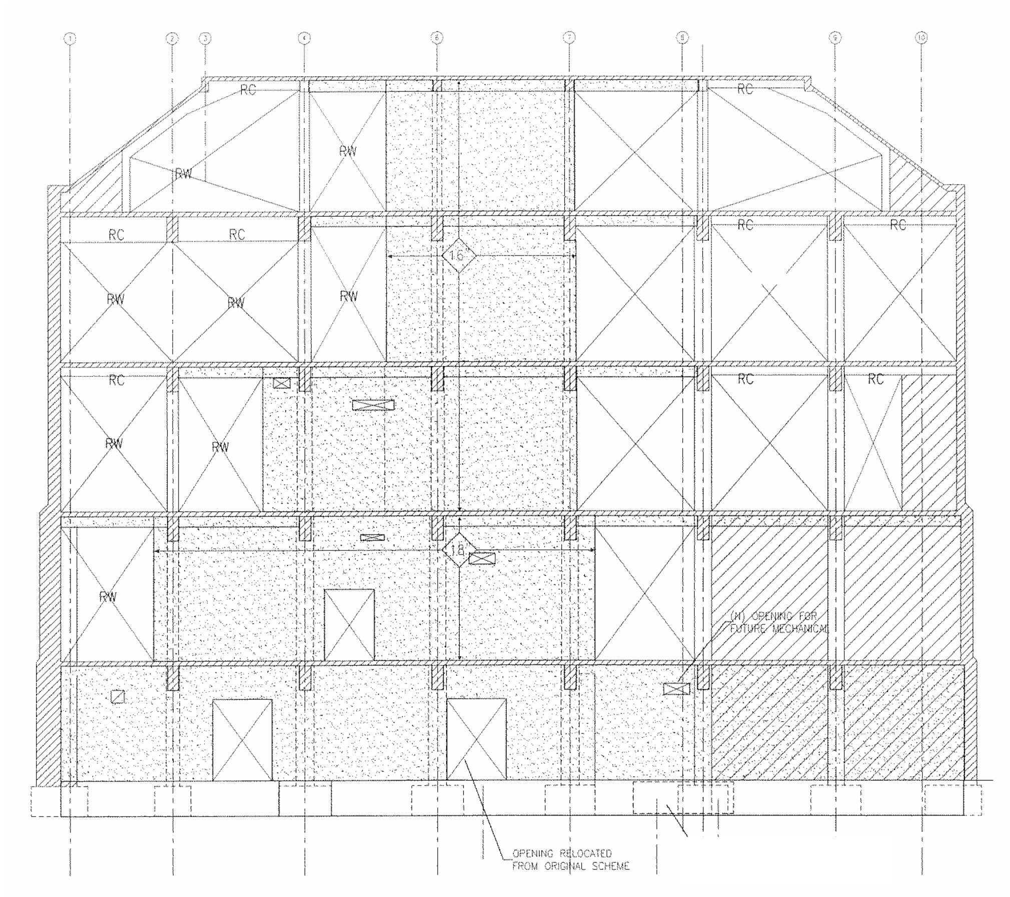

Figure 4: New Interior Shear Wall on Column Line B

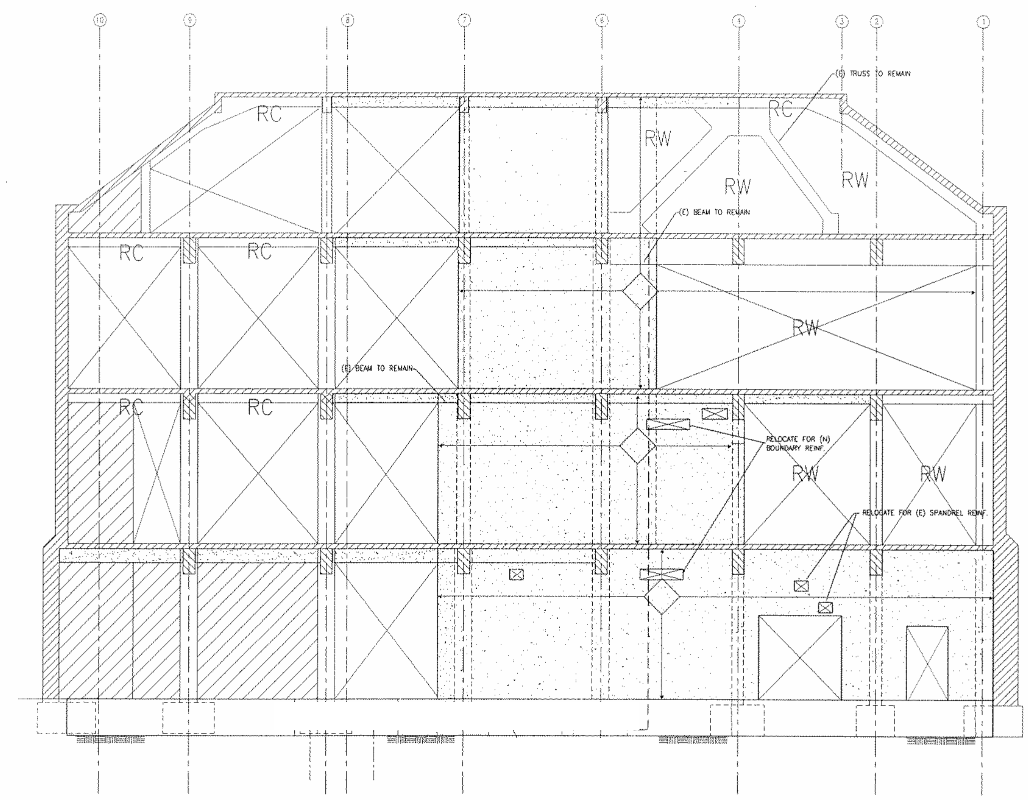

Figure 5: New Interior Shear Wall on Column Line K

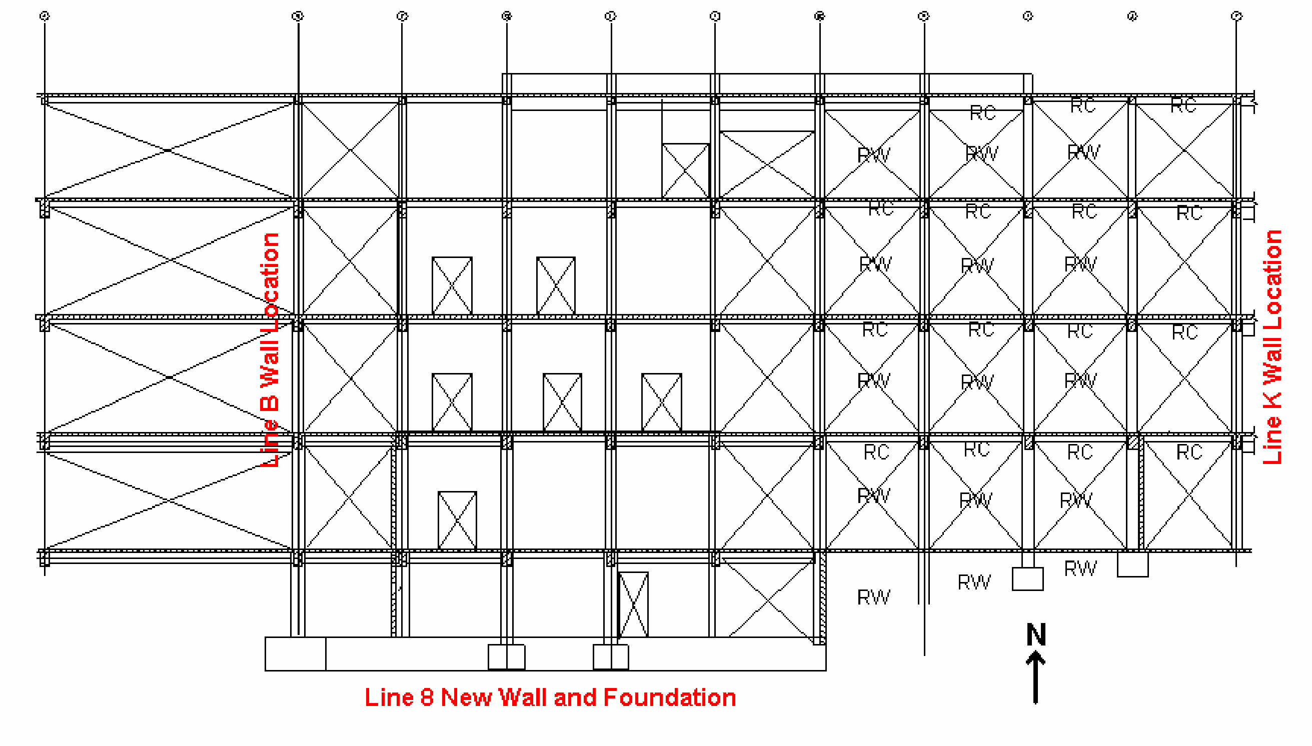

Figure 6: New Interior Shear Wall on Column Line 8

5. ANALYSIS APPROACH

Two and three-dimensional non-linear pushover analyses were used to validate the performance of the retrofit scheme. The SAP2000 computer program [2] was used to develop the models and perform the analyses.

The models incorporated non-linear flexural and shear hinges for the existing and new reinforced concrete components. The flexural hinge properties were developed using moment-curvature analysis and the deformation limits specified by FEMA 356 [4], as shown in Table 1. The shear hinge properties were developed using the provisions of FEMA 306 [5], which are based on approaches developed by Priestley et al. (1996) and Kowalsky et al. (1997). Most of the existing and new reinforced concrete components were found, or were designed, to be flexurally controlled. No pre-emptive shear failures are anticipated.

Non-linear soil springs were incorporated into the foundation modeling for both new and existing components. The foundation compression properties were developed by Geomatrix Consultants [6] and are summarized in Figure 7, and zero tensile capacity was assigned to permit uplift to occur as appropriate. Sensitivity studies were performed to assess the variation in target displacement with changes to the assumed soil properties and with vertical load.

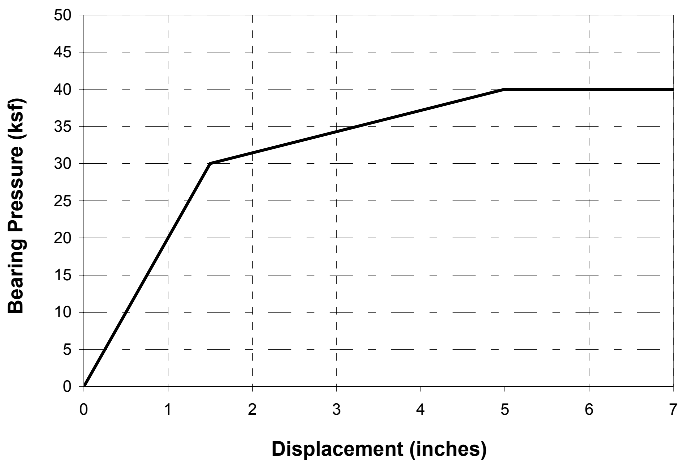

Figure 7: Soil Bearing Pressure vs. Vertical Displacement Relationship

In the three-dimensional analysis the existing exterior pier / spandrel walls were modeled in a simplified fashion to decrease the complexity of the computer analysis to a manageable level for both user and program. Essentially, each of the four existing exterior walls was represented in the three-dimensional model using one "stick" or "tree" that captured the overall stiffness and strength of the entire pier/spandrel system. An example of one of the four two-dimensional models is shown in Figure 13 and the three-dimensional model is shown in Figure 10.

The following analysis approach was used to determine the center of mass target displacements:

1. A two-dimensional pushover analysis of each of the four exterior pier/spandrel walls was performed using SAP2000. The life-safety and collapse prevention performance limits used for the existing piers and spandrels are listed in Table 1. The limits correspond to the FEMA 356 values for components with low axial load ($P < 0.1 \times A_g \times f'_c$) and low shear stress ($v < 3 \sqrt{f'_c}$). As permitted by FEMA 356 Section 3.4.3.2, the performance limits for secondary components were used since degradation was explicitly considered in the analysis.

Table 1: FEMA-356 Limits for Exterior Wall Components

Spandrel Flexural Hinges			Pier Flexural Hinges		
a=	0.020	Radians	a=	0.008	Radians
b=	0.035	Radians	b=	0.015	Radians
Life Safety Limit	0.020	Radians	Life Safety Limit	0.008	Radians
Collapse Prevention Limit	0.035	Radians	Collapse Prevention Limit	0.015	Radians

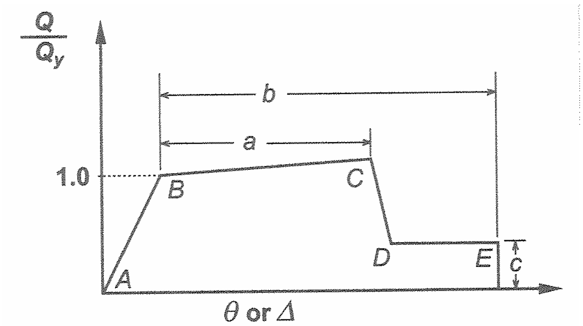

Figure 8: FEMA 356 Force – Deformation Relationship

2. A three dimensional model of the new walls, the existing interior stairwell walls and the interconnecting footings and grade beams was developed and a pushover curve for these components was generated in each primary direction (no torsion was considered).
3. The three pushover curves for each direction (two curves for the existing exterior walls and one for the interior new and existing walls) were combined to create the overall pushover curve for the entire building in each direction.
4. Target displacements were calculated using these curves, the seismic demand spectra in Figure 2, and the FEMA 356 target displacement procedure. The target displacements were computed at the roof level center-of-mass.

One of the primary concerns for the retrofit scheme was the torsional performance of the building. The new walls form a three-sided lateral system so the existing longitudinal walls are required provide resistance to torsion for transverse direction earthquake input as well as the bulk of the resistance to north-south earthquake input. To determine the maximum direct and torsional displacements for each exterior wall the following analysis approach was adopted:

1. For each exterior wall two-dimensional analysis, the pushover curve for each story, that is, the story shear vs. story deformation curve, was generated. This was then idealized as a bilinear system with degradation, as shown in Figure 9.
2. The three dimensional model, from Step 2 above (new interior shear walls, the existing interior shear walls, and the interconnecting grade beams) was modified to include a simplified “stick” or “tree” for each exterior wall. In each “tree”, non-linear shear hinges were added at each floor level with force-displacement properties assigned to

match the bi-linear curves (Figure 9) determined from the detailed two-dimensional model.

3. Three dimensional pushover analyses were performed in each of the four primary horizontal directions with 5% accidental mass eccentricity applied in the critical direction for the exterior wall under consideration. A total of eight different analysis cases were considered.

4. For transverse (east-west) direction earthquake loading, the existing longitudinal walls are the primary means of resisting torsion. These walls may experience some stiffness degradation due to earthquake loading in the longitudinal direction. The torsional analyses in the transverse direction were therefore performed with the two longitudinal walls pre-softened to account for 0.3 times the target displacement in the longitudinal direction, while the full ground motion was applied in the transverse direction.

5. The maximum displacement of each exterior wall was determined. Additional results extracted from three dimensional model for design purposes included the maximum flexural and shear demands on the new walls, the maximum uplift at the rocking walls on lines K and 8, and the maximum footing rotation demands.

6. The two-dimensional model of each exterior wall was then used to check the pier and spandrel deformations against the performance limits in Table 1, at the maximum exterior wall displacements determined from the previous step, for both the Level II and Level III earthquakes.

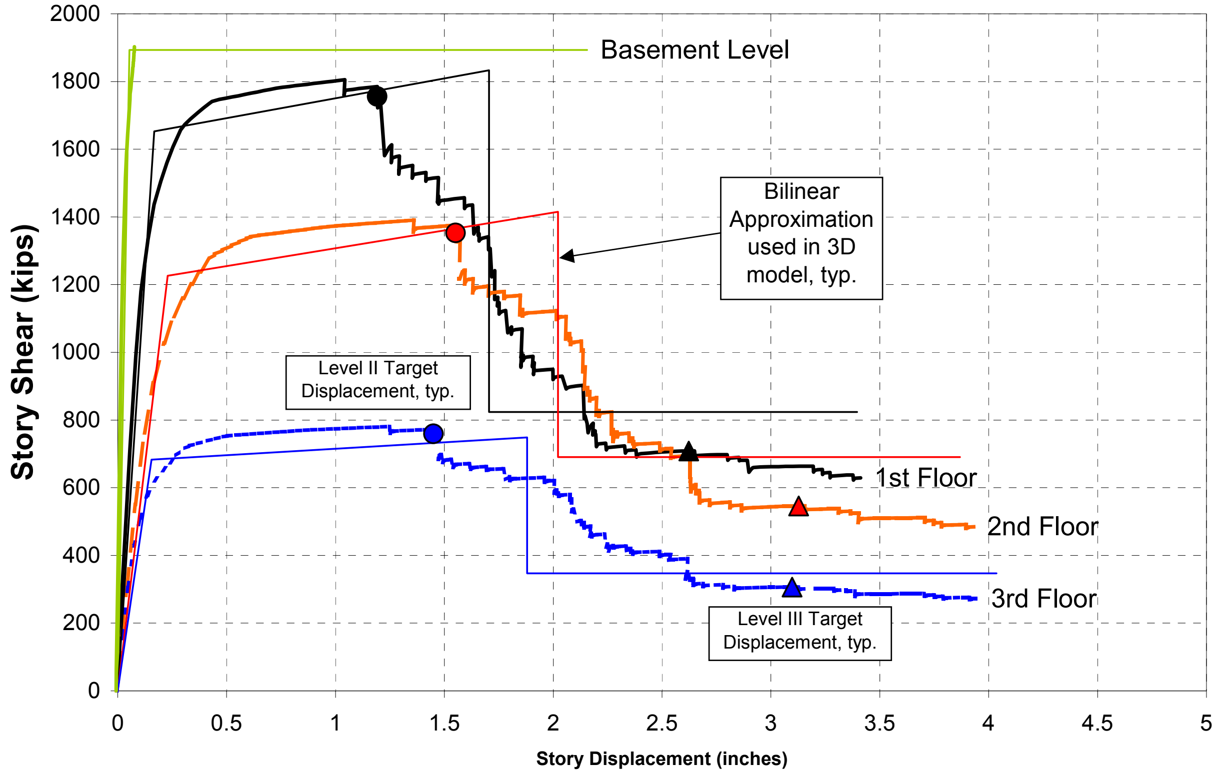

Figure 9: East Wall Story Shear – Story Displacement Pushover Curves

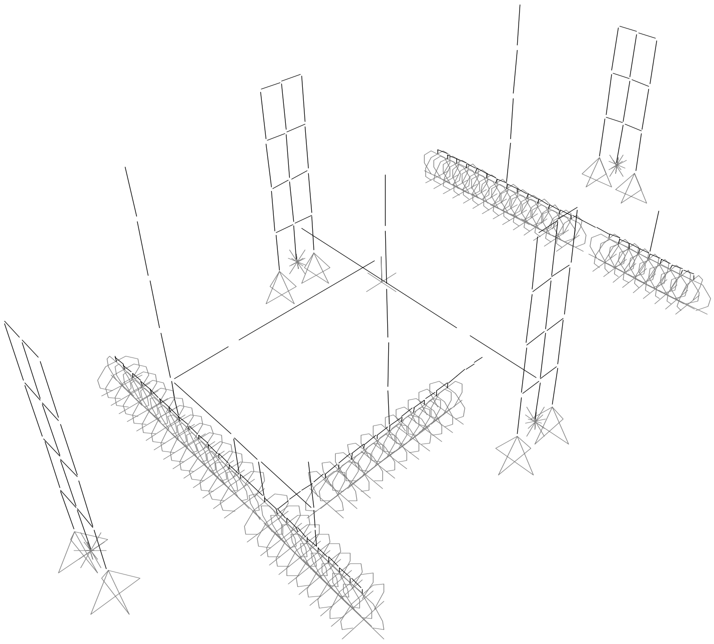

Figure 10: SAP2000 Three Dimensional Model with Simplified Exterior Wall Modeling (Looking northwest)

This analysis was required because a detailed three-dimensional model that included all the exterior wall components plus the interior new and existing walls would not run to completion. Regardless of the analysis solution strategy adopted, the maximum pushover displacement achieved was less than one quarter of the required target displacement. The primary reason for this limitation was that there were many degrading elements, some carrying relatively large forces, which lost a large portion of their load-carrying capacity at the same time. The need to incorporate non-linear springs for compression and uplift under the existing walls further complicated the analysis.

6. ANALYSIS RESULTS

8.1 Maximum Displacements

The pushover curves from the two-dimensional analyses in the transverse (east-to-west) and longitudinal (north-to-south) directions are shown in Figures 11 and 12 together with the target displacements for the Level II and Level III earthquakes. The figures show the relative contribution of the new and existing components to the overall pushover curve in each direction.

Figure 12 shows that for the transverse direction, the contribution of the existing north and south walls to the overall strength of the structure was relatively small, while in the longitudinal direction the situation was reversed. In the longitudinal direction this means that some degradation is visible in the overall pushover curve just after the Level II target displacement of 5.3 inches. This degradation amplified the Level III target displacement by approximately 25% via the C3 factor in the target displacement equation to approximately 11.0 inches. Torsional displacements for longitudinal direction earthquake loading were relatively small due to the high torsional stiffness provided by the new walls in the transverse direction.

In the transverse direction the contribution of the existing north and south walls to the overall strength of the structure was relatively small and no degradation was observed at the Level II or Level III target displacements of 5.0 inches and 8.1 inches respectively. Torsional displacements were much more significant in the transverse. The maximum north wall displacement at the roof level was 6.2 inches and 11.0 inches for Level II and Level III respectively, and the corresponding south wall displacements were 7.1 inches and 12.1 inches respectively.

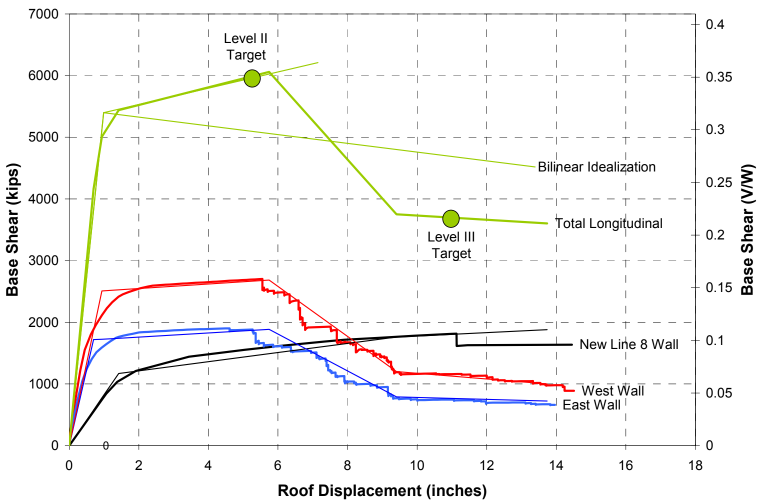

Figure 11: Longitudinal (North-South) Direction Pushover Curve

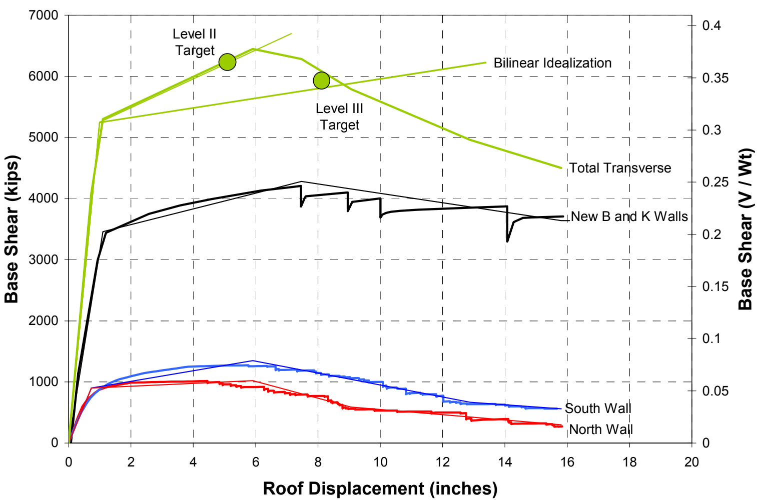

Figure 12: Transverse (East-West) Direction Pushover Curve

Flexural hinges are expected to form in the exterior piers at the bottom of the first story, the top of the third story, and at each end of the spandrels at other levels. The typical observed deformation pattern is shown in Figure 13. The existing pier and spandrel plastic rotation demands were checked against the performance limits in Table 1. The plastic rotation demand on the majority of piers and spandrels was found to be within the specified limits. Some spandrels adjacent to corner piers were found to very slightly exceed the permissible value (0.037 vs. 0.035 radians) due to concentrated rotation demands caused by rocking behavior of the corner L-shaped piers. This performance was considered acceptable by the design team, particularly since loss of vertical support for the slab was considered very unlikely.

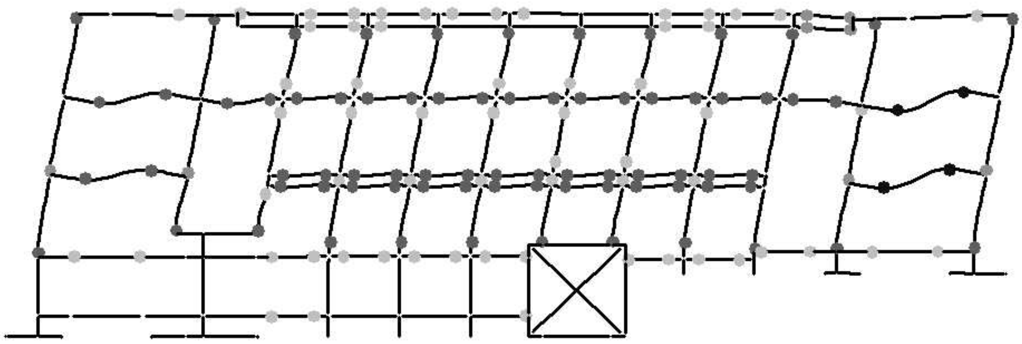

Figure 13: SAP2000 Two Dimensional Model at Level III Target Displacement

The plastic rotation demand at the first and third story piers hinges also exceeded the permissible FEMA 356 limit for both the Level II and Level III earthquakes. Of primary concern, the plastic hinge rotation for the Level III earthquake ranged from 0.017 to 0.022 (at a few locations). These components were examined in more detail to determine whether these demands could be accommodated within the overall global collapse prevention performance objective for the Level III earthquake.

8.2 Exterior Piers

The first story piers are of particular interest because of the higher gravity load demand and the increased potential for an overall story mechanism as a result of pier shear failure due to high flexural ductility demand. A typical section through one of these piers is shown in Figure 14. The presence of a spirally reinforced column at the core of the pier greatly improves the overall pier behavior. The flexural behavior of the overall pier and core section was investigated using moment-curvature analysis.

The variation in shear capacity of the overall pier section and the spiral core section with increasing flexural ductility demand was investigated using the provisions of FEMA 306 [5]. The presented methodology can be used to determine the shear capacity in the plastic hinge region for both low and high flexural ductility demands. The concrete and steel shear capacity for the overall pier section and the concrete core section were determined separately and were plotted against the applied shear demand determined from the pushover analysis. This curve is shown in Figure 15, which indicates that at no time in the analysis did the shear demand exceed the overall shear capacity of the section and therefore the pier section should therefore exhibit stable but degrading flexural hysteretic behavior. At the Level III earthquake it is expected that the outer edges of the section (the “ears” or “flanges”) will crush and loose confinement but the spirally confined core will continue to carry vertical and lateral loads.

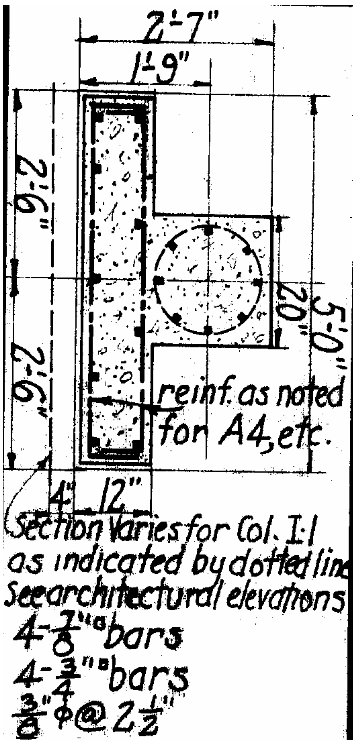

The possibility of a story shear mechanism developing at the 1st story is further reduced by the presence of additional components at this level that have shear capacity substantially in excess of their flexurally induced shear demand. These include the large existing piers at each corner of the building and the new wall on Line 8.

Since the first floor piers are critical to the seismic performance of the building it was appropriate to verify that the reinforcement shown on the structural drawings is in fact present in the building. The presence of longitudinal and spiral reinforcement was verified by NDT methods (Ferroscan and Radar).

Figure 14: Typical Pier Section at First Floor

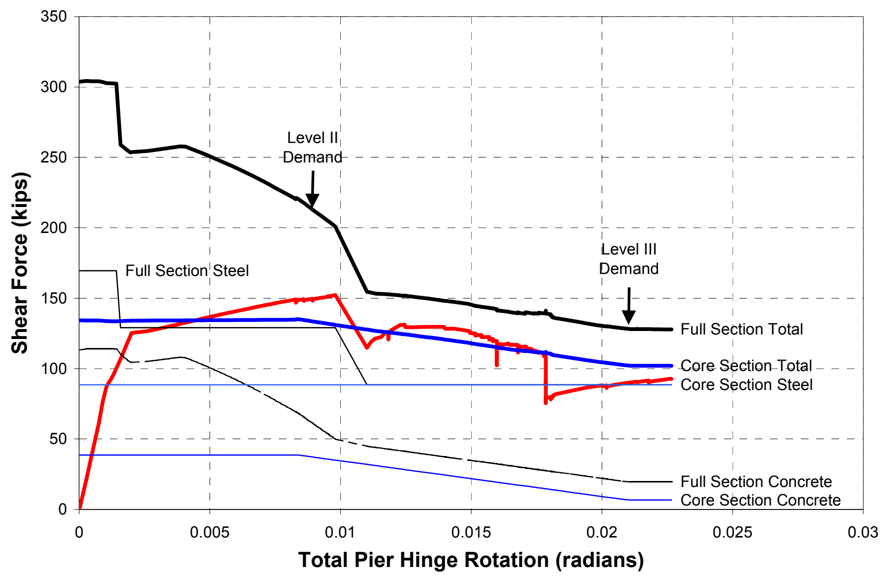

Figure 15: Pier Shear Demand and Shear Capacity vs. Total Pier Flexural Rotation Demand at 1st Floor

7. CONCLUDING REMARKS

The seismic strengthening scheme developed for the Le Conte Hall Seismic Corrections Project achieved the required objective of increasing the building's seismic performance rating from POOR to GOOD. The application of two and three dimensional non-linear pushover analysis allowed the scope of work to be substantially reduced from that originally envisaged with confidence that the required performance will be achieved in a major earthquake. The corresponding cost savings amounted to approximately 25% of the total structural cost of the project and significantly reduced the disruption to historic building finishes.

The presented retrofit scheme design and analysis illustrates some areas where performance based design procedures would benefit from additional development. These areas are summarized as follows:

1. Improvement in procedures to predict the target displacement of degrading systems and rocking systems. Data presented by Miranda et al. 2002 [8] indicate that the target displacements in the presented analysis may be significantly higher those that would result from non-linear time-history analysis.
2. A means to predict the target displacement for buildings with lateral resistance from multiple sources. In the case of Le Conte Hall, the lateral resistance comes from four sources; the degrading exterior pier / spandrel system, the degrading interior stairwell shear walls, and new interior rocking shear walls on lines K and 8, and the new yielding shear wall on line B.
3. Additional research on how many and what type of components may be permitted exceed the component level collapse prevention limits before global collapse will occur. A strict adherence to the component level limits appears to result in a conservative estimate of the collapse displacement capacity of the structure.

4. A more developed consensus definition for the global collapse prevention performance limit. Guidelines or commentary language to assist engineers in determining what constitutes collapse prevention and how and when engineering judgement should be applied.
5. Additional research on the behavior historic and irregular building components at collapse level deformations, such as the piers shown in Figure 14.

Preparation of final construction documents is presently in process and construction is scheduled to begin in July, 2003. The building is to be listed on the National Register of Historic Buildings.

9. KEYWORDS

Le Conte Hall, Pushover Analysis, Rocking, Torsion, FEMA 356, SAP2000, Concrete

10. REFERENCES

1. American Concrete Institute, *Building Code Requirements for Structural Concrete and Commentary*, ACI 318-95 and ACI 318R-95, 1995.
2. Computers and Structures, Inc., *SAP2000: Three Dimensional Static and Dynamic Finite Element Analysis and Design of Structures (version 7.45)*, Berkeley, CA. June 2001.
3. Degenkolb Engineers, Old Le Conte Hall, *Seismic Evaluation and Seismic Corrections*, May 1999.
4. Federal Emergency Management Agency, FEMA 356, *Prestandard and Commentary for the Seismic Rehabilitation of Buildings*, Washington D.C. November 2000.
5. Federal Emergency Management Agency, FEMA 306, *Evaluation of Earthquake Damaged Concrete and Masonry Buildings*, May 1999.
6. Geomatrix Consultants, *Geotechnical Study, Le Conte Hall Seismic Strengthening, University of California*, December 26, 2000.
7. Le Conte Hall Original Architectural, Structural, Mechanical and Electrical Drawings, John Galen Howard, February 13, 1922; Dwgs 1-10, 101-109, 201-203, 211-213, 221-223, 301-311, 401-402.
8. Miranda, E., and Akkar, S., Evaluation of Approximate Methods to Estimate Target Displacements in Nonlinear Static Procedures, *Proceedings 4th U.S.- Japan Workshop on Performance Based Seismic Design Methodology for Concrete Buildings*, Toba Japan, October 2002.
9. Paulay, T., and Priestley, M.J.N, *Seismic Design of Reinforced Concrete and Masonry Buildings*, John Wiley and Sons, New York, New York, 1992.
10. Planning, Design & Construction, *1997 Preliminary Seismic Evaluation*, University of California, Berkeley, Volumes 1 and 2, September 1997.
11. Rutherford & Chekene, *Old LeConte Hall, Preliminary Seismic Evaluation,* July 12, 1996.

Development of Real-time Residual Seismic Capacity Evaluation System

Koichi KUSUNOKI[1)] and Masaomi TESHIGAWARA[2)]

ABSTRACT

In order to reduce furthermore damage due to an aftershock and to reduce the number of refugee, a quick inspection on the damaged buildings must be carried out. However, the buildings have to be investigated one by one by engineers or researchers under the present situation. The judgment can vary according to the engineers' experiences and it takes long time to investigate all damaged buildings. This research aims to develop a new automatic and quick inspection system that has only few cheap accelerometers. This system makes it possible to indicate the safety level against an aftershock to inhabitants immediately.

1 INTRODUCTION

If a big earthquake occurs, many buildings are severely damaged due to the earthquake, and consequently it gives rise to many homeless. The damage level could increase due to an aftershock in some buildings. Thus enormous harm to the inhabitants in such buildings could occur. On the contrary, some people could get caught up in fear and would escape from even the buildings that have enough residual seismic capacity from the engineering point of view. Hence, the number of homeless can increase drastically. In order to reduce further damage due to an aftershock and to reduce the number of homeless, a quick inspection on the damaged buildings must be carried out soon after a main shock. However, under the present situation, the buildings have to be investigated one by one by engineers or researchers. For example, 5,068 engineers and 19 days were needed to investigate 46,000 buildings on a damaged area at the Kobe earthquake [JBDP, 1995]. Nineteen days were too long and yet the number of investigated buildings was not enough. Moreover, many buildings were judged as "Caution" level, which needs detailed investigation by engineers. "Caution" judgment is a gray zone and it could not take away anxieties from inhabitants. Furthermore, the current quick investigation system presents a dilemma since buildings should be investigated by visual observation of engineers. Thus, this judgment varies according to the engineers' experiences.

On the other hand, if it is possible to calculate the performance and demand curve [JBRP, 2000] from a measured acceleration of the basement and of each floor of a structure with cheap accelerometers, and further estimate the residual seismic capacity of a structure by comparing these curves, the problems mentioned above can be solved. To draw the

1Senior Researcher, Building Research Institute E-mail kusunoki@kenken.go.jp

2 Chief Research engineer, ditto

performance curve, the absolute response accelerations and relative response displacement on each floor are needed. A certain fixture is generally needed to measure the inter-story drift or the relative response displacement to the basement. This fixture can be obstructive for usage. On the contrary, it is easy to measure accelerations with accelerometers. If displacements can be derived from the accelerations with double integral, the performance curve of structures can be easily measured.

However, it is well-known that measured acceleration record can contain very small noise due to the non-linearity of the accelerometers and the noise in the measuring equipments [Iwan et al., 1985, Boore et al., 2001]. The noise level is ordinary very small, but the effect of the noise can be amplified very much if it is integrated twice [Iwan et Al., 1985]. Many researches were conducted on this topic in the past, but no algorithms that can integrate automatically acceleration record to displacement were proposed.

In this paper, a new real-time residual seismic capacity evaluation system was proposed. Furthermore, a new integral method to calculate the response displacement from the measured acceleration is proposed to develop the real-time residual seismic capacity evaluation system. Finally, the proposed integral method and the evaluation system were applied to the existing shaking table test results, and the validity of the method is confirmed.

2 CONFIGURATION OF THE SYSTEM AND OUTLINE OF THE EVALUATION

This system has basically two accelerometers and one judgment machine as shown in Fig. 1. The evaluation method is based on the performance design concept as shown in Fig. 2. The residual seismic capacity will be judged by comparing the measured performance curve of a structure and the measured demand curve.

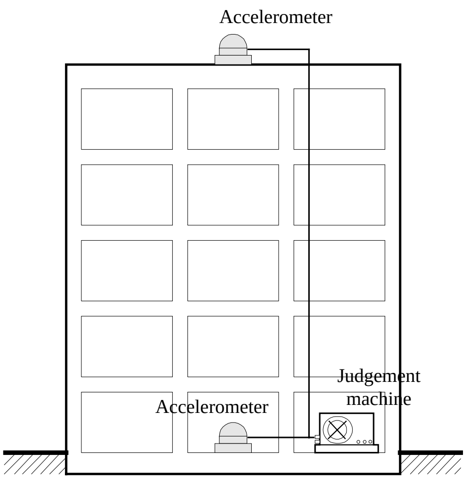

Fig. 1 Configuration of the system

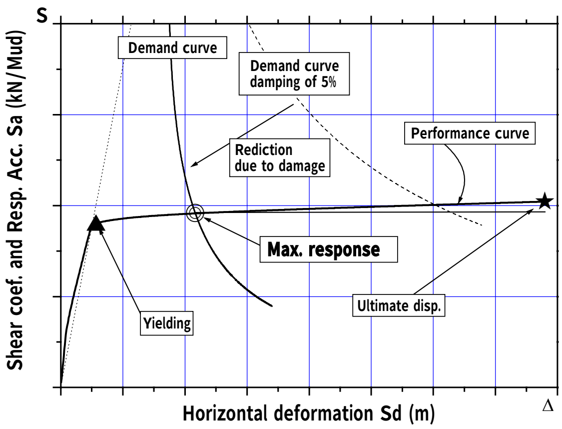

Fig. 2 Outline of the evaluation based on the Performance design concept

The performance curve is the relationship between the representative deformation D and the representative restoring force S, which shows the predominant response of a structure. The method to evaluate theses representative values is outlined below.

The calculated relative displacement vector to the basement $\{_M x\}$ from measured accelerations can be derived as Eq. 1 with the modal participation factor $_M\beta$, mode vector $\{_M u\}$, and the assumption that the $\{_M x\}$ is the unique vibration mode.

$$\{_M x\} = {}_M\beta \cdot \{_M u\} \cdot \Delta \qquad \text{Eq. 1}$$

The story shear (inertia force) of the first story $_M Q_B$ can be calculated using Eq. 2 with the measured absolute acceleration $\{_M \ddot{x} + \ddot{x}_0\}$ and mass m_i of each floor.

$$_M Q_B = \sum m_i \cdot \left(_M \ddot{x}_i + \ddot{x}_0\right) \qquad \text{Eq. 2}$$

The equation of motion of a multi-degree-of-freedom system can be abbreviated to a single-degree-of-freedom system as given in Eq. 3.

$$M \cdot \ddot{\Delta} + {}_M\tilde{C} \cdot \dot{\Delta} + {}_M\tilde{K} \cdot \Delta = -M \cdot \ddot{x}_0 \qquad \text{Eq. 3}$$

where, M is the total mass of a structure, $_M\tilde{C}$ is the equivalent damping, $_M\tilde{K}$ is the equivalent stiffness, and $\ddot{x}_0$ is the ground acceleration

The $_M Q_B$ can be calculated with Eq. 4. If the first mode is predominant enough, the calculated angular frequency, $_M\omega = \sqrt{\frac{_M\tilde{K}}{M}}$, can be the natural angular frequency of the first mode.

$$S = {}_M Q_B = M \cdot \ddot{\Delta} \qquad \text{Eq. 4}$$

Eq. 5 can be derived from Eq. 1 by deviding both sides by Δ. The inertia force acting on each floor $_M P_i$ can be derived as Eq. 6 by using Eq. 1 and Eq. 5.

$$_M\beta \cdot {}_M u_i = \frac{_M x_i}{\Delta} \qquad \text{Eq. 5}$$

$$_M P_i = m_i \cdot {}_M\beta \cdot {}_M u_i \cdot \ddot{\Delta} = m_i \cdot \ddot{\Delta} \cdot \frac{_M x_i}{\Delta} \qquad \text{Eq. 6}$$

The total mass M can also be derived from Eq. 4 and Eq. 6 since the total mass M is the sum of each floor mass, i.e.;

$$M = \frac{{}_M Q_B}{\ddot{\Delta}} = \frac{\sum m_i \cdot \ddot{\Delta} \cdot \frac{{}_M x_i}{\Delta}}{\ddot{\Delta}} = \frac{\sum m_i \cdot {}_M x_i}{\Delta} = \sum m_i$$

Therefore, the representative displacement Δ can be derived as Eq. 7.

$$\Delta = \frac{\sum m_i \cdot {}_M x_i}{\sum m_i} \qquad \text{Eq. 7}$$

The representative acceleration, $\ddot{\Delta}$ is applied to the representative restoring force, S ($S = {}_M Q_S / \sum m_i = \ddot{\Delta}$). If a system is elastic, the representative displacement, Δ and the representative acceleration, $\ddot{\Delta}$ can be calculated with Eq. 8, i.e.;

$$\ddot{\Delta}^2 + 2 \cdot {}_M h \cdot {}_M \omega \cdot \dot{\Delta} + {}_M \omega^2 \cdot \Delta = -\ddot{x}_0 \qquad \text{Eq. 8}$$

where, ${}_M h$ is the damping coefficient, and ${}_M \omega$ is the angular frequency

As a result, the maximum representative displacement Δ_{max} and the absolute acceleration $(\ddot{\Delta} + \ddot{x}_0)_{max}$ correspond to the value from the response displacement and acceleration spectrum with a damping coefficient of ${}_M h$.

On the other hand, the demand curve is the relationship between the response acceleration (Sa) and displacement (Sd) spectrum. The intersection point of the demand and performance curve shows the maximum elastic response. However, the damage of a structure can dissipate some amount of an input energy, thus the damping effect can be increased. Therefore, the demand curve can be reduced according to the damage (Fig. 2). The intersection point of the reduced demand and performance curves shows the maximum inelastic response.

Additionally, the following three challenging assumptions were applied for the judgment of the residual seismic capacity. These assumptions need further studies.

1. The mechanism of an aftershock is the same as the main shock, and the aftershock is always smaller than the main shock

With this assumption, the demand curve of the aftershock corresponds to the main shock.

2. The damping coefficient for the demand curve of an aftershock is 5%

In fact, if further damage occurred in a structure during an aftershock, an additional damping can be achieved, then the demand curve will be reduced. However, it is difficult now to estimate accurately the damping effect due to the damage during an aftershock. Therefore, the damping effect due to inelastic behavior during an aftershock is neglected and 5% viscous damping is taken into account for the judgment on the safe side. The residual seismic capacity can be calculated with the comparison of the demand curve with 5% damping and the performance curve. If the ratio of the Sa(=Sa_p) at the ultimate displacement on the performance curve to the Sa(=Sa_d) on the demand curve is greater than 1.0, the structure will be judged as SAFE, and if it is less than 1.0, it will be judged as UNSAFE.

3. The restoring force and the vibration mode will be constant after the maximum response is reached and less than the ultimate.

If the maximum response is less than the ultimate displacement, the performance curve to the ultimate displacement must be extrapolated. The restoring force and the vibration mode are assumed as constant after the maximum response reached to the ultimate displacement.

4. How to judge a structure as elastic

If a structure is elastic during a main shock, the performance curve calculated with the assumption (3) can be much underestimated since the restoring force at the ultimate displacement can be less than the yielding strength. Therefore, it must be judged separately if a structure is elastic. The elastic-inelastic judgment method is shown in Fig. 3. Firstly, the approximated stiffness of the envelope curve of the performance curve is calculated. Secondly, the error between the envelope curve and the approximated line, $\Delta Sd_{(i)}$, is calculated. If the ratio of the maximum value of, $\Delta Sd_{(i)}$, to the maximum response, Sd_{max}, is less than a tolerance, it is judged as elastic. In this study, a 5% tolerance is applied.

The judgment flowchart is shown in Fig. 4. The responses of a building and an input earthquake motion are measured by accelerometers, and the residual seismic capacity, i.e. how large the aftershock can be sustained by the building, is calculated from these measured accelerations. The safety level against an aftershock can be indicated just soon after a main shock. This System has a computer application, which can calculate the following items;

a) Integrate the measured accelerations twice to calculate the response displacements.
b) Calculate the base-shear coefficient and the representative displacement of the building with an assumed mode shape. (items 7 & 8 in Fig. 4)
c) Draw the performance curve of the structure. (item 9 in Fig. 4)
d) Draw the envelope curve of the performance curve. (item 10 in Fig. 4)
e) Calculate the response spectrum of the measured acceleration on the basement, and calculate the demand curve. (14 in Fig. 4)
f) Evaluate the residual seismic capacity of the building by means of the performance and demand curves.

Items 3, 6, and 11 in Fig. 4 must be defined prior to making a judgment. The item 3 (vibration mode shape) is to calculate the response accelerations on the floors where there are no accelerometers. For example, a linear or a constant distribution shape between measured floors can be applied. The item 6 (mass ratio) can be calculated from floor area ratio between each floor. At the moment, item 11 (ultimate displacement) can be defined from the corresponding adopted building code. However, in the future this can be carried out by placing a health-monitoring system.

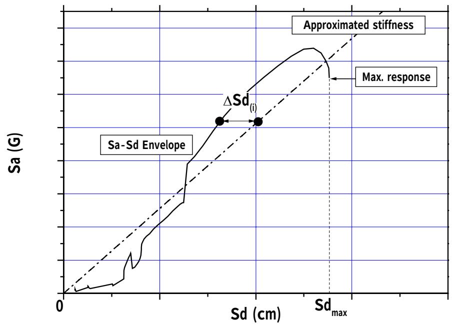

Fig. 3 Elastic-inelastic judgment

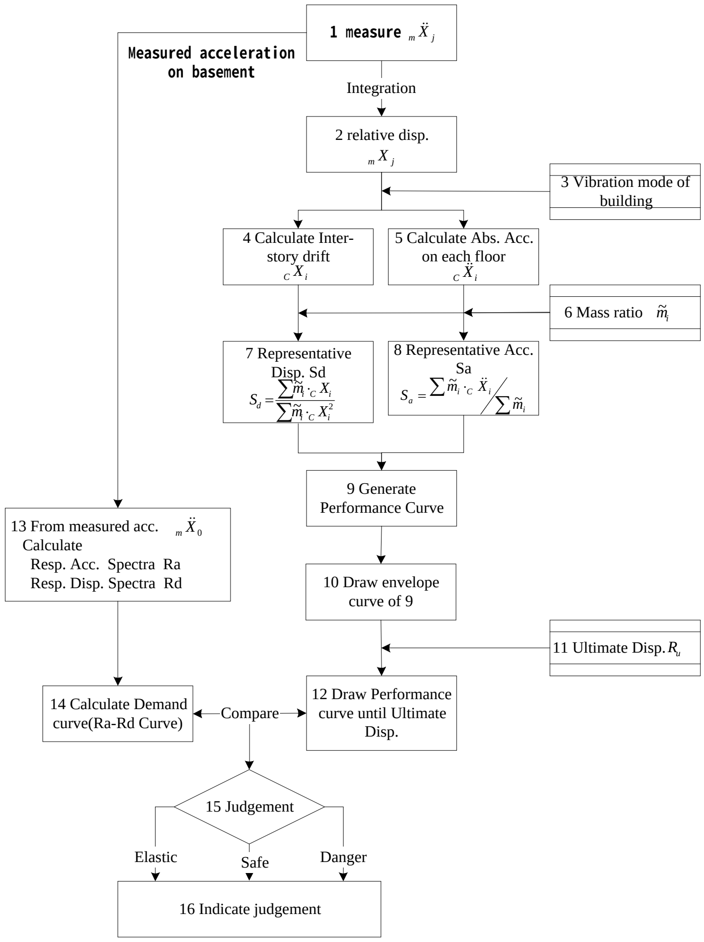

Fig. 4 Judgment flow chart

3 INTEGRATION METHOD TO CALCULATE DISPLACEMENT FROM ACCELERATION

In this proposed evaluation system, the response displacement is derived from the measured acceleration with double integral technique. If a displacement is calculated with the trapezoidal integral technique, it can diverge easily. Fig. 5 shows a measured acceleration and its displacement calculated with the trapezoidal integral technique. It can be seen that the calculated displacement diverged due to errors in the measured acceleration itself.

There are two ways to integrate acceleration, integration in frequency-domain and in time-domain. The Iwan's method was applied to the system by integrating in time-domain. The reason of the noise in the measured acceleration is supposed due to the non-linearity of accelerometers.

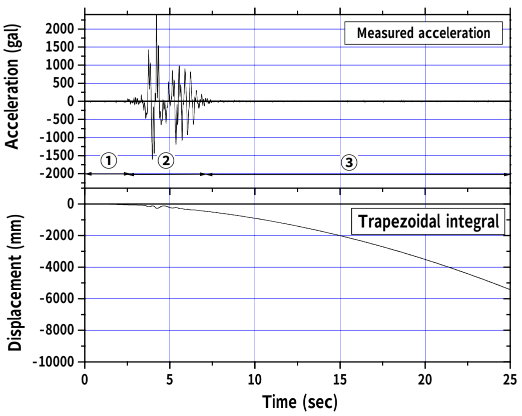

Fig. 5 Displacement calculated with the trapezoidal integral technique

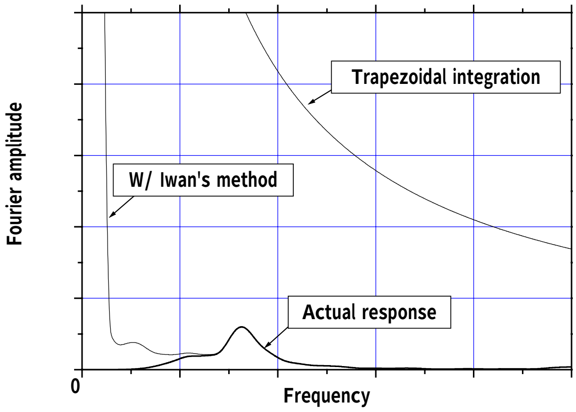

Fig. 6 Schematic diagram of Fourier spectra of velocities

The Iwan's method assumes that the errors that occurred during a principal shock are constant. However, since the error can vary during a principal shock, it is possible that relatively a long period error component cannot be removed by the Iwan's method. For example, the Fourier spectrum of actual response velocity integrated by the trapezoidal method can be hidden by the errors. On the other hand, a peak of Fourier spectrum of actual response at its natural frequency can be found if the Iwan's method is applied to remove errors from the measured acceleration. But if the Iwan's method does not remove errors successfully, error components can be found in low frequency domain. Thus, the band-pass filter is applied to remove the low frequency error that could not be removed by the Iwan's method in the proposed integral method. It is possible to find out the boundary between the error components and the actual response as shown in Fig. 6, because, a building structure has its predominant frequencies. Therefore, the proposed method has to be used carefully to integrate a measured ground acceleration since it has many random predominant frequencies.
The outline of Iwan's method and the proposed method are described below.

3.1 Iwan's method

An acceleration record is divided into three domains by the Iwan's method. These are as follows;

1. From the start to the time when the acceleration exceed Ao (the domain where the non-linearity of an accelerometer is not effective)
2. Between 1 and 2 (a principal shock domain)
3. After a principal shock (the maximum acceleration is less than A1)

In this paper, value of Ao of 10 gal and A1 of 50 gal were applied as in Iwan's research [Iwan et Al., 1985].

The noise level that occurred during a principal shock is assumed to be constant. The noise level before and after a principal shock are also assumed to be constant but of different values. The noise level before a principal shock can be calculated as the average of the measured acceleration record until the principal shock starts. At first, the calculated noise level before the principal shock is subtracted from the whole measured acceleration record. Then the adjusted acceleration record is integrated to calculate time history of velocity (Fig. 7). The velocity baseline shifts after a principal shock, is calculated with the linearization technique so that the velocity at long after principal shock can be zero. During the principal shock, the velocity baseline shift can be calculated by continuing at the boundary between and after the principal shock domain.

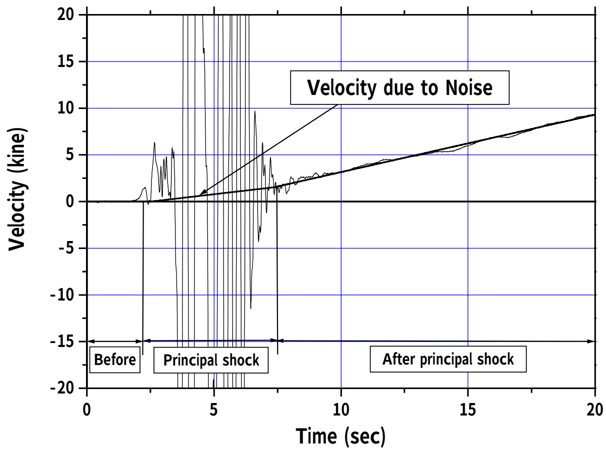

Fig. 7 Iwan's integral method (velocity)

3.2 Band-pass filter

The measured acceleration from the shaking table test of the 3-story steel structure [Morita et al., 2002], and the integrated displacement without using the Iwan's method are shown in Fig. 8. The Iwan's velocity baseline shift mentioned above is shown in Fig. 9, and its acceleration baseline shift is shown in Fig. 10. It is obvious from Fig. 9 that the calculated velocity baseline shift is not appropriate. The time-history of the adjusted velocity is elbowed during the principal shock, and the calculated displacement from the elbowed velocity can include much error. It can be the reason that several strong pulses are observed during the principal shock of Fig. 8, and the baseline shift could occur at each pulse because of the non-linearity of the accelerometers. As a result, the baseline shift during the principal shock could not be represented by the constant acceleration.

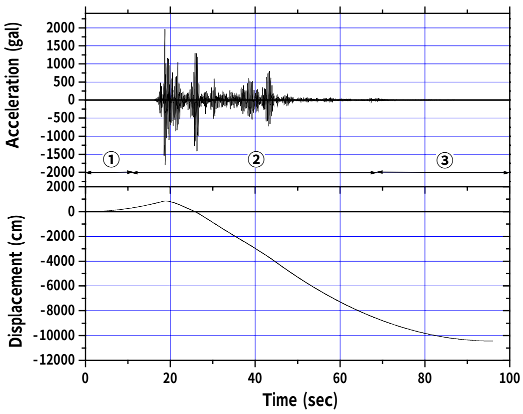

Fig. 8 Measured acceleration and the integrated displacement

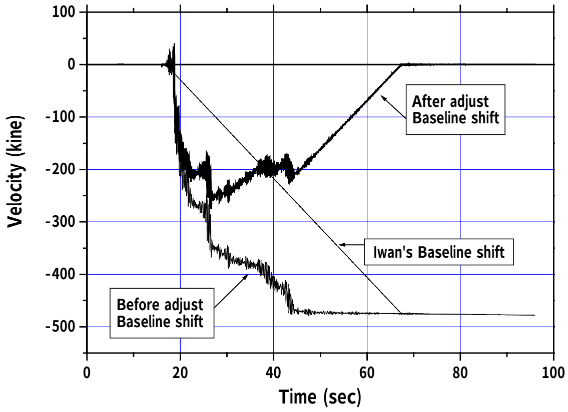

Fig. 9 Velocity without initial acceleration baseline shift and velocity baseline shift

Fig. 11 shows the Fourier amplitude of the integrated displacement from the time history of the elbowed velocity shown in Fig. 9. It can be observed that it contains much low-frequency (long period) components because of the elbowed shaped velocity. In order to remove the error components in frequency-domain, the proper lower and upper bound frequencies ω_L and ω_H must be found automatically. The proposed method to find out ω_L and ω_H is described below.

1) The power spectrum of the adjusted velocity with the Iwan's method is smoothed with the Parzen's Spectral Window [M. Osaki, 1994] (Fig. 12).

2) The frequency ${}_{min}\omega_i$ when the Fourier amplitude is a local minimum is selected. Sometimes more than one ${}_{min}\omega_i$ can be found. Three values of, ${}_{min}\omega_i$, were shown in Fig. 12 as an example. Then, the frequencies ${}_{max}\omega_i$ when the Fourier amplitude is a local maximum between ${}_{min}\omega_i$ and ${}_{min}\omega_{i+1}$, and the difference of the Fourier amplitudes, h_i, at ${}_{min}\omega_i$ and ${}_{max}\omega_i$ can be calculated. The ${}_{min}\omega_i$ of which h_i is a maximum is applied to the ω_L. Since h_2 was maximum in Fig. 12, ω_L was calculated as 1.8066 Hz. If the Fourier amplitude at the first natural frequency is greater than the Fourier amplitude for the value ω_L (F_2 in Fig. 12), an appropriate ω_L can be found. If it is not greater, a higher degree function must be applied to calculate the baseline shift during a principal shock. However, it was not needed in this study. If a measured acceleration contains no error, then ω_L is taken as 0 Hz since the power spectrum shows monotonous increasing function from 0 Hz to the first natural frequency.

3) The upper bound frequency ω_H was defined as 25 Hz since the frequency characteristic of the measuring equipment (frequency bandwidth able to be measured) was from a DC up to 30Hz.

4) The Butterworth filter, which is a kind of a band-pass filter, with its parameter of 4 [Boore, et al., 2001] is applied to Fourier spectrum of the calculated velocity with the Iwan's method from ω_L to ω_H. The Fourier spectra with and without the Butterworth filter are shown in Fig. 13.

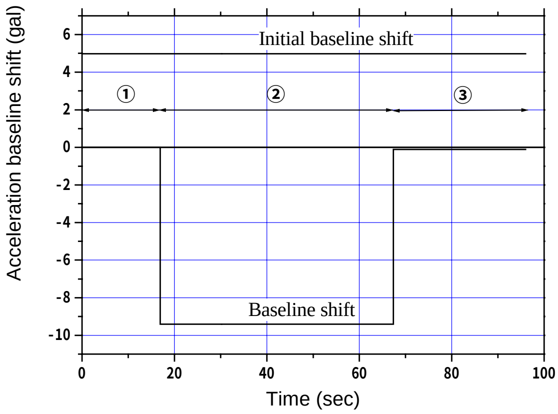

Fig. 10 Calculated baseline shift

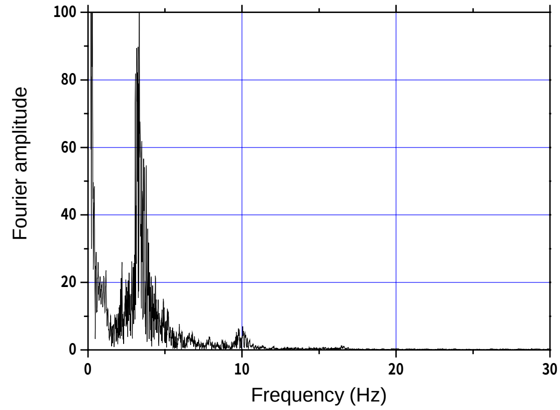

Fig. 11 Fourier amplitude of the integrated displacement (Iwan's method)

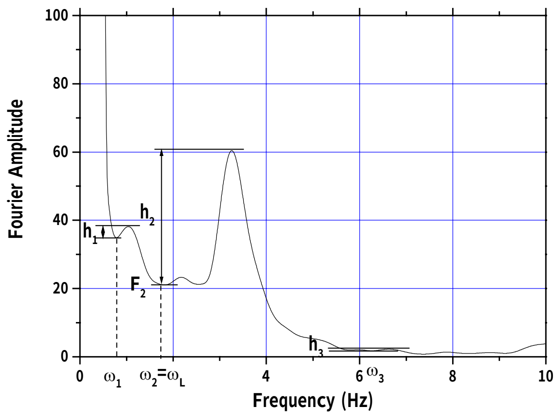

Fig. 12 Identification of the lower-bound frequency, ω_L

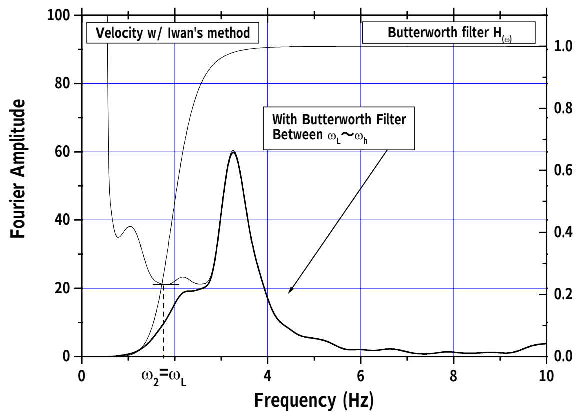

Fig. 13 Comparison of Fourier spectra with and without errors

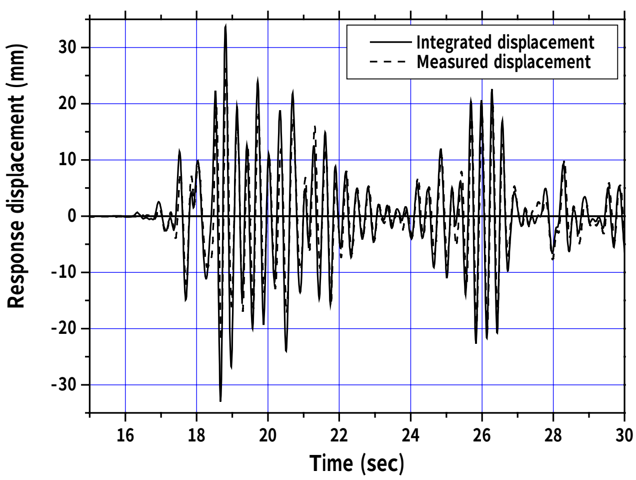

Fig. 14 Integrated displacement with band-pass filter and measured displacement

5) The displacement can be calculated from the velocity, which is calculated as the inverse Fourier transform of the Butterworth filtered velocity. The calculated displacement of the measured acceleration shown in Fig. 8, and the measured displacement during the shaking table test are shown in Fig. 14. It can be observed that the calculated displacement agrees well with the measured one.

4 APPLICABILITY WITH THE SHAKING TABLE TEST RESULT

The evaluation system and the integral method were applied to the shaking table test results carried out by Dr. Kumasawa [KUMASAWA et al., 2001] in order to confirm their validities, and the integrated displacements with the proposed method and the performance curve calculated with the integrated displacements were compared with the test results.

4.1 Outline of the shaking table test

The structure was scaled down by 1/2. Rigid slabs made of reinforced concrete provided the inertia forces on the shaking table. The mass of each floor was 76.9kN for the first floor and 78.0kN for the second floor. The varying factor of this experimental test was eccentricity. Accordingly, two of the four columns were located closer to the center of the slab than the others to provide mass eccentricity as shown in Fig. 15. The test results of the specimen without eccentricity was studied in this paper.

H-Shaped steel was used for the columns ($H-125\times125\times6.5\times9$ for the first floor and $H-100\times10\times6\times8$ for the second floor). The length of the column between top and bottom base plates was 1,500mm. Table 1 shows the strength of columns, story shear and story shear coefficients. Story shear coefficient for the first story is 1.43 and 1.85 for the second story. The natural period of the structure was 0.26 sec.

Table 1 Strength of the tested structure

	Yielding moment (kN*m)	Story shear at yielding (kN)
First story	41.4/14.3 [2.9]	220.8/76.3 (1.43)
Second story	26.6/9.3 [2.9]	141.9/49.5 (1.85)

Left-side value is for X Direction, right-side value for Y Direction
[] the ratio of yielding moment on X Direction to Y Direction
() Story Shear Coefficient

North-South component of JMA (Japan Meteorological agency) KOBE recorded at the Hyogo-Ken-Nambu earthquake in 1995 was used as the input motion. As mentioned above, the time axis was scaled down by 1/2. The input wave and its response acceleration spectrum are shown in Fig. 16. Five different PGAs of 200, 450, 900, 1640 and 2400 gal were input in order of level. PGAs in real size are 100, 225, 400, 820 and 1200 gal because of scale factors. The result with 2400 gal input was used in this paper.

The locations of sensors for measuring the accelerations and displacements were also shown in Fig. 15. The displacements of each floor and of the basement were measured from the outside of the shaking table. The response accelerations on each floor and of the table were measured with the accelerometers. The accelerometer had the rated flow of 5V and the measurable frequency characteristic of the DC to 100Hz. The time increment for measurement was 0.005 sec.

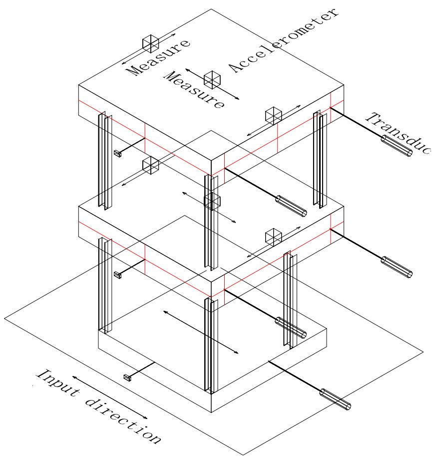

Fig. 15 Setup and measuring equipment

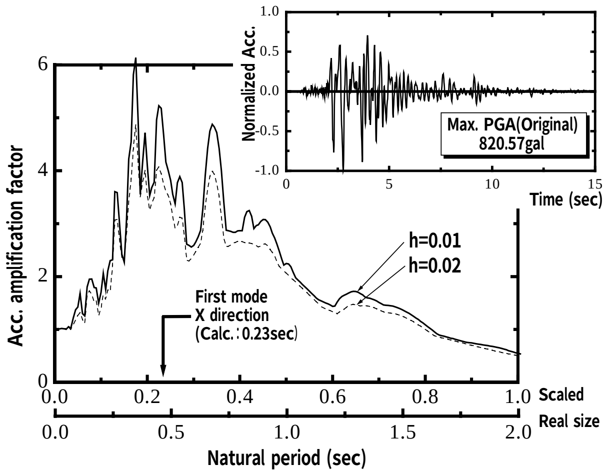

Fig. 16 Input motion

4.2 Residual seismic capacity evaluation

The residual seismic capacity evaluation of the proposed method was carried out with the shaking table test results. The measured acceleration of the basement, 2nd floor, and roof floor were used. The ultimate deformation angle of each floor was assumed as 1/50. The ultimate displacement was calculated as 31.4mm, since the height of each column was 1,570mm.

The comparison of measured and integrated displacements of each floor is shown in Fig. 17 to Fig. 19. It can be said from these figures that the integrated displacements on the 2nd and roof floor agreed very well with the measured displacements. Moreover, residual displacements calculated with the proposed integral method agreed well with measured residual ones. On the other hand, the response displacement of the basement after 6 seconds did not agree well with the measured displacement. While the measured residual displacement was about 20mm, the integrated residual displacement was almost zero. However, the difference of the two residual displacements can have no effect on the evaluation result, since the latter is carried out with the envelope of the performance curve.

The envelope of each performance curve calculated with the integrated and measured displacements is shown in Fig. 20. The envelope curve can be identified by selecting the Sd maxima steps of the performance curve. The envelope of the performance curve calculated with the integrated displacements agreed very well with the measured envelope curve.

Furthermore, the demand curve with the damping coefficient of 5% was superimposed on Fig. 20. Since the ultimate performance was less than the required demand capacity, this structure was judged as UNSAFE. That is, the safety ratio, which can be defined as the ratio of the representative restoring force (Sap) to that of the demand curve (Sad) for the same equivalent natural period, was 0.32. The safety ratio of 0.32 means that this structure can resist an aftershock of which PGA is 2400gal×0.32=768gal. Since the inter-story drift in the 2nd story at 4.2 sec was greater than the assumed ultimate displacement, therefore, the UNSAFE judgement can be reasonable.

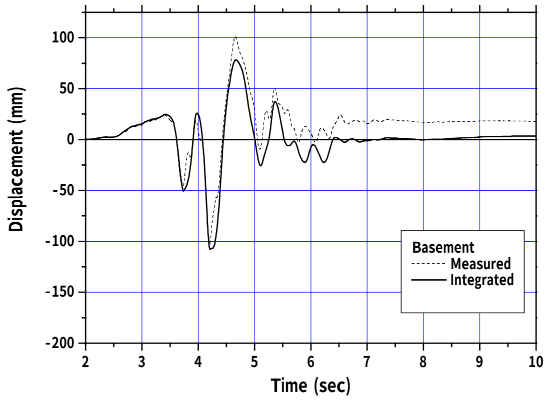

Fig. 17 Comparison of the response displacements (Basement)

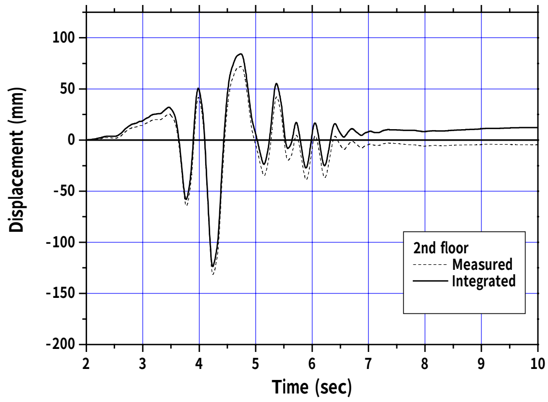

Fig. 18 Comparison of the response displacements (2nd floor)

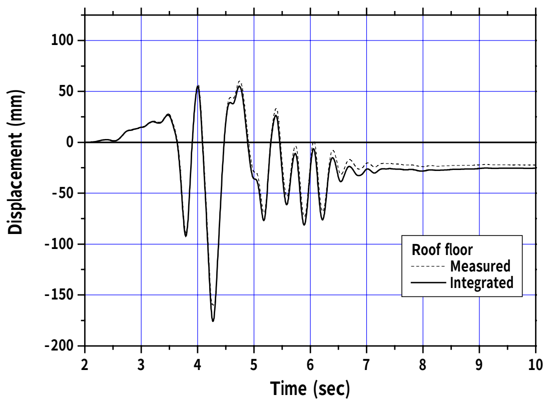

Fig. 19 Comparison of the response displacements (Roof floor)

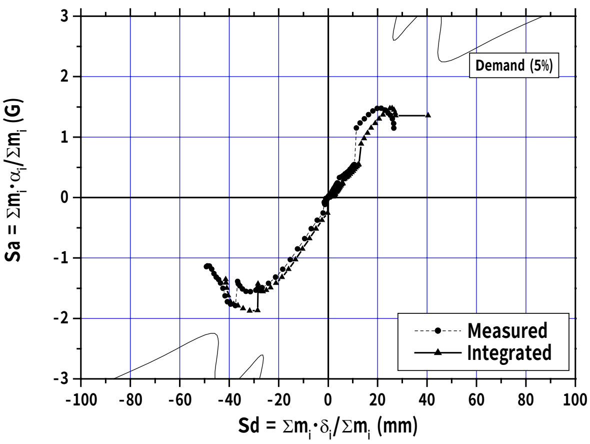

Fig. 20 Envelopes of the performance curves and the demand curve

5 CONCLUDING REMARKS

In order to develop the real-time residual seismic capacity evaluation system for improving the safety against an aftershock, the problem and the solution of the integral method, and the evaluation results with existing shaking table results, were discussed. Results obtained from the investigation can be summarized as follows;

1. The new residual seismic capacity evaluation method is proposed.
2. The Iwan's integral method cannot remove errors sufficiently for some acceleration record. However, The band-pass filter can remove the errors, which cannot be removed with the Iwan's method.
3. The new integral method and its algorithm for obtaining the lowermost frequency of the band-pass filter are proposed.
4. Since the proposed integral method applies to the characteristic of the structural vibration in which the predominant frequencies can be found with ease, more attention must be taken in order to use the proposed method to integrate a ground acceleration.
5. The integrated displacements from the measured acceleration at the shaking table test agree very well with the measured displacements. However, the residual displacement of the shaking table does not agree well with measured displacement.
6. The envelope of the performance curve calculated with the integrated displacement agrees very well with the measured envelope curve.
7. The validity of the proposed evaluation system was demonstrated with existing shaking table test results.

6 REFERENCES

Building Center of Japan (BCJ), Report on the reconnaissance committee on the building damages due to the Hanshin-Awaji Great Earthquake Disaster, 1995 – Summerization –, 1996.3 (in Japanese)

David M. Boore, Christopher D. Stephens, and William B. Joyner：Comments on baseline correction of digital strong-motion data: Examples from the 1999 Hector Mine, California, earthquake, BSSA, Vol. 1.3, 2001.12

Fumitoshi KUMASAWA et al., Experimental study on the dynamic response of steel frame structure with eccentricities, Summaries of technical papers of annual meeting, Architectural Institute of Japan, pp.829-832, 2001, 9

Iwan, W. D., et al.：Some Observations on Strong-motion Earthquake Measurement using a Digital Accelerograph, Bulletin of the Seismological Society of America, Vol. 75, pp. 1255-1246, 1985.10

Japan Building Disaster Prevention Association (JBDP), Kenchiku-Bosai July, 1995.7 (in Japanese)

K. Morita, Outline of damage detection test using large scale test frame, The earthquake engineering symposium, 2002 (now submitting)

M. Fumino, Residual seismic capacity evaluation from observed damages in R/C column, Proceedings of the Japan Concrete Institute, Vol. 23, No. 3, pp.1447-1452, 2000 (in Japanese)

M. Osaki, Revised manual for the spectral analysis for eathquake, Kashima-Syuppankai, 1994 (in Japanese)

SESSION B-2: COLUMN TESTS

Chaired by

♦ Mark Sinclair and Minehiro Nishiyama ♦

TEST AND ANALYSIS OF FULL-SCALE HIGH-STRENGTH CONCRETE COLUMNS

Yan Xiao[1]; Henry W. Yun [2]

ABSTRACT

Six full-scale high-strength concrete columns with compressive strength of above 63MPa were tested under cyclic lateral force and a constant axial load equal to 20% to 34% of the column axial load capacity. The 510 mm by 510 mm square columns were reinforced with 4 No. 29 and 4 No. 36 bars constituting a longitudinal steel ratio of 2.6% of the column gross sectional area. Main experimental parameters were the transverse reinforcement detail and the axial load level. This paper discusses the main results from the testing and analyses based on simple column models and FEM.

1. INTRODUCTION

Although an increasing amount of research (Hester, 1990; Li and Park 1994; Malhotra 1994; "Joint" 1997; Xiao and Martirossyan 1998; Bayrak and Sheikh 1998) on the seismic behavior of HSC columns is becoming available, tests on full-scale HSC columns are relatively limited. Full-scale testing of HSC columns requires large capacity loading facilities. In particular, the force required to simulate realistic axial load level of HSC columns in tall buildings becomes significantly large, making testing more difficult and costly. A new testing facility recently developed by the authors at the University of Southern California enables full-scale experimental testing on structural columns. This paper presents the experimental results on six full-scale HSC columns subjected to simulated seismic loading.

2. EXPERIMENTAL PROGRAM

2.1. Specimen Design

Six full-scale column specimens were designed to simulate typical columns in multi-story buildings in seismic regions. The testing matrix is shown in Table 1 and the specimen details are illustrated in Fig.1. The columns were 510 mm (20 in) by 510 mm (20 in.) square in cross-section with a height of 1778 mm (70 in) from the point of lateral loading to the top of the footing. The columns were reinforced with four No. 36 (ASTM No. 11, nominal diameter =35.8 mm =1.41 in) bars plus four No. 29 (ASTM No. 9, nominal diameter =28.7 mm =1.128 in) bars, constituting a longitudinal reinforcement ratio of 2.6%. The main testing parameters were the transverse reinforcement details and the axial load level.

1 Assoc. Prof., Dept. of Civil Engineering, University of Southern California, Kaprielian Hall, Los Angeles, CA 90089-2531, Email: yanxiao@usc.edu

2 Former graduate Research Assistant, University of Southern California, currently employed by the City of Los Angeles, Department of Building and Safety.

Table 1- Testing Matrix

Specimen	Longitudinal Steel	Transverse Steel for Column Potential Plastic Hinge Region	Concrete Strength f_c' (MPa)	Concrete Strength f_c' (MPa)*	Axial Load Ratio P/A_gf_c' (Axial Load)
FHC1-0.2		No.16 hoops &ties @100mm (f_y=445MPa)	64.1	-	0.2 (3334 kN)
FHC2-0.34	4 No.29 &	No.16 hoops &ties @100mm (f_y=445MPa)	62.1	75.5*	0.34 (5373 kN)
FHC3-0.22	4 No.36	No.16 hoops &ties @125mm (f_y=524MPa)	62.1	75.5*	0.22 (3630 kN)
FHC4-0.33	(f_y=473MPa)	No.16 hoops &ties @125mm (f_y=525MPa)	62.1	75.5*	0.33 (5240 kN)
FHC5-0.2		No.16 hoops &ties @150mm (f_y=445MPa)	64.1	-	0.2 (3334 kN)
FHC6-0.2		No.16 hoops &ties @150mm (f_y=524MPa)	64.1	-	0.2 (3334 kN)

Note: i. Specimen name designation example: FHC1-0.2 represents High-Strength Concrete Full-scale Flexural testing model column No.1 with an axial load ratio of 0.2; ii. Concrete strength, f_c', is based on average strength of three 152mm × 305mm cylinders cured in the air-dry condition; iii. f_c'*: concrete strength obtained from water-cured standard cylinder specimens; iv. Axial load ratio = $P/(A_gf_c')$; v. The nominal diameter is 28.7mm for No.29 bars; 35.8mm for No.36 bars; and 15.9mm for No.16 bars.

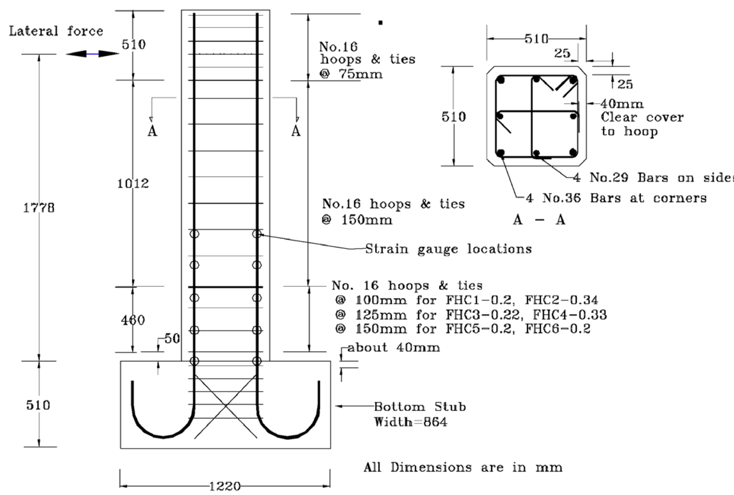

Fig. 1-Details of full-scale column specimens

In the seismic design provisions of ACI 318-99 (1999), the cross-sectional area of transverse reinforcement for the potential plastic hinge region of a column is specified by the following equations,

$$A_{sh} \geq 0.3\frac{sh_c f_c'}{f_{yh}}\left(\frac{A_g}{A_{ch}}-1\right) \tag{1a}$$

or,

$$A_{sh} \quad 0.09sh_c\frac{f_c}{f_{yh}} \tag{1b}$$

where, A_{sh} is the total transverse steel cross sectional area within the spacing s; h_c is the cross sectional dimension of the column core measured center-to-center of the outermost peripheral hoops; f_c' is the specified compressive strength of concrete; f_{yh} is the specified yield strength of the transverse reinforcement; A_g is the gross area of the column section; and A_{ch} is the cross sectional area of a column measured out-to-out of transverse reinforcement. It should be pointed out that in the following discussions and analysis all specified material strengths per design codes are replaced by using the actual strengths obtained from material tests. This was to reflect the research purpose of evaluating the adequacy of various design equations through actual testing, rather than providing safety factors for design. In earlier versions of the ACI 318 code, the hoop spacing is limited to one-quarter of the minimum dimension of the column or 100 mm , whichever is smaller. However, the hoop spacing in the ACI 318-99 code is changed to not exceeding: one-quarter of the minimum dimension of the member; six times the diameter of the longitudinal reinforcement, and s_x, given as,

$$s_x = 4 + \left(\frac{14 - h_x}{3} \right) \tag{2}$$

where h_x is the maximum horizontal spacing of hoop or crosstie legs on faces of the column, and both s_x and h_x are measured in inches. This change relaxed the requirements of the transverse reinforcement spacing in potential plastic hinge region up to 150 mm.

For the selected dimension of the specimens tested in this research, equation (1a) governs the determination of A_{sh}. Model columns FHC1-0.2 and FHC2-0.34 were transversely reinforced with No. 16 (nominal diameter =15.9 mm) hoops and cross ties spaced at 100 mm in the potential plastic hinge region with a length of 510 mm at the column end. The transverse reinforcements were spaced at 150 mm outside the plastic hinge region. The transverse reinforcement in the potential plastic hinge regions of these two specimens provided approximately 86% of the required confinement steel based on Eq. (1a) and actual material strengths. The spacing of the transverse reinforcement was more stringent than the ACI 318-99 requirements since the specimens were designed prior to the implementation of the relaxed spacing requirement.

In specimens FHC3-0.22 and FHC4-0.33, the spacing of the No.16 transverse reinforcement in the potential plastic hinge regions was increased to 125 mm. This spacing satisfied the of ACI 318-99, which relaxed the maximum spacing requirement for transverse reinforcement from 100 mm to 150 mm. Due to the use of higher strength transverse reinforcement in these two columns, the amount of transverse reinforcement was about 82% of that required by Eq. (1), comparatively close to that of specimens FHC1-0.2 and FHC2-0.34.

Specimen FHC5-0.2 was reinforced with No.16 hoops and ties spaced at 150 mm. This was at the limit allowed by the ACI 318-99 code. Consequently, FHC5-0.2 had approximately 57% of the confinement required by Eq.(1a). Higher strength steel was used in the transverse reinforcement for model column FHC6-0.2. In this specimen, the hoops and ties were spaced at 150mm (6in). The total cross-sectional area of transverse reinforcement was approximately equal to 68% of the value given by Eq. (1a).

All the hoops and ties satisfied the detailing requirements of ACI 318-99. Each set of transverse reinforcement consisted of a peripheral hoop with 135° hooks and a pair of cross ties with a 135° hook at one end and a 90° hook at the other end. The 90° hooks were alternated for the cross ties throughout the height of the column. The specimens were constructed with a heavily reinforced stub footing of 1219 mm × 864 mm × 508 mm.

2.2. Specimen Construction and Material Properties

Construction of the specimens was carried out at the Structural Laboratory of the University of Southern California with HSC supplied by a local concrete plant. The mixture proportions per m^3 of HSC were 187 kg water; 415 kg cement; 148 kg Class-F fly ash; 45 kg silica fume; 868 kg coarse aggregates; and 710 kg fine aggregates. The water-to-cementitious materials ratio was 0.30. Superplasticizer was also used to improve workability and setting time. The average slump at casting was about 150 mm. The compressive strength based on this mix proportion design doubles the typically upper strength of 34.5MPa for general use in seismic resisting elements in Southern California. Grade 420 steel with an average yield strength of 469 MPa was used for longitudinal reinforcing bars in all the columns. Three specimens were transversely reinforced with Grade 420 steel with an average yield strength of 445 MPa. The other three specimens had Grade 520 bars for transverse reinforcement with an average yield strength of 524 MPa.

2.3. Test Setup

A loading system that enables the full-scale testing of high-strength concrete columns was recently developed by the authors at the University of Southern California. The stub footing of the specimen was post tensioned to a stiff steel-concrete composite reaction beam. The reaction beam is 1.2 m wide and 5 m long, and is anchored to a deep concrete foundation. As shown in Fig.2(a), the testing system utilizes two actuators with 1334 kN capacity for cyclic loading in both lateral and axial directions. An axial force as large as 6200 kN can be applied to the specimen through a specially-designed lever arm that amplifies the force output of the vertical actuator by six times. Fig.2(b) schematically illustrates the concept of the lever arm system for axial loading. By setting the distance between the axis of the vertical connectors and the column axis equal to 1/5 of that between the vertical actuator and the column axis, an axial load of 6 times the actuator force can be applied to the specimen. As shown in Fig.2(b), if a lateral displacement Δ is induced, the applied axial load becomes inclined, and thus the true vertical load subjected by the column is the vertical component of the applied axial load. For a small lateral displacement, the true vertical load and the applied axial load can be considered approximately the same. On the other hand, the inclination of the applied axial force corresponding to Δ also has a horizontal component. Because this horizontal component is significant compared to the lateral load capacity of the column, it has to be subtracted from the horizontal actuator load to obtain the true lateral force applied to the column specimen.

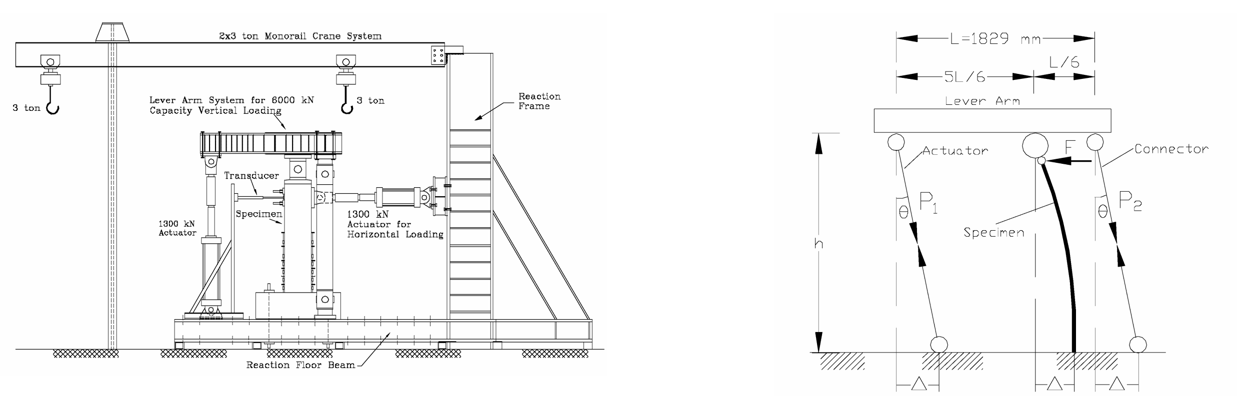

(a) **(b)**

Fig. 2-Full-scale testing system: (a) test setup; (b) lever arm system for axial loading

(a) (b) (c) (d)

Fig. 3. Crack Patterns of column FHC1-0.2 at: (a) 1.0% drift ratio; (b) 2.0% drift ratio; (c) 6.0% drift ratio; (d) failure.

2.5. Loading Procedure

During testing, the axial load was maintained approximately constant, whereas the lateral force was cycled under lateral displacement control conditions. Three single cycles corresponding to an increment of 0.25% peak drift ratio, Δ/L, were initially applied. Then, three repetitive loading cycles were applied for each of the peak drift ratios, Δ/L=1%, 1.5%, 2%, 3%, 4%, and 6%. For specimen FHC1-0.2, an additional cycle at 8% drift was also attempted.

3. EXPERIMENTAL RESULTS

3.1. General Observations

The six model columns developed stable responses, up to drift ratios ranging from 3% to 6% depending on the transverse reinforcement details and the axial load levels. Fig.3 illustrates the crack patterns for column FHC1-0.2 at various loading stages. Flexural cracks perpendicular to the column axis formed first in the lower half of the column at drift ratios less than 0.5%. Some of the flexural cracks became inclined and extended into the web zone of the columns due to the influence of shear when the drift ratio increased to 1.0%. The highest lateral load carrying capacity was typically recorded during the loading to approach the first peaks at a drift ratio of 2.0% for columns with an axial load ratio of 20% or 1.5% for columns with the axial load ratio above 30%. At the same stage, the concrete cover crushed at the toes of the column. The spalling of the concrete cover gradually spread over the lower portion of the column with the increase of both the loading cycles and the drift displacement. However, despite the concrete cover spalling, the confined core near the column end appeared to rotate in a stable manner, providing a satisfactory column performance until failure. The final failure of the columns was caused by longitudinal bar buckling and crushing of confined concrete core. No rupture of reinforcement was observed in any of the tests. The buckling of longitudinal bars appeared to be significantly severed by the opening of the 90-degree anchorage of the cross ties.

Although the concrete cover crushing initiated at the toes of the column, the most damaged zones appear to be in a portion about 200 mm to 300 mm above the critical section of the column. This is likely due to the extra confinement provided to the column end by the footing, as observed by Bayrak and Sheikh (1998). A closer examination of the tested specimens suggests the existence of a 45-degree triangular zone affected by the stub confinement. For this reason, it is suggested to consider a length of 0.5D as the zone affected by the footing confinement.

3.2. Hysteretic Responses

Detailed testing results were reported in Xiao et al. (2002). The main results are summarized in Table-2. Fig. 4 show lateral shear force – drift ratio hysteretic relationships for two full-scale HSC columns, as examples. The shear force values were obtained by subtracting the horizontal component of axial force from the applied lateral loads, for reasons discussed previously. The predicted flexural capacities, V_{fACI}, corresponding to an extreme concrete compressive strain of 0.003, as recommended by ACI 318-99, and based on actual material strengths are shown by dashed lines. The slopes of the dashed lines and the inclined solid line passing through the origin of the coordinates represent the P-Δ effect. Symbols in Figs. 4 mark various loading stages where physical changes, such as concrete crushing or steel yielding, were observed.

Table 2- Column Capacities

Specimen	${}_{ex}V_{1y}$ in kN (${}_{ex}V_{1y}$ / ${}_{an}V_{1y}$)	${}_{ex}V_{co}$ in kN (${}_{ex}V_{co}$ / ${}_{an}V_{co}$)	${}_{ex}V_{cc}$ in kN (${}_{ex}V_{cc}$ / ${}_{an}V_{cc}$)	Δ_{1y}/L	Δ_{co}/L	Δ_{y}/L	Δ_{u}/L
FHC1-0.2	701 (1.03)	755 (1.04)	751 (1.03)	1.25%	1.6%	1.34%	7.3%
FHC2-0.34	732 (1.09)	874 (1.15)	852 (1.11)	0.81%	1.17%	0.94%	3.76%
FHC3-0.22	670 (0.99)	783 (1.13)	723 (1.04)	1.25%	1.55%	1.35%	5.8%
FHC4-0.33	775 (1.13)	879 (1.16)	775 (1.02)	1.05%	1.32%	1.05%	4.0%
FHC5-0.2	658 (0.96)	769 (1.06)	715 (0.98)	1.04%	1.83%	1.13%	5.0%
FHC6-0.2	707 (1.03)	766 (1.05)	714 (0.98)	1.29%	1.75%	1.3%	6.0%

Note: subscripts, *ex* and *an* designate experimental and analytical values, respectively.

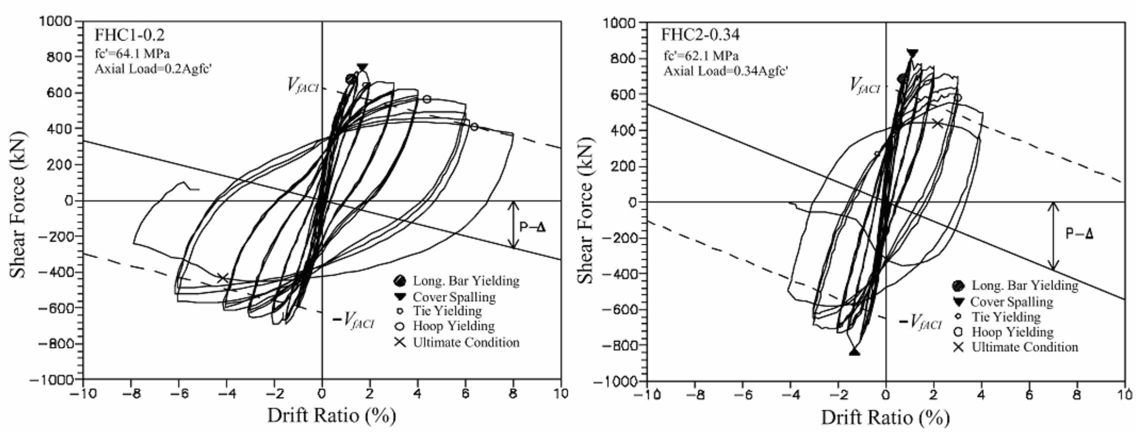

(a) **(b)**

Fig.4. Hysteresis loops of columns with 86% code-required transverse reinforcement: (a) FHC1-0.2; (b) FHC2-0.34.

The hysteretic behavior of the HSC columns appears to exhibit three stages: (i) the initial stage characterized by a full participation of both confined core concrete and the unconfined cover concrete; (ii) stable behavior with deformation contributed primarily by longitudinal steel yielding, cracking and straining of confined core concrete; and (iii) final failure. The termination of the initial stage and the beginning of the stable stage is typically marked by crushing and spalling of the unconfined cover concrete. The maximum lateral shear force carrying capacity was achieved by the HSC columns immediately before crushing of the cover concrete. The maximum shear force and the corresponding drift ratio depend mainly on the axial load level, and were not significantly affected by the configuration of transverse reinforcement. As shown in Figs. 4, all columns developed and exceeded the flexural capacity calculated according to ACI 318-99. Earlier tests ("Joint" 1997; Ibrahim and MacGregor 1997) have shown that the ACI code approach tends to overestimate the flexural strength of HSC columns failing in compression. All specimens tested in this study developed longitudinal bar yielding prior to concrete crushing, even for columns FHC2-0.34 and FHC4-0.33, both of which were predicted for a compression failure based on the ACI code approach. Other reasons why the current study did not show similar trends of previous tests may include: (i) loading condition differed from most previous tests where columns were tested under eccentric compression (Ibrahim and MacGregor 1997); (ii) possible effects of full-scale versus smaller scale specimens. The last point certainly deserves more studies in the future.

4. DISCUSSION ON ULTIMATE DEFORMATION

Although all the six specimens were of substandard design based on ACI 318 code (1999), the trend of their behavior shows that the code equations governing the transverse reinforcement design for earthquake resistant columns do not provide consistent performance level. The current code design for transverse reinforcement appears to be over-conservative for lower axial load levels but less conservative for higher axial load levels. Sheikh and Khoury (1998) also pointed out the deficiency of the ACI 318-95 provision for transverse confinement steel design based on test results of relatively smaller-scale columns.

The current trend of developing so-called performance based design requires the establishment of quantitative relationships between the design parameters and the expected seismic performance of structures or structural elements. Recently, Sheikh and Khoury (1998) proposed a performance based approach for confinement steel design. In their approach, the amount of confinement steel in a column hinge region is calculated based on the configuration, column axial load level and curvature ductility demands.

In this paper, an empirical approach is attempted to develop a performance-based design for transverse reinforcement of HSC columns. The column ultimate drift ratio, $(\Delta/H)_u$, is selected as the target performance index. The design parameters considered are the transverse confinement and the axial load level, using the following confinement index, α, and the axial load ratio, β.

$$\alpha = \frac{A_{sh} f_{yh}}{s h_c f_c'} \tag{3}$$

$$\beta = \frac{P}{A_g f_c'} \tag{4}$$

where, A_{sh} is the total transverse steel cross sectional area within spacing s; h_c is the cross sectional dimension of column core measured center-to-center of out-most peripheral hoops; f'_c

is specified compressive strength of concrete; f_{yh} is specified yield strength of transverse reinforcement; A_g is gross area of column section.

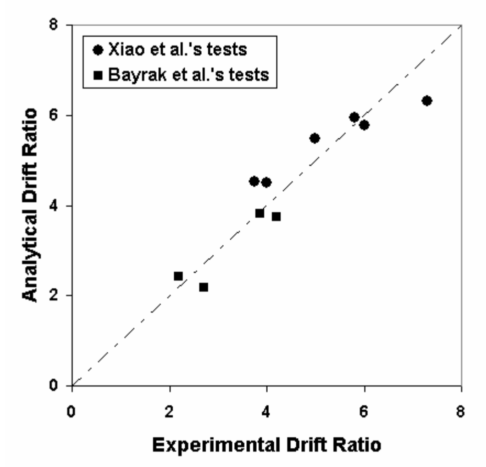

Fig.5. Comparison of drift ration calculated by proposed equation with test results

Based on regression analysis, the following statistical equation was obtained,

$$(\Delta / H)_u = 28\ln(\alpha + 1) + \frac{38}{\sqrt{\beta + 1}} - 31 \quad (\%) \tag{5}$$

The correlation between the analytical ultimate drift ratios and the test data from current study and Bayrak et al.'s tests (1998) is shown in Fig.5. Of course, due to the limited test data, the equation should not be extrapolated beyond the range of the tests.

5. ANALYSIS OF COLUMN PERFORMANCE

5.1. Approach

Three-dimensional FEM analysis was performed to attempt detailed understanding of the HSC column behavior and to evaluate if the existing analytical tools can provide decent prediction to the full-scale test results. Adina 900-node educational program Version 7.5 was used in the analysis. Two types of models analyzed are a column section model and a full-column model. The section model was to provide prediction to the initial axial loading behavior or the results of axial compression tests of HSC columns. The geometry of the section models is equivalent to a quarter of column section due to symmetry. Its thickness is equal to the spacing of transverse reinforcements with the transverse reinforcements placed at middle of the model thickness. The full-column model has its stub fixed in all directions and is geometrically equivalent to specimens FHC1-0.2 and FHC2-0.34 with experimental constant axial loading and statically induced lateral displacement increments.

The FEM models consist of 3-dimensional solid concrete 8-node elements, 3-dimensional bilinear elasto-plastic 2-node pipe and truss elements for steel reinforcements. The cross section of the pipe elements has their radius equal to one half of the diameter of steel bars. For the section model, pipe elements were used for longitudinal reinforcements and truss elements are used for all transverse reinforcements. A total of 442 elements are used for the section analysis. For the full-column model, only pipe elements were used for all reinforcements, after a failed attempt of using truss elements. The total number of elements for the full-column model analysis was 696.

The experimental compressive strength and ACI-318 code recommended Young's modulus for concrete were used for the concrete with a Poisson ratio of 0.15. True properties based on material testing were used for all reinforcements with a Poisson ratio of 0.3. The program is equipped with the Kupfer's concrete constitutive law. Nonlinear analysis was performed using fifty time steps of 0.2 seconds spanning a period of 10 seconds using displacement-based Full Newton Method with tolerance of 0.01 and 15 iterations for the section model, and energy-based BFGS Matrix Update method with line searches and with 300 iterations for the full-column model. The energy tolerance was set as 0.5 for the full-column model to improve convergence.

5.2. Analytical Results

Analytical results based on the section model provided very accurate predication for the initial axial loading stage of the full-scale column tests. To demonstrate the ability of the FEM analysis, a specimen in a previous axial loading test program (Xiao and Martirossyan, 1995, 2001) was analyzed and the comparison with the test results is shown in Fig.6. The analysis was able to capture the main features of the axial loading behavior for the ascending stress stage, however failed to track the post-peak behavior due to divergence after the onset of concrete model crushing.

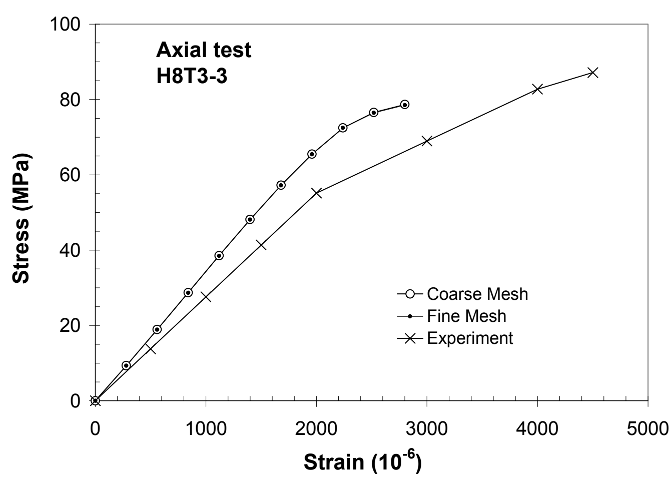

Fig.6. Comparison of analysis and axial loading test results (Xiao et al. 1995; Martirossyan and Xiao 2001)

The results of the three dimensional FEM push-over analysis for the two of the full-scale specimens are shown in Fig.7 (a) and (b), respectively. The analysis was able to provide reasonable prediction to the lateral force and deformation behavior up to the peak loading capacity. However, the onset of crushing of unconfined cover concrete elements resulted in the divergence of the program. The predicated behavior has a stiffness of about 10-20% higher than the test results. This was considered due to the fact that the analysis was performed for monotonic loading whereas the tests were cyclic. It was also identified that to achieve better agreement, the concrete modulus of elasticity should be based on actual values rather than the code specifications (Xiao et al. 1995). The analytical results of detailed stress and strain distributions in the full-scale column models also revealed useful information of the confined concrete and the reinforcement.

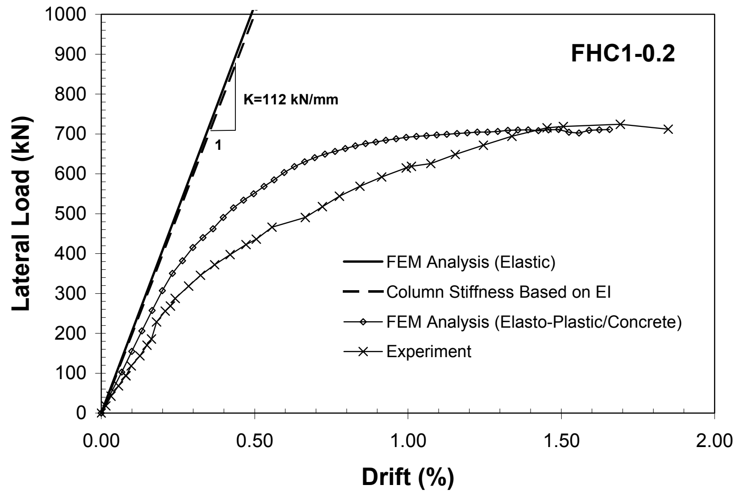

(a)

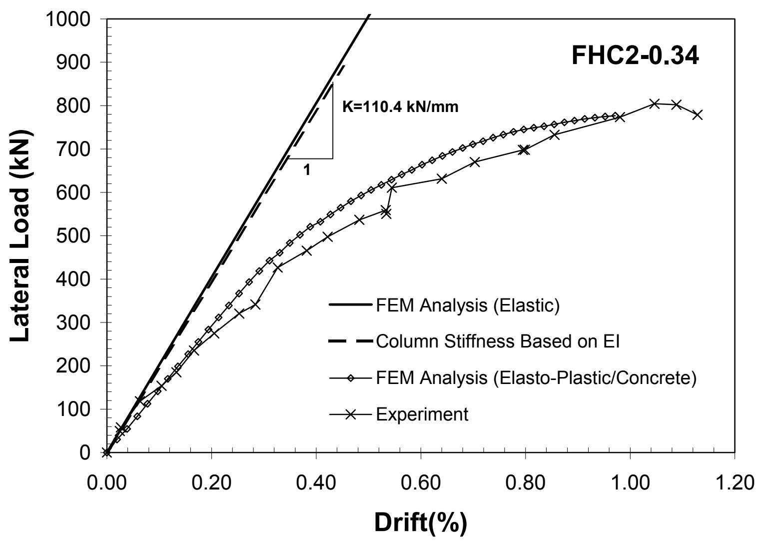

(b)

Fig.7. Comparison of analysis and full-scale HSC column tests: (a) column with axial load ratio of 0.2; (b) column with axial load ratio of 0.34.

6. CONCLUDING REMARKS

The main findings from the test results of the full-scale model HSC columns subjected to a constant axial load and cyclic lateral forces can be summarized as follows:

(1.) The hysteretic behavior of the HSC columns can be characterized by three distinct stages: (i.) the initial stage with the full participation of both confined core concrete and the unconfined cover concrete; (ii.) stable behavior with deformation contributed primarily by longitudinal steel yielding and straining of confined core concrete; and (iii.) final failure.

(2.) The termination of the initial stage or the beginning of the stable stage is marked by the crushing and spalling of unconfined cover concrete. The maximum lateral shear force carrying capacity is typically achieved by the HSC columns tested in the program at the crushing of cover concrete. The maximum shear force and the corresponding drift ratio depend mainly on the concrete section properties including the axial load levels, and are not significantly affected by the configuration of transverse reinforcement.

(3.) The stable behavior after concrete cover spalling, which is most important for seismic design, was significantly affected by both the level of axial load and the details of transverse reinforcement. Model columns reinforced with transverse reinforcement of more than 82% of the ACI 318-99 requirement developed ductile response with an ultimate drift ratio of 6.0% when the axial load was $0.2A_g f'_c$. The ultimate drift ratios decreased for model columns with less transverse reinforcement or higher axial load levels.

(4.) The failure of all the model columns was dominated by the buckling of longitudinal reinforcement, followed by the total crushing of core concrete. The failure might have been initiated or at least compounded by the opening of the 90 degree anchorage of the cross-ties.

(5.) The use of higher strength transverse reinforcement was found effective in providing additional confinement and ductility. In particular, increased transverse steel strength can effectively offset the negative effects due to widening of hoop spacing.

(6.) Analysis based on the equivalent compressive stress block corresponding to an ultimate concrete compressive strain of 0.003, as recommended by ACI 318-99, provides a predictable but conservative estimate to the flexural strength of the HSC full-scale column models tested in this study. The analysis based on a proposed stress-strain model for confined HSC can estimate the characteristic capacity values corresponding to major physical changes reasonably well.

(7.) Though the specimens were all substandard compared to the current ACI 318 code requirements for transverse reinforcement in the potential plastic hinge regions of a column, the test results show the trend that the current code provision appeared to be over-conservative for lower axial load levels but less conservative for higher axial load levels. An empirical equation was proposed to express the ultimate drift ratios of HSC columns with the axial load ratio and transverse reinforcement ratio.

(8.) Three dimensional FEM push-over analysis can provide reasonably good predications to the behavior of HSC columns before the peak load carrying capacity.

ACKNOWLEDGEMENTS

The research described in this paper has been funded by Carpenters/Contractors Cooperation Committee (CCCC), Inc. through collaboration with ESI Inc. The research project also received supports from Concrete Reinforcing Steel Institute (CRSI), Fontana Steel, Inc., and Transit Mixed Concrete, Corp. Cooperation from M. Pourzanjani, Dr. Roger Y. Li of ESI are warmly appreciated. The authors would like to thank Mr. H. Wu and Mr. T.T. Yaprak, Ph.D. graduate research assistants of the University of Southern California for their helps during testing.

REFERENCES

ACI Committee 318, (1999), "Building Code Requirements for Reinforced Concrete and Commentary (ACI 318-99/ACI 418R-99)," American Concrete Institute, Farmington Hills.

Bayrak, O.; and Sheikh, S.S., (1998), "Confinement Reinforcement Design Considerations for Ductile HSC Columns," *ASCE Journal of Structural Engineering*, Vol.124(9), September, pp.999-1010.

Hester, T. W., editor, (1990), "High-Strength Concrete," American Concrete Institute, Special Publication, SP-121, 786p.

Ibrahim, H.H.H., and MacGregor, J.G., (1997), "Modification of the ACI Rectangular Stress Block for High-Strength Concrete," *ACI Structural Journal*, American Concrete Institute, V.94, No.1, January-February, pp.40-48.

Li, B. and Park, R., (1994), "Strength and Ductility of Reinforced Concrete and Frames Constructed Using High-Strength Concrete," Research Report 94-5, Department of Civil Engineering, University of Canterbury, New Zealand, 389p.

Malhotra, V.M., editor, (1994), "High-Performance Concrete," American Concrete Institute, Special Publication, SP-149, 844p.

Martirossyan, A. (1998), "Performance of Reinforced High-Strength Concrete Columns," Ph.D. Thesis, Department of Civil Engineering, University of Southern California, Structural Engineering Research Project, Report No. USC-SERP-98/06.

Martirossyan, A. and Xiao, Y. (2001), "Flexural-Shear Behavior of High-Strength Concrete Short Columns," Earthquake Engineering Research Institute, *EERI Spectra*, V.17, No.4, November 2001, pp. 679-695.

Joint ACI-ASCE Committee 441, (1997), "High-Strength Concrete Columns: State of the Art," *ACI Structural Journal*, American Concrete Institute, V.94, No.3, May-June, pp.323-335.

Sheikh, S.A.; and Khoury, S.S., (1998), "A Performance-Based Approach for the Design of Confining Steel in Tied Columns," *ACI Structural Journal*, American Concrete Institute, V.94, No.4, July-August, pp.421-431.

Xiao, Y.; Anderson, J.C.; and Martirossyan, A., (1995), "Reinforcement Design for High Strength Concrete Columns Using Local Materials In Southern California," *USC Structural Engineering Research Report*, No. USC-SERR95/01, Department of Civil Engineering, University of Southern California, March 1995, 150p.

Xiao, Y.; Yun, H.W. (2002), "Full-Scale Experimental Studies on High-Strength Concrete Columns," American Society of Civil Engineers, *ACI Structural Journal,* Vol.99, No.2, March-April issue, pp. 199-207.

Xiao, Y. and Martirossyan, A., (1998), "Seismic Performance of High-Strength Concrete Columns," *ASCE Journal of Structural Engineering*, Vol.124(3), March, pp.241-251.

INTERFACE SHEAR TRANSFER FOR HIGH STRENGTH CONCRETE AND HIGH STRENGTH SHEAR FRICTION REINFORCEMENT

Susumu KONO[1], Hitoshi TANAKA[2], and Fumio WATANABE[1]

ABSTRACT

The shear transfer at construction joints for members was investigated experimentally using twenty-six direct shear type specimens in order to study the effects of high strength concrete, the high strength shear friction reinforcement, and interface roughness. The displacement-controlled cyclic loading was applied and shear stress transferred along the interface was separated into the contributions of concrete and dowel actions. In the dowel action, the flexural action dominates the shear-frictional reinforcement and the average tensile strain at the interface did not reach the yield strain at the peak stress. The assumption that reinforcement has yielded at the peak stress was not met in the test. In the concrete action, stress transfer depends on the concrete strength and the surface roughness and the combined effect of concrete strength and surface roughness needs to be considered in a design equation. If earthquake force acts cyclically to the interface, it is not safe to count on the experimental results based on the monotonic loading test since the shear resistance in the direction opposite to the virgin direction could become smaller. This effect is pronounced for specimens with coarse interface and considered to be caused by the wearing of the interlocking mechanism.

1: Department of Architecture, Kyoto University, Kyoto, Japan
2: Disaster Prevention Research Institute, Kyoto University, Kyoto, Japan

INTRODUCTION

Interface shear at construction joints is transferred mainly through concrete before cracking, and through both concrete and reinforcing bars after cracking. The shear transfer through concrete is called a concrete action in this paper and consists of friction resulting from the normal compressive stress and the interlock of aggregate protrusions. The shear transfer through reinforcing bars is called a dowel action. Total shear stress transferred at cracked interfaces can be predicted by summing the stresses due to the concrete and dowel actions. The shear friction method introduced in the ACI code [1] as well as in the Japanese building code [2] is useful to account for the interface shear transfer. Shear strength, V_n, is computed by Eq. (1) in the ACI code.

$$V_n = A_{vf} f_y \mu \qquad (1)$$

where A_{vf} and f_y are the area and specified yield strength of shear-friction reinforcement, respectively, and μ is the coefficient of friction. The value for μ is 1.4 for concrete placed

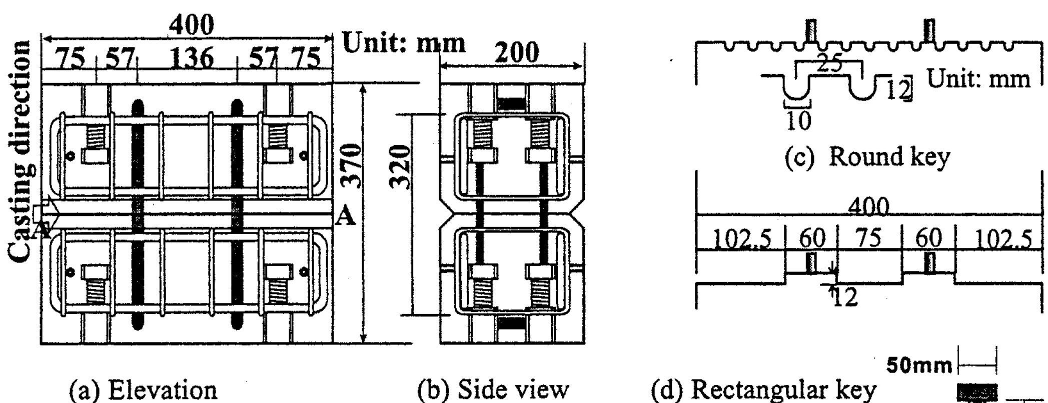

Figure 1 Dimension and reinforcement of column specimens

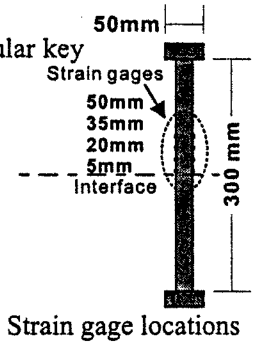

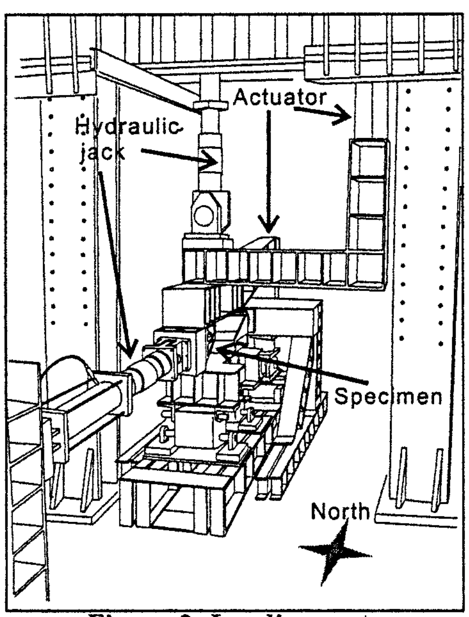

Figure 2 Loading system

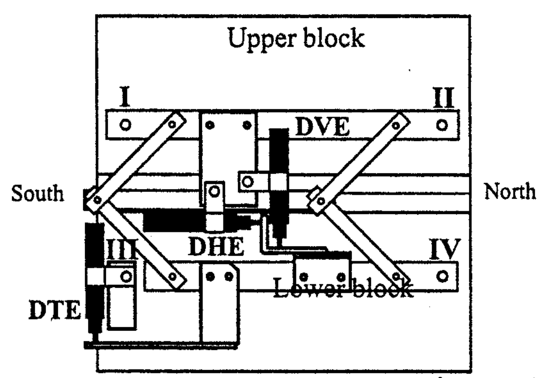

Figure 3 Displacement-measuring system
East Side

Table 1: Specimen designation, variables, and test results

Designation			Test variables				Shear capacity, slip, and opening						Shear capacity by ACI(*2)	
			Friction bar		Concrete		Positive side (Push)			Negative side (Pull)				
No.	Combination type	Dowel type	Fy (MPa)	Size and No.(*1)	f'c (MPa)	Surface finishing	Cap. (MPa)	Slip (mm)	Open (mm)	Cap. (MPa)	Slip (mm)	Open (mm)	ACI1 (MPa)	ACI2 (MPa)
1	H10-050PC	H10-050PD	999	4-D10	50	Plain	1.63	2.00	0.71	-1.61	-2.00	0.63	2.62	3.49
2	H10-050RC	H10-050RD				Roughened	5.30	0.84	0.61	-2.20	-1.47	1.59	4.36	6.29
3	H10-100PC	H10-100PD			100	Plain	2.21	2.01	0.22	-1.85	-1.81	0.30	2.62	3.49
4	H10-100RC	H10-100RD				Roughened	7.32	1.63	2.03	-3.55	-1.83	2.13	4.36	6.29
5	H10-100BC	H10-100BD				Round key	5.68	1.05	0.64	-2.82	-1.65	1.20	4.36	4.61
6	H10-100KC	H10-100KD				Rect. key	6.05	1.08	0.93	-3.29	-3.52	3.18	4.36	4.33
7	L19-045SC	L19-045SD	432	2-D19	45	Scratched	3.99	0.46	0.36	-3.23	-0.57	0.54	2.09	2.79
8	L25-045RC	L25-045RD	386	2-D25		Roughened	4.27	0.91	0.39	-3.17	-0.53	0.35	5.75	7.40
9	L25-045KC	L25-045KD				Rect. key	5.37	1.83	1.38	-3.31	-0.78	0.69	5.75	5.44
10	L19-110SC	L19-110SD	432	2-D19	110	Scratched	4.14	0.44	0.19	-3.15	-0.54	0.47	2.09	2.79
11	L25-110SC	L25-110SD	386	2-D25		Scratched	6.24	0.95	0.77	-3.89	-3.87	3.24	3.45	4.60
12	L25-110RC	L25-110RD				Roughened	6.18	0.48	0.20	-3.83	-0.31	0.21	5.75	7.40
13	L25-110KC	L25-110KD				Rect. key	6.67	0.89	1.02	-3.43	-1.06	1.02	5.75	5.44

*1: 4-D10 stands for four friction deformed bars with a diameter of 10 mm. 4-D10, 2-D19, and 2-D25 give the reinforcement ratio of 0.445%, 0.795%, and 1.458%, respectively.
*2: ACI1 and ACI2 are computed using Equations 1 and 2.

Table 2: Materials properties

	Nominal f'c (MPa)	Casting Sequence	f'c (MPa)	f't (MPa)	Ec (GPa)
Concrete	45	1st	44.1	3.49	30.8
		2nd	47.5	3.51	30.9
	50	1st	54.6	4.41	33.7
		2nd	45.4	4.44	29.2
	100	1st	103	15.7	35.4
		2nd	97.6	17.7	36.2
	110	1st	112	5.67	43.4
		2nd	112	5.58	43.2
Steel	Type	Diameter (mm)	fy (MPa)	fu (MPa)	Es (GPa)
	D10	10	999	1034	184
	D19	19	432	642	164
	D25	25	386	588	184

f'c: Compressive strength
f't: Tensile strength
Ec: Elastic modulus
fy: Yield strength
fu: Tensile strength
Es: Elastic modulus

Table 3: Coefficient used in ACI Equation

Surface finishing	μ	Ac (cm^2)
Plain	0.6	0
Scratched	0.6	0
Roughened	1.0	640
Round key	1.0	256
Rect. key	1.0	192

Note:
The friction coefficient is set 1.0 for shear keys. Crack forms along the foot of shear keys and along the plain interface elsewhere for keyed interface. The coefficient 1.4 is appropriate for shear key locations and 0.6 is appropriate along the plain interface. Value 1.0, which is the mean value of 1.4 and 0.6, was taken assuming the area of key and other region are same.

monolithically, 1.0 for concrete placed against hardened concrete with surface intentionally roughened, and 0.6 for concrete placed against hardened concrete not intentionally roughened. The commentary of the ACI code has Eq. (2) as an alternate equation since Eq. (1) tends to be conservative.

$$V_n = 0.8 A_{vf} f_y + A_c K_1 \qquad (2)$$

where A_c is the area of concrete section resisting shear transfer, K_1 is 2.8 MPa (400 psi) for normal weight concrete.

However, in the shear friction method the effects of the friction at the concrete interface and the dowel action of shear-friction reinforcement are experimentally evaluated by integrating them all into the frictional coefficient, and the contribution of the dowel action to the total shear transfer cannot be directly seen from the frictional coefficient given in the ACI code. In addition, the contribution of the dowel action varies not only with the mechanical properties of concrete and reinforcement but also with a relative displacement between concrete surfaces but this effect is not considered. Further the conventional shear friction method is not originally developed for members with high strength concrete and frictional reinforcement. Although Walraven el al. [3] and Mattock [4] studied the effects of concrete strength, the effects of cyclic loading with large displacement simulating the seismic loading are not included in their studies.

In this study, the interface shear transfer was investigated experimentally using direct shear tests on twenty-six specimens. Developing the test method originally proposed by Dulacska [5], shear stress transferred along the interface was separated into the contributions of concrete and dowel actions and the variation of those contribution with respect to cyclically loaded slip displacement is discussed. The specimens were made of high strength concrete and/or frictional reinforcement, and had five different interface roughness.

TEST SETUP

Specimen designs

As shown in Table 1, thirteen sets of specimens were prepared. Each set had two specimens; a combination type and a dowel type. The combination type specimens had prescribed interface finishing and two or four dowel bars embedded so that the external shear force was resisted by both the concrete and dowel actions. The dowel type specimens were prepared to isolate the dowel action by inserting double thin metal plates at the interface in order to eliminate the concrete action [5]. In this manner, the external shear force was resisted by the dowel action only. Specimen dimensions and reinforcement arrangement are shown in Fig. 1. The shear interface had an area of 640 cm^2. For combination type specimens, the lower block was cast first, a prescribed finishing made at the construction joint, and 3 days later the other half block cast. For dowel type specimens, lower and upper blocks were cast at a same time with double thin steel plates placed at the joint interface. The mechanical properties of concrete and friction reinforcement are shown in Table 2. The maximum aggregate size was 20 mm.

The shear interface had five kinds of finishing as indicated by Table 1. Plain surface had a flat trowelled interface. Scratched surface had a surface scratched with a wire brush several times but the surface condition was close to the plain surface. Roughened surface was generated by removing the surface mortar and exposing the aggregate before the surface hardened. This finishing is considered the intentionally roughened surface according to the ACI code whereas the scratched surface is deemed the not-intentionally roughened surface. Round key and rectangle keys had shear keys as shown in Fig. 1 (c) and (d), respectively.

Loading and measurement

Figure 2 shows the loading system used. The center of the horizontal hydraulic jack stayed at the same height as the shear plane so that the direct shear force acted on the shear plane without moment. The vertical hydraulic jack was used for dowel type specimens only. The vertical actuators set at the north and east side of the specimen automatically moved to enforce the upper and lower blocks to move parallel to each other. The inclination of the upper block with respect to the lower block was 1/2000 radian at maximum and considered negligible. For C type specimens, the horizontal force was applied cyclically and the opening and slip displacements were recorded. Two cycles were made at the displacements of 2 mm, 4 mm, and 8 mm for specimens with D10 friction bars whereas the same two cycles were made at the displacements of 0.5 mm, 1 mm, and 2 mm, and 4 mm for the other specimens. For dowel type specimens, the opening and slip were controlled so that the specimen experienced the identical displacement path with the companion combination type specimen as shown in Fig. 4. The dowel type specimens with D10 friction bars were loaded only for the first two cycles, basically at a slip of 2 mm. The shear resistance by the concrete action was computed by subtracting shear force of the dowel type specimen from the shear force of the companion type specimen.

Opening and slip displacements were measured at the both sides of a specimen as shown in Fig. 3. Strain gages were placed on the friction bars at 5 mm, 20 mm, 35 mm, and 50 mm from the interface in grooves as shown in Fig. 1(e).

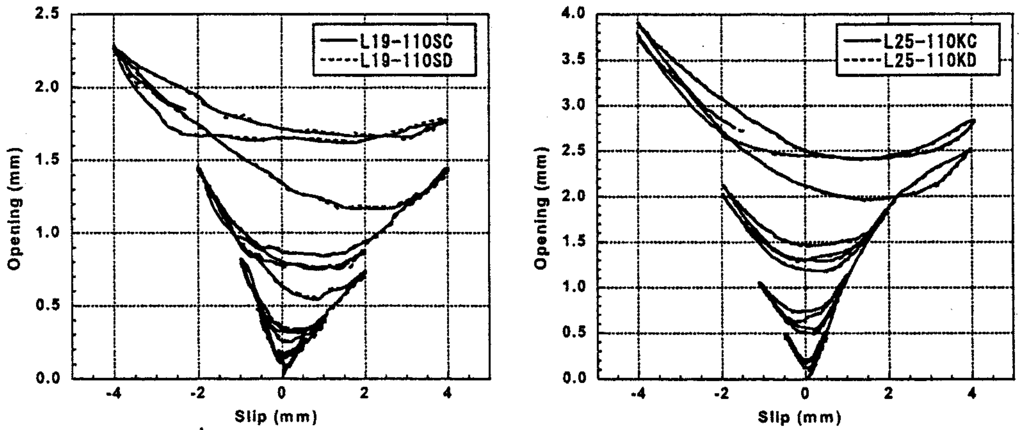

(a) L19-110S set (b) L25-110K set

Figure 4 Typical opening - slip relations for combination and dowel type specimens

TEST RESULTS

Strain distribution along the friction reinforcement

Figure 5 shows the strain distribution along the friction reinforcement at the first cycle of displacements of +0.5 mm, +1.0 mm, and +2.0 mm. Solid lines show the south side strains and dotted lines show the north side strains. It can be seen that the flexural action was dominant and the average tensile strain at the interface did not reach the yield strain at the peak stress. The fact that the frictional reinforcement does not yield at the interface at the peak shear stress was also shown by other studies [6][7][8] as well. Although some predictive equations for the shear capacity are based on the assumption that frictional bars have yielded at the peak stress, the assumption needs to be reconsidered.

Shear stress – slip relations

Figures 6 and 7 show shear stress- slip relations for all specimens. A combination type specimen and its companion dowel type specimen are drawn in one plot. All curves show slip type hysteresis and the stiffness for the experienced slip is much less than that for the virgin slip. The shear capacity and the corresponding slip and opening for both positive and negative directions are listed in Table 1. Also listed are predicted shear capacity using Eqs. (1) and (2) designated as ACI1 and ACI2, respectively. The friction coefficient μ and λ listed in Table 3 were used to calculate those values.

Although the ACI code states that a certain amount of slip and opening is necessary to reach the shear capacity, the magnitude of the slip is not clearly shown. Table 1 shows that slips at the peak stress ranged from 0.19 mm to 2.03 mm for the positive direction in which the maximum values were recorded for all specimens. Figure 4 and Table 1 show that the slip is accompanied by a same magnitude of the opening although smooth surface tends to have smaller opening. If a certain structure has an interface resisting the shear force by the shear friction mechanism, it needs to be taken into account that the shear capacity can be reached with this magnitude of slip and opening. The magnitude will change depending on the size and bond characteristics of friction bars and the mechanical properties of concrete.

Comparisons between H10-050PC and H10-100PC, and between L19-045SC and L19-110SC show that the shear capacity does not increase with the increase of concrete strength when the interface is smooth. However, comparisons between H10-050RC and H10-100RC, between L25-045RC and L25-110RC, and between L25-045KC and L25-110KC show that the shear capacity increases dramatically with the increase of concrete strength when the interface has a roughened or keyed surface. In this case the amount of enhancement in shear capacity was nearly same for roughened surface and keyed surface. Comparing shear capacity with the ACI code, Eq. (1) gives a very unconservative prediction for H10-050PC, H10-100PC, and L25-045RC. Specimens H10-050PC and H10-100PC had so smooth surface that

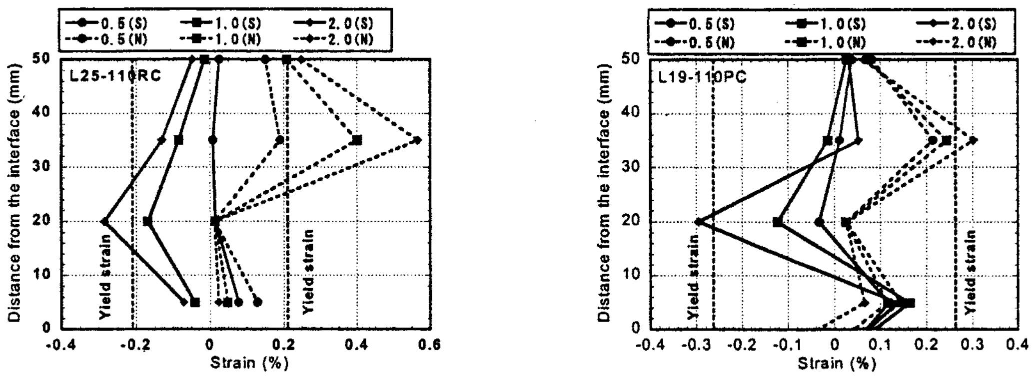

(a) L25-110RC (b) L19-110PC

Figure 5 Strain distribution along the bar

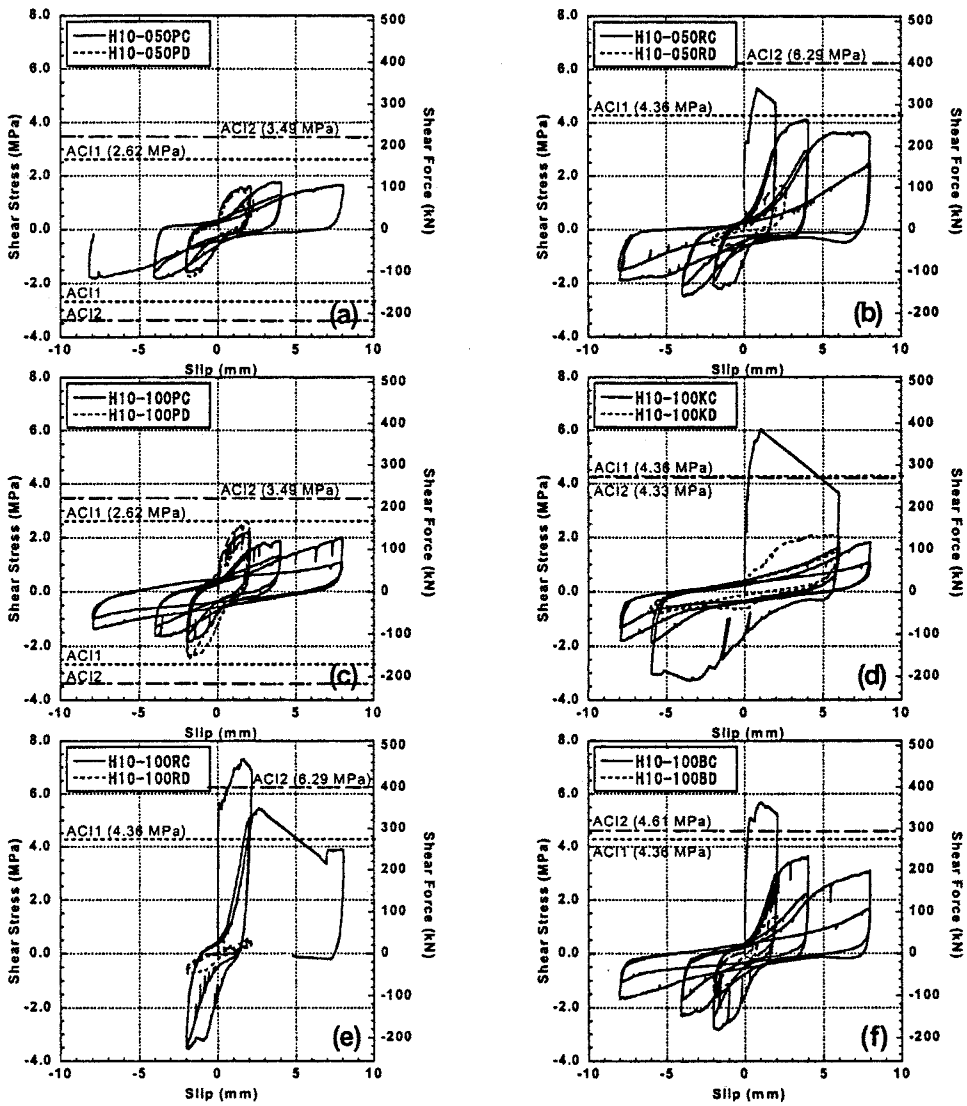

Figure 6 Shear stress and slip relations for specimens with D10 friction bars

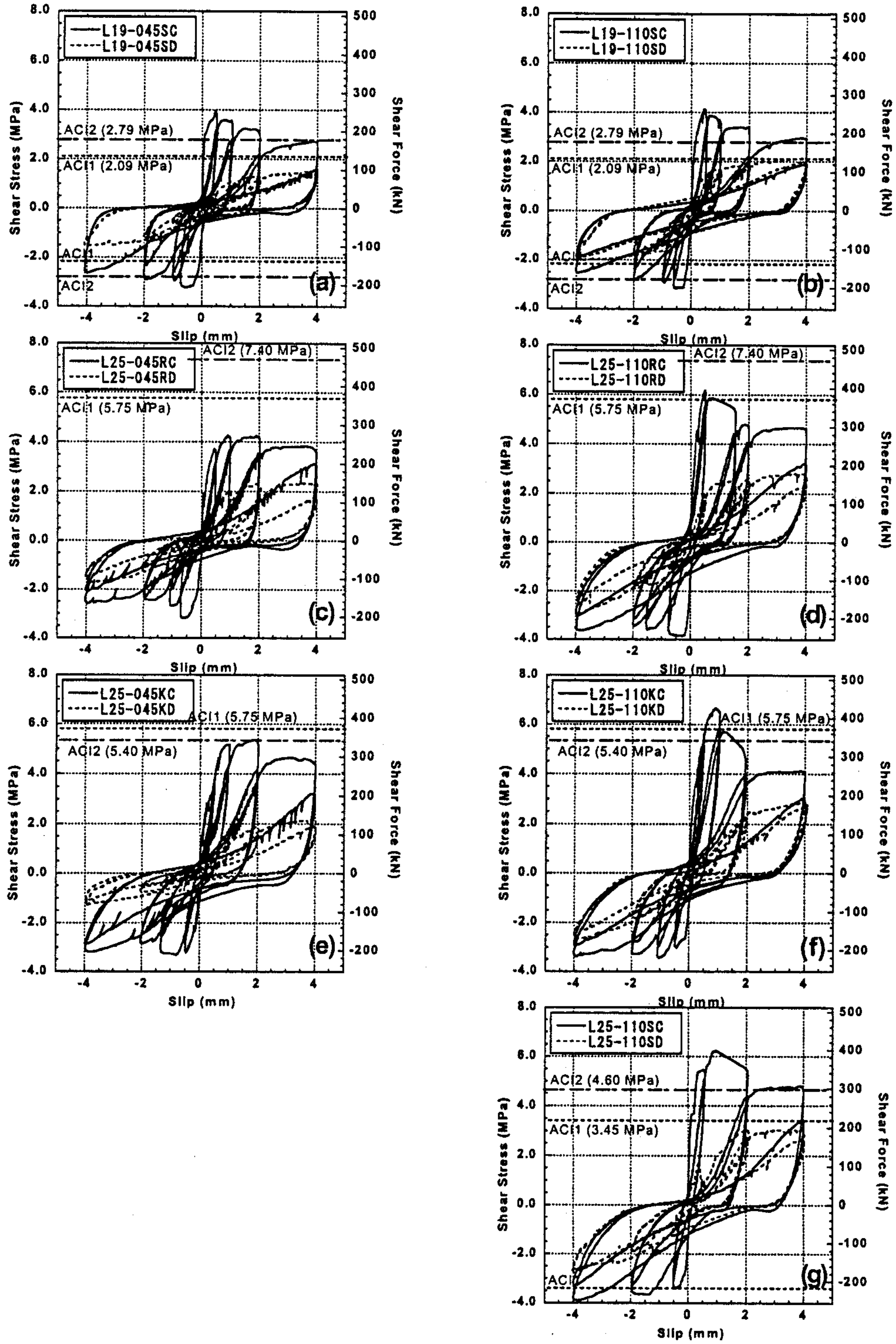

Figure 7 Shear stress and slip relations for specimens with D19 and D25 bars

the concrete action did not work and the dowel action was not enough to reach the shear capacity by itself. Specimens L25-045RC did not developed the enough concrete action as seen in Fig. 7(c).

Table 1 shows that shear capacity in the negative direction tends to be much smaller when the connection has roughened or keyed interface. It is not very surprising that the negative shear capacity becomes smaller after the shear capacity is reached at the positive side, which can be seen for H10-050RC, H10-100KC, H10-100RC, and H10-100BC, because mechanical interlocking is destructed in the positive direction. However, some specimens such as L25-110KC and L25-110SC also show much smaller negative shear stress for slip=-0.5 mm than the positive shear stress for slip=0.5 mm whereas the slip for the peak stress was 0.89 mm for L25-110KC and 0.95 mm for L25-110SC. Hence, the smaller negative shear stress happens even before the peak stress is reached in the positive direction. If earthquake force acts cyclically to the interface, it is not safe to count on the experimental results based on the monotonic loading test since the shear resistance in the direction opposite to the virgin direction could become smaller. This effect is pronounced for specimens with roughened or keyed interface and probably caused by wearing of the interlocking mechanism.

Contribution from concrete and dowel actions

Shear transfer is resisted by the concrete action and the dowel action as explained in the introduction. The variation of contribution of the concrete action can be computed from the test results using Eq. (3).

(Shear stress of combination type)
= (Shear stress of dowel type) + (Shear stress of concrete action) (3)

Equation 3 was applied at the reversing point of the first cycle for each prescribed displacement. The computed points were connected and shown in Figs. 8(c) and 9(c) for specimens with D19 or D25 reinforcement. The specimen designation has a letter "F" at the end although the specimens are fictitious and do not exist. Plots (a) and (b) are directly taken from the test results.

The contribution of the dowel action monotonically increases with the increase of slip but the contribution of the concrete action reaches the peak between 0.5 mm and 1.0 mm and decreases rapidly after the peak. A comparison between L19-045SC and L19-110SC shows that the concrete strength has slight influence on the dowel action and the concrete action when the surface condition is nearly smooth. However, when the surface is roughened or keyed, the contribution of the concrete action increases with the increase of the concrete strength.

Although it is not shown like Figs. 8 and 9, the contribution of concrete action for H10-050PC and H10-100PC is nearly zero and shear force is resisted by the dowel action only. Specimens with scratched surface, whose roughness looked closer to plain surface rather than roughened surface, show that the contribution of concrete action is nearly same as that with roughened surface. However, the former experiment by authors indicate that an incompletely scratched surface behaves like a plain surface. So the uncertainty is very large for the effect of surface roughness on the concrete action. Since the concrete action normally contributes to a great extent to the total shear resistance, an appropriate index representing surface roughness needs to be set in order to properly evaluate the contribution due to the concrete action.

The prediction of shear resistance from the dowel action is studied by Obuch et al. [7] in a good precision under a certain condition. Hence, establishing a good model for the concrete action is essential to the complete description of the shear friction mechanism. Since the results in Figs. 8 and 9 show that the concrete action and the dowel action is not independent but rather dependent on each other, these two actions need to be combined and analyzed together.

CONCLUSIONS

The interface shear transfer was investigated experimentally using direct shear tests. Shear stress transferred along the interface was separated into the contributions of concrete and dowel actions and the variation of those contributions with respect to slip displacement was

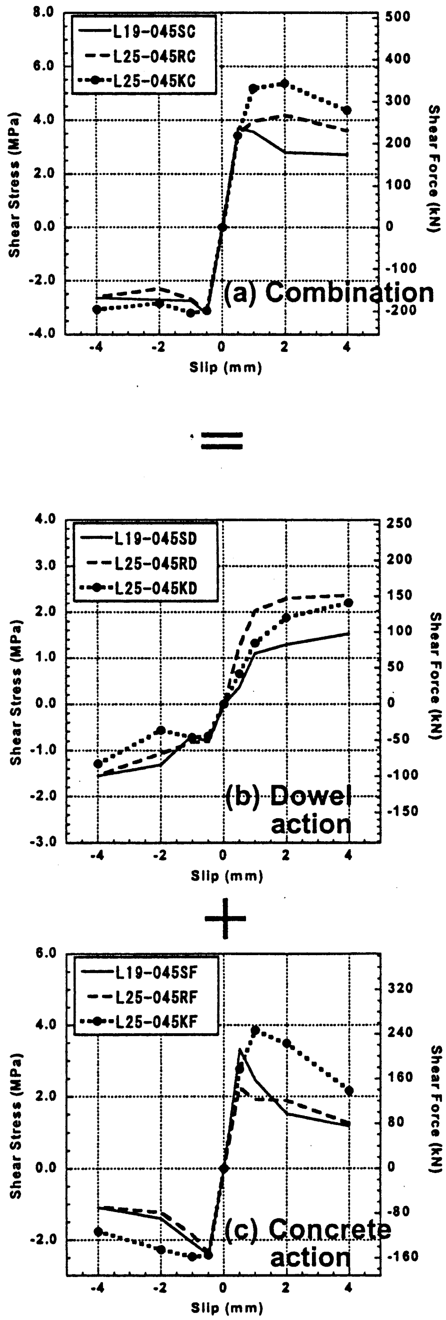

Figure 8 Contribution of mechanisms for f'c=45 MPa

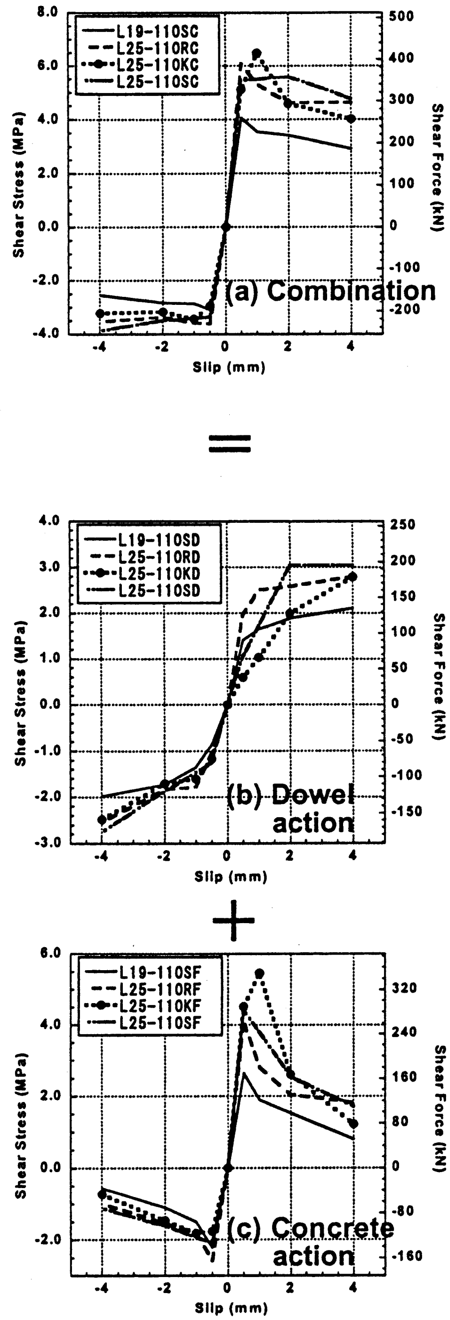

Figure 9 Contribution of mechanisms for f'c=110 MPa

discussed.

1. The flexural action dominates the shear-frictional reinforcement and the average tensile strain at the interface did not reach the yield strain at the peak stress. The assumption frequently used in many codes that reinforcement has yielded at the peak stress must be reconsidered.
2. Slips at the peak stress ranged from 0.19 mm to 2.03 mm accompanied by a same magnitude of opening. Type of shear-friction reinforcement, concrete, and surface condition had influences on these values.
3. With the increase of concrete strength, the shear capacity did not increase when the interface was smooth but increased dramatically when the interface was coarse. Hence the combined effect of concrete strength and surface roughness needs to be considered in a design equation.
4. If earthquake force acts cyclically to the interface, it is not always safe to count on the experimental results based on the monotonic loading test since the shear resistance in the direction opposite to the virgin direction could become smaller. This effect is pronounced for specimens with coarse interface and probably caused by the wearing of the interlocking mechanism.

ACKNOWLEDGMENTS

A part of this research was financially supported by Hirata Sadao Research Fellowship. The authors express their thanks to the former students N. Nagao and T. Kawanishi.

REFERENCES

1. ACI Committee 318 (1991), *Building Code Requirements for Reinforced Concrete*, American Concrete Institute, Detroit, MI.
2. Architecture Inst. of Japan (1982), "Standard for Structural Calculation of Prefabricated RC Structures with Shear-Walls." (In Japanese)
3. Walraven, J., Frenay, J., and Pruijssers, A. (1987), "Influence of Concrete Strength and Load History on the Shear Friction Capacity of Concrete Members," *PCI Journal, Jan.-Feb.*, pp. 66-84.
4. Mattock, A.H. (2001), "Shear Friction and High-Strength Concrete," *ACI Structural Journal, Vol. 98, No. 1, Jan.-Feb.*, pp. 50-59.
5. Dulacska, H. (1972), "Dowel Action of Reinforcement Crossing Cracks in Concrete," *ACI Journal, Dec.*, pp. 754-757.
6. Okamoto, H. et al. (1990-1992), "Shear Transfer between High Strength Precast and Cast-in-situ Concrete," *Summaries of Technical Papers of Annual Meeting, Architecture Institute of Japan*, pp. 539-540(1990), pp. 679-680(1991), pp. 773-774(1992). (In Japanese)
7. Obuchi, H. et al. (1997), "Study on shear transfer considering shear displacement in connection of precast concrete," *J. of Struct. and Constr. Eng.*, Architecture Inst. of Japan, No. 491, Jan., pp. 97-104. (In Japanese)
8. Kono, S. and Tanaka, H. (2000), "Interface shear transfer for high strength concrete and high strength reinforcement," *12th World Conference on Earthquake Engineering*, No. 641, Auckland.
9. Ali, M. A. and White, R.N. (1999), "Enhanced Contact Model for Shear Friction of Normal and High-Strength Concrete," *ACI Structural Journal, V. 96, No. 3, May-June,* pp. 348-360.
10. Mattock, A.H. and Hawkins, N.M. (1972), "Shear Transfer in RC Recent Research," *PCI Journal, March-April,* pp. 55-75.
11. Valluvan, R., Kreger, M.E., and Jirsa, J.(1999), "Evaluation of ACI 318-95 Shear-Friction Provisions," *ACI Structural Journal, Vol. 96, No. 4, July-Aug.*, pp. 473-481.

DISPLACEMENT-HISTORY EFFECTS ON THE DRIFT CAPACITY OF REINFORCED CONCRETE COLUMNS

S. Pujol[1]

ABSTRACT

Results from sixteen tests of reinforced concrete columns under different load histories are presented. It is concluded that the maximum drift that can be reached by a given column depends not only on the properties of the column but also on the displacement history.

1. INTRODUCTION

There is limited data on displacement-history effects for columns whose response may be dominated by shear. Probably for this reason, current analytical models (Aoyama 1993, Moehle et al. 2000, Priestley et al. 1994, FEMA 273 1997, Aschheim 2000) do not consider displacement history as a variable. A series of tests was designed to determine whether displacement history affects the drift capacity of reinforced concrete columns under inelastic displacement reversals (Pujol 2002). The results from these tests and their analyses are limited to cases where 1) drift cycles occur primarily in the plane defined by one of the principal axes of the cross section, 2) the drift capacity is not less than the drift at yield, 3) the maximum shear exceeds the shear at inclined cracking, 4) the "static" shear capacity is not less than the shear at yield, 5) the column core is effectively confined by transverse reinforcement, and 6) longitudinal reinforcement is restrained against buckling by transverse reinforcement.

2. EXPERIMENTAL PROGRAM

2.1 Specimen Geometry, Test Set-Up, and Displacement History

The experimental program included eight test assemblies (Table 1). An assembly consisted of two test specimens joined by a center stub. Each specimen was intended to represent a cantilever column under constant axial load and a point transverse load applied at its end. The center stub was intended to act as the base of the cantilevers. All assemblies were tested while simply supported. Transverse load was applied through the middle stub. Axial load was applied

[1] WJE Associates, 2200 Powell St., Suite 925, Emeryville, CA 94608. E-mail: spujol@wje.com
This study was developed at, Purdue University, School of Civil Engineering, West Lafayette, IN 47907.

through external post-tensioning rods. Fig. 1 shows the loading setup. The variables controlled in the experiments were the spacing of the hoops outside the center stub, the axial load (constant in each test), and the displacement schedule. Fig. 2 shows the dimensions of a typical test assembly.

The ranges of the variables considered were:

Maximum nominal unit shear stress $V/(b\,d\sqrt{f'_c})$	:	6 to 8 (stresses in psi)
Maximum core unit shear stress, $V/(A_c\sqrt{f'_c})$	:	10 to 13 (stresses in psi)
Axial load, P	:	0.08 to 0.21 $f'_c\,A_g$ (30 to 60 kips)
Transverse reinforcement ratio, $A_w/(b\,s)$	:	0.6% to 1.1%
Nominal unit transverse stress, $A_w f_{yw}/(b_c\,s)$	:	500 to 1000 psi
Maximum drift ratio, γ_{max}	:	3% to 4%

Where V is maximum shear force, b is cross-sectional width, d is effective depth, A_w is total cross-sectional area in a layer of transverse reinforcement, f_{yw} is transverse reinforcement unit yield stress, b_c is concrete core cross-sectional width (center-to-center of exterior transverse reinforcement), A_c is concrete core cross-sectional area (center-to-center of exterior transverse reinforcement), and s is hoop spacing.

The constants in the experiments were: concrete compressive strength (f'_c ,4.1 to 5.2 ksi), longitudinal reinforcement unit yield stress (f_y=65.7 ksi), longitudinal reinforcement ratio (ρ=2.4%), ratio of shear span a, to effective depth (d=2.7), and ratio of gross cross-sectional area to core area (A_g/A_c=2.0). The complete experimental program, including the displacement history for each test assembly described in terms of maximum drift ratio, is presented in Table 1. Relative rotation, or drift ratio, is defined in Fig. 3. The rotation of only one of the two specimens per test assembly could be controlled. As the tests progressed, damage, stiffness reduction, and rotation concentrated in one of the two cantilevers in each test assembly. The displacement at mid-span was controlled so that the larger of the two specimen rotations did not exceed the target maximum drift ratio. Relative-rotation targets were 1%, 2%, 3%, and 4%. All assemblies were designated using three numerals: the first numeral indicates the level of axial load as a percentage of the product f'_cA_g (where f'_c is the compressive strength of the concrete and A_g is the gross cross-sectional area), the second numeral indicates the maximum drift ratio reached during the initial displacement cycles, and the last numeral is the hoop spacing in inches. All tests were carried out until a reduction in average lateral stiffness of 50% or more was observed. Average stiffness is defined here as the slope of the line joining the peaks of the shear-drift ratio curve for a given cycle.

2.2 Materials

All test assemblies were fabricated using normal weight concrete (3/4 in. maximum aggregate size). Table 2 lists relevant mechanical properties of the concrete used. No.6 (3/4 in. diameter) A706 reinforcing bars were used as longitudinal reinforcement. Transverse reinforcement in each specimen was made out of No.2 (1/4 in. diameter) plain steel bars whose surfaces were roughened by rusting following the procedure described by Moehle (1980). Transverse reinforcement in the center stub was made with standard Grade 60 No. 3 (3/8" diameter) deformed bars. Table 3 shows the main properties of the reinforcement. Unit strain values in Table 3 include measurements made by two means: Measurements Group type EA-06-250BF-350 electrical strain gages and an MTS 634.25E-54 extensometer with a 2-in. gage length.

2.3 Data Collection

Measurements taken during the tests included: transverse and axial load, deflections, rotations, unit strains in the transverse and longitudinal reinforcement, deformations of the concrete surface, and crack widths. Electronic Whittemore gages were used to measure the changes in the distance between steel discs epoxy-glued to the concrete surface on one side of each test assembly. The mesh of reference points attached to the concrete is shown in Fig. 4.

3. TEST RESULTS

Figures 5 to 12 show shear-drift ratio curves recorded for the specimens where rotation and damage concentrated. Values of drift ratio were corrected for rotation of the joint as described in Fig. 3. Positive loads and rotations correspond to downward deflections (see Fig. 1 for reference).

All specimens developed inclined cracks before yielding of the longitudinal reinforcement. All specimens reached their full flexural capacity and developed inelastic deformations. Yielding was observed at a drift ratio of approximately 1%. Maximum nominal shear stresses ranged from 6 to $8\sqrt{f'_c}$ (f'_c in psi units). Fig. 13 shows specimens 10-3-3 at the end of the test, after all loose concrete was removed. Total disintegration of the concrete core was observed in all tests except for specimens 20-3-1½ where buckling of the reinforcement in the center stub caused a premature failure. The results from specimens 20-3-1½ are not included in the following discussions about load-history effects.

Comparisons between the responses of the test specimens can be made more conveniently in terms of average stiffness. Average stiffness is defined here as the slope of the line joining the peaks of the shear-drift ratio curve for a given cycle. For cycles of displacement in the inelastic range, the responses of the specimens were never stable. Stiffness decay with increasing number of cycles was always present for cycles at drift ratios larger than 1%, the drift ratio at yield. The rate at which average stiffness decreased increased with increasing number of displacement cycles. The final rate of stiffness decrease varied depending on the level of axial load. The higher axial load caused more abrupt stiffness loss during the final displacement cycles. The rate at which stiffness decreased with increasing number of cycles also varied depending on the spacing of the hoops in the columns. The smaller the hoop spacing, the larger was the number of cycles that could be sustained at a given maximum drift ratio.

Two series of experiments were carried out to study whether displacement history has an effect on drift capacity (specimens 10-2-3 and 10-3-3, and specimens 10-1-2¼, 10-2-2¼, and 10-3-2¼). In each series, similar specimens were subjected to different displacement histories. Specimens 10-1-2¼, 10-2-2¼, and 10-3-2¼ were subjected to the same axial load (30 kips) and had the same reinforcement details (2¼ in. hoop spacing). All three sets of specimens were tested at a drift ratio of 3%. Specimens 10-3-2¼ were displaced directly to a drift ratio of 3%. Specimens 10-1-2¼ were subjected to 7 cycles at a drift ratio of 1% (approximately the drift ratio at yield) and specimens 10-2-2¼ were subjected to 7 cycles at a drift ratio of 2% before application of cycles at 3%. The variation in average stiffness recorded for the specimens that failed in these assemblies is shown in Fig. 14. It can be seen that the damage caused by cycles at a drift ratio of 2% affected the response at 3%. On the other hand, damage caused by cycles at 1% did not accelerate the loss of stiffness with cycles at 3%. Stiffness loss during the final cycles applied to specimen 10-3-2 ¼ North occurred at a rate that was even higher than the final rate of stiffness reduction for specimen 10-1-2¼ South. This may be due to the lower strength of the concrete in specimens 10-3-2¼ (Table 2). Similarly, specimens 10-2-3 and 10-3-3 had the same axial load (30 kips) and the same amount of transverse reinforcement (3-in. hoop spacing) but were tested under different displacement histories. Specimens 10-2-3 were subjected to 7 cycles at a drift ratio of 2% before being tested at 3%. On the other hand, specimens 10-3-3 were tested directly at 3%. Again, the damage produced by cycles at 2% drift ratio caused the stiffness decrease with cycles at 3% to accelerate (Fig. 15). These observations indicate clearly that displacement history affected response under cyclic loading: the number of cycles that could be sustained at a given maximum drift ratio decreased with increasing number and amplitude of previous cycles in the inelastic range of response. The numbers of the cycles at which a relative reduction in average stiffness of 20% was observed are listed in Table 4.

3.1 Transverse Deformations

The relative movement between reference points at three different cross-sections was measured using Whittemore gages. These cross-sections will be referred to using numbers that increase sequentially from the base to the end of the specimens (Fig. 16). Section 1 is at 4 in. from the base. Sections 2 and 3 are at 8 and 16 in. from the base, respectively. Fig. 16 shows the sectional depth change at cycle peaks measured at sections 1, 2 and 3 for specimen 10-1-2¼ South. Extensions are plotted as positive values. The data indicate that, for specimen 10-1-2¼ South, cycles at a drift ratio of 1% did not cause continuous accumulation of transverse strains with increasing number of cycles. Cycles at larger drift ratios did cause accumulation of transverse strains. This continuous enlargement of the cross sections near the column base was observed in all the tests. Large transverse strains were associated with rapid stiffness decrease. In fact, stiffness loss of more than 20% was consistently measured only after transverse deformations larger than 0.25 in. (3% average unit strain) had taken place. This is illustrated in Fig. 17 and Table 4. This observation ties the overall response of a specimen under any given loading pattern to a single and easily identifiable variable: transverse deformation. A model for column drift capacity based on the observed relationship between stiffness reduction and transverse deformation is presented elsewhere (Pujol, 2002).

4. CONCLUSIONS

On the basis of the experimental data and their analyses, the following conclusions are made:

- Displacement cycles at drift ratios not exceeding the drift ratio at yield do not affect the drift capacity of a reinforced concrete column.
- Column drift capacity was found to be sensitive to displacement history. For columns cycled beyond yield, it decreases as a function of the amplitude and number of cycles the column has experienced.
- Column stiffness decreases with increasing number of cycles at drift ratios exceeding the drift ratio at yield. The reduction in stiffness exceeds 20% after transverse unit strains exceed 3%.

5. ACKNOWLEDGMENTS

The study presented was guided by Professors Mete A. Sozen and Julio Ramirez at Purdue University. The writer would like to express his deepest gratitude for their help, guidance and support.

6. REFERENCES

Aoyama, H. (1993). Design Philosophy for Shear in Earthquake Resistance in Japan. Earthquake Resistance of Reinforced Concrete Structures. Ed. Tsueno Okada. pp. 140-151.

Aschheim, M. (2000). Towards Improved Models of Shear Strength Degradation in Reinforced Concrete Members. *Structural Engineering and Mechanics.* Vol. 9. No. 6. pp. 601-613.

FEMA 273. (1997). Guidelines for the Seismic Rehabilitation of Buildings. NEHRP. Federal Emergency Management Agency. Washington DC.

Moehle, J. P., K. J. Elwood, and H. Sezen. (2000). Gravity Load Collapse of Building Frames During Earthquakes. M. Uzumeri Symposium. Special Publication. American Concrete Institute.

Moehle, J. P., and M. A. Sozen. (1980). Experiments to Study Earthquake Response of R/C Structures with Stiffness Interruptions. Structural Research Series No. 482. University of Illinois.

Priestley, M. J. N., R. Verma, and Y. Xiao. (1994). Seismic Shear Strength of Reinforced Concrete Columns. *ASCE Journal of Structural Engineering*. Vol. 120. No. 8. pp. 2310-2329.

Pujol, S. (2002). Drift Capacity of Reinforced Concrete Columns Subjected to Displacement Reversals. Ph.D. Thesis. Purdue University. West Lafayette. Indiana.

7. TABLES

Table 1 Experimental program.

Test Assembly	Hoop Spacing	Axial Load	No. of Cycles at Drift Ratio 1%	2%	3%	4%
	[in.]	[kip]				
10-2-3	3	30	0	7	7	0
10-3-1½	1½	30	0	0	7	11
10-3-3	3	30	0	0	9	0
10-3-2¼	2¼	30	0	0	19	0
20-3-1½	1½	60	0	0	7	10
20-3-3	3	60	0	0	9	0
10-2-2¼	2¼	30	0	7	16	0
10-1-2¼	2¼	30	7	0	20	0

Table 2 Mechanical properties of the concrete.

Assembly	Age	Compressive Strength (6x12in Cylinders) Samples	Average	Compressive Strength (4x8in Cylinders) Samples	Average	Tensile Strength (Split Cylinders) Samples	Average	Tensile Strength (Flexure Beam) Samples	Average	Modulus of Elasticity
	[days]		[psi]		[psi]		[psi]		[psi]	[psi]
10-2-3	285	3	4890	2	4470	3	460	3	820	4.15E+06
10-3-1½	334	3	4660	0	---	3	480	3	820	3.88E+06
Rounded Average			4800				470		820	4.02E+06
10-3-3	72	3	4340	0	---	3	440	2	800	3.78E+06
10-3-2¼	152	3	3970	3	3670	3	410	3	780	3.48E+06
20-3-1½	212	3	3980	0	---	3	440	2	800	3.41E+06
Rounded Average			4100				430		790	3.56E+06
20-3-3	54	3	5280	0	---	3	530	3	800	4.35E+06
10-2-2¼	80	3	5060	0	---	3	530	3	860	4.27E+06
10-1-2¼	106	3	5290	0	---	3	510	3	830	4.35E+06
Rounded Average			5200				520		830	4.32E+06

Note: All stresses calculated using nominal areas

Table 3 Mechanical properties of the steel.

		Modulus of Elasticity Based on Readings from		Yield Stress	Start of Strain Hardening Strain		Ultimate Stress
		Gage	Extensometer		Gage	Extensometer	
Bar Diameter	Coupon	ksi	ksi	ksi	Strain x 1E-6	Strain x 1E-6	ksi
3/4 in.	1	---	28,850	65.6	---	7,400	93.0
	2	27,600	28,350	66.0	10,000	7,500	93.6
	4	26,560	28,680	65.6	10,000	7,600	93.0
Rounded Average		27,100	28,600	65.7	10,000	7,500	93.2
1/4 in.*	1	---	31,110	60.2	---	14,900	76.6
	2	---	32,940	57.0	---	16,200	75.2
	3	30,170	32,420	60.0	---	17,000	76.4
	4	31,430	31,180	61.0	17,500	16,400	77.4
Rounded Average		30,800	31,900	59.6	17,500	16,100	76.4

All stresses calculated based on nominal areas.
* Maximum measured deviations from nominal diameter: ±0.005 in.

Table 4 Experimental results.

Test Assembly	Cycle # at 20 % or Larger Stiffness Decrease	Cycle # at 1/4-in. or Larger Transverse Deformation
10-2-3	12	11
10-3-1½	17	>10
10-3-3	7	6
10-3-2¼	15	15
20-3-1½	>16	>16
20-3-3	8	7
10-2-2¼	19	16
10-1-2¼	22	21

8. FIGURES

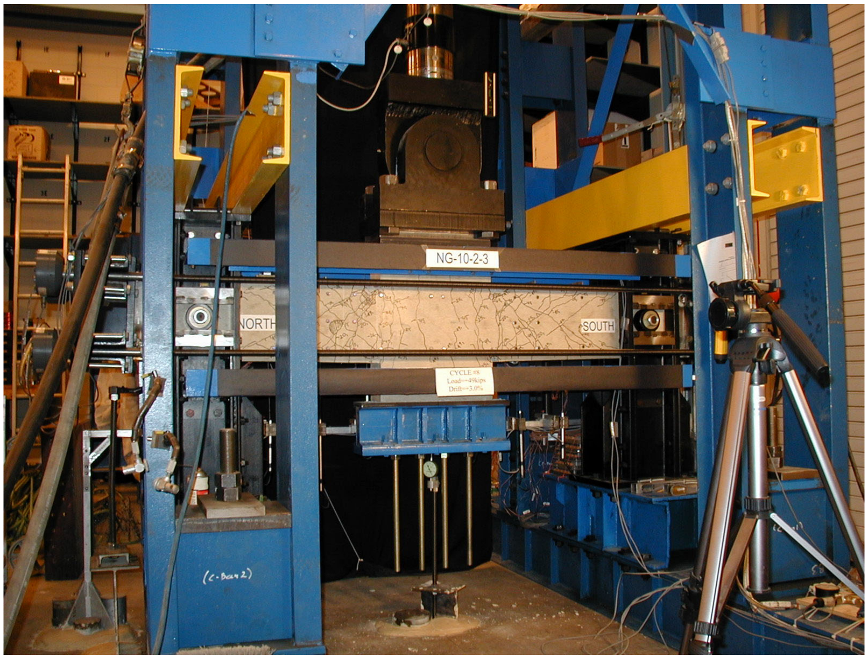

Figure 1 Test setup.

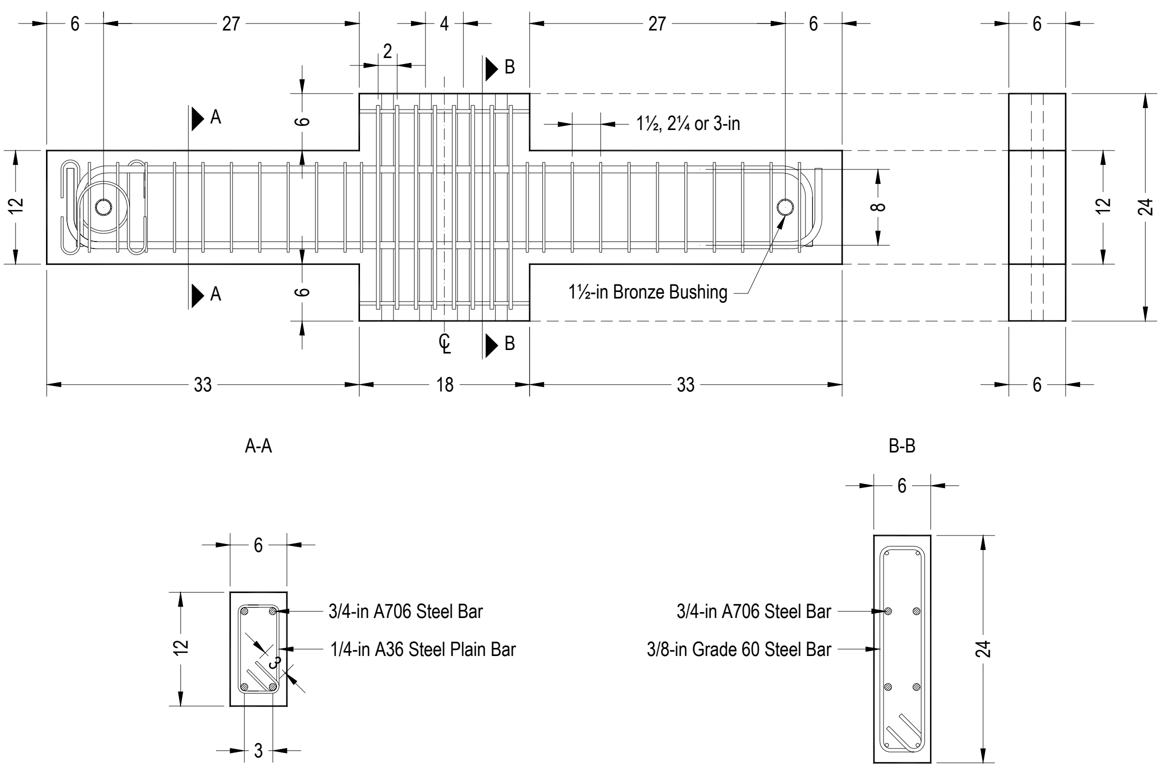

Figure 2 Test Assembly: nominal dimensions (in inches) and reinforcement details.

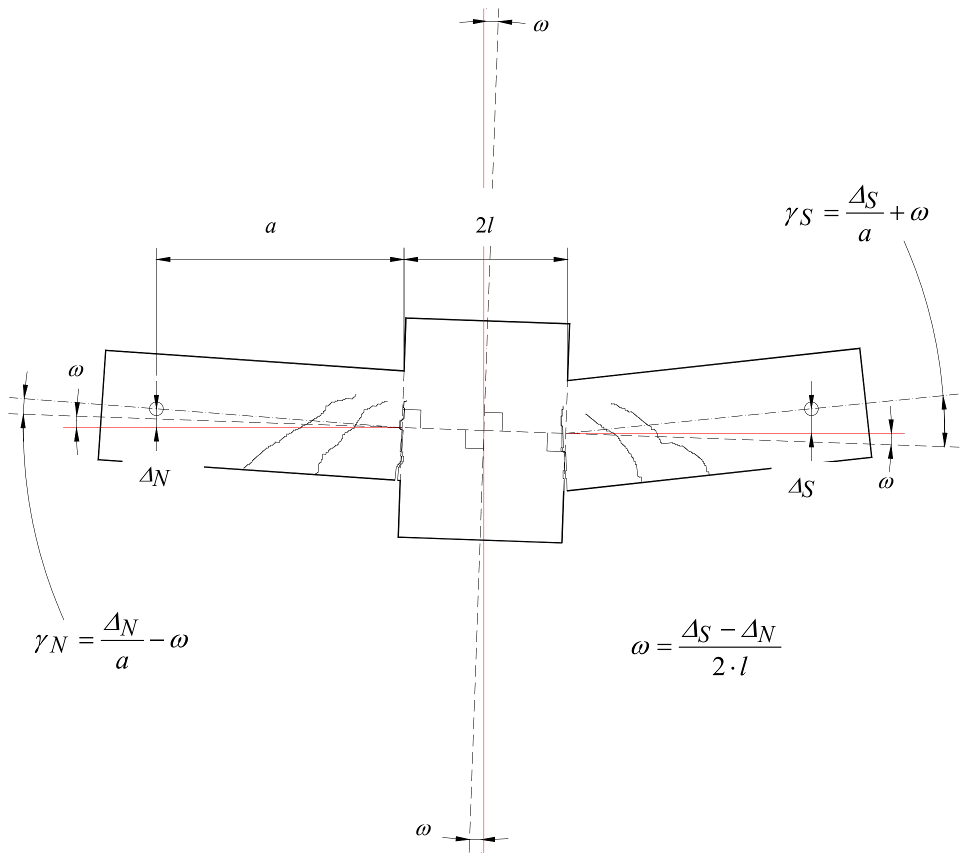

Figure 3 Definition of relative rotation or drift ratio.

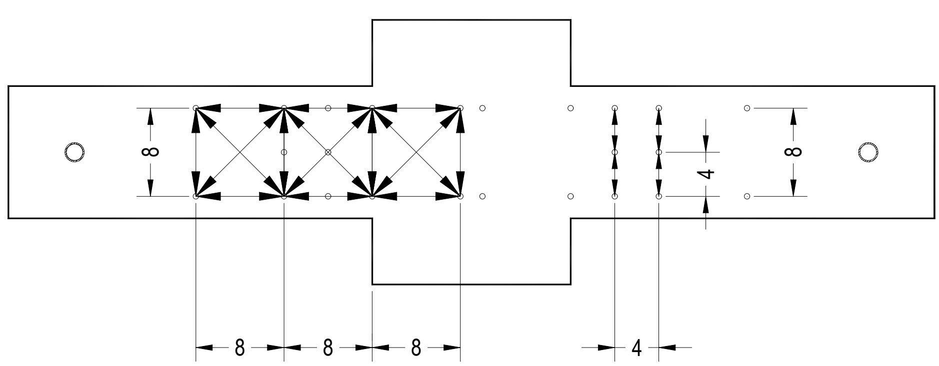

Figure 4 Mesh of Whittemore reference points (dimensions in inches).

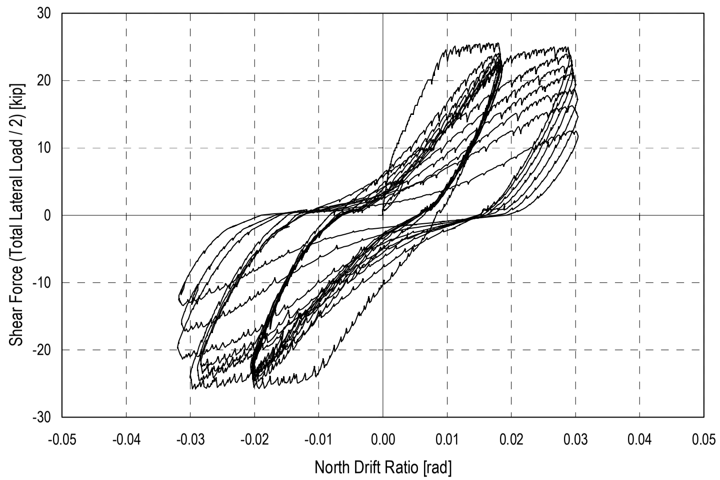

Figure 5 Shear-drift ratio response, specimen 10-2-3 North.

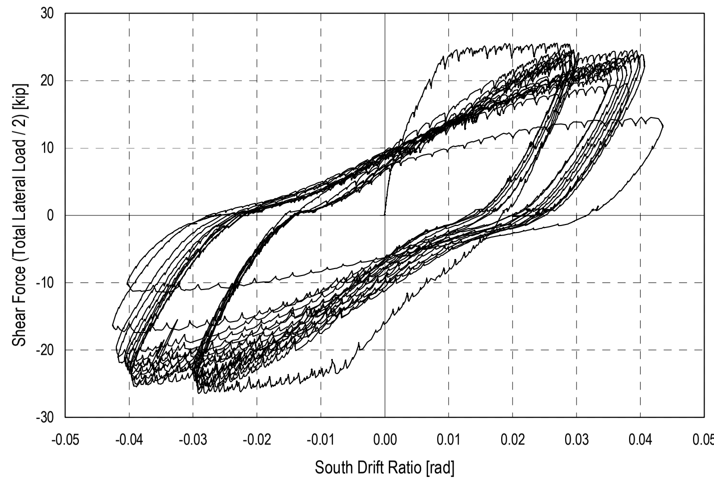

Figure 6 Shear-drift ratio response, specimen 10-3-1½ South.

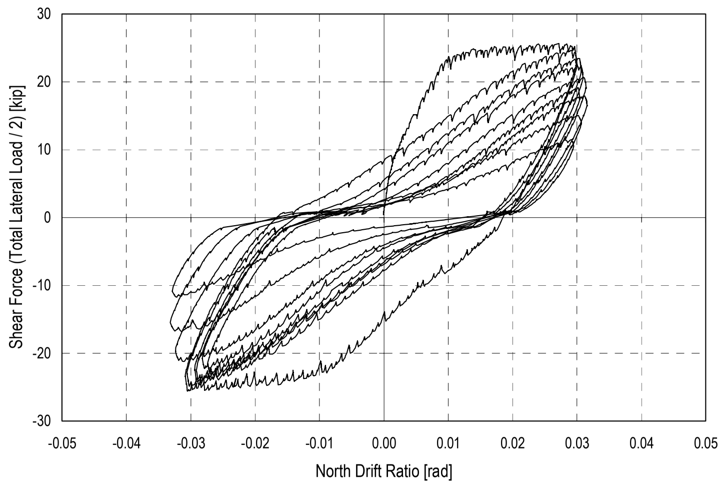

Figure 7 Shear-drift ratio response, specimen 10-3-3 North.

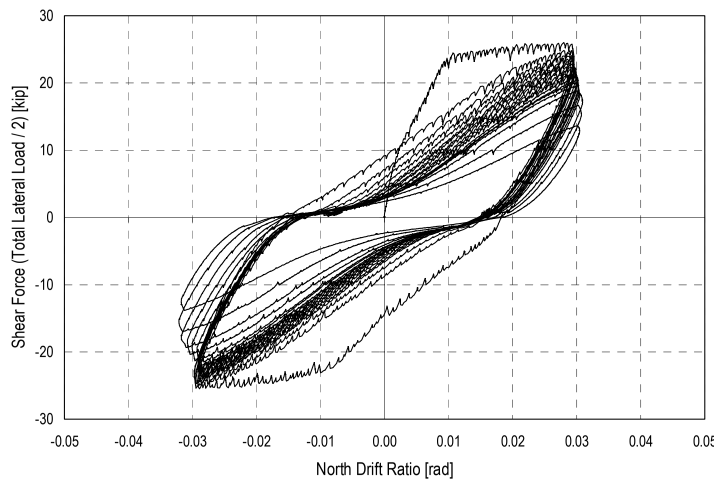

Figure 8 Shear-drift ratio response, specimen 10-3-2¼ North.

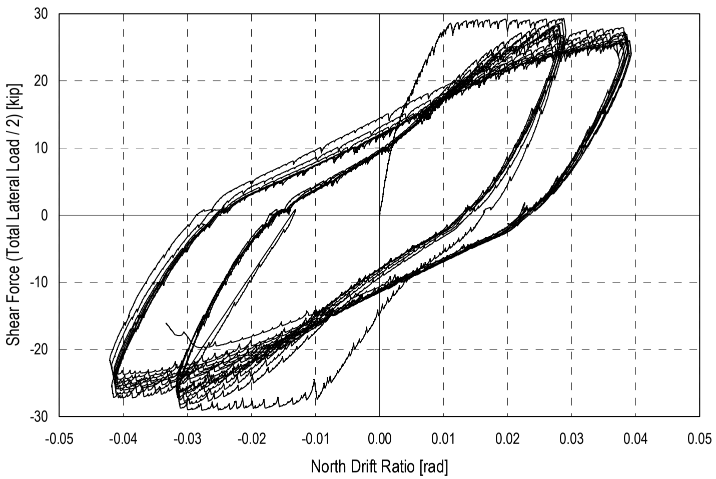

Figure 9 Shear-drift ratio response, specimen 20-3-1½ North.

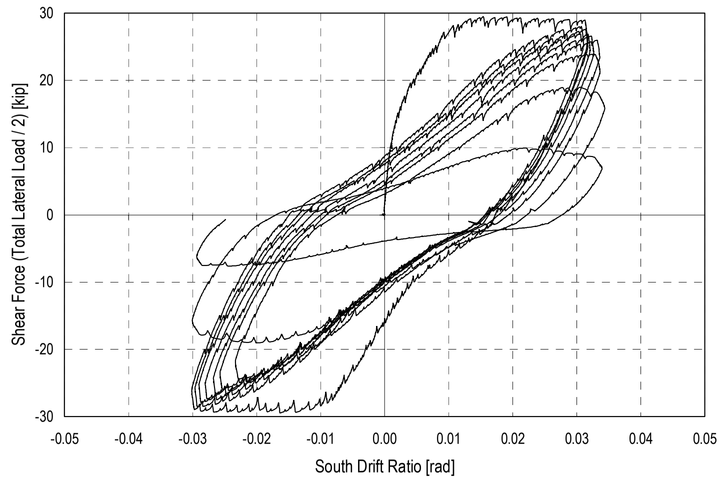

Figure 10 Shear-drift ratio response, specimen 20-3-3 South.

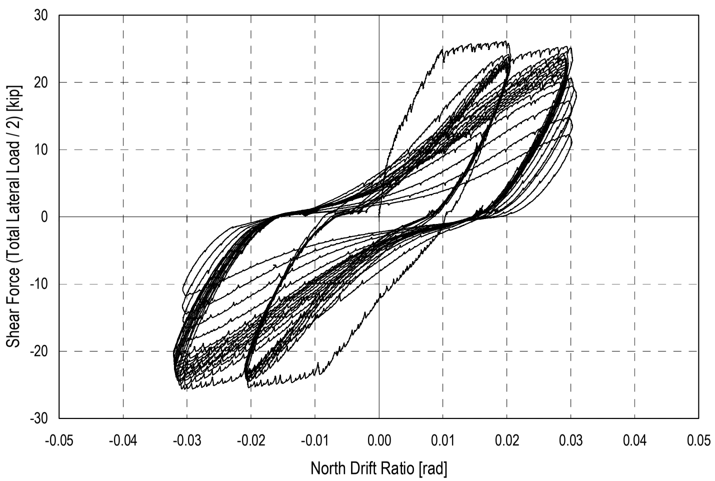

Figure 11 Shear-drift ratio response, specimen 10-2-2¼ North.

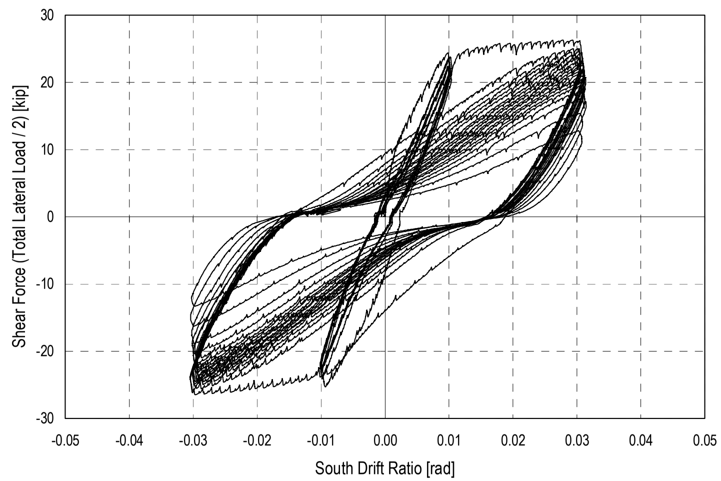

Figure 12 Shear-drift ratio response, specimen 10-1-2¼ South.

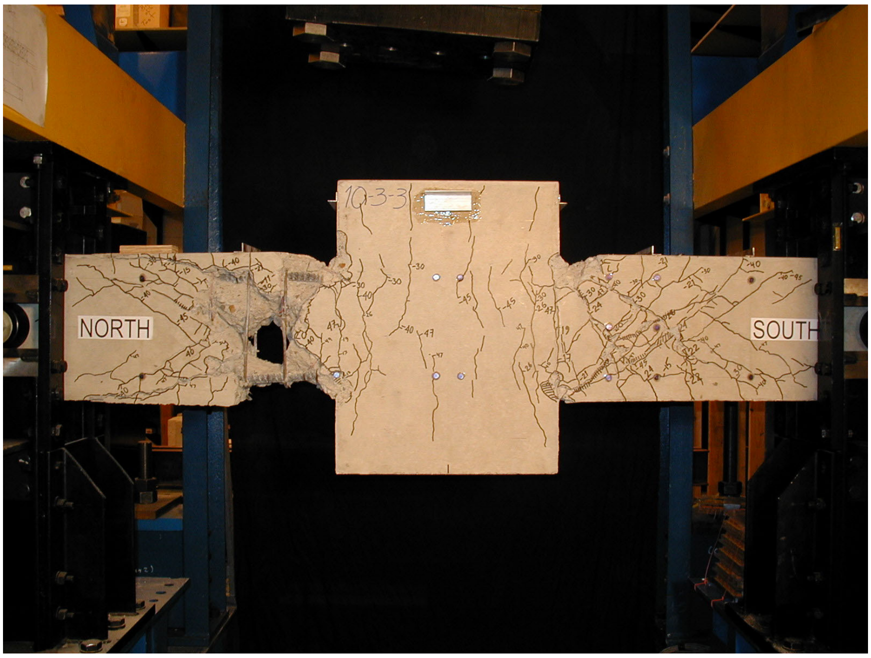

Figure 13 Specimens 10-3-3 at the end of the test, after removal of loose concrete.

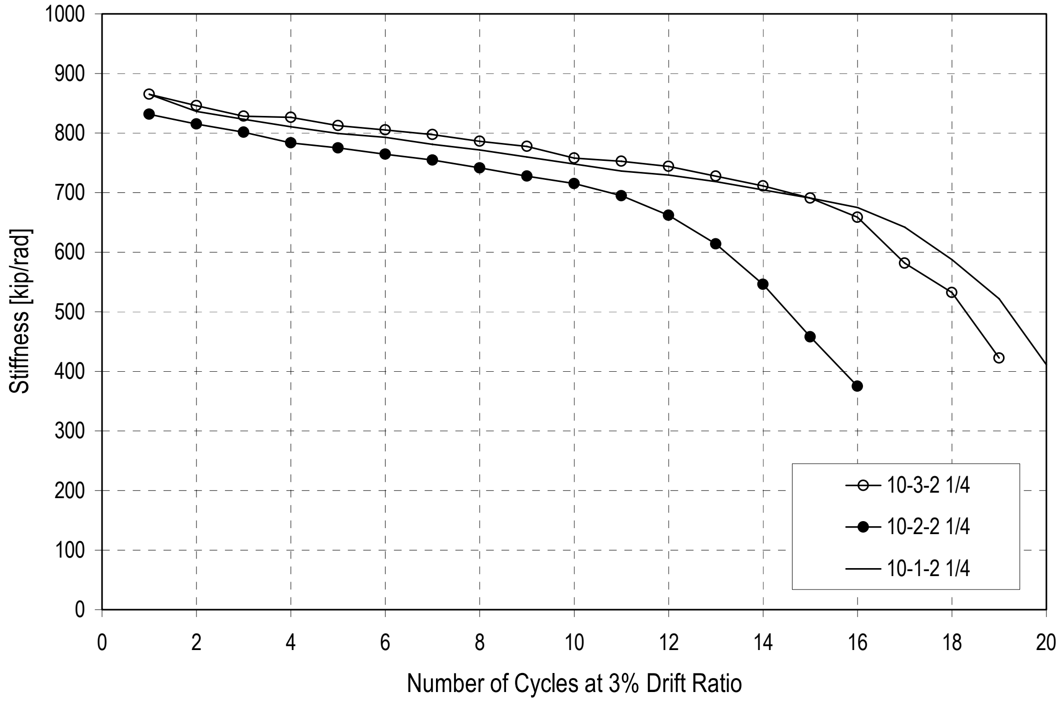

Figure 14 Average stiffness during cycles at 3% drift ratio for specimens 10-3-2¼ North, 10-2-2¼ North, and 10-1-2¼ South.

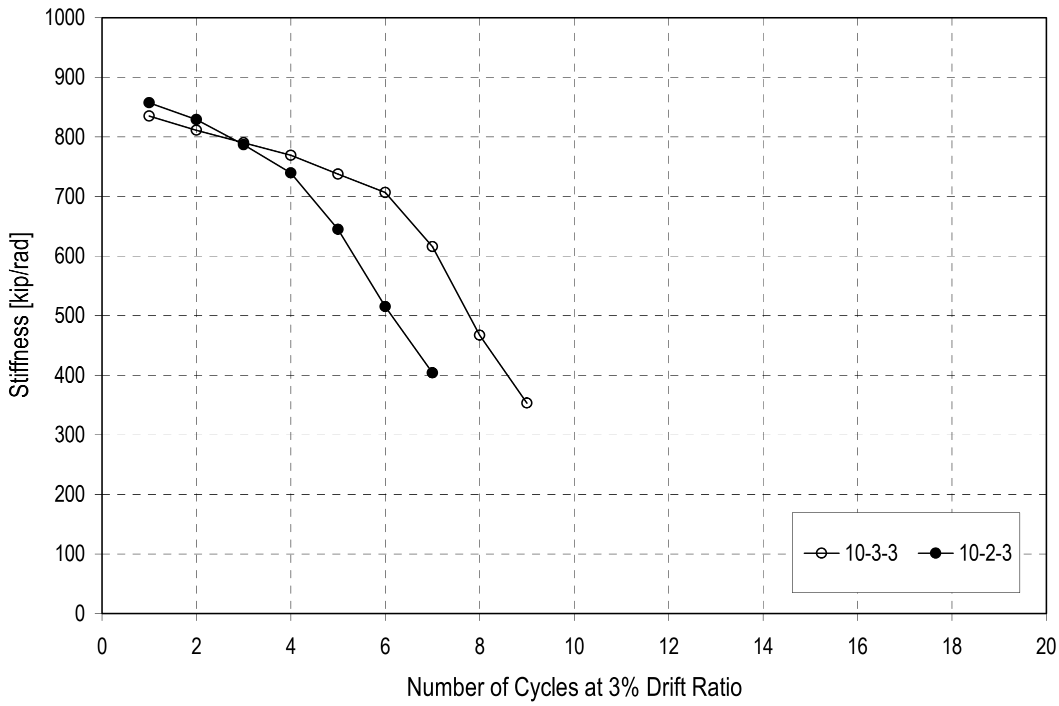

Figure 15 Average stiffness during cycles at 3% drift ratio for specimens 10-3-3 North, and 10-2-3 North.

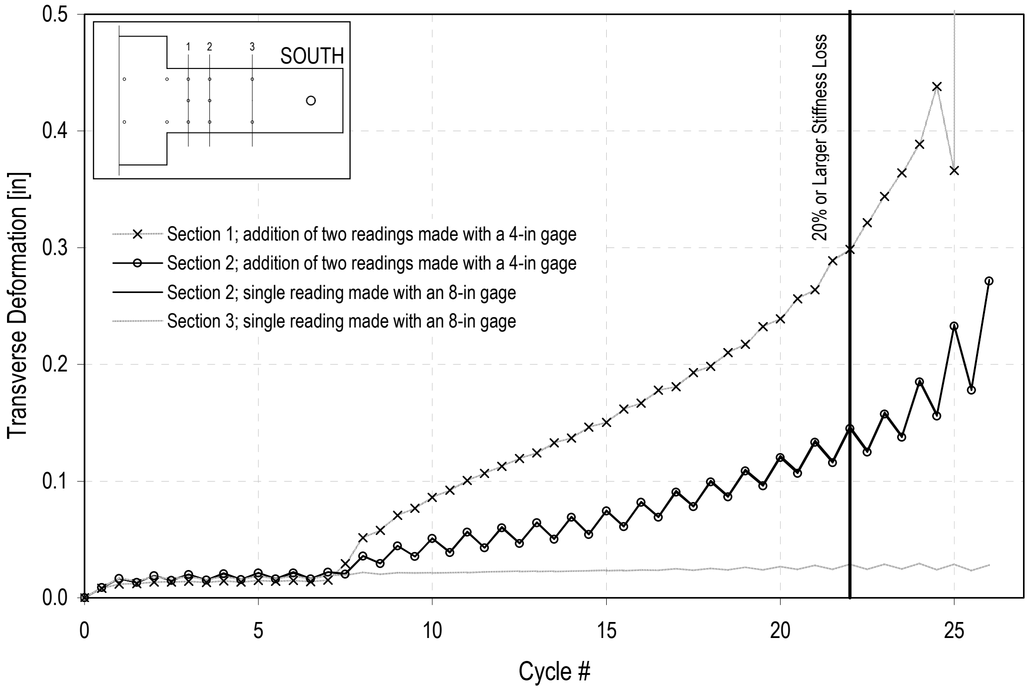

Figure 16 Transverse deformations, specimen 10-1-2¼ South.

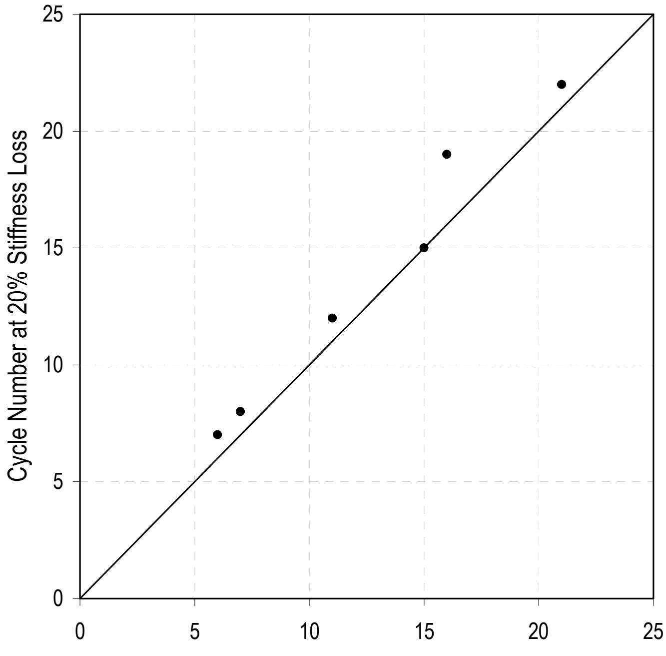

Figure 17 Experimental results.

SESSION B-3: BEAM-COLUMN JOINTS

Chaired by

♦ Hitoshi Tanaka and Yan Xiao ♦

Evaluation of Anchorage Strength of Beam Main Bars Anchored Mechanically in R/C Exterior Beam-Column Joints

A. TASAI [1] , T. KIYOHARA[2] and S. KATO[3]

ABSTRACT

The equation to estimate the mechanical anchorage strength for side cover splitting failure was improved based on the recent test data in Japan. Effect of anchorage length and distance between compressive and tensile resultants at critical section were considered in the equation, in addition to the effects of bearing area of anchorage plate, cover thickness of concrete, and lateral reinforcement in a joint. The equation predicted the mechanical anchorage strength appropriately.

1. INTRODUCTION

Mechanical anchorage method of beam main bars in exterior beam column joints has been diffused practically in Japan, especially in case of high-rise reinforced concrete buildings. The anchorage strength is usually estimated for the side cover splitting near the anchorage end plate by the equation, which was proposed in the New RC project in Japan (Murakami, Kubota, et al, 1993). The equation was obtained by regression from pull-out test results in consideration for some variables which affected pull-out strength. However, the equation imposes a restriction, because the effect of the anchorage length is not included in the equation.

---

1 Dept. of Architecture and Building Science, Faculty of Engineering, Yokohama National University, Yokohama 240-8501, Japan

Email: tasai@arc.ynu.ac.jp

2 Horie Engineering and Architectural Research Institute Co., Ltd., Tokyo 136-0073, Japan

Email:kiyoppy@m8.ffn.ne.jp

3 Master of Yokohama National University, Yokohama 240-8501, Japan

Email:s-kato@kajima.com

In this paper, in order to improve the equation, factors to influence the side cover splitting failure in the joint around the mechanically anchored beam main bars were investigated based on a new database which was made by referencing recent many test results in Japan. An equation for an anchorage strength of conventional bent-up rebar in a joint (Fjii and Morita, 1991) was used as reference as the improved equation.

2. INVESTGATED TEST DATA

In the database, test results of 148 pull-out specimens, which were reported from 1992 to 2001 in Japan, are included. The specimens were commonly loaded as simulating the condition of resultants in an exterior beam column joint, as shown **Fig.1**. The anchorage length ℓ_d was defined as a distance between a column face and an anchorage end plate of beam bars. The side cover thickness C_0 was defined as a distance between a center of the outer rebar and a column side surface.

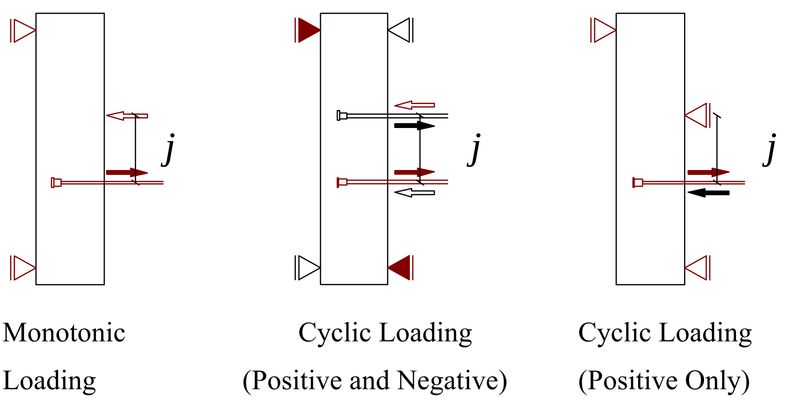

Fig. 1 Adopted Pull-out Tests in the Data-Base (j : Distance between Resultants)

According to the description in each paper, eighty five specimens failed in side cover splitting, twenty specimens in corn shape failure, fourteen specimens in joint failure, and fifteen specimens in fracture of rebar. The eighty-five specimens failed in the side cover splitting were adopted in the database to derive a new equation to estimate the anchorage strength. The reported maximum load of each specimen was identified as the anchorage strength.

3. DERIVATION OF EQUATION

3.1 Constitution of Equation

Investigation for test results of the eighty-five specimens revealed that the following five factors influenced the mechanical anchorage strength in side cover splitting, in addition to concrete strength.

k_1: Effect of bearing area of anchorage end plate
k_2: Effect of side cover thickness of concrete
k_3: Effect of distance between compressive and tensile resultants at critical section
k_4: Effect of anchorage length
k_5: Effect of lateral reinforcement in a joint

Effect of concrete strength was represented by approximated curves of anchorage strength as a function of concrete compressive strength of specimens with the same value in each k_i ($i = 1 \sim 5$). Each factor $k_1 \sim k_5$ was represented based on the strength rate for the anchorage strength of a benchmark specimen in a group with the same value in other factors. In this paper, the anchorage strength is expressed in terms of the maximum axial stress of anchored rebars obtained from the test. The anchorage strength σ is constituted by multiplying every k_i by the benchmark strength σ_{std} as a function of concrete strength as follows.

$$\sigma = k_1 \cdot k_2 \cdot k_3 \cdot k_4 \cdot k_5 \cdot \sigma_{std} \tag{1}$$

3.2 Formula of Influence Factors

Each influence factors k_i in the equation (1) was formulated by analyzing test data in the database, whose ranges are shown in **Table 1**.

Table 1 Range of Influence Factors in Adopted Pull-out Tests

influence factor	parameter range
concrete compressive strength : σ_B	19.3 ~ 76.0 (N/mm^2)
ratio of bearing area	2.70 ~5.84
side covering depth : C_0 / d_b	2.57~6.58
lever arm : j / 1_d	0.85~2.00
anchored length : $1_{d\,/}\,d_b$	7.89~18.67
$1_{d\,/}\,D_c$	0.50~0.84
ratio of lateral reinforcement : p_{jw}	0.00~1.10 (%)
ratio of peripheral hoop	0.00~0.63 (%)
ratio of core hoop	0.00~0.47 (%)
column size	300~650 (mm)

D_c : depth of column, d_b : diameter of reinforcing bar

(1) σ_{std} : Benchmark axial stress as a function of concrete compressive strength

There were six groups of total nineteen specimens in which varied only concrete strength. The anchorage strength vs. concrete strength relationship obtained from these specimens is shown in **Fig.2**. In the range of concrete strength σ_B lower than 50 N/mm^2,

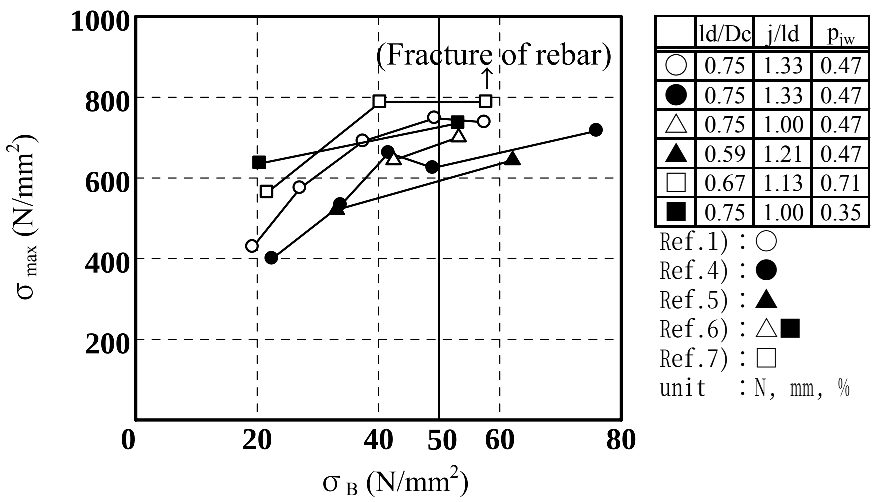

Fig. 2 Influence of Concrete Compressive Strength

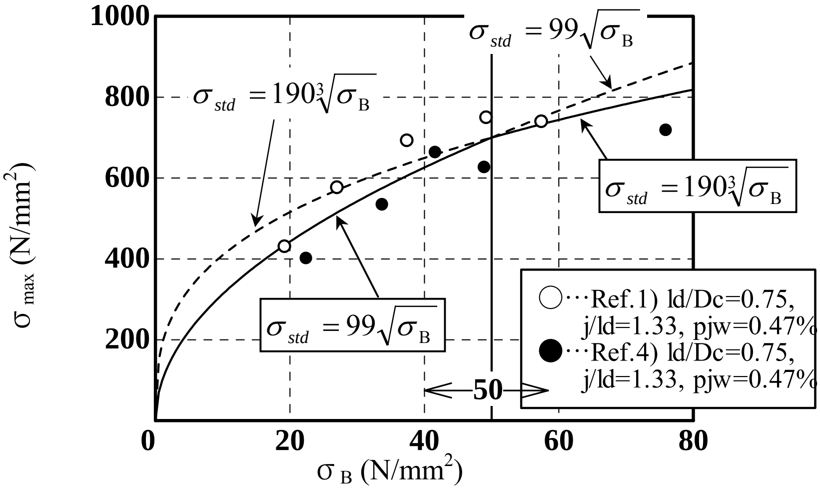

Fig. 3　Benchmark Axial Stress of an Anchored Bar

the anchorage strength increased proportionally to the concrete strength. However, in the range $\sigma_B > 50\ N/mm^2$, the anchorage strength did not increase so much. Ten specimens (denoted by the marks ○ and ● in the Figure) were selected to obtain the benchmark strength σ_{std}, because all influence factors of these specimens were equal to 1.0. In the range of $\sigma_B \leqq 50\ N/mm^2$, the anchorage strength was assumed to be proportional to the square of concrete strength and proportional to the cube of concrete strength in the range of $\sigma_B > 50\ N/mm^2$, as shown in **Fig.3**. Hence, the σ_{std} was expressed as follows.

$$\sigma_{std} = 99\sqrt{\sigma_B} \qquad \text{in } \sigma_B \leqq 50\ N/mm^2$$
$$\sigma_{std} = 190\sqrt[3]{\sigma_B} \qquad \text{in } 50\ N/mm^2 < \sigma_B \leqq 76\ N/mm^2 \qquad (2)$$

(2)　k_1: Effect of bearing area of anchorage end plate

The influence factor k_1 was represented by the same formula as the New RC equation, because the test data concerning bearing area was same as the original data for the New RC equation.

$$k_1 = 1 \qquad 2.7 \leqq \text{bearing area ratio} \leqq 6.0 \qquad (3)$$

(3)　k_2: Effect of side cover thickness of concrete

The influence factor k_2 was also represented by the same formula as the New RC equation, because the test data concerning side cover thickness of concrete was same as the original data for the New RC equation.

$$k_2 = 0.96 + 0.01\,(C_0 / d_b) \tag{4}$$

(4) k_3: Effect of distance between compressive and tensile resultants

Fujii and Morita have pointed out that the distance between compressive and tensile resultants in the critical section of a beam significantly influenced the anchorage strength in case of the conventional bent-up anchorage(1991). In the mechanical anchorage, the same effect was also assumed; i.e. the higher of the anchorage strength in the shorter of the distance. The anchorage strength decreased linearly to j/ℓ_d as shown in **Fig.4**. Therefore, the following formula was obtained.

$$k_3 = -0.16(j/\ell_d) + 1.22 \tag{5}$$

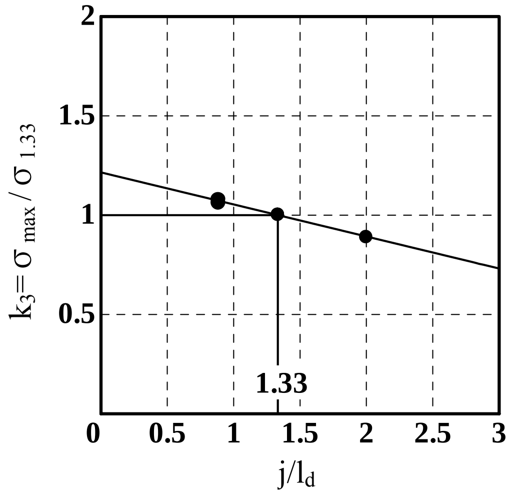

Fig. 4 Influence of the Distance between both Resultants
(j/l_d=4/3=1.33 was selected as the Benchmark)

(5) k_4: Effect of anchorage length

In the database, the anchorage length was varied in twenty specimens. The effect was studied as the ratio for the rebar diameter ℓ_d / d_b. However, the ratio j/ℓ_d also varied in conjunction with ℓ_d / d_b. The anchorage strength of the specimens was translated to the equivalent strength at $j / \ell_d = 4/3$ using equation (5), so that the effect of anchorage length could be estimated independently. Science the ratio ℓ_d / d_b was 11.8 in the specimen with $j/\ell_d = 4/3$, ℓ_d / d_b=11.8 was chosen as the benchmark. The anchorage strength increased proportionally to the anchorage length as shown in **Fig.5**. The formula for k_4 was obtained as follows.

$$k_4 = 0.032(\ell_d / d_b) + 0.63 \tag{6}$$

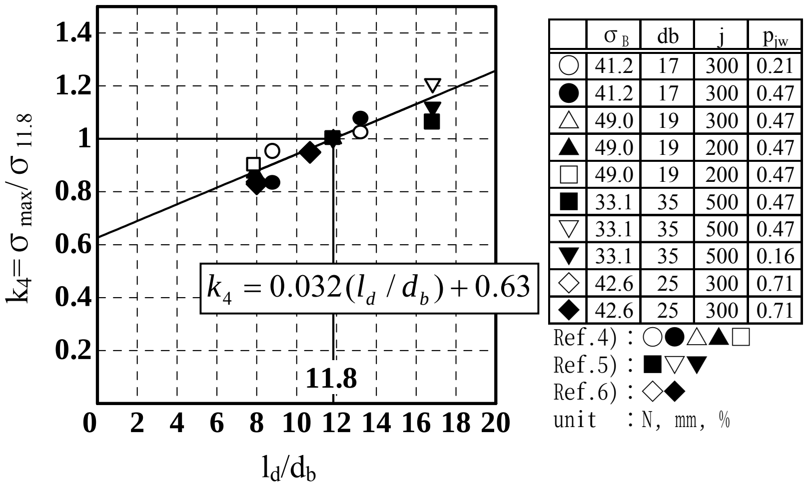

Fig. 5 Influence of Anchorage Length

(l_d/d_b=11.8 was selected as the Benchmark)

(6) k_5: Effect of lateral reinforcement in a joint

In the New RC equation, as the effect of lateral reinforcement in a joint, only peripheral hoops were considered. However, the database indicated that the core hoops developed almost the same effect as the peripheral hoops on the anchorage strength. In the improved equation, the effect of core hoops has been included. The ratio of lateral reinforcement p_{jw} was varied in total thirty-six specimens in the database. The anchorage strength is plotted versus p_{jw} in **Fig.6**. The strength increased linearly up to about p_{jw}=0.9%. The effect of lateral reinforcement was reported to decrease relatively in high strength concrete (Murakami, Kubota, 1997). In **Fig.7**, the test data is plotted in two cases of concrete strength for the same benchmark ratio of p_{jw}. The formula was determined by linear interpolation for the two cases, as follows.

for $p_{jw} \leqq 0.009$

$$k_5 = 51p_{jw} - (1.37p_{jw} - 0.0065)(\sigma_B - 27.2) + 0.76$$

for $p_{jw} > 0.009$

$$k_5 = 1.22 - 0.0059(\sigma_B - 27.2) \tag{7}$$

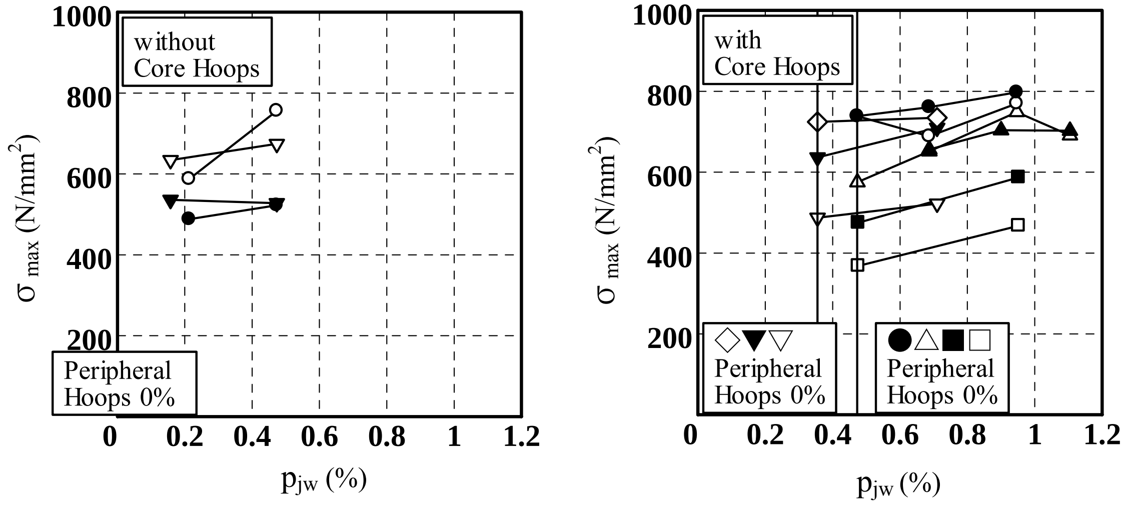

Fig. 6 Influence of Lateral Reinforcement

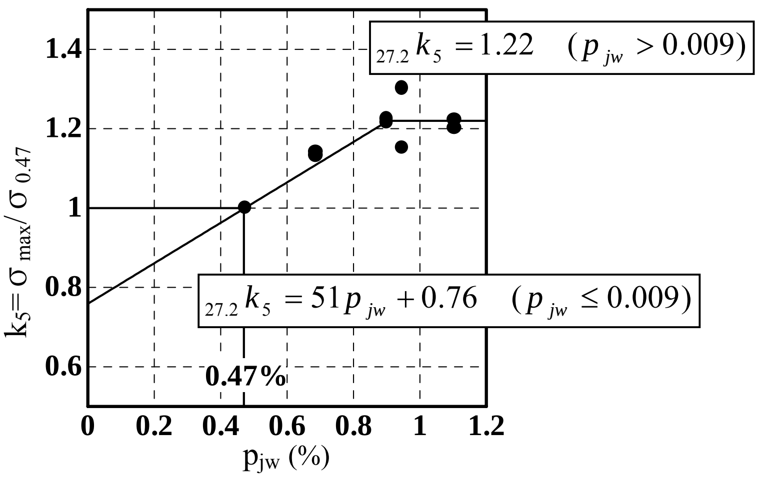

Fig. 7-1 Influence of Lateral Reinforcement in case of σ_B = 27.2N/mm^2

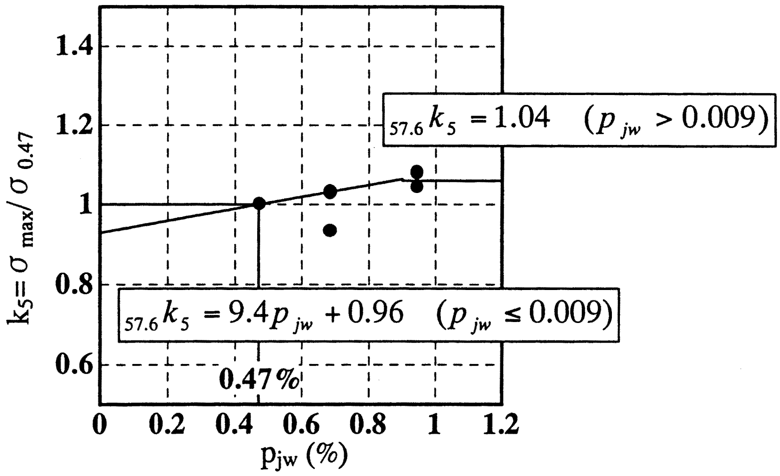

Fig. 7-2 Influence of Lateral Reinforcement in case of σ_B = 57.6N/mm^2

Finally, the mechanical anchorage strength for side cover splitting can be estimated by using equations (1) to (7).

3.3 Appropriateness of the Improved Equation

The calculated anchorage strength for side cover splitting was compared with the strength obtained from the test. The comparisons in three cases by the improved equation, by the New RC equation, and by the equation recommended by AIJ for the conventional bent-up anchorage after Fujii and Morita were represented in **Fig.8-1**, **Fig.8-2**, and **Fig.8-3**, respectively. Appropriateness of the improved equation (Ave.=1.012, SD=0.117) was remarkably better than that of the New RC equation (Ave.=0.942, SD=0.139).

However, in the improved equation, due to luck of test data, other many effects which may possibly influence the mechanical anchorage were not considered, for example, group effect of rebars, strength of hoops, layers of anchored rebars, width of compressive region in a beam, effect of orthogonal beams, difference between top and bottom rebar, column axial load, scale effect, and so on.

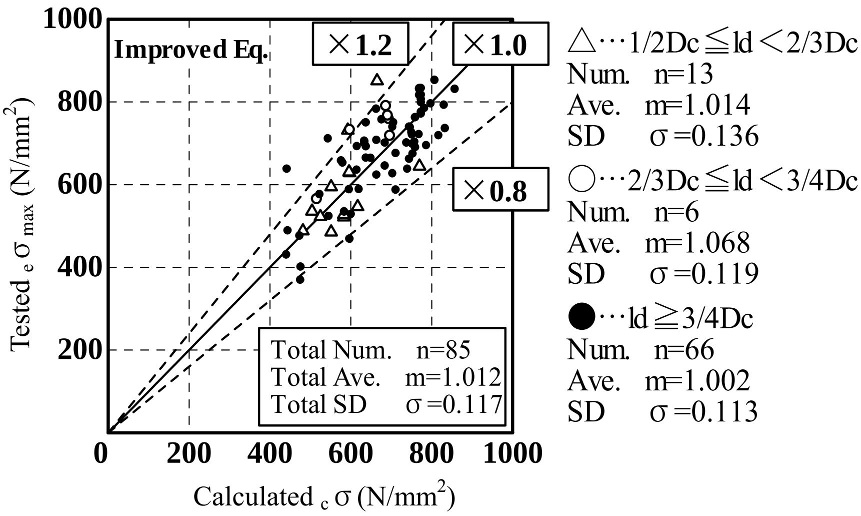

Fig. 8-1 Appropriateness of the Improved Equation

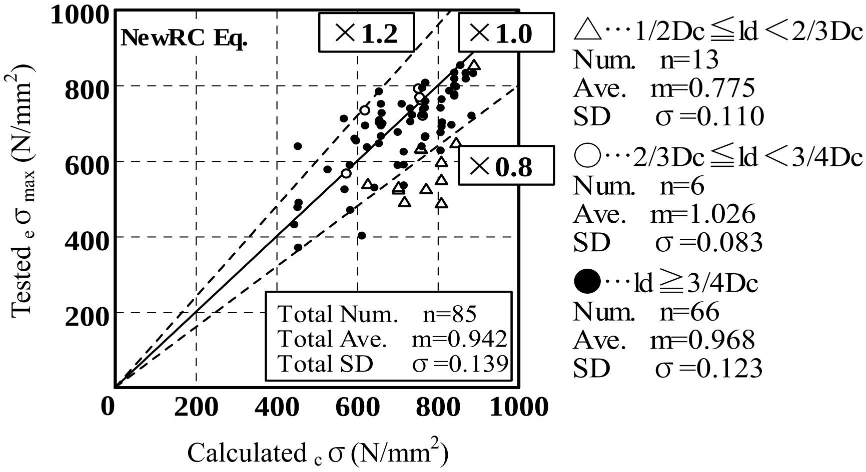

Fig. 8-2 Appropriateness of the NewRC Equation

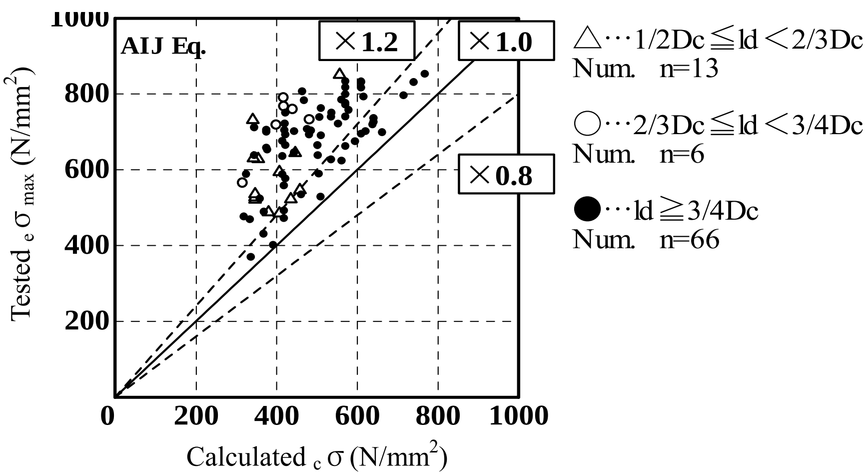

Fig. 8-3 Appropriateness of the equation in the AIJ Guidline

4. CONCLUSIONS

The equation to estimate the mechanical anchorage strength for the side cover splitting failure was improved based on the recent test data in Japan. Effect of anchorage length and distance between compressive and tensile resultants at critical section were considered in the equation, in addition to the effects of bearing area of anchorage plate, cover thickness of concrete, and lateral reinforcement in a joint. The equation predicted the mechanical anchorage strength appropriately.

REFERENCES

Murakami, M., Kubota, T., et al. (1993). Proposition of the empirical equation for mechanical anchorage strength of beam main bars in the exterior reinforced concrete beam-column joint. Summaries of AIJ annual meeting C: 125-128. (in Japanese)

Fujii, S., Morita, S., et al (1991). Reevaluation of anchorage strength for 90 degrees bent-up rebar. Transactions of AIJ 429: 65-75. (in Japanese)

AIJ. (1998). Design guidelines for earthquake resistant reinforced concrete buildings based on inelastic displacement concept. (in Japanese)

Murakami, M., Kubota, T., et al. (1992). Experiment on mechanical anchorage of beam main bars in reinforced concrete structure using high strength material(Part1, 2). Summaries of AIJ annual meeting C: 909-912. (in Japanese)

Konishi, H., Katoh, T. and Bessho, S. (1995). Experimental study on anchorage of RC beam rebar with new diviced anchor-plate. Proc. of JCI 17-2: 1195-1200. (in Japanese)

Murai, K., Okamoto, H., and Sugano, S. (1993). Experimental study on anchorage performance of beam main bars with knob at the end in the beam-column joint. Summaries of AIJ annual meeting C: 259-262. (in Japanese)

Murai, K., Yoshida, K., and Okamoto, H. (1994). Experimental study on anchorage performance of beam main bars with knob at the end in the beam-column joint. Summaries of AIJ annual meeting C: 683-684. (in Japanese)

Murakami, M., Kubota, T., et al. (1999). Mechanical anchorage strength by pull-out test (Part 1, 2). Summaries of AIJ annual meeting C: 527-530. (in Japanese)

Nakamura, K., Ichikawa, M., and Hayakawa, K. (2001). Development of mechanical anchorage used circular anchor plate (Part 1, 2). Summaries of AIJ annual meeting C: 107-110. (in Japanese)

Murakami, M., Kubota, T., et al. (1997). Evaluation of mechanical anchorage strength of beam main bars from pull-out test. Concrete Research and Technology of JCI 8-2: 1-10. (in Japanese)

MODELING THE EARTHQUAKE RESPONSE OF RC JOINTS

Laura N. LOWES[1]

ABSTRACT

Experimental investigation of the response of older and newly constructed RC beam-column joints indicates that inelastic joint action may determine global frame response under earthquake loading. A model is proposed to simulate the joint response under reversed-cyclic loading. This model provides a simple representation of the primary mechanisms that may determine inelastic behavior: failure of the joint core under shear loading and anchorage failure of beam and column longitudinal reinforcement embedded in the joint. The model is implemented as a four-node, 12-degree-of-freedom element that is appropriate for use with typical hysteretic beam-column elements in two-dimensional nonlinear analysis of RC structures. A simple calibration procedure is proposed to define joint behavior on the basis of the material, geometric and design parameters of the beam-column joint. Comparison of simulated and observed response suggests that the proposed model and calibration procedure are appropriate for use in predicting beam-column joint response.

INTRODUCTION

Typically, in simulating the seismic response of RC building frames, it is assumed that inelastic action is limited to flexural yielding of beams and columns. However, experimental data suggest the inelastic beam-column joint response may be significant both for newly designed and existing structures. Laboratory testing of building sub-assemblages with design details representative of pre-1970 construction shows that joints with little to no transverse reinforcement and relatively high bond-stress demand may exhibit severe stiffness and strength loss under cyclic loading (e.g., Walker 2001, Meinheit and Jirsa 1977). Experimental testing of joint designs more representative of current construction indicates that these joints also may exhibit inelastic deformation under severe earthquake loading (e.g., Park and Ruitong 1988, Meinheit and Jirsa 1977). Thus, simulation of RC frame response for design and evaluation requires simulation of inelastic joint action.

Here it is proposed that inelastic joint action be modeled by introducing a finite-volume joint element into the traditional line-element structural analysis model. The introduction of an independent joint element has several advantages. This enables explicit representation of inelastic joint action, ensures compatibility with the many beam-column line-elements developed by others, facilitates investigation of the impact of inelastic joint action on global structural response, and facilitates model development and calibration. The proposed model

[1] *Assistant Professor, Dept. of Civil Eng., University of Washington, Seattle, WA 98195-2700*

provides a simple representation of the mechanisms that may determine the hysteretic response of beam-column joints: anchorage of frame-member reinforcement in the joint core, shearing of joint-core concrete, and reduced capacity for shear transfer at the joint perimeter. The relative simplicity of the model minimizes the computational cost of representing joint action and contributes to the development of robust calibration procedures. Additionally, the proposed idealization facilitates the development of objective calibration procedures since experimental data characterizing specific RC response modes can be used.

PREVIOUSLY PROPOSED MODELS

The results of previous research include beam-column joint models of varying complexity. Early work to simulate inelastic joint action relied on empirical calibration of 'plastic-hinges' in beam-column line elements (e.g., Otani 1974). While this approach is computationally efficient, development of generally applicable and objective calibration procedures for this type of model is extremely difficult. The next generation of models employed zero-length rotational joint springs (e.g., Alath and Kunnath 1995). These models increase computational effort only slightly and decouple the action of beams, columns and joints; however, development of calibration procedures is still difficult since all inelastic joint action is lumped into a single load-deformation response. Recently, researchers have proposed using continuum-type models to simulate response within the joint. While this approach offers the potential for improved accuracy and objectivity, at the expense of added computational effort, to date only extremely simple idealizations of the joint region have been considered (e.g., Elmorsi et al. 2000).

Previous research suggests several approaches to modeling inelastic joint action; however, none of these approaches meets current modeling needs. Here a simple joint model is proposed that explicitly represents the mechanisms that may determine inelastic joint action. This model offers the potential for computational efficiency, objective and generally applicable calibration, reliability and robustness, and ease in use to investigate the impact of joint design on local and global response.

IDEALIZATION OF THE BEAM-COLUMN JOINT

Previous research identifies the mechanisms that determine inelastic response of beam-column joints; to predict response accurately, these mechanisms must be represented in the joint model. Fig. 1 shows an interior building joint under moderate to severe earthquake loading. Under this loading, it is expected that beams will develop nominal flexural strength at the joint perimeter and column longitudinal reinforcement will carry tensile stress that approaches the yield stress. Grey arrows in Fig. 1 represent load transferred from frame member longitudinal reinforcement into the joint-core concrete through bond. This force transfer results in shear loading of the joint core.

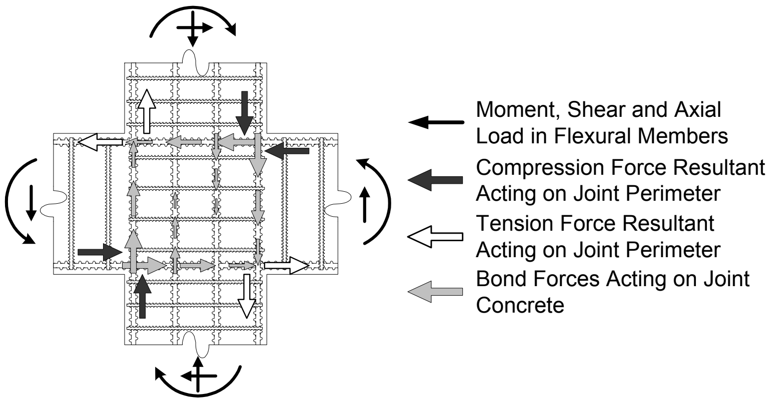

Figure 1. Building frame sub-assemblage.

The load distribution shown in Fig. 1 suggests that anchorage response may determine joint behavior. The bond-stress distribution determines, in part, the total load transferred into the joint. Thus, joint strength is a function of bond strength. A review by Bonacci and Pantazopoulou (1993) of interior building joint sub-assemblages tested in the laboratory under simulated earthquake loading found 19 of 86 sub-assemblages for which failure was determined, in part, by anchorage failure. The load distribution shown in Fig. 1 suggests also that shearing of joint-core concrete may contribute to inelastic response. In their review, Bonacci and Pantazopoulou (1993) found 51 of 86 sub-assemblages for which shear failure contributed to sub-assemblage failure.

Formulation of the Beam-Column Joint Element

Fig. 2 shows the currently proposed two-dimensional idealization of a beam-column joint. This idealization provides explicit representation of the mechanisms that may determine joint response. One-dimensional bar-slip springs are included in the model to represent inelastic action associated with anchorage failure. A shear-panel component represents inelastic action associated with shear failure of the joint core. Finally, interface-shear components are

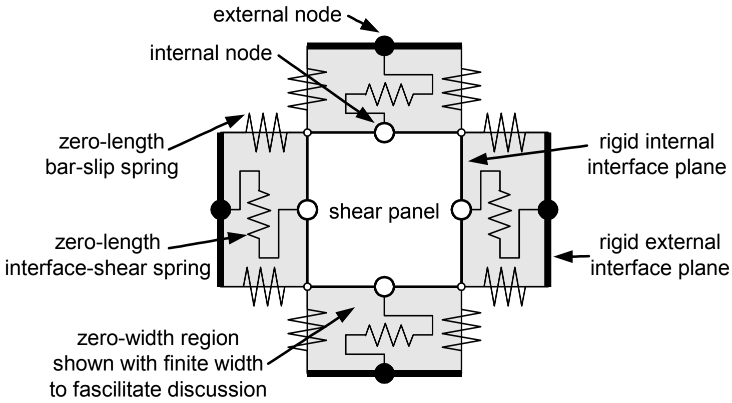

Figure 2: Joint model components.

included in the model to represent reduced capacity for shear transfer that may be observed under severe loading. In Fig. 2, the bar-slip and interface- shear springs are shown to have finite length. This is done to facilitate discussion; the model is implemented with the interior and exterior interface planes coincident in the undeformed configuration.

The joint model shown in Fig. 2 is incorporated into a four-node element for use in two-dimensional modeling of building frames. This element formulation is appropriate for use in a displacement-based incrementally advancing global solution scheme. Unlike the typical displacement-based element formulation in which the deformation state of the element is an assumed function of the element external nodal displacements, the deformation state of the joint element is defined by the displacement of four internal nodes, which are unique to element, and by the 12 generalized displacements imposed at the exterior nodes (Fig. 2). Thus, an iteration to solve for equilibrium of the entire structure requires an iterative solution within the element to determination the element deformation and load state. The element formulation is discussed in more detail in Lowes and Altoontash (2002).

CALIBRATION OF THE MODEL

Development of the proposed joint element requires definition of the load-deformation response of the bar-slip springs, shear-panel and interface-shear springs. This includes development of calibration procedures to enable simulation of joint response on the basis of material, geometric, and joint design parameters. Calibration procedures are developed using the results of previous experimental and analytical investigations. A general piecewise-linear load-deformation response model is developed that can be calibrated to represent observed one-dimensional response histories. Calibration procedures are discussed in more detail in Lowes and Altoontash (2002).

One-Dimensional Hysteretic Load-Deformation Response Model

A general hysteretic response model is proposed for use in simulating the response of the components that compose the element. A response envelope, an unload-reload path, and three damage rules that control evolution of these curves define the model. The response envelope is multi-linear, and the unload-reload path is tri-linear. Damage rules define deterioration in strength, unloading stiffness and reloading stiffness as a function of load history. Calibration of the hysteretic model requires 16 parameters to define the response envelopes, 6 parameters to define the two unload-reload paths and 12 parameters to define the hysteric damage rules. The following paragraphs discuss calibration of the one-dimensional hysteretic model to represent joint-element component response.

Calibration of the Shear-Panel Component

The Modified Compression Field Theory (MCFT) (Vecchio and Collins 1986) and experimental data provided by Stevens et al. (1991) are used as a basis for calibrating the shear-panel component of the joint element. The MCFT is used to define the envelope to the shear stress versus strain history for the panel. A subsequent study by Stevens et al. concludes that under reversed-cyclic loading, concrete compressive strength is substantially less and concrete tensile strength deteriorates more rapidly, than is observed under monotonic loading. These factors are incorporated into the proposed procedure for calibrating the envelope to the reversed-cyclic load history. Application of the MCFT implies that joint core response is determined by the compressive response of previously cracked concrete and the tensile response of reinforcing steel crossing concrete cracks. Additionally, application of the MCFT requires the assumptions that all load transfer through the joint occurs through shear.

The Stevens study (1991) extends the MCFT for the case of reversed-cyclic loading. Given the simplifying assumptions incorporated into the joint element, this cyclic model is considered too sophisticated for the current application. Instead, the experimental data provided by Stevens et al. are used to define the unload-reload path and damage rules of the general hysteretic one-dimensional response model. Specifically, unloading response defined to be relatively stiff until shear strength is approximately zero and reloading stiffness is defined to be minimal until a shear strain equal to approximately 25% of the previous peak strain is achieved. Damage rules are calibrated to represent observed response. Deterioration in stiffness and reloading strength is significant, but strength deterioration is minimal since the response envelope is calibrated for reversed-cyclic loading.

Calibration of the Bar-Slip Springs

Data from experimental testing of anchorage-zone specimens and assumptions about the bond stress distribution within the joint core are used to define a bar stress versus slip relationship for the beam-column joint model. Bar-slip spring force as a function of bar stress is defined on the basis of an assumed stress distribution at the perimeter of the beam-column joint.

The envelope to the bar stress versus slip relationship is developed on the basis of several simplifying assumptions about beam-column joint anchorage-zone response. First, bond stress along the anchored length of a reinforcing bar is assumed to be constant for reinforcement that remains elastic or piecewise constant for reinforcement loaded beyond yield. Second, slip is assumed to define the relative movement of the reinforcing bar with respect to the face of beam-column joint and is a function only of the strain distribution along the reinforcing bar. Third, the bar exhibits zero slip at the point of zero bar stress. Fourth on the basis of data provided by Eligehausen et al. (1983), bar stress is assumed to deteriorate once slip exceeds 3 mm (0.1 in.).

The results of experimental investigation indicate that bond strength is a function of the material state of the anchored bar as well as of the concrete and transverse reinforcing steel in the vicinity of the bar. Bond strength is relatively high if reinforcement is anchored in a compression zone and relatively low in a tension zone. Further, bond strength is reduced for reinforcement carrying stress in excess of the tensile yield strength and increased for reinforcement carrying compressive stress less than the compressive yield strength. Thus, in the joint in the vicinity of the column and beam flexural-tension zones (Fig. 1), relatively low bond strengths could be expected. In the vicinity of the flexural-compression zones, relatively high bond strengths could be expected.

Proposed average bond strength for the bond-zone conditions that develop within the joint are listed in Table 1. These values were developed using the results of previous investigations (Eligehausen et al. 1983, Shima et al. 1987, Viwathanatepa et al. 1979, Lowes 1999). Average bond strength values for regions where the reinforcing bar is elastic are computed using an experimentally defined maximum bond strength, the bond stress versus slip model proposed by Eligehausen et. Al. (1983), and the assumption that zero to maximum bond strength is developed along the elastic length of the bar. Average bond strength values for regions where the reinforcing bar has yielded are defined equal to the maximum bond strength value observed in the laboratory.

The results of reversed-cyclic anchorage tests conducted by Eligehausen et al. (1983) and Viwathanatepa et al. (1979) are used to define the unload-reload path parameters and damage model parameters included in the hysteretic response model.

Table 1. Average bond strength

Bar stress, fs (fy = yield strength)	Average Bond Strength, MPa (f_c = concrete compression strength, MPa)	Average Bond Strength, psi (f_c in psi)
Tension, fs < fy, Pull-out failure	$\tau_{ET} = 1.8\sqrt{f_c}$	$\tau_{ET} = 21\sqrt{f_c}$
Tension, fs < fy, splitting failure	$\tau_{ET} = 0.94 f_{ct}\sqrt{c/d_b}$	
Tension, fs > fy	$\tau_{YT} = 0.4\sqrt{f_c}$ to $0.05\sqrt{f_c}$	$\tau_{YT} = 4.8\sqrt{f_c}$ to $0.6\sqrt{f_c}$
Compression, |fs| < fy	$\tau_{EC} = 2.2\sqrt{f_c}$	$\tau_{EC} = 26\sqrt{f_c}$
Compression, |fs| > fy	$\tau_{YC} = 3.7\sqrt{f_c}$	$\tau_{YC} = 44\sqrt{f_c}$

Note: f_{ct} = concrete split-cylinder tensile strength, c = depth of clear concrete cover or half the bar-to-bar clear spacing, d_b = bar diameter.

Calibration of the Interface-Shear Springs

Under earthquake loading of a building frame (Fig. 1) flexural cracks will open in beams, and possibly columns, near the perimeter of the beam-column joint. If earthquake loading or bond strength deterioration is severe, cracks may not close upon load reversal and may widen with subsequent load cycles. As these cracks widen, capacity for shear transfer decreases and the flexibility of this shear-transfer mechanism increases. Ma et al. (1976) observed this phenomenon in an investigation of the earthquake response of RC beams in which the beams were cantilevered from relatively large concrete anchorage blocks and subjected to reversed-cyclic loading. This behavior is represented by the interface shear components of the beam-column joint element (Fig. 2).

Walraven (1981, 1994) investigated shear transfer across concrete crack surfaces under monotonic and cyclic loading. The results of these investigations include a model defining shear transfer strength as a function of slip on the interface and width of the interface crack. The results of these investigations include also data characterizing response under cyclic loading that are appropriate for use in developing a calibration procedure for the interface-shear springs.

EVALUATION OF THE PROPOSED MODEL

The proposed model is evaluated through comparison of simulated and observed response for a series of building frame sub-assemblages tested in the laboratory under pseudo-static reversed-cyclic loading by Park and Ruitong (1988). In this investigation, four sub-assemblages were designed to achieve different levels of ductility under simulated earthquake loading. The prototype specimen (Unit 1) was designed in accordance with NZS 3101:1982, The New Zealand Standard Code of Practice for the Design of Concrete Structures. The remaining specimens were designed with features that were expected to reduce joint strength and ductility capacity. These features included reduced normalized anchorage length for beam bars embedded in the joint (Units 2 and 4) and reduced joint shear capacity to demand ratio (Units 3 and 4). Joint shear capacity was defined, per NZS 3101, by the area of horizontal reinforcement provided as hoops in the joint core and the area of vertical reinforcement provided by column interior longitudinal reinforcement embedded in the joint core.

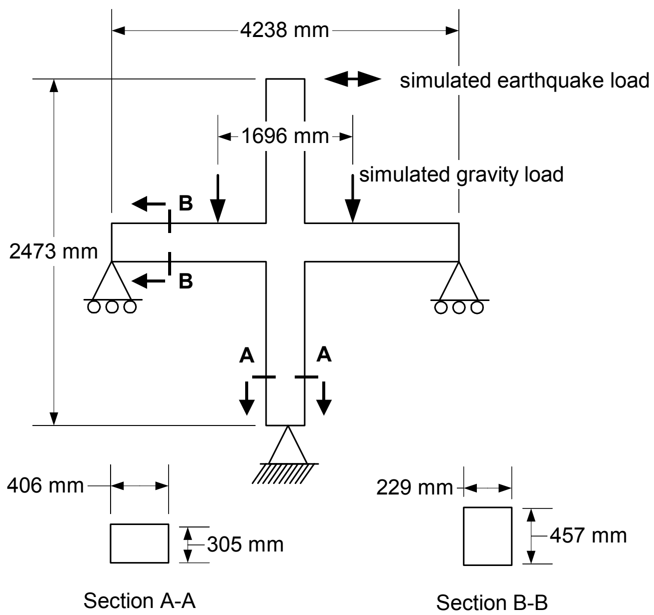

Figure 3. Sub-assemblage tested by Park et al. (1988)

Fig. 3 shows an idealization of the building frame sub-assemblages and the load distribution applied in the laboratory. Specimens were subjected to simulated earthquake loading by forcing the column tip through a prescribed pseudo-static cyclic displacement history. Joints were subjected to moderate shear demand, with the design joint shear stress less than $0.7\sqrt{f_c}$ MPa with f_c in MPa ($9\sqrt{f_c}$ psi with f_c in psi).

Numerical models were developed to simulate the Park and Ruitong experiment using Matlab (http://www.mathworks.com/); these models comprised lumped-plasticity beam-column elements and the proposed joint element. Beam and column response was simulated using the following assumptions:

- Elastic flexural stiffness is defined by cracked section properties.
- The envelope to the moment-rotation response of the plastic hinge is defined by the computed moment-curvature response of the beam-column cross-section and an assumed plastic-hinge length equal to half the depth of the beam-column element.
- The hysteretic response of the plastic-hinge is represented by the previously presented general one-dimension hysteretic response model with load-path parameters defined to represent the observed response of ductile reinforced concrete flexural elements.

The proposed constitutive models are used to define response of the joint model components using the material properties, joint geometry and reinforcement details provided by Park and Ruitong. In defining response of the shear-panel component, the horizontal transverse steel ratio was calculated using the total area of horizontal transverse steel provided in the joint while the vertical transverse steel ratio was calculated using the total area of longitudinal steel provided in the column. Park and Ruitong did not observe reduced capacity for shear transfer at the perimeter of the joint, and interface shear components were assumed to response elastically with a relatively large stiffness.

The proposed joint model may be evaluated through comparison of computed and observed load-displacement histories for the Park and Ruitong specimens; data for two of the specimens, Unit 1 and Unit 4, are shown in Fig. 4 and Fig. 5. The observed response history for Unit 1 shows significant energy dissipation and no strength loss; for Unit 4, the load-displacement history shows a more pinched response and strength loss at a displacement ductility demand of 5. Observed response histories for Units 2 and 3 are similar with Unit 2 exhibiting a significantly pinched load-displacement history as well as strength loss at a ductility demand of 5 and Unit 3 showing moderate pinching of the load-displacement history and minimal strength loss at a ductility demand of 7. The simulated histories exhibit the same fundamental characteristics as the observed histories; though strength loss is delayed until a ductility demand of 7 in the simulated histories.

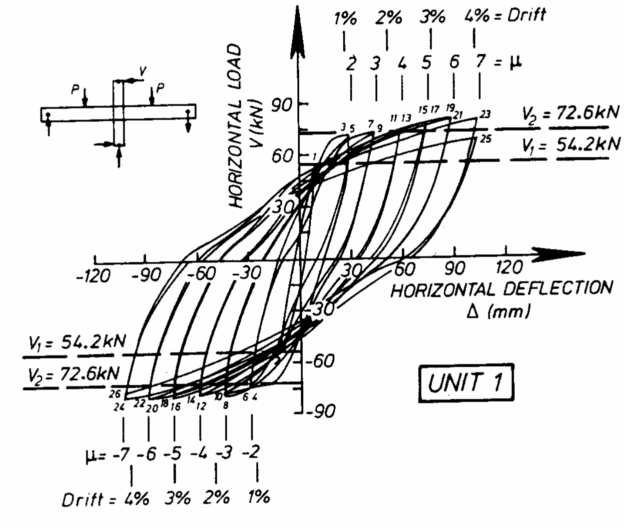

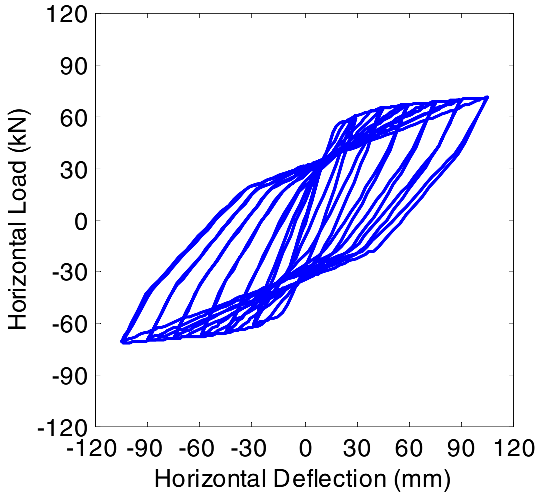

(b) Observed Response:
Unit 1 – Ductile Specimen

(c) Predicted Response:
Unit 1 – Ductile Specimen

Figure 4. Simulating the response of ductile building sub-assemblages.

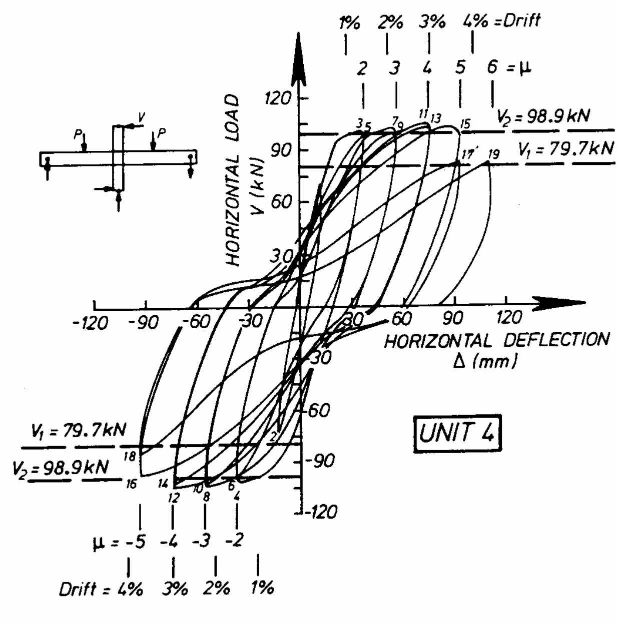

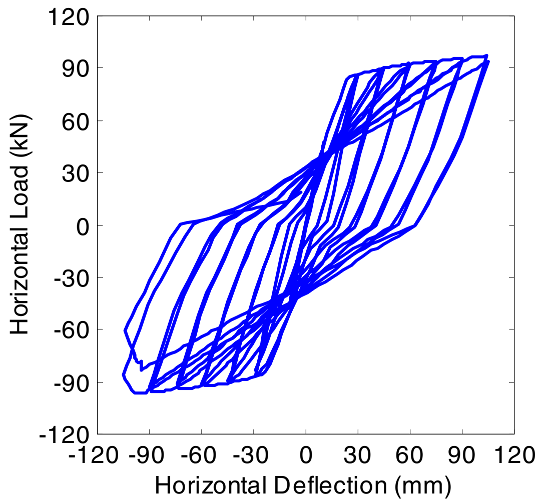

(d) Observed Response:
Unit 1 – Limited Ductility Specimen

(e) Simulated Response:
Unit 4 – Limited Ductility Specimen

Figure 5. Simulating the response of building sub-assemblages with limited ductility.

CONCLUSIONS

A beam-column joint element is developed for use with traditional beam-column line elements in two-dimensional modeling of RC structures under earthquake loading. The element provides a simple representation of the fundamental response mechanisms that determine component behavior. The simplicity of the formulation minimizes the computational effort required to simulate beam-column joint action. Additionally, the proposed formulation enhances the potential for reliable and robust simulation of a variety of structures. Finally, representation of the fundamental response mechanism provides the potential for objective calibration of the model. Comparison of simulated and observed response (Lowes and Altoontash 2002) indicates that the element is appropriate for use in investigating the impact of inelastic beam-column joint action on global structural response.

ACKNOWLEDGEMENTS

Support of this work was provided primarily by the Earthquake Engineering Research Centers Program of the National Science Foundation, under Award Number EEC-9701568 through the Pacific Earthquake Engineering Research Center (PEER).

REFERENCES

Alath, S., Kunnath, S.K. (1995). Modeling Inelastic Shear Deformation in RC Beam-Column Joints. *Eng. Mechanics: Proc. of the 10th Conference: University of Colorado at Boulder, May 1995*. Vol. 2. New York: ASCE, 822-825.

Bonacci, J.F. and Pantazopoulou, S.J. (1993). Parametric Investigation of Joint Mechanics. *ACI Str. Jo.* **90:1**, 61-71.

Eligehausen, R., Popov, E.P. and Bertero, V.V. (1983). Local Bond Stress-Slip Relationships of Deformed Bars Under Generalized Excitations. *Report UCB/EERC-83/23*. University of California, Berkeley

Elmorsi, M. Kianoush, M.R. and Tso, W.K. (2000). Modeling Bond-Slip Deformations in Reinforced Concrete Beam-Column. *Canadian Jo. of Civ. Eng.* **27**, 490-505.

Lowes, L.N. (1999). Finite Element Modeling of Reinforced Concrete Beam-Column Bridge Connections. *Diss*. University of California, Berkeley.

Lowes, L.N. and Altoontash, A. (2002) Modeling the Response of Reinforced Concrete Beam-Column Joints. *Jo. Str. Eng. ASCE*. (accepted for publication).

Ma, S.Y.M., V.V. Bertero and E.P. Popov (1976). Experimental and Analytical Studies on the Hysteretic Behavior of Reinforced Concrete Rectangular and T-Beams. *Earthquake Engineering Research Report 76/2*. University of California, Berkeley.

Meinheit, D.F. and Jirsa, J.O. (1977). The Shear Strength of Reinforced Concrete Beam-Column Joints. *CESRL Report No. 77-1*. University of Texas, Austin.

Otani, S. (1974). Inelastic Analysis of RC Frame Structures. *Jo. Str. Div. ASCE*. **100:ST7**, 1433-1449.

Park, R. and Ruitong, D. (1988). A Comparison of the Behavior of RC Joints Designed for Ductility and Limited Ductility. *B. of the New Zealand Nat. Soc. of Eq. Eng.* **21(4)**: 255-278.

Shima, H., Chou, L.L. and Okamura, H. (1987). Bond Characteristics in Post-Yield Range of Deformed Bars. *Concrete Library of JSCE* **10**: 113-124.

Stevens N.J., Uzumeri, S.M. and Collins, M.P. (1991). Reinforced-Concrete Subjected to Reversed-Cyclic Shear – Experiments and Constitutive Model. *ACI Str. Jo.* **88(2)**: 135-146.

Viawanthanatepa, S., Popov, E.P. and Bertero, V.V. (1979). Effects of Generalized Loadings on Bond of Reinforcing Bars Embedded in Confined Concrete Blocks. *Report UCB/EERC-79/22*. Berkeley: University of California.

Vecchio, F.J. and Collins, M.P. (1986). The Modified-Compression Field Theory for Reinforced-Concrete Elements Subjected to Shear. *Jo. ACI* **83(2)**: 219-231.

Walker, S.G. [2001]. Seismic Performance of Existing Reinforced Concrete Beam-Column Joints. *M.S. Thesis.* University of Washington, Seattle.

Walraven, J.C. (1981). Fundamental Analysis of Aggregate Interlock. *Jo. of the Str. Div. ASCE* **107:ST11**, 2245-2270.

Walraven, J.C. (1994). Rough Cracks Subjected to Earthquake Loading. *Jo. of Str. Eng, ASCE* **120:5**, 1510 –1524.

Keywords: beam-column joint, numerical model, structural analysis, bond, shear, earthquake response,

Structural Damage and Repair of Prestressed Concrete Beam-Column Assemblage

Minehiro Nishiyama[1]

ABSTRACT

Eight prestressed concrete beam-column joint assemblages were constructed. The experimental parameters for the first four test units were location of the anchorage plate and the diameter of the tendons. For the other four test units, three types of prestressing steel were used: round bars, strands and deformed bars. They were used for investigating the effect of bond characteristics on load-displacement curves of the test units. Cyclic loading tests were carried on these test units. The test results indicated that the location of the anchorage plates had significant influence on maximum loading capacity and hysteretic loops. Effect of difference in the tendons was not noticeable. Two of the test units were repaired and tested again. The cover concrete was replaced. The additional loadings were applied and a slight improvement in stiffness and capacity was observed in the small displacement range, but no difference in load-displacement curves in large ductility region was seen between before and after the repair.

1. INTRODUCTION

Prestress introduced into the beam through the joint of post-tensioned beam-column subassemblages has been considered to increase shear strength of the joint core because of its multi-axial state of stress with column axial load, and larger compressive block in the beam critical section, which results in larger compressive strut in the joint core. However, in some experiments on prestressed beam-column joints [1] it was revealed that prestress did not improve shear strength of the joint core. Effectiveness of prestress on shear strength of post-tensioned beam-column joints is still controversial.

The objectives of this paper are to make failure mechanism of post-tensioned beam-column subassemblages clear in terms of the anchorage location and bond characteristics between prestressing steel and grout mortar. The conclusions obtained in this study would be of importance for the practical design of prestressed concrete beam-column joints.

2. EXPERIMENTAL WORK

The experimental work is divided into two test series; in Series A the test parameters are location of anchorage of prestressing tendon and amount of prestressing force, in Series B the parameter is type of tendon, i.e., bond strength. Each test series consists of four prestressed concrete beam column joints. All test units had the same dimension of beams (200x300mm)

[1] *Department of Global Environment Engineering, Kyoto University, Kyoto, Japan*

Email: mn@archi.kyoto-u.ac.jp

and columns (300x300mm). They were beam-external column joint assemblages.

2.1 Series A

The experimental variables were location of anchorage of prestressing tendon (inside and outside the joint core) and amount of prestressing force (axial load level of $0.08f'_cA_b$ and $0.15f'_cA_b$; f'_c is the concrete compressive strength and A_b is the beam sectional area). The test unit is shown in Fig.1. Two of them are the test units whose prestressing steel bars were anchored to the steel plate (120x120, t=30mm) embedded in the joint core. The steel plate was located at the center of the joint core. In the other two, bars were anchored to the steel plate (300x200, t=30mm) attached to the column face. Two types of bars were used; one was 17mm in diameter round bar, and the other was 23mm in diameter round bar. They had the same amount of stress at the introduction of prestress into the beam, therefore, prestressing forces are different. The test units are summarized in Table 1. Mechanical properties of mild-strength reinforcement, prestressing steel, concrete and grout mortar are also summarized in Tables 2-5.

The test units were so designed as to fail in shear in the beam-column joint; the shear strength of the joint core calculated according to the AIJ (Architectural Institute of Japan) guidelines [2] was smaller than the input shear derived from the equilibrium of forces at the flexural strength as shown in Fig.2. The forces in the reinforcement and the compression force in the concrete were calculated based on the ACI318 equivalent rectangular stress block and the assumption that plane sections remain plane. The measured material strengths with the capacity reduction factor of unity were used in the calculation. The beams of all four test units were designed to have approximately the same flexural strength. The input shear and the shear strength of the test units are summarized in Table 6. The ratio of the shear strength to the input shear ranges from 0.57 to 0.74.

2.2 Series B

The variable in Series B was type of prestressing steel; round bars (SBPR1080/1230), deformed bars (SBPDL1080/1230) and strands (SWPR7AL) were used. The diameters of the tendons were 13.0mm, 12.6mm and 12.4mm, respectively. The test unit is illustrated in Fig.3. Test units in Series B are summarized in Table 7. Prestress was introduced up to about 80% of the nominal yield strength of the tendon. The beams of all four test units were designed to have approximately the same flexural strength. Mechanical properties of mild-strength reinforcement, prestressing steel, concrete and grout mortar are summarized in Table 8-11. The input shear and the shear strength of the test units obtained by the same procedure applied to the test units in Series A are summarized in Table 12. The units were so designed as to fail in joint shear. The results of pull-out tests on prestressing steels used in the test units are summarized in Table 13.

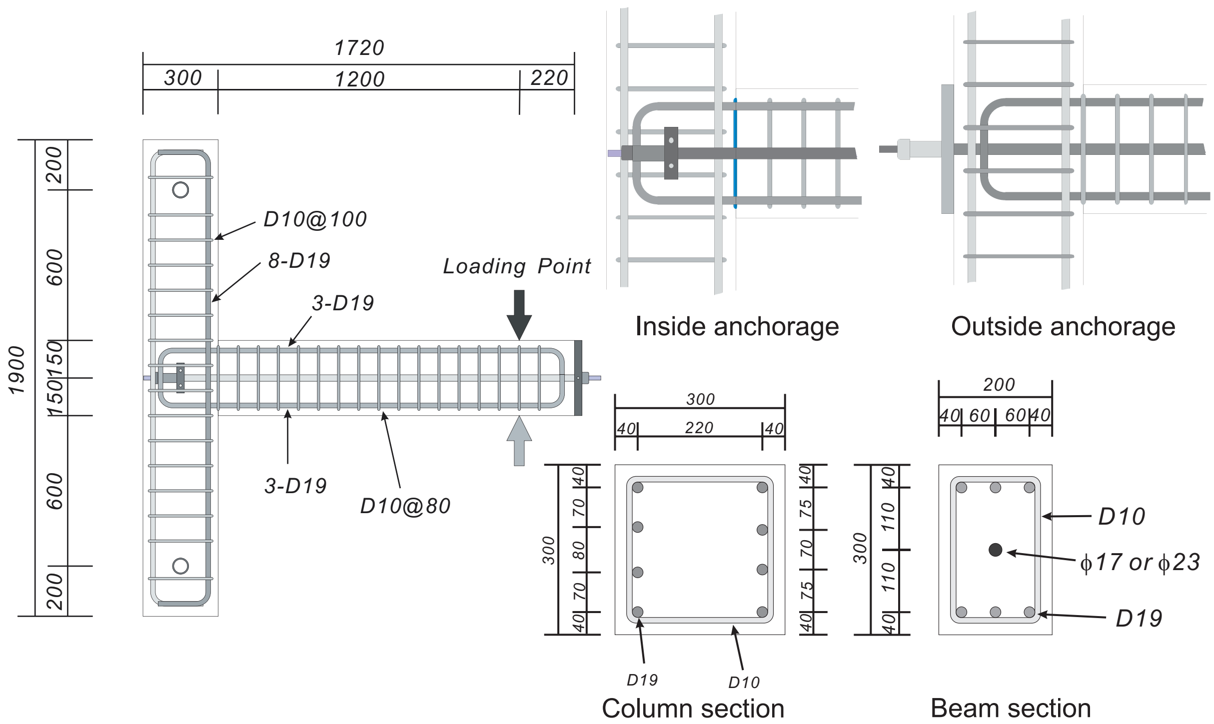

Fig.1 Series A Test unit

Table 1 Specification of Test units in Series A

Test unit	Anchorage location	Prestressing steel bar	Effective prestressing force, P_e [kN]	Prestress level, $P_e/A_b f'_c$
PC17-A	Outside	ϕ17	144.9	0.082
PC17-B	Inside		132.0	0.087
PC23-A	Outside	ϕ23	266.5	0.151
PC23-B	Inside		228.9	0.150

Table 2 Mechanical properties of mild steel used in test units in Series A

	Yield strength, f_y [N/mm^2]	Yield strain, ε_y [%]	Tensile strength, f_u [N/mm^2]	Young's modulus, E_s [10^5N/mm^2]
D19(SD295A)	372	0.235	545	1.56
D10(SD295A)	370	0.188	438	1.96

Table 3 Mechanical properties of prestressing steel used in test units in Series A

	Yield strength*, f_{py} [N/mm^2]	Yield strain, ε_{py} [%]	Tensile strength, f_{pu} [N/mm^2]	Young's modulus, E_{ps} [10^5N/mm^2]
ϕ17	1207	0.60	1286	2.00
ϕ23	1193	0.60	1290	2.00

* 0.2% off-set yield stress

Table 4 Mechanical properties of concrete used in test units in Series A

Test unit	Compressive strength, f'_c [N/mm^2]	Strain at f'_c, ε_o [%]	Tensile strength, f_t [N/mm^2]	Young's modulus, E_c [10^4N/mm^2]
PC17-A PC23-A	29.5	0.23	2.58	2.37
PC17-B PC23-B	25.4	0.21	2.25	2.38

Table 5 Mechanical properties of grout mortar used in test units in Series A

Test unit	Compressive strength, f'_c [N/mm^2]	Tensile strength, f_t [N/mm^2]	Young's modulus, E_c [10^4N/mm^2]
PC17-A PC23-A	33.9	2.76	1.37
PC17-B PC23-B	24.0	1.6	1.11

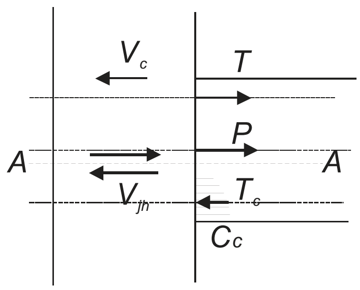

Fig.2 Input shear force of joint in test unit in Series A

Table 6 Input shear force and shear capacity of joints in test units in Series A

Test unit	M_{cal} [kNm]	V_{jh} [kN]	V_{ju} [kN]	V_{ju} / V_{jh}
PC17-A	91.0	517.9	381.5	0.74
PC17-B	89.9	518.8	343.6	0.66
PC23-A	115.3	636.4	381.5	0.60
PC23-B	110.0	598.5	343.6	0.57

M_{cal}: Theoretical maximum moment calculated using the ACI318 method
V_{jh}: Theoretical maximum applied horizontal shear force
V_{ju}: Joint shear strength calculated according to AIJ guidelines

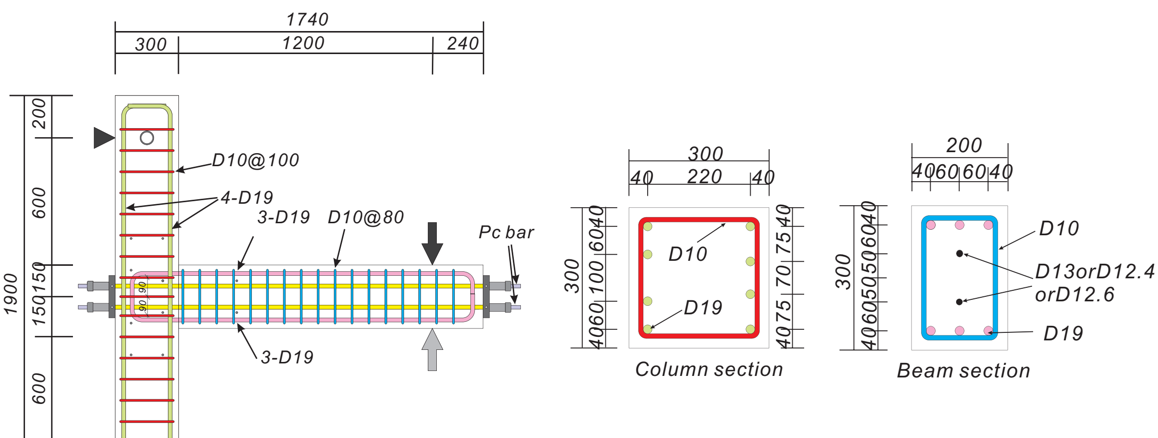

Fig.3 Series B Test unit

2.3 Loading setup

Both Series used the same loading setup. The unit was rotated by 90 degrees and set in the loading rig as shown in Fig.4. A horizontal load was applied at the end of the beam representing shear induced by seismic loading. The ends of the column were held on the same horizontal line between the pin and roller supports during the test and the applied beam load induced reactive shears at the ends of the column. By reversing the direction of the horizontal beam load, the effect of earthquake loading was simulated.

Table 7 Summary of Test units in Series B

Test unit	Prestressing tendon	Grout	Effective prestressing force, P_e [kN]	Prestress level, $P_e/A_bf'_c$
PC-K1	2-ϕ13 (round bar)	grouted	114.0	0.054
PC-K2	2-D12.6 (deformed bar)	grouted	111.0	0.053
PC-K3	2-ϕ12.4 (strands)	grouted	112.3	0.059
PC-KU	2-ϕ13 (round bar)	ungrouted	112.7	0.060

Table 8 Mechanical properties of mild steel used in test units in Series B

	Yield strength, f_y [N/mm^2]	Yield strain, ε_y [%]	Tensile strength, f_u [N/mm^2]	Young's modulus, E_s [10^{5}N/mm^2]
D19(SD295A)	345	0.192	540	1.80
D10(SD295A)	369	0.252	524	1.46

Table 9 Mechanical properties of prestressing steel used in test units in Series B

	Yield strength*, F_{py} [kN]	Yield strength*, f_{py} [N/mm^2]	Yield strain, ε_{py} [%]	Tensile strength, F_{pu} [kN]	Young's modulus, E_{ps} [10^{5}N/mm^2]
ϕ13 (SBPR1080/1230)	169.8	1279	0.64	175.2	2.00
D12.6 (SBPDL1080/1230)	150.4	1203	0.60	155.6	2.00
ϕ12.4 (SWPR7AL)	149.0	1604	0.83	168.0	1.92

* 0.2% off-set yield stress

Table 10 Mechanical properties of concrete used in test units in Series B

Test unit	Compressive strength, f'_c [N/mm^2]	Strain at f'c, ε_o [%]	Tensile strength, f_t [N/mm^2]	Young's modulus, E_c [10^{4}N/mm^2]
PC-K1 PC-K2	35.1	0.22	2.70	2.43
PC-K3 PC-KU	31.6	0.23	3.02	2.28

Table 11 Mechanical properties of grout mortar used in test units in Series B

Test unit	Compressive strength, f'_c [N/mm^2]	Tensile strength, f_t [N/mm^2]	Young's modulus, E_c [10^{4}N/mm^2]
PC-K1 PC-K2	44.6	2.08	1.42
PC-K3 PC-KU	41.5	2.25	1.50

Table 12 Input shear force and shear capacity of joints in test units in Series B

Test unit	M_{cal} [kNm]	V_{jh} [kN]	V_{ju} [kN]	V_{ju} / V_{jh}
PC-K1	90.72	428.8	289.5	0.68
PC-K2	89.04	468.7		0.62
PC-K3	89.16	453.5		0.64
PC-KU	86.40	455.4		0.63

M_{cal}: Theoretical maximum moment calculated using the ACI318 method
V_{jh}: Theoretical maximum applied horizontal shear force
V_{ju}: Joint shear strength calculated according to AIJ guidelines

Table 13 Results of pull-out tests on prestressing steel in test units in Series B

Pull-out test unit	No.1		No.2		No.3		Average	
	τ_y	S_y	τ_y	S_y	τ_y	S_y	τ_y	S_y
Round bar	5.28	0.075	4.65	0.089	4.01	0.138	4.65	0.101
Strand	7.90	0.162	7.04	0.114	8.05	0.095	7.66	0.124
Deformed bar	9.42	0.322	10.47	0.228	10.51	0.230	10.13	0.260

τ_y: bond strength [N/mm^2] S_y: Slip at bond strength [mm]

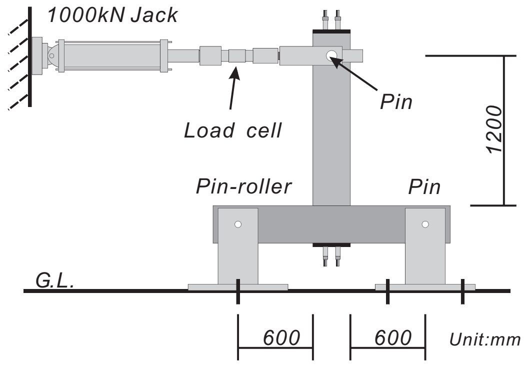

Fig.4 Loading setup

The first loading cycle was up to the beam rotation angle of 0.25%, and this was followed by a series of deflection controlled cycles in the inelastic range comprising two full cycles to each of the beam rotation angle of ±0.5%, ±1.0%, ±1.3%, ±2.0%, ±3.0%, ±5.0% and larger.

2.4 Measurements

Beam end deflection was measured by a linear displacement transducer which was attached to the pole fixed to the mid-height of the column. The deflection was consisted of the deformation of the beam, joint and column of half-height. It did not include the column deformation between the pin support and the place to which the measuring pole was fixed. Several cracks were found in this part of the column but the deformation of this part was considered small enough to be disregarded. Curvature and shear deformation of the beam in the potential plastic hinge region and shear distortion of the joint core were measured and calculated from the readings of the linear displacement transducers attached to the units by assuming curvature distribution along the beam.

Strain gauges were attached to the beam longitudinal reinforcement at the beginning of 90 degree hook, at the column face and at the center of these points. They were also attached to the joint transverse reinforcement on both sides of the column. The column reinforcement had strain gauges at the column critical faces and at the middle of the joint.

3. GENERAL BEHAVIOR OF TEST UNITS

3.1 Series A

Fig.5 shows the horizontal deflection at the end of the beam plotted against the corresponding load of the beam for each unit. The test units with the anchorage outside of the joint core were able to be loaded to well beyond the beam rotation angle of 1/20 with little reduction in moment capacity. In the units with the anchorage inside of the joint core, after the maximum moment had been reached at the beam rotation angle of approximately 5% in each direction, the subsequent reduction in stiffness and strength with pinched hysteresis was observed due to damage concentrating in the joint core. In PC17-B, the moment at the beam rotation angle of 1/13 was about 88% of the maximum moment capacity. In PC23-B, 20% reduction was ob-

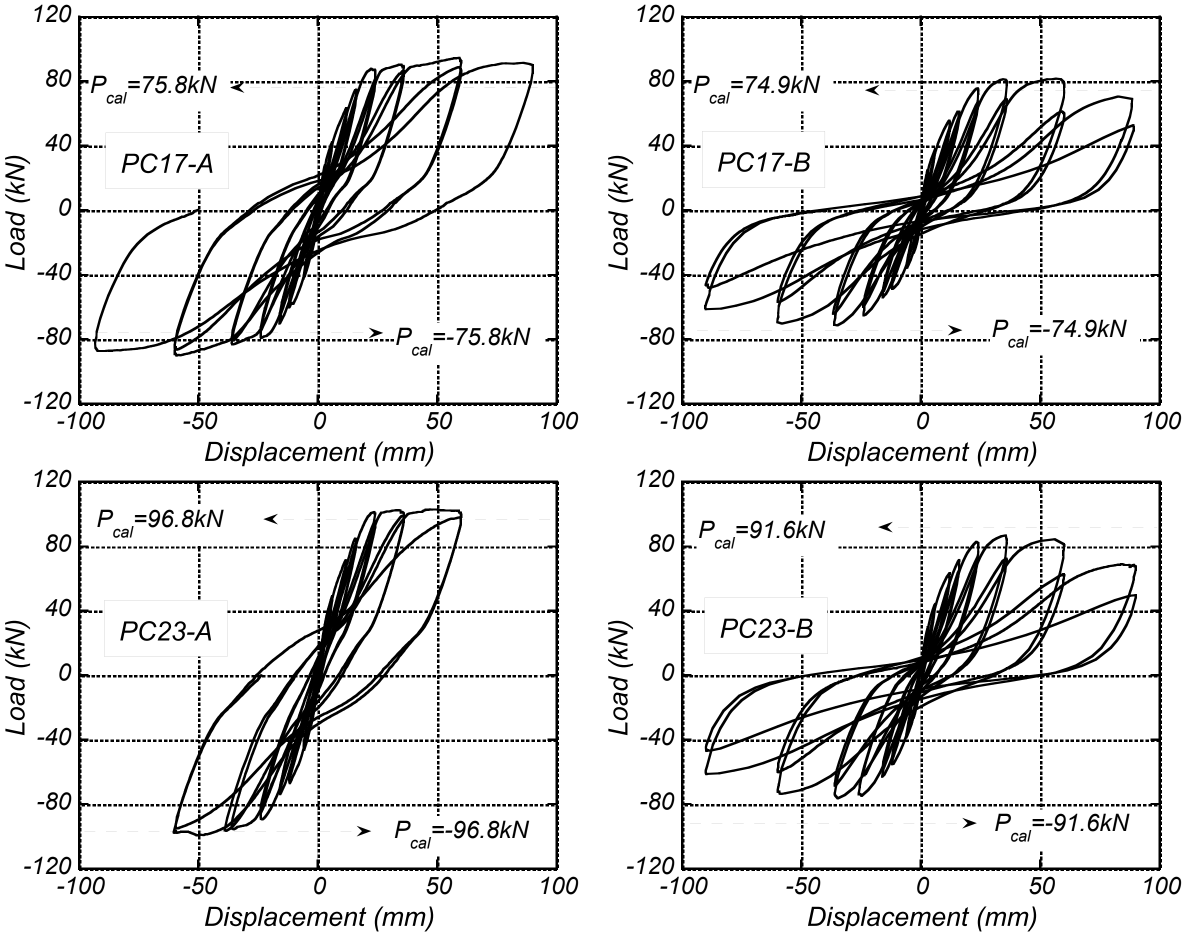

Fig.5 Load-deflection relations of test units in Series A

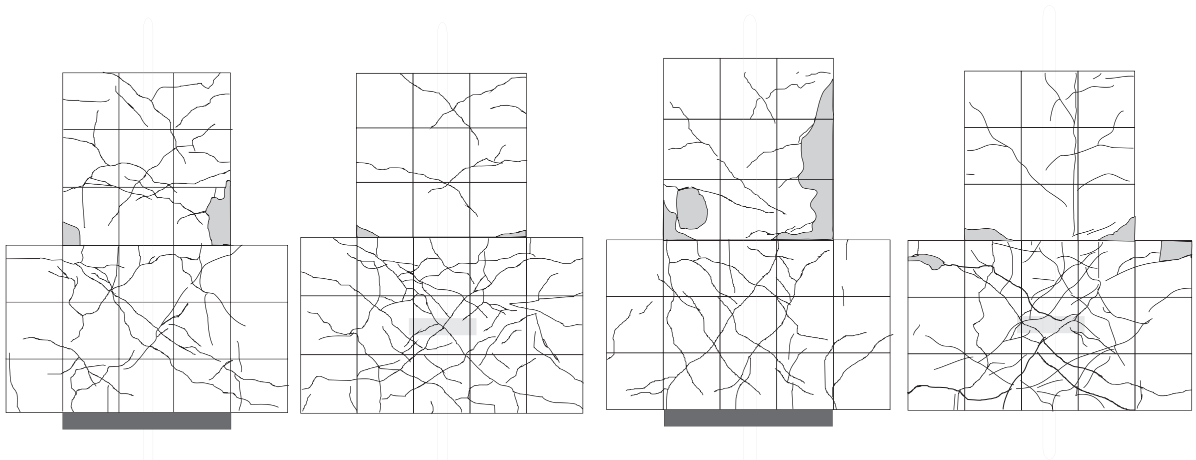

PC17-A **PC17-B** **PC23-A** **PC23-B**

Fig.6 Test units in Series A after loading

served at the final stage of loading.

P_{cal} is the load corresponding to the moment capacity calculated by the ACI318 method assuming that plane sections remain plane after bending and using the material strengths. The ratios of the maximum load capacities to P_{cal} are 1.27, 1.08, 1.17 and 0.98 for PC17-A, PC17-B, PC23-A and PC23-B, respectively. It should be noted that the calculated ideal load capacity was not attained in PC23-B with the inside anchorage. In PC17-B the ideal load capacity was not reached in the negative direction.

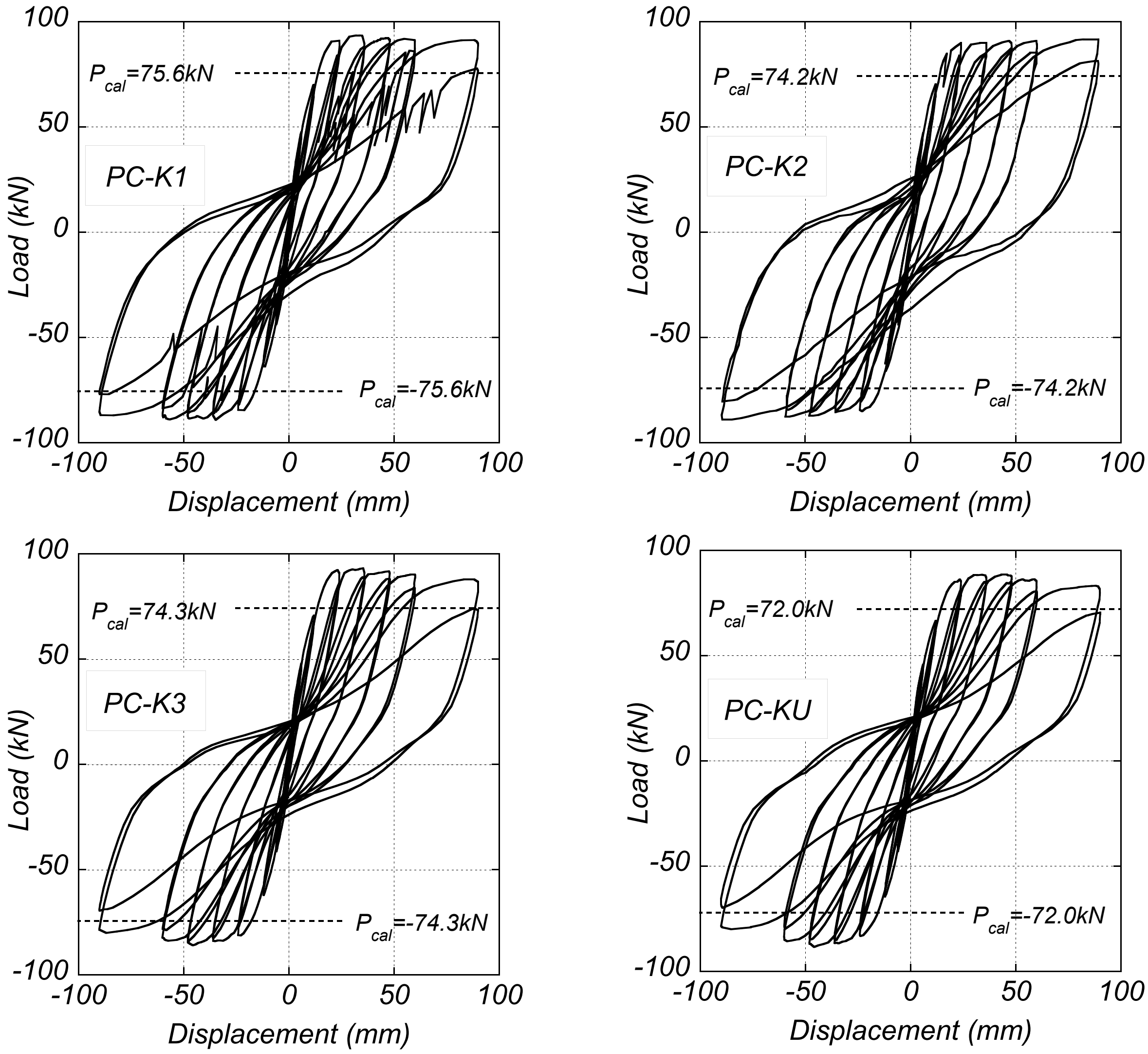

Fig.7 Load-deflection relations of test units in Series B

Fig.6 shows the test units after testing. In PC17-A and PC23-A with the anchorage outside the joint core, the damage such as concrete crushing and spalling of cover concrete concentrated in the beam plastic hinge region. In PC17-B and PC23-B with the anchorage inside the joint core, more visible cracks in the beam-column joint core were observed without serious damage in the beam plastic hinge region. In these units shear cracks in the joint core were connected to the cracks running along the column longitudinal reinforcement. It is noted that inclination of the shear cracks in PC17-A and PC23-A was steeper than that in the other two test units.

3.2 Series B

Fig.7 shows the horizontal deflection at the end of the beam plotted against the corresponding load of the beam for each unit. Although the test units were designed as to fail in shear in the joint prior to flexural yielding of the beam, stiffness reduction due to flexural yielding was observed before extensive shear cracks appeared in the joint. P_{cal} is the load corresponding to the moment capacity calculated by the ACI318 method. In PC-KU with ungrouted prestressing steel, the tendon stress was evaluated by the guidelines for design and construction of partially prestressed concrete published by AIJ [3]. The ratios of the load capacities to P_{cal} are 1.21, 1.22, 1.21 and 1.17 for PC-K1, PC-K2, PC-K3 and PC-KU, respectively. No significant difference is not observed in these load-displacement curves. This is because the contribution of prestressing steel to the load capacity is small; the ratio is approximately 6-7%.

Fig.8 shows the test units after testing. Solid circles in the figure indicate the location to which displacement transducers were attached. Concrete crushing and cover concrete spalling in the beam plastic hinge region occurred after yielding of the beam longitudinal reinforcement. Shear cracks in the joint were found at the beam rotation angle between 0.5% and 1.0% and their width did not become larger significantly. At the final stage of loading the crack width ranged from 1 to 1.5mm. In PC-K2 cracks run along the column longitudinal reinforcement on the side into which the beam was framed. The cracks opened widely as loading progressed.

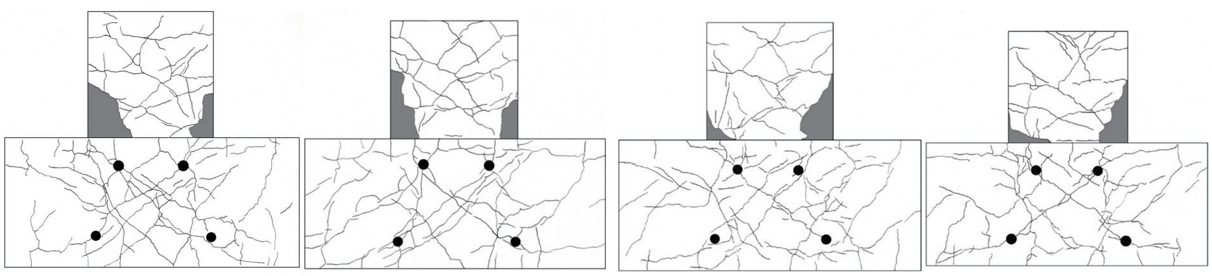

PC-K1　PC-K2　PC-K3　PC-KU

Fig.8 Test units in Series B after loading

4. REPAIR OF TEST UNITS

Many reports on repairing or strengthening of reinforced concrete members have been published, but little literature has not been made public for prestressed concrete members. Repair of prestressed concrete members is considered to be difficult due to the following reasons:
(1) Damage evaluation for prestressed concrete members has not been established yet. The same method for ordinary reinforced concrete members may not be applied.
(2) Prestressing force may disappear due to yielding of tendon and/or crushing of concrete.
(3) Replacement of core concrete and longitudinal reinforcement is difficult because of prestress.
(4) Prestressing tendons cannot be replaced and re-tensioning cannot be carried out if bonded system is used.
(5) Damage tends to concentrate into compressed concrete, not in steel reinforcement.
However, if unbonded system is used, replacement of prestressing steel and re-tensioning are possible. In this study, two test units PC-K2 and PC-KU used in Series B were repaired and tested again. Unbonded system was used for PC-KU, but in the first loading tests the unbonded tendons did not yield judging from the measurement of their tensile forces. Therefore, the tendons were not replaced. The tendons in PC-K2 are supposed to reach the yield stress,

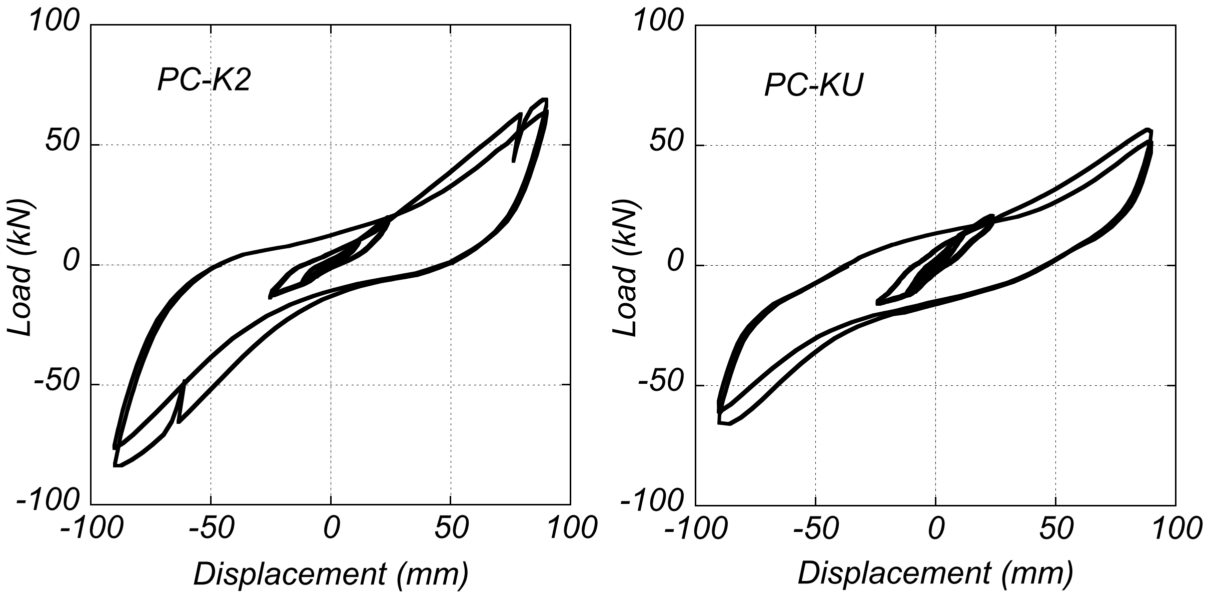

Fig.9 Load-displacement curves for the additional loading before repairing

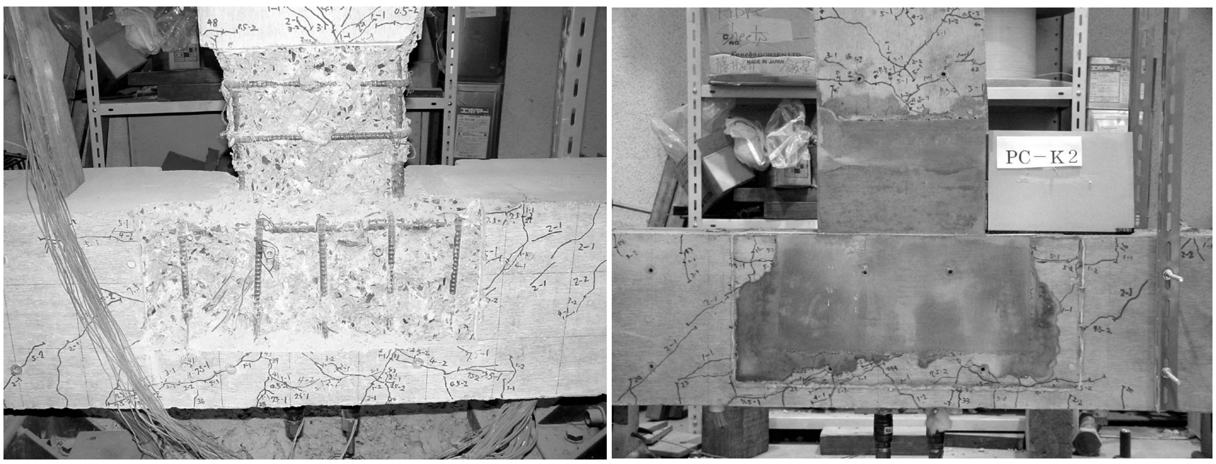

Photo 1 Removal of cover concrete for PC-KU and

Replacement of cover concrete for PC-K2

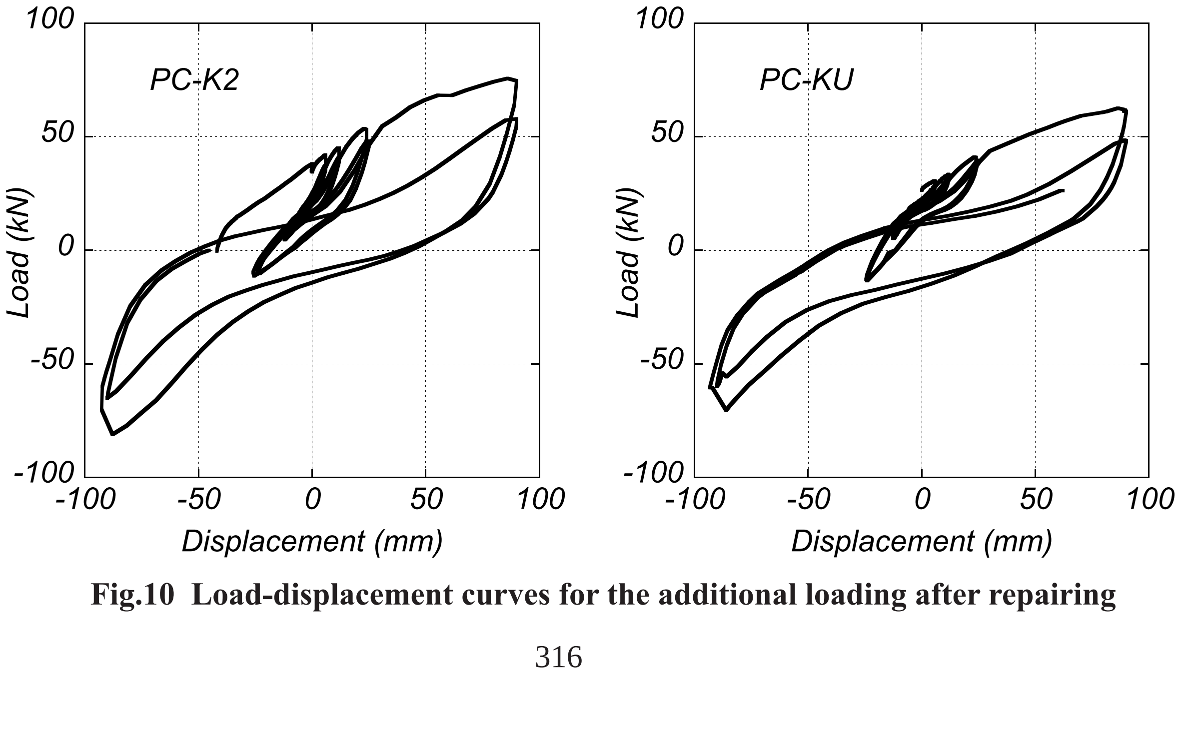

Fig.10 Load-displacement curves for the additional loading after repairing

although the measured tensile stresses were a little smaller than the yield strength. The tensile force was measured by a load cell attached at the end of the bar, therefore, the bond stress in the beam-column joint to the beam critical section should be accounted.

Before repairing additional loadings were applied. They consisted of two full cycles to each of beam rotation angle of ±0.5%, ±1.0%, ±2.0% and ±7.5%. Fig.9 shows load-displacement hysteresis curves obtained from the additional loadings. Significant degradation of stiffness and load carrying capacity is observed. Difference between the two test units is not noticeable although prestressing steel bars in PC-K2 were bonded and those in PC-KU were unbonded.

The repair work consisted of scraping of cover concrete and placement of new cover concrete as shown in Photo 1. Pre-mix type mortar was used for the cover concrete. The compressive strength and the elastic modulus at $1/3f'_c$ of the mortar at the time of the testing are 56.5 N/mm^2 and $1.99x10^4$ N/mm^2, respectively. After the repair work, another additional loadings were carried out. The same loading history as those before the repair work was used. The load-displacement curves obtained from the loadings are indicated in Fig.10. A slight improvement in stiffness and capacity can be observed in the small displacement range. However, after the first loading to the beam rotation angle of 7.5%, the curves are almost the same as those before the repair.

5. CONCLUSIONS

On the basis of the test results described in this paper the following conclusions are derived.

Series A:

(1) The maximum load capacity of the test units with the inside anchorage, PC17-B and PC23-B was smaller than that of the units with the outside anchorage, PC17-A and PC23-A. Even the ideal strength calculated by the ACI method was not attained in the units with the inside anchorage, PC17-B and PC23-B.

(2) The hysteresis loops obtained from the test units with the inside anchorage, PC17-B and PC23-B indicated reduction in capacity and pinching due to joint shear failure. Conversely, the units with the outside anchorage, PC17-A and PC23-A showed much better hysteresis loops even in the large ductility regions.

Series B:

(1) Bond strength between prestressing steel and grout mortar did not have a significant effect on the behavior of the test units. This is because the amount of prestressing steel was small compared with that of mild steel. Further study is needed.

(2) The proposal by the AIJ guidelines for the joint shear strength underestimated the joint strength of the test units.

Repair work:

(1) The repair work for the test units PC-K2 and PC-KU was conducted. The repair was

consisted of replacement of the cover concrete.

(2) A slight improvement in stiffness and capacity can be observed in the small displacement range. However, after the first loading to the beam rotation angle of 7.5%, the curves are almost the same as those before the repair.

6. REFERENCES

[1] Takashi KASHIWAZAKI and Hiroshi NOGUCHI: STRUCTURAL PERFORMANCES OF PRESTRESSED CONCRETE INTERIOR BEAM-COLUMN JOINTS, 12th World Conference on Earthquake Engineering, Auckland, New Zealand, Paper No.2342.

[2] Architectural Institute of Japan: Design Guidelines for Earthquake Resistant Reinforced Concrete Buildings Based on Inelastic Displacement Concept, 1999.

[3] Architectural Institute of Japan: Recommendations for Design and Construction of Partially Prestressed Concrete (Class III of Prestressed Concrete) Structures, 1986.

7. ACKNOWLEDGMENT

The author is grateful for the help of the students in the laboratory. In particular, thanks are due to Mr. F. Tono, Ms. Yue Wei, Mr. Y. Hamada and Mr. M. Adachi. Thanks are extended to Neturen, Co., Ltd. and Sumitomo Electric Industries, Ltd. for providing prestressing steel. The author appreciates Dr. K. Ashida of DENKA for his contribution to the repair work.

SESSION B-4: BEAM-COLUMN JOINTS

Chaired by

♦ Masaki Maeda and Santiago Pujol ♦

NEW MODEL FOR JOINT SHEAR FAILURE OF R/C EXTERIOR BEAM-COLUMN JOINTS

Hitoshi Shiohara[1]

ABSTRACT

A new analytical model for joint shear failure of reinforced concrete exterior beam-column joints is proposed. It is used for prediction of strength and failure modes and it is extended from a model for interior beam-column joints by the author. The model contains no empirical factors accounting the difference between exterior and interior joint. The both models consider four diagonal flexural critical sections in beam-column joints associating with joint shear deformation; or J-mode deformation. The equilibrium equations relate applied forces such as column shear, beam shear column and axial force, to the magnitude of stress resultants in steel and concrete at the critical sections. The equilibrium equations are combined with failure criteria for concrete, steel and bond to derive the maximum joint shear strength as an strength at optimal condition where bond resistance keeps its capacity in column or beam longitudinal bars passing through the beam-column joint for exterior or interior joint respectively. This paper focuses on demonstration of the models with numerical calculation. Calculated results are compared with average strength of test results based on Japanese laboratory tests. Calculated strengths by the models show good correlation with test results for both interior and exterior beam-column joints.

1. INTRODUCTION

For long time, the interior and exterior beam-column joint has been usually investigated by independent groups of researchers and there had been scarce contribution offering unified model of the behavior of the two different types of beam-column joint.

Early works of Paulay et al. (Pauley et al. 1978) established traditional truss and strut model to explain the shear resistance mechanism without making distinction of interior and exterior beam-column joints. But they gave no explanation to the reason why the strength of exterior joint is lower than that of interior joint based on the model. Key difference between them may be in the bond condition of column bar in exterior joint for a beam side and the opposite side. Cheung considered the interaction of bond deterioration of beam bars and joint shear strength (Cheung 1991)

1. *Associate Professor, Department of Architecture, Graduate School of Engineering, The University of Tokyo, Tokyo, 113-8656 Japan Email: shiohara@arch.t.u-tokyo.ac.jp*

based on the truss and strut model. But it is not mentioned on the distinction of exterior and interior joint. Lowes proposed a simple nonlinear model for beam-column joints consists of single R/C panel considering constitutive equations of reinforced concrete panel and bond-slip behavior and report a model applicable to both exterior and interior joints (Lowes 2002). However the model requires a non-linear solver of stiffness equations by incremental method and not simple to portray the effect of many factors on the behavior of beam-column joint. It is not revealed whether or not the model is applicable to both interior and exterior beam-column joint with common assumptions. No researchers have not succeed to give solution to the question quantitatively with simple mathematical model why the joint shear strengths for exterior and interior joint is different.

In contrast to the pessimistic situation of analytical model developing, design codes including ACI318 (ACI2002) and AIJ Guidelines (AIJ 1999) seem to pretend that the difference between exterior and interior joint is established with shape factor, although shape factor are given as an empirical factor based on laboratory testing. Moreover, they are arbitrarily extended for application to various configuration without justification, partly because it is difficult to carry out tests with such many factors in beam-column joints. Thus the provision in the codes neglect the effects of the most of parameters which may have influences on the behavior of beam-column joint.

Therefore this study attempts to provide a simple, comprehensive and unified model suitable for design codes, applicable for exterior beam-column joints and interior beam-column joints. A new model for interior beam-column joints was proposed by the author in the references (Shiohara 2001, 2002). In this paper, the model is extended for exterior beam-column joints. The both model contains no empirical factors accounting the difference between exterior and interior joint. This paper includes the principles, assumptions, mathematical formulation and numerical demonstration of the model. The numerical demonstration is provided and the correlation of the calculation and test results are examined.

2. JOINT SHEAR FAILURE MODEL FOR INTERIOR BEAM-COLUMN JOINT

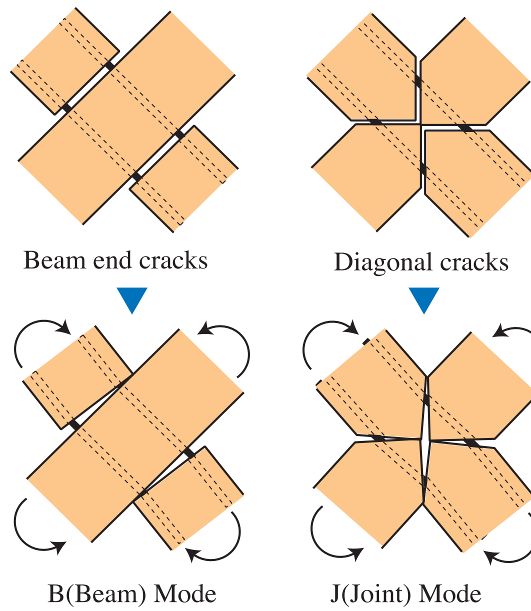

Figure 1: Two deformation mode for interior beam-column joint

A simple mathematical model for interior beam-column joints was proposed by the author (Shiohara 2001). The model is briefly summarized here. The model considers two sets of flexural critical sections associated with deformation modes, called J-mode and B-mode (Shiohara 2002). The basic idea of the critical section is similar to that of flexural theory where local curvature cause resistance by a pair of force resultants of tension and compression. B-mode considers critical section along column face, while J-mode considers four coupled critical sections which are on two diagonal lines as shown in Fig. 1. The equilibrium equations are used to relate applied force such as column shear, beam shear and column axial force, to the magnitude of stress resultants in steel, concrete at the critical sections and required averaged bond stress. Each material has its own properties such as yield strength and bond strength. The stress resultants can not exceeds their material strength and bond strength. Considering the equilibrium equations and restrictive conditions of material and bond strength, the maximum joint shear strength is derived as an force at optimal state when material strength and/or bond strength are reached. The joint shear strength of J-mode and B-mode are calculated independently. The strengths have close relation to the deformation modes. If the J-mode strength is smaller than that of B-mode strength, then J-mode deformation become dominant mode. The relation of the bond capacity and failure modes were discussed in detail in the reference (Shiohara 2002).

3. JOINT SHEAR FAILURE MODEL OF EXTERIOR BEAM-COLUMN JOINTS

3.1 Two Deformation Modes in Beam-Column Joints

The model for interior beam-column joints is extended to exterior beam-column joints. The B-mode deformation and J-mode deformation mode for exterior joint are depicted in Fig. 2. In exterior beam-column joints, beam bars need to be anchored in the beam-column joint. Two different J-mode deformation modes are identified, which include Type I, where beam bars are extended to outside of the layers of column longitudinal bar and anchored by anchorage devices as shown in Fig. 2(b) and Type II, where beam bars are anchored within core concrete of beam-column joint.

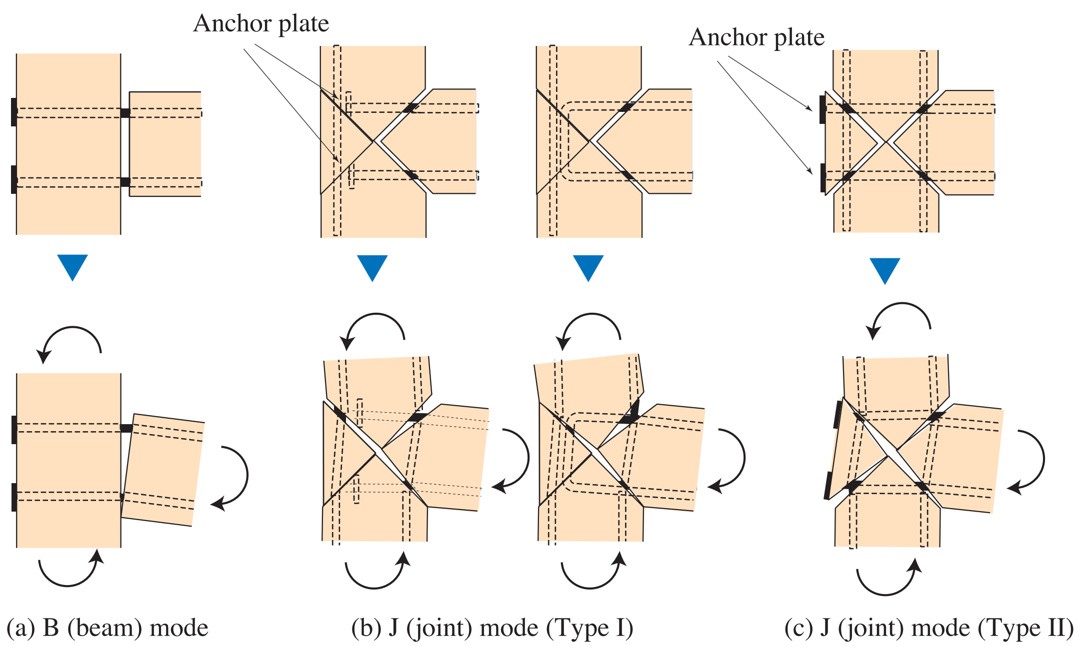

Figure 2: Three deformation mode for exterior beam-column joint

3.2 Assumption in Critical Sections

Figure 3 shows two sets of critical sections corresponding to B (Beam)-mode and J (Joint)-mode respectively. B-mode assumes critical sections at beam ends for flexural action of beams, while J-mode assumes diagonal lines as critical sections. To define the longitudinal stress in straight beam bars passing through at the critical sections, notations of T_3 and T_4 are used respectively. The assumption of plain section remains plain is not used, because in beam-column joint, the effects of bond slip is significant and not negligible. Thus the value of T_3 and T_4 are assumed as independent variables.

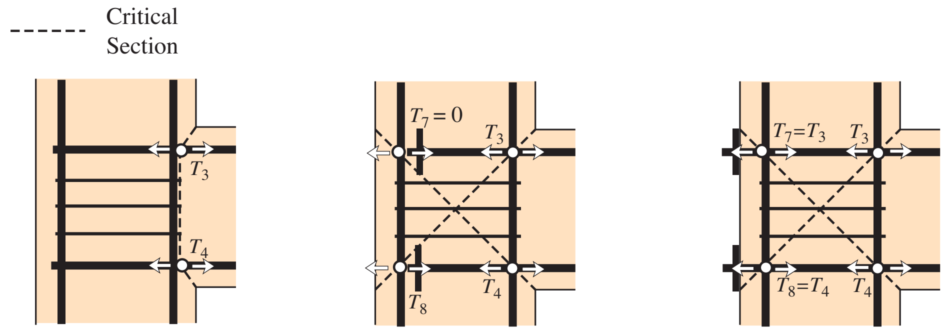

(a) Deformation mode due to crack at beam ends (Beam-mode)

(b) Deformation mode due to diagonal crack in beam-column joint (Joint-mode Type I)

(c) Deformation mode due to diagonal crack in beam-column joint (Joint-mode Type II)

Figure 3: Critical Sections for B-mode and J-mode

3.3 Generic Beam-Column Joint Substructure

The geometry and dimensions of generic substructure and external forces are defined in Fig. 4. Notations L_b and L_c is the distance of inflection point from the center of the joint respectively. Notations D_c and D_b define the depth of column and beam respectively. The other notations for dimension are defined in Fig. 4. The exterior beam-column joint is loaded with story shear V_c and axial force in Column N_c. The lower part of column is subjected to combination of N_c and V_b. The beam prestressing force T_p may be included in the formulation as a pair of constant applied forces in horizontal direction.

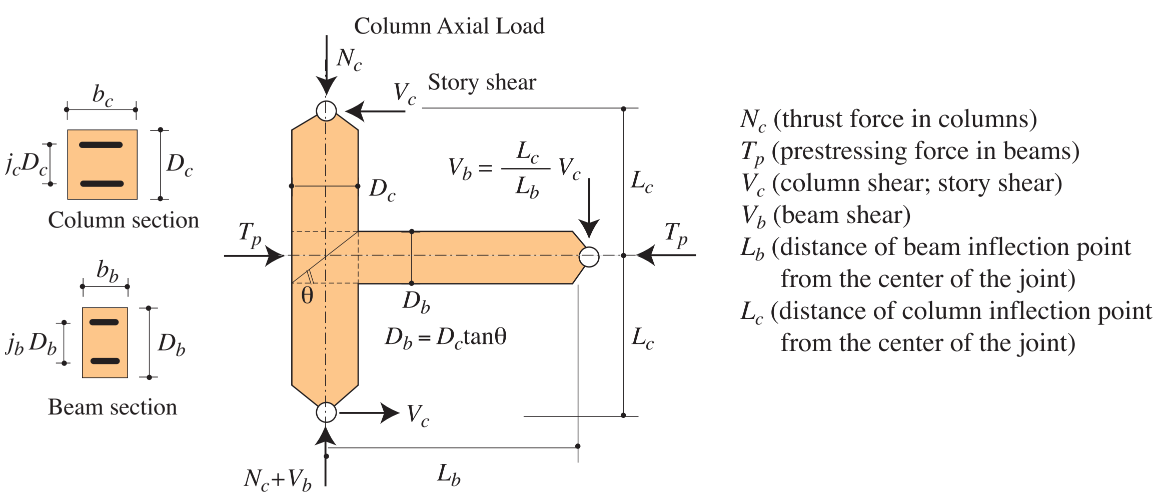

Figure 4: Notations for geometry of beam-colum substructure and applied forces

3.4 Notations for internal forces

Figure 5 shows the notations necessary to define the set of internal forces at the critical sections for the J-mode of exterior beam-column joint. The notations $T_1, T_2, T_3, T_4, T_5, T_6, T_7$ and T_8, represent the resultant tensile forces in longitudinal bars, while C_1, C_2, C_3 and C_4 represent the resultant compressive forces on the concrete boundaries. The values of C_1, C_2, C_3 and C_4 equal to the x component of compressive resultant in concrete. The direction of principle stress in concrete is assumed to be parallel to the diagonal line on the joint shear panel. The stress in concrete stress block is assumed σ_c.

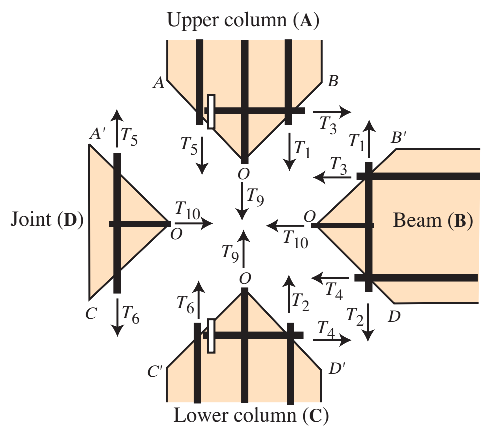

(a) Forces in reinforcements at critical sections (Type I : Anchorage of beam bars locate inside of column bars)

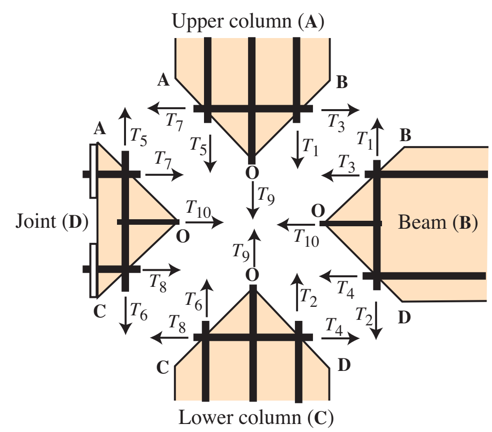

(b) Forces in reinforcements at critical sections (Type II : Anchorage of beam bars locate outside of column bars)

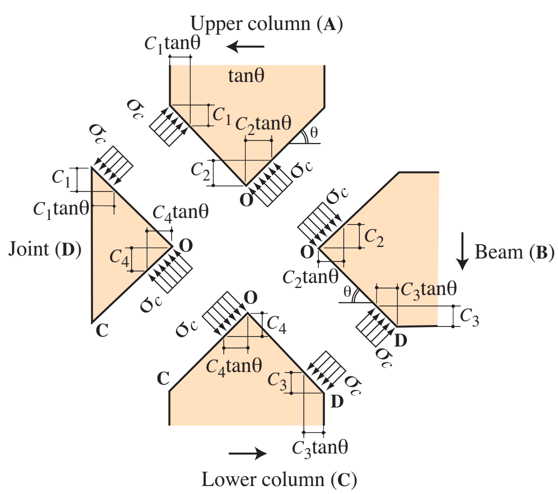

(c) Forces in concrete at critical sections

Figure 5: Notations for internal forces on critical sections of J-modes

3.5 Equilibrium in Forces Acting on the Segments

Three equations are necessary to define equilibrium for a rigid plane body. In this system, twelve equations exists to define equilibrium because a beam-column joint subassembledge consists of four rigid bodies. However the three equilibrium equations which describes the relation of applied forces already incorporated into them, the remaining number of independent equations is nine. Hence, the number or independent equilibrium equations is nine. They are given as follows. The equilibrium in *x* direction on the three free bodies **A**, **B**, **C** are expressed as,

$$T_3 - T_7 + C_1 - C_2 - V_c = 0 \tag{1}$$

$$-T_3 - T_4 + C_2 + C_3 - T_{10} - T_p = 0 \tag{2}$$

$$T_4 - T_8 - C_3 + C_4 + V_c = 0 \tag{3}$$

The equilibrium of forces in *y* direction on the three free bodies **A**, **B** and **C** are expressed as,

$$-T_1 - T_5 + C_1 \tan\theta + C_2 \tan\theta - T_9 - N_c = 0 \tag{4}$$

$$T_1 - T_2 - C_2 \tan\theta + C_3 \tan\theta - 2\left(V_c \cdot \frac{L_c}{L_b}\right) = 0 \tag{5}$$

$$T_2 + T_6 - C_3 \tan\theta - C_4 \tan\theta + T_9 + N_c + 2\left(V_c \cdot \frac{L_c}{L_b}\right) = 0 \tag{6}$$

The equilibrium of moment on the three free bodies **A**, **B** and **C** with respect to the center point **O** (see Fig. 5) are expressed as,

$$\frac{j_b D_b}{2}(T_7 - T_3) + \frac{j_c D_c}{2}(T_5 - T_1) + \frac{C_2^2}{2b_c \sigma_c \cos^2\theta} - C_1 \tan\theta\left(D_c - \frac{C_1 \tan\theta}{2b_c \sigma_c \cos^2\theta}\right) + L_c V_c = 0 \tag{7}$$

$$\frac{j_b D_b}{2}(T_3 - T_4) + \frac{j_c D_c}{2}(T_1 - T_2) - \frac{C_2^2}{2b_c \sigma_c \cos^2\theta} + C_3 \tan\theta\left(D_c - \frac{C_3 \tan\theta}{2b_c \sigma_c \cos^2\theta}\right) - 2L_c V_c = 0 \tag{8}$$

$$\frac{j_b D_b}{2}(T_4 - T_8) + \frac{j_c D_c}{2}(T_2 - T_6) + \frac{C_4^2}{2 b_c \sigma_c \cos^2\theta} - C_3 \tan\theta\left(D_c - \frac{C_3 \tan\theta}{2 b_c \sigma_c \cos^2\theta}\right) + L_c V_c = 0 \tag{9}$$

respectively. The simultaneous equations of second order from Eq. (1) to Eq. (9) yields four sets of solutions for nine unknown variables, provided the value of the other variables are fixed. When solutions are obtained, meaningful solution need to be selected. By solving the equations from Eq. (1) to Eq. (9), the story shear V_c is calculated.

4. STRENGTH OF EXTERIOR BEAM-COLUMN JOINTS

4.1 Assumptions

For the joints of Type I, the values T_7 and C_1 is assumed to be zero because horizontal reinforcing bars do not pass through the critical section at which T_7 is considered.

$$T_7 = 0 \text{ and } C_1 = 0 \qquad \text{(for Type I exterior joint)} \tag{10}$$

As a result, crack opens and no compressive force is transferred. To obtain the solution for joints of Type I, V_c, T_1, T_2, T_5, T_6, T_8, C_2, C_3 and C_4 are chosen as unknown variables, whereas, the T_3, T_4, T_p, T_9 and T_{10} is assumed to be given.

For Type II joint, two restrictive condition is added to the equilibrium condition. The force T_7 is assumed = $T_3/2$ and T_4 are assumed to be identical to and T_8 respectively. This is an assumption that the half of anchorage force of tensile beam bar are transferred to concrete at the anchorage end and the other half of the tensile force is transferred by bond in beam-column joint.

$$T_7 = T_3/2 \quad \text{and} \quad T_4 = T_8 \qquad \text{(for Type II exterior joint)} \tag{11}$$

To obtain the solution for joints of Type II, V_c, T_1, T_2, T_5, T_6, T_7, T_8, C_1, C_2, C_3 and C_4 are chosen as unknown variables, whereas, the T_3, T_4, T_p, T_9 and T_{10} is assumed to be given.

In all cases, the resultant force T_{10} is assumed that it equals to the yielding strength of joint shear reinforcement, while resultant force T_9 of zero is assumed. The longitudinal bars in columns and beams are assumed infinitely strong and never yield. The compressive stress of concrete stress block is assumed to be uniform within the thickness of column for J-mode critical section.

4.2 Failure criteria

In the past tests of exterior beam-column joint, it was reported that joint shear failure initiated when the anchorage force saturates in longitudinal bar in column on the beam side in beam-column joint (Shiohara et al. 2002). Thus, the following restrictive conditions are also taken into consideration to evaluate the joint shear capacity as follows. The total bond force B resisted by longitudinal bar in column on the beam side is expressed as the difference of stress resultants T_1 and T_2 as shown in Eq. (12) and not exceed the bond capacity B_u.

$$B = T_1 - T_2 < B_u \tag{12}$$

where, B_u: anchorage capacity of column bars, assumed to be estimated with Eq. (3) based on the test within beam-column joint. For the value of the k of 1.8 was suggested for modeling of bond capacity of non yielding tensile bar passing beam-column joint by Lowes (Lowes 2002).

$$B_u = k\sqrt{\sigma_B}\Sigma\varphi D_b \text{ (in N)} \tag{13}$$

where, $k\sqrt{\sigma_B}$: averaged bond strength in beam-column joint in MPa, and σ_B : concrete compressive strength in MPa, $\Sigma\varphi$: total perimeter length of longitudinal bar in the first layer of beam side in the column in mm, and D_b: beam depth in mm, D_c is used for D_b in the case of interior beam-column joint.

4.3 J-mode Strength

By solving the equilibrium equations and the other condition shown in Eq. (1-13), V_c are obtained as a function of T_3. Then pseudo joint shear $V_{j(pseudo)}$ and pseudo joint shear strength τ_{ju} of J-mode is derived from V_c by Eq. (14) and (15).

$$V_{j(pseudo)} = V_c\left(2 \times L_c\left(\frac{(L_b - (j_c D_c)/2)}{L_b} \cdot \frac{1}{j_b D_b}\right) - 1\right) \tag{14}$$

$$\tau_{ju} = \frac{V_{j(pseudo)}}{A_j} \tag{15}$$

where, $A_j = d_j(b_c + b_b/2)$: effective area of beam-column joint, d_j: effective depth of joint, full depth of column is used in US (ACI 2002) while the development length from column face to the anchor end is used for the AIJ Guidelines (AIJ 1999).

4.4 B-mode strength

By considering the equilibrium of horizontal force and moment at the critical section at the end of beam as shown in Fig. 6, the relation of the internal force T_3, T_4 and moment M_b at the critical section is derived as the Eq. 1.

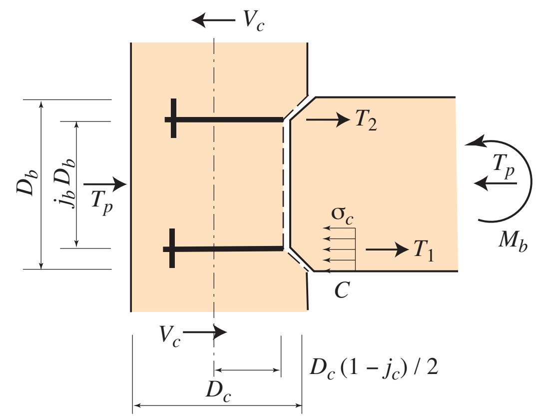

Figure 6: Notations for internal forces on critical sections of B-modes

When the J-mode strength is calculated by solving the equation as explained in the section 5.1, The value of T_3, T_4 is also obtained. Hence, the moment of B-mode is calculated using the Eq. (14) as a function of T_3.

$$M_b = \frac{T_3 - T_4}{2} j_b D_b + \frac{(T_3 + T_4 + T_p) D_b}{2}\left(1 - \frac{T_3 + T_4 + T_p}{b_b D_b \sigma_c}\right) \tag{16}$$

Then, the column shear V_c is obtained from Eq. (17) by considering the geometry of substructure and equilibrium condition.

$$V_c = \frac{M_b}{2(L_b - j_c(D_c/2))} \frac{L_b}{L_c} \tag{17}$$

Finally strength of B-mode is calculated as pseudo joint shear stress τ_{ju} using Eq. (14) and (15) as shown for J-mode strength.

5. NUMERICAL SOLUTION AND EXAMPLE

Table 2 lists the control parameters for analysis to demonstrate the models for both interior and exterior joints. The compressive stress of concrete stress block is assumed to be 85% of concrete compressive strength, typical value for flexural analysis. For exterior beam-column joint of Type II, the development length of beam bar in joint is assumed to 80% of column depth D_c. The equilibrium equations and assumptions for interior beam-column joint are not shown here but is described in detail in the reference (Shiohara 2002). To obtain the numerical solutions by solving the simultaneous equation, symbolic mathematical programing software Maple V was used. No post tensioning force T_p is assumed in this study, although it has some effects on the joint shear strength. It may be discussed in the other occasion.

Table 1: Parameter of control a beam-column joint subassembledge

Parameters	
L_b = 1500 mm	j_c = 0.75
L_c = 1000 mm	N_c = 100 kN
b_b = 250 mm	T_p = 0
b_c = 300 mm	σ_B = 30 MPa
D_b = 300 mm	p_w = 0.3%
D_c = 300 mm	f_y = 300 MPa
j_b = 0.75	σ_c = 85% of σ_B
beam (column) bars : 4-D13 (First layer)	
development length of beam bar = 0.8 D_c	

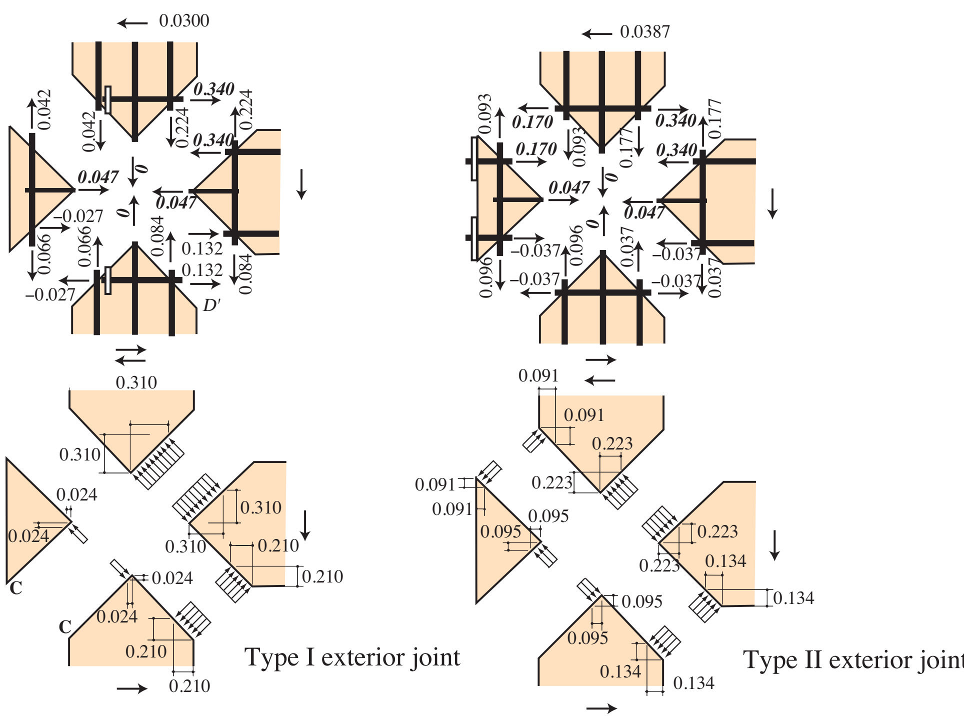

Figure 7: Calculated resultant forces for Type-I and Type-II exterior joints

Figure 7 shows calculated resultant forces in the two types of exterior beam-column joint with parameters in Table 2 which is calculated as a solution satisfy the equilibrium. These values are calculated at loading stage of $T_3 = 0.34$. The number in the figure is the value of resultant force divided by $b_c D_c \sigma_c$. The values shown in italic type face means the values are based on assumption and not derived by calculation.

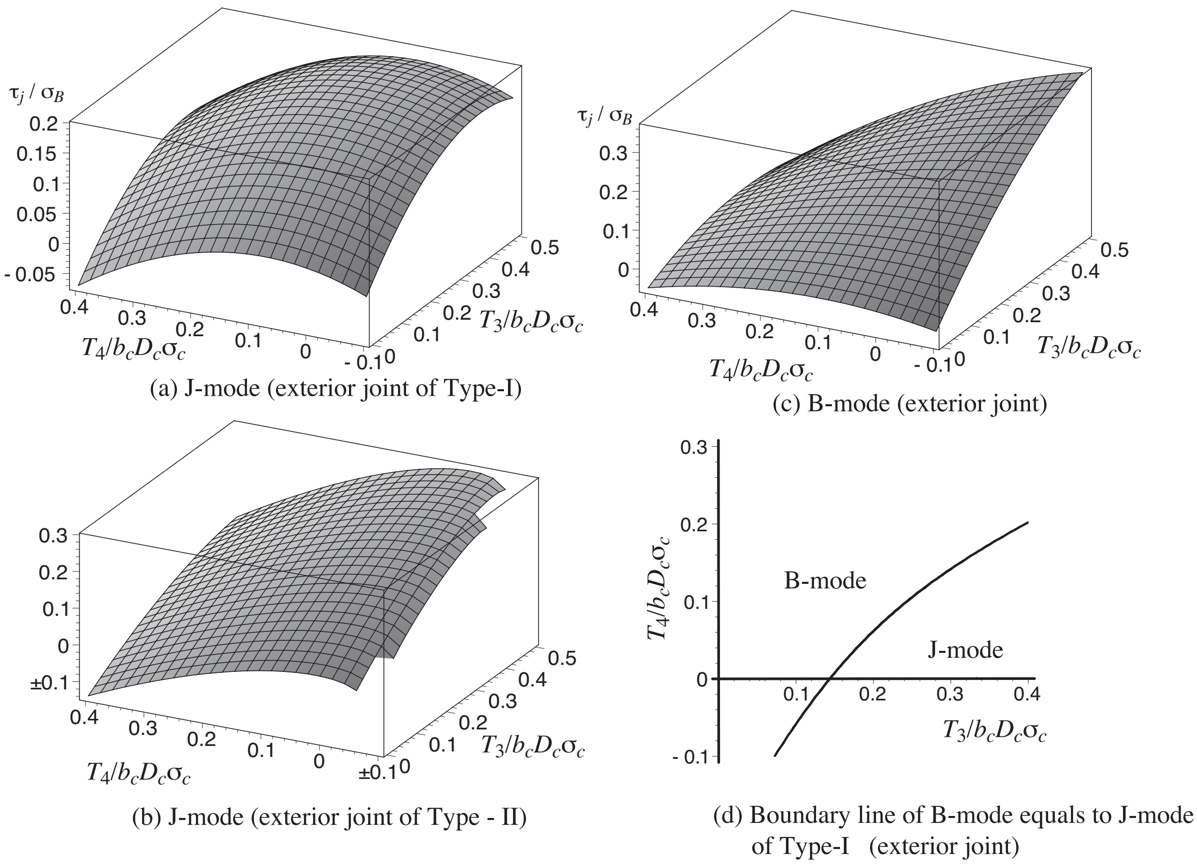

(a) J-mode (exterior joint of Type-I)

(c) B-mode (exterior joint)

(b) J-mode (exterior joint of Type - II)

(d) Boundary line of B-mode equals to J-mode of Type-I (exterior joint)

Figure 8: 3D plot of pseudo joint shear stress against stress resultant in beam bars

5.1 Relation of B-mode strength and J-mode strength

Figure 8 shows the three dimensional plot of pseudo joint shear stress τ_{ju} for three different deformation mode, J-mode (Type I), J-mode (Type-II) and B-mode, on the plane defined by (T_3, T_4), by neglecting the condition on bond of Eq. (12). The shapes of strength of J-mode has a peak less than 0.2 and look like a dome, whereas the shape of B-mode and J-mode (Type II) show monotonically increasing slope as T_3 and T_4 increase. It is similar to the interior beam-column joint reported in the reference (Shiohara 2002). However the joint shear strength are around half of that of interior beam-column joints.

5.2 Pseudo joint shear strength

Figure 9 shows the relation of T_1 (interior joint) or T_3 (exterior joint) and pseudo joint shear τ_{ju} considering restrictive condition of Eq. (16) for exterior beam-column joint

$$T_1 - T_2 = k\sqrt{\sigma_B}\Sigma\varphi D_b \quad k = 1.8 \tag{18}$$

and considering restrictive condition of Eq. (19) for interior beam-column joint.

$$T_1 - T_2 = k\sqrt{\sigma_B}\Sigma\varphi D_c \quad k = 1.8 \tag{19}$$

where, T_1 and T_2 are defined in reference (Shiohara 2002).

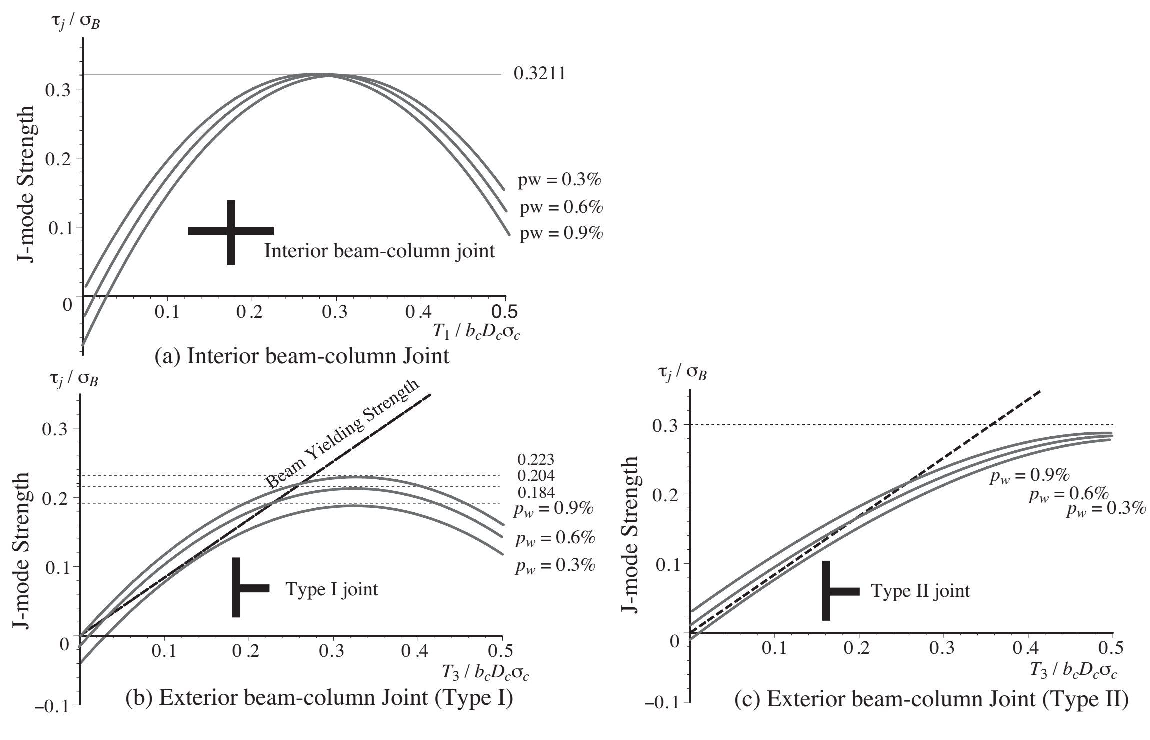

Figure 9: Relation of stress resultants in tensile longitudinal reinforcement in beam at column fact to pseudo joint shear strength

The joint shear strength, or the values of maximum pseudo joint shear stress normalized with concrete compressive strength are 0.3491, 0.188, > 0.28 for a) interior beam-column joint, b) exterior beam-column joint of Type-I and c) exterior beam-column joint of Type-II respectively. As shown in the Fig. 9, The strength of the exterior beam-column joints is 53% of the strength of the interior beam-column joint for Type-I, where as the strength of Type-II exterior joint, the strength is more than 80% of the interior beam-column joint. It is concluded that the beam-column joint with beam longitudinal bar anchored at opposite face of column has quite large capacity. It may be concluded if the exterior beam-column joint has non framing cantilever beam on opposite face and beam bars are anchored in the non framing beam, then the joint shear strength is larger than ordinary exterior beam-column joint like that of Type-II exterior joint. However, the strength is a little bit smaller than that of interior beam-column joint.

The calculated pseudo joint shear for the cases of p_w = 0.6% and p_w = 0.9% are also shown to examine the effects of the amount of joint shear reinforcement. Amount of joint shear reinforcement has no effect on the pseudo joint shear strength for interior joint. This fact agrees with current knowledge on the joint shear strength of beam-column joint based on tests described in design codes (ACI 2002, AIJ 1999). On the contrary, the calculated joint strength for exterior beam-column joint of Type-I increases with increasing of joint shear reinforcement ratio p_w. This fact also agrees with our knowledge, whereas the strength of Type-II joint is not affected by the p_w. It should be noted that the effect of joint shear reinforcement changes according to the type of anchorage of beam bars in exterior beam-column joints.

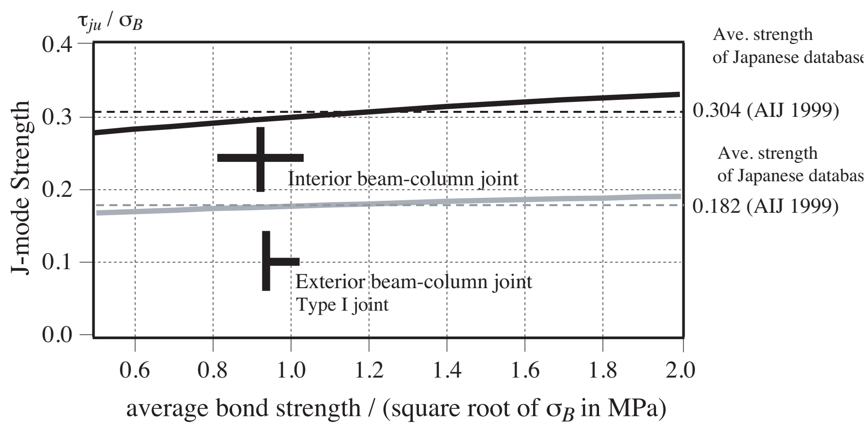

Figure 10: Effect of bond capacity

By comparison of joint strength of interior and exterior beam-column joint, shape factor adopted in current code seems to be larger for exterior beam-column joint. It means that interior beam-column joint has larger safety margin than exterior beam-column joint. For the exterior beam-column joint of Type II, the enhancement of performance may be admitted for this special detail in future revision of codes, typically used for exterior beam-column joint with post tension in beam and beam-column joint.

However, the assumptions in this paper neglect special cases, such as the premature yielding of column longitudinal reinforcement, which causes joint shear failure is not considered here. In addition to that, test results of exterior beam column joint showed joint shear failure initiated beam bar yielding, while story shear is much lower than calculated by flexural theory (Shiohara 2002). Hence the result of study here may gives higher strength than tests in some case. The premature yielding of bars may happen if the bending capacity of column is smaller or close to the flexural capacity of beam.

5.3 Effect of bond capacity on joint shear strength

As bond capacity is considered as an key factors for this model. It determines the strength and failure modes of beam-column joints. So the effects of the bond capacity is investigated. Figure 10 shows the calculated value of J-mode strength with parameter of *k* defined in Eq. (18) and (19). Larger value of *k* generally gives larger joint shear strength. However the joint strength is not proportional to the bond strength nor have significant effects. If bond capacity increase twice, the increase of joint shear strength remains approximately 10%. It may be concluded that the bond capacity is not so sensitive to the joint shear strength. Nonetheless it is essential, because this effect may explain the reason of enhancement in strength of beam-column joint with transverse beams observed in tests. Transverse beams covering beam-column joint is effective to increase the bond strength, as a result, joint shear strength increases.

The Fig. 10 also compare the calculation and the average strength reported in the commentary of AIJ Guidelines (AIJ 1999) derived from Japanese database of test of beam-column joint without transverse beams. They are given by the equations,

$$\tau_{ju} = 1.56 \times \sigma_B^{0.712} \quad \text{for interior beam-column joint} \tag{20}$$

$$\tau_{ju} = 1.13 \times \sigma_B^{0.718} \quad \text{for exterior beam-column joint} \tag{21}$$

where, τ_{ju} : joint shear strength and σ_B : concrete compressive strength.

So as to compare the interior and exterior joint shear strength based on same joint area A_j, the value of Eq.(21) are factored 80% in Figs.10 and 11, because Eq. (21) is based on the effective depth equal to development length from column face to the anchor end in AIJ Guidelines. For both interior and exterior joint, calculated values agree well with the average observed joint strength.

5.4 Effect of the other parameters on joint shear strength

While this model include large set of parameters, more dominant parameters affecting on joint shear strength are arbitrary selected and shown in Fig. 10. Figure 10 (a) shows the relation of joint shear reinforcement ratio and joint shear strength. It is worth noted again that the joint shear reinforcement ratio has significant effects for enhancing the joint shear strength only for Type-I exterior beam-column joint, while it has no effects on the shear strength of interior beam-column joints.

Figure 10(b) shows the other important factor seemingly affecting the joint shear strength much. It is the aspect ratio of beam-column joint panel. The aspect ratio is defined as the ratio of beam depth to column depth. For interior beam-column joint, larger aspect ratio gives lower joint shear strength, while larger aspect ratio gives larger joint shear strength for exterior beam-column joint. The aspect ratio has opposite effects to interior and exterior joint. It may be attributed to the location of bond capacity saturation happens. For interior beam-column joint, saturation of bond capacity happens in beam bars, while it happens in column bars for exterior beam-column joint. It is interesting and need to be investigated because prediction of the effect is very large compared to the other parameter. This factor may be taken into account as most important factor in future code revision.

Figure 10 (c) shows the relation of concrete strength and joint shear strength. It seems that joint shear strength is not proportional to concrete compressive strength. It is because the joint shear strength is partly governed by the bond capacity and it is assumed to be proportional to square root of concrete compressive strength in this study. If less concrete strength reduction factor is used for higher strength concrete, analysis will give smaller joint shear strength for higher strength concrete.

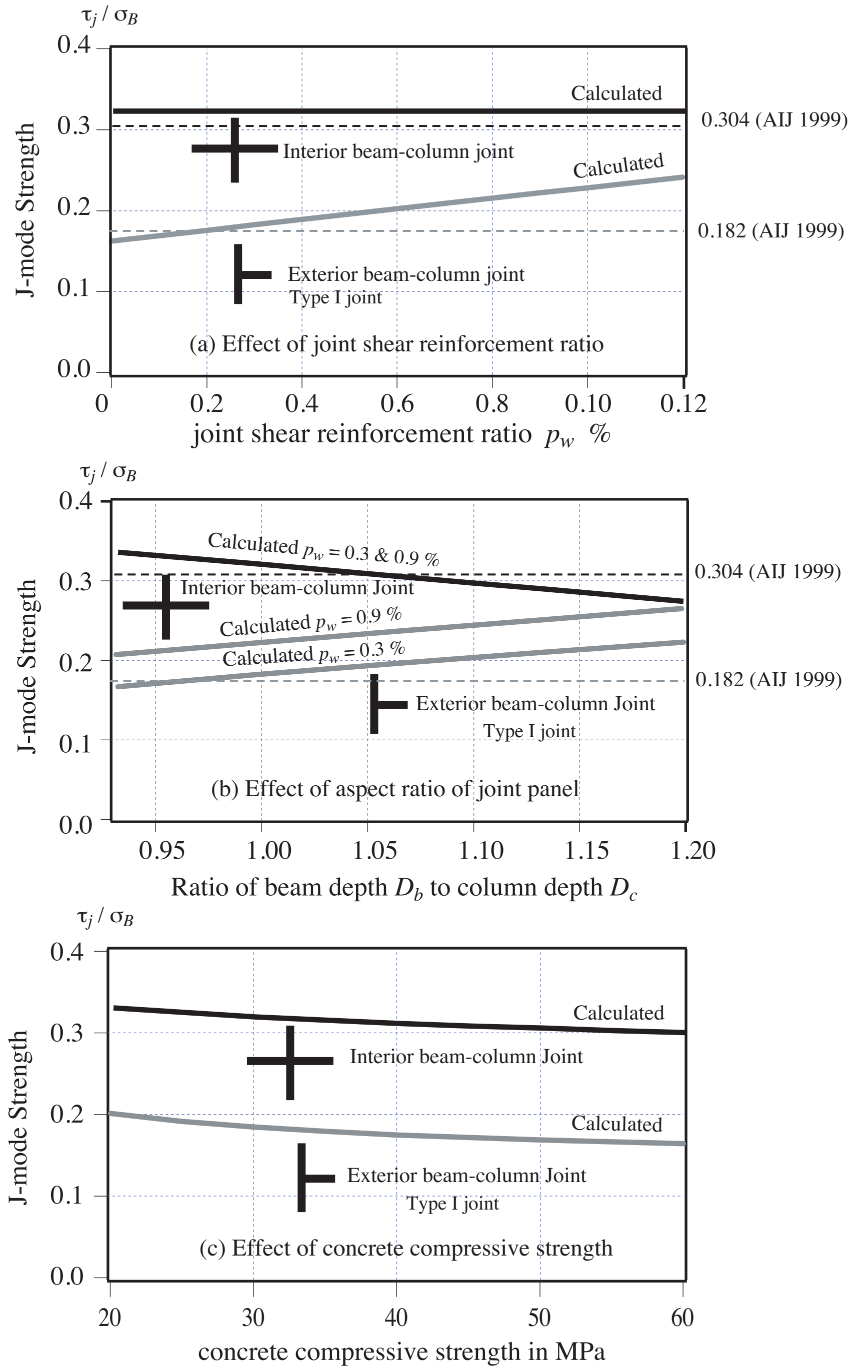

Figure 11: Calculated joint shear strength for controll specimen (see Table 2)

In reality, bond capacity may changes due to various factors such as axial force level of column due to confining effect or transverse beam covering joint. Bond strength is also affected by the thickness of cover concrete and location of bar in beam or column section as well as diameter of bars and number of bars, yielding of longitudinal steel and cyclic loading. They should be considered if necessary. The effect of bond deterioration due to loading history and yielding of reinforcing bars may cause strength decay for joint shear failure after beam yielding.

6. CONCLUSIONS

A new analytical models for joint shear failure of reinforced concrete exterior beam-column joints is proposed. It is a simple and comprehensive model extended from a similar model predicting strength and failure modes developed for interior beam-column joints. The model contains no empirical factors accounting the difference between exterior and interior joint like a shape factor adopted in current design code. The principles, assumptions, mathematical formulation and numerical demonstration of the model are described. The numerical demonstration is provided and the correlation of the calculation and test results are examined. It is concluded from the numerical calculation.

1. For both interior and exterior joint, calculated value agree well with the average observed joint strength derived from Japanese tests database of beam-column joint.
2. The beam-column joint with beam longitudinal bar anchored at opposite face of column has quite larger capacity. The enhancement of performance may need to be admitted for this special detail in future revision of codes.
3. It is predicted by the mode that joint shear reinforcement ratio has significant effects for enhancing the joint shear strength of exterior beam-column joint, while it has no effects on the shear strength of interior beam-column joints. This prediction well agrees with the state-of-the-art on the beam-column joint.
4. By comparison of joint strength of interior and exterior beam-column joint, shape factor adopted in current code seems to be larger for exterior beam-column joint. It means that interior beam-column joint is larger safety margin than exterior beam-column joint.
5. As bond capacity increase the joint shear strength increase, because the bond capacity is key parameter in the new models. Nevertheless the joint strength is not proportional to the bond strength nor have significant effects.

6. For interior beam-column joint with larger aspect ratio gives lower joint shear strength, while larger aspect ratio gives larger joint shear strength for exterior beam-column joint. The aspect ratio has opposite effects to interior and exterior joint.

7. REFERENCES

American Concrete Institute (ACI). (2002). “Building Code Requirements for Structural concrete and Commentary.” ACI 318-02, Farmington Hills, Michigan.

Architectural Institute of Japan (AIJ), (1999). “Design Guideline for Earthquake Resistant Reinforced Concrete buildings Based on Inelastic Displacement Concept” Tokyo, Japan. (in Japanese)

Cheung, P. C., Paulay, T. and Park, R., (1991). “Some Possible Revisions to the Seismic Provisions of the New Zealand Concrete Design Code for Moment Resisting Frames,” Proceeding of the Pacific Conference on Earthquake Engineering, New Zealand, November 1991, 79-90.

Lowes, L. N. and A. Altoontash, (2002). “Modeling the Response of RC Building Beam-column Joints subjected to Earthquake Loading,” Proceedings of the Seventh U.S. National Conference on Earthquake Engineering (7NCEE), July 21-25, 2002, Boston, Massachusetts.

Paulay, T., Park, R., and Priestley, M. J. N., (1978). “Reinforced Concrete Beam-Column Joints Under Seismic Actions.” Journal of ACI, 75 (11), 585-593.

Shiohara, H., (2001). “New Model for Shear Failure of RC Interior Beam-Column Connections,” Journal of Structural Engineering, ASCE, Vol. 127, No. 2, February 2001, 152-160.

Shiohara, H., (2002). “Effects of Interaction between Joint Shear and Anchorage Force within R/C beam-column Joints on their Strength and Failure Modes, Proceedings of the Seventh U.S. National Conference on Earthquake Engineering (7NCEE), July 21-25, 2002, Boston, Massachusetts.

Shiohara, H., A. T. Sato, S. Otani and T. Matsumori, (2002). “Effects of Beam Prestressing Force on the Strength and Failure Mode of R/C Exterior Beam-Column Joints,” Proceedings of the first fib congress, October 14-28, 2002, Osaka, Japan.

DEVELOPMENT OF BOLTED CONNECTIONS FOR STEEL REINFORCED CONCRETE COMPOSITE STRUCTURES

Yan XIAO [1]; J. C. ANDERSON [1]

Yuntian WU [2]

ABSTRACT

One of the most significant lessons learned from the 1994 Northridge earthquake and the 1995 Kobe earthquake was the cracking and brittle failure of welded moment connections of modern steel buildings. Several important progresses have since been made, resulting in improved designs. One possible solution for improving the design and construction of moment resisting frame (MRF) buildings ranging in height from mid-rise to high-rise may be the adoption of composite steel and concrete MRF systems in the regions of high seismicity. Because of the existence of reinforced concrete and the high stiffness in a composite MRF, the deformation demand to the encased steel joints becomes less than in a pure steel MRF. Smoother force transfer mechanisms with less stress concentration can be expected in a composite beam-to-column connection. Thus, the development of composite MRFs can provide the structural design and construction professions with an alternative structural system. In order to improve the constructability and meanwhile ensure excellent seismic behavior, several innovative composite connection details were conceived and will be studied by the authors. This paper describes the proposed concepts and analysis of testing specimens.

1. INTRODUCTION

1.1. Background

One of the most significant lessons learned from the 1994 Northridge earthquake and the 1995 Kobe earthquake was the cracking and brittle failure of welded moment connections of modern steel buildings [Bertero et al. 1994, 1995]. Several important progresses have since been made, resulting in improved designs [Anderson et al. 2001, SAC FEMA 350, Xiao and Mahin 2000 edited].

One possible solution for improving the design and construction of moment resisting frame (MRF) buildings ranging in height from mid-rise to high-rise may be the adoption of composite steel and concrete MRF systems in the regions of high seismicity. Because of the existence of reinforced concrete and the high stiffness in a composite MRF, the deformation demand to the encased steel joints becomes less than in a pure steel MRF. Smoother force transfer mechanisms with less stress concentration can be expected in a composite beam-to-column connection. Thus, at least the development of composite MRFs can provide the structural design and construction professions with an alternative structural system.

1. Dept. of Civil Engineering, University of Southern California, Kaprielian Hall, Los Angeles, CA 90089-2531, Email: yanxiao@usc.edu
2. College of Civil Engineering, Hunan University, Changsha, Hunan, China.

In general, composite steel and concrete structures have the following advantages compared with steel structures:

i. By encasing steel shapes in reinforced concrete or using concrete filled tubular columns, a composite system can provide high lateral stiffness which is important for tall buildings.
ii. Buckling behavior of steel shapes can be significantly improved.
iii. Composite structures or structural members have relatively high rigidity and damping against vibration, thus are especially desirable for residential, hotel and office buildings. The concrete finishing is also favored architecturally.
iv. The combination with concrete not only provides the above mechanical merits, but also can also greatly improve fire resistance.

On the other hand, composite steel and concrete structures have the following advantages compared with reinforced concrete (RC) structures:

i. Properly designed composite steel and concrete members can prevent the brittle failure mode of reinforced concrete members and have significant ductility.
ii. The size of the members can be made smaller thus increasing strength/weight ratios.
iii. The encased steel frame can be used as formwork during construction.

In the United States, most of the previous research on composite frames has been focused on reinforced concrete steel (RCS) connections between reinforced concrete columns and steel beams [ASCE Task 1994; Deierlein et al. 1989; Griffis 1986; Leon et al. 1996; Sheikh et al. 1989]. In a typical RCS system, a small steel section is encased in the column primarily for erection purposes rather than for transferring forces. Research carried out by others (Peng, Ricles and Lu 2000) has indicated that innovative details using post-tensioning and bolting can provide adequate strengths and ductility for steel or concrete filled tubular (CFT) MRF structures. Only limited research has been performed to evaluate the seismic performance of SRC connections that consists of SRC column and steel beam [Chou and Uang 1998, 2000]. Through an NSF sponsored project, Uang and Chou tested two full-scale subassemblies with steel-encased reinforced concrete (SRC) columns and steel beams to evaluate the seismic performance of the connection details. Promising seismic behavior has been observed in their research for connections with reduced steel beam section as well as using offset doubler plates. However, the details investigated by Uang et al. were still quite complicated with the requirement of a welded steel beam to column connection.

1.2. Proposed SRC-MRF Connections

In order to improve the constructability and meanwhile ensure excellent seismic behavior, several innovative composite connection details were conceived by the PIs. It is proposed herein to develop a new type of composite steel and concrete moment resisting frame system using bolted end plate connections without the need of field welding. Three types of connection details are suggested herein.

<u>Type-1: SRC Column and Steel Beam with Bolted Unstiffened End Plate (BUEP) Connection</u>
As shown in Fig.1, the steel beam has a factory-welded end plate, which is bolted to the encased steel column. The moment transfer relies on: the high-tension bolts which connect the end plate of the beam to the encased steel; hoops; concrete struts. It is expected that the doubler plates or continuity plates could be eliminated. If necessary, offset stiffeners as shown by Chou and Uang [1998, 2000] can also be used. The suggested construction process for this type of structure is,

(i) erecting steel columns;
(ii) bolting the end plates of steel beams to the steel columns;
(iii) installing reinforcing bars for the columns;
(iv) forming and casting concrete of the columns (and slabs).

In this case, if the construction tolerance for bolting the steel beams is of concern, stub beams with end plates can be bolted to the steel columns to form so-called "Christmas Tree" types connections. And then drop-in steel beams can be connected to the stub beams at the offset locations where the moments were the smallest. The tolerance problem can also be solved by purposely making the beams slightly short leaving gaps between the end plates and the steel columns, which will be filled with shims before tensioning the bolts.

Type-2: Post-tensioned Steel Beam to SRC Column Connection
The type-2 connection intends to further simplify the design by mainly relying on post-tensioning the connection zone to develop the required force transfer mechanism. As shown in Fig.2, the simply bolted steel beam to column connection is encased in reinforced concrete, which is then post-tensioned. The post-tensioning of the connection zone of the SRC column provides a strong clamping action to the connection zone and can be designed to eliminate cracking thus engaging the full participation of concrete in resistance. The suggested construction process is,

(i) erecting steel columns;
(ii) bolting the end plates of steel beams to the columns;
(iii) installing reinforcing bars to the columns
(iv) forming and casting concrete to the columns (and slabs);
(v) after curing the SRC columns, post-tensioning the connection zones. If necessary, steel bearing plates can be used, as shown in Fig.2.

The foreseeable advantages of this type of connection includes: using only a limited number of bolts, which need not be high-tension, for connecting the end plates of the steel beam to the steel column thus relaxing the tolerance of construction; no need for doubler plates or continuity plates for the encased steel column; reducing reinforcement congestion in the connection zone; etc.

Type-3: Post-tensioned Steel Beam to PC Column Connection
As shown in Fig.3, this type of connection has a detail with directly connecting the end plate of the steel beam to the column by post-tensioning. This creates more freedoms for the design, as the columns can be SRC, RC, and particularly suitable for precast (PC) construction of the columns. Fig.3 schematically depicts a connection with steel beam post-tensioned to a PC column.

The connection proposed herein is different compared with Peng et al.'s post-tensioned connections [Peng et al. 2000; Rojas et al. 2002] where the post-tensioning is for the entire length of the steel beams in a floor. Previous research on joints between reinforced concrete walls and steel coupling beams provides useful references to the proposed study [Shahrooz et al. 2000; Shen and Kurama 2000].

Guidelines for the seismic design of composite moment frames (C-MRF) in the United States were first introduced in the 1994 NEHRP Recommended Seismic Provisions [FEMA 1994]. The design guidelines for composite connection in the NEHRP Provisions are based on a combination of stringent requirements from both the ACI code [1999] and AISC Seismic Provisions [1999]. No specific connection details are presented in the provisions. Related research on the C-MRF connections conducted in Japan mainly consisted of SRC column and SRC beam, which is a more expensive construction type and has not been favored by the US construction industry. Thus, the proposed research faces a significant challenge in a new field where design provisions need to be explored. Specifically, the following design issues will be challenged.

i. Can a special moment resisting frame be made by using bolted SRC or PC columns and steel beams, particularly without reducing the beam section?
ii. Can the doubler plate recommended by FEMA 350 [2000] for BUEP connections be eliminated in the composite connection?
iii. Can the continuity plates recommended by FEMA 350 [2000] for bolted unstiffened end plate (BUEP) connections be eliminated in the composite connection?
iv. Can the stringent transverse reinforcement requirements specified by ACI 318 (1999) be relaxed for the SRC columns?
v. Whether a larger shape than W24 recommended by FEMA for BUEP connections can be used for the proposed composite connection?

2. RESEARCH OBJECTIVES AND SCOPE

The research program is to investigate the seismic performance and to develop guidelines for design of bolted steel beam to SRC composite connections. The followings are the detailed objectives of this program:

i. To define and to provide constructable details using available materials for the proposed three types of connections with a range of section sizes.
ii. To develop and evaluate design methods for the connections to ensure a ductile behavior of the composite MRF system for suitable design in high seismic regions.
iii. To evaluate the stress transfer and resisting mechanisms in the composite connections with the proposed details, through experiments and analyses.
iv. To critically evaluate the current provisions for composite structure design and to provide rational design guidelines.

3. PROPOSED DESIGN APPROACH

A performance design approach is proposed and followed in the selection of the specimens. The approach includes the following steps:

i. To choose a mechanism where plastic hinges occurring at the ends of the steel beams and at the base of the first floor columns;
ii. Design concrete or steel-concrete composite columns for sufficient flexural and shear strength and ductility to ensure the mechanism;
iii. Design the end plates and selection of post-tensioning bolts;

iv. Beam-column joint shear check following two criteria: (1) joint shear cracking check by comparing the principal tensile stress with the concrete tensile strength; (2) if joint shear cracking is identified in (1), then conduct strut-and-tie analysis to determine the shear reinforcement.

4. EXPERIMENTAL PROGRAM

Four large-scale SRC-MRF connection models will be tested using the test configurations shown in Fig.4. Three exterior connection models, each representing one of the proposed composite MRF structures, will be designed and tested. Another test will be conducted for interior connection configuration. During each test, axial load will be applied to the column while cyclic transverse forces will be applied to the beam tips. In order to take full advantages of existing data and testing experiences at the laboratory, it is planned to use AISC W24x76 steel beams. Selection of this steel shape will allow to compare the test results of the current project with those conducted for welded SRC column and steel beam connections by Uang et al. (Chou and Uang 1998, 2000) and the welded steel connections tested by the authors (2000, 2002).

4.1. Design of Steel Beam Bolted to RC Column Connection Specimen

Based on the proposed design procedure and considering the dimensions of Uang's specimens, the exterior connection details were chosen and shown in Fig.5. The design and analysis of the specimen are described hereafter. Note that the strength reduction factors are taken to be unit for the design of specimens.

4.1.1. Flexural strength of steel beam

For seismic design, the nominal strength of the steel beam can be calculated as the plastic moment, M_p,

$$M_p=F_yZ \tag{1}$$

where, F_y is the yield strength of the steel and Z is the plastic section modulus. The corresponding shear V_p in the steel beam with a clear shear span length l_b can then be determined as,

$$V_p=M_p/l_b \tag{2}$$

The AISC W24x76 beam has a plastic section modulus Z=3.28x10^6 mm^3 (200 in.^{3}). If ASTM A572 Grade 50 Steel (yield strength Fy = 345 MPa = 50 ksi) is used, then the plastic moment is calculated as Mp=FyZ=1130 kNm (10,000 kip-in.), and the shear force corresponding to the plastic moment is, Vp=Mp/Lb = 1130/3.125 = 361.2 kN.

4.1.2. Reinforced concrete column design

The shear demands in the columns and the moment demands at column ends should be calculated based on the plastic moments acting at the ends of beam. For a story height of 3.4 m, the shear in the columns is calculated as V_c = 358 kN, and the moment demand at the beam column interface is then 464 kNm. Based on ACI-318 codes, the reinforcements for the 510x510 square column with concrete strength of f_c' = 35 MPa (5.08 ksi) are determined and shown in

Fig.5. The column is reinforced with 10 No. 25 (nominal diameter = 25.4mm) A706 (nominal yield strength = 420 MPa) bars, constituting a total longitudinal steel ratio of 2%.

4.1.3. End plate

The thickness of the end plate can be designed based on the so-called tee-stub analogy (AISC 2001). A thickness of 38 mm (1.5 in.) is chosen for the endplate of the W24x76 steel beam.

4.1.4. Post-tensioned bolts

Two possible approaches can be considered in the design of the post-tensioned bolts, similar to elastic and ultimate design approaches for prestressed concrete beam. The first method is based on a no-tension criterion, and the resultant of the linearly distributed stresses in the steel end plate and the concrete column interface needs to resist the moment demand, M_p. For the specimens studied in this research, such approach would result in impractically large endplate. Thus the ultimate design approach is suggested. The suggested approach is based on a resisting mechanism shown in Fig.6, where the bolts on the tension side resists tension at their ultimate capacities and the concrete rectangular stress block based on ACI 318 codes provides the compressive resistant. It is also suggested that the compressive strength of the concrete for the design can be amplified as a bearing strength using $\sqrt{b_c / b_{ep}}$, here b_c and b_{ep} are the widths of the concrete column and the endplate, respectively. The compression zone depth can then be calculated as,

$$a = \frac{N_{bt} \phi R_n}{0.85 b_{ep} f_c ' \sqrt{b_c / b_{ep}}} \tag{3}$$

where, N_{bt} is the number of the rows of bolts on the tension side; and ϕR_n is the nominal capacity of one row of bolts. The nominal moment capacity, M_{nep}, at the interface of the bearing plate and column can be calculated by taking moment about the center of the compression zone.

$$M_{nep} = \phi R_n \sum (h_{bi} - a/2) \tag{4}$$

where, h_{bi} is the depth of the *i*-th row of bolts measured from the bottom edge of the endplate.

Based on the suggested approach, 14 M22 (nominal diameter 22 mm) A490 bolts aligned in 7 rows are chosen. The required pretension for the M22 A490 bolt is 221 kN (49.7 kip) and the tensile strength neglecting shear is 779 MPa (113 ksi).

4.1.5. Joint shear – cracking check

A conservative design of the beam-column connection is to size the connection zone big enough to eliminate the possibility of joint shear cracking. Similar to the method proposed for column-footing connection (Xiao et al. 1996), principal tensile stress can be calculated and compared with the tensile strength of concrete. As shown in Fig.7(a), the tensile and compressive resultants and shear forces at each of the beam-column interface sections can be analyzed for the ultimate loading condition corresponding to M_p. Note the special feature of the proposed bolted connection where the tension force in at the beam end $N_{bt}\phi R_n$ is transmitted to the other side of the beam-column connection. Applying these forces on the boundary of the connection zone, the average normal and shear stresses in the horizontal and vertical sections, shown in Fig.7 (b) and (c), can be estimated as follows,

$$f_x = \frac{N_{bt}\phi R_n}{b_j h_{jv}} \quad \text{(5-a)}, \qquad f_y = \frac{C_c + C_s - T_s}{b_j h_{jh}} \quad \text{(5-b)}$$

$$\tau_{xy} = \frac{N_{bt}\phi R_n - V_c}{b_j h_{jh}} \quad \text{(5-c)}, \qquad \tau_{yx} = \frac{C_c + C_s + T_s}{b_j h_{jv}} \quad \text{(5-d)}$$

where, b_j is the joint width; h_{jh} and h_{jv} are the depths of the horizontal and vertical sections, respectively. For simplicity, b_j and h_{jh} can be taken as the column width and depth, whereas h_{jv} can be taken as the depth of the steel beam. Note that theoretically τ_{xy} and τ_{yx} are the same magnitude. If they are calculated with different values due to different assumptions for the horizontal and vertical sections, the larger value should be used. The principal tensile stress can then be calculated based on the subtraction operation of the following equations,

$$p_{\substack{c\\t}} = \left(\frac{f_x + f_y}{2}\right) \pm \sqrt{\left(\frac{f_x - f_y}{2}\right)^2 + \tau^2} \qquad (6)$$

If the calculated principal tensile stress p_t exceeds $0.29\sqrt{f_c'}$ (Priestley et al. 1996), cracking is expected in the connection and additional reinforcement is needed for the shear resistance in the joint region. For the exterior connection specimen in this study, the principal tensile stress is calculated as 4.5 MPa > $0.29\sqrt{f_c'}$ =1.7 MPa. It is deemed impractical and inefficient design to further enlarge the column size, thus further analysis for a cracked connection is necessary.

4.1.6. Joint shear – strut-and-tie model

The resulting forces corresponding to the ultimate condition are applied on the boundary of the connection zone with the dimension of the column section and the height of the endplate, as shown in Fig.8 (a). By combining the compressive forces provided by the concrete and compressive steel bars in the column sections and assuming nodes at the intersections of the application lines of various resulting forces, the first simple strut-and-tie model can be constructed as illustrated in Fig.8 (b). For the given conditions, the forces in the elements of the model are analyzed and marked for tension by "T", compression by "C" and zero element by "0", in Fig.8 (b). It is interesting to note that all the horizontal elements which suppose to be ties for a conventional join are subjected to compressive forces, while two of the intended struts (struts 2-3 and 6-7) actually become ties, indicating tensile stress fields in those directions. If assuming no tensile forced can be carried by the concrete struts, the revised strut-and-tie model shown in Fig.8(c) should be considered. The analysis of the revised strut-and-tie model indicates that the horizontal joint reinforcements are only needed near the vicinities of the column ends. It is most important to notice that the tensile forces in vertical ties 1-3, 3-5, 4-6 and 6-8 are all larger than the yield forces of the tensile bars. This indicates the needs of providing additional vertical reinforcements in the connection region.

5. SUMMARY

Steel – concrete composite moment resisting frame systems are proposed along with several innovative connection details. The proposed connections involve post-tensioning the shop-welded endplates of the steel beams to the concrete, precast and prestressed concrete or steel and concrete columns. There is no field welding necessary, eliminating the problems of the welded steel connections. A rational design approach is also suggested for the design of the elements and the beam-to-column connection. The trial design of the testing specimens based on the proposed methods revealed some important features of the connection.

ACKNOWLEDGEMENTS

The research described in this paper is supported by the National Science Foundation under the contract number CMS-0220067. The NSF project director is Dr. Perumalsamy N Balaguru. The project is also conducted as the international collaboration between the University of Southern California of USA and the Hunan University of China. Testing at the Hunan University is sponsored by the Cheung Kong Scholarship of the Ministry of Education and the Hunan Construction Committee. The international collaboration is facilitated by the travel supports of the NSF US-China Cooperative Program managed at the Multi-disciplinary Center for Earthquake Engineering Research (MCEER). The authors would like to appreciate the supports of various sponsoring agencies.

REFERENCES

ACI318, (1999), "Building Code Requirements for Reinforced Concrete," American Concrete Institute, Detroit.

AIJ, (1991), "Standards for Structural Calculation of Steel Reinforced Concrete Structures," Architectural Institute of Japan.

AISC, (2001), "Load and Resistance Factor Design," Manual of Steel Construction, Third edition, American Institute of Steel Construction, Chicago.

Anderson, C.J.; Duan, J.; Xiao, Y.; Maranian, P. (2002) "Cyclic testing of moment connections upgraded with weld overlay." Accepted for publication *Journal of Structural Engineering*, ASCE, March.

Anderson, C.J., et.al., (1995), "Seismic Behavior of HSC Exterior Beam-To-Column Connections," Department of Civil Engineering, University of Southern California.

ASCE Task Committee (1994), "Guidelines for Design of Joints Between Steel Beams and Reinforced Concrete Columns," *Journal of Structural Engineering*, American Society of Civil Engineers, Vol.120, No.8, August, pp.2330-2357.

Bertero, V.V.; Anderson, J.C.; and Krawinkler, H. (1994), "Performance of Steel Building Structures During the Northridge Earthquake," Earthquake Engineering Research Center, Report No. UCB/EERC-94-09, August.

Bertero, V.V. et.al., and Xiao, Y., (1995), "Seismological and Engineering Aspects of The January 17, 1995 Hyogoken-Nanbu (Kobe) Earthquake," Earthquake Engineering Research Center, No. UCB/EERC-95/10, University of California, Berkeley, November, 250p.

Chou CC, Uang CM. (1998), “Experimental and analytical studies of two types of moment connections for composite special moment frames.” Report No. SSRP 98-12, San Diego, La Jolla, (CA): Department of Structural Engineering, University of California, 1998.

Chou, C.C. and Uang, C.M., (2000) “Experimental Studies of Composite-SMF Connections with Reinforced-Concrete-Encased Column and Steel Beams,” Composite and Hybrid Structures – Proceedings of 6th ASCCS Conference, Xiao and Mahin, editors, Los Angeles, March 22-24, pp. 729-736.

CIB, (1990), "Trends in Building Construction Techniques Worldwide, "International Council for Building Research Studies and Documentation.

CERF, (1993), "High-Performance Construction Materials and Systems - an Essential Program for America and Its Infrastructure," Civil Engineering Research Foundation, Technical Report, 93-5011, April.

Deierlein, G.G., Sheikh, T.M.; Yura, J.A.; and Jirsa, J.O. (1989), “Beam-column moment connections for composite frames: Part 2.” Journal of Structural Engineering, ASCE, 115(11), 2877-2896.

FEMA (1994), “Recommended provisions for the development of seismic regulations for new buildings,” Washington, (DC): FEMA-222A, National Earthquake Hazards Reduction Program, Building Seismic Safety Council, 1994.

Griffis, L., (1986), "Some Design Considerations for Composite-Frame Structures," *AISC Engineering Journal*, 23(2), pp.59-64.

Moor, W., and Gosain, N., (1985), "Mixed Systems: Past Practices, Recent Experience and Future Direction," *Composite and Mixed Construction*, C. Roeder, ed., ASCE, New York, N.Y., pp138-149.

Peng, S.W.; Ricles, J.M.; Sause, R.; and Lu, L.W. (2000) “Experimental evaluation of a Post-tensioned Moment Connection for Steel and Composite Frames in Seismic Zone.” Composite and Hybrid Structures – Proceedings of 6th ASCCS Conference, Xiao and Mahin, editors, Los Angeles, March 22-24, pp. 721-728.

Priestley, M.J.N.; Seible, F.; and Calvi, M., (1996), “Seismic Design and Retrofit of Bridges,” *Wiley Interscience*, 686p.

Shahrooz, B.M.; Deason, J.T.; and Tunc, G. (2000) “Cyclic Beahvior of Outrigger Beam-Wall Connections.” Composite and Hybrid Structures – Proceedings of 6th ASCCS Conference, Xiao and Mahin, editors, Los Angeles, March 22-24, pp. 785-793.

Sheikh, T.M.; Deierlein, G.G.; Yura, J.A.; and Jirsa, J.O. (1989) “Beam-column moment connections for composite frames: Part 1.” Journal of Structural Engineering, ASCE, 115(11), 2858-2876.

Shen, Q. and Kurama, Y.C. (2000) “Lateral Load Behavior of Unbonded Post-tensioned Hybrid Coupled Walls.” Composite and Hybrid Structures – Proceedings of 6th ASCCS Conference, Xiao and Mahin, editors, Los Angeles, March 22-24, pp. 793-800.

Xiao, Y.; Anderson, J.C.; and Yaprak, T.T., (2001) “Shear Strength of Steel and Concrete Composite Columns,” Proceedings of Sixth Pacific Structural Steel Conference, Beijing, China, October 15-17, 2001, pp.1171-1176.

Xiao, Y.; Priestley, M.J.N.; and Seible, F., (1996), “Seismic Assessment and Retrofit of Bridge Column Footings," American Concrete Institute, *ACI Structural Journal*, Vol.93, No.1, January-February, pp.79-94.

Xiao, Y.; and Mahin, S. edited, “Composite and Hybrid Structures,’’ Vol.1 and 2, Proceedings of 6th ASCCS International Conference, Los Angeles, March 22-24, 2000, 1220p, ISBN 0-9679749-0-9.

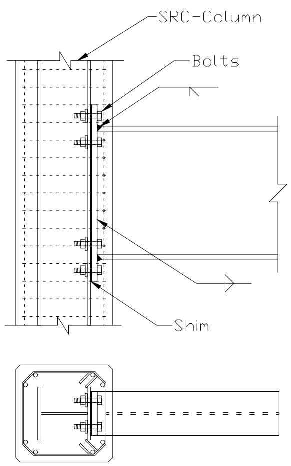

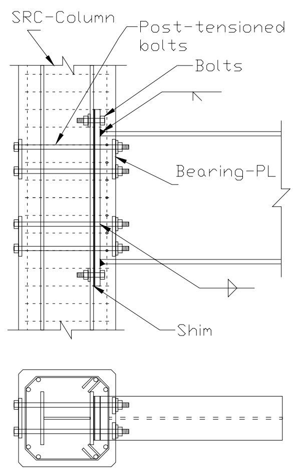

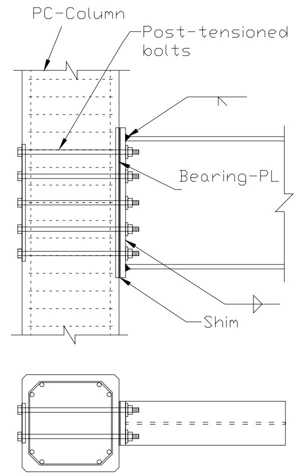

Fig.1. Type-1: **Fig.2. Type-2** **Fig.3. Type-3**

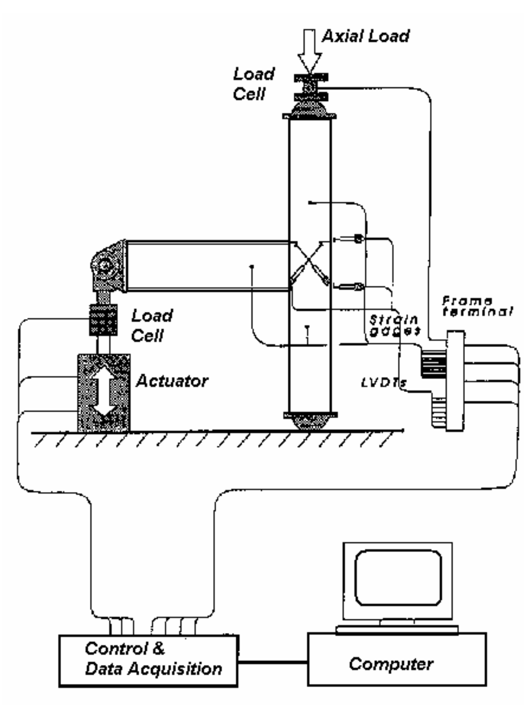

Fig. 4. Test Setup

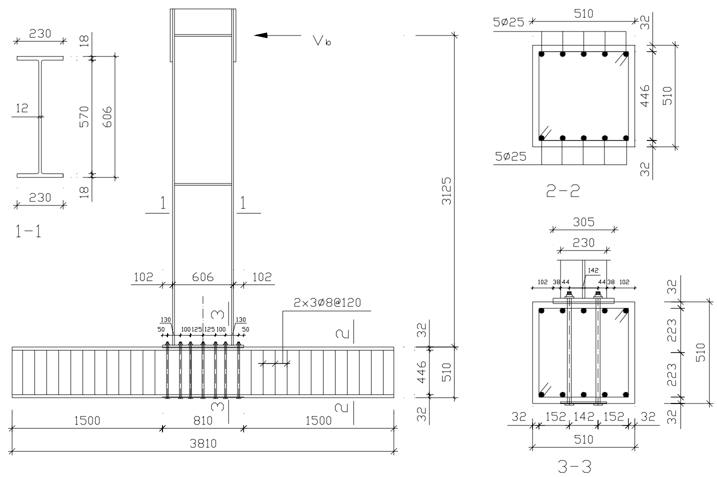

Fig.5. Model exterior connection subassembly details

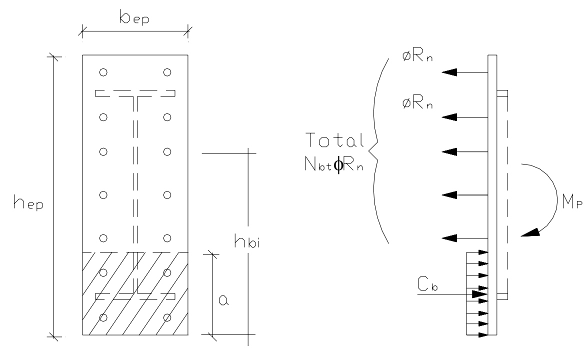

Fig.6. Ultimate condition at endplate and column interface

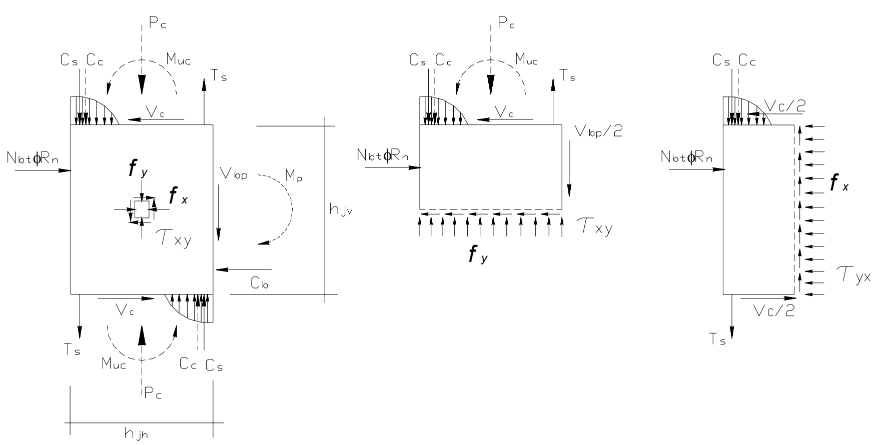

(a) **(b)** **(c)**

Fig.7. Joint shear stresses

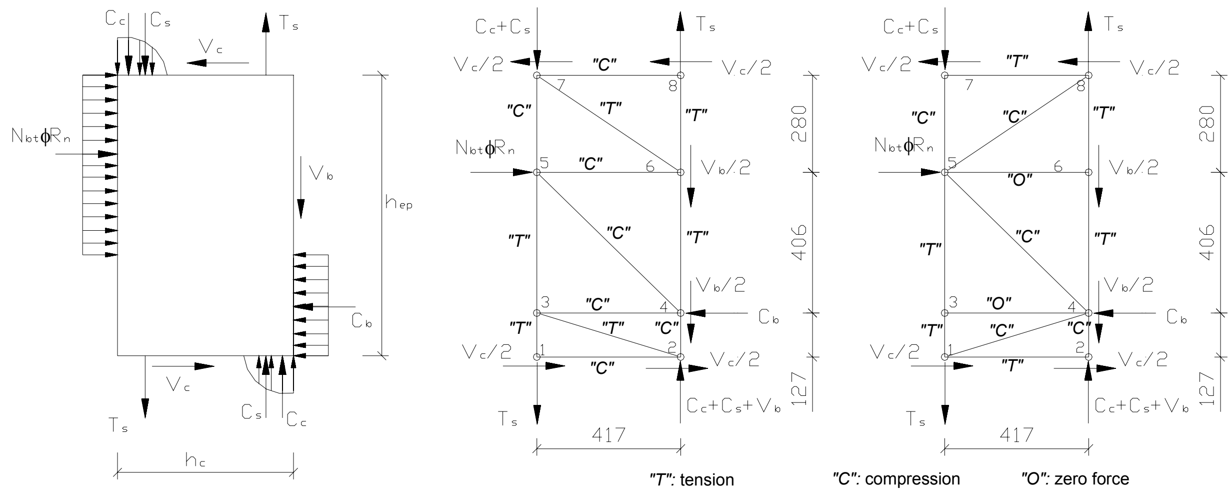

(a) (b) (c)

Fig.8. Strut-and-tie models

Paper prepared for the Fourth US -Japan
Workshop on Performance-Based Engineering
for R/C Building Structures, Toba, Japan,
October 22-24, 2002

Shear Failure Mechanism of Precast Prestressed Concrete Beam-Column Joints Assembled by Post-tensioning Steel Bars

KITAYAMA Kazuhiro [*1], KISHIDA Shinji [*2] and MORIYAMA Kensaku [*3]

ABSTRACT

Prestressed concrete beam-column subassemblage specimens, which were prefabricated by passing post-tensioning deformed bars through precast RC beams and column, were tested under reversed cyclic loading. Beam-column joint panel failed in shear for specimens provided bond between post-tensioning bars and concrete by grout injection, whereas concrete compressive failure due to flexural moment was observed at beam ends for unbonded specimen. To study on horizontal shear force input to joint panel, concrete compressive stress distribution acting on beam critical section was researched through measuring concrete normal strains by gauges stuck on beam surface. Central region of joint panel concrete in some height was subjected to horizontal compression by concrete stress blocks on beam critical sections on both sides of a joint. This means that all concrete compressive force at beam crtical section was not necessarily introduced to a joint panel. The joint input shear force, which was computed using measured tensile forces of post-tensioning steel bars and accounting for non-contribution of the compressive force in middle height of a joint to horizontal shear, deteriorated with the decrease in story shear force. Shear strength in interior beam-column joint obtained by above-mentioned method agreed well with shear strength predicted by AIJ provision proposed for RC beam-column joints.

1. INTRODUCTION

Shear strength in reinforced concrete (RC) beam-column joints can be obtained by Design Guidelines of Architectural Institute of Japan [1], which depends on both the joint shape such as interior, exterior or knee joint and the concrete compressive strength. Whereas, the strength in precast prestressed concrete beam-column joints assembled by post-tensioning steel bars called as PCaPC has not been estimated quantitatively. There are few tests in which joint panel failure is studied for PCaPC beam-column subassemblages [2]. Therefore PCaPC beam-column joint specimens were tested under reversed cyclic lateral loading and column axial loading to study the joint failure mechanism.

---

*1 Associate Professor, Graduate School of Engineering, Tokyo Metropolitan University, Dr. Eng.
Email : kitak@ecomp.metro-u.ac.jp

*2 Research Associate, Graduate School of Engineering, Tokyo Metropolitan University, Dr. Eng.
Email : skishida@ecomp.metro-u.ac.jp

*3 Graduate student, Tokyo Metropolitan University
Email : moriken@ecomp.metro-u.ac.jp

Table 1 Properties of specimens

Specimens	BNU	BHH1	BHH2	BHH3
Post-tensioning Steel Bars	2-D32		2-D36	
Specified Concrete Strength of Column	60MPa		30MPa	
Column Axial Load (Compression, Stress Ratio)	937kN (0.13)		469kN (0.13)	
Mortal of Vertical Joint	Normal Strength	High Strength		
Grout	None	High Strength		
Shape of Subassemblage	Interior Beam-Column Joint			Exterior
Ratio of Initial Tensile Stress to Yield Strength of Post-tensioning Steel Bar	0.7			
Steel Factor*1	0.279			
Specified Concrete Strength of Beam	60MPa			
Column longitudinal Bars	4-D32 (SBPR 930/1080)			
Joint Lateral Bars	2-D10 2 sets			

D32（SBPR 930/1080）：Sheath- 49mm, D36（SBPR 930/1080）：Sheath -56mm

*1 Steel factor： $q = \dfrac{a_y \cdot \sigma_y + a_{py} \cdot \sigma_{py}}{bD \cdot \sigma_B}$, where, D ：depth of section,

a_y ：Section area of longitudinal steel bar, σ_y ：Yield stress of longitudinal steel bar,
a_{py} ：Section area of post-tensioning steel bar, σ_B ：Concrete compressive strength
σ_{py} ：Yield stress of post-tensioning steel bar， b ：Width of section

Table 2 Material properties of joint mortal

Joint Mortal		Compressive Strength, MPa	Secant Modulus, GPa	Tensile Strength, MPa
Normal	BNU	64.9	22.0	4.37
High	BHH1	105.3	39.1	4.07
	BHH2	101.8	37.0	4.07
	BHH3	100.1	36.1	4.07

Table 3 Material properties of grout

Grout		Compressive Strength, MPa	Secant Modulus, GPa	Tensile Strength, MPa
-	BNU	-	-	-
High	BHH1	118.3	32.5	4.91
	BHH2	112.0	31.9	4.91
	BHH3	109.2	31.6	4.91

Table 4 Material properties of steel bars

Diameter		Yield Strength, MPa	Young's Modulus, GPa	Yield Strain, %
D32	BNU, BHH1	1014.4	195.1	0.720*1
D36	BHH2, BHH3	1023.6	211.1	0.685*1
Column Longitudinal Bar (D32)		1014.4	195.1	0.720*1
Beam Longitudinal Bar (D13)		396.4	184.4	0.226
Reinforcing Bar (D10)		418.7	187.0	0.225

*1 Yield strain was determined nominally by 0.2% offset method.

Table 5 Material properties of concrete

Specimens	Compressive Strength, MPa	Strain at Maximum Strength, %	Secant Modulus, GPa	Tensile Strength, MPa
BNU	76.6	0.258	41.1	4.45
BHH1	77.2	0.260	41.1	
BHH2*1	43.0	0.216	33.1	2.99
	71.7	0.255	39.7	4.45
BHH3*1	39.9	0.212	32.2	2.99
	67.4	0.257	38.0	4.45

*1 Upper column:concrete of column , Lower column: concrete of beam

2. OUTLINE OF TEST

2.1 SPECIMENS

Properties of specimens are summarized in Table 1. Section dimensions and reinforcement details are shown in Fig.1. Three plane cruciform and one exterior beam-column joint specimens with two-fifth scale to actual frames were tested. Beam and column elements were precast separately. Post-tensioning steel bars with deformed surface were used to connect precast RC beams and column for all specimens. Therefore beam longitudinal bars were terminated at column face without passing through a beam-column joint panel. The gap with the width of 20 mm between precast beam and column was filled with normal or high strength mortal. Bond along post-tensioning steel bars was provided by injecting high strength grout mortal into the sheath except for Specimen BNU. Unbonded post-tensioning steel bars were used for Specimen BNU. The column section was square with 350mm depth. The depth and width of a beam section were 400mm and 250mm, respectively. Two sets of 2-D10 were arranged in a beam-column joint region as the lateral reinforcement for all specimens. The length from the center of column to the pin-roller support of beam end was1600mm. The height from the center of beam to the loading point on the top of the column or to the bottom support was 1415mm. The shear span ratio was 4.0 in the column and 4.3 in the beam, respectively.

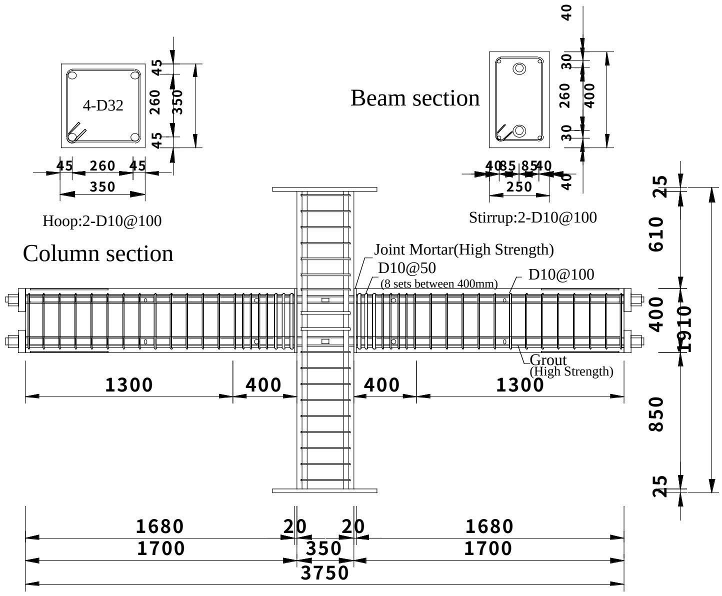

Fig. 1 Section dimensions and reinforcement details

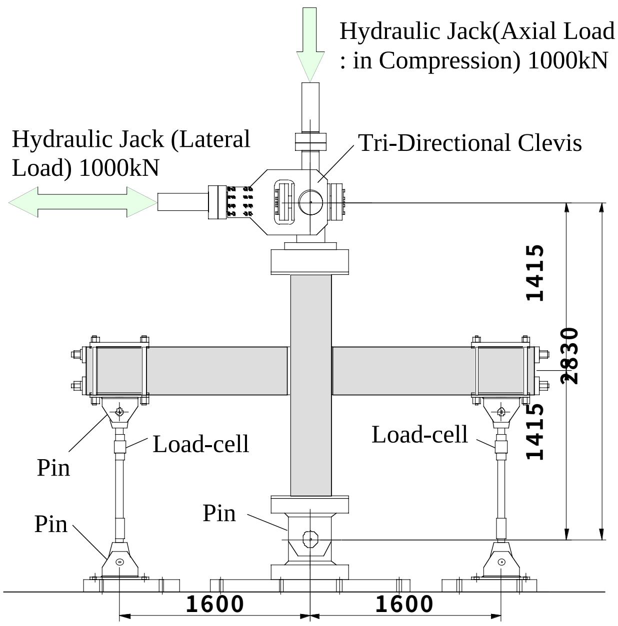

Fig. 2 Loading apparatus

Specimens BNU and BHH1 were designed to develop beam yielding. Concrete compressive strength of 30MPa for a column and the diameter of 36mm for a post-tensioning steel bar were chosen to cause joint shear failure for Specimens BHH2 and BHH3. The amount of the stirrup in beam hinge regions was increased to two times more than that in elastic region. Specimen BHH3 is the exterior beam-column joint. The post-tensioning steel beam bars were anchored with the anchor plates outside the column face. Material properties of concrete, mortal, grout and steel are listed in Tables 2,3,4 and 5.

2.2 LOADING METHOD AND INSTRUMENTATION

The loading system is shown in Fig.2. The beam ends were supported by horizontal rollers, while the bottom of the column was supported by a mechanical hinge. The reversed horizontal load and the constant axial load in compression were applied at the top of the column. All Specimens were controlled by the story drift angle for one cycle of 1/400, two cycles of 1/200 and 1/100, one cycle of 1/66, two cycles of 1/50, one cycle of 1/33 and two cycles of 1/25. Lateral force applied to the top of a column, column axial load and shear forces of both beam ends were measured by load-cells. Story drift, beam and column deflections, and local displacement of a joint panel were measured by displacement transducers. Strains of prestressing steel bars, beam bars, column bars and the joint lateral reinforcement were measured by strain gauges. Moreover, concrete strain distribution at the beam end adjacent to column face was measured by concrete strain gauges stuck on concrete surface (see Fig.7).

3. TEST RESULTS

3.1 CRACK PATTERNS AND FAILURE MODE

Crack patterns at the end of test are shown in Fig.3. Flexural cracks in beams and column and diagonal shear cracks in a joint panel were observed for all specimens. The column longitudinal bars did not yield. Joint lateral reinforcement yielded for all specimens. Post-tensioning steel bars passing through beams yielded for Specimen BHH1. On the contrary, for other specimens post-tensioning steel bars of the beam did not yield. Diagonal joint shear cracks expanded considerably. The shell concrete spalled off in a joint panel except for Specimen BNU. The diagonal shear cracks were not observed in beams for all specimens. Concrete compressive failure at beam ends occurred for Specimen BNU without diagonal crack opening in a joint panel. It was concluded that Specimens BHH2 and BHH3 failed in joint shear, Specimen BNU failed by concrete compression at beam ends due to bending moment and Specimen BHH1 failed eventually in joint shear after the post-tensioning steel bars yielded.

3.2 STORY SHEAR - DRIFT RELATIONSHIP

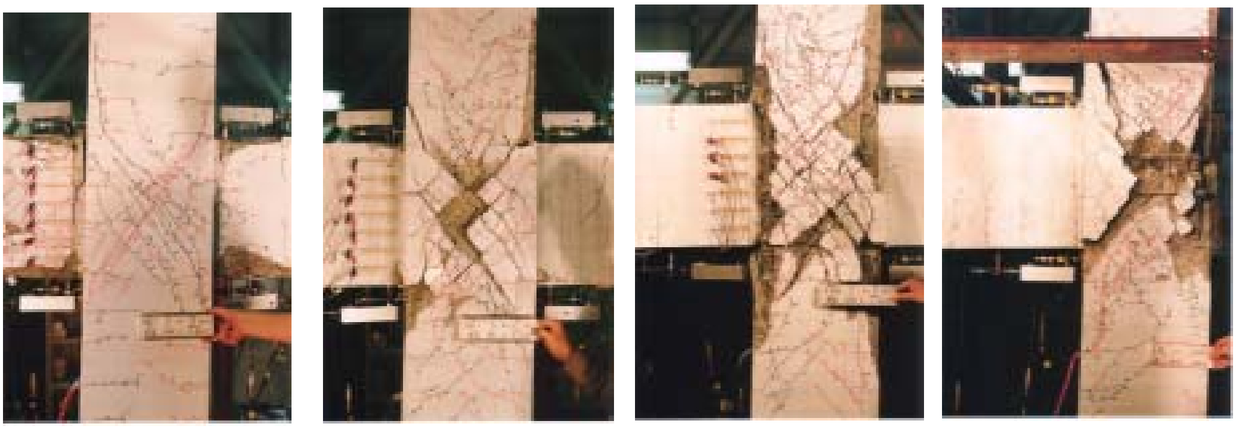

(a) Specimen BNU (b) Specimen BHH1 (c) Specimen BHH2 (d) Specimen BHH3

Fig. 3 Crack patterns at end of test

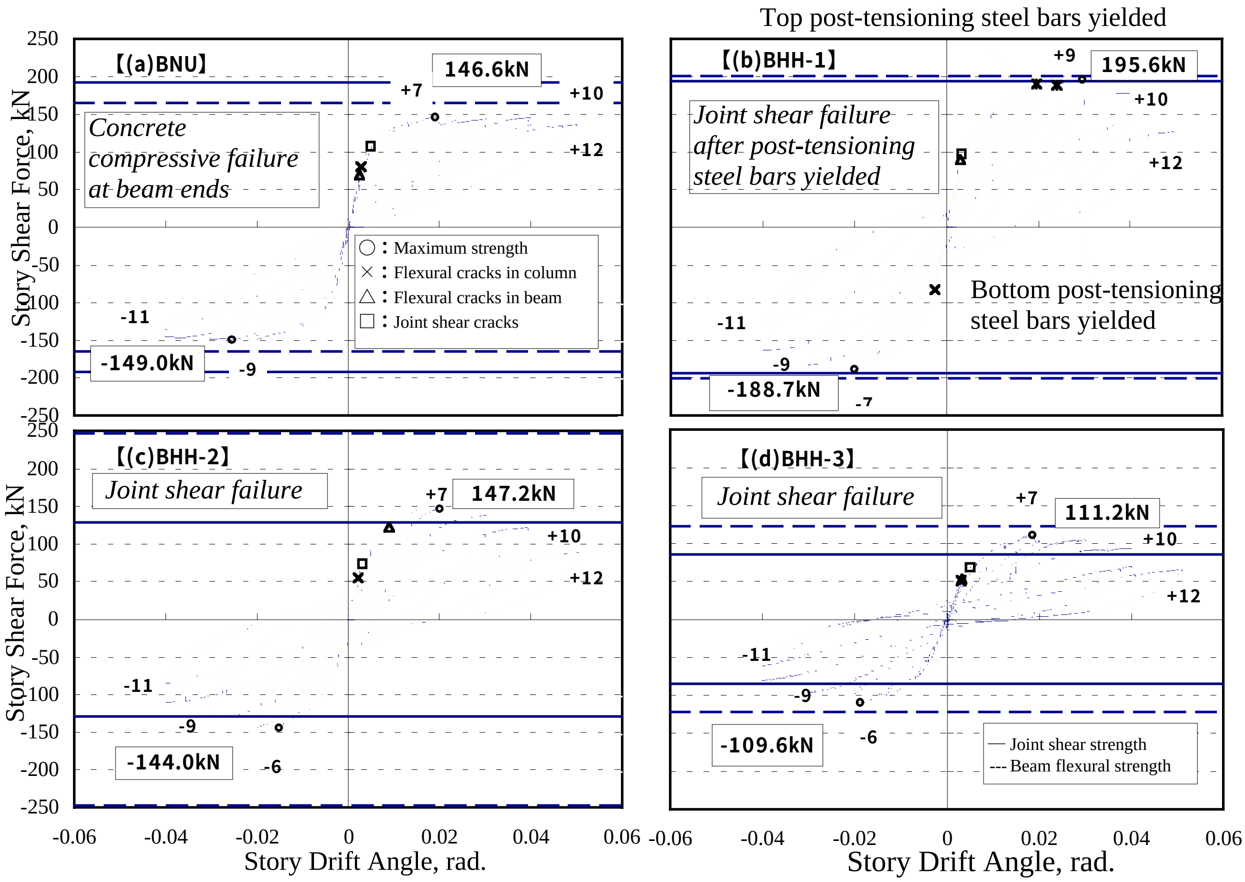

Fig. 4 Story shear - drift relations

The story shear force - story drift relationships are shown in Fig.4. The story shear force was computed from moment equilibrium between measured beam shear forces and the horizontal force at the loading point on the top of the column. The occurrence of flexural cracking in beams and column, diagonal shear cracking in a joint panel and yielding of post-tensioning steel bars are marked in Fig.4. The joint shear strength computed according to Architectural Institute of Japan (AIJ)[1] and beam flexural strength are shown by a solid line and a dotted line respectively in Fig.4. The lever arm lengths in beam and column section were assumed to be 289mm and 267mm respectively when joint shear strength was converted to corresponding story shear force. Beam flexural strength was calculated by the section analysis on the basis of the assumption that plane sections remain plane. The story shear reached the maximum force at the story drift angle of 1.5% for Specimen BHH3, 2% for Specimen BHH2 and 3% for Specimens BNU and BHH1. The measured maximum story shear for Specimens BHH2 and BHH3 was larger than the calculated nominal strength, whereas that for other two specimens was smaller than the calculated strength. The story shear force decreased gradually after story shear force reached the maximum value.

3.3 DISPLACEMENT CONTRIBUTION

The contribution of deformation of beams, column and joint panel to the story drift was calculated and shown in Fig.5. The horizontal axis represents the measured story drift. Total of each components did not always correspond with the directly measured story drift, including a little tolerance to use the measured value for each components. The beam-column joint panel deformation was large from the start of test and increased until the story drift angle of 3% for Specimens BHH2 and BHH3. The beam deformation shared more than 60 percent of the total story drift for Specimen BNU. The beam-column joint panel deformation for Specimen BHH1 increased radically after the story drift angle of 3% at which damage of concrete in a joint panel became severe and post-tensioning steel bars yielded.

4. DISCUSSIONS

The stresses of post-tensioning steel bars used in the paper were obtained from strains

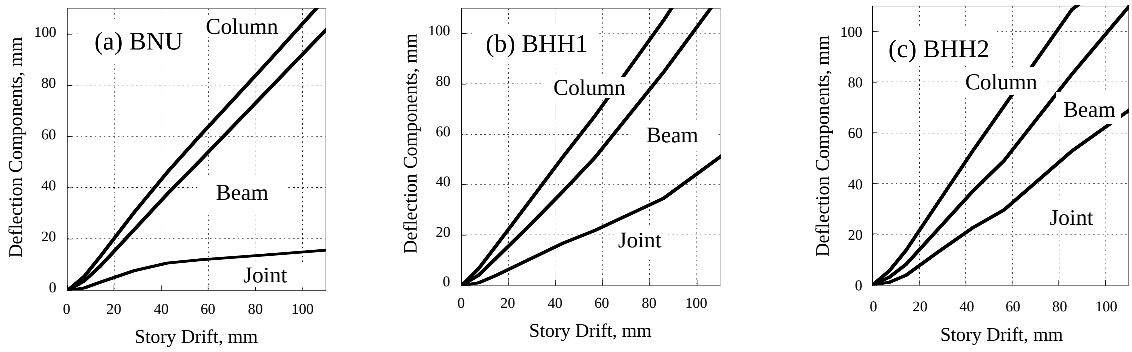

(a) Concrete compressive failure at beam ends

(b) Joint shear failure after yielding of post-tensioning steel bars

(c) Joint shear failure

Fig. 5 Deflection components to story drift

measured by strain gauges through hexa-linear stress - strain relationship model as shown in Fig.6, where stress of the deformed post-tensioning steel bar with the diameter of 32mm was traced as a instance with measured strain.

4.1 COMPARISON BETWEEN MEASURED AND COMPUTED STORY SHEAR

The comparisons between test results and calculations are shown in Table 6. Diagonal shear crack strength in a joint panel (τ_{cr}) was obtained by Equation (1) based on the principal stress field taking account of the prestress to a beam (σ_p :σ_p < 0) and the axial compressive stress to a column(σ_o : σ_o< 0).

$$\tau_{cr} = \sqrt{f_t^2 - f_t(\sigma_o + \sigma_p) + \sigma_o \cdot \sigma_p} \qquad (1)$$

where f_t is a concrete tensile strength. Compressive stress σ_p was obtained by dividing initial prestress force to a beam by the product of column width and beam depth. Measured joint shear stress was computed from Equations (2) or (3) assuming that joint shear resistant area is the product of column depth and the average of beam and column width. Measured joint shear stress at joint diagonal crack was smaller than computed crack strength for all specimens since uniform compressive stress field as supposed in Equation (1) was not formed in a joint panel due to separation between beam and column at beam critical sections.

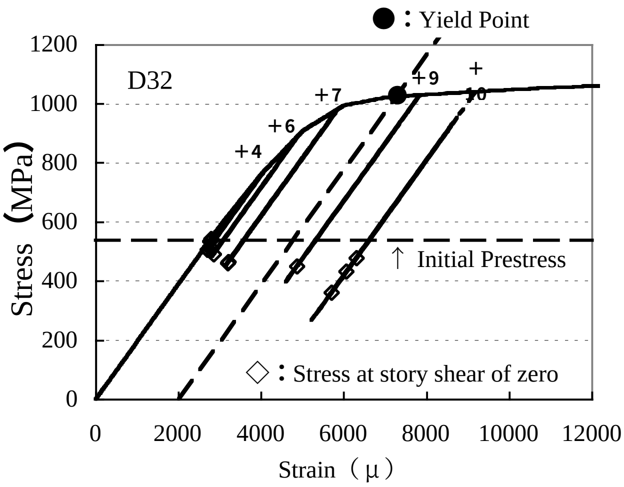

Fig. 6 Hexa-linear stress-strain model

Table 6 Test results

Specimen	BNU	BHH1	BHH2	BHH3
Measured Story Shear Force at Joint Shear Crack (kN)	107	97	74	69
Measured Story Shear Strength at Positive Loading (kN)	147	196	147	111
Corresponding Story Drift Angle (rad.)	0.02	0.03	0.02	0.015
Measured Story Shear Strength at Negative Loading (kN)	149	189	144	110
Corresponding Story Drift Angle (rad.)	0.03	0.02	0.015	0.015
* Measured Joint Shear stress at Joint Shear Crack (MPa)	7.8	7.7	6.9	5.2
** Computed Joint Shear Crack Strength (MPa)	11.1	11.0	8.3	8.3
* Measured Maximum Joint Shear stress (MPa)	10.2	14.4	12.6	8.6
*** Computed Joint Shear Strength (MPa)	17.6	17.7	11.6	8.3

* Joint shear force was obtained by Eqs. (2) or (3).
**Joint shear crack strength computed according to Reference[4]
*** Average joint shear strength computed according to Reference[1]

4.2 TRANSITION OF NEUTRAL AXIS DEPTH

Concrete strain gauges as shown in Fig.7 were stuck on the surface of a beam at the location of 60 mm apart from a beam critical section. Change of the neutral axis position on a beam critical section was investigated by using concrete strain distribution. Method for deciding the beam neutral axis position is explained for example by Fig.8. Measured compressive strain distribution at the locations of C1 from C4, excluding tensile strains at the locations of C5 from C7, was approximated by the line induced from least squares method. Hence the neutral axis position was decided as the point at which obtained strain line crosses the vertical axis of zero strain. The shape of concrete compressive stress block can be assumed as triangle as shown in Fig.8.

Transitions of the neutral axis position are shown in Fig.9 for all specimens. The neutral axis depth for Specimens BHH2 and BHH3 which failed in joint shear was greater than the half of beam depth, i.e., 200 mm, during tests. In other words central region of joint panel concrete in some height was subjected to horizontal compression by concrete stress blocks on beam critical sections on both sides of a joint as shown in Fig.11 (b). This means that all concrete compressive force at beam crtical section was not necessarily introduced to a joint panel as a horizontal shear. This is investigated quantitatively in next section.

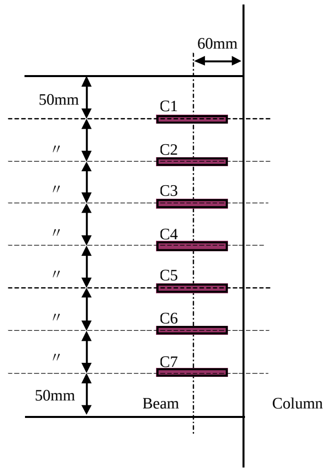

Fig. 7 Location of concrete srain gauges on beam surface

4.3 JOINT INPUT SHEAR FORCE

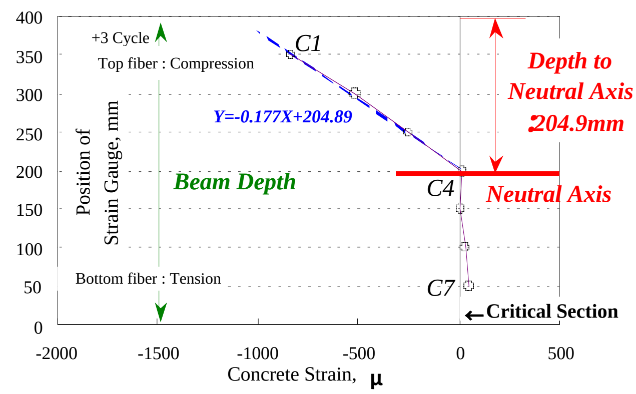

Fig. 8 Determination for beam neutral axis depth

Envelope curves of relationship between joint shear stress and shear distortion are shown in Fig.10. The joint shear average strength calculated according to AIJ provisions [1] is also shown by a solid line. Joint input shear force denoted as V_{jh} was computed by Equations (2) or (3) according to the definition shown in Fig.11. As mentioned in Section 4.2, it is necessary to consider two cases which one is 1) that the distance from the extreme compression fiber to neutral axis (depth of compressive stress distribution) is less than the half of beam depth as illustrated in Fig.11 (a), the other is 2) that it is greater than the half of

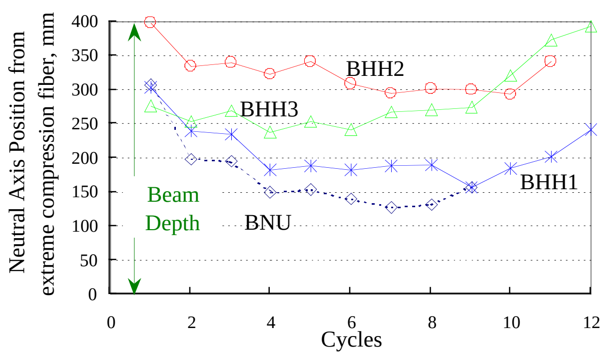

Fig. 9 Transition of beam neutral axis depth

beam depth as illustrated in Fig.11 (b). In the second case, the maximum joint shear force can be obtained mathematically along horizontal section at the center of joint depth. Therefore joint input shear force was computed as Equation (3).

1) In case that depth of compressive stress block is less than the half of beam depth;

$$V_{jh} = P_{t1} + P_{b2} - V_c \qquad (2)$$

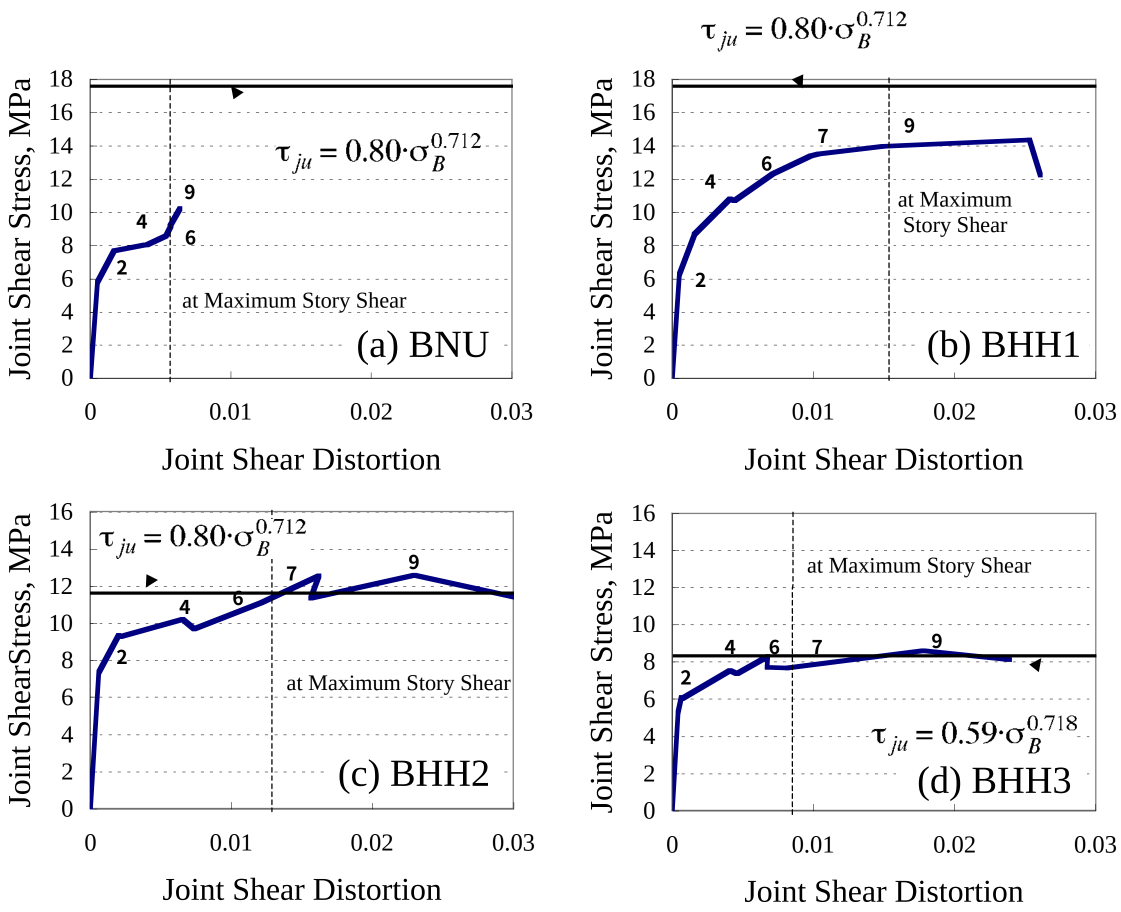

Fig. 10 Joint shear stress - shear distortion relations

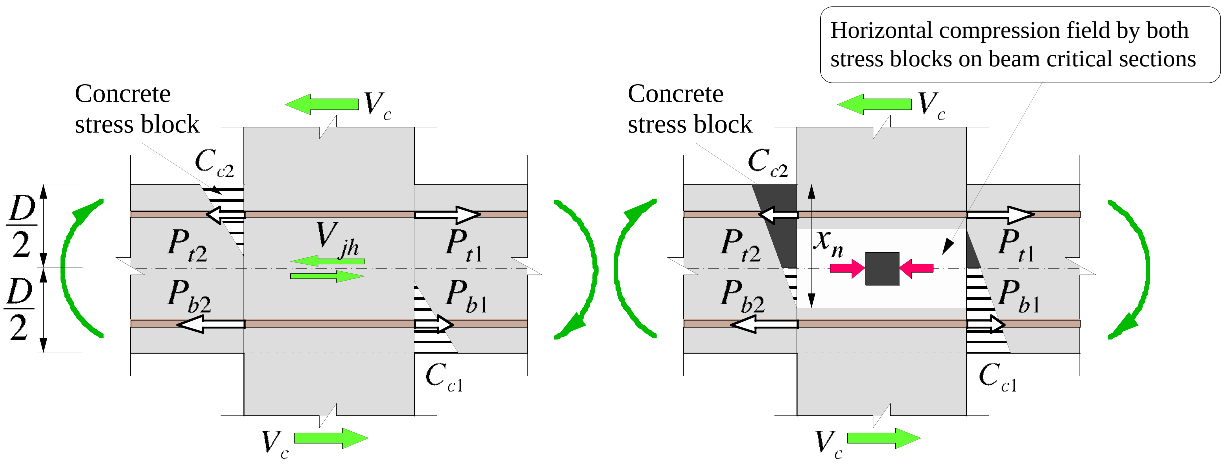

(a) In case that depth of concrete stress block is less than half of beam depth

(b) In case that depth of concrete stress block is greater than half of beam depth

Fig. 11 Stress acting on joint panel

2) In case that depth of compressive stress block denoted as x_n in Fig.11 (b) is greater than the half of beam depth;

$$V_{jh} = \alpha_1 C_{c2} - P_{t2} + P_{t1} - \alpha_2 C_{c1} - V_c \qquad (3)$$

$$C_{c1} = P_{t1} + P_{b1} \qquad (4)$$

$$C_{c2} = P_{t2} + P_{b2} \qquad (5)$$

$$\alpha_1 = 1 - \alpha_2 \qquad (6)$$

$$\alpha_2 = \frac{\left(x_n - \frac{D}{2}\right)^2}{x_n^2} \qquad (7)$$

where P_{t1} and P_{t2} are measured tensile forces of the top post-tensioning steel bar, P_{b1} and P_{b2} are measured tensile forces of the bottom post-tensioning steel bar, C_{c1} and C_{c2} are concrete compressive resultant forces and V_c is measured story shear force.

Joint shear strength for Specimens BHH2 and BHH3 which was computed by Equation (3) agreed well with average strength predicted by AIJ provisions [1]. For these specimens failed in joint panel, joint shear force reached the strength at the joint shear distortion of 2% approximately after story shear force attained the maximum. For Specimen BNU which failed by concrete flexural compression at beam ends, joint shear force continued to increase even during keeping story shear force almost constant.

Equation (2) is used customarily for taking joint input shear force. Therefore joint input shear forces computed by Equations (2) and (3) were compared in Fig.12 for Specimen BHH2. Solid line shows shear force computed by Equation (2) and dotted line by Equation (3). The joint shear force calculated by customary method, i.e., Equation (2) was 1.1 times greater than that calculated by Equation (3). It is noted that the overlapping of concrete stress blocks across a joint panel on opposite beam critical sections should be considered when joint input shear force is computed in tests.

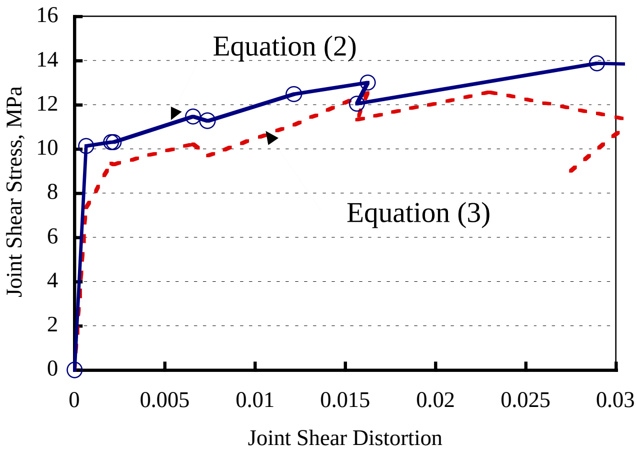

Fig. 12 Difference of joint shear stress between two computing methods

4.4 LOCATION OF COMPRESSIVE RESULTANT FORCE ON BEAM CRITICAL SECTION

With the aim of understanding the stress state around beam-column joint panel, the position of the concrete compressive resultant force on a beam critical section was computed using tensile forces of post-tensioning steel bars and beam bending moment calculated from measured beam shear. The transition of location of compressive resultant forces, tensile resultant forces and lever arm length are shown in Fig13. The specific examples at the story drift angle of 2% are shown in Fig.14. Compressive resultant force was located between top post-tensioning steel bar and the extreme compression fiber for all specimens. The lever

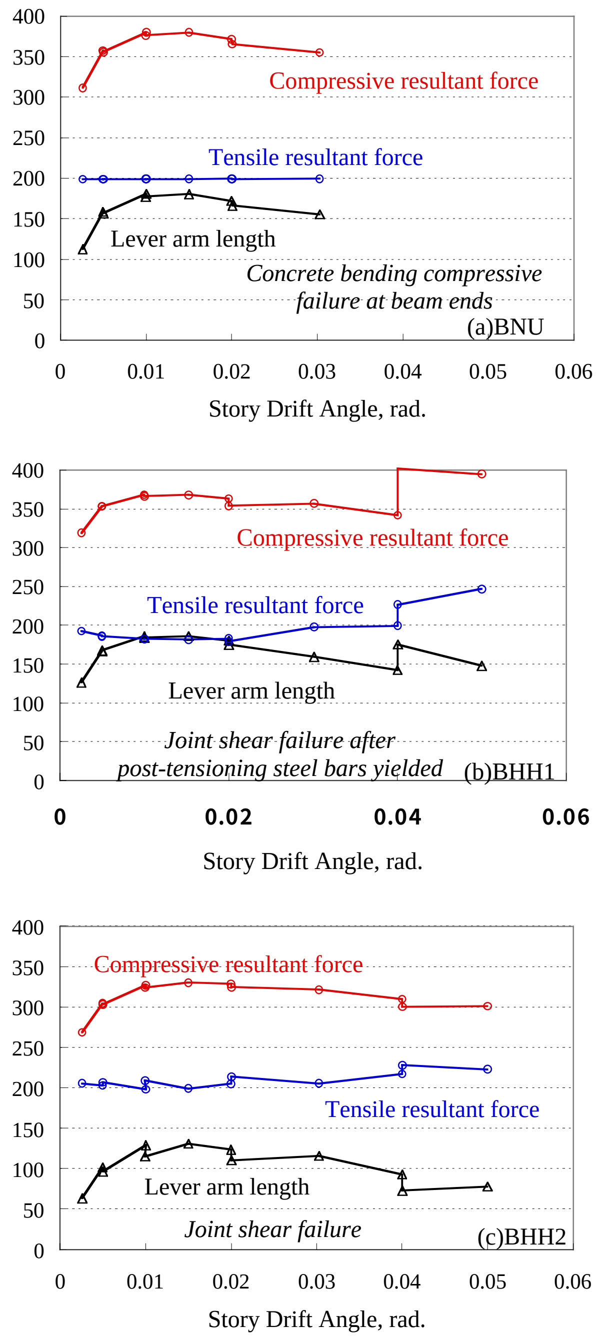

Fig. 13 Transition of location of compressive, tensile resultant forces and lever arm length on beam critical section

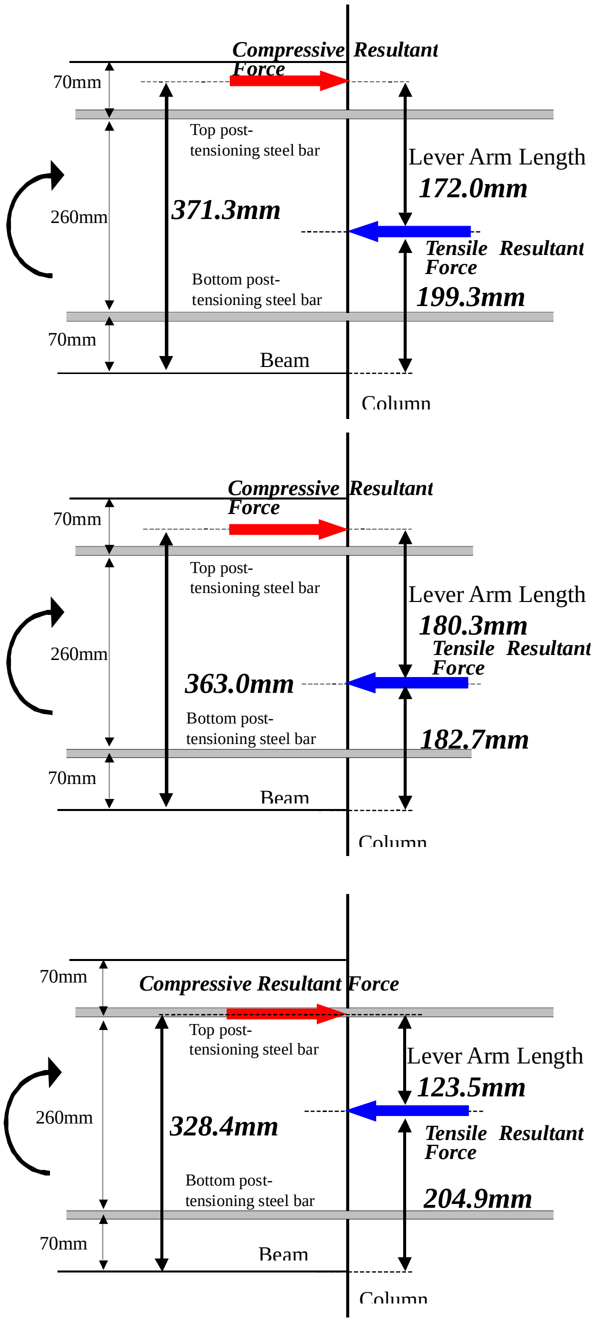

Fig. 14 Location of compressive, tensile resultant forces and lever arm length at story drift angle of 2 %

arm lengths changed from 0.3d to 0.6d (d : 330mm).

Lever arm length on prestressed beam section was shorter than that on general RC sections because the tensile resultant force of top and bottom post-tensioning steel bars was located near the center of beam section during a test.

The reason why the story shear force declined after the strength is that tensile resultant force was kept constant after the post-tensioning steel bars yielded, wheras the lever arm length gradually decreased as shown in Fig.13.

4.5 BOND ALONG BEAM POST-TENSIONING STEEL BARS

The average bond stresses along a beam post-tensioning steel bars within a joint for all specimens are shown in Fig.15. The average bond stress was computed by the difference between beam post-tensioning steel bar forces at opposite column faces. Bond stress of 1 MPa for Specimen BHH2 was kept to the story drift angle of 1.5% and decreased whereas the tensile force of beam post-tensioning steel bars at critical sections increased to the story drift angle of 3.0%. It is judged that the decrease in bond stress along beam post-tensioning steel bars within a joint panel resulted from bond deterioration. Bond strength for Specimen BHH1 was greater than that for other specimens since high strength concrete was cast for the column. The bond deteriorated before the story shear force reached the maximum for all specimens.

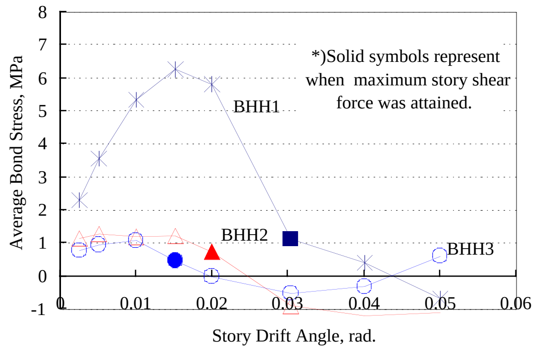

Fig. 15 Average bond stress along beam post-tensioning steel bar within joint

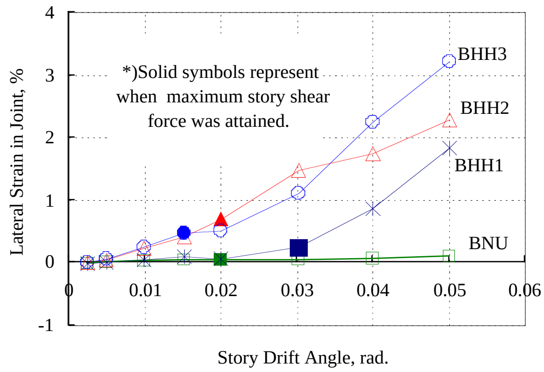

Fig. 16 Lateral strain in joint panel

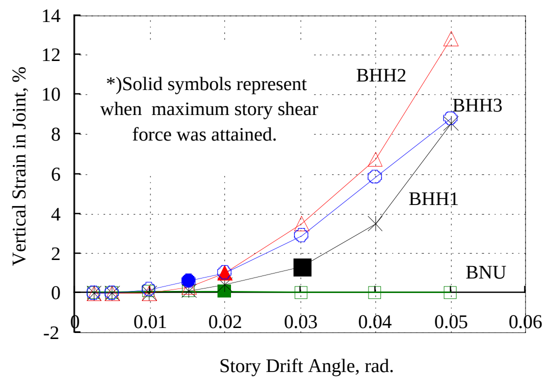

Fig. 17 Vertical strain in joint panel

4.6 DEFORMATION OF JOINT PANEL

The lateral and vertical average strains in a joint panel are shown in Figs.16 and 17,

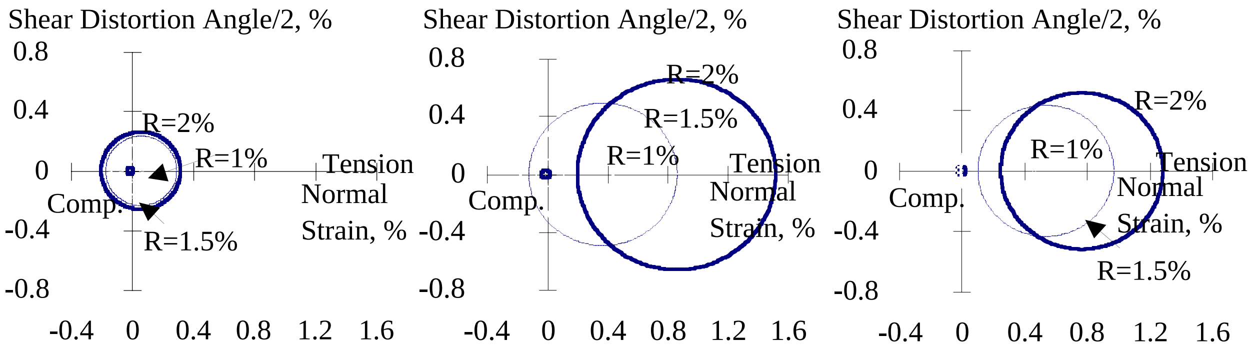

(a) Specimen BNU (b) Specimen BHH2 (c) Specimen BHH3

Fig. 18 Mohr's strain circles for joint panel

respectively. These strains were computed by using average displacements measured by two horizontal and vertical displacement transducers. Both lateral and vertical average tensile strains kept increasing after the story shear force reached the maximum for all specimens. Both average strains were negligible for Specimen BNU, which did not fail in joint shear.

Mohr's strain circles are shown in Fig.18 to the story drift angle of 2% to investigate deformation characteristics of a joint panel in more detail. The larger Mohr's circle is, the severer the damage in a joint panel is. The strain circles of Specimens BHH2 and BHH3 which failed in joint shear were larger than that for Specimen BNU. Centers of circle shifted largely to the tensile side. This indicates that the joint panel concrete expanded isotropically with the increase in a story drift. Joint shear failure for both specimens was caused by the concrete expansion.

The strain circle for Specimen BNU that did not fail in joint shear was small. Center of circle was located at the origin and the Mohr's strain circle became large like as concentric circles.

5. CONCLUSIONS

The following conclusions can be drawn from the present study:

(1) Interior and exterior beam-column joints which were made of assembling precast RC beams and column through post-tensioning steel bars failed in shear.

(2) The depth of compressive stress block computed by the concrete strains at beam critical section was larger than the half of beam depth. This indicates that joint panel concrete in central

height was subjected to horizontal compression by concrete stress blocks on beam critical sections on both sides of a joint. Therefore all concrete compressive force on beam critical section did not necessarily contribute to joint input shear.

(3) The joint input shear force was computed by using the measured tensile forces of post-tensioning steel bars and considering that two concrete compressive stress blocks on opposite beam critical sections of a joint panel overlapped as mentioned above.

(a) Joint shear force reduced with the decrease in story shear force after the joint panel failed by shear.

(b) Shear strength of PCaPC beam-column joints can be estimated by the prediction formula for usual RC beam-column joints.

(4) Joint failure was caused by the expansion of joint core concrete.

ACKNOWLEDGMENT

The authors would like to thank Dr. MARUTA Makoto and Ms. KIMURA Akiko, research engineers in Kajima Technical Research Instiute, for their cooperative works.

REFERENCES

[1] Architectural Institute of Japan : Design Guideline for Earthquake Resistant Reinforced Concrete Buildings Based on Inelastic Displacement Concept,1999, (in Japanese).

[2] Beniya, N., T. Kashiwazaki and H. Noguchi : An Experimental Study on Shear Behavior of Prestressed Concrete Beam-Column Connection, *Proceedings of the Japan Concrete Institute*, Vol.19, No.2, pp.1179-1184, 1997, (in Japanese).

[3] Architectural Institute of Japan : Standard for Structural Design and Construction of Prestressed Concrete Structures,1998, (in Japanese).

[4] Architectural Institute of Japan : Design Method of Prestressed (Reinforced) Concrete Structural Members -Actual Situation and Future, 2000.4, (in Japanese).

PLENARY SESSION II: RESOLUTIONS AND CLOSING

Chaired by

♦ Jack Moehle and Toshimi Kabeyasawa ♦

RESOLUTIONS

Recent urban earthquakes have caused significant economic losses, injuries, and fatalities in both the U.S. and Japan. This was evident in the U.S. during the 1994 Northridge earthquake, and in Japan during the 1995 Hyogo-ken Nambu earthquake. These and other earthquakes, such as the recent earthquakes in Turkey, Taiwan, and Seattle, point out the need for effective and practical methods for

- evaluating and rehabilitating existing hazardous buildings and
- designing new buildings for more reliable and improved performance.

While great progress previously has been made in engineering for earthquake resistance, suggested frameworks for performance-based earthquake engineering will accelerate progress by focusing efforts and bridging gaps. This will lead to a future of earthquake engineering that will include increased emphasis on quantitative measures of performance over qualitative measures, precision over approximation, reliability over uncertainty, and intelligent engineering and life-cycle cost design over minimum capital cost design.

The papers presented at the First, Second, Third, and Fourth U.S.-Japan Workshop on Performance-Based Earthquake Engineering Methodology for Reinforced Concrete Building Structures demonstrate progress being made in performance-based earthquake engineering. In the Fourth Workshop, presentations in the plenary session described the currently revised ACI code in the U.S. and Japanese state of practice in the design of seismically isolated buildings. Two working group sessions covered the most recent research findings related to analysis and performance assessment in support of performance-based design. Discussion of the presented papers enhanced understanding and advanced the state of the art in performance-based earthquake engineering. Important outcomes of the Workshop include:

(a) Better understanding of the present state of knowledge and practice of performance-based earthquake engineering, especially the requirements of the recently revised ACI code and design practice on base-isolation systems;

(b) Detailed understanding of seismic demands, especially the use of analysis methods, system monitoring, performance assessment, and fatality estimation for performance-based earthquake engineering of reinforced concrete buildings;

(c) Detailed understanding of seismic capacities of structures and members, especially reinforced concrete columns, full-scale columns, beam-column joints, and the dynamic behavior of frames;

(d) Identification of common areas of concern, areas of needed advancement, and areas that would benefit from joint study.

The topic of performance-based earthquake engineering is a particularly effective one for workshop discussion because it brings together and promotes common focus of experts in ground motion, analysis, and design, and because its format is not constrained by prescriptive code requirements that vary from one country to another. Understanding of the work of individuals with different expertise was achieved in ways that would not be possible without meeting in this format.

The Workshop was a successful continuation of progress made in more than two decades of cooperative U.S.-Japan research in earthquake engineering. The success at this Workshop suggests that the two countries will benefit from continued cooperation. The reasons for continued cooperation include:

(a) the two countries have a shared need to develop improved methods for seismic design and evaluation;

(b) in both countries, there is a need for integrated analytical and experimental approaches, which is promoted in this meeting format; and

(c) each side brings unique data, experience, knowledge, and facilities, the sharing of which benefits all.

These discussions are best accomplished through face-to-face meetings of extended duration such as occur in a workshop format.

Therefore, the following recommendations are offered:

(1) Because of the rapid rate at which new information and applications are being achieved, the importance of advances to Japan and the U.S., and the success of the first, second, third and fourth Workshops, the participants recommend that the Fifth U.S.-Japan Workshop on Performance-Based Seismic Engineering Methodology for Reinforced Concrete Building Structures be organized by the Japan side, September 9–11, 2003. Consideration also should be

given to convening or participating in a major international workshop on the theme subject around one year later.

(2) At future workshops, several topics for focused discussion should be considered. A reduced number of these should be the focus of the fifth Workshop:

(a) simplified and rigorous methods for predicting seismic demands:

- (i) identification of extreme earthquake
- (ii) continuation of the topic on inelastic displacement demands for SDOF and MDOF systems
- (iii) practical application of advanced analysis methods
- (iv) use of probabilistic bases for PBEE incorporating uncertainty and variability
- (v) performance of strength-degrading structures
- (vi) seismic demands including life-cycle loss and fatality estimation

(b) simplified and rigorous methods for predicting seismic capacities:

- (i) definitions and measures of performance
- (ii) modeling of damage and definition of reparability
- (iii) hysteretic energy dissipation of members
- (iv) deformations at loss of lateral and gravity load capacity of members
- (v) continuation of the topic of residual gravity load capacity of members
- (vi) damage models including cumulative and cyclic effects
- (vii) exchange of data base on test results
- (viii) behavior of nonstructural component

(c) design methodology to bring these together:

- (i) validation of performance-based earthquake engineering methods
- (ii) assessment of system performance need to be carried out based on component performance
- (iii) evaluation of moderate damage for assessment of damage repair cost
- (iv) development of performance-derived design criteria

(d) knowledge-based rapid post-earthquake response

(i) development and verification of sensor and monitoring system

(ii) residual performance assessment of damaged structures

(iii) development and verification of retrofit technology

(3) At the fifth Workshop, the following format should be considered:

(a) Focus on two to four topics, emphasizing presentation of papers on those topics coupled with special theme sessions to examine topics in greater detail; and

(b) Participation of researchers, professional engineers, representatives of code-writing organizations, representatives of national organizations responsible for construction, and leading international participants.

(4) Cooperative activities between individual participants from the U.S. and Japan are encouraged to address problems of mutual concern. Efforts should be undertaken to facilitate exchange of personnel, including students, faculty, and professional researchers and practitioners, as well as of information on technical issues and applications. Funding agencies are encouraged to support these activities.

PEER REPORTS

PEER reports are available from the National Information Service for Earthquake Engineering (NISEE). To order PEER reports, please contact the Pacific Earthquake Engineering Research Center, 1301 South 46th Street, Richmond, California 94804-4698. Tel.: (510) 231-9468; Fax: (510) 231-9461.

PEER 2002/21 *Fourth U.S.-Japan Workshop on Performance-Based Earthquake Engineering Methodology for Reinforced Concrete Building Structures*. December 2002.

PEER 2002/20 *Barriers to Adoption and Implementation of PBEE Innovations.* Peter J. May. August 2002.

PEER 2002/19 *Economic-Engineered Integrated Models for Earthquakes: Socioeconomic Impacts.* Peter Gordon, James E. Moore II, and Harry W. Richardson. July 2002.

PEER 2002/18 *Assessment of Reinforced Concrete Building Exterior Joints with Substandard Details.* Chris P. Pantelides, Jon Hansen, Justin Nadauld, and Lawrence D. Reaveley. May 2002.

PEER 2002/17 *Structural Characterization and Seismic Response Analysis of a Highway Overcrossing Equipped with Elastomeric Bearings and Fluid Dampers: A Case Study.* Nicos Makris and Jian Zhang. November 2002.

PEER 2002/16 *Estimation of Uncertainty in Geotechnical Properties for Performance-Based Earthquake Engineering.* Allen L. Jones, Steven L. Kramer, and Pedro Arduino. December 2002.

PEER 2002/15 *Seismic Behavior of Bridge Columns Subjected to Various Loading Patterns.* Asadollah Esmaeily-Gh. and Yan Xiao. December 2002.

PEER 2002/14 *Inelastic Seismic Response of Extended Pile Shaft Supported Bridge Structures.* T.C. Hutchinson, R.W. Boulanger, Y.H. Chai, and I.M. Idriss. December 2002.

PEER 2002/13 *Probabilistic Models and Fragility Estimates for Bridge Components and Systems.* Paolo Gardoni, Armen Der Kiureghian, and Khalid M. Mosalam. June 2002.

PEER 2002/12 *Effects of Fault Dip and Slip Rake on Near-Source Ground Motions: Why Chi-Chi Was a Relatively Mild M7.6 Earthquake.* Brad T. Aagaard, John F. Hall, and Thomas H. Heaton. December 2002.

PEER 2002/11 *Analytical and Experimental Study of Fiber-Reinforced Strip Isolators*. James M. Kelly and Shakhzod M. Takhirov. September 2002.

PEER 2002/10 *Centrifuge Modeling of Settlement and Lateral Spreading with Comparisons to Numerical Analyses***.** Sivapalan Gajan and Bruce L. Kutter. January 2003.

PEER 2002/09 *Documentation and Analysis of Field Case Histories of Seismic Compression during the 1994 Northridge, California, Earthquake.* Jonathan P. Stewart, Patrick M. Smith, Daniel H. Whang, and Jonathan D. Bray. October 2002.

PEER 2002/08 *Component Testing, Stability Analysis and Characterization of Buckling-Restrained Unbonded Braces™.* Cameron Black, Nicos Makris, and Ian Aiken. September 2002.

PEER 2002/07 *Seismic Performance of Pile-Wharf Connections.* Charles W. Roeder, Robert Graff, Jennifer Soderstrom, and Jun Han Yoo. December 2001.

PEER 2002/06 *The Use of Benefit-Cost Analysis for Evaluation of Performance-Based Earthquake Engineering Decisions*. Richard O. Zerbe and Anthony Falit-Baiamonte. September 2001.

PEER 2002/05 *Guidelines, Specifications, and Seismic Performance Characterization of Nonstructural Building Components and Equipment*. André Filiatrault, Constantin Christopoulos, and Christopher Stearns. September 2001.

PEER 2002/04 *Consortium of Organizations for Strong-Motion Observation Systems and the Pacific Earthquake Engineering Research Center Lifelines Program: Invited Workshop on Archiving and Web Dissemination of Geotechnical Data, 4–5 October 2001*. September 2002.

PEER 2002/03 *Investigation of Sensitivity of Building Loss Estimates to Major Uncertain Variables for the Van Nuys Testbed.* Keith A. Porter, James L. Beck, and Rustem V. Shaikhutdinov. August 2002.

PEER 2002/02 *The Third U.S.-Japan Workshop on Performance-Based Earthquake Engineering Methodology for Reinforced Concrete Building Structures*. July 2002.

PEER 2002/01 *Nonstructural Loss Estimation: The UC Berkeley Case Study. Mary C. Comerio and John C. Stallmeyer.* December 2001.

PEER 2001/16 *Statistics of SDF-System Estimate of Roof Displacement for Pushover Analysis of Buildings.* Anil K. Chopra, Rakesh K. Goel, and Chatpan Chintanapakdee. December 2001.

PEER 2001/15 *Damage to Bridges during the 2001 Nisqually Earthquake.* R. Tyler Ranf, Marc O. Eberhard, and Michael P. Berry. November 2001.

PEER 2001/14 *Rocking Response of Equipment Anchored to a Base Foundation.* Nicos Makris and Cameron J. Black. September 2001.

PEER 2001/13 *Modeling Soil Liquefaction Hazards for Performance-Based Earthquake Engineering.* Steven L. Kramer and Ahmed-W. Elgamal. February 2001.

PEER 2001/12 *Development of Geotechnical Capabilities in OpenSees.* Boris Jeremic. September 2001.

PEER 2001/11 *Analytical and Experimental Study of Fiber-Reinforced Elastomeric Isolators*. James M. Kelly and Shakhzod M. Takhirov. September 2001.

PEER 2001/10 *Amplification Factors for Spectral Acceleration in Active Regions.* Jonathan P. Stewart, Andrew H. Liu, Yoojoong Choi, and Mehmet B. Baturay. December 2001.

PEER 2001/09 *Ground Motion Evaluation Procedures for Performance-Based Design.* Jonathan P. Stewart, Shyh-Jeng Chiou, Jonathan D. Bray, Robert W. Graves, Paul G. Somerville, and Norman A. Abrahamson. September 2001.

PEER 2001/08 *Experimental and Computational Evaluation of Reinforced Concrete Bridge Beam-Column Connections for Seismic Performance*. Clay J. Naito, Jack P. Moehle, and Khalid M. Mosalam. November 2001.

PEER 2001/07 *The Rocking Spectrum and the Shortcomings of Design Guidelines.* Nicos Makris and Dimitrios Konstantinidis. August 2001.

PEER 2001/06 *Development of an Electrical Substation Equipment Performance Database for Evaluation of Equipment Fragilities*. Thalia Agnanos. April 1999.

PEER 2001/05 *Stiffness Analysis of Fiber-Reinforced Elastomeric Isolators.* Hsiang-Chuan Tsai and James M. Kelly. May 2001.

PEER 2001/04 *Organizational and Societal Considerations for Performance-Based Earthquake Engineering.* Peter J. May. April 2001.

PEER 2001/03 *A Modal Pushover Analysis Procedure to Estimate Seismic Demands for Buildings: Theory and Preliminary Evaluation.* Anil K. Chopra and Rakesh K. Goel. January 2001.

PEER 2001/02 *Seismic Response Analysis of Highway Overcrossings Including Soil-Structure Interaction.* Jian Zhang and Nicos Makris. March 2001.

PEER 2001/01 *Experimental Study of Large Seismic Steel Beam-to-Column Connections.* Egor P. Popov and Shakhzod M. Takhirov. November 2000.

PEER 2000/10 *The Second U.S.-Japan Workshop on Performance-Based Earthquake Engineering Methodology for Reinforced Concrete Building Structures.* March 2000.

PEER 2000/09 *Structural Engineering Reconnaissance of the August 17, 1999 Earthquake: Kocaeli (Izmit), Turkey.* Halil Sezen, Kenneth J. Elwood, Andrew S. Whittaker, Khalid Mosalam, John J. Wallace, and John F. Stanton. December 2000.

PEER 2000/08 *Behavior of Reinforced Concrete Bridge Columns Having Varying Aspect Ratios and Varying Lengths of Confinement.* Anthony J. Calderone, Dawn E. Lehman, and Jack P. Moehle. January 2001.

PEER 2000/07 *Cover-Plate and Flange-Plate Reinforced Steel Moment-Resisting Connections.* Taejin Kim, Andrew S. Whittaker, Amir S. Gilani, Vitelmo V. Bertero, and Shakhzod M. Takhirov. September 2000.

PEER 2000/06 *Seismic Evaluation and Analysis of 230-kV Disconnect Switches.* Amir S. J. Gilani, Andrew S. Whittaker, Gregory L. Fenves, Chun-Hao Chen, Henry Ho, and Eric Fujisaki. July 2000.

PEER 2000/05 *Performance-Based Evaluation of Exterior Reinforced Concrete Building Joints for Seismic Excitation.* Chandra Clyde, Chris P. Pantelides, and Lawrence D. Reaveley. July 2000.

PEER 2000/04 *An Evaluation of Seismic Energy Demand: An Attenuation Approach.* Chung-Che Chou and Chia-Ming Uang. July 1999.

PEER 2000/03 *Framing Earthquake Retrofitting Decisions: The Case of Hillside Homes in Los Angeles.* Detlof von Winterfeldt, Nels Roselund, and Alicia Kitsuse. March 2000.

PEER 2000/02 *U.S.-Japan Workshop on the Effects of Near-Field Earthquake Shaking.* Andrew Whittaker, ed. July 2000.

PEER 2000/01 *Further Studies on Seismic Interaction in Interconnected Electrical Substation Equipment.* Armen Der Kiureghian, Kee-Jeung Hong, and Jerome L. Sackman. November 1999.

PEER 1999/14 *Seismic Evaluation and Retrofit of 230-kV Porcelain Transformer Bushings*. Amir S. Gilani, Andrew S. Whittaker, Gregory L. Fenves, and Eric Fujisaki. December 1999.

PEER 1999/13 *Building Vulnerability Studies: Modeling and Evaluation of Tilt-up and Steel Reinforced Concrete Buildings.* John W. Wallace, Jonathan P. Stewart, and Andrew S. Whittaker, editors. December 1999.

PEER 1999/12 *Rehabilitation of Nonductile RC Frame Building Using Encasement Plates and Energy-Dissipating Devices.* Mehrdad Sasani, Vitelmo V. Bertero, James C. Anderson. December 1999.

PEER 1999/11 *Performance Evaluation Database for Concrete Bridge Components and Systems under Simulated Seismic Loads.* Yael D. Hose and Frieder Seible. November 1999.

PEER 1999/10 *U.S.-Japan Workshop on Performance-Based Earthquake Engineering Methodology for Reinforced Concrete Building Structures.* December 1999.

PEER 1999/09 *Performance Improvement of Long Period Building Structures Subjected to Severe Pulse-Type Ground Motions*. James C. Anderson, Vitelmo V. Bertero, and Raul Bertero. October 1999.

PEER 1999/08 *Envelopes for Seismic Response Vectors.* Charles Menun and Armen Der Kiureghian. July 1999.

PEER 1999/07 *Documentation of Strengths and Weaknesses of Current Computer Analysis Methods for Seismic Performance of Reinforced Concrete Members.* William F. Cofer. November 1999.

PEER 1999/06 *Rocking Response and Overturning of Anchored Equipment under Seismic Excitations.* Nicos Makris and Jian Zhang. November 1999.

PEER 1999/05 *Seismic Evaluation of 550 kV Porcelain Transformer Bushings.* Amir S. Gilani, Andrew S. Whittaker, Gregory L. Fenves, and Eric Fujisaki. October 1999.

PEER 1999/04 *Adoption and Enforcement of Earthquake Risk-Reduction Measures.* Peter J. May, Raymond J. Burby, T. Jens Feeley, and Robert Wood.

PEER 1999/03 *Task 3 Characterization of Site Response General Site Categories*. Adrian Rodriguez-Marek, Jonathan D. Bray, and Norman Abrahamson. February 1999.

PEER 1999/02 *Capacity-Demand-Diagram Methods for Estimating Seismic Deformation of Inelastic Structures: SDF Systems*. Anil K. Chopra and Rakesh Goel. April 1999.

PEER 1999/01 *Interaction in Interconnected Electrical Substation Equipment Subjected to Earthquake Ground Motions.* Armen Der Kiureghian, Jerome L. Sackman, and Kee-Jeung Hong. February 1999.

PEER 1998/08 *Behavior and Failure Analysis of a Multiple-Frame Highway Bridge in the 1994 Northridge Earthquake.* Gregory L. Fenves and Michael Ellery. December 1998.

PEER 1998/07 *Empirical Evaluation of Inertial Soil-Structure Interaction Effects.* Jonathan P. Stewart, Raymond B. Seed, and Gregory L. Fenves. November 1998.

PEER 1998/06 *Effect of Damping Mechanisms on the Response of Seismic Isolated Structures.* Nicos Makris and Shih-Po Chang. November 1998.

PEER 1998/05 *Rocking Response and Overturning of Equipment under Horizontal Pulse-Type Motions.* Nicos Makris and Yiannis Roussos. October 1998.

PEER 1998/04 *Pacific Earthquake Engineering Research Invitational Workshop Proceedings, May 14–15, 1998: Defining the Links between Planning, Policy Analysis, Economics and Earthquake Engineering.* Mary Comerio and Peter Gordon. September 1998.

PEER 1998/03 *Repair/Upgrade Procedures for Welded Beam to Column Connections.* James C. Anderson and Xiaojing Duan. May 1998.

PEER 1998/02 *Seismic Evaluation of 196 kV Porcelain Transformer Bushings.* Amir S. Gilani, Juan W. Chavez, Gregory L. Fenves, and Andrew S. Whittaker. May 1998.

PEER 1998/01 *Seismic Performance of Well-Confined Concrete Bridge Columns.* Dawn E. Lehman and Jack P. Moehle. December 2000.